

Thin Composite Two-Way Flooring System for Steel Structural Systems

AISC Milek Fellowship Final Report

Prepared for AISC by:

Eugene Boadi-Danquah, Ph.D., P.E. (Lincoln University)

Duncan MacLachlan, MS (Kiewit Engineering)

Brian Robertson, MS (Burns & McDonnell)

Tristan Yount, MS (University of Kansas)

Matthew Fadden, Ph.D., P.E. (Wiss, Janney, Elstner Associates)

William Collins, Ph.D., P.E. (University of Kansas)

TABLE OF CONTENTS

Chapter 1: Introduction.....	10
1.1 Problem Description	10
1.2 Goal of Research.....	11
1.3 Organization.....	11
1.4 Acknowledgements.....	13
Chapter 2: Lightweight Modular Steel Floor System for Rapidly Constructible and Reconfigurable Buildings	14
2.1 Abstract.....	14
2.2 Introduction.....	15
2.3 RCRMSF Concept and Design	17
2.3.1 RCRMSF Description.....	17
2.4 Performance Assessment	18
2.4.1 Deflection Assessment.....	18
2.4.2 Plate Yielding Assessment.....	19
2.4.3 Connector Design.....	20
2.5 Finite Element Analysis Parametric Study	20
2.6 Description of Finite Element Model	21
2.7 Parametric Study and Results	23
2.8 RCRMSF Performance	24
2.9 Conclusions and Recommendations	28
Chapter 3: Cyclic Behavior of Steel-to-Steel Screws and Powder-Actuated Fastener Connections in Single Shear.....	30
3.1 Abstract.....	30
3.2 Introduction.....	30
3.3 Objectives and Scope.....	32
3.4 Background on Fastener Strength and Characterization.....	33
3.4.1 Screw Shear Strength Estimate.....	33
3.4.2 PAF Shear Strength Estimate.....	34
3.4.3 Cyclic Loading Protocol	34
3.4.4 Pinching4 Material Model	36
3.5 Experimental Program	38
3.5.1 Test Setup.....	39
3.5.2 Instrumentation	41

3.5.3	Material Properties	41
3.5.4	Test Matrix	41
3.5.5	Displacement Protocol	42
3.5.6	Pinching4 Parameters Determination	42
3.6	Results	43
3.6.1	Peak Loads and Failure Modes	44
3.6.2	Pinching4 Model Parameters	51
3.7	Discussion	51
3.8	Conclusions	52
Chapter 4: Behavior of a Lightweight Modular Steel Floor Diaphragm under Quasi-static Cyclic Loading. I: Experimental Evaluation.....		54
4.1	Abstract	54
4.2	Introduction	55
4.2.1	Modular Steel Floor System	57
4.3	Diaphragm Test program	59
4.3.1	Test Frame	59
4.3.2	Test Details	62
4.3.3	Loading and Instrumentation	62
4.4	Finite Element Modeling	65
4.4.1	Gravity Load Analyses	66
4.4.2	Lateral Load Analyses	67
4.4.3	User-defined Connector Elements	67
4.5	Results and Discussion	70
4.6	Conclusions	76
Chapter 5: Behavior of a Lightweight Modular Steel Floor Diaphragm under Quasi-static Cyclic Loading. II: Parametric Finite Element Analyses		78
5.1	Abstract	78
5.2	Introduction	78
5.3	Diaphragm Assessment of Floor System	80
5.4	Finite Element Modeling	83
5.4.1	Elements and Meshing	85
5.4.2	Interactions	86
5.4.3	User-defined Connector Elements	87
5.4.4	Gravity Load Analyses	89
5.4.5	Cyclic Load Analysis	89

5.5	Results and Discussion	91
5.6	Conclusions.....	97
Chapter 6:	Parametric Analysis of Vibrations in a Lightweight Two-Way Steel Floor System	99
6.1	Abstract.....	99
6.2	Introduction.....	99
6.3	Rapidly Constructible and Reconfigurable Modular Steel Floor System.....	102
6.4	Vibration Serviceability Design Assessment.....	104
6.5	Finite Element Model Description.....	107
6.5.1	Material and Mesh Properties	108
6.5.2	Boundary Conditions	109
6.5.3	Loading	110
6.6	Parametric Study Results and Discussion.....	111
6.6.1	Single Bay FEA Natural Frequency Results and Discussion	115
6.6.2	Single Bay FEA Acceleration Response Results and Discussion	118
6.6.3	Suitability of the RCRMSF for Walking Vibrations	123
6.6.4	3x3 Bay Parametric Study Results and Discussion	124
6.6.5	Rhythmic Loading Parametric Study Results and Discussion.....	127
6.7	Conclusions.....	128
Chapter 7:	Vibration Serviceability Testing of a Lightweight Cold-Formed Steel Floor System	131
7.1	Abstract.....	131
7.2	Introduction.....	132
7.2.1	Acceptability Criteria.....	132
7.2.2	Lightweight Cold-Formed Floor System	133
7.3	Test Procedure	133
7.4	Finite Element Modeling	135
7.5	Experimental Testing	136
7.5.1	Test Matrix.....	136
7.5.2	Supporting Frame Details	137
7.5.3	Floor System Details.....	138
7.6	Results.....	145
7.6.1	In Situ Response	146
7.6.2	Calibration of Finite Element Models.....	149
7.6.3	FE Model Response	149

7.7	Conclusions.....	150
Chapter 8:	A Novel Loading Procedure for Finite Element Prediction of Walking-Induced Vibrations	151
8.1	Abstract.....	151
8.2	Introduction.....	152
8.3	Structures of Interest.....	154
8.4	Finite Element Modeling	156
8.4.1	Material and Mesh Properties	157
8.4.2	Damping.....	158
8.4.3	Boundary Conditions	162
8.4.4	Loading: Design Guide Procedures	162
8.4.5	Loading: Walking Procedure	164
8.5	Experimental Testing	166
8.6	Results & Discussion	168
8.6.1	Pedestrian Footbridge	169
8.6.2	One-Way Composite Floor	170
8.6.3	Experimental Cold-Formed Floors	170
8.7	Conclusions.....	172
	References.....	174
	APPENDIX A: Cyclic Load-displacement Response (Screws).....	179
	APPENDIX B: Cyclic Load-displacement Response (PAF).....	207
	APPENDIX C: Fastener Peak Load Summary.....	212
	APPENDIX D: Positive Backbone Parameters.....	215
	APPENDIX E: Negative Backbone Parameters	221
	APPENDIX F: Unloading-reloading Parameters	227
	APPENDIX G: Sample Matlab code for generating <i>pinching4</i> parameters.....	230
	APPENDIX H: Photos of Test Frame Construction and Floor Assembly	241
	APPENDIX I: Individual gage readings for diaphragm tests	246
	APPENDIX J: Test Frame Shop Drawings.....	250
Chapter 9:	APPENDIX K: Test Frame Construction Photos.....	268
	APPENDIX L: Floor Fabrication Drawings	271
Chapter 10:	APPENDIX M: Floor Fabrication Photos.....	280
	APPENDIX N: Instrumentation and Testing for Serviceability	285
	APPENDIX O: Heel Drop Response Spectra Plots, Floor D203 (D8)	288
	APPENDIX P: Walking Testing, Floor D203 (D8).....	305

APPENDIX Q: Heel Drop Response Spectra Plots, Floor D254 (D10)	350
APPENDIX R: Walking Testing, Floor D254 (D10)	373
APPENDIX S: Sample FORTRAN Code	418

LIST OF FIGURES

Fig. 2- 1: RCRMSF system concept	17
Fig. 2- 2: Details of channel cut-outs.....	18
Fig. 2- 3: Yield line analysis collapse mechanism.....	20
Fig. 2- 4: Typical section geometry of channel and channel layout showing typical.....	23
Fig. 2- 5: Finite elements part model showing mesh regions	23
Fig. 2- 6: Typical load vs displacement plot (varying plate thickness)	25
Fig. 2- 7: Parametric study results; (a) displacements varying t_p and t_c (b) peak	27
Fig. 3- 1: The lightweight modular steel floor system.....	31
Fig. 3- 2: Schematic cyclic displacement protocol in accordance with FEMA 461 (2007)	35
Fig. 3- 3: Schematic representation of Δ_o and Δ_m estimates from monotonic test results	36
Fig. 3- 4: <i>Pinching4</i> hysteresis parameters from Mazzoni et al. (2006).....	37
Fig. 3- 5: Test setup for a) screws and b) powder-actuated fasteners.....	39
Fig. 3- 6: Location of Optotrak markers for monitoring slip.....	40
Fig. 3- 7: Monotonic load vs displacement plots for a) screws b) powder-actuated fasteners	43
Fig. 3- 8: Cyclic force-deformation response for 54-54-10-Q1	44
Fig. 4- 1: The lightweight modular steel floor system.....	58
Fig. 4- 2: Plan view of cantilever diaphragm setup adapted from ASTM E455 (2019a).....	60
Fig. 4- 3: Diaphragm test frame setup	61
Fig. 4- 4: Floor diaphragm assembly showing preliminary gravity loads	63
Fig. 4- 5: Diaphragm Cyclic displacement protocol in accordance with FEMA 461.....	64
Fig. 4- 6: Representative FE model for gravity and diaphragm assessment.....	66
Fig. 4- 7: Load vs displacement response for gravity tests.....	70
Fig. 4- 8: Load vs displacement response for bare frame tests	72
Fig. 4- 9: Lateral load vs displacement response for Floor 1 (60 mm = 1.1 % drift)	73
Fig. 4- 10: Lateral load vs displacement response for Floor 2 (60 mm = 1.1 % drift)	74
Fig. 5- 1: Schematic layout for diaphragm (SDI 2015)	80
Fig. 5- 2: Schematic layout for assessing peak diaphragm load capacity.....	82
Fig. 5- 3: Typical FE model showing assembled instances and mesh regions	86
Fig. 5- 4: Estimate of Δ_o from a) Floor 1 test result b) Floor 2 test result	90
Fig. 5- 5: Cyclic displacement protocol	91
Fig. 5- 6: Load vs. displacement response under uniformly distributed gravity loads.....	92
Fig. 5- 7: Cyclic load vs displacement response for varying (a and b) purlin depth, and (c and d) plate thickness (100 mm = 1.8 % drift).....	93
Fig. 5- 8: Variations in unit shear strength and dissipated energy with varying (a and c) plate thickness, and (b and d) purlin depth	94

Fig. 6- 1: RCRMSF floor details.....	103
Fig. 6- 2: 3x3 bay arrangement and dimensions	108
Fig. 6- 3: Finite element model.....	109
Fig. 6- 4: Walking and aerobic load history	111
Fig. 6- 5: Cross-section showing RCRMSF parameters.....	112
Fig. 6- 6: Abaqus FEA results showing floor accelerations as a result of (a) global vibrational behavior of the top plate and (b) local vibrational behavior present in the bottom plate as shown by variations within channel lines.....	115
Fig. 6- 7: Single bay parametric study natural frequency results varying: (a) plate thickness (b) channel thickness (c) channel depth and (d) channel spacing	116
Fig. 6- 8: Sample finite element analysis time histories: (a) low frequency floor P1.37-C1.72-D203-S610 (b) high frequency floor P1.37-C1.72-D305-S610.....	119
Fig. 6- 9: Single bay parametric study acceleration results varying: (a) plate thickness (b) channel thickness (c) channel depth and (d) channel spacing.....	120
Fig. 6- 10: Acceleration vs. natural frequency for single bay floors	121
Fig. 6- 11: 3x3 bay parametric study results: (a) natural frequency (b) acceleration	125
Fig. 6- 12: Rhythmic loading parametric study acceleration results	128
Fig. 7- 1: Test frame.....	138
Fig. 7- 2: Purlin flange and web profile cut-out.....	139
Fig. 7- 3: Orthogonally arranged purlins	140
Fig. 7- 4: Notched bottom plate of the center panel and top plate lap-splice pieces	141
Fig. 7- 5: Completed floor panel.....	142
Fig. 7- 6: Floor panels being lowered into place	143
Fig. 7- 7: Splice plates being installed over the splice seats of the center-top plate and the top plate of the exterior panel	144
Fig. 7- 8: Perimeter purlins nailed to the flanges of the test frame girders using Hilti brand powder actuated fasteners	144
Fig. 7- 9: Measured heel drop response spectra for floor D203 (D8).....	147
Fig. 7- 10: Measured heel drop response spectra for floor D254 (D8).....	147
Fig. 7- 11: Measured walking time history for floor D203 (D8)	148
Fig. 7- 12: Measured walking time history for floor D254 (D10)	148
Fig. 8- 1: Cross section of the pedestrian footbridge from AISC DG11 2016 (a) and cross section of the composite floor from Perry et al. 2003 (b)	155
Fig. 8- 2: Typical cold-formed steel floor system.....	156
Fig. 8- 3: Comparison of the response spectra by modal analysis and direct dynamics for the a) pedestrian bridge, b) composite floor system	162
Fig. 8- 4: Time history of ground reaction force due to a footfall	165
Fig. 8- 5: Acceleration-time history for the D203 (D8) a) walking model and c) experimental data and the D254 (D10) b) walking model and d) experimental data.....	172

LIST OF TABLES

Table 2- 1: Steel gages with equivalent minimum thicknesses and bending radii	21
Table 2- 2: Range of parameters considered for FE modelling	24
Table 2- 3: Comparison between estimated displacements at 2.4 kPa, collapse load	26
Table 3- 1: <i>Pinching4</i> parameters definitions (Mazzoni et al. 2006)	38
Table 3- 2: Mechanical properties test report	40
Table 3- 3: Peak loads vs AISI/SDI predicted maximum loads	45
Table 3- 4: Positive displacement backbone parameters	46
Table 3- 5: Positive force backbone parameters	47
Table 3- 6: Negative displacement backbone parameters.....	48
Table 3- 7: Negative force backbone parameters	49
Table 3- 8: Unloading-reloading parameters	50
Table 4- 1: Estimated weight of frame and floors	62
Table 4- 2: Diaphragm test summary.....	62
Table 4- 3: Incremental patch loads for gravity tests.....	63
Table 4- 4: <i>Pinching4</i> parameters definitions (Mazzoni et al. 2005)	68
Table 4- 5: <i>Pinching4</i> parameters of PAF and screw	69
Table 4- 6: Stiffness under gravity patch loads	70
Table 4- 7: Computed net shear deflections from lateral diaphragm tests	73
Table 4- 8: Summary of peak loads and dissipated energy from lateral cyclic tests	74
Table 5- 1: Connector shear strength values.....	83
Table 5- 2: Model designations with corresponding geometric parameters	84
Table 5- 3: <i>Pinching4</i> parameters for powder-actuated fasteners (Boadi-Danquah et al. 2019a) 87	87
Table 5- 4: <i>Pinching4</i> parameters for No. 12 screws (Boadi-Danquah et al. 2019a).....	88
Table 5- 5: Parametric study results.....	95
Table 6- 1. Parametric study configurations (bold indicates parameter varied from base configuration P1.37-C1.72-D254-S610).....	113
Table 6- 2. Parametric study results for walking load (bold indicates parameter varied from base configuration P1.37-C1.72-D254-S610; HFF=high frequency floor; LFF=low frequency).....	114
Table 6- 3. Parametric study results for 3x3 configurations under walking load and single bay configurations subjected to rhythmic loading (bold indicates parameter varied from base configuration P1.37-C1.72-D254-S610).....	125
Table 6- 4. Lowest weight floor configurations for each depth, d, to satisfy ISO vibration limits (minimum plate thickness, t_p , and channel thickness, t_c). Channel spacing, s, is 610 mm in all cases	127
Table 7- 1. Step frequency at which walking testing was conducted	137
Table 7- 2. Measured panel weight and equivalent floor dead load	142
Table 7- 3. Measured natural frequencies from the experimental systems and predicted natural frequencies from the calibrated FE models	145

Table 7- 4. Measured equivalent sinusoidal peak accelerations (ESPA) from the experimental systems and predicted ESPA from the calibrated FE models	146
Table 7- 5. Predictions from uncalibrated FE models	149
Table 8- 1. Recommended viscous damping ratios for floor components	159
Table 8- 2. Recommended viscous damping ratios for model materials	161
Table 8- 3. FE model damping values	161
Table 8- 4. Natural frequencies predicted by AISC Design Guide 11 (2016) and FEA.....	169
Table 8- 5. Equivalent sinusoidal peak accelerations predicted by AISC Design Guide 11 (2016) and FEA for varying evaluation methods	169
Table 8- 6. Effective weight as calculated by AISC Design Guide 11 (2016) and Abaqus/CAE	169
Table 8- 7. Comparison of natural frequencies predicted from FEA and experimental testing .	171
Table 8- 8. Comparison of equivalent sinusoidal peak accelerations determined from FEA and experimental testing	171

Chapter 1: Introduction

1.1 Problem Description

To promote economically and environmentally sustainable design, modern structures must be adaptable to the needs of rapidly changing markets and building occupancies. At the same time, these structures are required to withstand extreme loading events such as seismic activity or blast. These demands of modern structures are coupled with requirements of structural engineers to find sustainable methodologies to reduce material wastage from construction, as natural resources become scarcer (Wang et al. 2015, Ross et al. 2016).

Rapidly constructible and adaptable structures provide a new paradigm that has the potential to address rapidly changing economic and occupancy needs. These adaptable structures require modularity and integration of mechanical, electrical and plumbing systems. Modularity results in many benefits including flexibility and re-use, less material wastage, increased construction speed, and rapid component replacement after a hazardous event. The use of modular adaptable structures also addresses demands of modern structures by allowing a building's use to change to meet market needs. Such systems can be adapted quickly for reuse or be deconstructed, moved, and reconstructed at a different location. Likewise, in the case of an extreme event, a resilient modular system will experience repairable damage with an inherent ability for components to be replaced if necessary.

It is essential that the self-weight of these modular and adaptable systems is kept as low as can be practically achieved. From a construction and logistical perspective, low self-weight enhances the practical use of the system. It also minimizes inertial forces transmitted during seismic activity. While these attributes provide both economic and life-safety resilience, no current modular adaptable structural system has all these characteristics.

1.2 Goal of Research

The goal of this research work is to develop a lightweight, two-way flooring system that has the ability to integrate better with structural and non-structural building components. The system is required to be modular to maximize construction speed and reconfiguration, and have a potential to accommodate building service within its depth to minimize floor-to-floor heights. It is considered therefore that, that the use of steel as primary structural components will result in a lighter and more resilient flooring system, providing lower seismic weight and increased structural ductility due to its inherent properties and versatility.

1.3 Organization

This report is organized into eight chapters, each a modified manuscript detailing different aspects of the project. Chapter 2 presents a manuscript published in the *International Journal of Computational Methods and Experimental Measurements*. The chapter introduces the concept of the novel modular floor system, and presents the design formulations and analytical results for service load deflection and strength assessment under gravity loads. Chapters 3, 4, and 5 consist of manuscripts of papers prepared for submission to technical journals. Chapter 3 covers the experimental testing and characterization of fasteners and connectors applicable to the novel modular floor system. Chapters 4 and 5 are companion manuscripts examining gravity load and cyclic diaphragm behavior of the floor system. Chapter 4 presents experimental testing and supporting finite element (FE) model development, while Chapter 5 details the FE modeling methods used, expanding them into a parametric study of the floor system's diaphragm performance. Chapter 6 is composed of a manuscript accepted for publication in the *ASCE Journal of Structural Engineering* and provides further background on the development and parametric

vibrations study of the proposed floor system using FE methods. Chapter 7 presents data and findings from experimental testing conducted on two full-scale floor systems to evaluate them for vibration serviceability performance under walking loads. Chapter 8 presents a newly developed FE loading technique for predicting floor accelerations due to walking events and assesses the efficacy of the method and identify areas for improvement.

Results of individual connector tests and a summary of key values are included in Appendices A through C. The *pinching4* material model, capable of representing the hysteretic behavior of fasteners, is utilized for defining the cyclic behavior of the connectors tested. The parameters for defining the *pinching4* models, generated from the test results are included in Appendices D through F. Matlab code for generating *Pinching4* parameters for numeric modeling is provided in Appendix G. Photos of the diaphragm test setup are included in Appendix H, and individual displacement gage readings for diaphragm tests are included in Appendix I. Shop drawings for fabrication of the test frame are included in Appendix J. Photos of construction of the test frame are included in Appendix K. Floor panel fabrication drawings are included in Appendix L. Photos of floor panel fabrication are included in Appendix M. Photos of the instrumentation and test procedure for evaluating vibration serviceability are included in Appendix N. Appendices O-R include raw test data from heel drop testing for floor D203 (D8), walking test data from floor D203 (D8), heel drop testing for floor D254 (D10), and walking test data from floor D254 (D10). Appendix S includes the FORTRAN code used to apply the walking loading developed for FE modeling.

1.4 Acknowledgements

This research was made possible through funding provided by the American Institute of Steel Construction Milek Faculty Fellowship. The authors are indebted to many people for their help and support on this project. Specifically, the authors would like to thank Sabrea Platz, David Woody, Kent Dye, Zahra Andalib, and Abdulaziz Almarshad for their involvement. Materials and fabrication were provided in part by the Bradbury Group, Central Plains Steel, Kansas City Structural Steel, Hilti, and Simpson Strong-Tie.

Chapter 2: Lightweight Modular Steel Floor System for Rapidly Constructible and Reconfigurable Buildings

2.1 Abstract

Rapid construction, modularity, deconstruction, and reconfiguration facilitate economy and sustainability allowing for changes in a building's use over time. Typical one-way composite steel/concrete floor systems lend themselves to terminal construction practices that make assumptions about the occupancy and usage needs that must last through the life of the structure. To address this, a lightweight rapidly constructible and reconfigurable modular steel floor (RCRMSF) system that utilizes two-way bending behavior and cold-formed steel building materials has been developed. RCRMSF improves upon the efficiency benefits of traditional composite steel/concrete flooring systems, reducing beam and girder usage and size, and allowing for highly flexible building configurations and mobility. The system consists of a series of prefabricated panels composed of a grid of cold-formed steel channels running in orthogonal directions sandwiched together by steel plates. A simple performance assessment has been formulated and a finite element model parametric study has been carried out in Abaqus finite element analysis (FEA) software. The results of the developed performance assessment and FEA study show that RCRMSF systems are suitable for rapidly constructible buildings in terms of strength and serviceability providing an initial step to fully modular and reconfigurable steel buildings.

2.2 Introduction

As natural resources become scarcer, structural engineering must find sustainable design methodologies to reduce material usage. At the same time, structures must remain resilient to economic changes and the effects of extreme loads such as earthquakes. While most buildings remain static, rapidly constructible and movable building structures provide a new paradigm that can address these needs. These structures require modularity, reconfigurability, rapid constructability and integration of mechanical, electrical and plumbing systems (M/E/P). No current system has all these characteristics. These attributes provide both economic and life-safety resilience. If building use needs to change to meet market needs, the system can adapt quickly for reuse or be deconstructed, moved, and reconstructed for reuse at a different location. Likewise, if an extreme event takes place a resilient system will show reduced damage and have the ability to replace modular components if necessary. It is envisioned that structures of the future will be completely movable with limited site preparation using modular and rapidly constructible design and construction practices. Rapidly constructible and reconfigurable modular steel floor (RCRMSF) systems will play a key role in these kit-of-part systems.

One of many barriers to making movable and rapidly constructible steel structures are typical one-way composite steel/concrete floor systems pervasive to commercial, residential, and industrial construction. A multitude of flooring systems (Girder slab 2015, Hsu et al. 2014, Hanaor 2000, Colaco 1972), have been developed to improve upon the performance of standard flooring system including systems that consider Design for Deconstruction (DfD) (Wang et al. 2015, Uy et al. 2015). Regardless, one-way composite floors result in large gravity loads and high inertial forces that lead to unnecessary material usage and damage during extreme events. Limited research has been focused on analyzing and developing lighter floor systems for steel structures,

considering the two-way bending behavior (Schaad 2005, Ahmed et al. 2002). Two-way steel systems are possible and show promising results, but they have not been implemented in construction.

While movable and modular structures are not currently popular in the United States, a recent study among architects, engineers, general contractors, and owners found that construction speed, reduced costs, site safety, and quality can be improved with modular construction (Bernstein et al. 2011). At the same time, material waste and impact on the environment can be reduced creating more sustainable buildings (Bernstein et al. 2011). Currently many prefabricated building components are already available; however, lightweight, integrated, and reconfigurable building components, especially floor systems, are limited or non-existent.

In an attempt to increase the suitability and utility of these building components for construction, the development of the RCRMSF system addresses many of the limitations to the current state-of-the-art. RCRMSF's are envisioned to be one of many rapidly constructible, modular building components that are designed to integrate M/E/P and non-structural systems and use advanced analysis methods such as two-way action, allowing for adaptable building structures of the future. RCRMSF's inherently in their design increase the versatility of structural systems, improve integration of non-structural components, allow for modular design, and use new detailing to enhance constructability, economy, and resiliency. Additionally, as few assumptions as possible about the future use of the RCRMSF's are considered such that a robust and versatile system is achieved.

This paper focuses on the development of a RCRMSF for rapidly constructible and reconfigurable structures. A strength and serviceability analysis procedure was developed for preliminary design and a finite element model parametric study was carried out to predict and

understand RCRMSF system performance. The results of this research will lead to design recommendations and construction procedures for the next generation of highly adaptive building structures.

2.3 RCRMSF Concept and Design

2.3.1 RCRMSF Description

The RCRMSF system is just one building component of future integrated modular structures. The RCRMSF system is comprised of individual rectangular panels fabricated from thin-gauge steel top and bottom plates with a sandwiched grillage of cold formed channels (Fig. 2- 1). To form the grillage, channels are placed in an orthogonal arrangement with even spacing. Fig. 2- 2 shows the profiling that is used to allow the channels to meet this configuration within each panel. The channels can be further detailed to allow for integration of M/E/P components during fabrication. Self-drilling self-tapping screws are used to connect the plates to channels. The floor is topped with a thin layer of gypsum concrete to aid in fire proofing, acoustics, and finishing.

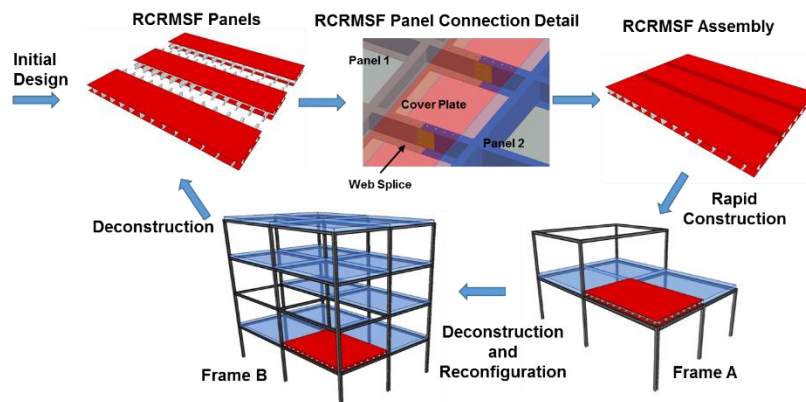


Fig. 2- 1: RCRMSF system concept

As shown in Fig. 2- 1, the RCRMSF panels can be shipped to the construction site, lifted into the skeleton structure, and rapidly constructed with web splices and cover plates using screw

connections. As previously described, RCRMSFs are designed such that the structure can be deconstructed, moved or reconfigured, and reconstructed. This is achieved through simple unscrewing of the panels and rapid construction in a new structure (i.e. Frame A to Frame B). If no longer needed, the panels can be taken down to make space until needs change. Overall, this design creates a highly adaptable flooring system.

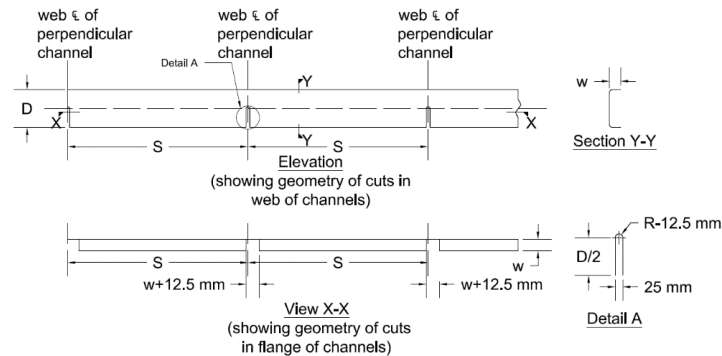


Fig. 2- 2: Details of channel cut-outs

2.4 Performance Assessment

The procedure for assessing the structural performance of RCRMSF is formulated based on three failure limit states: (1) excessive deflection, (2) yielding of sandwich plates and (3) failure of connectors at the interface between plates and channels. This assessment considers the monolithic performance of the constructed panel within a structural bay ignoring the panel connection detail.

2.4.1 Deflection Assessment

Allowable deflections of the RCRMSF are bounded by limits set in the International Building Code (IBC 2015). For floor members, the deflection shall not exceed $l/360$ for live loads or $l/240$ for a combination of live and dead loads, where l represents the shorter span of the assembled deck.

Estimation of the system's deflection under service loads is based on the plate bending theory by Timoshenko and Woinowsky-Krieger (1959). The deflection of a simply supported rectangular plate under uniform loading is expressed as;

$$\Delta_{max} = \alpha \frac{qa^4}{F} \quad (2- 1)$$

$$F = \frac{Eh^3}{12(1-\nu^2)} \quad (2- 2)$$

where Δ_{max} is the maximum displacement, α is a coefficient dependent on the aspect ratio (longer span, b to shorter span, a) and q is the pressure loading. F represents the flexural rigidity, estimated using eqn. (2- 2) for a rectangular plate with thickness, h , elastic modulus, E , and Poisson's ratio, ν .

For the equations above to be applicable to the RCRMSF, the flexural rigidity has been modified to account for the use of the plate pair and the stiffness contributions from the channels in the two orthogonal directions. The result is a modified flexural rigidity, expressed as;

$$F_{mod} = \frac{E(H^3 - D^3)}{12(1-\nu^2)} \quad (2- 3)$$

$$H = D + 2t_m \quad (2- 4)$$

where D is the overall height of channel (space between plates) and t_m is the thickness of plate, modified to account for the stiffness contribution of the sandwiched channels. The contribution of the layer of gypsum concrete to the system stiffness is ignored for this assessment as it is not used for strength purposes.

2.4.2 Plate Yielding Assessment

The process of assessing the ultimate load of the RCRMSF is based on plate yield line theory. The application of the yield line theory for this assessment involves the utilization of the primary collapse mechanisms as shown in Fig. 2- 3. The ultimate collapse load is obtained by

equating the external work done by an applied load, q , to the internal work done in rotating yield lines. For efficiency in this system, however, it is desirable for no plate yielding to occur up to the deflection limits.

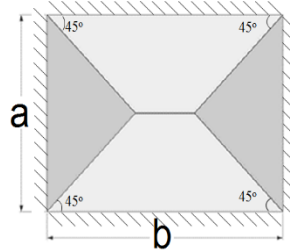


Fig. 2- 3: Yield line analysis collapse mechanism

2.4.3 Connector Design

Screw connectors are provided to transfer the full shear at the interface between the plates and channel up to the point where the plates fully yield as such connector failure does not govern the assessment and performance of the system. The shear capacity of each connector, Q_n is determined in accordance with the provisions of section E4.3 of AISI S100 (2012). The capacity of the total number of connectors provided is required to exceed the total force required to fully yield the plate, F_s .

The magnitude of F_s depends on the yield strength of the steel, f_y , the thickness of the steel plate, t_p and the spacing between the channels, s , and is computed as

$$F_s = f_y s t_p \quad (2- 5)$$

ΣQ_n therefore should exceed F_s . The total number of connectors is determined for shear transfer in the (shorter) stiffer direction only, and spaced to evenly cover the two orthogonal directions.

2.5 Finite Element Analysis Parametric Study

Finite element models were created to assess the strength and serviceability performance of the system, and a parametric study carried out to assess the effects of varying certain critical

parameters on the performance of the system. For this study, the FEA models considered a monolithic panel and did not account for connectors which splice the individual panels of the RCRMSF.

2.6 Description of Finite Element Model

The finite element models were generated in Abaqus FEA (Version 6.14) (2014) to support the performance assessment formulated earlier and to study the influence of different parameters on the strength of the system. The geometry of the steel component, including the width (w), depth (D), and thickness (t), was taken as that reported in the SSMA Product Technical Guide (2014). Additionally, the fastener details were taken from Hilti Product Technical Guide (2015). Steel gages studied with their equivalent minimum thicknesses and inside bend radii (for channels) are as summarized in Table 2- 1.

Table 2- 1: Steel gages with equivalent minimum thicknesses and bending radii

Steel Gage	Minimum thickness, t (mm)	Inside bend radius, r (mm)
16	1.37	2.16
14	1.72	2.72
12	2.45	3.87

The plates, channels and gypsum concrete topping were modeled using 3-D shell elements. The material properties of the steel components were assumed isotropic with an elastic modulus $E= 200$ GPa (29,000 ksi) and Poison’s ratio $\nu = 0.30$. For this nonlinear analysis, an elastic-perfectly plastic material behavior was assumed, with yield stress defined as $\sigma_y = 345$ MPa (50 ksi). The gypsum concrete topping was assumed to be isotropic with a linear elastic behavior and an elastic modulus of $E= 11.7$ GPa (1,700 ksi). The value was selected to limit the structural contribution of the gypsum concrete to the overall stiffness of the system. Its inclusion in the model however ensures uniform load distribution across the top plate without inducing local

displacements (depressions) within the channel grid spaces. Within all regions, 4-node thin or thick shell elements (S4R) with reduced integration, hourglass control, and considering finite member strains were used.

The element mesh sizes were selected to balance accuracy and efficiency of the model. The top and bottom plates were modeled using rectangular elements of approximately 50 mm square. The lightweight concrete topping was modeled using rectangular elements of approximately 100 mm square and the channels were modeled using mixed quad dominated elements of approximately 40 mm square size. Screw connectors at the interface between the steel plates and channels were specified using mesh independent point fasteners, with sections assembled as “beam type” connectors. In all cases, the numbers of point fasteners specified meet or exceed the minimum number required for full shear transfer. The steel-to-steel contact in the model was defined as hard normal contact with allowance for separation and the tangential behavior defined using a friction coefficient of 0.35. The interaction between the gypsum concrete topping and the steel top plate was defined using a tie constraint.

Boundary conditions were applied to represent a rectangular deck, simply supported along all four sides. By definition, the global X, Y and Z axes of the models represent the transverse, longitudinal and vertical directions of the flooring system, respectively. Translation in the Z-direction was restrained along all four edges of the bottom plate. Additionally, X-translation was restrained along one longitudinal edge, and Y-translation restrained at a single corner node to prevent rigid body motion, without consequently developing horizontal reactions.

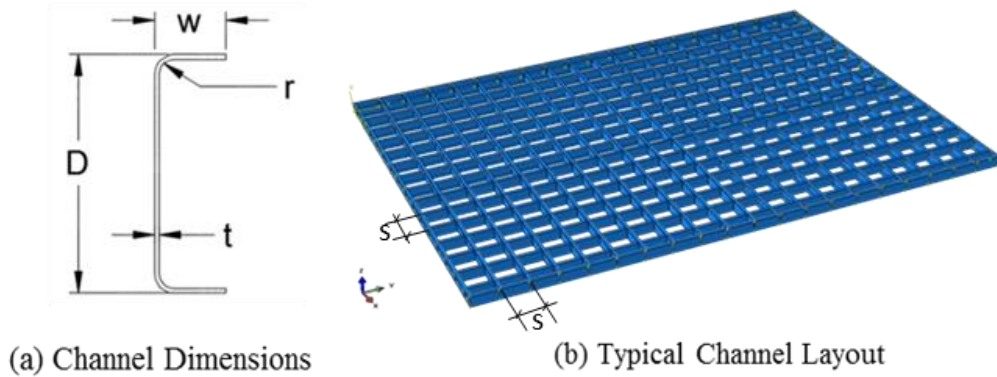


Fig. 2- 4: Typical section geometry of channel and channel layout showing typical spacing (s) of 610 mm (2 ft)

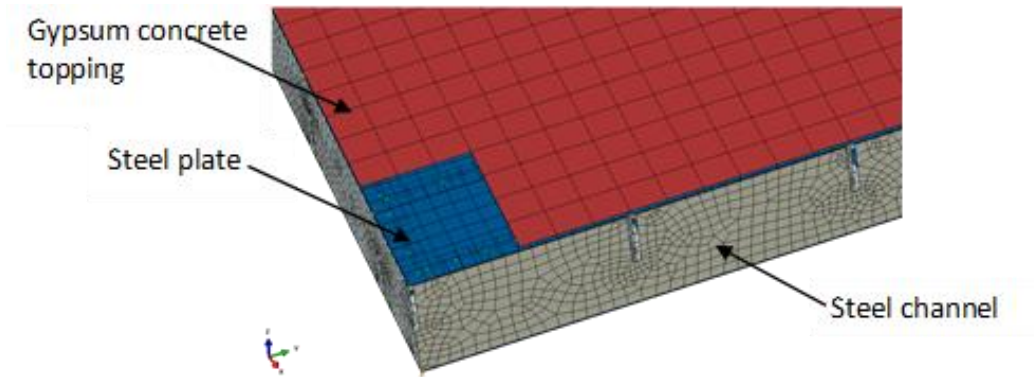


Fig. 2- 5: Finite elements part model showing mesh regions

A uniform pressure was applied over the surface of the gypsum concrete topping. The loading was applied with a ramp type amplitude from 0 to a maximum value of 21 kPa (432 psf). For this study, peak loads were recorded after analysis, as the load along the ramp at which the last converging solution was obtained.

2.7 Parametric Study and Results

These studies were conducted to investigate influence of four parameters, including: plate thickness (t_p), channel thickness (t_c), channel depth (D) and channel spacing (s), on strength characteristics of the system. The range of the parameters considered for service load conditions are represented in Table 2- 2.

A base model with $t_p = 1.37$ mm, $t_c = 1.72$ mm, $D = 254$ mm and $s = 610$ mm was created. The parameters, including the plate thickness (t_p), channel thickness (t_c), depth of channel (D) and channel spacing (s) were varied as shown in Table 2. In all cases, the width (w) of the channel flange was kept constant at 76.2 mm (3 in.).

For all the models studied, the peak load was recorded as the load value at which the web of the perimeter channels buckled due to support reactions. Since the higher magnitude of shear is carried in the shorter (stiffer) direction, the 12.2 m (40 ft) perimeter channels had a higher susceptibility to buckling at the supports.

Table 2- 2: Range of parameters considered for FE modelling

CHANNELS									
Depth, D (mm)		203	254				305		
Spacing, s (mm)		610	610		1220	1830	610		
PLATES	Thickness, t (mm)	t_c \ / t_p	1.72	2.45	1.72	1.37	1.72	1.72	1.72
			2.45						
	1.72								
	1.37								

LEGEND

- Base Model
- Varying t_p
- Varying t_c
- Varying s
- Varying D

2.8 RCRMSF Performance

In order to assess the strength performance of the system, the results of the parametric study were interpreted and compared to results based on the formulated performance assessment to validate the anticipated response of the system to static loading.

From the parametric study, typical load-displacement curves and failure mode can be seen in Fig. 2- 6. Table 2- 3 and Fig. 2- 7 report results from parametric study. The highest peak load recorded was 10.68 kPa for the floor with $t_p = 2.45$ mm, $t_c = 1.72$ mm, $D = 254$ mm and $s = 610$ mm. The lowest peak load recorded was 3.16 kPa for $t_p = 1.37$ mm, $t_c = 1.72$ mm, $D = 254$ mm, and $s = 1830$ mm. For all variations in parameters, the perimeter channels buckled at the peak loads as shown on Fig. 2- 6. The highest displacement at 2.4 kPa ($\Delta_{2.4}$) was recorded as 11.91 mm for $t_p = 1.37$ mm,

$t_c=1.72$ mm, $D=203$ mm, and $s=610$ mm. The lowest displacement at 2.4 kPa ($A_{2.4}$) was recorded as 5.4 mm for $t_p=2.45$ mm, $t_c=1.72$ mm, $D=254$ mm, and $s=610$ mm.

Increasing t_p from 1.37 mm to 1.72 mm resulted in a reduction in displacement by 1.1 mm, compared to a reduction of 0.28 mm for increasing t_c by the same magnitude, at 2.4 kPa load, holding s and D constant, Fig. 2- 7a. Similarly, increasing t_p from 1.72 mm to 2.45 mm resulted in a reduction in displacement of 1.46 mm, compared to a reduction of 0.43 mm for increasing t_c by the same magnitude at 2.4 kPa load. As expected, for the spacing considered and constant channel depth, the thickness of the steel plates had a greater influence on the overall stiffness of the system than the thicknesses of the channels due to their larger influence on the moment of inertia.

It was observed that the recorded peak loads were similar for varying plate thickness, Fig. 2- 7b. An increase in t_c from 1.37 mm to 1.72 mm, however resulted in an increase in peak load by 4.34 kPa. A further increase of 0.18 kPa was recorded for t_c increase from 1.72 mm to 2.45 mm. This indicated that, increasing the wall thickness of the channel had a greater influence on the recorded peak loads, due to buckling of thin walls at the support.

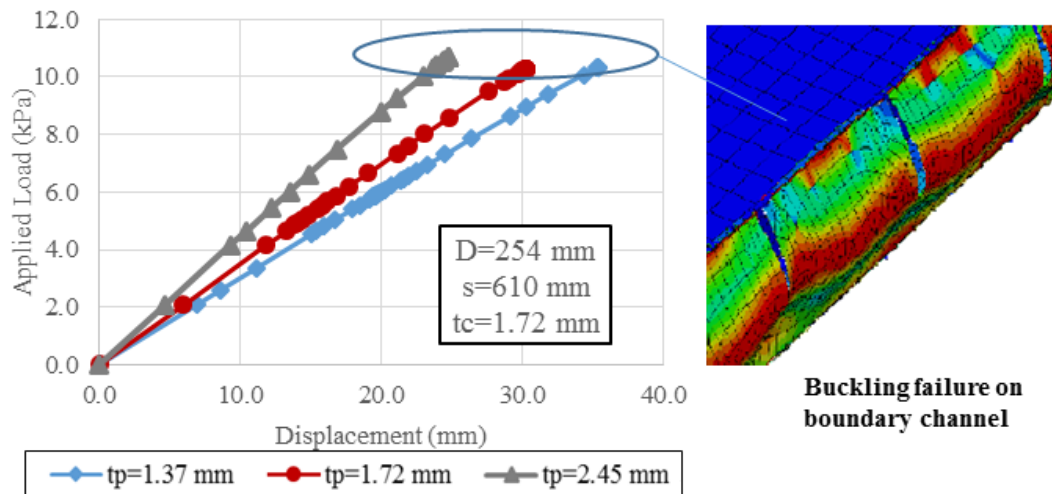


Fig. 2- 6: Typical load vs displacement plot (varying plate thickness)

Table 2- 3: Comparison between estimated displacements at 2.4 kPa, collapse load based on Yield Line Analysis, and FE model results

Plate Thickness t_p (mm)	Channel Thickness t_c (mm)	Channel Depth D (mm)	Channel Spacing s (mm)	Theo. Disp. $\Delta_{2.4}$ (mm)	FE Model Disp. (mm)	Yield Line Peak (kPa)	FE Peak Load (kPa)
1.37	1.72	254	610	9.14	7.96	34.10	10.34
1.72	1.72	254	610	7.54	6.86	41.09	10.29
2.45	1.72	254	610	5.51	5.40	55.68	10.68
1.37	1.37	254	610	9.50	8.25	32.68	6.00
1.37	2.45	254	610	8.48	7.53	36.92	10.52
1.37	1.72	203	610	14.45	11.91	26.89	6.70
1.37	1.72	305	610	6.27	5.78	41.52	8.42
1.37	1.72	254	1220	10.11	9.14	29.77	4.55
1.37	1.72	254	1830	10.47	10.34	28.77	3.16

Only minor reduction in system stiffness from increasing the channel spacing (s) from 610 mm to 1830 mm was observed based on an increase in deflection of 2.38 mm at 2.4 kPa loading, Fig. 2- 7c. The highest peak loads at channel spacings (s) of 1220 mm and 1830 mm were less than 4.8 kPa, hence variations in system deflections at 4.8 kPa were not plotted. Increasing channel depths (D), with all other parameters kept constant, resulted in an increase in the system's stiffness as a result of the corresponding increase in the system's flexural rigidity.

A peak load drop of 5.8 kPa was observed from increasing channel spacing (s) from 610 mm to 1220 mm and a further drop of 1.4 kPa from increasing from 1220 mm to 1830 mm, Fig. 2- 7d. This was a direct result of a proportional increase in the shear load taken by the perimeter channels, increasing their susceptibility to buckling. Reducing the depth of the channel from 305 mm to 254 mm with all other parameters constant, resulted in an increase in the peak load from 8.42 kPa to 10.34 kPa. This is due to the fact that the 305 mm deep channel is more slender, thus more susceptible to web buckling. Reducing the channel depth further from 254 mm to 203 mm reduced the peak load from 8.42 kPa to 6.70 kPa. The change in trend was due to the fact that the

reduction in depth resulted in a reduced system stiffness and consequently, higher rotations in the top plate, resulting in buckling in the perimeter channels at a lower load.

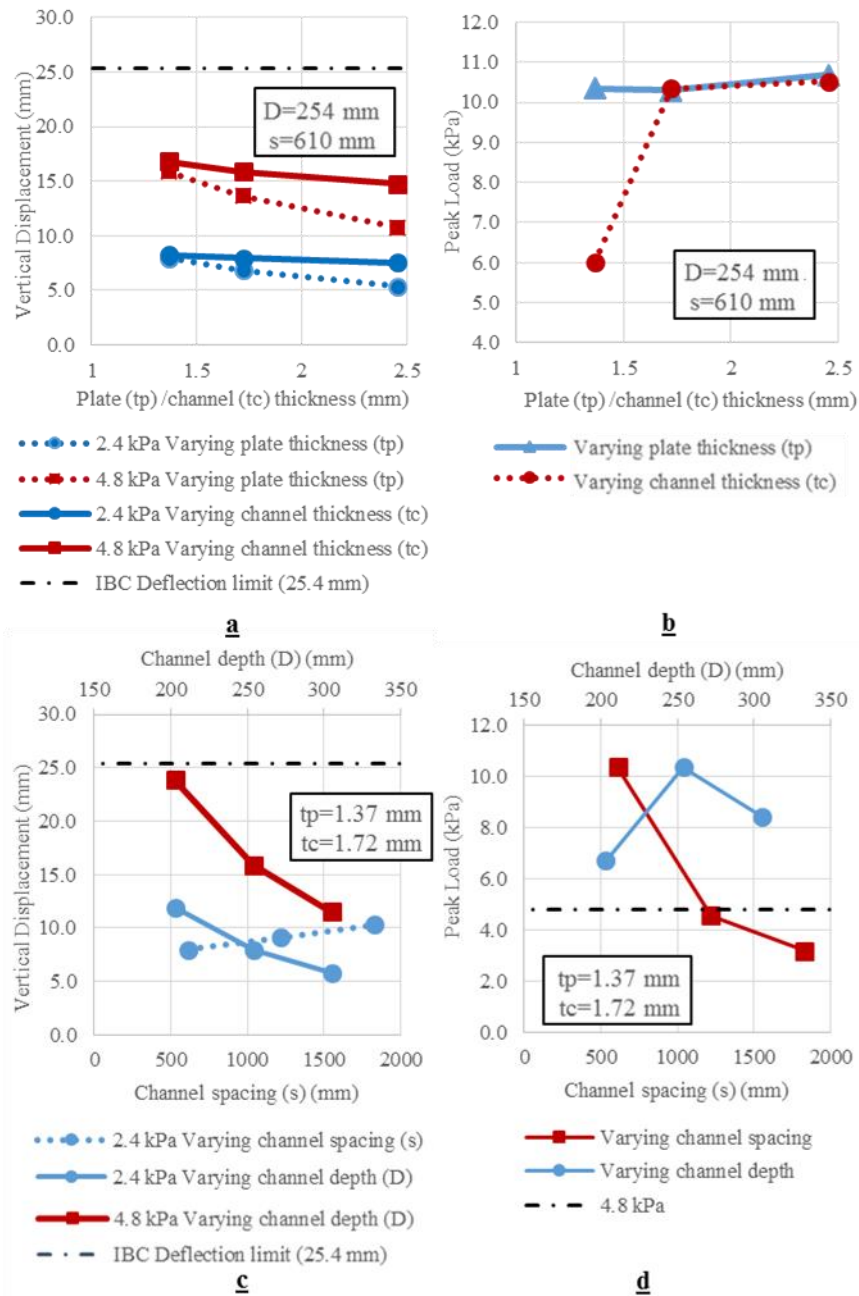


Fig. 2- 7: Parametric study results; (a) displacements varying t_p and t_c (b) peak load recorded varying t_p and t_c (c) displacements at loads varying s and D (d) peak load recorded varying s and D .

Comparison of the system's displacement at 2.4 kPa (50 psf) and estimated loads using the formulated design procedure to the results from the finite element parametric studies is as shown in Table 2- 3. It was observed that, while the gypsum concrete was included in the models in order to limit local displacements in the top plate, its contribution to the overall stiffness of the floor became more significant with lower plate thicknesses and shallower deck depth. This was seen in a difference of 2.54 mm between the estimated displacement and displacement recorded from the FE model for the $t_p=1.37$ mm and 203 mm channel depth. For the 1220 mm spaced channels, more significant shear load was transferred to the perimeter and the perimeter channels began to buckle at a load below 2.4 kPa causing some plastic deformation in addition to the plate's elastic displacement. These additional plastic deformations offset the stiffness contribution of the lightweight concrete, resulting in the "false" agreement between the two values.

In all cases, a lower peak load was recorded from the FE models compared to the load estimated using yield line analysis. The highest difference in load is for the plate thickness of 2.45 mm, where the estimated collapse load from yield line analysis was 55.68 kPa compared to a load of 10.68 kPa from the FE model. This disparity is a result of the channels buckling around the perimeter well ahead of the onset of plate yielding.

2.9 Conclusions and Recommendations

In this study, a novel RCRMSF system was developed. A performance assessment was undertaken and verified through a parametric finite element analysis. The parametric studies found that (a) steel plate thickness, (b) channel thickness, (c) channel depth, and (d) channel spacing each had a distinct effect on system performance

Overall, the RCRMSF has shown adequate strength capacity to support live loads in excess of 2.4 kPa (50 psf), recommended for office use in accordance with the International Building

Code (IBC 2015). Higher strength capacities are attainable with the right selection of the parameters that control the stiffness and load response of the system. It is recommended that in order to utilize the full capacity of the top and bottom plates, channels should be optimally sized and spaced to reduce buckling prior to the onset of plate yielding. Alternatively, extra perimeter reinforcement can be used to reduce the effects of web buckling on the system prior to plate yielding. Overall the RCRMSF system provides a suitable alternative to the typical design and construction of steel structures and allows for rapid, modular construction.

Chapter 3: Cyclic Behavior of Steel-to-Steel Screws and Powder-Actuated Fastener Connections in Single Shear

3.1 Abstract

An experimental program was undertaken to assess the cyclic performance of screw and powder-actuated fastener connections in light-gage steel. Nine unique joints composed of steel ranging from 16-gage to 12-gage, with single-lap connections made with No. 10 and No. 12 screws, as well as powder-actuated fasteners were examined, with goals of comparing peak loads with code formulations and characterizing the hysteretic behavior. The unique joint types were subjected first to a monotonic displacement protocol, the load-deformation response for which was used to determine an appropriate unified displacement protocol for cyclic testing. The screw joints were subjected to quasi-static, 0.5 Hz, and 3 Hz cyclic displacement protocols, and PAF joint have were subjected to only the quasi-static cyclic displacement protocol. The peak loads recorded from the tests generally have a close agreement to strength values from code formulations. Increasing the loading rate generally increased the peak loads recorded. Additionally, parameters for characterizing the cyclic load-deformation backbone, and unloading-reloading response have been derived specifically for the joint configurations from the quasi-static results of the experimental program.

3.2 Introduction

A lightweight modular floor system has been previously developed using light-gage steel plates and Z-purlins. The floor system is comprised of individual panels assembled within a structural steel frame and spliced together using self-drilling screws, as shown in Fig. 3- 1. A full description of the floor system can be found in Boadi-Danquah et al. (2016, 2018). In addition to

carrying gravity loads, the floor system also serves to transmit lateral forces to the structure's vertical lateral force resisting system (LFRS) through diaphragm action.

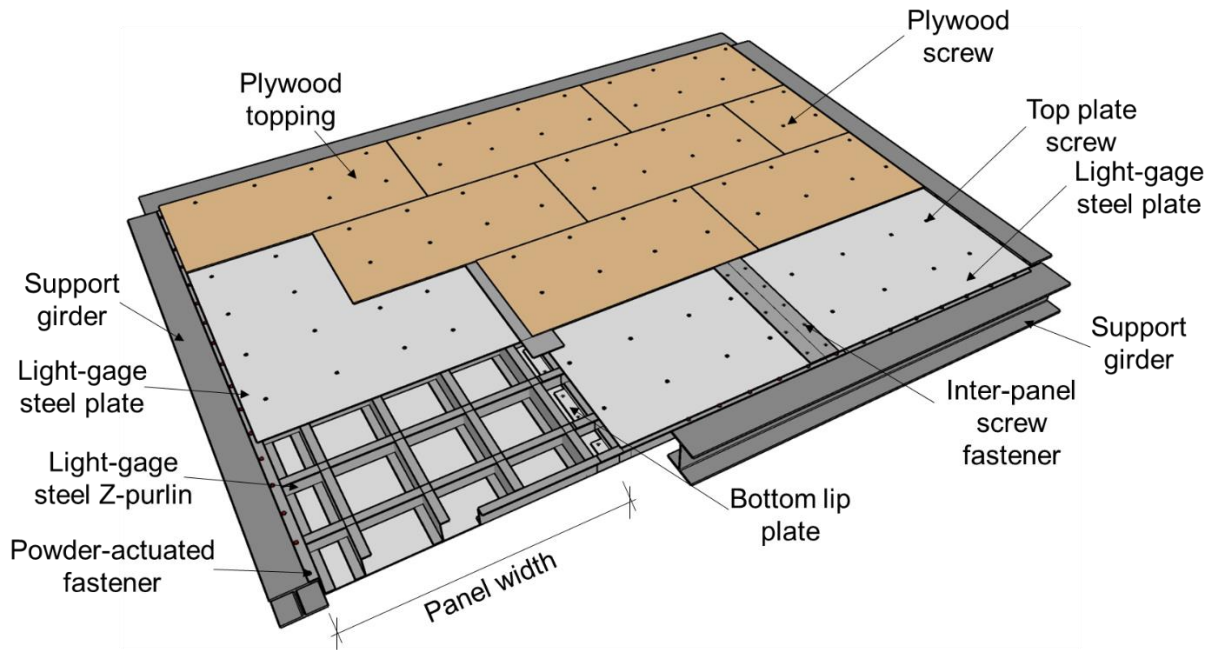


Fig. 3- 1: The lightweight modular steel floor system

Under lateral loading, inter-panel screw fasteners transfer longitudinal shear forces from one panel to the other, and powder-actuated fasteners (PAFs) transfer forces between panels and the supporting girder flange. Overall diaphragm performance is primarily dependent on the performance of both inter-panel and perimeter connectors (SDI 2015, Rogers and Tremblay 2003a & b, Essa et al. 2003, Luttrell 1996). There are proven finite element (FE) tools available to analytically assess the behavior of steel deck diaphragms in lieu of experimental testing (DDS 2016, Ding 2015, Mazzoni et al. 2006). However, these tools all require connectors to be characterized by their hysteretic characteristics, including response backbone, unloading-reloading paths, stiffness/strength degradations as applicable.

To assess the diaphragm behavior of the floor system under reversed cyclic loading, simulating a seismic event, characterization of fastener performance under cyclic loading is

necessary. Researchers (Tao et al. 2017, Peterman et al. 2014, Peterman et al. 2013) have examined the cyclic constitutive behavior of screws and other fastener types in light-gage steel. However, results are not directly applicable to the developed lightweight steel floor, due to the thickness of the steel members required to satisfy vibration serviceability criteria (Robertson et al. 2017). Research presented in this dissertation therefore contributes the required constitutive behavior for screw and PAF fasteners, applicable to the developed lightweight floor system from results of an experimental program.

The experimental program examined six unique single lap screw-fastened joints and three PAF joints. All joints were first tested using a monotonic displacement protocol, with load-displacement results used to determine the appropriate cyclic loading protocol in accordance with FEMA 461 (2007). Identical joints were then tested under the quasi-static cyclic displacement protocol. Additionally, screw-fastened joints were also tested under a cyclic displacement protocol similar to the quasi-static cyclic tests, with load rates increased to 0.5 Hz and 3.0 Hz, consistent with previous research (Rogers and Tremblay 2003a, 2003b). The recorded connector shear strengths, P_c , were compared to applicable code-predicted shear strength values, P_d (SDI 2015, AISI 2016). Additionally, the general connection behavior, backbone characteristics, and cyclic constitutive parameters were determined from these experimental results. Finally, the effects of varying the cyclic loading rate on the screw behavior was assessed.

3.3 Objectives and Scope

The goal of this research was to develop experiment-based connector cyclic models, capable of being incorporated into numerical models to predict the overall diaphragm cyclic behavior of the developed lightweight floor system. The range of parameters selected for this study

includes plate thicknesses previously deemed satisfactory for vibration performance (Robertson et al. 2017) and recommended fasteners for a prototype floor (Boadi-Danquah et al. 2016, 2018).

3.4 Background on Fastener Strength and Characterization

3.4.1 Screw Shear Strength Estimate

Provisions for estimating the nominal shear resistance of screw fasteners limited by bearing and tilting can be found in AISI's North American Specification for the Design of Cold-Formed Steel Structural Members (AISI 2016). For a single shear lap, these provisions are empirically-based equations, expressing the nominal shear strength of the sheet per screw, P_{nv} , in terms of ply thicknesses, screw diameter, and tensile strength of the steel sheets. Three equations are provided for calculating P_{nv} :

$$P_{nv} = 4.2(t_2^3 d)^{1/2} F_{u2} \quad (1)$$

$$P_{nv} = 2.7t_1 d F_{u1} \quad (2)$$

$$P_{nv} = 2.7t_2 d F_{u2} \quad (3)$$

where t_1 is the thickness of the steel ply in contact with the screw head or washer, t_2 is the thickness of ply not in contact with the screw head or washer, d is the diameter of the screw, and F_{u1} and F_{u2} are the respective tensile strengths of the steel members. For $t_1/t_2 < 1.0$, P_{nv} is taken as the smallest of equations (1), (2) or (3), and for $t_1/t_2 > 2.5$, only equations (2) and (3) apply. For $1.0 < t_1/t_2 < 2.5$, linearly-interpolated values between the minimum value of P_{nv} from equations (2) and (3), and the value of P_{nv} from equation (1) are acceptable.

Where shear strength of the screwed joint is limited by shear failure of the screw, P_{nv} is taken to be the nominal shear resistance of the screw, P_{nvs} , as reported by the screw manufacturer or determined by independent testing.

3.4.2 PAF Shear Strength Estimate

Shear strength, Q_f and stiffness, S_f of powder-actuated fasteners can be predicted from empirically-based equations in the SDI Diaphragm Design Manual (2015). Equations are specific for producer and PAF size, and apply to base metal thicknesses, t between 0.71 mm (0.028 in.) and 1.52 mm (0.060 in.). The empirically-derived equations provide Q_f and S_f in units of kN and kN/mm respectively as;

$$Q_f = 9.81t(1 - t/25.4) \text{ kN} \quad (4)$$

$$S_f = 1000\sqrt{t} / 21.6, \text{ kN/mm} \quad (5)$$

3.4.3 Cyclic Loading Protocol

FEMA 461(2007) establishes a quasi-static displacement-controlled protocol appropriate for hysteretic testing of a single specimen. The recommended loading history, presented schematically in Fig. 3- 2, consists of repeated displacement cycles, incrementally increasing in amplitude. At each displacement amplitude, two cycles are applied to the specimen, following which displacement values are increased by 40% for the subsequent two cycles.

The starting displacement amplitude is determined based on an estimate of the deformation corresponding to damage initiation, Δ_o . FEMA 461 (2007) requires a minimum of six displacement cycles prior to reaching Δ_o . Researchers have found this requirement to be challenging when testing fasteners in light-gage steel due to the plasticity occurring at low load levels (Tao et al. 2017).

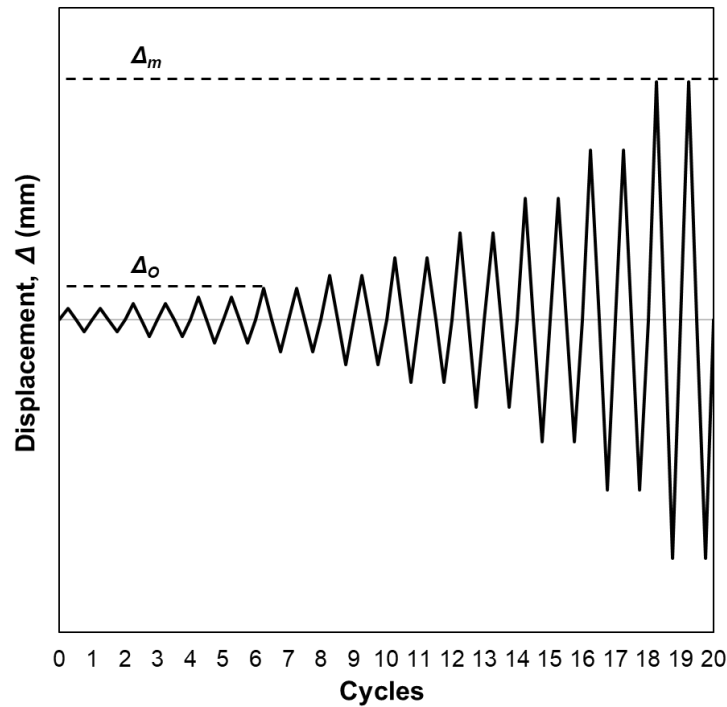


Fig. 3- 2: Schematic cyclic displacement protocol in accordance with FEMA 461 (2007)

The targeted deformation Δ_m corresponding to maximum load, Δ_m , is also required to be defined, for which a minimum of ten displacement cycles are required prior to reaching. Essa et al. (2003) defines appropriate displacement ranges to be used in cyclic tests floor diaphragm test as shown in Fig. 3- 3. The two deformation values, Δ_o and Δ_m , are determined from a monotonic test: Δ_o is determined by assuming that the test specimen remains elastic based on the secant stiffness up to the peak load, and Δ_m determined as displacement corresponding to the peak load as shown in Fig. 3- 3. Previous tests (Tao et al. 2017, Peterman et al. 2013, 2014) of fasteners in cold-formed steel using FEMA 461 (2007) typically do not define Δ_m , and continuously increase displacement amplitudes beyond Δ_o by a factor of 1.4 until the fastener loses load-carrying capacity.

3.4.4 *Pinching4* Material Model

Several hysteretic models for simulating behavior fastener behavior in light-gage steel have been proposed and improved over time (Ibarra et al. 2005, Lowes LN and Altoontash 2003, Folz and Filiatrault 2001, Foschi 1974). The *pinching4* material model, widely adopted, and currently used in OpeenSees (Mazzoni 2006) is capable of simulating cyclic behavior of fasteners in sheathed walls. The material model represents a pinched load-deformation response with strength and stiffness degradation under cyclic loads (Mazzoni 2006). The cyclic response of the *pinching4* model is characterized by a quadri-linear backbone as shown in Fig. 3- 4, with unloading-reloading response defined by six parameters. Definitions of the backbone parameters are as presented in Table 3- 1 (Mazzoni et al. 2006).

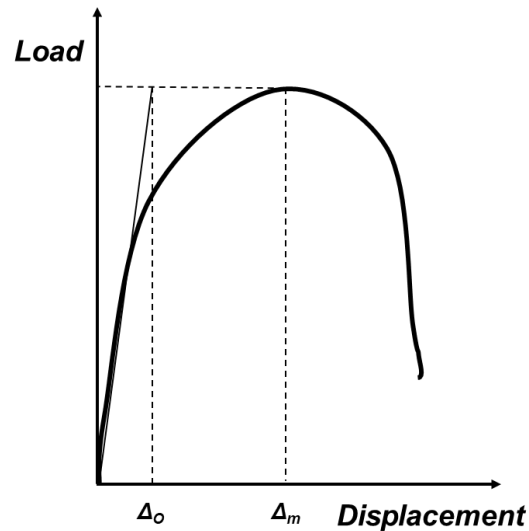


Fig. 3- 3: Schematic representation of Δ_o and Δ_m estimates from monotonic test results

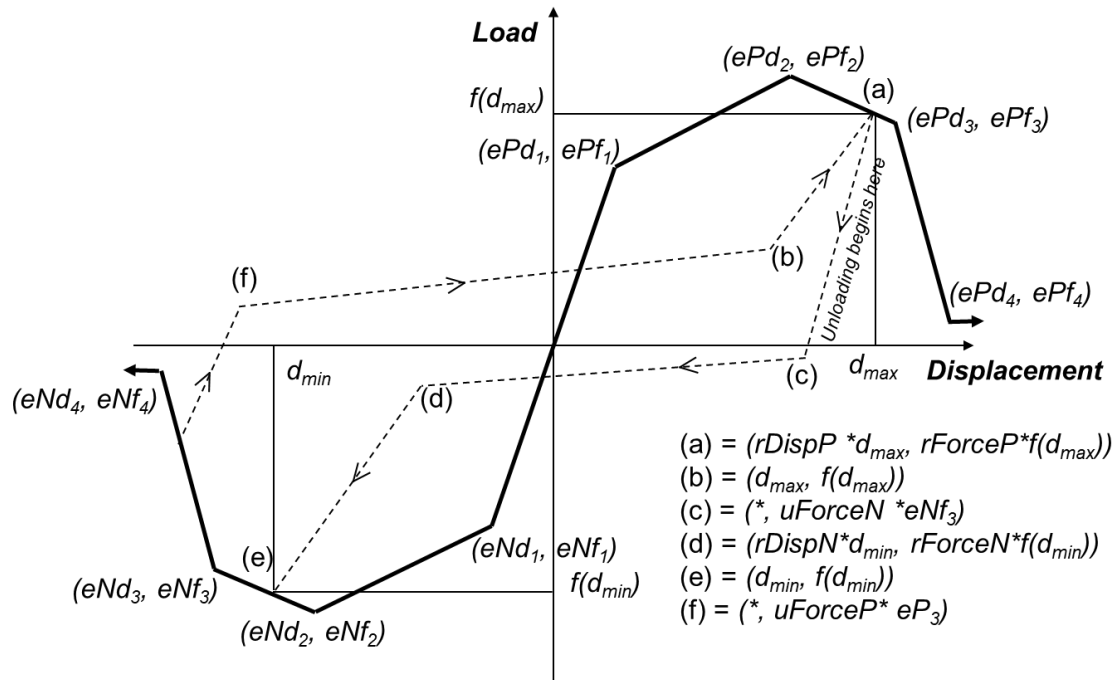


Fig. 3- 4: *Pinching4* hysteresis parameters from Mazzoni et al. (2006)

The source-code of the *pinching4* material model, as incorporated in Opensees (Mazzoni et al. 2006) has been adapted by Ding (2016) for use as a user-element (UEL) sub-routine in Abaqus 2016 (DSS 2016) and has been successfully used to simulate the lateral behavior of sheathed shear walls.

Table 3- 1: *Pinching4* parameters definitions (Mazzoni et al. 2006)

Pinching4 parameter	Definition
<i>ePf1, ePf2, ePf3, ePf4</i>	Values defining force points on the positive response envelope
<i>ePd1, ePd2, ePd3, ePd4</i>	Values defining deformation points on the positive response envelope
<i>eNf1, eNf2, eNf3, eNf4</i>	Values defining force points on the negative response envelope
<i>eNd1, eNd2, eNd3, eNd4</i>	Values defining deformation points on the negative response envelope
<i>rDispP</i>	Value defining the ratio of the deformation at which reloading occurs to the maximum historic deformation demand
<i>fFoceP</i>	Value defining the ratio of the force at which reloading begins to force corresponding to the maximum historic deformation demand
<i>uForceP</i>	Value defining the ratio of strength developed upon unloading from negative load to the maximum strength developed under monotonic loading
<i>rDispN</i>	Value defining the ratio of the deformation at which reloading occurs to the minimum historic deformation demand
<i>fFoceN</i>	Value defining the ratio of the force at which reloading begins to force corresponding to the minimum historic deformation demand
<i>uForceN</i>	Value defining the ratio of strength developed upon unloading from negative load to the minimum strength developed under monotonic loading

3.5 Experimental Program

The experimental setup for testing screws was in accordance with section 7.2 of AISI's Test Standard for Determining the Tensile and Shear Strengths of Steel Screws (AISI 2017). It was ensured, per requirements of AISI-S904 (2017), that the loading was applied centrally across the lap joint. Two screw sizes were tested, X1B1016 (No. 10) and X1B1214 (No. 12) (Simpson Strongtie 2019). The thickness of the steel plies ranged from 1.48 mm (0.057 in.) to 2.48 mm

(0.098in.). The same range of plate thicknesses was used in the examination of *X-ENP-19* powder-actuated fasteners (Hilti 2015).

3.5.1 Test Setup

All specimens were tested using a Landmark servo-hydraulic test frame (MTS, Eden Prairie, MN). For the screw tests, the joints were made from 150 mm (6 in.) deep light-gage steel purlins. Two 250 mm (10 in.) long purlins are placed back-to-back with a minimum overlap of 50 mm (2 in.), and a single screw was driven through at a minimum edge distance of 25 mm (1 in.). To minimize eccentric loading and to ensure a firm grip on the ends of the specimen, a 125 mm (5 in.) purlin piece and 6 mm (0.25 in.) thick backer plate was bolted to each end as shown in Fig. 3-5a.

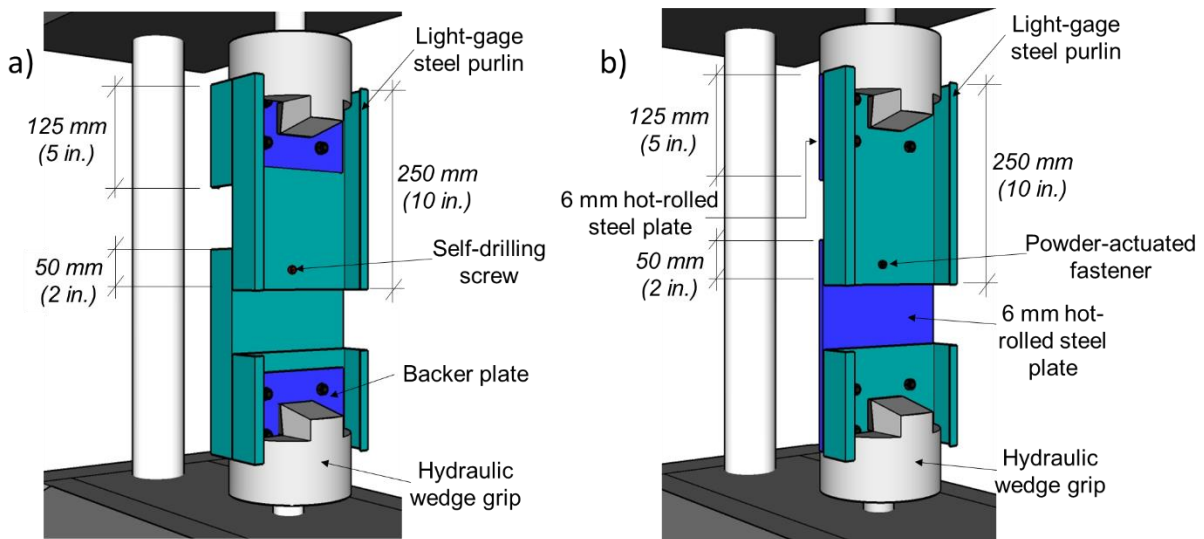


Fig. 3- 5: Test setup for a) screws and b) powder-actuated fasteners

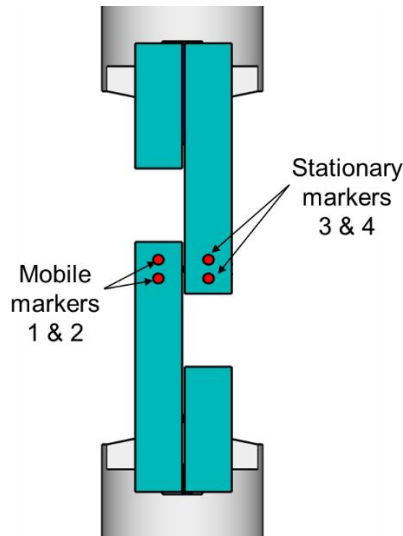


Fig. 3- 6: Location of Optotrak markers for monitoring slip

Table 3- 2: Mechanical properties test report

Designation	Mill thickness designatio	Nominal thickness	Coating	Yield strength	Tensile strength	Elongation
		mm (in.)		N/mm ² (ksi)	N/mm ² (ksi)	%
6 in. 16G 1-5/8 in.	54	1.48 (0.057)	A60	504.0 (73.1)	587.4 (85.2)	25
6 in. 14G 1-5/8 in.	68	1.81 (0.071)	A90	367.5 (53.3)	532.3 (77.2)	26
6 in. 12G 1-5/8 in.	97	2.48 (0.098)	A60	356.5 (51.7)	519.9 (75.4)	26
Flat Bar / ¼ x 6	N/A	6.35 (0.25)	N/A	407.5 (59.1)	529.5 (76.8)	25

The PAF joints were made by driving a single HILTI X-ENP-19 (Hilti 2015) nail through a purlin and a 6 mm (0.25 in.) thick plate of hot-rolled steel. The purlin end had 125 mm x 6 mm (5 in. x 0.25 in.) thick plate bolted to it and the plate end had a 125 mm (5 in.) purlin piece connected to it, ensuring lateral symmetry and preventing eccentric loading as shown in Fig. 3- 5b. For both the screw and PAF joints, load was applied to both the top and bottom ends of the joint through hydraulic wedge grips.

3.5.2 Instrumentation

The test frame's built-in force and displacement transducers were used for all force and deformation measurements, respectively. As shown in Fig. 3- 6, four Optotrak (NDI 2005) markers were attached to the specimen to monitor slip in accordance with AISI-904 (2017). The test frame's crosshead to which the upper grip is attached was adjusted and locked in place, ensuring a firm grip on the top half of the test specimen at the start of each test. The bottom half of the specimen was held in the bottom grip attached to the test frame's actuator head. Markers 1 and 2 were mobile, as they were attached to the bottom half of the specimen, while markers 3 and 4 were stationary, attached to the top half of the specimen.

3.5.3 Material Properties

Mechanical properties of the light-gage structural studs and hot-rolled steel plates used in the tests are presented in Table 3- 2, based on manufacturers' mechanical properties test report.

3.5.4 Test Matrix

Nine unique joint configurations results in a total of seventy-two (72) tests. Test name designations for screw testing corresponded to the mill thickness designations (SSMA 2015) of the steel in mils, the fastener size, and the displacement rate. Monotonic tests were represented by *M*, quasi-static cyclic by *Q*, and higher rate cyclic tests were represented by *S* and *F* for 0.5 Hz and 3 Hz, respectively. For example, test 54-54-10-Q1 represents two 1.48 mm (0.057 in.) thick purlins fastened with a No. 10 screw, subjected to the quasi-static cyclic displacement loading protocol. The final number '1' designates the first in a series of similar tests. Similarly, for the PAF tests, 54-PAF-Q1 represents the first 1.45 mm (0.057 in.) thick purlin with a single HILTI X-ENP-19 (Hilti 2015) nail, subjected to the quasi-static cyclic displacement loading protocol.

3.5.5 Displacement Protocol

Monotonic testing was performed at a constant displacement rate of 0.025 mm/s (0.001 in./s) as recommended in Okasha (2004). The results initially obtained from the monotonic tests were used to determine appropriate displacement amplitudes for cyclic tests. Cyclic testing utilized the FEMA loading protocol described in section 3.4.3, with a minimum of 6 cycles applied prior to reaching a pre-determined value of Δ_o . A unified approach was used to determine this value of Δ_o , based on the least ductile monotonic test results considering all joint configurations, and applying the secant stiffness method (Essa et al. 2003). The FEMA cyclic displacement protocol is specified for quasi-static testing. However, to examine rate effects on fastener behavior, the displacement protocol was also applied at loading rates of 0.5 Hz and 3 Hz.

3.5.6 Pinching4 Parameters Determination

The *pinching4* positive and negative backbone parameters were determined by minimizing the sum of the squared error between the model's force prediction and test results. The backbone of the test results was first determined using Matlab's *boundary* command, with a shrink factor of 1.0. Matlab's *fminsearch* routine was used to optimize the desired backbone parameters for error minimization. Anchor points from test results were selected as follows; ePd_2 =displacement at peak positive load, ePf_2 =peak positive load, ePd_4 =displacement at fastener failure/most extreme positive displacement and $ePf_4=0$; eNd_2 =displacement at peak negative load, eNf_2 =peak negative load, eNd_4 =displacement at fastener failure/most extreme negative displacement and $eNf_4=0$. These anchor points were kept outside the optimization loop for stability.

The unloading-reloading parameters were determined by minimizing the error between the total hysteretic area between the *pinching4* model and the test results. For stability in the optimization process, $uForceP$ was selected to be equal to $uForceN$, and $rForceP$ was set equal to

rForceN. The four parameters reflected the width of the band around the x-axis for the respective tests results. While *uForceP* and *uForceN* represent the ratio of the force value to a fixed magnitude of force (eNf_3 , ePf_3), *rForceP* and *rForceN* relate force to varying force values along the backbone of the pinching model. *rForceP* and *rForceN* values were therefore optimized using the respective average forces in the 1st and 4th quadrants (positive and negative) of the test results.

3.6 Results

Monotonic test results for both the screw fasteners and the PAFs, used to determine the cyclic loading protocol, are presented in Fig. 3- 7. The response of 97-97-12-M, the least ductile of the screw-fastened joint configurations, was used to develop the unified cyclic displacement protocol for all tests. The magnitude of Δ_o was selected as 0.15 mm (0.006 in.) based on assuming elastic behavior, determined using secant stiffness up to the peak load (Essa et al. 2003).

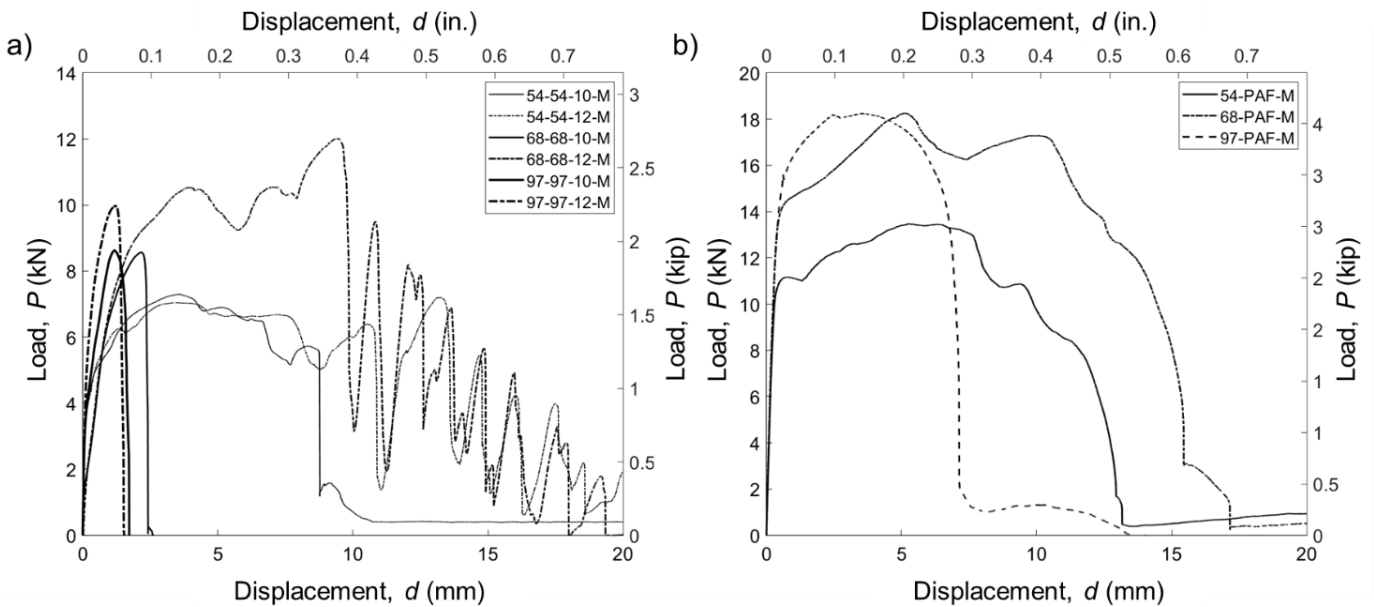


Fig. 3- 7: Monotonic load vs displacement plots for a) screws b) powder-actuated fasteners

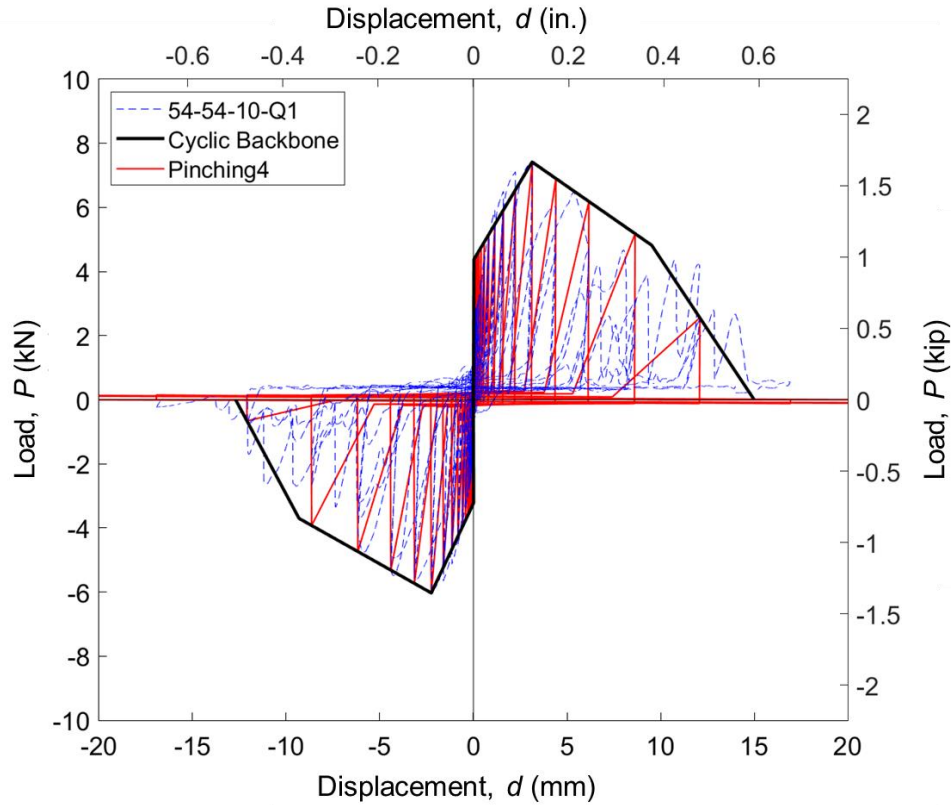


Fig. 3- 8: Cyclic force-deformation response for 54-54-10-Q1

3.6.1 Peak Loads and Failure Modes

The average peak load, P_c , for each respective joint configuration and cyclic loading rate is compared with code-based estimates and presented in Table 3- 3. Peak loads, failure modes, and comparisons with empirically-based code equations for individual tests are presented in Appendix C.

Table 3- 3: Peak loads vs AISI/SDI predicted maximum loads

Test	Loading rate	Peak Load	CoV	AISI/SDI	
		P_c kN (kip)		P_d kN (kip)	P_c/P_d
54-54-10	Q	7.2 (1.6)	0.038	7.2 (1.6)	1.00
	0.5 Hz	7.9 (1.8)	0.027	7.2 (1.6)	1.10
	3.0 Hz	7.4 (1.7)	0.040	7.2 (1.6)	1.03
54-54-12	Q	7.5 (1.7)	0.015	10.1 (2.3)	0.74
	0.5 Hz	7.4 (1.7)	0.054	10.1 (2.3)	0.73
	3.0 Hz	7.9 (1.8)	0.037	10.1 (2.3)	0.78
68-68-10	Q	8.0 (1.8)	0.027	7.2 (1.6)	1.11
	0.5 Hz	8.7 (2.0)	0.033	7.2 (1.6)	1.20
	3.0 Hz	8.4 (1.9)	0.042	7.2 (1.6)	1.17
68-68-12	Q	10.3 (2.3)	0.051	11.2 (2.5)	0.92
	0.5 Hz	10.3 (2.3)	0.037	11.2 (2.5)	0.92
	3.0 Hz	10.3 (2.3)	0.053	11.2 (2.5)	0.92
97-97-10	Q	9.1 (2.0)	0.140	7.2 (1.6)	1.26
	0.5 Hz	8.0 (1.8)	0.016	7.2 (1.6)	1.11
	3.0 Hz	8.3 (1.9)	0.038	7.2 (1.6)	1.15
97-97-12	Q	10.2 (2.3)	0.037	11.2 (2.5)	0.91
	0.5 Hz	11.0 (2.5)	0.023	11.2 (2.5)	0.98
	3.0 Hz	11.0 (2.5)	0.016	11.2 (2.5)	0.98
54-PAF	Q	12.1 (2.7)	0.045	13.4 (3.0)	0.90
68-PAF	Q	15.5 (3.5)	0.030	16.5 (3.7)	0.94
97-PAF	Q	15.1 (3.4)	0.026	22.0 (4.9)	0.69

Table 3- 4: Positive displacement backbone parameters

Test	Loading		<i>ePd1</i> mm (in.)	<i>ePd2</i> mm (in.)	<i>ePd3</i> mm (in.)	<i>ePd4</i> mm (in.)
54-54-10	<i>Q</i>	<i>Mean</i>	0.030 (0.001)	3.56 (0.14)	8.26 (0.33)	13.33 (0.52)
		<i>CoV</i>	0.996	0.204	0.135	0.115
	0.5Hz	<i>Mean</i>	0.037 (0.001)	3.12 (0.12)	6.21 (0.24)	8.87 (0.35)
		<i>CoV</i>	0.849	0.000	0.277	0.335
	3.0Hz	<i>Mean</i>	0.033 (0.001)	3.01 (0.12)	6.35 (0.25)	9.50 (0.37)
		<i>CoV</i>	1.039	0.012	0.083	0.091
54-54-12	<i>Q</i>	<i>Mean</i>	0.030 (0.001)	3.14 (0.12)	8.51 (0.34)	13.00 (0.51)
		<i>CoV</i>	0.925	0.001	0.241	0.134
	0.5Hz	<i>Mean</i>	0.032 (0.001)	2.82 (0.11)	9.81 (0.39)	14.00 (0.55)
		<i>CoV</i>	0.893	0.184	0.207	0.124
	3.0Hz	<i>Mean</i>	0.080 (0.003)	4.78 (0.19)	8.01 (0.32)	11.00 (0.43)
		<i>CoV</i>	0.179	0.675	0.222	0.000
68-68-10	<i>Q</i>	<i>Mean</i>	0.013 (0.000)	1.87 (0.07)	1.93 (0.08)	2.23 (0.09)
		<i>CoV</i>	0.867	0.124	0.014	0.026
	0.5Hz	<i>Mean</i>	0.044 (0.002)	2.11 (0.08)	2.19 (0.09)	2.43 (0.10)
		<i>CoV</i>	0.332	0.226	0.139	0.166
	3.0Hz	<i>Mean</i>	0.076 (0.003)	1.72 (0.07)	1.94 (0.08)	2.13 (0.08)
		<i>CoV</i>	0.398	0.164	0.082	0.054
68-68-12	<i>Q</i>	<i>Mean</i>	0.016 (0.001)	4.64 (0.18)	7.35 (0.29)	9.67 (0.38)
		<i>CoV</i>	1.732	0.597	0.202	0.208
	0.5Hz	<i>Mean</i>	0.045 (0.002)	3.10 (0.12)	6.15 (0.24)	9.50 (0.37)
		<i>CoV</i>	0.587	0.009	0.186	0.139
	3.0Hz	<i>Mean</i>	0.109 (0.004)	3.41 (0.13)	5.51 (0.22)	8.49 (0.33)
		<i>CoV</i>	0.640	0.198	0.191	0.178
97-97-10	<i>Q</i>	<i>Mean</i>	0.001 (0.000)	1.08 (0.04)	1.30 (0.05)	1.21 (0.05)
		<i>CoV</i>	1.732	0.246	0.318	0.279
	0.5Hz	<i>Mean</i>	0.033 (0.001)	0.92 (0.04)	1.22 (0.05)	1.09 (0.04)
		<i>CoV</i>	0.450	0.201	0.123	0.224
	3.0Hz	<i>Mean</i>	0.063 (0.002)	1.08 (0.04)	1.45 (0.06)	1.46 (0.06)
		<i>CoV</i>	0.562	0.037	0.129	0.160
97-97-12	<i>Q</i>	<i>Mean</i>	0.015 (0.001)	1.54 (0.06)	1.91 (0.08)	2.00 (0.08)
		<i>CoV</i>	1.732	0.077	0.164	0.182
	0.5Hz	<i>Mean</i>	0.071 (0.003)	1.73 (0.07)	2.05 (0.08)	1.96 (0.08)
		<i>CoV</i>	0.141	0.145	0.187	0.213
	3.0Hz	<i>Mean</i>	0.103 (0.004)	1.56 (0.06)	2.08 (0.08)	2.15 (0.08)
		<i>CoV</i>	0.350	0.001	0.100	0.077
54-PAF	<i>Q</i>	<i>Mean</i>	0.161 (0.006)	2.01 (0.08)	15.04 (0.59)	15.75 (0.62)
		<i>CoV</i>	0.162	0.031	0.340	0.340
68-PAF	<i>Q</i>	<i>Mean</i>	0.089 (0.003)	3.24 (0.13)	4.00 (0.16)	4.40 (0.17)
		<i>CoV</i>	0.137	0.204	0.198	0.233
97-PAF	<i>Q</i>	<i>Mean</i>	0.102 (0.004)	0.74 (0.03)	2.25 (0.09)	4.06 (0.16)
		<i>CoV</i>	0.218	0.017	0.008	0.000

Table 3- 5: Positive force backbone parameters

Test	Loading		<i>ePf1</i>	<i>ePf2</i>	<i>ePf3</i>	<i>ePf4</i>
			kN (kip)	kN (kip)	kN (kip)	kN (kip)
54-54-10	<i>Q</i>	<i>Mean</i>	4.41 (0.99)	7.23 (1.62)	4.77 (1.07)	0.0 (0.0)
		<i>CoV</i>	0.095	0.038	0.059	
	0.5Hz	<i>Mean</i>	4.14 (0.93)	7.51 (1.69)	4.87 (1.09)	0.0 (0.0)
		<i>CoV</i>	0.132	0.066	0.064	
	3.0Hz	<i>Mean</i>	3.96 (0.89)	7.37 (1.66)	4.71 (1.06)	0.0 (0.0)
		<i>CoV</i>	0.124	0.054	0.068	
54-54-12	<i>Q</i>	<i>Mean</i>	4.32 (0.97)	7.46 (1.68)	4.90 (1.10)	0.0 (0.0)
		<i>CoV</i>	0.134	0.015	0.043	
	0.5Hz	<i>Mean</i>	4.08 (0.92)	7.37 (1.66)	4.70 (1.06)	0.0 (0.0)
		<i>CoV</i>	0.143	0.054	0.099	
	3.0Hz	<i>Mean</i>	4.57 (1.03)	7.91 (1.78)	5.16 (1.16)	0.0 (0.0)
		<i>CoV</i>	0.073	0.037	0.050	
68-68-10	<i>Q</i>	<i>Mean</i>	4.98 (1.12)	7.90 (1.78)	5.33 (1.20)	0.0 (0.0)
		<i>CoV</i>	0.072	0.048	0.053	
	0.5Hz	<i>Mean</i>	5.03 (1.13)	8.66 (1.95)	5.70 (1.28)	0.0 (0.0)
		<i>CoV</i>	0.082	0.033	0.029	
	3.0Hz	<i>Mean</i>	4.84 (1.09)	8.35 (1.88)	5.52 (1.24)	0.0 (0.0)
		<i>CoV</i>	0.045	0.042	0.042	
68-68-12	<i>Q</i>	<i>Mean</i>	5.94 (1.34)	10.19 (2.29)	6.70 (1.51)	0.0 (0.0)
		<i>CoV</i>	0.073	0.074	0.069	
	0.5Hz	<i>Mean</i>	6.19 (1.39)	10.34 (2.32)	6.94 (1.56)	0.0 (0.0)
		<i>CoV</i>	0.066	0.037	0.031	
	3.0Hz	<i>Mean</i>	6.23 (1.40)	10.30 (2.31)	6.70 (1.51)	0.0 (0.0)
		<i>CoV</i>	0.067	0.053	0.051	
97-97-10	<i>Q</i>	<i>Mean</i>	4.31 (0.97)	7.23 (1.62)	4.70 (1.06)	0.0 (0.0)
		<i>CoV</i>	0.194	0.234	0.210	
	0.5Hz	<i>Mean</i>	4.35 (0.98)	7.71 (1.73)	5.02 (1.13)	0.0 (0.0)
		<i>CoV</i>	0.083	0.066	0.063	
	3.0Hz	<i>Mean</i>	4.75 (1.07)	8.25 (1.85)	5.34 (1.20)	0.0 (0.0)
		<i>CoV</i>	0.028	0.027	0.023	
97-97-12	<i>Q</i>	<i>Mean</i>	6.34 (1.43)	10.01 (2.25)	6.74 (1.51)	0.0 (0.0)
		<i>CoV</i>	0.014	0.017	0.011	
	0.5Hz	<i>Mean</i>	6.37 (1.43)	10.98 (2.47)	7.29 (1.64)	0.0 (0.0)
		<i>CoV</i>	0.020	0.023	0.036	
	3.0Hz	<i>Mean</i>	6.49 (1.46)	11.03 (2.48)	7.19 (1.61)	0.0 (0.0)
		<i>CoV</i>	0.042	0.016	0.016	
54-PAF	<i>Q</i>	<i>Mean</i>	10.46 (2.35)	12.08 (2.72)	9.47 (2.13)	0.0 (0.0)
		<i>CoV</i>	0.091	0.044	0.045	
68-PAF	<i>Q</i>	<i>Mean</i>	14.98 (3.37)	15.41 (3.46)	10.03 (2.25)	0.0 (0.0)
		<i>CoV</i>	0.041	0.017	0.009	
97-PAF	<i>Q</i>	<i>Mean</i>	12.04 (2.70)	15.08 (3.39)	4.88 (1.10)	0.0 (0.0)
		<i>CoV</i>	0.023	0.026	0.023	

Table 3- 6: Negative displacement backbone parameters

Test	Loading		<i>eNd1</i> mm (in.)	<i>eNd2</i> mm (in.)	<i>eNd3</i> mm (in.)	<i>eNd4</i> mm (in.)
54-54-10	<i>Q</i>	<i>Mean</i>	-0.005 (0.000)	-2.24 (-0.09)	-7.65 (-0.30)	-11.23 (-0.44)
		<i>CoV</i>	-1.732	-0.002	-0.208	-0.175
	0.5Hz	<i>Mean</i>	-0.021 (-0.001)	-3.12 (-0.12)	-6.28 (-0.25)	-9.08 (-0.36)
		<i>CoV</i>	-1.656	0.000	-0.406	-0.278
	3.0Hz	<i>Mean</i>	-0.013 (-0.001)	-3.01 (-0.12)	-5.34 (-0.21)	-8.54 (-0.34)
		<i>CoV</i>	-0.613	0.000	-0.092	-0.093
54-54-12	<i>Q</i>	<i>Mean</i>	-0.030 (-0.001)	-2.25 (-0.09)	-7.56 (-0.30)	-12.23 (-0.48)
		<i>CoV</i>	-0.358	0.000	-0.053	-0.033
	0.5Hz	<i>Mean</i>	-0.010 (0.000)	-2.82 (-0.11)	-8.11 (-0.32)	-13.00 (-0.51)
		<i>CoV</i>	-0.577	-0.183	-0.303	-0.308
	3.0Hz	<i>Mean</i>	-0.006 (0.000)	-3.02 (-0.12)	-6.01 (-0.24)	-9.00 (-0.35)
		<i>CoV</i>	-0.933	-0.006	-0.085	0.000
68-68-10	<i>Q</i>	<i>Mean</i>	-0.016 (-0.001)	-1.60 (-0.06)	-1.88 (-0.07)	-2.03 (-0.08)
		<i>CoV</i>	-1.732	-0.006	-0.185	-0.186
	0.5Hz	<i>Mean</i>	0.000 (0.000)	-1.79 (-0.07)	-1.97 (-0.08)	-2.00 (-0.08)
		<i>CoV</i>	0.000	-0.206	-0.195	-0.173
	3.0Hz	<i>Mean</i>	-0.035 (-0.001)	-1.64 (-0.06)	-1.61 (-0.06)	-1.80 (-0.07)
		<i>CoV</i>	-0.701	-0.163	-0.216	-0.192
68-68-12	<i>Q</i>	<i>Mean</i>	-0.043 (-0.002)	-4.15 (-0.16)	-5.71 (-0.22)	-8.13 (-0.32)
		<i>CoV</i>	-0.214	-0.419	-0.074	-0.123
	0.5Hz	<i>Mean</i>	-0.002 (0.000)	-3.12 (-0.12)	-6.35 (-0.25)	-8.89 (-0.35)
		<i>CoV</i>	-1.732	0.000	-0.115	0.000
	3.0Hz	<i>Mean</i>	-0.084 (-0.003)	-3.12 (-0.12)	-4.93 (-0.19)	-7.86 (-0.31)
		<i>CoV</i>	-0.280	-0.332	-0.140	-0.138
97-97-10	<i>Q</i>	<i>Mean</i>	-0.006 (0.000)	-0.92 (-0.04)	-1.20 (-0.05)	-1.19 (-0.05)
		<i>CoV</i>	-1.732	-0.212	-0.409	-0.354
	0.5Hz	<i>Mean</i>	-0.002 (0.000)	-0.73 (-0.03)	-1.06 (-0.04)	-1.20 (-0.05)
		<i>CoV</i>	-0.099	-0.185	-0.337	-0.328
	3.0Hz	<i>Mean</i>	-0.029 (-0.001)	-0.99 (-0.04)	-1.15 (-0.05)	-1.07 (-0.04)
		<i>CoV</i>	-1.184	-0.183	-0.127	-0.206
97-97-12	<i>Q</i>	<i>Mean</i>	-0.029 (-0.001)	-1.45 (-0.06)	-1.79 (-0.07)	-1.84 (-0.07)
		<i>CoV</i>	-1.463	-0.183	-0.181	-0.223
	0.5Hz	<i>Mean</i>	-0.010 (0.000)	-1.43 (-0.06)	-1.80 (-0.07)	-1.70 (-0.07)
		<i>CoV</i>	-1.732	-0.184	-0.089	-0.103
	3.0Hz	<i>Mean</i>	-0.113 (-0.004)	-1.52 (-0.06)	-1.51 (-0.06)	-1.58 (-0.06)
		<i>CoV</i>	-0.108	-4.564	-0.339	0.000
54-PAF	<i>Q</i>	<i>Mean</i>	-0.107 (-0.004)	-5.46 (-0.22)	-19.71 (-0.78)	-21.34 (-0.84)
		<i>CoV</i>	-0.107	-1.270	-0.026	0.000
68-PAF	<i>Q</i>	<i>Mean</i>	-0.011 (0.000)	-2.58 (-0.10)	-4.46 (-0.18)	-4.40 (-0.17)
		<i>CoV</i>	-1.255	-0.182	-0.249	-0.233
97-PAF	<i>Q</i>	<i>Mean</i>	-0.013 (-0.001)	-0.53 (-0.02)	-2.80 (-0.11)	-4.06 (-0.16)
		<i>CoV</i>	-1.128	0.000	-0.180	0.000

Table 3- 7: Negative force backbone parameters

Test	Loading		<i>eNf1</i> kN (<i>kip</i>)	<i>eNf2</i> kN (<i>kip</i>)	<i>eNf3</i> kN (<i>kip</i>)	<i>eNf4</i> kN (<i>kip</i>)
54-54-10	<i>Q</i>	<i>Mean</i>	-3.44 (-0.77)	-6.20 (-1.39)	-4.00 (-0.90)	0.0 (0.0)
		<i>CoV</i>	-0.114	-0.024	-0.064	
	0.5Hz	<i>Mean</i>	-4.05 (-0.91)	-7.05 (-1.58)	-4.52 (-1.02)	0.0 (0.0)
		<i>CoV</i>	-0.193	-0.131	-0.153	
	3.0Hz	<i>Mean</i>	-4.10 (-0.92)	-6.61 (-1.49)	-4.40 (-0.99)	0.0 (0.0)
		<i>CoV</i>	-0.089	-0.066	-0.066	
54-54-12	<i>Q</i>	<i>Mean</i>	-4.13 (-0.93)	-6.66 (-1.50)	-4.48 (-1.01)	0.0 (0.0)
		<i>CoV</i>	-0.039	-0.025	-0.022	
	0.5Hz	<i>Mean</i>	-4.27 (-0.96)	-6.72 (-1.51)	-4.59 (-1.03)	0.0 (0.0)
		<i>CoV</i>	-0.087	-0.087	-0.086	
	3.0Hz	<i>Mean</i>	-3.82 (-0.86)	-6.85 (-1.54)	-4.50 (-1.01)	0.0 (0.0)
		<i>CoV</i>	-0.054	-0.068	-0.032	
68-68-10	<i>Q</i>	<i>Mean</i>	-4.53 (-1.02)	-7.74 (-1.74)	-5.01 (-1.13)	0.0 (0.0)
		<i>CoV</i>	-0.011	-0.028	-0.007	
	0.5Hz	<i>Mean</i>	-4.34 (-0.98)	-7.97 (-1.79)	-5.13 (-1.15)	0.0 (0.0)
		<i>CoV</i>	-0.126	-0.019	-0.049	
	3.0Hz	<i>Mean</i>	-4.52 (-1.02)	-7.63 (-1.72)	-5.08 (-1.14)	0.0 (0.0)
		<i>CoV</i>	-0.051	-0.029	-0.041	
68-68-12	<i>Q</i>	<i>Mean</i>	-5.81 (-1.31)	-9.19 (-2.06)	-6.26 (-1.41)	0.0 (0.0)
		<i>CoV</i>	-0.069	-0.059	-0.057	
	0.5Hz	<i>Mean</i>	-5.18 (-1.16)	-9.49 (-2.13)	-6.11 (-1.37)	0.0 (0.0)
		<i>CoV</i>	-0.060	-0.079	-0.042	
	3.0Hz	<i>Mean</i>	-5.81 (-1.31)	-9.34 (-2.10)	-6.23 (-1.40)	0.0 (0.0)
		<i>CoV</i>	-0.083	-0.081	-0.096	
97-97-10	<i>Q</i>	<i>Mean</i>	-5.98 (-1.34)	-8.85 (-1.99)	-6.11 (-1.37)	0.0 (0.0)
		<i>CoV</i>	-0.275	-0.166	-0.208	
	0.5Hz	<i>Mean</i>	-4.71 (-1.06)	-7.40 (-1.66)	-5.02 (-1.13)	0.0 (0.0)
		<i>CoV</i>	-0.067	-0.066	-0.066	
	3.0Hz	<i>Mean</i>	-4.27 (-0.96)	-7.37 (-1.66)	-4.84 (-1.09)	0.0 (0.0)
		<i>CoV</i>	-0.124	-0.167	-0.180	
97-97-12	<i>Q</i>	<i>Mean</i>	-6.01 (-1.35)	-9.69 (-2.18)	-6.49 (-1.46)	0.0 (0.0)
		<i>CoV</i>	-0.098	-0.084	-0.093	
	0.5Hz	<i>Mean</i>	-5.85 (-1.31)	-9.97 (-2.24)	-6.55 (-1.47)	0.0 (0.0)
		<i>CoV</i>	-0.086	-0.063	-0.053	
	3.0Hz	<i>Mean</i>	-5.80 (-1.30)	-9.83 (-2.21)	-6.44 (-1.45)	0.0 (0.0)
		<i>CoV</i>	-0.213	-0.077	-0.113	
54-PAF	<i>Q</i>	<i>Mean</i>	-11.28 (-2.53)	-11.56 (-2.60)	-9.30 (-2.09)	0.0 (0.0)
		<i>CoV</i>	-0.109	-0.065	-0.078	
68-PAF	<i>Q</i>	<i>Mean</i>	-16.57 (-3.72)	-15.45 (-3.47)	-10.19 (-2.29)	0.0 (0.0)
		<i>CoV</i>	-0.014	-0.035	-0.038	
97-PAF	<i>Q</i>	<i>Mean</i>	-11.08 (-2.49)	-14.07 (-3.16)	-4.50 (-1.01)	0.0 (0.0)
		<i>CoV</i>	-0.294	-0.040	-0.084	

Table 3- 8: Unloading-reloading parameters

Test	Loading rate		<i>rDispP</i>	<i>rForceP</i>	<i>rDispN</i>	<i>rForceN</i>	<i>uForceP</i>	<i>uForceN</i>
54-54-10	<i>Q</i>	<i>Mean</i>	0.470	0.035	0.470	0.036	0.020	0.020
		<i>CoV</i>	0.358	0.059	0.358	0.062	0.000	0.000
	0.5Hz	<i>Mean</i>	0.536	0.041	0.536	0.039	0.020	0.020
		<i>CoV</i>	0.099	0.064	0.099	0.048	0.000	0.000
	3.0Hz	<i>Mean</i>	0.464	0.040	0.464	0.038	0.020	0.020
		<i>CoV</i>	0.423	0.023	0.423	0.034	0.000	0.000
54-54-12	<i>Q</i>	<i>Mean</i>	0.356	0.036	0.356	0.035	0.020	0.020
		<i>CoV</i>	0.357	0.011	0.357	0.015	0.000	0.000
	0.5Hz	<i>Mean</i>	0.367	0.035	0.367	0.034	0.020	0.020
		<i>CoV</i>	0.217	0.029	0.217	0.080	0.000	0.000
	3.0Hz	<i>Mean</i>	0.359	0.039	0.359	0.039	0.020	0.020
		<i>CoV</i>	0.088	0.039	0.088	0.040	0.000	0.000
68-68-10	<i>Q</i>	<i>Mean</i>	0.901	0.025	0.901	0.026	0.010	0.010
		<i>CoV</i>	0.039	0.026	0.039	0.082	0.000	0.000
	0.5Hz	<i>Mean</i>	0.792	0.027	0.792	0.027	0.010	0.010
		<i>CoV</i>	0.149	0.117	0.149	0.071	0.000	0.000
	3.0Hz	<i>Mean</i>	0.800	0.027	0.800	0.028	0.010	0.010
		<i>CoV</i>	0.103	0.104	0.103	0.046	0.060	0.060
68-68-12	<i>Q</i>	<i>Mean</i>	0.450	0.038	0.450	0.038	0.020	0.020
		<i>CoV</i>	0.102	0.077	0.102	0.019	0.000	0.000
	0.5Hz	<i>Mean</i>	0.542	0.038	0.542	0.038	0.020	0.020
		<i>CoV</i>	0.119	0.011	0.119	0.027	0.000	0.000
	3.0Hz	<i>Mean</i>	0.380	0.042	0.380	0.040	0.020	0.020
		<i>CoV</i>	0.285	0.016	0.285	0.041	0.000	0.000
97-97-10	<i>Q</i>	<i>Mean</i>	0.928	0.014	0.928	0.013	0.005	0.005
		<i>CoV</i>	0.056	0.068	0.056	0.073	0.000	0.000
	0.5Hz	<i>Mean</i>	0.410	0.020	0.410	0.019	0.007	0.007
		<i>CoV</i>	0.913	0.412	0.913	0.367	0.433	0.433
	3.0Hz	<i>Mean</i>	0.547	0.020	0.547	0.021	0.007	0.007
		<i>CoV</i>	0.240	0.524	0.240	0.555	0.433	0.433
97-97-12	<i>Q</i>	<i>Mean</i>	0.543	0.012	0.543	0.013	0.005	0.005
		<i>CoV</i>	0.167	0.059	0.167	0.011	0.000	0.000
	0.5Hz	<i>Mean</i>	0.661	0.013	0.661	0.013	0.005	0.005
		<i>CoV</i>	0.192	0.059	0.192	0.050	0.000	0.000
	3.0Hz	<i>Mean</i>	0.508	0.014	0.508	0.016	0.005	0.005
		<i>CoV</i>	0.311	0.100	0.311	0.029	0.000	0.000
54-PAF	<i>Q</i>	<i>Mean</i>	0.706	0.073	0.706	0.062	0.050	0.050
		<i>CoV</i>	0.028	0.067	0.028	0.027	0.000	0.000
68-PAF	<i>Q</i>	<i>Mean</i>	0.605	0.016	0.605	0.015	0.010	0.010
		<i>CoV</i>	0.151	0.021	0.151	0.045	0.000	0.000
97-PAF	<i>Q</i>	<i>Mean</i>	0.634	0.011	0.634	0.010	0.005	0.005
		<i>CoV</i>	0.027	0.057	0.027	0.051	0.000	0.000

3.6.2 *Pinching4* Model Parameters

For each cyclic test, *pinching4* hysteretic models were generated, with parameters optimized using as described in Section 3.5.6. A total of 63 hysteretic models were generated for all tests, with a typical plot presented in Fig. 3- 7. The average of the parameters taken from the optimized parameters for the respective joints and loading rates are summarized in Tables 3- 4 through 3- 8. The full set of cyclic hysteretic parameters used for generating the *pinching4* models for all tests are presented as supplemental information, S2.

3.7 Discussion

The predominant modes of failure in the screw joints were found to be tilting and bearing in 54-54-10, 54-54-12 and 68-68-12, and screw shear failure in 68-68-10, 97-97-10 and 97-97-12. Across the six unique screw joints tested, increasing the loading rate typically increased the average peak load, P_c . The highest increase in peak load occurred in 97-97-12, from 10.2 kN (2.3 kips) in the monotonic test to 11.0 kN (2.5 kips) when tested at 3 Hz, an increase in peak force of 8%. This was consistent with the increasing yield strength in the material around the screw shank due to increase in the strain rate, prior to screw shear failure. Joint 97-97-10 showed an anomaly, with the highest average peak load occurring in the monotonic test. This was the result of joint 97-97-10 being the worst case for shear failure (thickest plate and smallest screw diameter). In the joint, screw shear dominates the response of the joint to displacement, hence there was very little effect on the overall response from screw bearing on the material and yielding around the screw. There was no clear consistent pattern in the screw joints response, between increasing the loading rate from 0.5 Hz to 3.0 Hz.

All screw joints tested showed values of P_c within 27% of AISI-S100 (2016) screw joint shear strength prediction. Joint 54-54-10, tested under quasi-static cyclic load was within 1% of

the AISI-S100 (2016) shear strength prediction, and showed the best agreement. Joint 54-54-12, tested under 0.5 Hz cyclic load was within 27% of the AISI-S100 (2016) shear strength prediction, and showed the worst agreement of the screw joints tested.

The PAFs were not tested under varying load rates, hence only their response under quasi-static cyclic loads are discussed. The dominant failure mode was found to be bearing and tear-out in the light-gage steel in 54-PAF and 68-PAF, and tilting and pull-out in 97-PAF. The average values of P_c in 54-PAF and 68-PAF were within 10% of SDI (2015) predicted values. 97-PAF was considered anomalous because unlike the other joints, it was unable to mobilize its full joint shear strength prior to pull-out due to relatively shallow embedment.

The derived backbone parameters derived are interdependent, and for each unique joint and loading rate, they collectively describe the *pinching4* hysteretic model aimed at minimizing error in the overall cyclic behavior when incorporated in numeric modeling. Individual parameters are not comparable across different joint types, however, the degree of consistency of a particular parameter for a particular joint type and loading rate is reflected in the magnitude of their coefficients of variation (*CoV*) as indicated in Tables 3- 4 through 3- 8. The backbone parameters $ePd4$ and $eNd4$ provided for screw joints dominated by tilting and bearing failure are influenced by the length of screw and thread patterns, and are only applicable to this set of tests.

3.8 Conclusions

Light-gage steel screw and PAF joints were tested under monotonic and cyclic loads. The thickness of the light-gage steel plates and diameter of the screw fasteners were varied to assess the joint peak load performance and to determine hysteretic backbone and pinching path parameters for analytical modeling. Peak loads recorded across all screw joints generally showed

good agreement with code-predicted values. It was observed that, increasing the loading rate from quasi-static to 0.5 Hz and 3.0 Hz generally increased the peak loads recorded for the screw joints.

Though SDI (2015) sets an upper plate thickness limit of 1.52 mm (0.06 in.) for computing the shear strength, Q_f of the HILTI X-ENP-19 (Hilti 2015) PAF, it was observed from the test results that full shear strength was mobilized in a PAF joint with a plate thickness of 1.81 mm (0.071 in.). The SDI (2015) upper plate thickness limit could therefore be increased safely to 1.81 mm (0.071 in.) based on test results. It was observed however that in PAF joints with 2.48 mm (0.098 in.) thick plates, the thickness of the plate resulted in shallow embedment lengths of the PAFs in the support steel, leading to fastener pull-out precluding the full magnitude of Q_f from being mobilized. This observation implies that a plate thickness of 2.48 mm (0.098 in.) is above a suitable upper limit for computing Q_f based on SDI (2015) provisions.

Pinching4 hysteretic models have been generated for all joints tested cyclically, and these models are capable of representing the hysteretic behavior of these joints for analytical studies. Overall, this work contributes additional load-displacement, hysteresis characterization and general screw and PAF fastener behavior information, currently not available in published literature.

Chapter 4: Behavior of a Lightweight Modular Steel Floor

Diaphragm under Quasi-static Cyclic Loading. I: Experimental

Evaluation

4.1 Abstract

A lightweight modular steel floor system was developed at the University of Kansas in an effort to make modern structures more environmentally and economically sustainable. This research investigates the diaphragm behavior of the floor system using a cantilever diaphragm setup of two full-scale prototype floors, tested experimentally with a quasi-static cyclic displacement protocol and supported by non-linear finite element (FE) simulations. FE simulations were performed using incorporated fastener constitutive relationships developed from cyclic tests of single lap joints. The floors were tested to determine their stiffness under gravity loads prior to diaphragm testing.

The results obtained showed agreement between the gravity load stiffnesses recorded in the experimental results and the FE models. Additionally, peak loads and hysteretic areas recorded from the experiments and FE models showed trends indicating that the FE modeling technique used can be utilized for further parametric study of the floor system. The observed hysteretic behavior of the floor system from both the experiment and FE analysis indicated that the floor system can provide an alternative solution to current seismic design and construction practices, by potentially acting as an energy dissipating fuse during seismic activity.

4.2 Introduction

Construction and demolition of buildings are large consumers of natural resources and thus have significant associated environmental impacts (Wang et al. 2015). As natural resources become more scarce, structural engineers need to find innovative solutions to reduce material waste, both in terms of design methodologies and construction details. One approach to this is to make structures more rapidly constructible and adaptable to changes in occupancy and use (Ross et al. 2016, Boadi-Danquah et al. 2017a). Adaptable structures require modularity to allow for changes in building use to meet market needs. Such systems can be quickly adapted for reuse, or be deconstructed, moved, and reconstructed at a different location. Similarly, in the case of an extreme event such as a blast or earthquake, a resilient modular system should be limited to exhibiting repairable damage, and possess an inherent ability for components to be replaced. It is essential that the self-weight of these systems is kept low, enhancing the practical use of the system from a construction perspective and reducing inertial forces transmitted during seismic events, thereby minimizing damage. While these attributes provide both economic and life-safety resilience, no current system has all these characteristics.

In addition to serving as the primary gravity load resisting component of a building structure, floor systems are often responsible for transmitting lateral loads to the lateral force resisting system (LFRS) through diaphragm action. Under seismic loading, diaphragms transfer the inertial forces within a building to the seismic force resisting system (SFRS), while also providing lateral support to vertical elements in a framed structure (Moehle et al. 2010). The multiple roles of the floor in a framed building present the floor as a key area where innovation can be applied to make structures more efficient to meet future demands. Various systems have been developed to either improve upon the performance of conventional floor systems, including

systems that consider Design for Deconstruction (DfD) (Wang et al. 2015), or as a new paradigm aimed to facilitate reuse of materials (Colaco 1972, Hanaor 2000, Hsu et al. 2014). The most common of these systems utilize one-way bending behavior, resulting in large gravity loads from self-weight, and high inertia forces during extreme loading events. Limited research has been focused on utilizing two-way bending behavior to achieve lighter floors for steel structures (Ahmed et al. 2002 and Schaad 2005).

This paper presents a new lightweight modular two-way steel floor system that enables easy repair and reuse of components. The paper presents the vertical gravity load behavior and cyclic lateral diaphragm performance of the floor system, evaluated through two full-scale floor tests and non-linear finite element (FE) modeling. Initial static gravity load testing evaluated the displacement at the center of the floor and was compared with the central displacement of the FE model. Lateral diaphragm testing utilized a cantilevered test setup based on ASTM E455 (2019a), with a cyclic displacement protocol adapted from FEMA 461 (2007) applied to the free end. The results obtained from the experimental tests were used to validate non-linear FE models. For diaphragm assessment, a comparison was made between the average peak loads and the total dissipated energy obtained from the area of the hysteretic response in the experimental test, and the corresponding peak loads and hysteretic areas in the FE models. This comparison informed the suitability of the modeling technique for further parametric study.

The objective of the study presented in this paper is to assess the inelastic response of the novel lightweight modular floor system to an applied cyclic load, representing a seismic excitation, using both experimental and non-linear FE modeling of two full-scale prototype floors.

4.2.1 *Modular Steel Floor System*

The developed modular floor system is made of individual panels connected using a splice plate, as shown in Fig. 4- 1. Each panel is comprised of orthogonally-arranged light-gage steel Z-purlins, sandwiched between top and bottom light-gage steel plates. The orthogonal arrangement is achieved by cutting out the flanges and webs to permit perpendicular fitting of the purlins (Boadi-Danquah et al. 2017a). The top steel plate is connected to the top flanges of the purlins using self-drilling screws. The bottom plate is connected to the bottom flanges of the purlins using flare-bevel groove welds between the purlin bend radius and plate, and fillet welds between the edge of the purlin bottom flange and plate. The panels are assembled within a structural steel frame and spliced using light-gage steel cover plates and self-drilling screws. Along the perimeter, the floor system is connected to the supporting frame using powder-actuated fasteners (PAF). This detail is essential to facilitate the diaphragm performance of the floor system. After assembly, the floor is topped with plywood. The plywood topping limits buckling in the top plate, adds fire protection, helps with acoustics, and provides general load distribution. The floor has been developed to span an entire structural bay without need for intermediate beam supports.

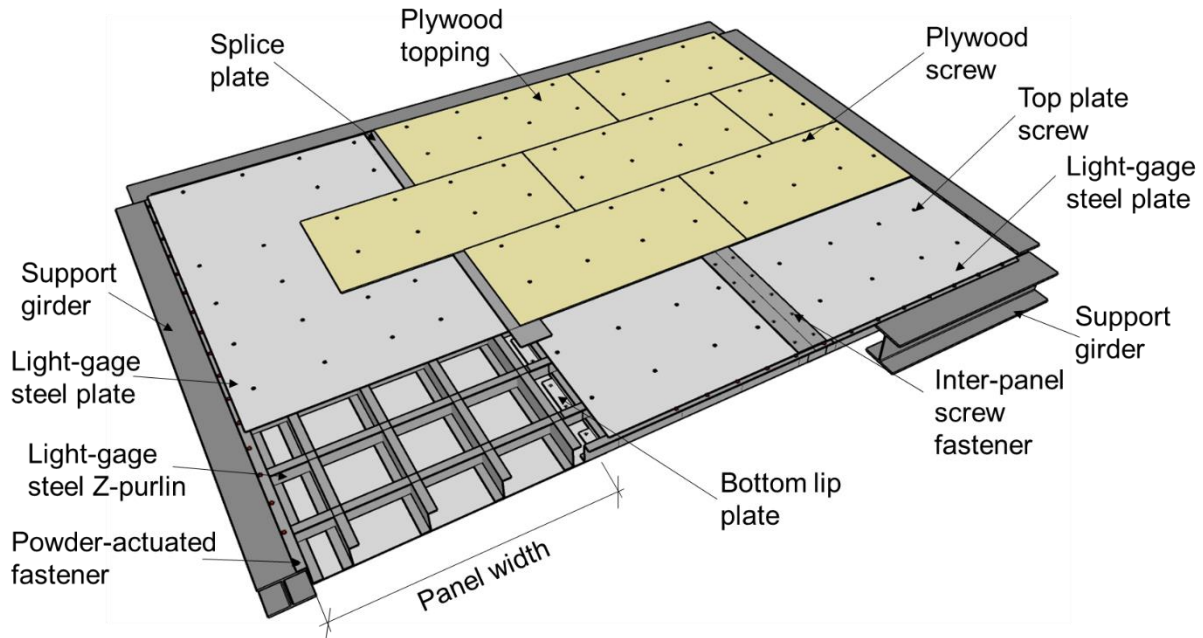


Fig. 4- 1: The lightweight modular steel floor system

The floor can be transported to the construction site as individual pre-fabricated panels, which are then lifted into place and assembled within the structural steel frame. Assembled panels can be deconstructed, moved, and reconfigured by unscrewing the panels, detaching them from support girders, repairing damaged components, and adapting them to form part of a new framed structure (Boadi-Danquah et al. 2017a). The system leverages the high mechanical strength-to-weight ratio of steel and two-way bending action to attain light weight. Additionally, panelizing the floor system ensures that modular and rapid construction can be achieved.

An analytical assessment of strength and vibration performance of the floor behavior under gravity loads was developed and presented in Boadi-Danquah et al. (2017a), Robertson et al. (2017) and MacLachlan et al. (2019). Additionally, the effects of varying the plate thickness, t_p , purlin thickness, t_c , purlin spacing, s , and purlin depth, d , on strength and vibration behavior of the floor system were also investigated and reported in the same publications. Structural assessment under gravity loads is based on multiple strength and serviceability limit states; yielding of

sandwich plate, failure of connectors at the interface between plates and Z-purlins, failure of panel-to-panel connection, web buckling of perimeter purlins, excessive deflection, and excessive vibration (Boadi-Danquah et al. 2017a and Robertson et al. 2017). Assessments were made using standard design codes and methodologies, adapted for the developed floor system and augmented by FE modeling in Abaqus CAE (DSS 2016). Performance assessments for gravity loads indicate the most severe gravity load limit are service load deflections and vibrations.

4.3 Diaphragm Test program

4.3.1 Test Frame

The cantilever diaphragm test was designed and arranged in accordance with ASTM E455 (2019a), shown schematically in Fig. 4- 2. The standard requires that test frame members meet minimum building design requirements, which resulted in the use of W360 x 134 (W14 x 90) members based on preliminary design of a 7.3 m x 5.5 m (24 ft x 18 ft) structural bay, with the floor subjected 2.4 kPa (50 psf) office loading (IBC 2015). The test frame is comprised of a pair of 5.5 m (18 ft) long transverse girders and pair of 7.3 m (24 ft) long longitudinal girders. One longitudinal girder was pinned at its two ends, and the opposite longitudinal girder, serving as the loading girder, was allowed to rack under transverse loading. The pinned corners of the test frame represented in Fig. 4- 2 were achieved by connecting the corners of the frame using double angle shear tabs to support braces, anchored to a concrete strong floor by means of post-tensioned anchor rods shown in Fig. 4- 3. The loading girder was additionally supported by three intermediate bearing supports, located at approximately quarter points along the girder length as shown in Fig. 4- 3. Polished steel plates were welded to the underside of the bottom flange of the loading girder and lubricated to minimize the effects of friction during cyclic testing.

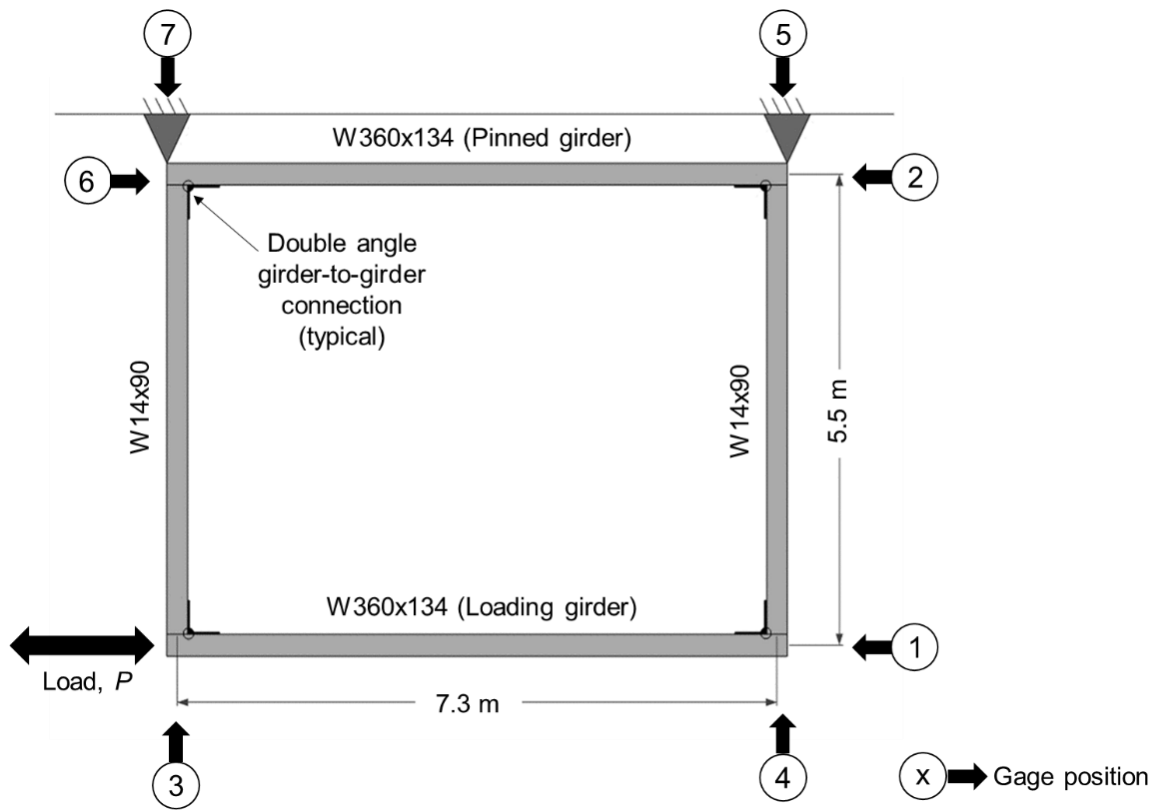


Fig. 4- 2: Plan view of cantilever diaphragm setup adapted from ASTM E455 (2019a)

Girder-to-girder connections were also made of double angle shear tabs as shown in Fig. 4- 3. Additional details of the frame and floor construction are presented in MacLachlan (2019).

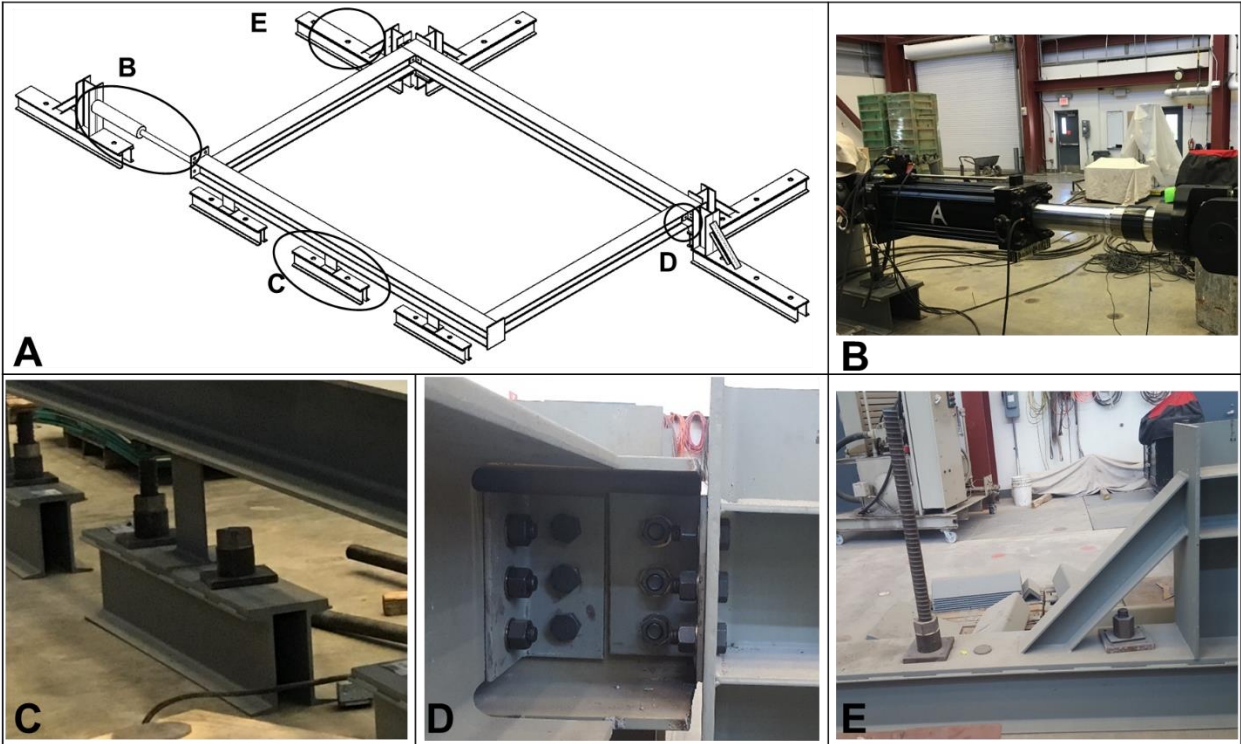


Fig. 4- 3: Diaphragm test frame setup

Prior to starting each full-scale cyclic test, a preliminary monotonic lateral test was performed to evaluate the stiffness of the bare steel frame and to estimate magnitude of the static friction force between the loading girder and the intermediate bearing supports. This was necessary to adjust load data for static friction effects, for comparison with FE models. The bare frame was also evaluated analytically with an FE model for comparison, using the geometric properties of W360 x 134 (W14 x 90) steel to ensure analytical model frame had similar lateral stiffness to the physical frame. The floor system was assembled within the test frame after the bare frame lateral test, and a gravity load test was performed initially to assess its load-carrying capacity. Estimated weights of frame assembly and floor dead loads are summarized in Table 4- 2.

Table 4- 1: Estimated weight of frame and floors

Bare frame	Floor 1	Floor 2
kN (kip)	kN (kip)	kN (kip)
35 (7.9)	23.7 (5.3)	26.2 (5.9)

4.3.2 Test Details

Floor systems of two (2) different structural depths, $D= 208$ mm (8.2 in.) and $D= 259$ mm (10.2 in.), were fabricated from 2.46 mm thick (12-gage) light-gage steel for testing. A summary of the floors’ geometric parameters is shown in Table 4- 2. Each floor system was comprised of three panels, each with an approximate width of 2.4 m (8 ft) and length of 5.1 m (16.6 ft). The perimeter of the assembled panels was connected to the support girders using PAFs spaced at approximately 305 mm (1 ft) centers. For each panel, No. 12 self-drilling screws spaced at approximately 305 mm (1 ft) centers were used to connect the top steel plates to the top flange of the purlins. In between panels, No. 12 self-drilling screws approximately 305 mm (1 ft) centers were used to connect both the bottom lip-plates and the top splice plates to adjacent panels.

Table 4- 2: Diaphragm test summary

Floor	Purlin depth	Plate thickness	Purlin thickness	Purlin spacing (avg)
	mm (in.)	mm (in.)	mm (in.)	mm (ft)
1	203 (8)	2.46 (0.097)	2.46 (0.097)	610 (2)
2	254 (10)	2.46 (0.097)	2.46 (0.097)	610 (2)

4.3.3 Loading and Instrumentation

Initial gravity load tests were performed by loading the floor assembly with an approximately uniform dead load as shown in Fig. 4- 4. The magnitudes of the applied dead loads were pre-determined, and were comprised of both pre-weighed floor panels and pallets of steel plates. The total loads applied were 77.2 kN and 74.7 kN (17.3 kips and 16.8 kips), for Floors 1 and 2 respectively. The dead loads were applied over a footprint of 5.1 m x 2.4 m (16.6 ft x 8 ft)

in five loading increments summarized in Table 4- 2. Three concrete blocks were placed underneath the pinned longitudinal girder to replicate the bearing supports underneath the loading girder, creating symmetric boundary conditions for gravity load testing. The displacement at the center of the mid-panel, was recorded using a displacement transducer placed at the geometric center of the assembled floor underneath the floor.



Fig. 4- 4: Floor diaphragm assembly showing preliminary gravity loads

Table 4- 3: Incremental patch loads for gravity tests

Step	Floor 1 Load	Floor 2 Load
	kN (kip)	kN (kip)
1	9.1 (2.0)	8.2 (1.8)
2	18.0 (4.0)	16.3 (3.7)
3	26.2 (5.9)	23.7 (5.3)
4	41.6 (9.3)	39.1 (8.8)
5	77.2 (17.3)	74.7 (16.8)

FEMA 461-established (2007) quasi-static displacement-controlled protocol was used for the lateral cyclic testing. At each displacement amplitude, two cycles were applied to the floor diaphragm, following which displacement values were increased by 40% for the subsequent two cycles. The starting displacement amplitude was determined based on an estimate of the deformation corresponding to damage initiation, Δ_o . FEMA 461 (2007) requires a minimum of six

displacement cycles prior to reaching Δ_o . The magnitude of Δ_o is usually assessed through monotonic diaphragm testing of a floor with similar geometric and mechanical properties. In the absence of such preliminary monotonic test results, an approximate FE assessment and recommendations for establishing Δ_o found in Essa et al. (2003) were used for estimating Δ_o . From the FE assessment and recommendations in Essa et al. (2003), the magnitude of $\Delta_o = 3.81$ mm (0.15 in.) was selected. The targeted deformation corresponding to maximum load, Δ_m , was also required to be defined, for which a minimum of ten displacement cycles were required prior to reaching. The magnitude of Δ_m , was set to 78.6 mm (3.1 in.), to prevent yielding of the web of the transverse frame members. The final displacement protocol used for the diaphragm testing is as shown in Fig. 4- 5.

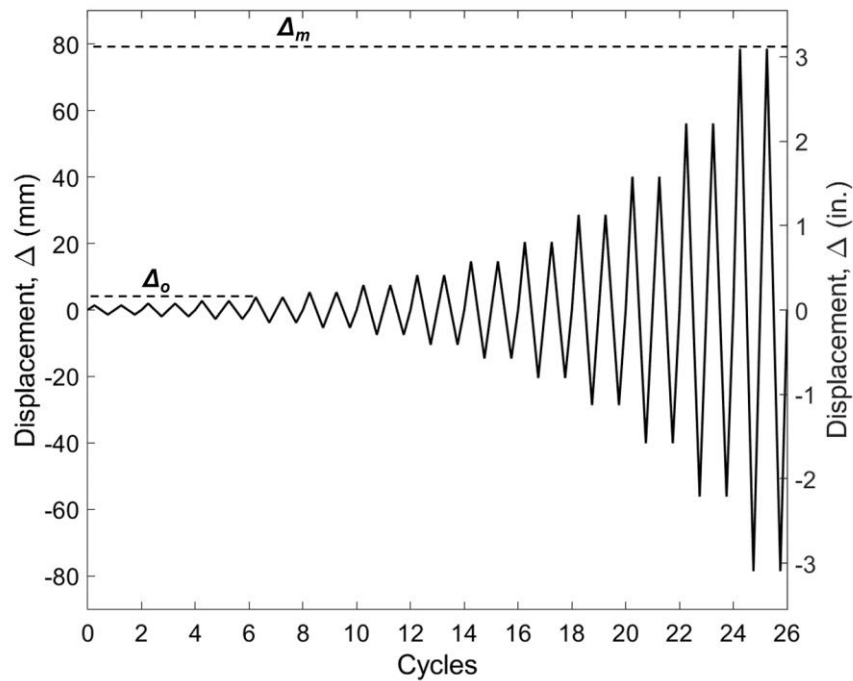


Fig. 4- 5: Diaphragm Cyclic displacement protocol in accordance with FEMA 461

The displacement protocol was applied using a 980 kN (220 kip) actuator. The quasi-static loading rate was specified as 0.1 mm/s (0.004 in./s) (Essa et al. 2003). This rate was considered slow enough to eliminate any dynamic effects during testing. Corresponding force measurements for each value of applied displacements were recorded from the actuator's built-in load cell. Deflections at all frame corners were recorded in the longitudinal (x) and transverse (y) directions from displacement transducers and optical measuring devices as shown in Fig. 4- 2. The x deflection of the loading girder was recorded at gage position 1. At gage positions 2 and 6, x deflections in the pin supports were recorded. The y deflections in the pin supports were recorded at gage positions 5 and 7. Auxiliary y deflections were also recorded at gage positions 3 and 4.

4.4 Finite Element Modeling

Finite element models, with geometric and mechanical parameters corresponding to the experimental tests, were generated using Abaqus CAE (DSS 2016) to assess the response of the floor systems to lateral cyclic loads. Similar to the fabricated floors, the analytical models were initially assessed for gravity load carrying capacity prior to the lateral cyclic assessment. 3D shell elements were used to model the light-gage steel plates and light-gage purlins. The material was modeled as isotropic with linear-elastic material behavior. An elastic modulus of 200 GPa (29,000 ksi) and a Poisson's ratio of 0.3 were used for all steel. Mesh sensitivity was analyzed to ensure the selected element mesh sizes were adequate to balance accuracy and efficiency of the model. The top and bottom steel plates were modeled using rectangular elements sized at approximately 50 mm (2 in.) square, purlins were modeled using mixed quad dominated elements sized at approximately 50 mm (2 in.) square, and the support girders were meshed with elements approximately 100 mm (4 in.) square. A representative FE model is as shown in Fig. 4- 6.

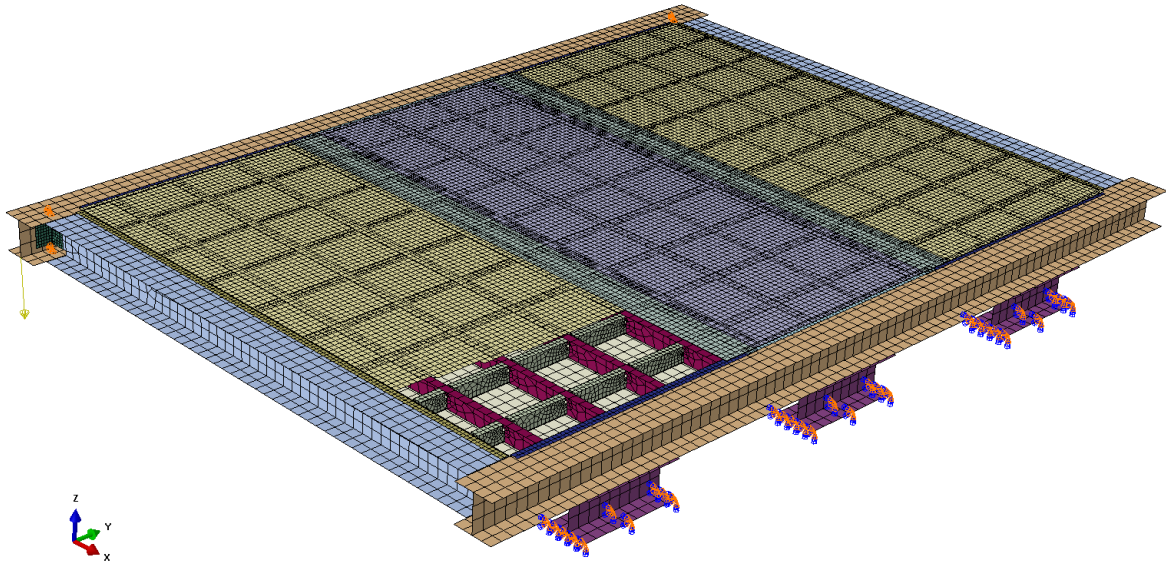


Fig. 4- 6: Representative FE model for gravity and diaphragm assessment

The thicknesses of the light-gage steel plates and purlins for the study were modeled with the gage thicknesses listed in Table 4- 2. The screw fasteners connecting the top plates to the top flanges of the purlins were modeled using mesh independent, rigid point-based fasteners (Boadi-Danquah et al. 2017b). The inter-panel and the perimeter screw fasteners were modeled by defining an Abaqus user-element (UEL), with radial-thrust element behavior. The constitutive behavior of the UEL was obtained from prior cyclic testing of a single-lap joints (Boadi-Danquah et al. 2019). Mesh types and sizes were selected to balance computational efficiency and accuracy, following a mesh sensitivity analysis. Full numeric modeling details are provided in the companion paper to this paper.

4.4.1 Gravity Load Analyses

Boundary conditions for the analytical gravity assessment were established to replicate those in the experimental test setup as shown in Fig. 4- 6. Bearing supports were modeled as

reduced length 915 mm (3 ft) long frame members, with bottom flange fully fixed. A frictionless hard contact was defined between the top face of the top flange of the bearing support members and the underside of the bottom flange of the longitudinal girders. Loading was applied uniformly with a ramp amplitude over the 2.4 m x 2.4 m (8 ft x 8 ft) footprint in contact with top plate of the assembled floor, and the corresponding displacement at the center of the assembled floor was measured at each increment of load.

4.4.2 *Lateral Load Analyses*

Analytical boundary conditions for the lateral analyses also replicated the experimental setup. Pin supports were defined by restraining the x , y , and z translational degrees of freedom at the points of contact between support braces and the pinned longitudinal girder, eliminating the need to explicitly model support braces. The lateral cyclic loading was applied as a unit displacement of the loading girder, with a tabulated varying amplitude set to reflect measured net longitudinal displacements measured during experimental testing.

4.4.3 *User-defined Connector Elements*

The UEL connector elements were incorporated for the perimeter fasteners using a subroutine developed as a Fortran source code by Ding (2015) for use with Abaqus CAE. The subroutine was developed through the modification of the source code of the *pinching4* material model in OpenSees (Mazzoni et al. 2005). *Pinching4* is an OpenSees material model used for calibrating cold-formed steel sheeting connection tests (Bian et al. 2014; Ngo 2014; Peterman and Schafer 2013). The cyclic connector response is characterized by connector backbone and unloading-reloading parameters derived from the results of cyclic tests of screw and PAFs presented in Boadi-Danquah et al. (2019). Backbone and unloading-reloading parameters are listed and described in Table 4- 4. The parameters define the relative load-displacement behavior for a node-pair with one

pinned and the other with translational degree-of-freedom released. Using 41 parameters, a realistic connector hysteresis response curve can be defined for each node-pair (Ding 2015). Defined behavior includes the backbone curve, material state change, and strength and stiffness degradation, which are defined as inputs for computational modeling.

Table 4- 4: *Pinching4* parameters definitions (Mazzoni et al. 2005)

Pinching4 parameter	Definition
<i>ePf1, ePf2, ePf3, ePf4</i>	Values defining force points on the positive response envelope
<i>ePd1, ePd2, ePd3, ePd4</i>	Values defining deformation points on the positive response envelope
<i>eNf1, eNf2, eNf3, eNf4</i>	Values defining force points on the negative response envelope
<i>eNd1, eNd2, eNd3, eNd4</i>	Values defining deformation points on the negative response envelope
<i>rDispP</i>	Value defining the ratio of the deformation at which reloading occurs to the maximum historic deformation demand
<i>fFoceP</i>	Value defining the ratio of the force at which reloading begins to force corresponding to the maximum historic deformation demand
<i>uForceP</i>	Value defining the ratio of strength developed upon unloading from negative load to the maximum strength developed under monotonic loading
<i>rDispN</i>	Value defining the ratio of the deformation at which reloading occurs to the minimum historic deformation demand
<i>fFoceN</i>	Value defining the ratio of the force at which reloading begins to force corresponding to the minimum historic deformation demand
<i>uForceN</i>	Value defining the ratio of strength developed upon unloading from negative load to the minimum strength developed under monotonic loading

The constitutive model for the perimeter PAF was derived from the cyclic test of a single lap-joint of a HILTI X-ENP-19 in 2.46 mm thick (12-gage), A36 steel (ASTM 2019b, Boadi-Danquah et al. 2019). Similarly, the constitutive model for the inter-panel screw fastener was

derived from the cyclic test of a single lap-joint of No.12 (*X1B1214*) screw in A50 12-gage (2.48 mm) steel (Simpson 2019, Boadi-Danquah et al. 2019). Table 4- 5 summarizes the constitutive parameters used for defining the UEL and radial thrust envelopes of the PAF and screw fasteners.

Table 4- 5: *Pinching4* parameters of PAF and screw

Pinching4 parameter	Powder-actuated fastener (PAF)	Screw
<i>ePd1</i> [mm (in.)]	0.10 (0.004)	0.015 (0.0006)
<i>ePd2</i> [mm (in.)]	0.74 (0.03)	1.54 (0.061)
<i>ePd3</i> [mm (in.)]	2.25 (0.09)	1.91 (0.075)
<i>ePd4</i> [mm (in.)]	4.06 (0.16)	2.00 (0.079)
<i>ePf1</i> [kN (kip)]	12.04 (2.71)	6.34 (1.43)
<i>ePf2</i> [kN (kip)]	15.08 (3.47)	10.00 (0.39)
<i>ePf3</i> [kN (kip)]	4.88 (1.1)	6.74 (1.51)
<i>ePf4</i> [kN (kip)]	0.005 (0.001)	0.005 (0.001)
<i>eNd1</i> [mm (in.)]	-0.10 (-0.004)	-0.015 (-0.0006)
<i>eNd2</i> [mm (in.)]	-0.74 (-0.03)	-1.54 (-0.061)
<i>eNd3</i> [mm (in.)]	-2.25 (-0.09)	-1.91 (-0.075)
<i>eNd4</i> [mm (in.)]	-4.06 (-0.16)	-2.00 (-0.079)
<i>eNf1</i> [kN (kip)]	-12.04 (-2.71)	-6.34 (-1.43)
<i>eNf2</i> [kN (kip)]	-15.08 (-3.47)	-10.00 (-0.39)
<i>eNf3</i> [kN (kip)]	-4.88 (-1.1)	-6.74 (-1.51)
<i>eNf4</i> [kN (kip)]	-0.005 (-0.001)	-0.005 (-0.001)
<i>rDispP</i>	0.634	0.543
<i>fFoceP</i>	0.01	0.012
<i>uForceP</i>	0.005	0.005
<i>rDispN</i>	0.634	0.543
<i>fFoceN</i>	0.01	0.012
<i>uForceN</i>	0.005	0.005

The values indicated in Table 4- 5 cover the backbone and unloading-reloading parameters. Additional parameters defining cyclic strength/stiffness degradation are set to zero and the fastener damage type is set as “cycle” (Mazzoni et al. 2005, Ding 2015).

4.5 Results and Discussion

The gravity test results are presented in Fig. 4- 7 as applied load versus vertical displacement at the center of the floor for Floor 1 and Floor 2. The stiffness of the floor under the monotonically-increasing patch loading computed is as summarized in Table 4- 6. The stiffness of the FE model for Floor 1 was found to be within 13% of the stiffness from the experimental test, and the stiffness of the FE model for Floor 2 within 3% of the stiffness from the experimental test.

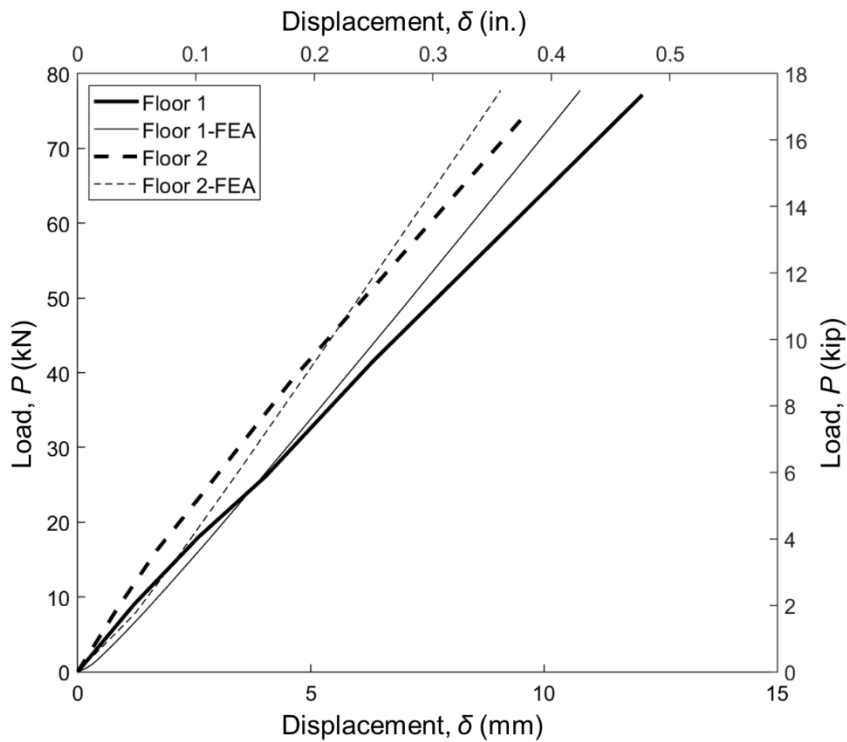


Fig. 4- 7: Load vs displacement response for gravity tests

Table 4- 6: Stiffness under gravity patch loads

Floor	Experimental stiffness N/mm (kip/in)	FE stiffness N/mm (kip/in)	Ratio FE/Experiment
1	6.32 (36.1)	7.17 (40.9)	1.13
2	7.66 (43.7)	7.87 (44.9)	1.03

The recorded load versus displacement from the 980 kN (220 kip) actuator for the bare frame lateral tests is as shown in Fig. 4- 8. From the results, a static frictional force of 2.4 kN (0.54 kip) was found to have developed at the onset of the bare frame displacement for Floor 1, and a static frictional force of 4.3 kN (0.97 kip) was found to have developed at the onset of the bare frame displacement for Floor 1. The magnitudes of static frictional force relative to the weights of the floor assembly in Table 4- 1 are therefore estimated as 4.03 kN (0.95 kip) for Floor 1, and 7.52 (1.69 kip) for Floor 2. Since the resistance of the frame was greater than 2% of the recorded peak loads for the respective floors, the test results have been adjusted to compensate for the frame resistance (ASTM 2019a) for comparison with FE models. From the results of the two bare frame tests, the stiffness of the bare frame was computed as 14.8 N/mm (83.9 lb/in). It was ensured that the estimated frame stiffness from the bare frame tests matched the stiffness of the frame model in the FE analysis. It is noted that, the test frame response was influenced by the effects of variable values kinetic coefficient of friction over 75 mm (3 in.), hence the non-linear response.

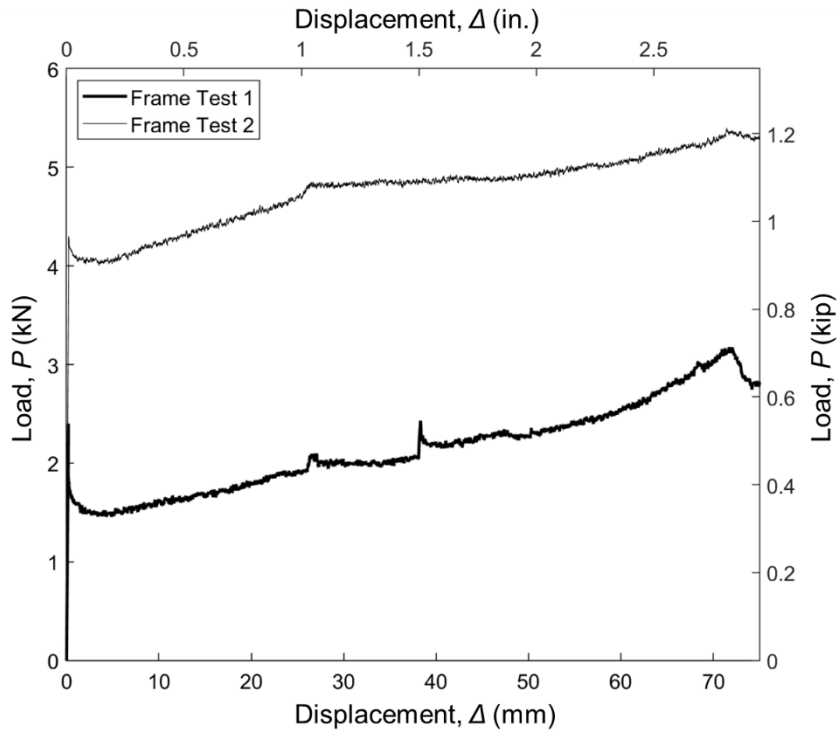


Fig. 4- 8: Load vs displacement response for bare frame tests

The net shear deflections in the diaphragm were computed from adjusting recorded displacements in gage 1 by displacement readings in gages 2, 5, and 7, shown in Fig. 4- 2. The computed net shear deflections were applied as input displacements for the FE analysis, and are summarized in Table 4- 7. The test and FE load versus displacement response for Floor 1 and Floor 2 are shown in Fig. 4- 9 and Fig. 4- 10, respectively. The average peak loads were computed from the mean of the positive peak load in the first quadrant and the absolute value of the negative peak load in the third quadrant. The average peak loads have been summarized in Table 4- 8. There was a difference of 16% between the average peak load in Floor 1 and its corresponding FE model, and a difference of 10% between the average peak load in Floor 2 and its corresponding FE model.

Table 4- 7: Computed net shear deflections from lateral diaphragm tests

Cycle	Floor 1		Floor 2	
	Peak disp. (+) mm (in.)	Peak disp. (-) mm (in.)	Peak disp. (+) mm (in.)	Peak disp. (-) mm (in.)
1,2	1.39 (0.055)	-1.39 (-0.055)	1.39 (0.055)	-1.39 (-0.055)
3,4	1.95 (0.077)	-1.95 (-0.077)	1.95 (0.077)	-1.95 (-0.077)
5,6	2.73 (0.107)	-2.73 (-0.107)	2.73 (0.107)	-2.73 (-0.107)
7,8	3.81 (0.15)	-3.81 (-0.15)	3.81 (0.15)	-3.81 (-0.15)
9,10	4.83 (0.19)	-4.57 (-0.18)	5.33 (0.21)	-5.33 (-0.21)
11,12	6.35 (0.25)	-5.84 (-0.23)	7.47 (0.294)	-7.47 (-0.294)
13,14	10.16 (0.40)	-7.62 (-0.30)	10.45 (0.412)	-10.45 (-0.412)
15,16	13.97 (0.55)	-10.41 (-0.41)	14.62 (0.575)	-14.62 (-0.575)
17,18	19.3 (0.76)	-14.73 (-0.58)	18.03 (0.71)	-20.46 (-0.806)
19,20	26.42 (1.04)	-19.56 (-0.77)	20.57 (0.81)	-28.45 (-1.12)
21,22	38.86 (1.53)	-25.91 (-1.02)	38.61 (1.52)	-29.72 (-1.17)
23,24	51.82 (2.04)	-45.72 (-1.80)	48.26 (1.90)	-55.12 (-2.17)
25,26	73.66 (2.90)	-66.04 (-2.60)	67.56 (2.66)	-64.26 (-2.53)

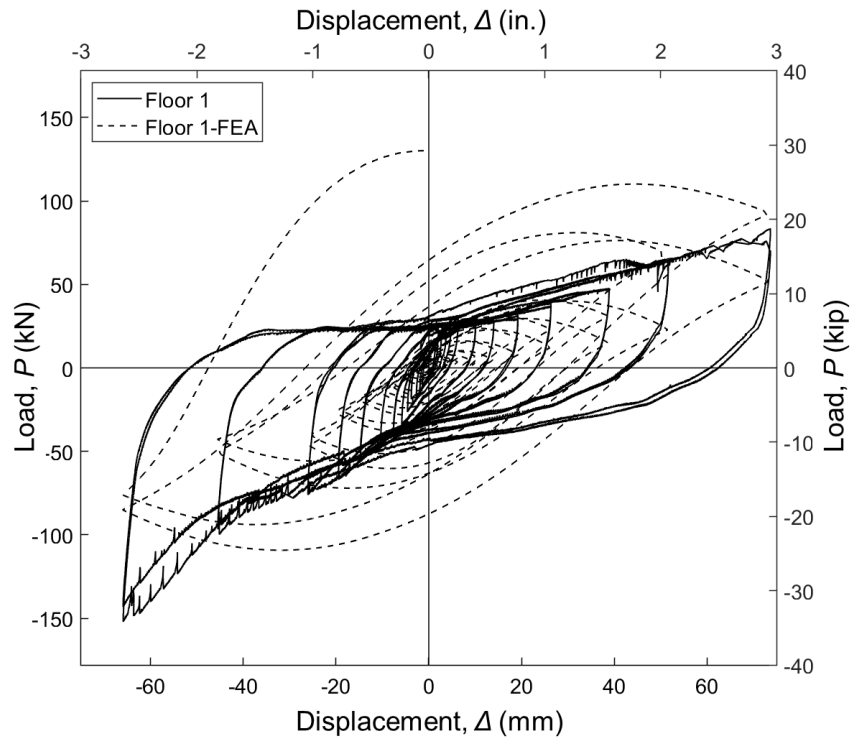


Fig. 4- 9: Lateral load vs displacement response for Floor 1 (60 mm = 1.1 % drift)

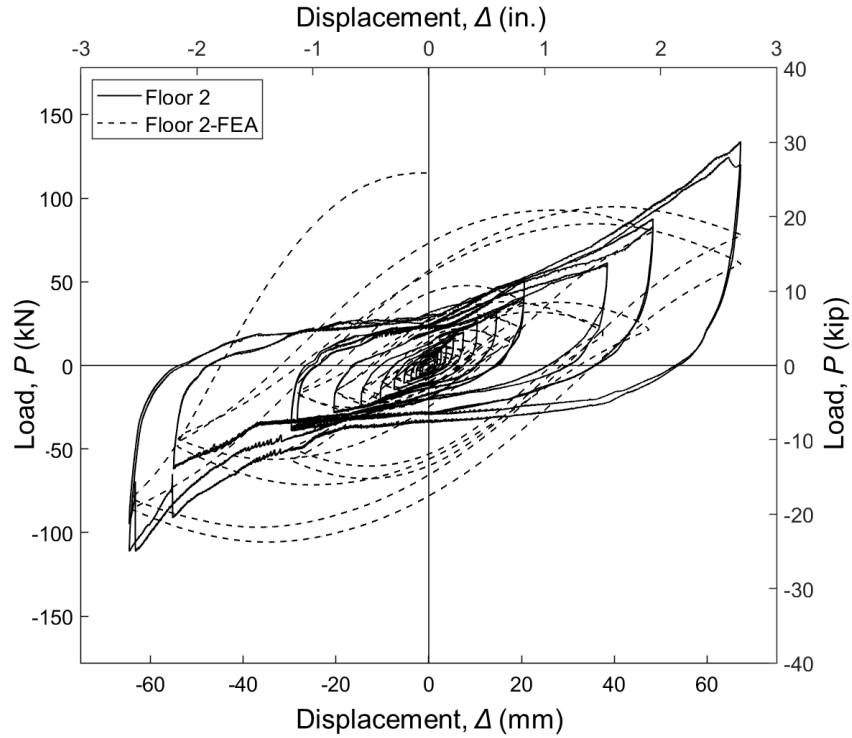


Fig. 4- 10: Lateral load vs displacement response for Floor 2 (60 mm = 1.1 % drift)

Table 4- 8: Summary of peak loads and dissipated energy from lateral cyclic tests

Floor	Experiment avg. peak load kN (kip)	FE avg. peak load kN (kip)	Ratio FE/Exp.	Experiment dissipated energy kN-m (kip-in.)	FE dissipated energy kN-m (kip-in.)	Ratio FE/Exp.
1	117.8 (26.5)	119.7 (26.9)	1.01	55.2 (488.6)	48.1 (425.7)	0.87
2	122.7 (27.6)	110.4 (24.8)	0.90	47.0 (415.9)	48.8 (431.9)	1.04

The dissipated energy for each floor was computed from the area of the hysteresis curve generated from the load-deformation response of the floors. The dissipated energies for Floor 1 and 2 have been summarized in Table 4- 8. The difference in dissipated energy between the floors and their corresponding FE models were found to be 13% and 4% for Floor 1 and Floor 2, respectively.

Overall, the average recorded peak loads showed good agreement with the analytical models. Towards the peak displacement amplitudes, the experimental test results typically showed stiffening in the load response, compared to softening in the response of the analytical models. The stiffening is attributable to closing and tightening of gaps in the constructed modular system towards the peak displacements, making the floor system stiffer laterally, and resulting in peak loads being mobilized sharply. The analytical models however did not include explicit definition of these lateral stiffening effects, hence the overall response was defined by the connector behavior and the floor geometric parameters specified. Additional observed differences between experimental results and analytical model peak loads are attributable to potential disparities in individual fastener behavior between results from single-lap tests results used for developing constitutive models, and fasteners used in the actual prototype construction.

Similarly, the dissipated energy between the experimental test and FE showed good agreement. It is noted from Fig. 4- 9 and 4- 10 that the unloading-reloading paths in the FE models are different from the experimental tests. This is attributed to the fact that fastener *pinching* properties used for the FE modeling were optimized for force and dissipated area prediction (Boadi-Danquah et al. 2019). Additionally, no stiffness or strength degradation factors were included in the fastener property definitions. These assumptions for fastener optimizations described in in Boadi-Danquah et al. (2019) imply that fastener constitutive models used are capable of predicting peak loads and dissipated energy, not necessarily following similar unloading-reloading paths as experimental testing.

In addition to identified contributors to the disparities between peak loads, dissipated energies and general hysteresis recorded for the experimental test and numerical modeling, defining a frictionless contact between loading girder and bearing supports, discounted any kinetic

friction effects on the load values recorded from numerical analysis. Also, though the assumption of a linear-elastic material definition for the floor components in the numerical analysis was essential, due to non-linear effects around connectors already captured in the *pinching4* material model, any material non-linear response outside the zone of influence of the connectors were not captured in the numerical models.

4.6 Conclusions

This research program examined the diaphragm strength characteristics and inelastic behavior under quasi-static cyclic loads for two prototypes of a novel modular steel floor system. The program also assessed the system for gravity load-carrying capacity. Understanding these characteristics is the first step towards establishing the floor system as part of an alternative solution to current seismic design and construction practices. The following conclusions were obtained from the results of the tests and analyses.

1. From the diaphragm lateral tests, both Floor 1 and Floor 2 showed stable hysteretic behavior under cyclic loading.
2. Analytically, viscous damping factors can be estimated from the hysteretic areas recorded from experimental tests for dynamic analysis of a structure that incorporates the novel floor system. Practically, the stable hysteresis implies that floor diaphragm can potentially dissipate energy during seismic activity, and consequently reduce the demands on the SFRS in a steel-framed building.
3. From assuming a linear-elastic material behavior for FE models, the stiffness of the floor system under gravity loads, estimated from the experiments closely matched the stiffness computed from FE simulations. This implies that FE simulation method can be used to assess the floor system's behavior under gravity loads, within the elastic range, for different

floor geometric parameters, based on an approximately uniformly distributed load across the entire floor surface.

4. The incorporated fastener numerical model showed similar peak lateral loads and areas of hysteresis as experimental tests under lateral cyclic loading. However, loading paths varied between numerical and experimental results. The modeling technique therefore can be utilized as an approximate method for estimating peak lateral loads and hysteretic areas of the floor system with varying geometric and mechanical parameters.
5. To predict the overall lateral response of the floor system under cyclic loading more accurately using numerical modeling, further research into developing representative models capable of predicting lateral stiffening effects in the modular floor system is required. Additionally, fastener constitutive behavior should be developed to include strength/stiffness degradation parameters.

Chapter 5: Behavior of a Lightweight Modular Steel Floor

Diaphragm under Quasi-static Cyclic Loading. II: Parametric

Finite Element Analyses

5.1 Abstract

This paper uses a finite element (FE) approach which has been validated by results from two full-scale experimental tests to explore the diaphragm behavior of a lightweight modular steel floor system under lateral cyclic loading. Nine non-linear FE models, representing a full-scale (7.3 m × 5.5 m) cantilever diaphragm have been developed in Abaqus CAE. A user-element (UEL) sub-routine has been used to approximate the behavior of fasteners in the floor system. A uniformly-distributed gravity load was initially applied to the floors to establish adequate gravity load carrying capacity. A lateral quasi-static cyclic displacement protocol developed based on results from a physical test was applied afterwards. From the results obtained, the unit shear strength, energy dissipation, and general response of the floor diaphragm have been computed and described. The observed characteristic properties of the floor system imply that it can provide an alternative solution to current seismic design and construction practices.

5.2 Introduction

This paper is the second part of a study aimed at characterizing the diaphragm behavior of a novel lightweight modular two-way steel floor system that enables easy repair and reuse of components. The floor system is assembled from individual panels, each comprising orthogonally-arranged light-gage steel purlins, welded at the bottom to a light-gage steel plate, and connected at the top to a light-gage steel plate using self-drilling screws (Boadi-Danquah et al. 2016). Two

full-scale prototypes of the floor have been tested under quasi-static cyclic loading, with assembly details and results presented in Boadi-Danquah et al. (2019b). The results presented in the first part of the study were augmented by results from finite element (FE) modeling, incorporating fastener constitutive models developed earlier (Boadi-Danquah et al. 2019a). This paper details the FE modeling approach used to augment experimental results, and examines the effects of varying plate thickness, t_p , and depth, d , on the behavior of the floor diaphragm. A 7.3 m \times 5.5 m (24 ft \times 18 ft) structural bay size was used, for which nine non-linear finite FE models with varying t_p and d were developed. This represents the floor system occupying a structural bay with no requirement for intermediate support beams.

Each floor configuration was initially assessed for its gravity load carrying capacity prior to assessing diaphragm performance. A cantilever diaphragm setup was used for the diaphragm assessment, based on ASTM E455 (2016) provisions, with a cyclic displacement protocol developed from recommendations in FEMA-461 (2007). The amplitudes of the cyclic displacement protocol were determined based on physical test results (Boadi-Danquah et al. 2019b).

For the gravity assessments, the peak displacement recorded from the FE assessments were compared against service load displacement limits in IBC (2015). For the diaphragm assessments, load capacity of the cantilever diaphragm, P_u , based on provisions in SDI (2015) and recommendations in Luttrell (1996) were estimated for all models. Additionally, the peak load, P_{ult} , equivalent to the diaphragm's maximum load recorded within the applied cyclic displacement range was extracted from the FE assessments for all models. These values of P_{ult} were then used to compute the diaphragms' unit shear strength, S_{ult} . Finally, the dissipated energy under cyclic

loading was determined from the results of each model by computing the area within the load-displacement hysteretic curves.

The objective of the study presented in this paper is to assess the influence of varying t_p and d on the diaphragm unit shear strength and the dissipated energy, using a numerical modeling approach introduced in Boadi-Danquah et al (2019b).

5.3 Diaphragm Assessment of Floor System

The floor diaphragm is typically characterized by the diaphragm unit shear strength, S_{ult} , and diaphragm shear stiffness, G' . The magnitude of S_{ult} defines how much shear load the diaphragm can sustain, while G' relative to the supporting frame's stiffness defines how the diaphragm distributes lateral loads to adjacent frames (Boadi-Danquah et al. 2017). Provisions in

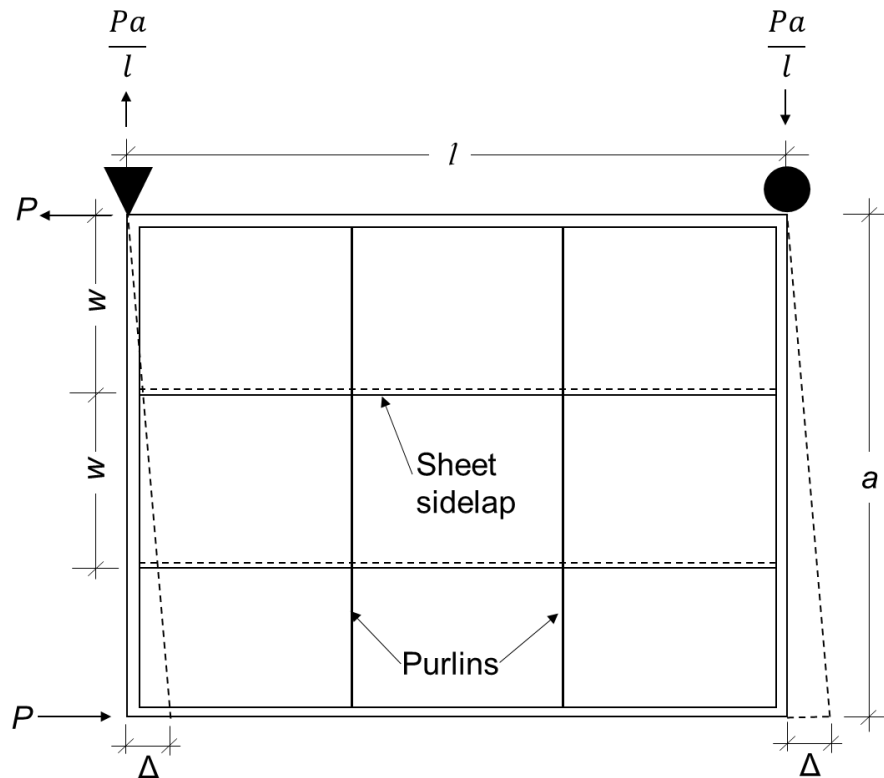


Fig. 5- 1: Schematic layout for diaphragm (SDI 2015)

the Steel Deck Institute (SDI) Diaphragm Design Manual (SDI 2015) for assessing S_{ult} and G' are derived from recommendations in Luttrell (1996), which assumes a simple cantilever diaphragm with three profiled steel deck panels as shown in Fig. 5- 1.

The magnitude of S_{ult} for a profiled steel deck diaphragm can be limited by the strength of the fasteners, local buckling in plates, or by general plate-like buckling of the whole diaphragm area (SDI 2015). The provisions in SDI (2015) are specific to profiled steel decks. However, with some modification, the fastener limitations can be applied to the developed lightweight steel floor system. Based on the layout and configuration used in this study, the magnitude of S_{ult} can be obtained from assuming equilibrium of the center panel (Luttrell 1996). For an applied load, P , acting along the panel length, l , the magnitude of the ultimate load, P_u , based on equilibrium of an interior panel as shown in Fig. 5- 2, can be computed using Eq. 1, adapted from SDI (2015) and Luttrell (1996).

$$P_u = \frac{l}{a} (n_s Q_s + 2 \frac{M_c}{w}) \quad (1)$$

The number of interior fasteners along a vertical column for each panel is represented by n_s and Q_s is the interior connector shear strength. Values of Q_s are computed in accordance with AISI (2012) provisions or recorded from a shear lap test (AISI 2013). M_c is the end-of-panel coupling resistance developed in the interior panels' perimeter fasteners (Luttrell 1996), and w is the width of the panel. M_c is computed based on the perimeter connector strength, Q_f as;

$$M_c = n_e Q_f \left(\frac{w}{6} \right) \quad (2)$$

where n_e is the number of perimeter fasteners for an interior panel. However, it is noted that the true magnitude of M_c depends on the ability of the edge-most panels to resist compression (Luttrell 1996). The equations do not capture limitations due to local buckling in plates and general plate-like buckling of the whole diaphragm. For this study, values of both Q_s and Q_f were obtained from

single lap shear tests for screws and powder-actuated fasteners (PAFs) (Boadi-Danquah et al. 2019a). Table 5- 1 shows values of Q_s and Q_f for the range of plate thickness applicable to this study. The values shown are from test results of X1B1214 (No. 12) screws (Simpson Strong-Tie 2019) and X-ENP-19 PAFs (Hilti 2015).

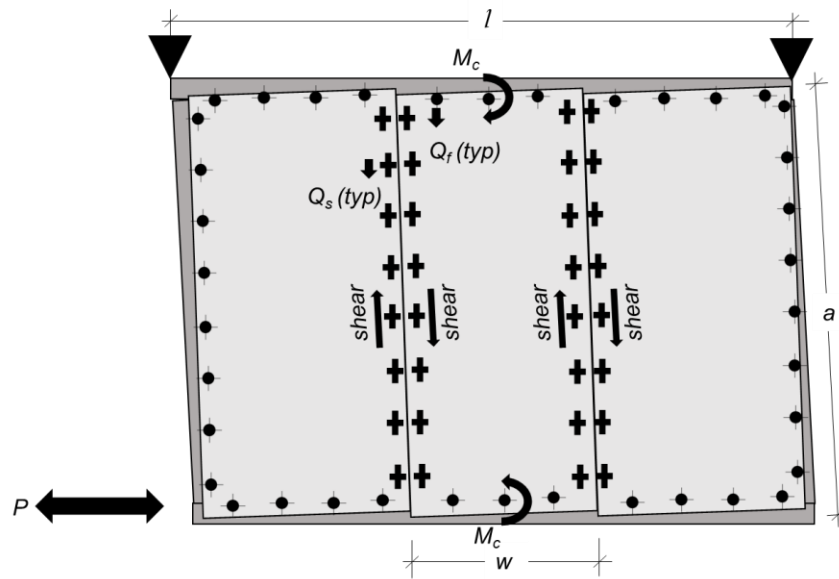


Fig. 5- 2: Schematic layout for assessing peak diaphragm load capacity

There are provisions in SDI (2015) for estimating G' , but these estimates are applicable to profiled steel decks only. In the absence of applicable provisions, the magnitude of G' can be computed from monotonic testing a cantilever diaphragm setup (Bagwell 2007, SDI 2015, ASTM 2016). For a cantilever diaphragm test, G' is estimated from the slope of the linear portion of the load-displacement result of the diaphragm test. Where there is no obvious linear portion in the load-displacement results, O'Brien et. al (2016) estimates G' from the ratio of 40% of the recorded peak load, P_u , to its corresponding displacement. This ensures that the diaphragm is characterized only within its elastic behavior range. This elastic characterization of the diaphragm is essential,

since current seismic design codes recommend that inelastic behavior be limited to seismic force resisting systems (SFRS), such as buckling-restrained braces in a steel frame.

Table 5- 1: Connector shear strength values

Plate/purlin gage	Plate/purlin thickness t mm (in.)	Screw shear strength Q_s kN (kip)	PAF shear strength Q_f kN (kip)
16	1.37 (0.054)	7.46 (1.68)	12.10 (2.72)
14	1.72 (0.068)	10.33 (2.32)	15.54 (3.49)
12	2.45 (0.096)	10.19 (2.29)	15.08 (3.39)

An alternative approach considers inelastic response occurring in diaphragms, thereby reducing demands on the SFRS (Tremblay et al. 2004, O’Brien et al. 2016). With this approach, the floor diaphragm could be considered as ductile fuse element in the lateral load path and sustain large inelastic deformation cycles without significant strength degradation. Therefore, there is need to evaluate the inelastic performance of the floor system under cyclic loading to determine strength and stiffness degradation, energy dissipation, and general hysteresis (Rogers and Tremblay 2003a, 2003b). Finite element modeling provides a tool to evaluate some of the general inelastic response of the developed floor system under cyclic loading. This paper focuses on a parametric study of the inelastic behavior of the floor diaphragm under cyclic loading, using a non-linear FE method, informed by the results of two full-scale diaphragm tests (Boadi-Danquah et al. 2019b).

5.4 Finite Element Modeling

Finite element models of the floor system were generated using Abaqus CAE (DSS 2016) to assess the effects of varying plate thickness and floor depth on the inelastic response to lateral

cyclic loads. The models were assessed to establish their gravity load-carrying capacity prior to the lateral cyclic assessment. Nine models were developed to assess the behavior of the floor system in this parametric analysis. The values of t_p and the purlin thickness, t_c , considered for the study were taken as the minimum design thicknesses for the relevant designated gage, as reported in the SSMA Product Technical Guide (SSMA 2015). Each floor configuration was assigned a designation corresponding to the values of the relevant parameters, details of which are presented in Table 5- 2. For example, the base configuration with $t_p = 2.45$ mm, $t_c = 2.45$ mm, and $d = 254$ mm was named P245-C245-D254. In this study, purlins were kept at an average spacing, s , of 610 mm (2 ft) to reflect the average spacing used in the experimental study (Boadi-Danquah et al. 2019b). Plate thicknesses of 1.37 mm (0.054 in.), 1.72 mm (0.068 in.), and 2.45 mm (0.096 in.) were considered, along with purlin depths of 203 mm (8 in.), 254 mm (10 in.), and 305mm (12 in.). Plate thickness was varied from 1.37 mm (0.054 in.) to 2.45 mm (0.096 in.) while maintaining constant floor depth. The influence of purlin depth was also examined, evaluating three values of d from 203 mm (8 in.) to 305 mm (12 in.) while holding plate thickness constant.

Table 5- 2: Model designations with corresponding geometric parameters

Model Designation	Plate Thickness t_p mm (in.)	Purlin Thickness t_c mm (in.)	Purlin Depth d mm (in.)
P137-C137-D203	1.37 (0.054)	1.37 (0.054)	203 (8)
P172-C172-D203	1.72 (0.068)	1.72 (0.068)	203 (8)
P245-C245-D203	2.45 (0.096)	2.45 (0.096)	203 (8)
P137-C137-D254	1.37 (0.054)	1.37 (0.054)	254 (10)
P172-C172-D254	1.72 (0.068)	1.72 (0.068)	254 (10)
P245-C245-D254	2.45 (0.096)	2.45 (0.096)	254 (10)
P137-C137-D305	1.37 (0.054)	1.37 (0.054)	305 (12)
P172-C172-D305	1.72 (0.068)	1.72 (0.068)	305 (12)
P245-C245-D305	2.45 (0.096)	2.45 (0.096)	305 (12)

5.4.1 *Elements and Meshing*

3D shell elements were used to model the plywood, steel plates, purlins, support girder, and double angles at the girder-to-girder connections. All steel and plywood elements were considered to be isotropic, with linear-elastic material behavior. An elastic modulus, $E_s= 200$ GPa (29,000 ksi) and a Poisson's ratio of 0.3 was specified for steel in all models. An elastic modulus, $E_p= 0.7$ GPa (100 ksi), and a Poisson's ratio of 0.25 was specified for the plywood for gravity load analysis. The low value of E_p specified for the plywood accounts for discontinuities in its layout, and also ensures that its stiffness contribution to the gravity load response of the system is limited. The element mesh sizes were selected to balance accuracy and efficiency in computation, following mesh sensitivity and convergence studies. The top and bottom steel plates were modeled using 4-node quadrilateral shell elements with reduced integration (S4R), sized at approximately 50 mm (2 in.) square, purlins were modeled using S4R-dominated elements, sized at approximately 50 mm (2 in.) square, and the support girders were meshed to approximately 100 mm (4 in.) square S4R elements as shown in Fig. 5- 3. For the gravity load assessment, the plywood was modeled using approximately 100 mm (4 in.) square S4R elements.

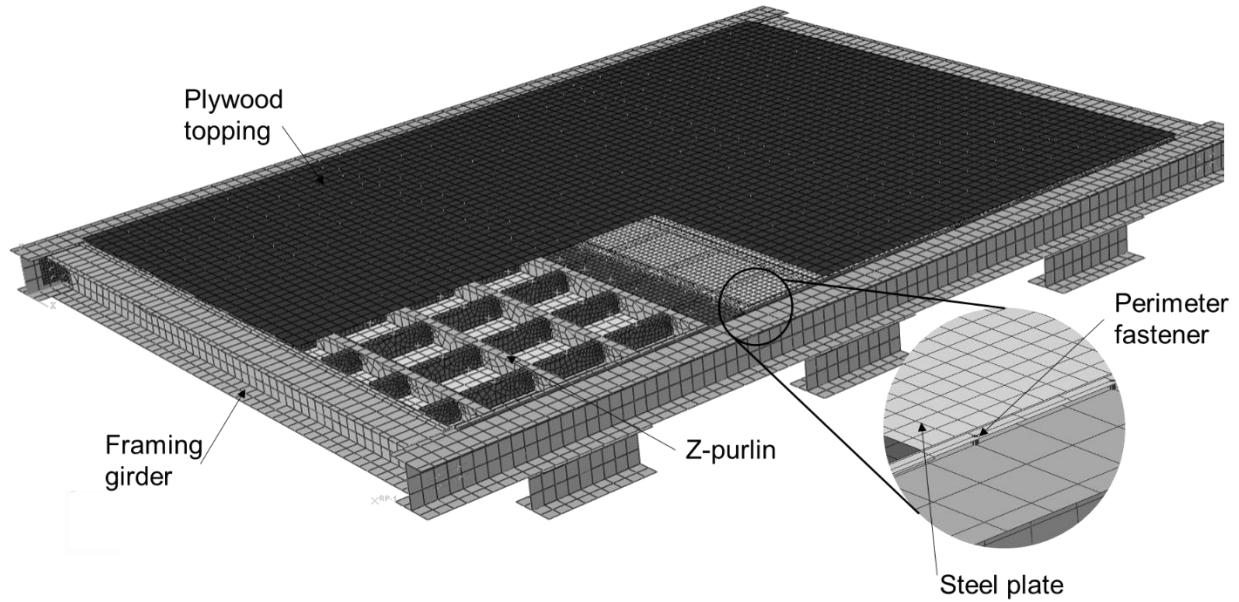


Fig. 5- 3: Typical FE model showing assembled instances and mesh regions

5.4.2 Interactions

Steel-to-steel contact was specified as hard normal contact, with frictionless tangential interaction. Welded zones between the purlins and plates were modeled using a tie-constraint. For gravity assessments, the plywood was attached to the top of the steel plates using rigid mesh-independent point-based fasteners following a 305 mm (1 ft) square grid pattern. For all the models studied, both inter-panel and perimeter connectors were spaced at 305 mm (1 ft) on-center. For the gravity assessments, the inter-panel and perimeter connectors were defined using radial thrust connector elements. No. 12 screw fasteners (Simpson Strong-Tie 2019) were specified at the top plate and inter-panel connections, and X-ENP-19 PAFs (Hilti 2015) were specified at the perimeter fasteners with corresponding backbone behavior prescribed as applicable (Boadi-Danquah et al. 2019a).

However, for lateral cyclic assessment, built-in Abaqus FE connector elements are not able to fully define the constitutive behavior of the fasteners. An Abaqus user-element (UEL) was used

to define the fastener cyclic behavior by defining the behavior for node-pairs at fastener locations. To achieve this, the models were carefully partitioned to create in-plate coincident nodes for the UEL to be defined.

5.4.3 User-defined Connector Elements

The constitutive parameters used to define fastener behavior were obtained from parameters optimized in Boadi-Danquah et al. (2019a) following the *pinching4* for material model (Mazzoni et al. 2005), as summarized in Table 5- 3 for PAFs, and in Table 5- 4 for screws.

Table 5- 3: *Pinching4* parameters for powder-actuated fasteners (Boadi-Danquah et al. 2019a)

Pinching4 parameter	PAF in		
	12-gage	14-gage	16-gage
<i>ePd1</i> [mm (in.)]	0.10 (0.004)	0.10 (0.004)	0.15 (0.006)
<i>ePd2</i> [mm (in.)]	0.74 (0.03)	3.30 (0.13)	2.01 (0.08)
<i>ePd3</i> [mm (in.)]	2.25 (0.09)	29.46 (1.16)	27.74 (1.09)
<i>ePd4</i> [mm (in.)]	4.06 (0.16)	29.72 (1.17)	28.45 (1.12)
<i>ePf1</i> [kN (kip)]	12.04 (2.71)	15.00 (3.37)	36.32 (2.35)
<i>ePf2</i> [kN (kip)]	15.08 (3.47)	15.44 (3.47)	12.10 (2.72)
<i>ePf3</i> [kN (kip)]	4.88 (1.1)	10.01 (2.25)	9.48 (2.13)
<i>ePf4</i> [kN (kip)]	0.005 (0.001)	0.22 (0.05)	0.22 (0.05)
<i>eNd1</i> [mm (in.)]	-0.10 (-0.004)	-0.10 (0.004)	-0.15 (-0.006)
<i>eNd2</i> [mm (in.)]	-0.74 (-0.03)	-3.30 (0.13)	-2.01 (-0.08)
<i>eNd3</i> [mm (in.)]	-2.25 (-0.09)	-29.46 (1.16)	-27.74 (-1.09)
<i>eNd4</i> [mm (in.)]	-4.06 (-0.16)	-29.72 (1.17)	-28.45 (-1.12)
<i>eNf1</i> [kN (kip)]	-12.04 (-2.71)	-15.00 (3.37)	-36.32 (-2.35)
<i>eNf2</i> [kN (kip)]	-15.08 (-3.47)	-15.44 (3.47)	-12.10 (-2.72)
<i>eNf3</i> [kN (kip)]	-4.88 (-1.1)	-10.01 (2.25)	-9.48 (-2.13)
<i>eNf4</i> [kN (kip)]	-0.005 (-0.001)	-0.22 (0.05)	-0.22 (-0.05)
<i>rDispP</i>	0.634	0.605	0.706
<i>fFoceP</i>	0.01	0.016	0.073
<i>uForceP</i>	0.005	0.01	0.05
<i>rDispN</i>	0.634	0.605	0.706
<i>fFoceN</i>	0.01	0.016	0.073
<i>uForceN</i>	0.005	0.01	0.05

Table 5- 4: *Pinching4* parameters for No. 12 screws (Boadi-Danquah et al. 2019a)

Pinching4 parameter	No. 12 screws in		
	12-gage	14-gage	16-gage
<i>ePd1</i> [mm (in.)]	0.015 (0.0006)	0.016 (0.001)	0.030 (0.001)
<i>ePd2</i> [mm (in.)]	1.54 (0.061)	4.64 (0.18)	3.14 (0.12)
<i>ePd3</i> [mm (in.)]	1.91 (0.075)	7.35 (0.29)	8.51 (0.34)
<i>ePd4</i> [mm (in.)]	2.00 (0.079)	9.67 (0.38)	13.00 (0.51)
<i>ePf1</i> [kN (kip)]	6.34 (1.43)	5.94 (1.34)	4.32 (0.97)
<i>ePf2</i> [kN (kip)]	10.00 (0.39)	10.19 (2.29)	7.46 (1.68)
<i>ePf3</i> [kN (kip)]	6.74 (1.51)	6.70 (1.51)	4.90 (1.10)
<i>ePf4</i> [kN (kip)]	0.005 (0.001)	0.005 (0.001)	0.005 (0.001)
<i>eNd1</i> [mm (in.)]	-0.015 (-0.0006)	-0.016 (-0.001)	-0.030 (-0.001)
<i>eNd2</i> [mm (in.)]	-1.54 (-0.061)	-4.64 (-0.18)	-3.14 (-0.12)
<i>eNd3</i> [mm (in.)]	-1.91 (-0.075)	-7.35 (-0.29)	-8.51 (-0.34)
<i>eNd4</i> [mm (in.)]	-2.00 (-0.079)	-9.67 (-0.38)	-13.00 (-0.51)
<i>eNf1</i> [kN (kip)]	-6.34 (-1.43)	-5.94 (-1.34)	-4.32 (-0.97)
<i>eNf2</i> [kN (kip)]	-10.00 (-0.39)	-10.19 (-2.29)	-7.46 (-1.68)
<i>eNf3</i> [kN (kip)]	-6.74 (-1.51)	-6.70 (-1.51)	-4.90 (-1.10)
<i>eNf4</i> [kN (kip)]	-0.005 (-0.001)	-0.005 (-0.001)	-0.005 (-0.001)
<i>rDispP</i>	0.543	0.450	0.356
<i>fFoceP</i>	0.012	0.038	0.036
<i>uForceP</i>	0.005	0.02	0.02
<i>rDispN</i>	0.543	0.450	0.356
<i>fFoceN</i>	0.012	0.038	0.036
<i>uForceN</i>	0.005	0.02	0.02

The values in Tables 5- 3 and 5- 4 include the parameters that define the backbone and unloading-reloading paths for the respective fasteners. Since the values shown were optimized for force and hysteretic area prediction, similar to previous work (Tao et al. 2017 and Peterman et al. 2013) involving calibrating fastener behavior against experimental results, utilizing them will be adequate for predicting diaphragm forces (Ngo 2014) and hysteretic areas generated under cyclic loading, without necessarily following the true load paths.

5.4.4 Gravity Load Analyses

For models under gravity loads, boundary conditions were applied to represent a deck supported along all four sides, restrained vertically by bearing on the supporting flange of the frame girders. Horizontal and vertical restraints were provided at corners of the supporting frame to represent column supports, and to prevent rigid body motion during analysis. The support girders were made infinitely stiff to ensure that vertical displacements occurred only in the floor. Loading was applied as a uniformly distributed load to the surface of the plywood topping with displacement recorded at the center of the floor. The applied loads were ramped up to 5 kPa (105 psf). Gravity load performance was established using the IBC (2015) recommended load of 2.4 kPa (50 psf), equivalent to office uniform live load, and comparing central deflection to a limit of $a/360$, where width of the floor, a , is equal to 5.5 m (18 ft).

5.4.5 Cyclic Load Analysis

FEMA 461 (2007) displacement protocol, appropriate for quasi-static cyclic testing of a single specimen, is defined using two predetermined targeted deformation points, Δ_o and Δ_m . The magnitude of Δ_o represents deformation equivalent to damage initiation and is typically obtained from a performed monotonic test. A minimum of six displacement cycles are required prior to reaching Δ_o . The magnitude of Δ_m represents targeted deformation corresponding to maximum load, and requires a minimum of ten cycles prior to reaching. Δ_o and Δ_m were obtained from experimental diaphragm test results (Boadi-Danquah et al. 2019b). The value of Δ_o was taken as the measured displacement corresponding to 40% of the recorded positive peak loads (O'Brien et. al 2016) from Floor 1 and Floor 2 test results, as shown in Fig. 5- 4. This limit was considered the end of elastic behavior in the diaphragms tested cyclically (O'Brien et. al 2016, Essa et al. 2003). Between Floor 1 and Floor 2 test results, the lower value of $\Delta_o = 19$ mm (0.75 in.) was used to

calibrate the protocol for the parametric analysis. The value of Δ_m was set at 100 mm (4 in.), considered adequate to capture ample details on the floor’s diaphragm behavior for parametric study. The resulting displacement protocol used in the analytical evaluation is shown in Fig. 5- 5, with six displacement cycles, prior to reaching a Δ_o value of 19 mm (0.75 in.), and a total of sixteen cycles prior to reaching a Δ_m value of 100 mm (4 in.).

The cyclic displacement protocol was applied in the models by specifying a unit displacement along the face of the girder at the cantilever end of the diaphragm setup, and applying a variable amplitude to reflect the peak displacements in Fig. 5- 5. The loads corresponding to the applied displacements were obtained from the reactions measured in the pinned corners of the frame in the plane of the applied displacements.

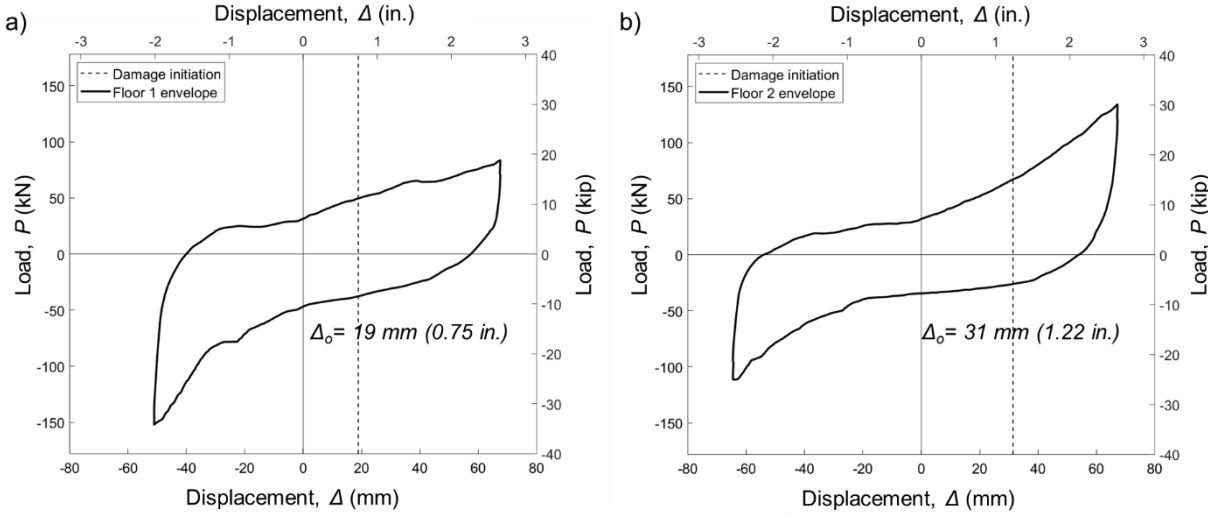


Fig. 5- 4: Estimate of Δ_o from a) Floor 1 test result b) Floor 2 test result

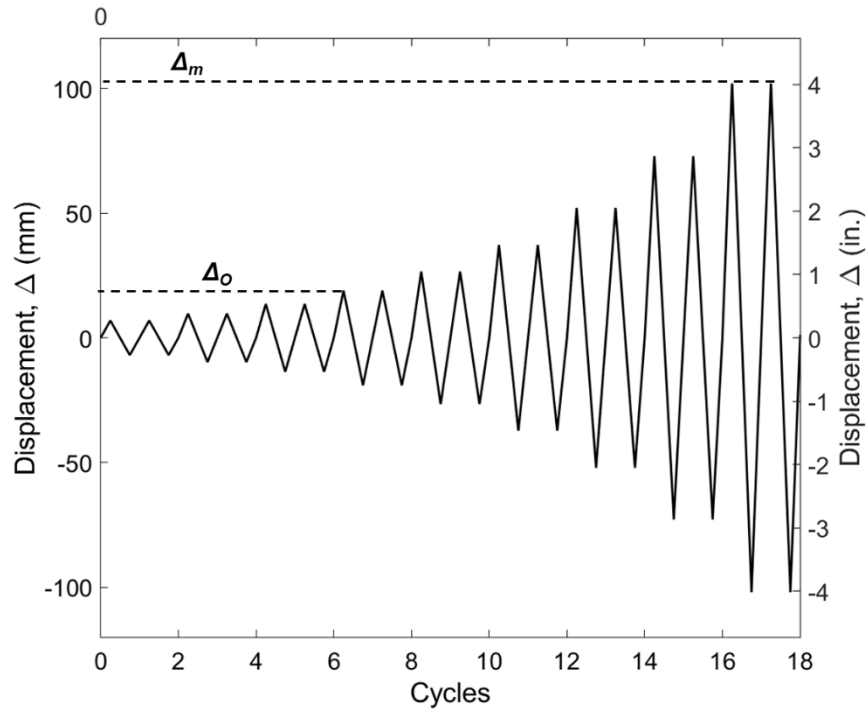


Fig. 5- 5: Cyclic displacement protocol

5.5 Results and Discussion

The *pinching4* material model has been used extensively in OpenSees (Mazzoni et al. 2005) to simulate connector behavior between sheathing and cold-formed sections in complex systems, and has been previously adapted (Ding 2015) for use with the commercial finite element program Abaqus CAE. The compatibility of this material model with Abaqus CAE, its capability to predict lateral system behavior at the connector level, and consequently overall behavior, have been further demonstrated by Ding (2015). This research further demonstrates the effectiveness of the Abaqus-adapted *pinching4* material model in simulating connector behavior in a complex floor diaphragm to understand overall diaphragm behavior.

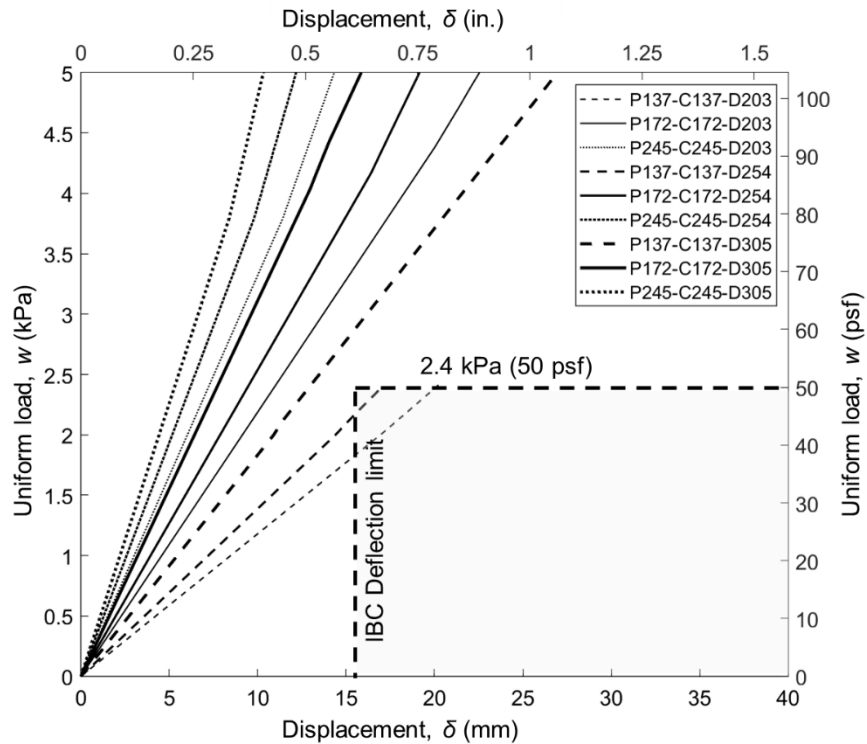


Fig. 5- 6: Load vs. displacement response under uniformly distributed gravity loads

The results of the FE gravity assessment were used to initially establish adequate service load carrying capacity for the floor configurations considered for the diaphragm study. The governing criterion for this assessment was the deflection limit in accordance with IBC (IBC 2015) at 2.4 kPa (50 psf), which is the minimum acceptable uniformly-distributed office live load. In Fig. 5- 6, displacements at the center of the floor system have been plotted against the applied uniformly distributed gravity loads for the range of parameters considered. The deflection limit in accordance with IBC (IBC 2015) was computed as 15.3 mm (0.6 in.) based on the plan dimensions of the floors studied. The maximum displacement at 2.4 kPa (50 psf) uniform loading was recorded as 20 mm (0.79 in.) for P137-C137-D203, and the minimum displacement of 6 mm (0.24 in.) was recorded for P245-C245-D356. Floors P137-C137-D203 and P137-C137-D203 had displacements exceeding the IBC (2015) limit, hence did not meet the acceptability criterion for service load

deflection. All other floor configurations studied had acceptable vertical displacements under 2.4 kPa (50 psf) uniform loading.

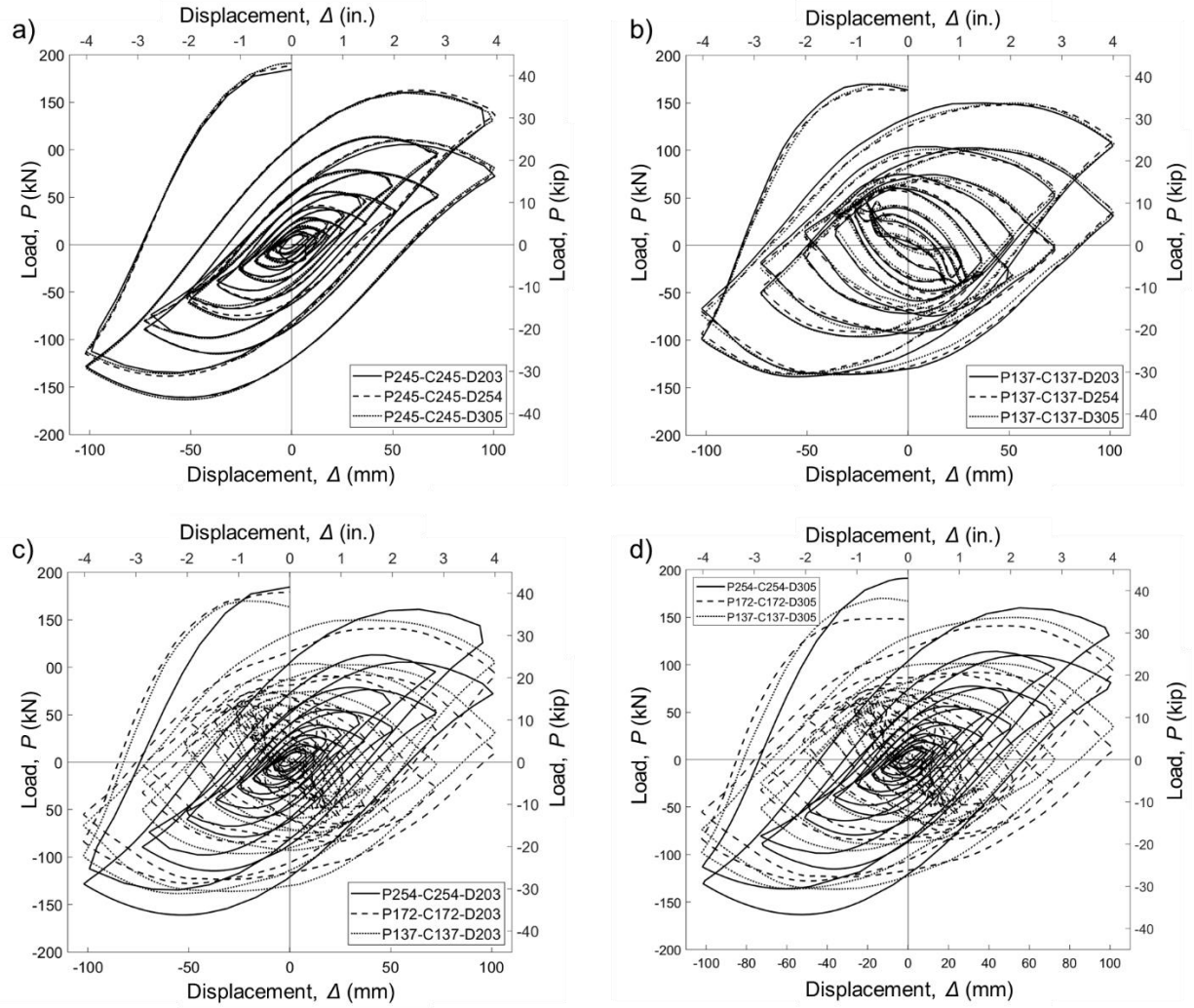


Fig. 5- 7: Cyclic load vs displacement response for varying (a and b) purlin depth, and (c and d) plate thickness (100 mm = 1.8 % drift)

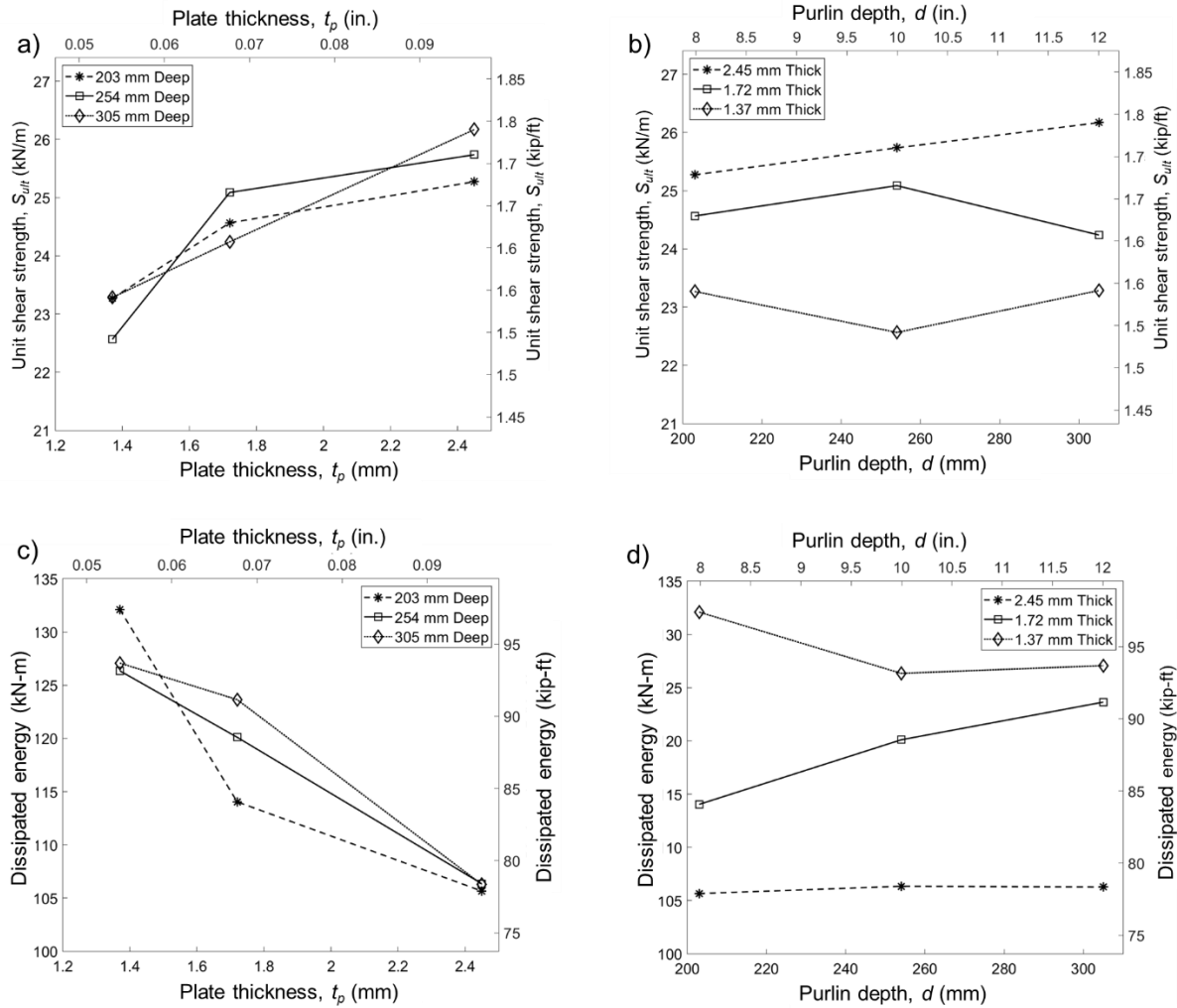


Fig. 5- 8: Variations in unit shear strength and dissipated energy with varying (a and c) plate thickness, and (b and d) purlin depth

The hysteretic response of the floor system under the cyclic displacement protocol is presented in Fig. 5- 7. Behavior associated with varying channel depth, d , and plate thickness, t_p , is presented in Fig. 5- 7. The magnitudes of S_{ult} and dissipated energy were determined from the hysteretic response of the system. Under cyclic displacements, the peak loads, P_{ult} , are the highest magnitude of load recorded for each floor configuration within the displacement range considered. The unit shear, S_{ult} of each floor system configuration is the respective peak load divided by the diaphragm length. Energy dissipation of the diaphragms was determined from the area within the

hysteresis plots. The magnitudes of P_{ult} , S_{ult} , and the dissipated energy are summarized in Table 5-5. The highest S_{ult} of 25.7 kN/m (1.8 kip/ft) was recorded for $t_p = 2.45$ mm (0.096) in P245-C245-D254, and the highest energy dissipation of 132.1 kN-m (97.4 kip-ft) was recorded for $t_p = 1.37$ mm (0.054 in.) in P137-C137-D203. The lowest S_{ult} of 22.6 kN/m (1.5 kip/ft) was recorded for $t_p = 1.37$ mm (0.054 in.) in P137-C137-D254, and the lowest energy dissipation of 105.7 kN-m (78.0 kip-ft) was recorded for $t_p = 2.45$ mm (0.096 in.) in P245-C245-D203.

Table 5- 5: Parametric study results

Model designation	Dissipated energy kN-m (kip-ft)	Unit shear	Peak load	Load (Eq. 1)
		S_{ult} kN/m (kip/ft)	P_{ult} kN (kip)	P_u kN (kip)
P137-C137-D203	132.1 (97.4)	23.3 (1.6)	169.9 (38.2)	221.6 (49.8)
P172-C172-D203	114.0 (84.1)	24.6 (1.7)	179.3 (40.3)	302.2 (67.9)
P245-C245-D203	105.7 (78.0)	25.3 (1.7)	184.5 (41.5)	297.3 (66.8)
P137-C137-D254	126.4 (93.2)	22.6 (1.5)	164.7 (37.0)	221.6 (49.8)
P172-C172-D254	120.1 (88.6)	25.1 (1.7)	183.1 (41.2)	302.2 (67.9)
P245-C245-D254	106.4 (78.5)	25.7 (1.8)	187.9 (42.2)	297.3 (66.8)
P137-C137-D305	127.1 (93.7)	23.3 (1.6)	170.0 (38.2)	221.6 (49.8)
P172-C172-D305	123.6 (91.2)	24.2 (1.7)	176.9 (39.8)	302.2 (67.9)
P245-C245-D305	106.3 (78.4)	26.2 (1.8)	191.0 (42.9)	297.3 (66.8)

Under lateral cyclic loading, varying t_p and d had unique effects on S_{ult} , and the dissipated energy as shown in Fig. 5- 8. At $d = 203$ mm (8 in.), when t_p was increased from 1.37 mm (0.054 in.) to 2.45 mm (0.097 in.), S_{ult} increased by 2.0 kN/m (0.1 kip/ft), and dissipated energy decreased by 26.4 kN-m (19.4 kip-ft). Similarly, at $d = 254$ mm (10 in.), when t_p was increased from 1.37 mm (0.054 in.) to 2.45 mm (0.097 in.), S_{ult} increased by 3.1 kN/m (0.3 kip/ft), and dissipated energy decreased by 20.0 kN-m (14.7 kip-ft). Finally, at $d = 305$ mm (12 in.), when t_p was increased from 1.37 mm (0.054 in.) to 2.45 mm (0.097 in.), S_{ult} increased by 2.9 kN/m (0.2 kip/ft), and dissipated energy decreased by 20.8 kN-m (15.3 kip-ft).

At $t_p = 1.37$ mm (0.054 in.), increasing depth from 203 mm (8 in.) to 305 mm (12 in.), resulted in an initial decrease of 0.7 kN/m (0.1 kip/ft) in S_{ult} between 203 mm (8 in.) deep and 254 mm (10 in.) deep, and an increase of 0.7 kN/m (0.1 kip/ft) between 254 mm (10 in.) deep and 305 mm (12 in.) deep. The dissipated energy reduced by 5.7 kN-m (4.2 kip-ft) between 203 mm (8 in.) deep and 254 mm (10 in.) deep, and increased by 0.7 kN-m (0.5 kip-ft) between 254 mm (10 in.) deep and 305 mm (12 in.) deep. At $t_p = 1.72$ mm (0.067 in.), increasing depth from 203 mm (8 in.) to 305 mm (12 in.), resulted in an initial increase of 0.5 kN/m (0.1 kip/ft) in S_{ult} between 203 mm (8 in.) deep and 254 mm (10 in.) deep, and a decrease of 0.9 kN/m (0.1 kip/ft) between 254 mm (10 in.) deep and 305 mm (12 in.) deep. The dissipated energy increased by 6.1 kN-m (4.5 kip-ft) between 203 mm (8 in.) deep and 254 mm (10 in.) deep and increased further by 3.5 kN-m (2.6 kip-ft) between 254 mm (10 in.) deep and 305 mm (12 in.) deep. Finally, at $t_p = 2.45$ mm (0.097 in.), increasing depth from 203 mm (8 in.) to 305 mm (12 in.), resulted in an initial decrease of 0.4 kN/m (0.1 kip/ft) in S_{ult} between 203 mm (8 in.) deep and 254 mm (10 in.) deep, and further increase of 0.5 kN/m (0.1 kip/ft) between 254 mm (10 in.) deep and 305 mm (12 in.) deep. The dissipated energy increased by 0.7 kN-m (0.5 kip-ft) between 203 mm (8 in.) deep and 254 mm (10 in.) deep, and reduced by 0.1 kN-m (0.1 kip-ft) between 254 mm (10 in.) deep and 305 mm (12 in.) deep. Increasing d had minimal effect on both S_{ult} and energy dissipation for the range of parameters considered, in comparison to increasing t_p . The magnitudes of change in S_{ult} and dissipated energy observed for varying d indicates little sensitivity of diaphragm characteristics to changes in d for the range of parameters studied.

The diaphragm load capacity, P_u , was computed using Eq. 1, based on SDI (2015) provisions. The computed values of P_u are presented in Table 5- 5 for the range of parameters considered in this study. The values of P_u were computed on the basis of rigid connector behavior

up to its peak, resulting in an upper bound diaphragm load capacity. From the values of P_u shown in Table 5- 5, plate thickness of $t_p = 1.72$ mm (0.067 in.) had the highest P_u of 302.2 kN (67.9 kip), followed by $t_p = 2.45$ mm (0.096 in.) with P_u of 297.3 kN and $t_p = 1.37$ mm (0.054 in.) with P_u of 221.6 kN. These values were consistent with perimeter fastener shear strength values shown in Table 5- 1. Test results presented in Boadi-Danquah et al. (2019a) showed that, at $t_p = 2.45$ mm (0.096 in.), the shear strength of PAFs were limited by fastener pull-out at lower lateral displacements, in comparison to the same PAFs in $t_p = 1.72$ mm (0.067 in.) and $t_p = 1.37$ mm (0.054 in.).

The response of cold-formed steel lateral load resisting systems is typically dominated by the local behavior at the fastener level (SDI 2015, Rogers and Tremblay 2003a & b, Essa et al. 2003, Luttrell 1996). This behavior was observed for all floor configurations studied, based on the assumptions made in numerical modeling.

5.6 Conclusions

This research has determined the diaphragm characteristics and inelastic behavior under quasi-static cyclic loads for varying plate thickness and purlin depth for different configurations of a novel modular steel floor system, as well as their gravity load carrying capacity. The following conclusions were obtained from the results of the analyses.

1. The *pinching4* material model-based Abaqus UEL was capable of simulating hysteretic behavior at the connector level, and consequently, overall diaphragm behavior.
2. For the range of parameters considered for the study, the diaphragm unit shear strength and energy dissipation of the floor diaphragm were sensitive to the plate thickness.
3. For the range of parameters considered for the study, depth had an insignificant effect on both the diaphragm unit shear strength of the floor system and its energy dissipation

capacity.

4. Estimated energy dissipation values can aid the estimation of an equivalent viscous damping ratio for dynamic analysis of structural systems incorporating the novel floor system.
5. Under cyclic loading, the seismic demands on the floor system can be increased to push it beyond its normal elastic function into the inelastic range, in order to dissipate some energy and consequently reduce the loads on the SFRS.

Chapter 6: Parametric Analysis of Vibrations in a Lightweight Two-Way Steel Floor System

6.1 Abstract

There is a lack of rapidly constructible, modular, and lightweight structural components and systems used for building construction. Such structures will in the future be able to sustainably and cost effectively meet new, changing demands for structures such as changing occupancies and extreme events. In an effort towards making structures more efficient, a lightweight, rapidly constructible and reconfigurable, modular steel floor (RCRMSF) system has been developed using cold formed steel components. Current design guidelines for vibrations are written for conventional structural systems and the suitability of the lightweight RCRMSF to resist vibrations due to human activity is unclear. To assess the dynamic behavior a design assessment has been adopted and high fidelity finite element models have been created. A parametric study was conducted to investigate the effect of important design parameters on the vibration response and serviceability of the RCRMSF for walking and rhythmic loading. The parametric study found that many RCRMSF configurations could be classified as high frequency floors and that the RCRMSF can meet serviceability limits with adequate design parameters.

6.2 Introduction

In practice there is limited use of modular structural components for rapid construction (Schoenborn 2012) leading to a lack of systems which facilitate this practice. Design and construction practices often assume that a structure's purpose will not significantly change during its service life. As a result, structures are not readily adaptable to changes in occupancy or use.

Modular design and construction, while not inherently adaptable, can allow for details suitable for rapid construction and reconfiguration of its components. Modular design also lends itself to low structural mass, as components are typically transported to a construction site. Lightweight structures provide another benefit through reduced material usage and diminished inertial forces developed during a seismic event. As an added benefit, damaged modular components can be designed to be replaced after an extreme loading event, reducing the time and cost of repairs. Thus, rapidly constructible, modular, and lightweight structures serve as a possible alternative to the status quo. However, no pervasively used flooring, cladding, or framing system has all these characteristics for building construction and as such experimental and analytical data are lacking.

Currently, one-way composite steel/concrete floor systems are extremely common in steel framed buildings, popular for their simplicity of construction, use of steel deck as a form, and utilization of composite behavior. Nevertheless, these steel/concrete composite floors are not lightweight, lend themselves to terminal construction practices, require collaboration between trades, and need significant time for construction and curing. Many flooring systems have been developed to improve upon typical composite steel/concrete floors (El-Sheikh 1996, Hsu et al. 2014). Recently, Boadi-Danqah et al. (2017) introduced a lightweight rapidly constructible and reconfigurable modular steel floor (RCRMSF) as a possible alternative. The RCRMSF is designed to take advantage of two-way action, can span bays of 12.2 m by 9.1 m with no intermediate beams, and for this study ranges in mass from 63 kg/m² to 92 kg/m². To maintain a low structural weight and rapid constructability, the RCRMSF is composed of predominantly cold-formed steel components, self-drilling self-tapping screws, and a thin cement board topping. The use of lighter, cold-formed steel components in this system allows for increased depth without greatly increasing weight, allowing for longer spans that meet deflection requirements which often govern floor

design (ICC 2012). Due to the high span-to-depth ratio and lightweight characteristics of the RCRMSF, assessment of induced vibrations from walking is essential (Robertson et al. 2017, Boadi-Danqah et al. 2017).

Guidance and limitations for floor vibrations to ensure comfort are provided in the American Institute of Steel Construction (AISC) Design Guide (DG) 11: Floor Vibrations Due to Human Activity 2nd Edition (Murray et al. 2016), Steel Construction Institute (SCI) P354 (Smith et al. 2007), and the International Standards Organization (ISO) 10137:2007 (ISO 2007). Methods for dealing with vibration issues have become more sophisticated as they have become more prevalent, and AISC DG11 (Murray et al. 2016) has been updated to account for high frequency floors, sensitive equipment, and finite element modeling methods. The design method found in AISC DG 11 (2016) uses the estimated fundamental natural frequency to predict the acceleration response and compares it to the ISO (2007) limit for floor acceleration based on occupant comfort (ISO limit).

Predominantly cold-formed steel floors, such as the RCRMSF, have been shown to have satisfactory behavior for floor vibrations due to walking (Xu 2011, Parnell et al. 2010). However, it is unclear if the existing vibration design methodologies are able to characterize the RCRMSF system, as these methodologies have been developed for conventional flooring systems. Considering that the RCRMSF is lightweight, has no intermediate beams, and has the potential to behave as a high frequency floor, alternative methods for evaluation will need to be considered (Robertson et al. 2017). For flooring systems with unknown properties, finite element modeling can also be used to predict floor vibration properties and acceleration response to harmonic loading (Davis et al. 2014, Da Silva et al. 2014).

The objective of this research is to assess the serviceability of the RCRMSF in office building configurations for walking induced vibrations and generate a simplified approach to evaluate the floor system using hand calculations. Methods from AISC DG 11 (Murray et al. 2016) and plate theory (Timoshenko and Woinowsky-Krieger 1959) are used in a design assessment (DA) to predict the acceleration response due to walking vibrations. High fidelity finite element models have been created in Abaqus Finite Element Analysis (FEA) software (DSS 2014) to better understand the RCRMSF vibrational behavior and assess the efficacy of a simplified DA. Ultimately, the DA and FEA have been used to provide analytical data and complete a parametric study to better understand the effect of important design parameters on dynamic behavior of the RCRMSF.

6.3 Rapidly Constructible and Reconfigurable Modular Steel Floor System

The RCRMSF system is comprised of a grillage of cold-formed steel channels, evenly spaced and running in two orthogonal directions (Fig. 6- 1). Track sections were selected for the channels according to the Steel Stud Manufacturers Association (SSMA) (2015). To develop two-way action the channels are profiled to run in both directions. Further profiling of the channel web can allow electrical, mechanical, and plumbing services to be placed within the floor depth (Boadi-Danquah et al. 2017). Sandwiching the channels are two light gauge steel plates fastened by self-drilling screws and welds. A 15.9 mm thick topping layer of cement board is attached to the top plate to improve load distribution, fireproofing, acoustics, finishing, and mitigate local vibrations. The RCRMSF can be transported to the construction site as pre-assembled individual panels. These panels can be connected using screwed web splices and cover plates framing directly onto the four perimeter girders of the bay without using intermediate beams. If necessary the RCRMSF panels

can be deconstructed by removing the cover plate and web splices, and then reconfigured as part of a new frame. RCRMSFs are intended to be one of many lightweight, modular, and adaptable building components of future structures.

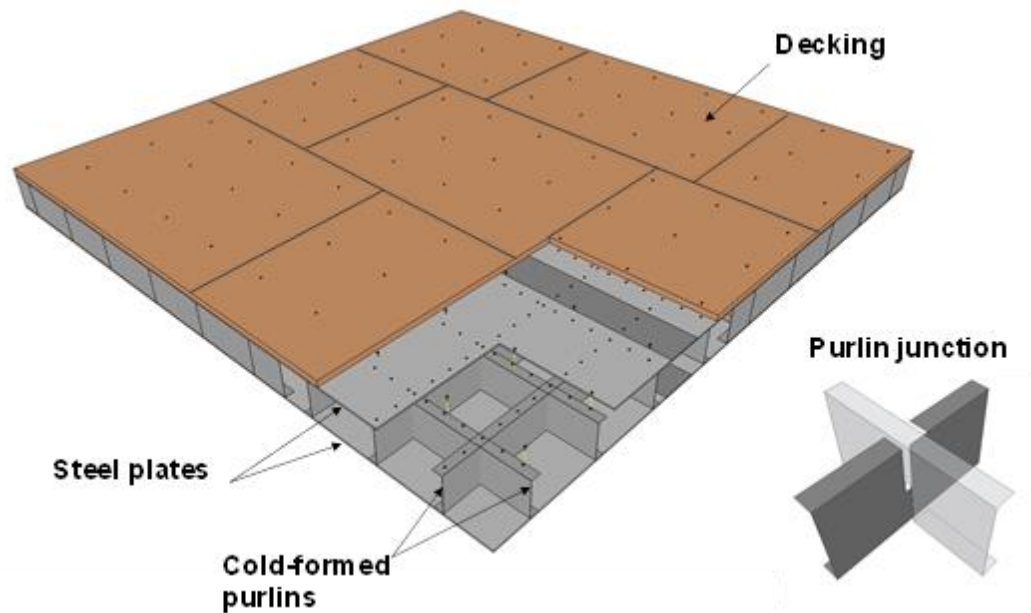


Fig. 6- 1: RCRMSF floor details

For this research, a 12.2 m by 9.1 m bay size was used. Girders were chosen based on realistic wide-flange sections given in the AISC Steel Construction Manual (AISC 2011) to meet deflection requirements (ICC 2012) for a 2.4 kPa (50 psf) live load. The bay was assumed to be interior and the load on the girders was doubled to account for adjacent bays. In selection of girders, the 9.1 m (30 ft) span had a triangular tributary area while the 12.2 m (40 ft) span had a trapezoidal tributary area. To maintain limited floor-to-floor heights, W18 series girders were used and the lightest section that met strength and deflections requirements (ICC 2012) was selected. The RCRMSF sits directly on top of wide flanged girders; W18 x 192 in the 12.2 m direction and

W18 x 97 in the 9.1 m direction (AISC 2011). Although only a typical office is being considered, floor parameters could be altered to fit different applications such as residences, shopping malls, or exercise facilities.

6.4 Vibration Serviceability Design Assessment

The vibration analysis in AISC DG11 (Murray et al. 2016) was adapted to apply to the RCRMSF to help determine its suitability to resist human induced vibrations. For this study, the system is assumed to be monolithic and the inter-panel connection detail is not considered. Amplitudes due to walking are small enough that some connections, especially beam-column type connections, can be modeled as fixed due to the friction in the connection (Murray et al. 2016). It has been shown that the inclusion of panel connections does not significantly affect the behavior of the system under low load amplitudes (Boadi-Danquah et al. 2017). In order to analyze the vibration response, the natural frequency (f_n) must first be predicted. To do this, displacement under a uniformly distributed gravity load (q) was estimated based on plate theory for a simply supported rectangular plate (Timoshenko and Woinowsky-Krieger 1959) (Equation 1);

$$\Delta = \alpha \frac{q a^4}{D} \quad (1)$$

where Δ is the mid-bay deflection and α is the aspect ratio coefficient based on the ratio of the long span (b) to the short span (a). For a floor size of 12.2 m x 9.1 m the b/a ratio is 1.33 and the alpha (α) is interpolated to 0.0066 (Timoshenko and Woinowsky-Krieger 1959).

The flexural rigidity for a rectangular plate (D) is based on the modulus of elasticity ($E = 11.7$ GPa), Poisson's ratio ($\nu = 0.3$), and plate thickness. To account for the use of the sandwich plates and the stiffness contributions from the channels running in both directions, the

channel depth (d) is subtracted from the overall floor depth, and the sandwich plate thickness is increased to account for the channel stiffness. This results in Equation 2;

$$D = \frac{E(H^3 - d^3)}{12(1 - \nu^2)} \quad (2)$$

where H is the total modified floor depth accounting for the increased or modified plate thickness (t_m) (Equation 3). The modified plate thickness (t_m) is found by first summing the moment of inertia of the channels and the sandwich plates to find the moment of inertia for the real section (I_{real}). An equivalent moment of inertia ($I_{equiv.}$) is then formulated for two plates without channels, separated by depth (d) with spacing (s) and set equal to I_{real} ($I_{equiv.} = I_{real}$) to solve for the modified thickness (Equation 4). This is an adapted approach from Timoshenko Woinowsky-Krieger (1959) and only applies to equivalent orthogonal channel spacing.

$$H = d + 2t_m \quad (3)$$

$$I_{real} = \frac{s(2t_m + d)^3}{12} - \frac{sd^3}{12} \quad (4)$$

The natural frequency was predicted based on Szilard (2004) (Equation 5);

$$f_n = \frac{2}{\pi^2} \sqrt{\frac{g}{\Delta_{total}}} \quad (5)$$

where g is the acceleration due to gravity and Δ_{total} is the sum of the mid-span deflection of the floor (Δ) and the girders under the gravity load (q) for the case of combined girder panel and beam/joist panel mode. The fundamental natural frequency was used to determine if floors were low (≤ 9 Hz) or high frequency floors (≥ 9 Hz). Low frequency floors are subject to resonant build-up from walking excitation, while high frequency floors do not reach resonance from walking excitation and their response to walking resembles a response to a series of impulses (Murray et al. 2016).

Floor vibrations are often presented in terms of acceleration because it is easy to measure using an accelerometer (Parnell et al. 2010). The low and high frequency floors acceleration response can be predicted according to AISC DG 11;

$$\frac{a_{low}}{g} = \frac{P_o e^{-0.35(f_n)}}{\beta W} \quad (6)$$

$$\frac{a_{high}}{g} = \left(\frac{2\pi f_n R R_M I_{eff}}{W} \right) \sqrt{\frac{1 - e^{-4\pi h \beta}}{\pi h \beta}} \quad (7)$$

$$I_{eff} = \frac{f_{step}^{1.43}}{f_n^{1.30}} \frac{Q}{17.8} \quad (8)$$

where the acceleration response of a low frequency floor is a_{low} (Equation 6) and the acceleration response of a high frequency floor is a_{high} (Equation 7) using an effective impulse (Equation 8). For low frequency floors, the effective weight (W) is calculated using Equation 9, damping (β) is assumed to be 2.5% of critical damping (typical of electronic offices with lower live loads), the force (P_o is taken as 289 N), the step frequency (f_{step}) is taken as 2.2 Hz, and the step frequency harmonic matching the natural frequency (f_n), is 5 for $f_n=9-11$ Hz, 6 for $f_n=11-13.2$ Hz, and 7 for $f_n=13.2-15.4$ Hz (Murray et al. 2016). The calculation for high frequency floors involves different terms, notably the higher mode factor (R_M) and a calibration factor (R) (Murray et al. 2016). The effective impulse I_{eff} (Equation 8) is calculated using the step frequency and system natural frequency along with the bodyweight, Q which is taken as 747 N. The step frequency harmonic (h) is taken from Murray et al. 2016.

Methods from Murray et al. (2016) were adapted to find the effective weight (W) by combining the long ($i=b$) and short direction ($i=a$) panel modes;

$$W = \frac{\Delta_a}{\Delta_b + \Delta_a} W_{gb} + \frac{\Delta_b}{\Delta_a + \Delta_b} W_{ga} \quad (9)$$

Where Δ_a is the girder deflection in the short direction (9.14 m), Δ_b is the girder deflection in the long direction (12.2 m), W_{gi} is the effective weight of each panel mode (Equation 10);

$$W_{gi} = w B_i L \quad (10)$$

with the girder weight per unit length (w), the effective panel width for the respective panel mode (B_i), and the girder span (L). The effective panel width for each mode is found using Equation 11;

$$B_i = C_g \left(\frac{D_f}{D_g} \right)^{1/4} L \leq \left(\frac{2}{3} \right) \text{ floor width} \quad (11)$$

using the constant C_g , taken as 1.8, the floor transformed moment of inertia in one direction (D_f) and the girder transformed moment of inertia (D_G).

The influence of higher modes beyond the fundamental mode is accounted for in the higher mode factor (R_M). For the single bay analysis, the R_M was taken as 1. Finite element analysis was used to examine higher mode impact and indicated that for a single bay the higher mode contribution was negligible. Therefore, there was no impact of additional modes between 0 Hz and 20 Hz. Design Guide 11 (Murray et al. 2016) allows for Equation 7 to be calibrated using the calibration factor (R), determined from experimental studies. In the absence of experimental data, and uncalibrated R value is specified to be 1.

6.5 Finite Element Model Description

Abaqus FEA (Version 6.14) (DSS 2014) was used to generate the finite element models of single bay and 3x3 bay configurations (Fig. 6- 2). The models were used to study the behavior of the RCRMSF under dynamic loading. Recommendations from AISC DG 11 (Murray et al. 2016) and SCI P354 (Smith et al. 2007) were followed to build the models for a typical electronic office. In each model, an eigenvalue analysis was conducted to find each mode and natural frequency. The models were then loaded with a dynamic load for 10 seconds and the acceleration time history was recorded over the 10 seconds of loading. This load duration was chosen to ensure adequate time for resonant build-up to appear if applicable and evaluate the steady state acceleration of the

floor system. Contributions of modes with frequencies less than 20 Hz were considered in computing the acceleration time history. The acceleration time histories were then measured and compared to the ISO limit for offices.

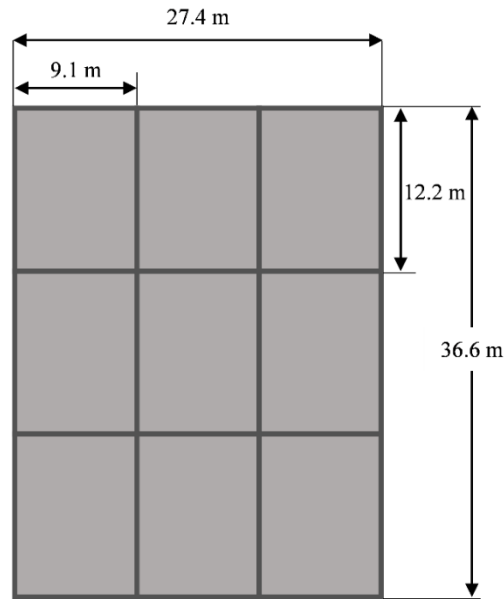


Fig. 6- 2: 3x3 bay arrangement and dimensions

6.5.1 *Material and Mesh Properties*

Three dimension (3-D) shell elements (SR4) were selected for the cement board, steel plates, and channels while beam elements (B31) were used for the girders (Fig. 6- 3). Steel plates and cement board were meshed into 76.2 mm square elements, the beams were meshed into 76.2 mm long elements and the channels were globally seeded at 76.2 mm. An initial mesh size equivalent to 1/10 the bay size was selected and refined until further reductions in mesh size no longer produced changes in natural frequency greater than 0.05 to 0.1 Hz. (Murray et al. 2016). Due to the low load range of the dynamic loads considered, all of the materials were modeled with linear elastic

behavior. The steel elements were assumed to have a density of $\rho=7,850 \text{ kg/m}^3$, elastic modulus of $E=200 \text{ GPa}$, and a Poisson's ratio of $\nu=0.30$ and the cement board was assumed to have a density of $\rho=933 \text{ kg/m}^3$, an elastic modulus of $E=11.7 \text{ GPa}$, and a Poisson's ratio of $\nu=0.20$ (USG 2016). Damping equivalent to 2.5% of critical damping, a design value suggested for an electronic office, was applied to each mode of vibration (Murray et al. 2016). An additional mass of 58.6 kg/m^2 was added to the mass of the steel plates to account for the presence of occupants and non-structural components based on recommendations from Murray et al. (2016).

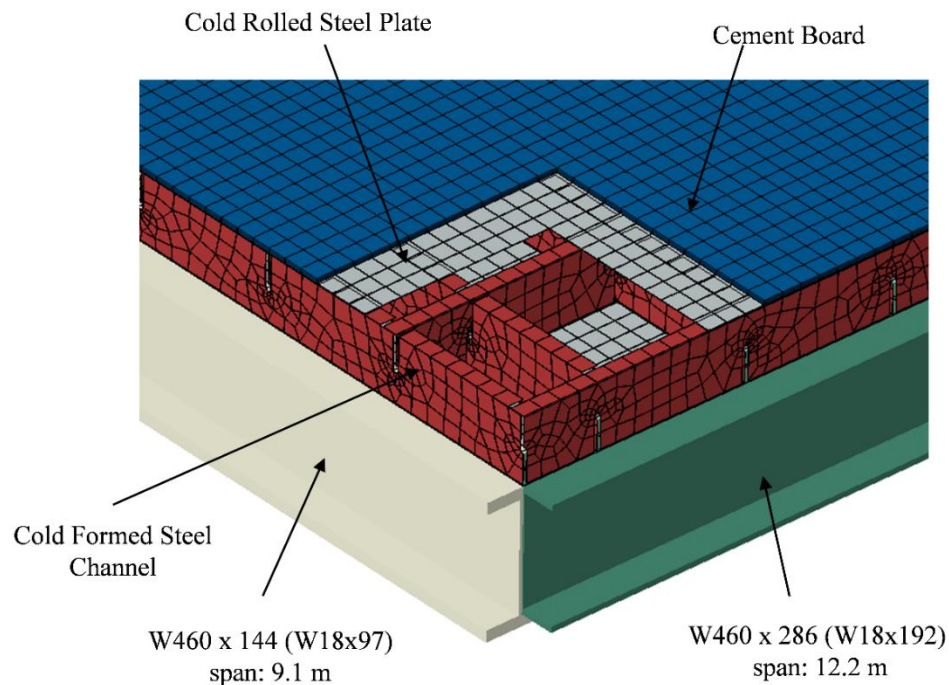


Fig. 6- 3: Finite element model

6.5.2 Boundary Conditions

Based on findings in Boadi-Danquah et al. (2017) and recommendations by AISC DG 11 (Murray et al. 2016), the configurations were built as monolithic systems with all tie constraints connecting the plates to the flanges of the channels, the bottom of the cement board to the top

plate, and the perimeter beams to the underside of bottom plate. Murray et al. justify simplifying modeling assumptions for dynamic analysis of walking vibrations due to the low amplitude of vibrations from human loading and friction in the system that may resist local effects. The orthogonally arranged channels are tied only to the plate and are not connected to each other. For the low amplitudes of floor vibrations, friction in the beam-column connection causes it to effectively behave as a moment connection (Murray et al. 2016, Smith et al. 2007). Therefore, the beam ends were fixed in single bay configurations and fixed connections were applied to the beams at the corners of each bay for the 3x3 bay arrangement. For the 3x3 bay configuration, adjoining panels were tied to create continuity across bays.

6.5.3 Loading

Two types of loading were applied to the models, a time dependent walking loading and a time dependent rhythmic loading. Both loads were applied to the top of the cement board in the center of the bay; in the 3x3 bay arrangement the load was applied in the same location in the central bay. The forcing function (F) for both the walking and rhythmic loads are based on a Fourier series approximation of each load;

$$F(t) = \sum_{i=1}^4 P(\alpha_i \cos 2\pi i f_{step} t) \quad (12)$$

with dynamic coefficient (α) for each harmonic number (i). Loading frequencies (f_{step}) were individually selected for each model such that the frequency would generate the largest response within the recommended range of 1.6–2.2 Hz (Murray et al. 2016) (Fig. 6- 4). Low frequency floors ($f_n < 9$ Hz) were loaded with the lowest walking frequency that would generate resonance and maximize response; for RCRMSF, only the 4th harmonic ($i=4$) generated resonance. High frequency floors ($f_n \geq 9$ Hz) were loaded with the maximum walking frequency of 2.2 Hz. The

acceleration response to the dynamic loads were measured at the point of loading, mid-bay on top of the cement board, and at the same location in the central bay for the 3x3 bay arrangement.

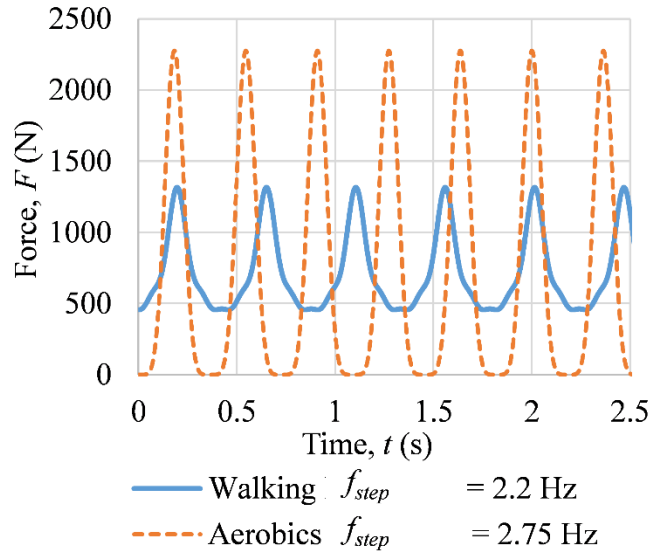


Fig. 6- 4: Walking and aerobic load history

6.6 Parametric Study Results and Discussion

A parametric study was conducted to examine the effect of plate thickness (t_p), channel thickness (t_c), channel depth (d), and channel spacing (s) on the vibration performance of the RCRMSF (Fig. 6- 5). Each model in the single bay arrangement was evaluated using the DA and FEA to determine the natural frequencies and predict the acceleration response to walking excitation. Using the FEA on a subset of RCRMSF configurations, 3x3 bay configurations were studied to examine the effect of including surrounding bays and a single bay configurations were evaluated for rhythmic loading. Each RCRMSF configuration was given a designation corresponding to the values of its parameters; for example, the base configuration with $t_p=1.37$ mm, $t_c=1.72$ mm, $d=254$ mm, and $s=610$ mm was named P1.37-C1.72-D245-S610. For the entire parametric study, plate thicknesses varied between 1.37 mm and 3.0 mm, channel thicknesses

varied between 1.09 mm and 3.0 mm, channel depths varied between 203 mm and 406 mm, and channel spacing varied between 610 mm and 1830 mm (Table 6- 1).

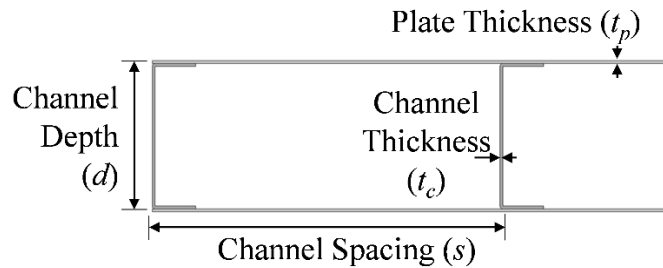


Fig. 6- 5: Cross-section showing RCRMSF parameters

For the FEA, acceleration time histories were converted to equivalent sinusoidal peak acceleration (ESPA) and the maximum ESPA over the entire time history is presented (A_{ESPA}). The DA results are presented in terms of predicted peak acceleration (A_p). The parametric study results of both the FEA and DA are presented in Table 6- 2. The f_n of each configuration was used to classify each floor as a high frequency floor or low frequency floor and to compare to the ISO limit for offices. The ISO limit increases with higher natural frequencies; therefore the ISO limit was adjusted based on the predicted f_n . The resulting limit was used to determine the serviceability of the floor (Table 6 -2). Both the FEA and DA show similar changes in natural frequency and peak accelerations with changes in t_p , t_c , and d . However, the FEA can capture local vibrations (Fig. 6- 6) and other sensitivities not feasible to consider using the DA. Because of this and for brevity the following discussion focuses primarily on the FEA model results unless otherwise specified.

Table 6- 1. Parametric study configurations (bold indicates parameter varied from base configuration P1.37-C1.72-D254-S610)

Model	Plate	Channel	Channel	Channel	Parameter Varied	3x3 Bay Model	Rhythmic Loading
	Thickness	Thickness	Depth	Spacing			
	t_p (mm)	t_c (mm)	d (mm)	s (mm)			
P1.37-C1.72-D254-S610	1.37	1.72	254	610	Base Model	X	X
P1.72 -C1.72-D254-S610	1.72	1.72	254	610	t_p	X	X
P2.45 -C1.72-D254-S610	2.45	1.72	254	610		X	X
P3.00 -C1.72-D254-S610	3	1.72	254	610		X	X
P1.37-C 1.37 -D254-S610	1.37	1.37	254	610	t_c	-	-
P1.37-C 2.45 -D254-S610	1.37	2.45	254	610		-	-
P1.37-C1.72- D203 -S610	1.37	1.72	203	610	d	X	X
P1.37-C1.72- D305 -S610	1.37	1.72	305	610		X	X
P1.37-C1.72- D406 -S610	1.37	2.45	406	610		-	-
P1.37-C1.72-D254- S1220	1.37	1.72	254	1220	s	-	-
P1.37-C1.72-D254- S1829	1.37	1.72	254	1830		-	-
P1.72-C1.37 -D254-S610	1.72	1.37	254	610	t_p & t_c	-	-
P2.45-C1.37 -D254-S610	2.45	1.37	254	610		-	-
P3.00-C1.37 -D254-S610	3	1.37	254	610		-	-
P1.72-C2.45 -D254-S610	1.72	2.45	254	610		-	-
P2.45-C2.45 -D254-S610	2.45	2.45	254	610		-	-
P3.00-C2.45 -D254-S610	3	2.45	254	610		-	-
P1.72-C1.72-D203 -S610	1.72	1.72	203	610	t_p & d	X	X
P2.45-C1.72-D203 -S610	2.45	1.72	203	610		X	X
P3.00-C1.72-D203 -S610	3	1.72	203	610		X	X
P1.72-C1.72-D305 -S610	1.72	1.72	305	610		X	X
P2.45-C1.72-D305 -S610	2.45	1.72	305	610		X	X
P3.00-C1.72-D305 -S610	3	1.72	305	610		X	X
P1.72-C1.72-D406 -S610	1.72	2.45	406	610		-	-
P2.45-C1.72-D406 -S610	2.45	2.45	406	610		-	-
P3.00-C1.72-D406 -S610	3	2.45	406	610		-	-
P1.72-C1.72-D254-S1220	1.72	1.72	254	1220	t_p & s	-	-
P2.45-C1.72-D254-S1220	2.45	1.72	254	1220		-	-
P3.00-C1.72-D254-S1220	3	1.72	254	1220		-	-
P1.72-C1.72-D254-S1830	1.72	1.72	254	1830		-	-
P2.45-C1.72-D254-S1830	2.45	1.72	254	1830		-	-
P3.00-C1.72-D254-S1830	3	1.72	254	1830		-	-
P1.37-C 1.09 -D203-S610	1.37	1.09	203	610	t_c & d	-	-
P1.37-C 1.37 -D203-S610	1.37	1.37	203	610		-	-
P1.37-C 2.45 -D305-S610	1.37	2.45	305	610		-	-
P1.37-C 3.00 -D305-S610	1.37	3	305	610		-	-
P1.37-C 1.37 -D254- S1220	1.37	1.37	254	1220	t_c & s	-	-
P1.37-C 2.45 -D254- S1220	1.37	2.45	254	1220		-	-
P1.37-C 1.37 -D254- S1830	1.37	1.37	254	1830		-	-
P1.37-C 2.45 -D254- S1830	1.37	2.45	254	1830		-	-
P1.37-C1.72- D203-S1220	1.37	1.72	203	1220	d & s	-	-
P1.37-C1.72- D305-S1220	1.37	1.72	305	1220		-	-
P1.37-C1.72- D203-S1830	1.37	1.72	203	1830		-	-
P1.37-C1.72- D305-S1830	1.37	1.72	305	1830		-	-

Table 6- 2. Parametric study results for walking load (bold indicates parameter varied from base configuration P1.37-C1.72-D254-S610; HFF=high frequency floor; LFF=low frequency)

Model	FEA, f_n (Hz)	FEA, A_{ESPA} (%g)	DA, f_n (Hz)	DA, A_P (%g)	FEA ISO Limit	FEA, Floor Type	FEA, Vibration Check	DA ISO Limit	DA, Floor Type	DA, Vibration Check
P1.37-C1.72-D254-S610	9.26	0.93	8.84	0.72	0.58	HFF	FAIL	0.55	LFF	FAIL
P1.72 -C1.72-D254-S610	9.72	0.60	9.33	0.78	0.61	HFF	PASS	0.58	HFF	FAIL
P2.45 -C1.72-D254-S610	10.43	0.45	10.05	0.69	0.65	HFF	PASS	0.63	HFF	FAIL
P3.00 -C1.72-D254-S610	10.77	0.40	10.40	0.64	0.67	HFF	PASS	0.65	HFF	PASS
P1.37- C1.37 -D254-S610	9.21	1.03	8.86	0.74	0.58	HFF	FAIL	0.55	LFF	FAIL
P1.37- C2.45 -D254-S610	9.31	0.82	8.81	0.68	0.58	HFF	FAIL	0.55	LFF	FAIL
P1.37-C1.72- D203 -S610	7.88	2.13	7.35	1.24	0.50	LFF	FAIL	0.50	LFF	FAIL
P1.37-C1.72- D305 -S610	10.56	0.49	10.17	0.78	0.66	HFF	PASS	0.64	HFF	FAIL
P1.37-C1.72- D406 -S610	13.22	0.32	12.30	0.70	0.83	HFF	PASS	0.77	HFF	PASS
P1.37-C1.72-D254- S1220	10.20	0.69	8.84	0.78	0.64	HFF	FAIL	0.55	LFF	FAIL
P1.37-C1.72-D254- S1829	10.20	0.65	8.79	0.81	0.64	HFF	FAIL	0.55	LFF	FAIL
P1.72-C1.37 -D254-S610	9.72	0.63	9.37	0.80	0.61	HFF	FAIL	0.59	HFF	FAIL
P2.45-C1.37 -D254-S610	10.43	0.47	10.11	0.71	0.65	HFF	PASS	0.63	HFF	FAIL
P3.00-C1.37 -D254-S610	10.73	0.42	10.47	0.66	0.67	HFF	PASS	0.65	HFF	FAIL
P1.72-C2.45 -D254-S610	9.80	0.56	9.26	0.73	0.61	HFF	PASS	0.58	HFF	FAIL
P2.45-C2.45 -D254-S610	10.50	0.43	9.92	0.66	0.66	HFF	PASS	0.62	HFF	FAIL
P3.00-C2.45 -D254-S610	10.83	0.38	10.24	0.61	0.68	HFF	PASS	0.64	HFF	PASS
P1.72-C1.72-D203 -S610	8.28	2.03	7.81	1.01	0.52	LFF	FAIL	0.50	LFF	FAIL
P2.45-C1.72-D203 -S610	8.95	1.54	8.51	0.72	0.56	LFF	FAIL	0.53	LFF	FAIL
P3.00-C1.72-D203 -S610	9.27	0.80	8.88	0.59	0.58	HFF	FAIL	0.55	LFF	FAIL
P1.72-C1.72-D305 -S610	11.05	0.43	10.66	0.73	0.69	HFF	PASS	0.67	HFF	FAIL
P2.45-C1.72-D305 -S610	11.90	0.37	11.33	0.66	0.74	HFF	PASS	0.71	HFF	PASS
P3.00-C1.72-D305 -S610	12.14	0.33	11.64	0.61	0.76	HFF	PASS	0.73	HFF	PASS
P1.72-C1.72-D406 -S610	12.22	0.29	12.73	0.67	0.76	HFF	PASS	0.80	HFF	PASS
P2.45-C1.72-D406 -S610	12.51	0.23	13.25	0.60	0.78	HFF	PASS	0.83	HFF	PASS
P3.00-C1.72-D406 -S610	12.93	0.19	13.43	0.57	0.81	HFF	PASS	0.84	HFF	PASS
P1.72-C1.72-D254-S1220	10.97	0.53	9.39	0.84	0.69	HFF	PASS	0.59	HFF	FAIL
P2.45-C1.72-D254-S1220	12.36	0.49	10.18	0.74	0.77	HFF	PASS	0.64	HFF	FAIL
P3.00-C1.72-D254-S1220	9.60	0.41	10.56	0.68	0.60	HFF	PASS	0.66	HFF	FAIL
P1.72-C1.72-D254-S1830	8.96	0.52	9.37	0.85	0.56	LFF	PASS	0.59	HFF	FAIL
P2.45-C1.72-D254-S1830	10.46	0.47	10.18	0.75	0.65	HFF	PASS	0.64	HFF	FAIL
P3.00-C1.72-D254-S1830	11.02	0.39	10.58	0.69	0.69	HFF	PASS	0.66	HFF	FAIL
P1.37- C1.09-D203 -S610	7.73	2.27	7.34	1.32	0.50	LFF	FAIL	0.50	LFF	FAIL
P1.37- C1.37-D203 -S610	7.83	2.23	7.35	1.28	0.50	LFF	FAIL	0.50	LFF	FAIL
P1.37- C2.45-D305 -S610	11.50	0.44	10.09	0.72	0.72	HFF	PASS	0.63	HFF	FAIL
P1.37- C3.00-D305 -S610	12.76	0.48	10.23	0.69	0.80	HFF	PASS	0.64	HFF	FAIL
P1.37- C1.37-D254-S1220	10.09	0.72	8.84	0.80	0.63	HFF	FAIL	0.55	LFF	FAIL
P1.37- C2.45-D254-S1220	10.30	0.59	8.81	0.76	0.64	HFF	PASS	0.55	LFF	FAIL
P1.37- C1.37-D254-S1830	11.13	0.68	8.80	0.82	0.70	HFF	PASS	0.55	LFF	FAIL
P1.37- C2.45-D254-S1830	10.34	0.62	8.75	0.80	0.65	HFF	PASS	0.55	LFF	FAIL
P1.37-C1.72- D203-S1220	9.21	1.03	7.31	1.35	0.58	HFF	FAIL	0.50	LFF	FAIL
P1.37-C1.72- D203-S1220	12.06	0.59	10.21	0.85	0.75	HFF	PASS	0.64	HFF	FAIL
P1.37-C1.72- D305-S1830	9.19	0.68	7.27	1.40	0.57	HFF	FAIL	0.50	LFF	FAIL
P1.37-C1.72- D305-S1830	11.81	0.62	10.16	0.87	0.74	HFF	PASS	0.64	HFF	FAIL

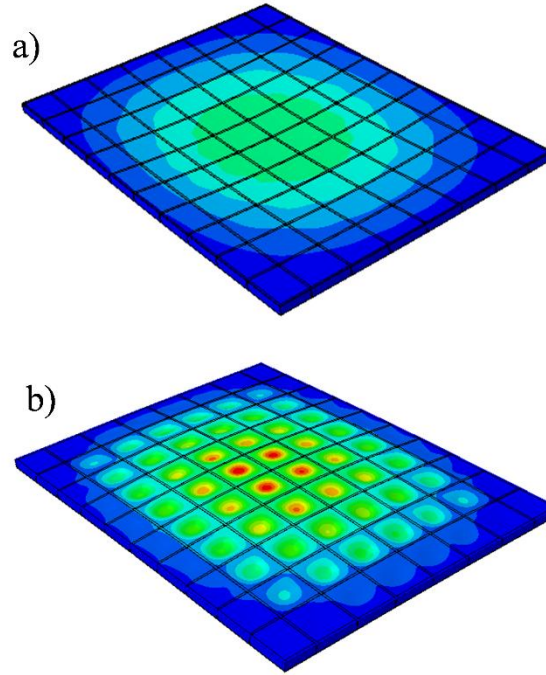


Fig. 6- 6: Abaqus FEA results showing floor accelerations as a result of (a) global vibrational behavior of the top plate and (b) local vibrational behavior present in the bottom plate as shown by variations within channel lines

6.6.1 Single Bay FEA Natural Frequency Results and Discussion

In the course of the FEA parametric study, the natural frequency and acceleration time history were recorded for each model. The fundamental natural frequencies of each single bay model in the parametric study are displayed in Fig. 6- 7 for varying (a) t_p , (b) t_c , (c) d , and (d) s . For configurations with $s=1220$ mm and 1830 mm, bottom plate local vibrations were observed. These local vibrations were not present in the top plates as a result of the restraint provided by the topping. In cases with localized vibrations, the fundamental natural frequency was chosen as the lowest frequency of the mode that exhibited global vibration behavior.

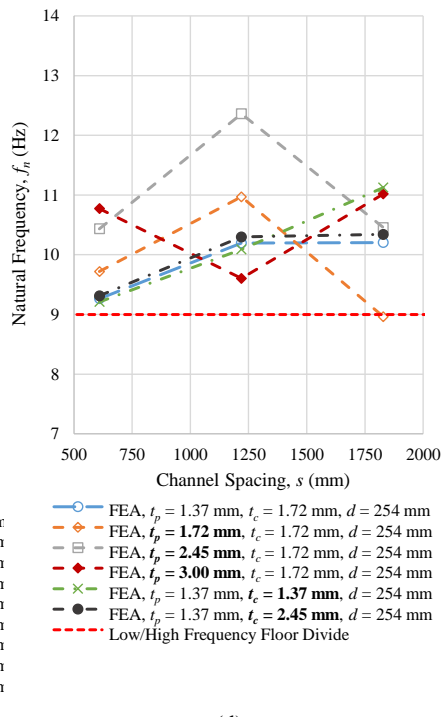
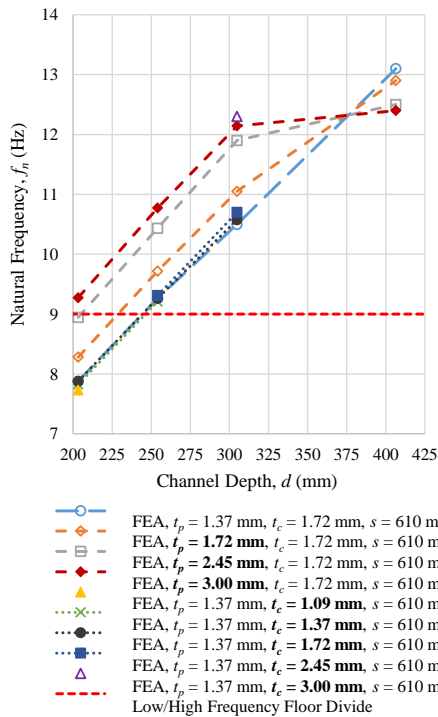
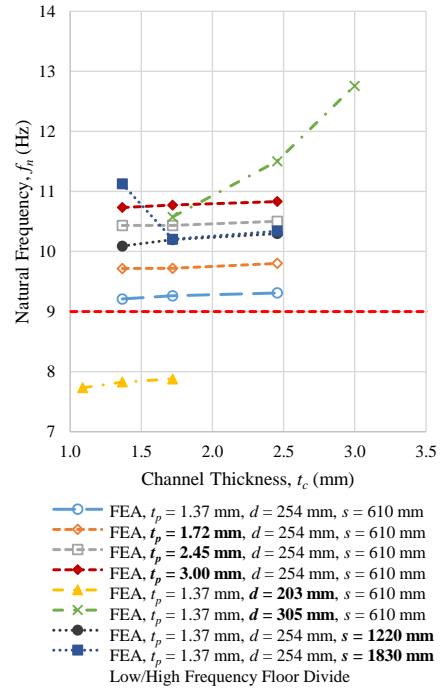
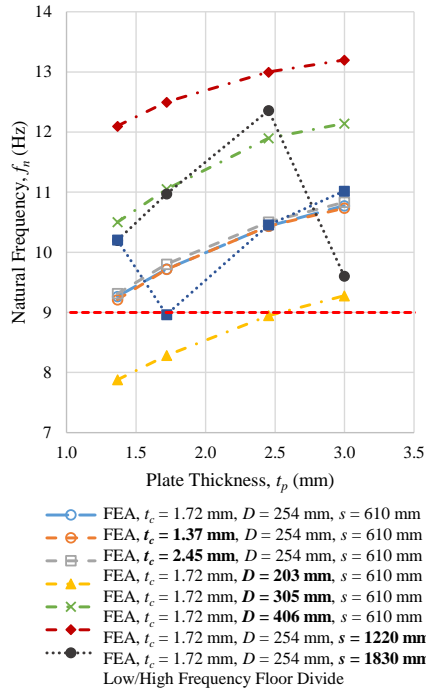


Fig. 6- 7: Single bay parametric study natural frequency results varying: (a) plate thickness (b) channel thickness (c) channel depth and (d) channel spacing

For the FEA, the maximum f_n of 13.22 Hz occurred in P1.37-C1.72-D406-S610 and the minimum f_n of 7.73 Hz occurred in P1.37-C1.09-D203-S610. For the DA the maximum f_n of 13.43 Hz occurred in P3.00-C1.72-D406-S610 and the minimum f_n of 7.27 Hz occurred in P1.37-C1.72-D305-S1830. The study found that 38 of 44 configurations were high frequency floors ($f_n \geq 9$ Hz), and the DA found 27 of 44 configurations were high frequency floors.

Increases in plate thickness, t_p , were positively related to increases in f_n . Each time t_p was increased, the f_n also increased, except when $s \geq 1220$ mm and local vibrations were observed. The average f_n for all configurations with $t_p = 1.37$ mm was 9.90 Hz and the average f_n for all configurations with $t_p = 3.00$ mm was 10.80 Hz. This results in a slight increase of 0.90 Hz between the two plate thicknesses regardless of other parameters. Increases in t_p increased both the mass and stiffness of the system, and resulted in increased f_n . For each increase in t_c , f_n also increased, except when $s \geq 1830$ mm. The average f_n for all configurations with $t_c = 1.37$ mm was 10.23 Hz and the average f_n for all configurations with $t_c = 2.45$ mm was 10.73 Hz. This results in an increase of 0.50 Hz between the two channel thicknesses. However, at increased depth (305 mm) channel the effect of increasing channel thickness becomes more pronounced as a deeper and more flexurally stiff channel is used. Increases in channel depth, d , always led to an increase in f_n . The average f_n for all configurations with $d = 203$ mm was 8.46 Hz and the average f_n for all configurations with $d = 406$ mm was 12.70 Hz. This was an increase of 4.24 Hz between the two channel depths regardless of other parameters. Increasing d was by far the most effective means of increasing natural frequency as a result of greatly increased stiffness with little increased mass.

Changes in parameters t_p , t_c , and d , showed no clear trend with increasing $s \geq 1220$ mm. Due to local vibrations, increasing s from 610-1830 mm led to both increases and decreases in f_n . The relationship between mass, stiffness, and local vibrations due to changes in s is complex and a

clear trend could not be determined. Regardless, the average f_n for configurations with $s=610$ mm was 9.86 Hz and the average f_n for configurations with $s=1830$ mm was 10.33 Hz, resulting in a small difference of 0.47 Hz between the two channel spacing. As a result, changing spacing is not an effective method for modifying system natural frequency. Overall, changes in d had the largest impact on f_n , followed by changes in t_p , t_c , and s .

High frequency floors are less susceptible to resonant buildup and therefore are less likely to exhibit excessive vibrations. When $t_p \geq 3.00$ mm, each of the configurations were high frequency floors. When $d \geq 254$ mm and $t_p \geq 1.37$ mm, configurations were also high frequency floors, except P1.72-C1.72-D254-S1830. All configurations with $d \geq 254$ mm and configurations with $d=203$ mm and $t_p \geq 3.00$ mm were high frequency floors (Fig. 6- 7(c)). The effect of t_c and s on the floor type is less clear, however $d \geq 254$ mm and $t_c \geq 1.37$ satisfy high frequency floor limits when $s = 610$ mm.

6.6.2 *Single Bay FEA Acceleration Response Results and Discussion*

For measured acceleration time histories, A_{ESPA} should be compared with the ISO limit to determine serviceability of a floor. The A_{ESPA} is calculated using a 2 second rolling root mean square (RMS) of the acceleration time history and multiplied by the ratio between RMS and peak ($\sqrt{2}$) (Davis et al. 2014). For a typical office building, accelerations higher than 0.5% gravitational acceleration (g) are deemed unacceptable by the ISO limits (Murray et al. 2016). Fig. 6- 8(a) and (b) show the first 5 seconds of the acceleration time history and A_{ESPA} of (a) a sample low frequency floor, P1.37-C1.72-D203-S610, (b) a sample high frequency floor, P1.37-C1.72-D305-S610. The maximum A_{ESPA} over the entire time history of each single bay model is plotted for varying (a) t_p , (b) t_c , (c) d , and (d) s (Fig. 6-9). The resulting A_{ESPA} were compared to ISO limit for offices (Table

6 -2). In Fig. 6- 9 the minimum ISO limit for an office is plotted as a reference. However, the ISO limit increases with increasing natural frequency for $f_n > 9$ Hz (Fig. 6- 10).

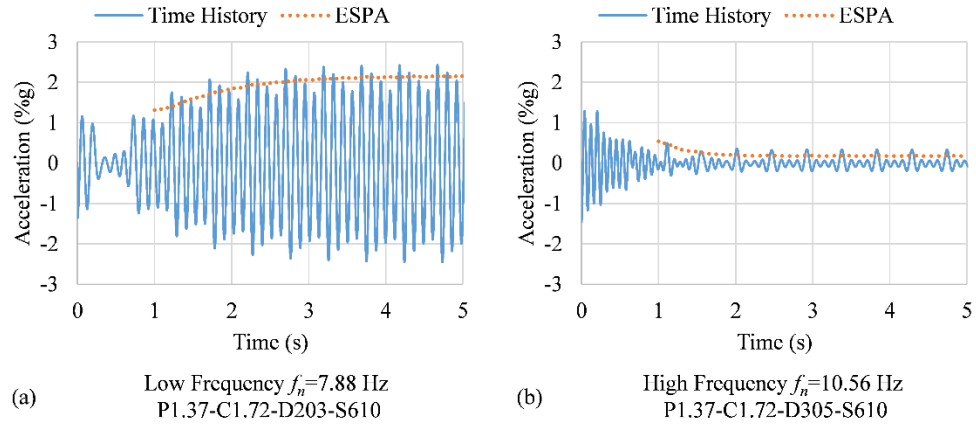


Fig. 6- 8: Sample finite element analysis time histories: (a) low frequency floor P1.37-C1.72-D203-S610 (b) high frequency floor P1.37-C1.72-D305-S610

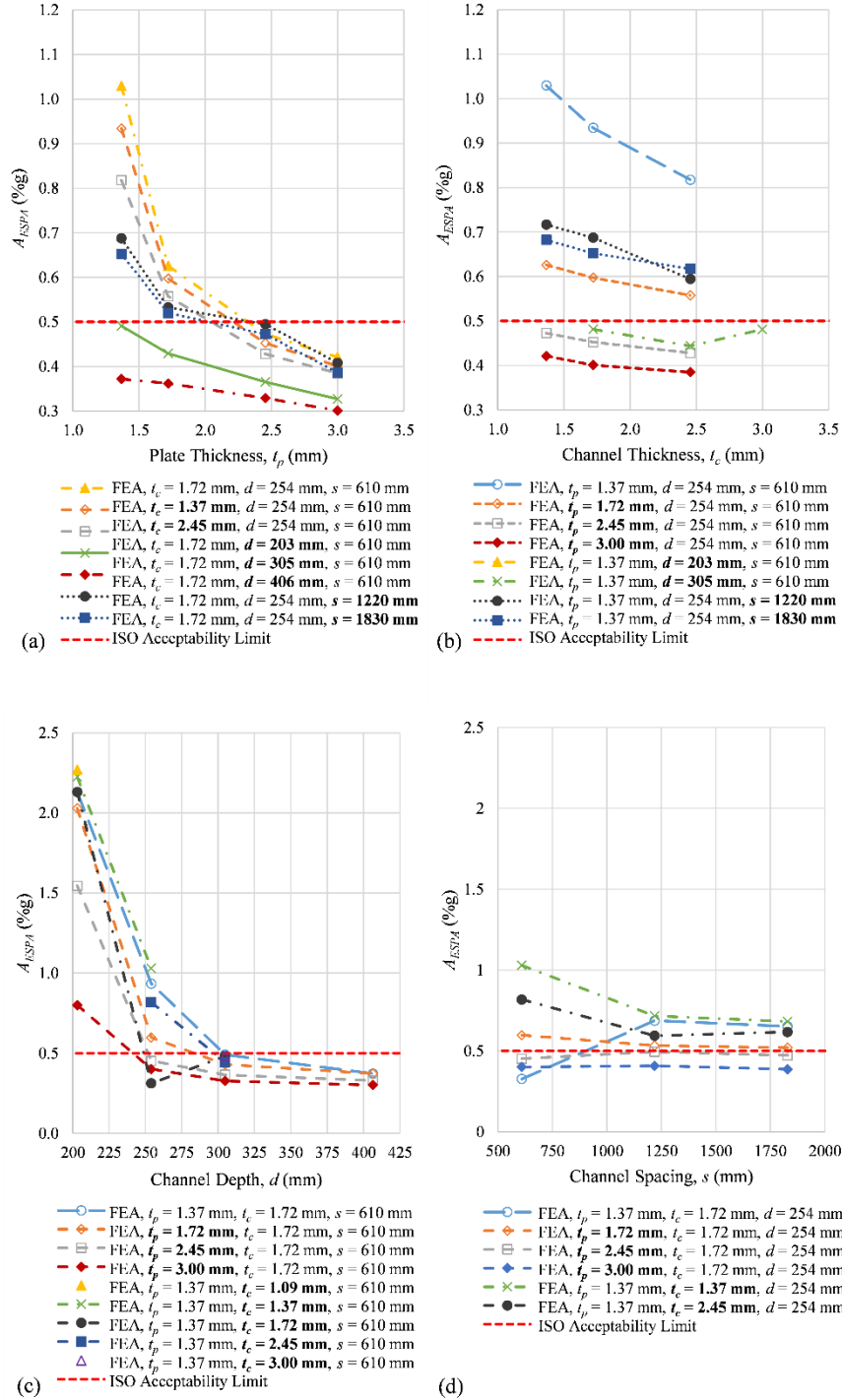


Fig. 6- 9: Single bay parametric study acceleration results varying: (a) plate thickness (b) channel thickness (c) channel depth and (d) channel spacing

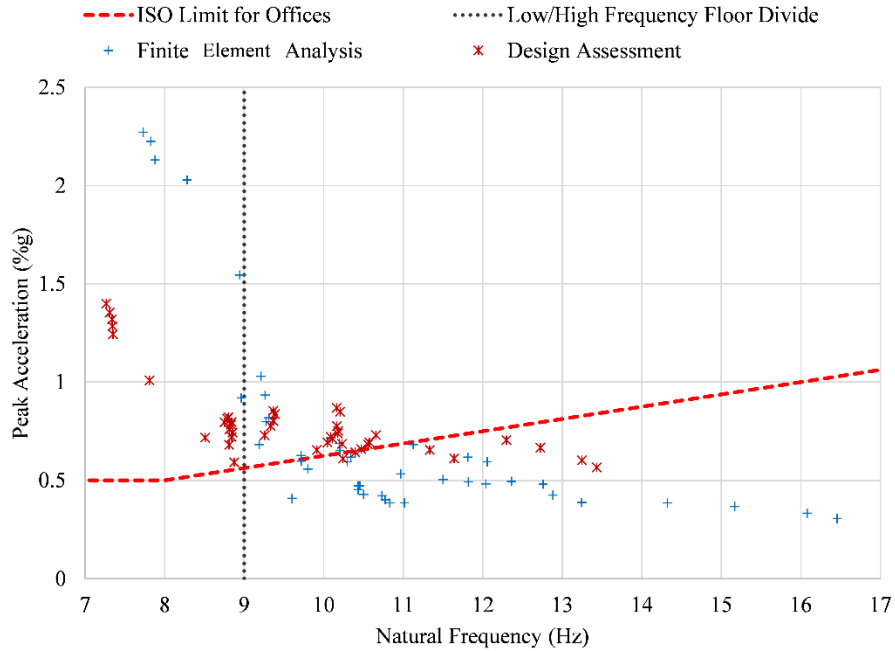


Fig. 6- 10: Acceleration vs. natural frequency for single bay floors

For the FEA, the maximum A_{ESPA} of 2.27 %g occurred in P1.37-C1.09-D203-S610 and the minimum A_{ESPA} of 0.19 %g occurred in P3.00-C1.72-D406-S610. For the DA the maximum A_{ESPA} of 1.40 %g occurred in P1.37-C1.72-D203-S1830 and the minimum A_{ESPA} of 0.57 %g occurred in P3.00-C1.72-D406-S610. The FEA found that 28 out of 44 configurations met ISO limit for offices; while the DA found that 8 out of 44 configurations met the ISO limit for offices. Notably, none of the low frequency floors met ISO limits for offices. It is worth noting that analytical discrepancies between FEA and DA predicted accelerations are not abnormal. This can likely be attributed to the respective methods used to determine the participating mass of the system, where the FEA method will calculate eigenvectors to obtain the mode shapes and the DA relies on the deflected shape (Perry 2003). The effective mass of the system can be determined experimentally and compared to the FEA and DA and used to calibrate each.

The parametric study results showed that f_n was inversely related to A_{ESPA} . For example, increases in t_p , t_c , d , and s resulted in increases in f_n but decreases in A_{ESPA} . When $s \geq 1220$ mm, increases in t_p and t_c did not always result in decreases in A_{ESPA} due to the presence of local vibrations. Several floors, both low and high frequency, had a natural frequency near the fourth harmonic of the walking load. It was observed that these floors experienced some effect of resonant build-up and resulted in greater accelerations. For example, P2.45-C1.72-D203-S610 had a natural frequency of 9.06 Hz and excessively high vibrations, $A_{ESPA}=1.25$ %g were observed from examination of the acceleration time history. Furthermore, while high frequency floors often do not have vibration serviceability problems, those RCRMSF systems with natural frequencies near the fourth harmonic experienced greater accelerations. As a result, designing based on f_n alone is not sufficient to characterize the serviceability of the RCRMSF.

Increases in t_p led to decreases in A_{ESPA} for all configurations, except P1.72-C1.72-D254-S1830 due to local vibrations (Fig. 6- 9(a)). The average A_{ESPA} for all configurations with $t_p=1.37$ mm was 0.86 %g and the average A_{ESPA} for all configurations with $t_p=3.00$ mm was 0.40 %g. This was a decrease of 0.46 %g between the two plate thicknesses. Increasing t_c also led to decreases in A_{ESPA} (Fig. 6- 9(b)) The average A_{ESPA} for all configurations with $t_c=1.37$ mm was 0.66 %g and the average A_{ESPA} for all configurations with $t_c=2.54$ mm was 0.54 %g. This was a decrease of 0.12 %g between the channel thicknesses. Similar to t_p and t_c , increasing d resulted reduced A_{ESPA} (Fig. 6- 9(c)). The average A_{ESPA} for all configurations with $d=203$ mm was 1.89 %g and the average A_{ESPA} for all configurations with $d=406$ mm was 0.27 %g. This was a decrease of 1.62 %g regardless of other parameters. Increasing d was the most effective at reducing A_{ESPA} . However at larger depths, the effect of increasing d on A_{ESPA} diminished; the average acceleration for

configurations with $d = 305$ mm was 0.48 %g whereas configurations with $d = 406$ mm was 0.26 %g, a decrease of 0.22 %g.

In general, parameters t_p , t_c , and d were inversely related to A_{ESPA} except when $s \geq 1220$ mm. Due to local vibrations, changes in s did not have a clear correlation to changes in accelerations and resulted in measured vibrations that may not always be the worst case accelerations, especially at low plate thicknesses, such as for P1.37-C1.72-D254-S610 (Fig. 6-9(d)). Regardless, most configurations provided some predictability and the average A_{ESPA} for configurations with $s=610$ mm was 0.74 %g and the average A_{ESPA} for configurations with $s=1800$ mm was 0.55 %g. This showed a decrease of 0.19 %g. Overall, increasing d led to the largest reduction in A_{ESPA} followed by t_p . In the range of values considered, increasing spacing or channel thickness only had a marginal effect.

6.6.3 Suitability of the RCRMSF for Walking Vibrations

The acceleration limits given by the ISO baseline curve, factored for occupancy and use, is sensitive to the structure's natural frequency (ISO 2007). To compare peak accelerations to the ISO limit for offices, the peak acceleration of the floors are plotted versus the natural frequencies for both the FEA and DA (Fig. 6- 10). The natural frequencies from the DA were predicted using Equation 6-5 and accelerations were predicted using Equation 6-6 for low frequency floors and Equation 6-7 for high frequency floors.

In both the FEA and DA, it is observed that the low frequency floors did not satisfy the ISO limit for offices. Low frequency floors with f_n less than or equal to 9 Hz show significantly higher peak accelerations than high frequency floors (Fig. 6-10). Overall, the FEA predicted higher f_n than the DA by an average of 1.09 Hz and on average the DA predicted 0.30 %g higher peak acceleration than the FEA for each configuration.

The RCRMSF in a single bay configuration can meet the ISO limit for offices with the appropriate configurations of channel depth, plate thickness, and channel thickness, regardless of if the DA or FEA is used to evaluate the system (Table 6- 4). However since the DA was unable to account for local vibrational behavior in the bottom plate, which may affect serviceability at larger channel spacing, a spacing no larger than 610 mm is suggested unless remediation measures are considered on the bottom plate. The lowest weight acceptable configurations of P3.00-C1.72-D254-S610, P2.45-C1.72-D305-S610, and P1.37-C1.72-D406-S610 are suggested when evaluating performance using the DA. For evaluations conducted using FEA, lowest weight acceptable configurations P1.72-C1.72-D254-S610, P1.37-C2.45-D254-S610, and P1.37-C1.72-D305-S610 are suggested.

6.6.4 *3x3 Bay Parametric Study Results and Discussion*

Part of the FEA single bay parametric study was repeated for a 3x3 bay layout to examine the effect of surrounding bays on vibration performance of the RCRMSF. The configurations assessed in the 3x3 bay parametric study are indicated in Table 6 -1; only t_p and d were varied in the 3x3 bay parametric study as they had the largest effect on performance for the single bay configuration (Fig. 6- 11). The results of this assessment are shown in Table 6- 3. Configurations with 3x3 bay arrangement had a higher f_n by an average of 0.51 Hz and a lower A_{ESPA} by an average of 0.52 %g than single bay configurations with the same parameters.

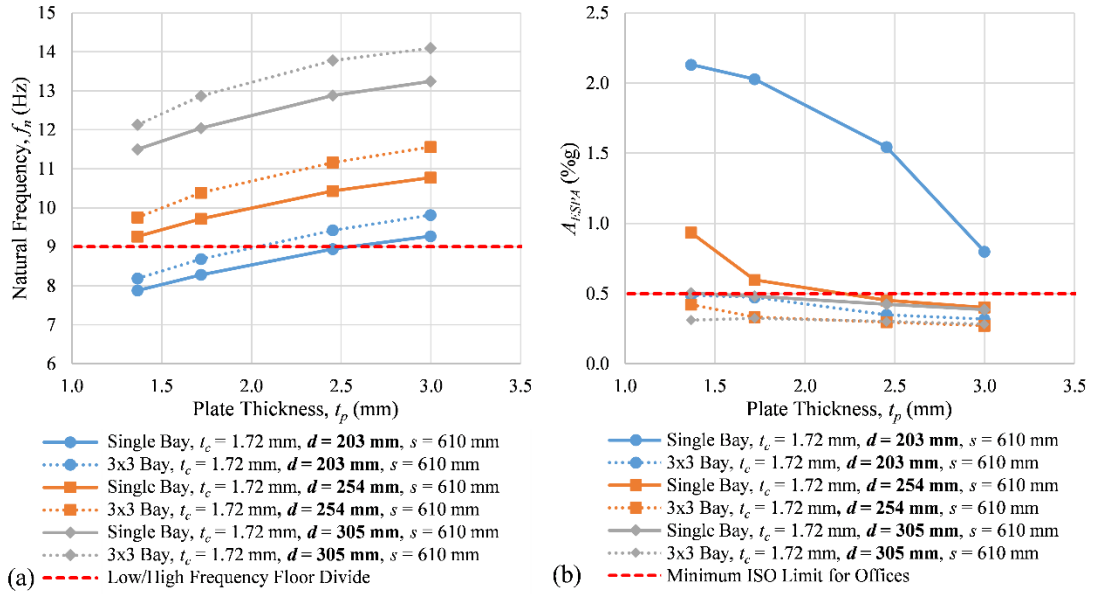


Fig. 6- 11: 3x3 bay parametric study results: (a) natural frequency (b) acceleration

Table 6- 3. Parametric study results for 3x3 configurations under walking load and single bay configurations subjected to rhythmic loading (bold indicates parameter varied from base configuration P1.37-C1.72-D254-S610)

Model	3x3 Bay				Single Bay, Rhythmic Loading	
	FEA f_n (Hz)	FEA A_{ESPA} (%g)	FEA ISO Limit	FEA Serviceability	FEA A_{ESPA} (%g)	FEA Serviceability
P1.37-C1.72- D203 -S610	8.19	0.49	0.51	PASS	4.40	FAIL
P1.72 -C1.72- D203 -S610	8.69	0.47	0.54	PASS	4.11	FAIL
P2.45 -C1.72- D203 -S610	9.42	0.35	0.59	PASS	1.30	PASS
P3.00 -C1.72- D203 -S610	9.82	0.32	0.61	PASS	0.91	PASS
P1.37-C1.72-D254-S610	9.75	0.42	0.61	PASS	1.05	PASS
P1.72 -C1.72-D254-S610	10.39	0.33	0.65	PASS	0.77	PASS
P2.45 -C1.72-D254-S610	11.16	0.30	0.70	PASS	0.53	PASS
P3.00 -C1.72-D254-S610	11.56	0.27	0.72	PASS	0.44	PASS
P1.37-C1.72- D305 -S610	12.13	0.31	0.76	PASS	0.48	PASS
P1.72 -C1.72- D305 -S610	12.87	0.32	0.80	PASS	0.42	PASS
P2.45 -C1.72- D305 -S610	11.81	0.37	0.74	PASS	0.32	PASS
P3.00 -C1.72- D305 -S610	14.10	0.28	0.88	PASS	0.28	PASS

As was also observed in the single bay parametric study, increases in t_p and d were positively related to f_n , and inversely related to A_{ESPA} . For configurations with $t_p=1.37$ mm the average f_n was 9.72 Hz and the average A_{ESPA} was 0.88 %g. Configurations with $t_p=3.00$ had an average f_n of 10.90 Hz and average A_{ESPA} of 0.49 %g. The change in f_n and A_{ESPA} between configurations with the two plate thicknesses was an increase of 1.18 Hz and a decrease of 0.39 %g, respectively. The configurations with $d=203$ mm had an average f_n of 9.03 Hz and average A_{ESPA} of 0.41 %g. For configurations with $d=305$ mm the average f_n was 13.20 Hz and the average A_{ESPA} was 0.30 %g. The change in f_n and A_{ESPA} between configurations with the two channel depths was an increase of 4.19 Hz and a decrease of 0.10 %g, respectively. Increasing both t_p and d was successful in significantly improving the vibration behavior of the RCRMSF when considering the effect of surrounding bays. Lowest weight acceptable configurations for 3x3 bays include P2.45-C1.72-D203-S610, P1.37-C1.72-D254-S610, and P1.37-C1.72-D305-S610 (Table 6- 4). When considering surrounding bays, the A_{ESPA} for low frequency floors was significantly less than the A_{ESPA} for the single bay configuration and even low frequency floors exhibited acceptable performance.

Table 6- 4. Lowest weight floor configurations for each depth, d , to satisfy ISO vibration limits (minimum plate thickness, t_p , and channel thickness, t_c). Channel spacing, s , is 610 mm in all cases

Case	t_p (mm)	t_c (mm)	d (mm)
Single Bay (DA)	3	1.72	254
	2.45	1.72	305
	1.37	1.72	406
Single Bay (FEA)	1.72	1.72	254
	2.45	1.37	
	1.37	1.72	305
	1.37	1.72	406
3x3 Bay (FEA)	2.45	1.72	203
	1.37	1.72	254
	1.37	1.72	305
Rhythmic Loading (FEA)	2.45	1.72	203
	1.37	1.72	254
	1.37	1.72	305

6.6.5 Rhythmic Loading Parametric Study Results and Discussion

Floors used in exercise facilities are often subject to rhythmic loads. For this reason, a study of RCRMSF single bay finite element models experiencing rhythmic loading was conducted for selected configurations (Table 6 -1). Aerobic loading was chosen as the rhythmic load because it is the most intense rhythmic loading prescribed in AISC DG 11 (Murray et al. 2016).

The results of the rhythmic loading parametric study are shown in Table 6 -3 and Fig. 6-12: Rhythmic loading parametric study acceleration results. As expected, acceleration response was generally higher for aerobic loads than it was for walking loads. Increases in t_p and d resulted in decreases in A_{ESPA} as was seen in the walking load parametric study. The results are compared to the recommended limit for weightlifting in AISC DG 11 (1.5 %g) for a floor with a shared use

of aerobics and weightlifting (Murray et al. 2016). Lowest weight acceptable configurations to satisfy the weightlifting limit include P2.45-C1.72-D203-S610, P1.37-C1.72-D254-S610, and P1.37-C1.72-D305-S610 (Table 6 -4). It should be noted that the higher ISO tolerable vibration limit for aerobic activity allows for a shallower channel depth in some instances than could be tolerated for walking activity in offices.

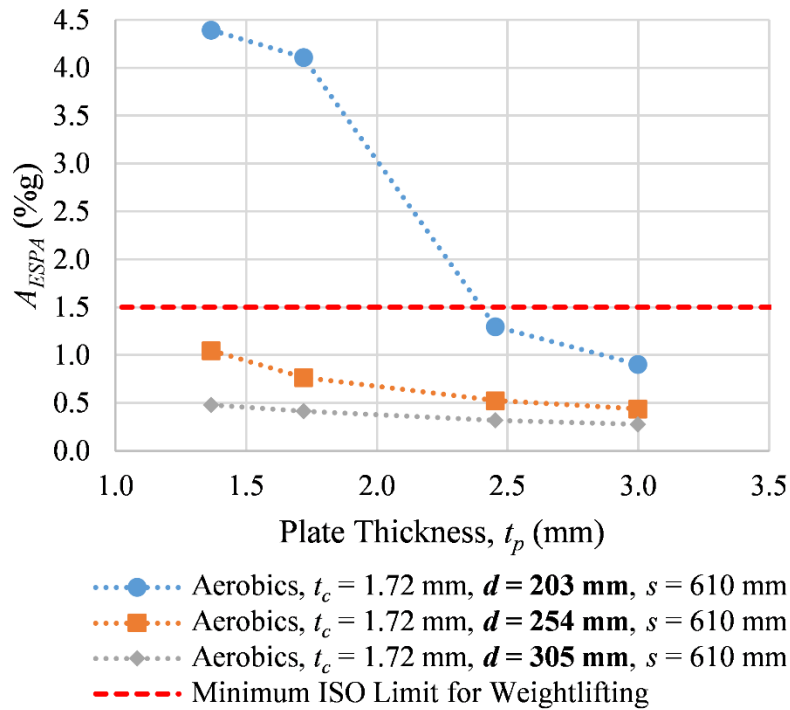


Fig. 6- 12: Rhythmic loading parametric study acceleration results

6.7 Conclusions

A novel, cold-formed steel flooring system has been developed, and its vibration serviceability has been assessed using a design assessment and finite element modeling. To better understand the vibration behavior and serviceability of lightweight cold-formed steel flooring systems, a parametric study of four parameters pertinent to the RCRMSF (t_p , t_c , d , and s) was

conducted for 44 floors in a single bay configuration and the natural frequencies and accelerations were compared. Of significance is the large number of systems categorized as high frequency floors, where the behavior of high frequency flooring systems is continuing to be understood and analytical and experimental data is lacking. The effect of surrounding bays was examined using a 3x3 bay FEA model. A rhythmic aerobics load was applied to examine suitability of the RCRMSF in an exercise facility. The following conclusions were made:

For the RCRMSF, increasing d , t_p , t_c , and s raised the natural frequency and reduced the acceleration response to walking. The average f_n increased 4.24 Hz and the average A_{ESPA} decreased 1.62 %g with increasing depth. It was also observed that when increasing plate thickness the average f_n increased 0.90 Hz and the average A_{ESPA} decreased 0.46 %g. When channel thickness increased, the average f_n increased 0.50 Hz and the average A_{ESPA} decreased 0.12 %g. Increasing spacing between channels increased the average f_n by 0.47 Hz and the average A_{ESPA} decreased by 0.19 %g. As a result, both d and t_p had a large impact, while t_c and s had a small impact on performance.

Low frequency floors in the parametric study experienced resonant build-up, which led to excessively high vibrations. High frequency floors often had lower A_{ESPA} than low frequency floors, and many satisfied ISO limits. Lowest weight acceptable configurations of P3.00-C1.72-D254-S610, P2.45-C1.72-D305-S610, and P1.37-C1.72-D406-S610 are suggested when evaluating performance using the DA. Lowest weight acceptable configurations of P1.72-C1.72-D254-S610, P1.37-C2.45-D254-S610, and P1.37-C1.72-D305-S610 are suggested for performance evaluations using FEA. Rhythmic (aerobic) loading response of a single bay was also examined using FEA, and higher acceleration response was observed than present under walking

load. The lowest weight acceptable configurations of P2.45-C1.72-D203-S610, P1.37-C1.72-D254-S610, and P1.37-C1.72-D305-S610 are recommended for rhythmic loading.

Overall the DA produced more conservative results than the FEA. Comparison of the FEA and DA showed that the DA predicted lower natural frequencies than the FEA by an average of 1.56 Hz. In general, DA predicted higher acceleration response than the FEA by an average of 0.19 %g. The FEA and DA predicted similar trends in behavior for varying t_p , t_c , and d , but different behavior for varying s . This was because the DA could not capture effects of local vibrations, whereas the FEA could account for this behavior.

At a higher channel spacing of $s \geq 1220$ mm, the FEA captured effects of local vibrations on global behavior for which the DA was not able to account. For this reason, a higher channel spacing ($s \geq 1220$ mm) is not suggested unless a detail is used to limit local vibrations.

A parametric study was also conducted for a 3x3 bay arrangement to assess the impact of surrounding bays on RCRMSF vibration performance. Configurations with 3x3 bay arrangement had higher f_n by an average of 0.51 Hz and lower A_{ESPA} by an average of 0.52 %g than single bay configurations with the same parameters. Including the impact of surrounding bays significantly improved the ability of the RCRMSF to resist walking vibrations. Lowest weight acceptable configurations for 3x3 bays evaluated using FEA include P2.45-C1.72-D203-S610, P1.37-C1.72-D254-S610, and P1.37-C1.72-D305-S610.

Chapter 7: Vibration Serviceability Testing of a Lightweight Cold-Formed Steel Floor System

7.1 Abstract

Predicting and designing for vibration serviceability in floor systems is increasingly important for the structural engineer. Walking-induced vibrations can render an otherwise structurally sound floor system unusable due to occupant discomfort. Cold-formed steel structures may be especially susceptible to complaints of excessive vibrations due to their light nature. A vibration serviceability assessment for a lightweight, cold-formed steel floor system was conducted by way of finite element analysis and a simplified evaluation method to determine its response to walking-induced vibrations. The natural frequencies of two experimental floor systems were determined by way of heel drop impact testing, and walking tests were conducted to evaluate floor accelerations with respect to ISO serviceability limits. Calibrated finite element models were used to predict the performance of the experimental floors with an additional mass to account for additional dead and live loads. The floors were determined to be unacceptable by ISO serviceability limits and areas for further investigation were identified. Improving connections between floor panels and conducting a more in-depth experimental modal analysis may provide a path forward for rectifying serviceability concerns.

7.2 Introduction

Designing and assessing floors for vibration serviceability problems are increasingly important as complaints of lively floors become more common with increasing span lengths and decreasing live loads (Murray 2011). As the popularity of cold-formed steel construction rises, it is important to be able to assess the performance of these structures (Parnell et al. 2010). Cold-formed steel floor systems may be especially susceptible to annoying vibrations as they are often lightweight and exhibit less mass and structural damping than more traditional floor systems (Hanagan et al. 2003). It has been shown that cold-formed steel floor systems often satisfy vibration limits (Xu 2011); however, there is still a need to perform due diligence to avoid problematic floors.

7.2.1 Acceptability Criteria

Comfort limits for evaluating the serviceability of floor structures are laid out by the International Organization for Standardization (ISO) (ISO 2007). These limits establish acceptable peak accelerations defined as a percent of gravity, %g, depending on the type of structure, expected activities, and natural frequency of the structure. The most stringent of these acceptability limits, 0.5%g, occurs in the frequency range of 4 to 8 Hz, which is the range which may cause excessive discomfort in humans (Murray et al. 2016). Beyond 8 Hz the specified limit increases rapidly (ISO 2007).

Significant work has gone towards the prediction and measurement of accelerations in floor structures for comparison with the ISO limits. *The American Institute of Steel Construction Design Guide 11: Floor Vibrations Due to Human Activity 2nd Edition* (AISC DG11) (Murray et al. 2016)

has extensive guidelines for predicting acceleration response of structures largely as a function of the estimated natural frequency. As structures have become more irregular and the prevalence of computer modeling increased, additional methods for finite element (FE) modeling of floor structures for studying walking response have been developed and incorporated into AISC DG11. Developments in field testing of existing structures for remediating serviceability problems has also provided engineers with additional tools for designing with walking-induced vibrations in mind.

7.2.2 Lightweight Cold-Formed Floor System

A cold-formed steel floor system has been introduced in an attempt to utilize cold-formed steel construction to achieve a light steel floor system capable of spanning great distances and leverage light, cold-formed steel elements to achieve increased depth without greatly increased weight (Boadi-Danquah et al. 2017).

The lightweight nature of this system necessitates extensive FE modeling and experimental testing to assess the vibration performance of the floor system when subjected to walking-induced vibrations. Two floor systems were constructed and tested in situ by way of a simplified evaluation method (Davis 2014) to verify FE modeling techniques and compare the dynamic response to ISO limits.

7.3 Test Procedure

An initial assessment of the performance of the cold-formed steel floor system when subjected to walking-induced vibrations was carried out using a simplified evaluation method. This method consists of performing a heel drop test and analyzing the acceleration time-history in the frequency domain to determine the heel drop response spectra. Once the natural frequency of

the floor is determined from the heel drop response spectra, walking testing is conducted and the acceleration time-history is converted to an equivalent sinusoidal peak acceleration (ESPA) for evaluation with the ISO serviceability limits (Davis 2014).

The heel drop test is performed by having an individual standing on the floor rise onto their toes and then drop forcefully, recording acceleration time-history with accelerometers. This impact applies adequate force in the 1-20 Hz range for analyzing the response spectra. This frequency range is also that which may be excited by walking and felt by occupants (Davis 2014).

While adequate for obtaining responsive frequencies, the only information necessary for carrying out walking testing, the heel drop method has limitations when compared to experimental modal analysis. Heel drops do not provide adequate information for characterizing modal properties including damping and mode shapes (Davis 2014) and cannot be used to construct a frequency response function (Murray 2011). However, it has been demonstrated that heel drops do provide accurate estimations of natural frequencies and are a suitable method for evaluating responsive floors (Murray 2011).

Following heel drop tests and the determination of the floor natural frequency, walking tests were conducted to obtain acceleration time history data for measuring accelerations. The natural frequency is used to determine the step frequency an evaluator must match in order to elicit the greatest response in the floor. Walking tests are ideally conducted at a step frequency between 1.8 and 2.2 Hz, characteristic of typical occupant step frequencies and matching the lowest possible harmonic of the natural frequency (Davis 2014). A metronome was used to assist in matching the desired step frequency. Walking paths were chosen based on the greatest expected floor response, generally crossing the center of floor bay.

Accelerometers were placed at locations with the highest anticipated response in order to obtain the acceleration-time history during walking testing. This data was converted to a rolling root mean square acceleration and then converted to ESPA by multiplying the RMS acceleration by the square root of two, allowing for comparison with the ISO limits in terms of percent of gravity, %g (Davis 2014). As they may be subject to resonant build-up, low frequency floors, characterized by a natural frequency less than 9 Hz, a two second interval is suggested for computing the RMS acceleration. Walking events on high frequency floors, those with natural frequencies greater than 9 Hz, are more likely to resemble a series of impulses and the RMS acceleration is computed using a time interval following an apparent impulse (Murray 2016 et al.).

7.4 Finite Element Modeling

Abaqus/CAE (DSS 2016) was used to generate FE models to perform initial predictions of floor system behavior. Guidelines for constructing and evaluating FE models for vibration serviceability studies are presented in AISC DG11 (2016) and include recommendations for mesh size, damping ratios, and post-processing evaluation.

Experimental models utilized 3D shell elements for the steel plates and purlins. Dynamic amplitudes are typically small enough to assume all materials behave linearly elastically (Robertson 2017). The steel material was defined as having a density of $\rho=7849 \text{ kg/m}^3$ (490 lb/ft³), an elastic modulus of $E=200 \text{ GPa}$ (29,000 ksi), and Poisson's ratio of $\nu=0.30$. Additionally a mass representative of a human weighing 747 N (168 lb) was included at the center of the floor for evaluating the frequency response.

The floor system was modeled as a monolithic panel with continuous purlins in each direction. Top and bottom plates were tied to the purlins. These assumptions are based on the fact

that connections may behave as a moment connection due to the friction in the connection and the small amplitudes of vibrations (Murray et al. 2016).

Meshing sizes were selected that were $1/10^{\text{th}}$ the bay size and refined until further reductions in mesh sized produced no change in natural frequency (Murray et al. 2016). Modal damping was applied to the system on the order of 1% of critical damping per AISC DG11 recommendations for critical damping ratios resulting from the structural system (Murray et al. 2016).

7.5 Experimental Testing

In situ vibration serviceability testing was conducted on two cold-formed steel floor systems. The tests aimed to evaluate the performance of the floors due to walking-induced vibrations by characterizing the response spectra of the floors due to a human impact and recording acceleration time-history due to walking events. This data was used to calibrate FE models of the floor system and then evaluated using Abaqus/CAE finite element analysis software (DSS 2016) with a superimposed distributed load of 2.4 kPa (50 psf) to account for dead and live loads that may be expected in an electronic office fit-out (Boadi-Danquah et al. 2017).

7.5.1 Test Matrix

Floor systems consisted of twelve gage cold-formed steel purlins and plate topped with OSB sheathing and supported by perimeter girders in a test frame. The depth of the purlins varied between the floors, one utilizing 203 mm purlins (8 in.) and the other utilizing 254 mm purlins (10 in.). These will be referred to as D203 (D8) and D254 (D10), respectively. Each floor was subjected to a series of tests in accordance with the simplified evaluation method. A series of three heel drop tests were carried out by three individuals to determine the response spectra of the floor

system. Once the natural frequency of each floor was determined, each individual traversed the floor six times: three times along the longitudinal span and three times along the transverse span. Walking was conducted at a step frequency determined to match the lowest harmonic of the fundamental frequency found by the heel drop test for each floor as shown in Table 7 -1. Data was recorded from five accelerometers positioned along the centerlines of the longitudinal and transverse spans at quarter points.

Table 7- 1. Step frequency at which walking testing was conducted

Walking Pace	
Floor	f_{step} (Hz)
D203 (D8)	2
D254 (D10)	1.9

7.5.2 Supporting Frame Details

The test frame illustrated in Fig. 7- 1 was constructed with wide flange sections and was used to represent structural framing during floor system evaluation. The test frame consisted of W360x134 (W14x90) girders on all sides with inside dimensions for the floor clear span of 6.93 m (273 in.) x 5.08 m (200 in.). As a result of the significantly higher mass and stiffness of the test frame relative to the floor specimens the influence of the frame was not included in the results (Parnell et al. 2010). Girder-to-girder connections consisted of double angle shear tabs. One side of the frame was fully pinned to support braces at the ends and where girders connected to the web, also utilizing double angle shear tabs. The opposite side of the frame was supported by three intermediary bearing supports located approximately at the quarter points. This atypical framing

detail was necessary for diaphragm behavior testing unrelated to the vibration serviceability and was explicitly modeled in the FE analyses of the floor to capture any influence on behavior.

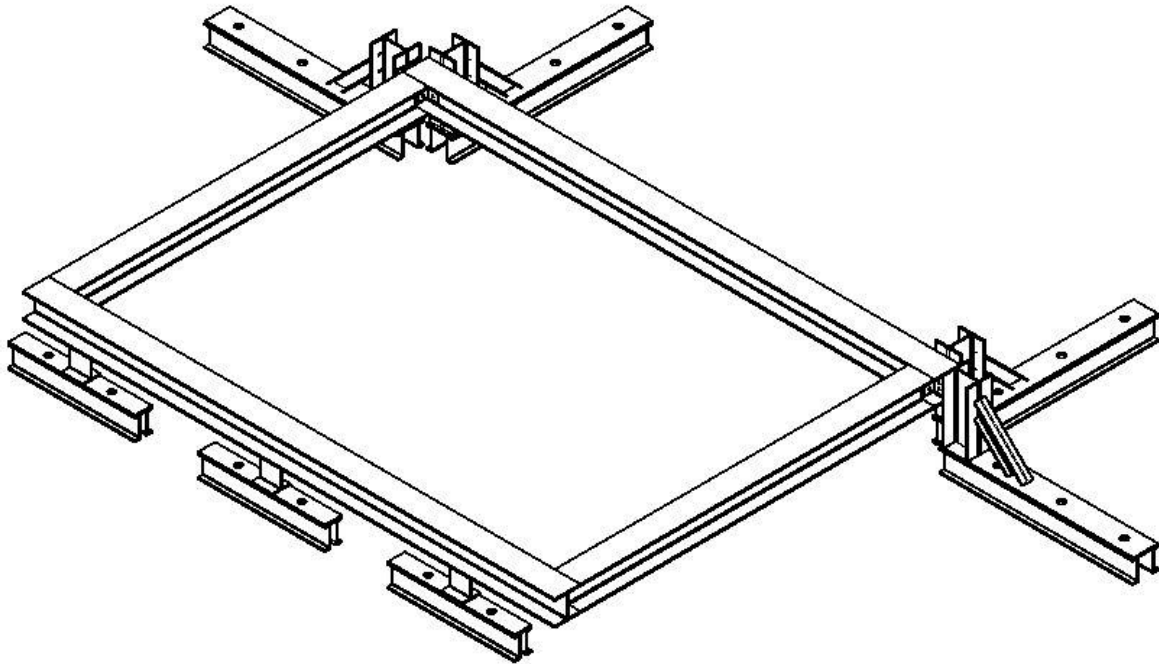


Fig. 7- 1: Test frame

7.5.3 Floor System Details

The floor systems were fabricated out of cold-formed steel purlins and cold-rolled steel plates. Each floor system consisted of three panels: two like exterior panels and one unique center panel. Exterior panels utilized a bottom plate dimension of 5.08 m (200 in.) x 2.44 m (96 in.) and top plate dimension of 5.23 m (206 in.) x 2.29 m (90 in.). The center panel utilized a bottom plate dimension of 5.08 m (200 in.) x 2.44 m (96 in.) and top plate dimension of 5.23 m (206 in.) x 2.03 cm (80 in.).

Purlins were cut to length utilizing a plasma cutter. A profile was cut out of the flanges and webs of the purlins as shown in Fig. 7- 2 to allow for the purlins to interlock in an orthogonal grid

as seen in Fig. 7- 3. Center-line spacing between the web cut-outs was 0.61 m (24 in.) to allow for an inside 0.61 m (24 in.) x 0.61 m (24 in.) grid of purlins. The ends of purlins coinciding with the perimeter had the bottom flange notched out 76 mm (3 in.) from the end to prevent the purlins from sitting atop each other.



Fig. 7- 2: Purlin flange and web profile cut-out



Fig. 7- 3: Orthogonally arranged purlins

Cold-rolled steel plates were obtained in 1.5 m (5 ft) x 3 m (10 ft) sheets and joined to form the desired plate size with a CJP groove weld. The bottom plate of the center panel had 100 mm (4 in.) x 203 mm (8 in.) notches cut out of the edges as shown in Fig. 7-4. These notches rest on bottom plate of the edge panel when the center panel is installed. This is to allow for joining the bottom plates with self-tapping screws. The top plate of the center panel had 305 mm (12 in.) x 203 mm (8 in.) splice seats welded to the underside in between purlins as seen in Fig. 7-4. This allowed for the attachment of splice plates across the tops of the panels utilizing self-tapping screws.



Fig. 7- 4: Notched bottom plate of the center panel and top plate lap-splice pieces

A panel was constructed by welding perimeter purlins to the bottom plates with the top flanges facing out, allowing the purlin flanges to seat on the framing girder flanges. The interior grid of purlins were laid out as shown in Fig. 7- 5 and welded to the bottom plate. Once the interior grid of purlins was welded to the bottom plate the top plate was installed on each panel. The edges of the top plate were welded to the flanges of the perimeter purlins and self-tapping screws were used to attach the plate to the interior grid of purlins every 0.3 m (1 ft). A completed edge panel is shown in Fig. 7-5.

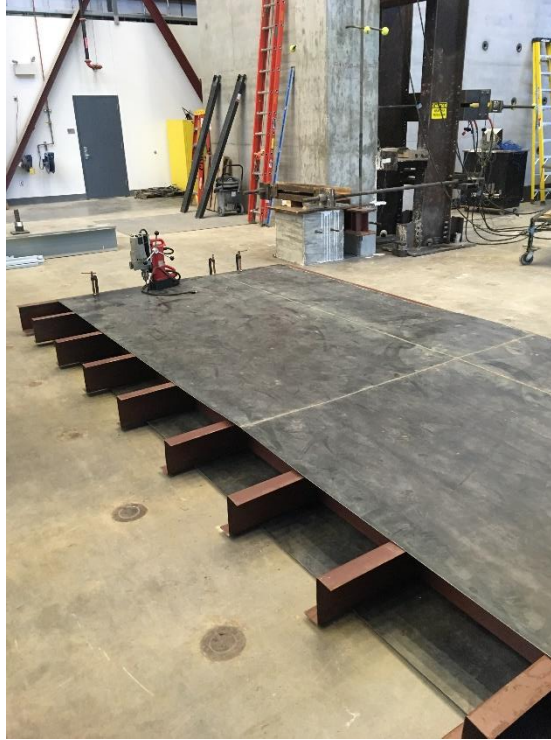


Fig. 7- 5: Completed floor panel

The weight of each constructed panel is reported in Table 7 -2 including the equivalent total floor dead load.

Table 7- 2. Measured panel weight and equivalent floor dead load

System Weight, kN (lbf)				
Floor	Exterior Panel 1	Exterior Panel 2	Center Panel	Dead Load, kPa (psf)
D203 (D8)	8.09 (1,818)	8.19 (1,841)	7.42 (1,668)	0.68 (14.3)
D254 (D10)	9.05 (2,035)	8.96 (2,015)	8.16 (1,835)	0.74 (15.5)

To provide auxiliary support for each panel, angle seats were bolted to the webs of the supporting girders as a bearing support for perimeter purlins. Exterior panels were set into place before the center panel was set on top of them such as in Fig. 7- 6, with extended purlins and

bottom plate notches resting on top of those of the exterior panels. Self-tapping screws were utilized to tie the bottom plates together, with two self-tapping screws used at each notch overlap. Top plates were joined with 0.3 m (1 ft) wide splice plates that were attached to the top plate splices of the center panel and top plates of the exterior panels as in Fig. 7- 7. Two self-tapping screws were driven into each tooth and two driven into the top plates of the exterior panels across from the splice. The OSB sheathing covered the floor system and was attached with self-tapping screws. Lastly, the top flanges of the panels were nailed to the flanges of the support frame using Hilti brand powder actuated fasteners spaced at 0.3 m (1 ft), as shown in Fig. 7- 8.



Fig. 7- 6: Floor panels being lowered into place



Fig. 7- 7: Splice plates being installed over the splice seats of the center-top plate and the top plate of the exterior panel



Fig. 7- 8: Perimeter purlins nailed to the flanges of the test frame girders using Hilti brand powder actuated fasteners

7.6 Results

The results presented below include the natural frequency of the in situ floor systems compared with the predicted natural frequency of the FE models for the purpose of evaluating the accuracy of the FE models. Following the natural frequency data is the measured and predicted ESPA for the in situ floor systems and FE models, respectively. This data is evaluated against the ISO serviceability limit of 0.5 %g as required by ISO 2007. These results do not account for the stiffness or mass contributions of the frame (Parnell et al. 2010).

The natural frequencies determined from the heel drop response spectra and FE modeling are reported in Table 7 -3. Floor D203 (D8) was found to have a natural frequency of 10.3 Hz. The FE model predicted a natural frequency of 10.9 Hz, within 6% of the experimental value. Floor D254 (D10) was found to have a natural frequency of 9.6 Hz. The FE model predicted a natural frequency of 11.0 Hz, within 13% of the experimental value. The FE models with a superimposed mass predicted a natural frequency of 7.3 Hz for floor D203 (D8) and 7.7 Hz for floor D254 (D10).

Table 7- 3. Measured natural frequencies from the experimental systems and predicted natural frequencies from the calibrated FE models

Natural Frequency (Hz)			
Floor	Experimental	Model	Model + Mass
D203 (D8)	10.3	10.9	7.3
D254 (D10)	9.6	11	7.7

The ESPA for the in situ floor systems and FE models are reported in Table 7 -4. The experimentally determined ESPA for floor D203 (D8) was 10.24 %g while the FE model predicted 12.37 %g, these were within 17%. Floor D254 (D10) had an experimental ESPA of 11.83 %g

compared to a predicted ESPA of 12.56 %g, within 6%. To account for components that may be present in an office space setting, FE analyses were also performed including an additional uniform load of 2.4 kPa (50 psf) applied to the plates as an equivalent mass. Floor D203 (D8) was predicted to have an ESPA of 2.3 %g and floor D254 (D10) was predicted to have one of 2.57 %g. These are both in exceedance of the 0.5 %g limit set by the ISO standards (ISO 2007).

Table 7- 4. Measured equivalent sinusoidal peak accelerations (ESPA) from the experimental systems and predicted ESPA from the calibrated FE models

Floor	ESPA (%g)		
	Experimental	Model	Model + Mass
D203 (D8)	10.24	12.37	2.3
D254 (D10)	11.83	12.56	2.57

7.6.1 *In Situ Response*

Heel drop testing determined a natural frequency of approximately 10.3 Hz for floor D203 (D8) and 9.4 Hz for floor D254 (D10) as shown in Fig. 7- 9 and Fig. 7- 10, respectively. Walking testing determined an ESPA of 10.24 %g for floor D203 (D8) and 11.83 %g for floor D254 (D10). These measured accelerations are useful for comparing the in situ response with the response predicted by FE modeling. They are not to be compared to the ISO limits as the in situ floor was tested without any distributed load other than self-weight and would not be representative of realistic floor loading.

A representative walking time-history for each respective floor is presented in Fig. 7- 11 and Fig. 7- 12. The qualitative waveform shown in each figure confirm that the floors behave as high frequency floors ($f_n > 9$ Hz) in that they do not undergo resonant build-up (Murray et al. 2016). This is consistent with the determined natural frequencies for floor D203 (D8) and D254

(D10) of 10.3 Hz and 9.6 Hz, respectively. Additionally, the input of the walking testing was found to be broadband enough to causes significant modal contribution between 1-10 Hz.

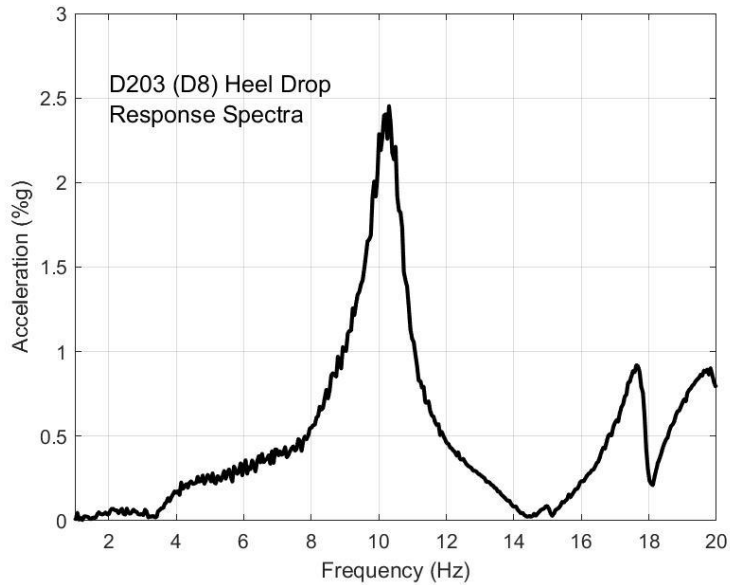


Fig. 7- 9: Measured heel drop response spectra for floor D203 (D8)

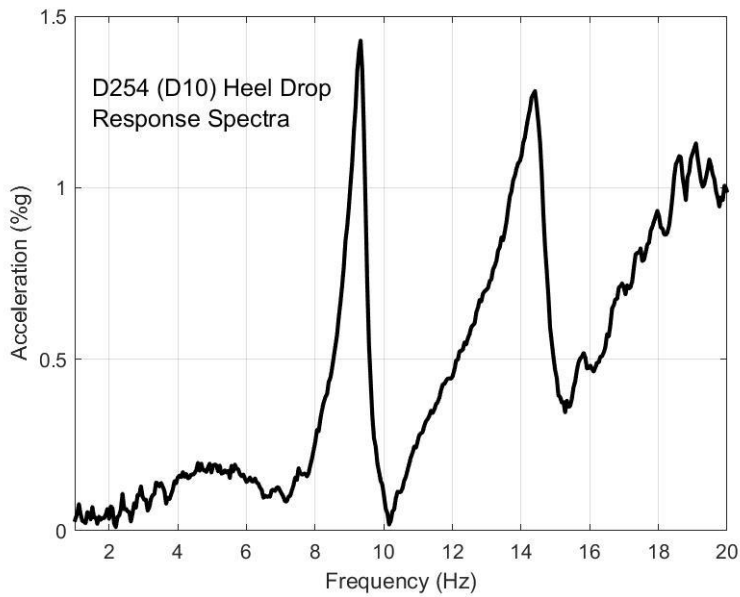


Fig. 7- 10: Measured heel drop response spectra for floor D254 (D8)

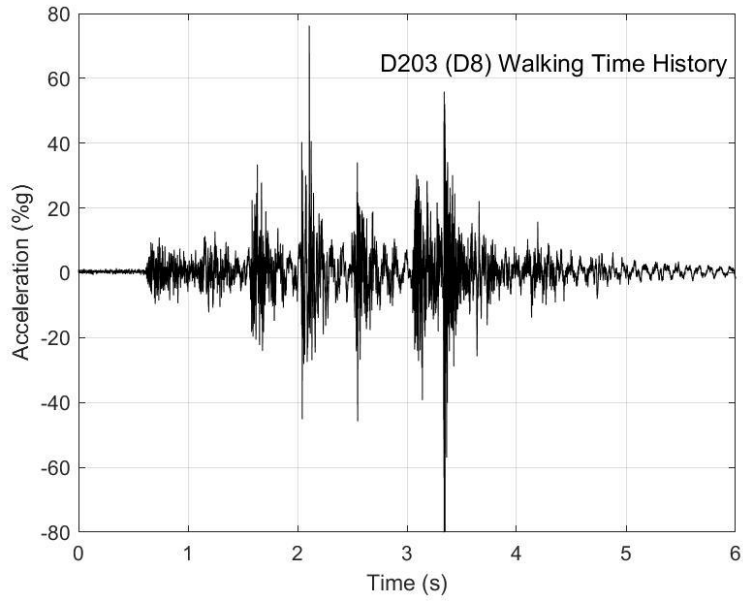


Fig. 7- 11: Measured walking time history for floor D203 (D8)

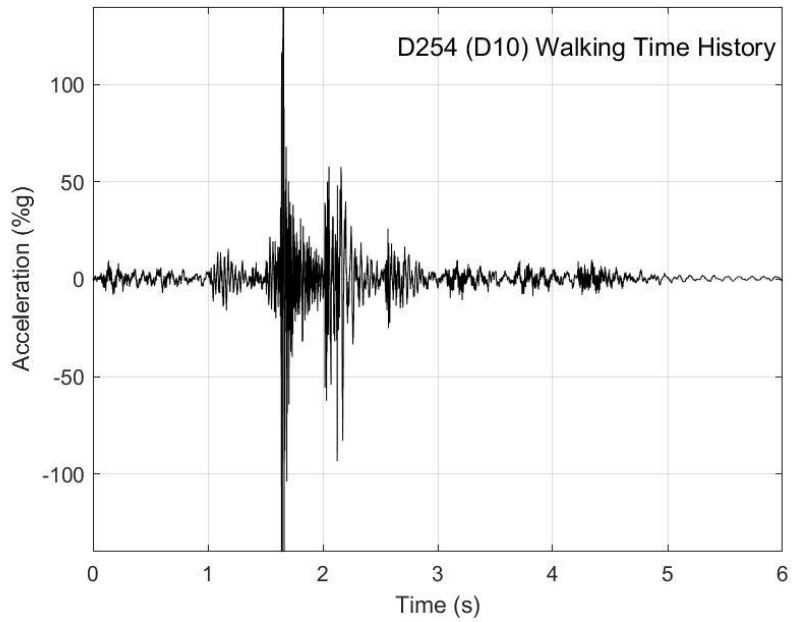


Fig. 7- 12: Measured walking time history for floor D254 (D10)

7.6.2 Calibration of Finite Element Models

Refinement of FE models was required as the predicted natural frequencies of the initial models shown in Table 7 -5 varied greatly from the experimental results in Table 7 -3. It was determined that the assumption of a monolithic floor with continuous purlins was not adequate for predicting the behavior of the system. Calibration of the model consisted of creating individual panels and modeling the inter-panel connections using a hard contact interaction in Abaqus/CAE (DSS 2016). The measured and predicted natural frequency of the D203 (D8) floor system was within 6% while those of the D254 (D10) floor were within 13% after calibration. This is an improvement upon the initial predicted natural frequency which varied from the measured natural frequency by 62% and 96% for the D203 (D8) and D254 (D10) floors, respectively.

Table 7- 5. Predictions from uncalibrated FE models

Natural Frequency Predictions	
Floor	Natural Frequency (Hz)
D203 (D8)	16.7
D254 (D10)	18.9

7.6.3 FE Model Response

Finite element models predicted a natural frequency of approximately 11.1 Hz for floor system D203 (D8) and approximately 11.3 Hz for floor system D254 (D10). A modal dynamic analysis of the FE model corresponding to the in situ systems was conducted in accordance with AISC DG 11. This analysis predicted an ESPA of 12.37 %g for the D203 (D8) floor and 12.56 %g for the D254 (D10) floor. The analysis of the floors accounting for an additional equivalent mass of 2.4 kPa (50 psf) predicted an ESPA of 2.3 %g for the D203 (D8) floor and 2.57 %g for the D254

(D10) floor. These results would suggest that the floor system in its current design would not satisfy ISO vibration limits of 0.5 %g (ISO 2007).

7.7 Conclusions

There is close agreement between the natural frequencies obtained from the heel drop spectra and the calibrated FE models to support the predicted acceleration response of the floor systems due to walking. This is further supported by the agreement between the measured and predicted ESPA. For floor systems modeled with an additional equivalent mass of 2.4 kPa (50 psf) the predicted accelerations due to walking are 2.3 %g for floor D203 (D8) and 2.57 %g for floor D254 (D10). These exceed the ISO vibration serviceability limit of 0.5 %g for these structures.

When modeling this floor system it is crucial that the inter-panel connection detail be modeled as it exists in situ. This involves modeling discontinuous purlins and panels and utilizing contact interaction rather than tied behavior. The simplifying assumptions of a monolithic system utilizing continuous purlins is not adequate for characterizing the system.

The failure of the floor systems to meet ISO serviceability criteria warrants a more in-depth study of this flooring system. Reducing flexibility at the inter-panel connections may help to increase the system stiffness and damping such that it meets serviceability criteria. Considering the extremely low weight of the floor system it would likely benefit not only from the increased stiffness of an improved inter-panel connection but also from increased structural damping that may be introduced through an improved inter-panel connection. More detailed experimental modal analyses may yield further insight to the modal properties of the systems to help in improving vibration serviceability behavior.

Chapter 8: A Novel Loading Procedure for Finite Element Prediction of Walking-Induced Vibrations

8.1 Abstract

With the increasing floor spans and decreasing dead loads of modern building construction, floor vibrations are becoming a greater concern for the structural engineer. Predicting the acceleration response of floor structures due to walking excitation is important for the proper design of floors as well as the evaluation and remediation of vibration serviceability problems in existing structures. Current design provisions in AISC Design Guide 11 for evaluating and designing for vibrations include hand calculation methods for conventional floor systems as well as finite element (FE) methods for evaluating unique structural configurations that may exhibit irregularities. A novel loading procedure for evaluating floor vibrations due to occupant loading has been developed and applied to Abaqus/CAE using a direct dynamic approach and DLOAD subroutine. This procedure uses a unique subroutine to apply a dynamically-applied moving load to a structure, representative of the human gait, to produce an acceleration response time history. Use of the subroutine allows the designer to specify step frequency, pressure, and gait, and can include multiple walkers and complex paths. This can be useful for the designer in identifying problem areas of large floors as well as studying dynamic build-up present in low frequency floors. Several FE models have been created and their predicted dynamic response under the established FE design procedures and this approach have been evaluated. Initial findings suggest this FE method may be suitable for evaluating floor vibrations resulting from walking.

8.2 Introduction

Advances in materials and design methods have allowed structural engineers to design lighter floors spanning greater distances, resulting in increased susceptibility to human-induced structural vibrations (Boice 2003). Lively floors can remain structurally safe but become unusable if the vibrations from walking or other dynamic pedestrian loading become intolerable. The International Organization for Standardization provides tolerability limits for floor structures based on their natural frequency, f_n , and expressed as acceleration as a percent of gravity, %g (ISO 2007). For offices and residences the peak acceleration limits are the lowest, 0.5 %g, for vibrations in the range of 4-8 Hz, and increase rapidly above 8 Hz. The American Institute of Steel Construction (AISC) provides guidance for predicting the natural frequency and acceleration response due to various loadings in *AISC Steel Design Guide 11: Floor Vibrations Due to Humans Activities* (DG 11, Murray et al. 2016). Included are provisions for evaluating dynamic behavior of floor systems, either by hand calculations or FE analysis. Hand calculations may be suitable for floor structures that are symmetric by the configuration of their structural framing and have a uniform distribution of dead and live loads throughout the floor area. The FE method is ideal for atypical floor structures or other pedestrian structures such as stairways that may not have typical structural framing. Floors which have great irregularities in load distribution or support sensitive equipment should also be evaluated by FE methods (Murray et al. 2016).

Evaluating a structure using FE modeling as detailed in Chapter 7 of AISC DG11 (2016) consists of plotting the frequency response function (FRF) for a structure using a unit sinusoidal force applied at some location, i . With the response spectrum a designer can identify the responsive frequencies at a point, j , on a structure as well as the associated response magnitudes expressed as %g/lbf. Acceleration is predicted differently for floors with natural frequencies above and below

9 Hz, classified as high and low frequency floors, respectively. Low frequency floors have the potential for resonant build-up from walking loads. Typical step frequency is between 1.8 and 2.2 Hz, that frequency or harmonics of it may excite a low frequency floor with enough energy at or near its natural frequency to cause excessive vibration. Design Guide 11 states that the first four harmonics should be considered for design purposes, leading to the 9 Hz threshold for low and high frequency floors. Floors with a natural frequency above 9 Hz are not likely to undergo resonant buildup and are evaluated by considering contributions of the first four modes resulting from an applied impulse.

Another method of evaluating a floor using FE modeling involves applying a forcing function to excite the floor. The same forcing function is used for all types of floors and is a Fourier series including contributions from the step frequency and the next three harmonics. Design for different activities can be achieved by appropriately adjusting the step frequency.

The respective FE methods tend to predict similar accelerations; however, these methods may differ from the accelerations predicted by the AISC DG11 (2016) provisions. This is thought to be a result of the difference between each method's ability to predict and model certain characteristics such as participating mass and mode shapes (Alvis 2001). Discrepancies in the effective mass between FE models and AISC DG11 (2016) provisions have been observed that would help explain diverging predicted accelerations. (Perry 2003). Accounting for damping in FE models is often done by including the effects of viscous modal damping in the solution procedure. Investigating ways to incorporate energy dispersion as frictional or material damping may help improve the accuracy of models (Alvis 2001). The forcing methods in the FE models must also be considered, and it has been observed that the transient nature of walking may produce better predictions (Sladki 1999).

An alternative walking loading method has been developed for Abaqus/CAE (DSS 2016) that applies a load representative of walking to a floor structure solved using a direct dynamics procedure. The use of this method provides the structural engineer with an additional tool to determine if certain walking paths or events may prove problematic to a floor system. This can be beneficial to floor systems with irregular framing or irregular masses, those which may have sensitive equipment near a walking lane, or other cases where the area of concern is not necessarily the center of the bay. To evaluate this procedure the natural frequency and accelerations were predicted for two baseline structures and then compared to results obtained using the AISC DG11 (2016) provisions, the Fourier series FE method, the FRF FE method, and the walking FE model. These two structures, a pedestrian footbridge and composite floor of known properties, were chosen to act as baselines for validating this new approach. Two additional floor structures were constructed and tested in situ specifically to test the efficacy of the new walking modeling approach compared to actual walking response.

8.3 Structures of Interest

Four structures were modeled for this study. Two structures from the literature were examined for the purpose of verifying results, and two were based on floor systems designed and fabricated by the authors. A pedestrian footbridge, schematically presented in Fig. 8- 1(a), was modeled after a design example included in AISC DG11 (2016). This structure consisted of a 0.15 m (6 in.) deep, 6 m (10 ft) wide concrete deck supported by W530x66 (W21x44) girders spaced 2.1 m (7 ft) on center. The span length is 12.2 m (40 ft). Damping was assumed to be 1% of critical as suggested for outdoor footbridges (Murray et al. 2016). The one-way composite floor shown in Fig. 8- 1(b) was modeled based on work performed by Perry et al. (2003). The structure was a

single bay floor system spanning 12.2 m (40 ft) by 9.1 m (30 ft). The floor consisted of a 0.13 m (5.25 in.) concrete deck supported by W460x52 (W18x35) beams spaced 1.8 m (6 ft) on center with continuous wall supports at the ends.

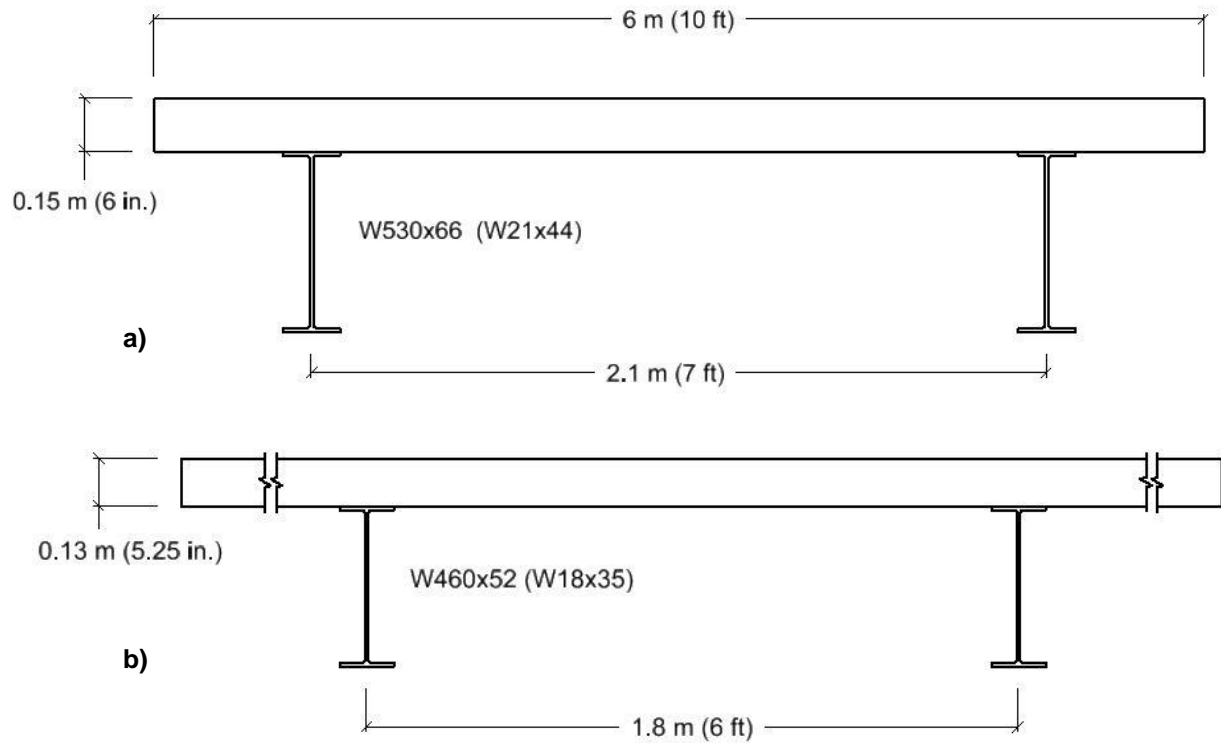


Fig. 8- 1: Cross section of the pedestrian footbridge from AISC DG11 2016 (a) and cross section of the composite floor from Perry et al. 2003 (b)

For experimental validation of the walking prediction method, two modular, lightweight cold formed steel floors, as introduced by Boadi-Danquah et al. (2017) and shown in Fig. 8- 2, were modeled and tested. The floors consisted of orthogonally arranged purlins sandwiched between plates and supported by perimeter girders. Each system consisted of 12 gage cold-formed steel purlins and plate with the depth of the purlins varied between the two systems. One system utilized a purlin depth of 203 mm (8 in.) and the other system utilized a purlin depth of 254 mm (10 in.). These will be referred to as floors D203 (D8) and D254 (D10), respectively.

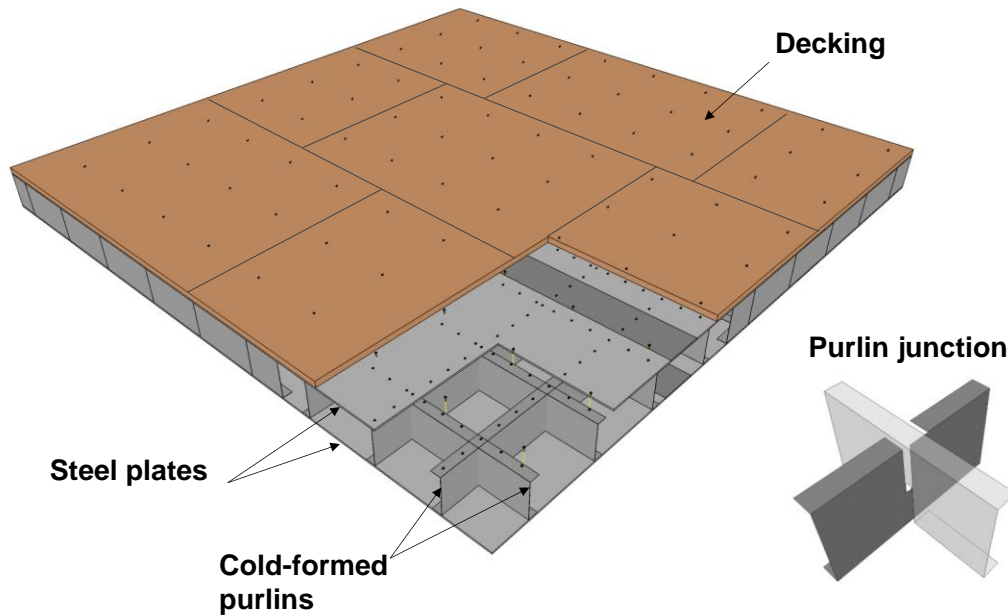


Fig. 8- 2: Typical cold-formed steel floor system

8.4 Finite Element Modeling

Abaqus/CAE was used for the FE modeling in this study. Guidelines for constructing FE models are presented in AISC DG11 (2016) which include suggestions for mesh size, damping ratios, and post-processing evaluation. For each structure the natural frequency, damping as a percent of critical, and equivalent sinusoidal peak acceleration (ESPA) were determined. Dynamic analysis of the floor structures was carried out by linear dynamic analysis using modal superposition for the Design Guide procedures and direct dynamics for the alternative method. In the evaluation of ESPA, as well as for the application of Rayleigh damping, modes at frequencies

above 20 Hz were neglected as these are outside the range of frequencies excited by human walking (Murray et al. 2016).

8.4.1 *Material and Mesh Properties*

The pedestrian footbridge and composite floor models consisted of concrete decking tied to supporting girders or joists. Three-dimensional (3-D) shell elements and beam elements were used for the concrete decking and supporting members, respectively. Both experimental models used 3-D shell elements for the steel plates, cement board, and purlins. Dynamic loading from occupants is typically small, and all materials were modeled assuming linear-elastic behavior. The steel material was defined as having a density of $\rho=7849 \text{ kg/m}^3$ (490 lb/ft^3), an elastic modulus of $E=200 \text{ GPa}$ ($29,000 \text{ ksi}$), and Poisson's ratio of $\nu=0.30$. Concrete material was defined as having a density of $\rho=2323 \text{ kg/m}^3$ (145 lb/ft^3), strength $f'_c=27.6 \text{ MPa}$ ($4,000 \text{ psi}$), dynamic elastic modulus of $1.35E_c=32.5 \text{ GPa}$ (4712 ksi) (Murray et al. 2016), Poisson's ratio of 0.2, and a shear modulus $G_c=13.5 \text{ GPa}$ (1963 ksi) calculated in accordance with Equation 4-1 (Murray et al. 2016).

$$G_c = \frac{1.35E_c}{2(1+\nu)} \quad (4-1)$$

For the cold-formed floors the cement board was defined as having a density of $\rho=929 \text{ kg/m}^3$ (58 lb/ft^3), an elastic modulus of $E=11.7 \text{ GPa}$ (1700 ksi), and a Poisson's ratio of $\nu=0.20$ (USG 2016). A mesh size sensitivity analysis was performed for each model, with initial square element mesh dimensions of one-tenth the bay size. Mesh sizes were reduced until further refinement produced less than 0.1 Hz change in natural frequency (Murray et al. 2016).

8.4.2 *Damping*

Damping as it relates to structural dynamics is a mechanism by which energy dissipation results in reduced response of a structural system. (Stevenson 1980). It is important to somehow account for damping present in the structural system. For the evaluation of floor structures, types of damping to be considered primarily include material damping and structural damping. Material damping relates to energy loss in the material as a result of stress cycling and is often small and insensitive to varying stress levels below yield (Stevenson 1980). Structural damping often has a larger impact on the behavior of the structure and the structural joints often contribute more towards energy dissipation than the behavior of the materials (Adhikari 2000). Understanding and prescribing damping values to a structure can be difficult as it may be a function of several factors including displacement, velocity, stress, and other variables. These mechanisms by which energy is dissipated in a dynamic system are often non-linear or cannot be neatly categorized as linear-viscous or linear-hysteretic damping (Adhikari 2000). A simplified viscous damping model is often used for structural design and expressed as a percent of critical. These values can be determined experimentally or taken from accepted design guidelines.

Linear modal analysis steps in Abaqus/CAE allow for the user to directly define a critical damping factor for each eigenmode, where critical damping is the amount of damping that will cause a system to return to static equilibrium without oscillation (DSS 2016). This method of applying damping to the system is strictly a mathematical concept and is not rooted in any physical basis of the model, limiting it to use in mode-based linear applications (DSS 2016). For models evaluated using modal superposition a critical damping value, 1% of critical for the pedestrian footbridge and 2.5% for the other structures, was assigned for all eigenmodes below 20 Hz. These values are determined by summing viscous damping ratios for various structural and non-structural

components as shown in Table 8 -1 and recommended by AISC DG11 (2016). For the pedestrian footbridge this consisted of solely using the viscous damping ratio recommend for the effects of the structural system. The floor structures consisted of the ratios recommended for effects of the structural system, ceiling/ductwork below, and the electronic office fit out.

Table 8- 1. Recommended viscous damping ratios for floor components

Component Damping Values	
System	Viscous Damping Ratio ζ
Structural System	0.01
Ceiling/Ductwork	0.01
Electronic Office	0.005
Paper Office	0.01
Partitions	0.02-0.05

Damping in direct dynamics procedures in Abaqus/CAE cannot be defined as easily as in modal superposition. Direct dynamics procedures involve the direct integration of the equations of motion of the system and a physical representation of damping is required. Abaqus/CAE provides several sources of damping the user can define for direct procedures, and sources can be defined independently or in combination. Sources include material and element damping, global damping, and damping due to time integration (DSS 2016). Material and element damping along with global damping were used to apply damping to direct dynamics models. Abaqus/CAE uses the Rayleigh damping model of viscous damping, presented in Equation 4-2, which uses coefficients for mass proportional damping, α , and stiffness proportional damping, β , to achieve damping at a given percent of critical damping for the frequencies of interest. Damping at a single mode can be defined or expressed using Equation 4-3. To describe damping across a range of modes the system of equations in Equation 4-4 can be solved for the desired frequencies and

damping ratios. An important nuance of using Rayleigh damping is that it will produce the desired percent of critical damping at the lower and upper frequencies specified. However, modes in between those frequencies will be underdamped, while modes outside of those will be overdamped (Wilson 2004).

$$C = \alpha M + \beta K \quad (4-2)$$

$$\zeta_n = \frac{1}{2\omega_n} \alpha + \frac{\omega_n}{2} \beta \quad (4-3)$$

$$\begin{bmatrix} \zeta_i \\ \zeta_j \end{bmatrix} = \frac{1}{2} \begin{bmatrix} \frac{1}{\omega_i} & \omega_i \\ \frac{1}{\omega_j} & \omega_j \end{bmatrix} \begin{bmatrix} \alpha \\ \beta \end{bmatrix} \quad (4-4)$$

Models analyzed using direct dynamics utilized material damping with the viscous damping ratios outlined in Table 8 -1 (Bachmann 1995). Global damping parameters were calculated in accordance with viscous damping ratios in Table 8 -2. By summing the damping ratio of relevant structural and non-structural features one arrives at the total value of damping to assume (Murray et al. 2016). To ensure that the proper level of damping was applied to the models, a direct steady state analysis was conducted to generate the response spectra for each respective baseline model and damping was calculated using the half-power bandwidth method. The desired and measured damping values are summarized in Table 8 -3. Desired damping values are determined in accordance with AISC DG 11 (2016) values for pedestrian bridges and electronic offices, respectively. All modeling procedures for the footbridge were able to achieve the desired amount of damping. Damping for the composite floor was achieved with the modal procedure and was within 4% of the desired value for the direct procedure. The response spectra resulting from modal and direct dynamics were plotted together for comparison in Fig. 8- 3. The natural frequencies

predicted by both FE methods for the pedestrian bridge were within 1% of each other. The natural frequencies predicted by the FE methods for the composite floor structure varied slightly, varying only 5% between the methods. The composite floor as modeled by the direct procedure may be influenced more by higher modes as a result of underdamping inherent with the Rayleigh damping model. Reasonable agreement, both quantitatively and qualitatively, was achieved between the two methods across all models.

Table 8- 2. Recommended viscous damping ratios for model materials

Material Damping Ratios	
System	Viscous Damping Ratio ζ
RC - Uncracked	0.007-0.01
Composite	0.002-0.003
Steel	0.001-0.002

Table 8- 3. FE model damping values

Damping (% Critical)			
Structure	Desired	Modal Procedure	Direct Procedure
Footbridge	0.01	0.01	0.01
Composite Floor	0.025	0.025	0.026

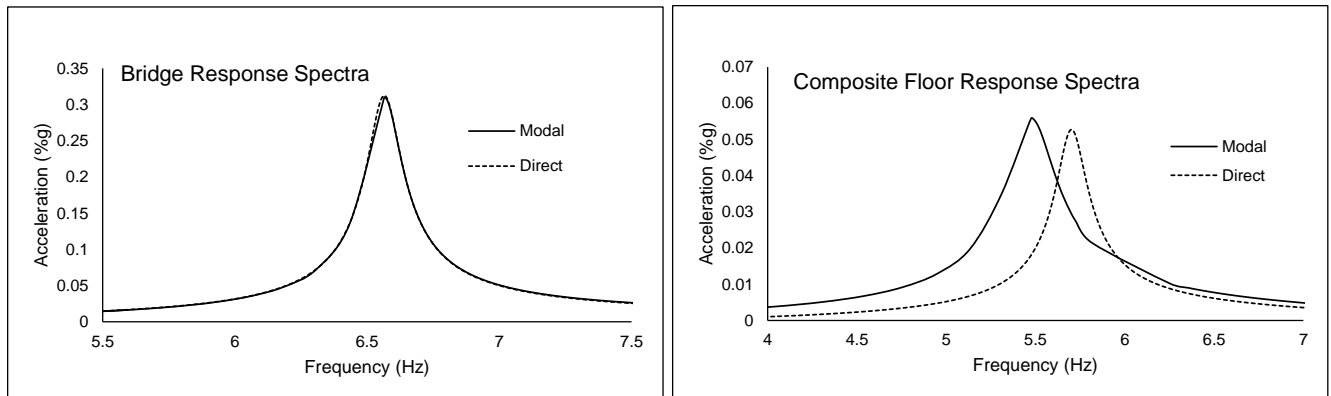


Fig. 8- 3: Comparison of the response spectra by modal analysis and direct dynamics for the a) pedestrian bridge, b) composite floor system

8.4.3 *Boundary Conditions*

The low amplitudes associated with floor vibrations allow for simplifying assumptions of boundary conditions between connecting and supporting elements (Murray et al. 2016). Floor structures were modeled monolithically with tie constraints connecting all elements (Boadi-Danquah et al. 2017). The beam ends were modeled as fixed due to the friction present in the beam-column and beam-girder connections which, at low amplitudes, essentially behave as moment connections (Smith et al. 2007).

8.4.4 *Loading: Design Guide Procedures*

Baseline models were evaluated by the hand calculation procedure outlined in AISC DG11 (2016). Additionally, three types of loadings were applied to the models at the point of interest: a time dependent forcing function, a unit sinusoidal load, and the aforementioned moving walking load. For the forcing function and unit sinusoidal load the point of interest was assumed to be that

which corresponds to the maximum mode shape value, typically the center of the bay or midspan. The moving walking load traversed the length of the floor along the centerline in the long direction.

The forcing function, $F(t)$, is based on a Fourier series approximation of the time dependent harmonic force components of walking, including the step frequency and the subsequent three harmonics.

$$F(t) = \sum_{i=1}^4 P(\alpha_i \cos i f_{step} 2\pi t) \quad (4-5)$$

Recommended values for this equation are provided in AISC DG11 (2016). For this study the person's weight P was taken as 747 N (168 lbf). The coefficient α_i is a dynamic coefficient for the i th harmonic of interest. The step frequency of the individual, f_{step} , was taken as 2 Hz. The coefficient i is simply the harmonic multiple of interest of the step frequency (Murray et al. 2016). It has been shown the vibration of a floor structure is typically dominated by a single mode, that which is closest to resonance (Murray et al. 2016). The participation of other modes, up to the fourth harmonic, were included for the purpose of evaluating if other modes produced significant response.

Resonant response of the floor structures was predicted by way of the Frequency Response Function (FRF) method (Murray et al. 2016). This method consists of applying a unit sinusoidal load at the point of interest and generating a response spectrum. There are two procedures for this method depending on if the floor is classified as low frequency or high frequency. Prediction of peak accelerations for low frequency floors utilizes Equation 4-6, consisting of the maximum magnitude obtained from the response spectrum by a value for body weight, Q , a dynamic coefficient, α , and a resonant build-up factor, ρ .

$$a_p = FRF_{Max} \alpha Q \rho \quad (4-6)$$

The body weight was taken as 747 N (168 lbf). The dynamic coefficient is calculated from Equation 4-7, where f_n is the natural frequency of the floor.

$$\alpha = 0.09e^{-0.075f_n} \quad (4-7)$$

The resonant build-up factor is calculated differently based on the assumed viscous damping ratio, β . All structures modeled had an assumed damping ratio between 1% and 3% of critical, and Equation 4-8 was used to determine ρ .

$$\rho = 12.5\beta + 0.625 \quad (4-8)$$

8.4.5 *Loading: Walking Procedure*

The body weight, step frequency, stride length, and walking path for the human induced load applied to the Abaqus/CAE model were controlled using a FORTRAN DLOAD subroutine, included as supplementary material, that was developed specially for this modeling procedure. A distributed pressure load was applied to the entirety of the floor surface to allow for control of foot width and length as well as path using FORTRAN code. The subroutine was adapted from a subroutine developed for applying moving pressure loads from tires (Cambridge 2011) to fit the requirements for modeling walking. To achieve a discontinuous loading rather than a rolling pressure load the subroutine was adapted to incorporate the stride length and duration of foot pressure on the floor.

A footfall is characterized by a heel-strike and toe-strike occurring in a time period of 0.5 to 0.6 seconds, with a ground reaction force between 1.2 and 1.4 times the bodyweight (Newland

2003). To model a footfall, the reaction force time-history for each step was divided into two parts: the heel-strike and the toe-strike (Bard 2008) for a bodyweight of 747 N (168 lbf) (Fig. 8- 4). For this model, the path with which the load traversed was defined to be linear. The dimensions of the foot were defined to be 76.2 mm (3 in.) wide by 305 mm (12 in.) long. Both the path and the foot dimensions were defined in the subroutine using the Abaqus/CAE universal coordinate system. Step frequency was controlled by determining a corresponding velocity and multiplying coordinate positions defined for the heel and toe position by the velocity and time step, creating a 76.2 mm (3 in.) x 305 mm (12 in.) strip that moved along the structure. To ensure that the load was applied only at the points of interest and not continuously, a stride length was defined, and the remainder of the current heel coordinate was evaluated with the desired stride length to determine when to apply the load. A bodyweight of 747 N (168 lbf) was used for modeling an occupant and the step frequency was defined as 2 Hz and the stride length as 0.76 m (2.5 ft).

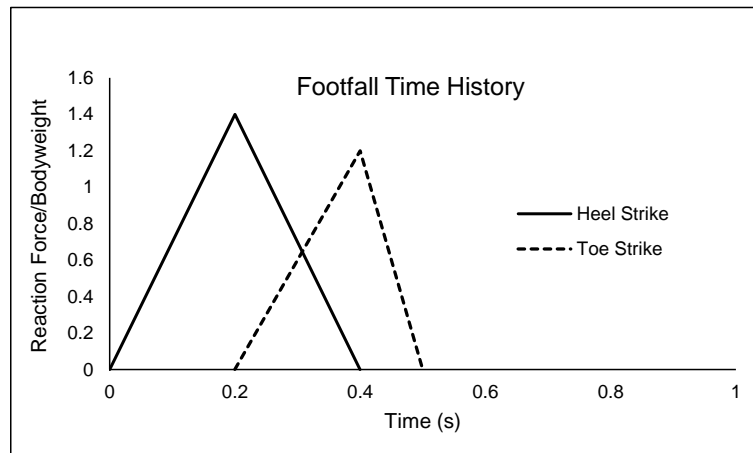


Fig. 8- 4: Time history of ground reaction force due to a footfall

By using the DLOAD subroutine the designer may define several characteristics of occupant loading. Furthermore, the code may be adapted to include multiple occupants and can be developed for more complex, non-linear paths.

8.5 Experimental Testing

Two cold-formed steel floors systems as described above were fabricated and tested in accordance with a simplified evaluation methodology (Davis 2014). Each system consisted of 12 gage cold-formed steel purlins and plate with the depth of the purlins varied between the two systems. One system utilized a purlin depth of 203 mm (8 in.) and the other system utilized a purlin depth of 254 mm (10 in.). These will be referred to as floors D203 (D8) and D254 (D10), respectively.

Fabrication of these test specimens consisted of plasma cutting a profile out of the flange and web of the purlins spaced at 0.61 m (24 in.) to allow the purlins to interlock and create an orthogonal grid. Cold-formed plates were plasma cut into desired sizes and then welded together using a CJP groove weld to form the bottom and top plates of the system. Purlins were placed around the perimeter of the bottom plate with the top flanges facing outwards. The grid of interlocking purlins was arranged on the bottom plate and all purlins were welded to the bottom plate where the edge of the flange on one side and the bend in the web on the other met the plate. The top plate was then placed on top of the grid of purlins. The edges of the plate were welded to the perimeter purlins while self-tapping screws tied the top plate to the inner grid of purlins. This procedure produces a single floor panel. Each floor system consisted of three floor panels which were then installed one at a time inside a test frame consisting of W360x134 (W14x90) girders with inside dimensions of 6.9 m (273 in.) x 5.1 m (200 in.). The perimeter purlins were attached

to the top flanges of the test frame using Hilti brand powder actuated fasteners. The panels were tied together using 12 gage splice plates and self-tapping screws. A decking consisting of sheets of 1.2 m (4 ft) x 2.4 m (8 ft) OSB sheathing with 10 mm (0.4375 in.) thickness was attached to the top plates of the floor system using self-tapping screws to complete the in situ system.

Evaluation of the experimental systems consisted of instrumenting the floor with accelerometers at the center of the floor and the quarter points along the centerlines and obtaining the responsive frequencies before conducting walking testing. To estimate the responsive frequencies of the floor system heel drop tests were conducted involving an individual on the floor system rising onto their toes and dropping their heels forcefully onto the floor. Acceleration time history is recorded from this impact and can be analyzed in the frequency domain to obtain responsive frequencies. This simplified method is adequate in place of experimental modal analysis in that the natural frequency estimate is the only parameter required for subsequent testing and the heel drop produces ample force between 1 and 20 Hz (Davis 2014).

Once the responsive frequencies of the floor system are obtained from the heel drop spectra, walking testing may be conducted. The step frequency for the test is determined based on the fundamental frequency of the floor system. A step frequency is chosen that is between 1.5-2.2 Hz and matches the lowest harmonic of the fundamental frequency (Davis 2014). While an individual traverses the floor system at the determined step frequency, acceleration time history data is collected from the measurement stations. To evaluate the recorded acceleration relative to the ISO limits, the ESPA must be determined. This is done by computing the rolling root mean square (RMS) acceleration and multiplying it by the square root of two. For low frequency floors an interval of two seconds is recommend for calculating RMS acceleration (Davis 2014). For high

frequency floors where the response resembles a series of impulses rather than resonant buildup, the RMS is often calculated following an applied impulse.

8.6 Results & Discussion

The predicted natural frequencies and peak accelerations for the baseline models are presented below. A study of these baseline models was conducted to verify the suitability of the developed direct dynamics procedure for predicting natural frequency and walking accelerations. A summary of natural frequency predictions can be found in Table 8 -4 and indicates that the developed FE method matched the established design guide method within 0.06% for the footbridge and 1% for the composite floor. Similarly, to verify the developed FE method is suitable for evaluating accelerations due to walking, the baseline structures were evaluated with several methods as shown in Table 8 -5. The pedestrian footbridge obtained similar results across all methods and the predicted effective weights which governs acceleration response are shown Table 8 -6. The composite floor FE models all diverged from the different methods. It is seen in Table 8 -6 that the effective or participating weight for the composite floor is predicted to be different by the design guide method and FE methods. Another possible explanation for the proposed method to over-predict accelerations of the composite floor are related to the damping model. Rayleigh damping allows the designer to specify a percent of critical damping at two frequencies, however frequencies within that range will be underdamped. If the composite floor experiences vibration at frequencies in between those specified by the Rayleigh model they contribute to overall behavior disproportionately.

Table 8- 4. Natural frequencies predicted by AISC Design Guide 11 (2016) and FEA

Natural Frequencies (Hz)		
Structure	DG	FEA
Footbridge	6.61	6.57
Composite Floor	5.53	5.47

Table 8- 5. Equivalent sinusoidal peak accelerations predicted by AISC Design Guide 11 (2016) and FEA for varying evaluation methods

ESPA (%g)				
Structure	DG	Fourier Series	FRF	Walking
Footbridge	2.69	2.76	2.1	2.86
Composite Floor	0.29	0.37	0.41	0.87

Table 8- 6. Effective weight as calculated by AISC Design Guide 11 (2016) and Abaqus/CAE

Effective Weight, kN (kips)		
Structure	DG	FEA
Footbridge	144.5 (32.5)	128.6 (28.9)
Composite	449 (101)	302.5 (68)

8.6.1 *Pedestrian Footbridge*

For the evaluated footbridge the design guide predicted natural frequency was 6.61 Hz, while the natural frequency predicted by the direct FE method was 6.57 Hz. Acceleration predictions resulted in values of 2.69, 2.76, 2.1, and 2.86 %g for the AISC DG11, the Fourier series, the FRF, and the walking model methods, respectively. Close agreement between all methods can be explained by the simplicity of the system. The effective panel width calculated by

the Design Guide ends up simply being the width of the system because the footbridge will vibrate as a beam (Murray et al. 2016).

8.6.2 *One-Way Composite Floor*

The AISC DG11 (2016) procedure for predicting natural frequency resulted in a calculated natural frequency of 5.53 Hz, which can be compared with 5.47 Hz resulting from an eigenvalue analysis conducted through Abaqus/CAE. Predicted accelerations of 0.29, 0.37, 0.41, and 0.87 %g were calculated by the AISC DG11, Fourier series, FRF, and walking model methods, respectively.

The FE models under-predicted the participating mass in comparison to AISC DG11 (2016): 302.5 kN (68 kips) compared to 449 kN (101 kips). Some of this variation may be attributed to differences in mode shape. The AISC DG11 (2016) method assumes the deflected shape of the floor under gravity loading represents the fundamental mode shape, whereas the FE methods calculate the eigenvectors. Furthermore, modes in between the upper and lower bounds of the specified Rayleigh damping parameters will be under-damped. If there are contributions from these modes to the overall response they may be overestimated, especially in the walking model where the damping is applied over a range rather than at specific frequencies. In examining the acceleration-time history of this model, it also appears that there is some type of resonant build-up that may result in the increase RMS acceleration resulting in increased predicted ESPA.

8.6.3 *Experimental Cold-Formed Floors*

The walking modeling FE method predicted natural frequencies and peak accelerations close to the experimental data. Finite element analysis by the developed method predicted a natural frequency within 8% of the experimental data for floor D203 (D8) and within 17% for floor D254

(D10) as shown in Table 8 -7. Accelerations predicted by the developed walking method were within 3% for floor D203 (D8) and 33% for floor D254 (D10) as shown in Table 8 -8. Acceleration time histories for the walking FE method and experimental testing are included in Fig. 8- 5. It is important to note that peak accelerations cannot be compared directly from these plots as they are not converted to ESPA and are presented on different acceleration scales. Instead they are able to show qualitatively that the floors respond to the modeled and real footfall as an impulse load followed by free vibration, characteristic of high frequency floors.

Table 8- 7. Comparison of natural frequencies predicted from FEA and experimental testing

Natural Frequencies (Hz)		
Structure	FEA	Experimental
D203 (D8)	10.9	10.3
D254 (D10)	11.0	9.6

Table 8- 8. Comparison of equivalent sinusoidal peak accelerations determined from FEA and experimental testing

ESPA (%g)		
Structure	FEA	Experimental
D203 (D8)	10.57	10.24
D254 (D10)	15.82	11.83

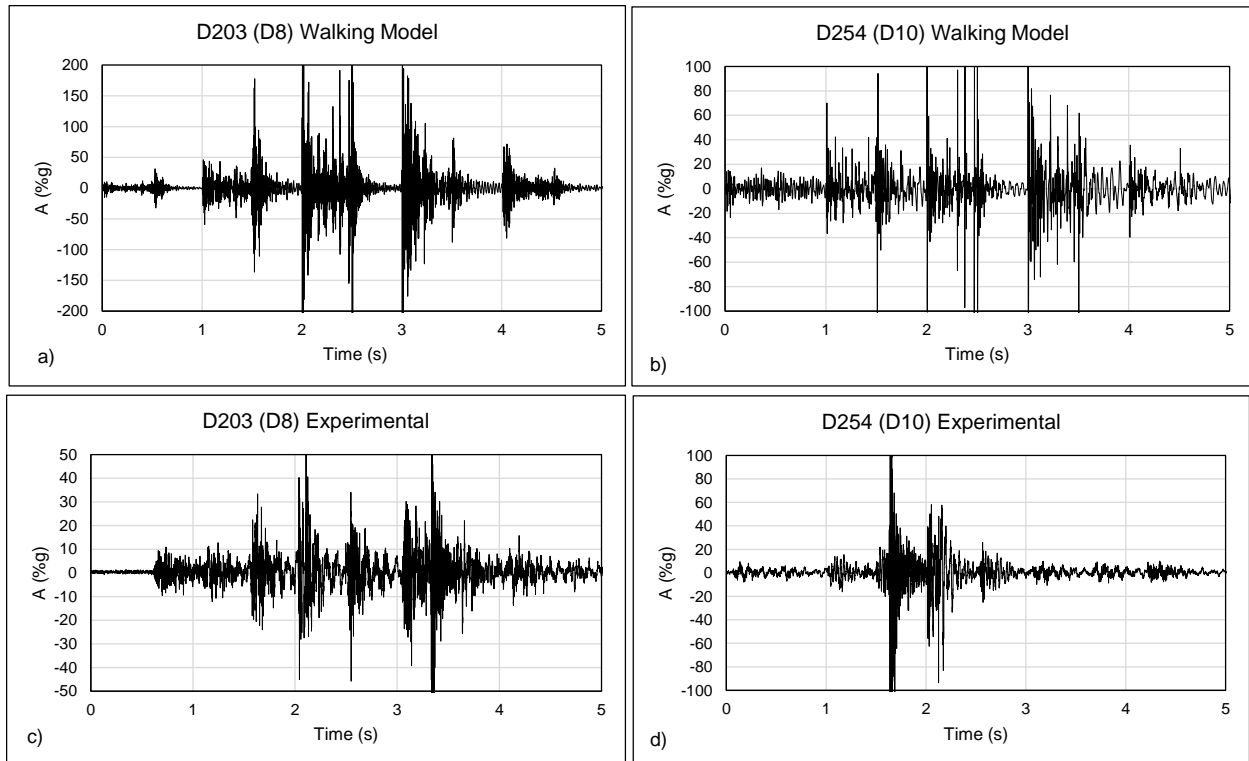


Fig. 8- 5: Acceleration-time history for the D203 (D8) a) walking model and c) experimental data and the D254 (D10) b) walking model and d) experimental data

8.7 Conclusions

Initial findings suggest the newly developed walking model approach for predicting dynamic behavior of floors through finite element analysis may be suitable for evaluating vibration serviceability. Further experimental testing will help to validate this approach and calibrate FE models.

Through the use of baseline models the direct dynamics procedure used to implement the walking model was evaluated. It was shown to be adequate at capturing the response of simply vibrating systems such as a pedestrian bridge. For more complex models a better understanding of the damping in the structure and how it may be translated to the model may help improve accuracy.

It was shown that both the AISC DG11 (2016) and the FE modeling method predict natural frequencies in agreement with each other; however, a slight divergence was noted in the prediction of accelerations. Several possibilities for this divergent behavior, including different predicted participating mass, effects of material damping, and the impact of using deflected shape vs. calculated mode shapes, were highlighted.

Experimental data helped to further verify the ability of the direct dynamics method for modeling the modal properties of a structure. The experimental data validated the ability of the walking method for capturing the response of a structure to a walking event. Further calibration of this method through additional experimental testing may be beneficial for refining the methods by which the walking event is applied to the structure.

References

- Ahmed, E., Badaruzzaman, W. W., & Wright, H. D. (2002). Two-way bending behavior of profiled steel sheet dry board composite panel system. *Thin-walled structures*, 40(11), 971-990.
- AISC (2017). *Steel construction manual*. American Institute of Steel Construction. 15th Edition.
- AISI (2013). AISI-S100-13. Test Standard for Cold-formed Steel Connections. American Iron and Steel Institute, Washington, D.C.
- AISI (2012). AISI-S100-12. North American Specification for the Design of Cold-Formed Steel Structural Members. American Iron and Steel Institute, Washington, D.C.
- ASTM (2016). "Standard method for static load testing of framed floor or roof diaphragm constructions for buildings." *ASTM E455-16*, West Conshohocken, PA.
- Bernstein, H.M., Gudgel, J.E., Laquidara-Carr, D. (2011). "Prefabrication and modularization: Increasing productivity in the construction industry". *Smart Market Report*, ed. McGraw-Hill Construction. NIST.
- Bian, G., Buonopane, S. G., Ngo, H. H., & Schafer, B. W. (2014). "Fastener-based computational models with application to cold-formed steel shear walls." *22nd International Specialty Conference on Cold-Formed Steel Structures*. Missouri, USA
- Boadi-Danquah, E., Robertson, B., Fadden, M., Sutley, E. J., and Colistra, J. (2017a). "Lightweight modular steel floor system for rapidly constructible and reconfigurable buildings." *International Journal of Computational Methods and Experimental Measurements*, 5(4), 562-573.

- Boadi-Danquah E., Maclachlan D., Fadden M. (2017b). "Lightweight Rapidly Constructible and Reconfigurable Modular Steel Floor Diaphragm: Cyclic Performance." 3rd Huixian International Forum on Earthquake Engineering for Young Researchers, Illinois-USA.
- Boadi-Danquah E., Yount T., Collins W., Fadden M. (2019a). "Cyclic Behavior of Single Shear Steel-to-Steel Screws and Powder-Actuated Fastener Connections" Manuscript in preparation.
- Boadi-Danquah E., MacLachlan, D., Collins W., Fadden M. (2019b). "Behavior of a lightweight modular steel floor diaphragm under quasi-static cyclic loading I: Experimental Evaluation" Manuscript in preparation.
- CGC (2016). Tile and Flooring Solution. Data Sheet- *CGC Durock Brand Cement Board*.
- Colaco, J. P. (1972). Stub-girder system for high-rise buildings. *Engineering Journal-American Institute of Steel Construction Inc*, 9(3), 89-95.
- Ding, C. (2015). "Monotonic and cyclic simulation of screw-fastened connections for Cold-Formed Steel Framing". Virginia Polytechnic Institute and State University.
- Dassault Systems Simulia (DDS) (2016). "Abaqus CAE version 2016 ", Dassault Systemes Simulia Corp.
- Dassault Systems Simulia (DDS) (2014). "Abaqus CAE version 2014 ", Dassault Systemes Simulia Corp.
- Essa, H. S., Tremblay, R., & Rogers, C. A. (2003). Behavior of roof deck diaphragms under quasistatic cyclic loading. *Journal of Structural Engineering*, 129(12), 1658-1666.
- FEMA (2007). Interim Testing Protocols for Determining the Seismic Performance Characteristics of Structural and Nonstructural Components, Federal Emergency Management Agency (Report No. FEMA-461.)

Girder Slab (2015). Girder Slab Composite Steel and Precast System.

www.girder-slab.com

Hanaor, A. (2000). Tests of composite beams with cold-formed sections. *Journal of Constructional Steel Research*, 54(2), 245-264.

Hilti (2015) Direct Fastening Technical Guide 2015. *North American Product Technical Guide*. Ed 15, 161-167.

Hsu, C. T. T., Punurai, S., Punurai, W., & Majdi, Y. (2014). New composite beams having cold-formed steel joists and concrete slab. *Engineering structures*, 71, 187-200.

IBC (2015). International Building Code, International Code Council, Country Club Hills, Illinois.

Luttrell, L. (1996). Designing Roof and Floor Diaphragms. *Modern Steel Construction*, Chicago, IL.

MacLachlan, D. (2019). *Vibration serviceability assessment of a lightweight cold-formed steel floor system* (Masters thesis, University of Kansas).

Mazzoni, S., McKenna, F., & Fenves, G. L. (2005). OpenSees command language manual. *Pacific Earthquake Engineering Research (PEER) Center*, 264.

Moehle, J. P., Hooper, J. D., Kelly, D. J., & Meyer, T. R. (2010). Seismic design of cast-in-place concrete diaphragms, chords, and collectors. *Seismic design technical brief, US Department of Commerce, Building and Fire Research Laboratory, National Institute of Standards and Technology*.

Ngo, H.H. (2014). "Numerical and experimental studies of wood sheathed cold-formed steel framed shear walls." John Hopkins University, Baltimore, Maryland.

O'Brien, P., Florig, S., Moen, C. D., & Eatherton, M. R. (2016). Characterizing the Load Deformation Behaviour of Steel Deck Diaphragms.

- Peterman, K. D., & Schafer, B. W. (2013). Hysteretic shear response of fasteners connecting sheathing to cold-formed steel studs. In Research report, CFS-NEES, RR04.
- Robertson, B., Boadi-Danquah, E., Fadden, M., Sutley, E. J., Collistra, J. (2017). "Lightweight rapidly constructible and reconfigurable modular steel floor system: Serviceability analysis and design." *7th Biennial Architectural Engineering Institute Conference 2017*, Oklahoma City, Oklahoma.
- Rogers, C. A., & Tremblay, R. (2003a). Inelastic seismic response of side lap fasteners for steel roof deck diaphragms. *Journal of Structural Engineering*, 129(12), 1637-1646.
- Rogers, C. A., & Tremblay, R. (2003b). Inelastic seismic response of frame fasteners for steel roof deck diaphragms. *Journal of Structural Engineering*, 129(12), 1647-1657.
- Ross, B. E., Chen, D. A., Conejos, S., & Khademi, A. (2016). Enabling adaptable buildings: Results of a preliminary expert survey. *Procedia Engineering*, 145, 420-427.
- Schaad, J. A. (2005). *Two-Way Steel Floor System Using Open-Web Joists* (Doctoral dissertation, Marquette University).
- SDI (Steel Deck Institute). (2015). *Diaphragm Design Manual*, 4th Edition. Steel Deck Institute
- Simpson Strong-Tie. (2019). *Strong-Drive Self-drilling X Metal Screws*. Product Information
- SSMA (Steel Studs Manufacturers Association). (2015) *Product Technical Guide*.
- Timoshenko, S. P., & Woinowsky-Krieger, S. (1959). *Theory of Plates and Shells*. McGraw-hill: New York, Toronto and London.
- Tremblay, R., Rogers, C. A., Yang, W., & Martin, E. (2004). Ductile design of steel roof deck diaphragms for earthquake resistance. In *Proceedings of the 13th World Conference on Earthquake Engineering, Vancouver, Canada. Paper (No. 1997)*.

Uy, B., Patel, V.I. and Li, D. (2015). Behaviour and design of connections for demountable steel and composite structures, Keynote, *11th International Conference on Advances in Steel and Concrete Composite Structures*. Tsinghua University, Beijing, China.

Wang, L., Webster, M. D., & Hajjar, J. F. (2015). “Diaphragm Behavior of Deconstructable Composite Floor Systems”. Proc. *8th International Conference on Behavior of Steel Structures in Seismic Areas*. Shanghai, China.

APPENDIX A: Cyclic Load-displacement Response (Screws)

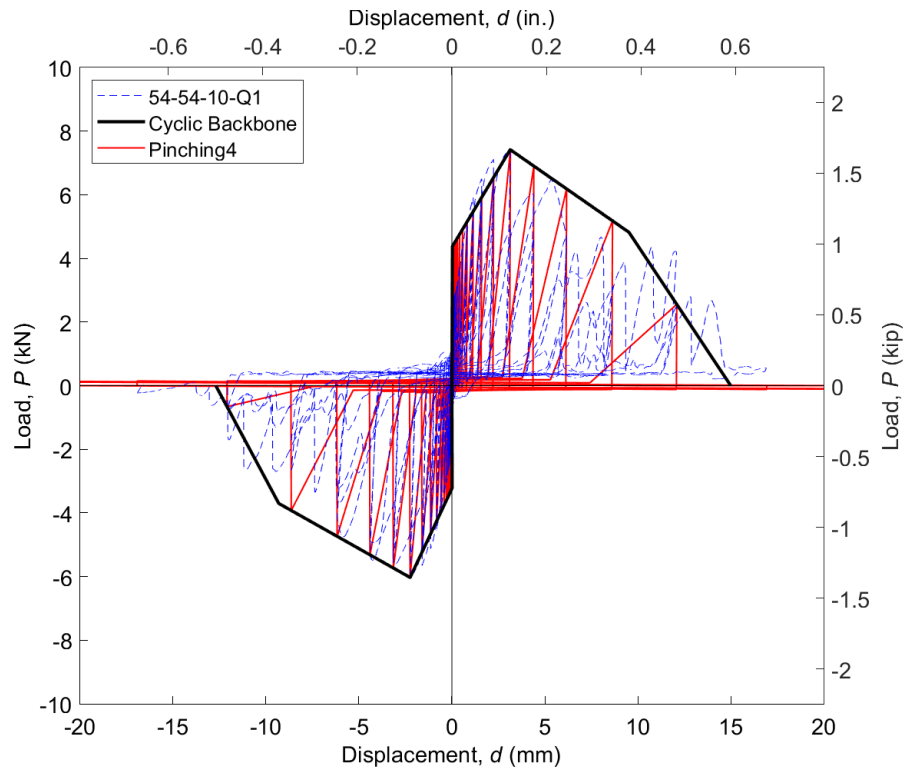


Fig. A-1: Cyclic load-displacement response for 54-54-10-Q1

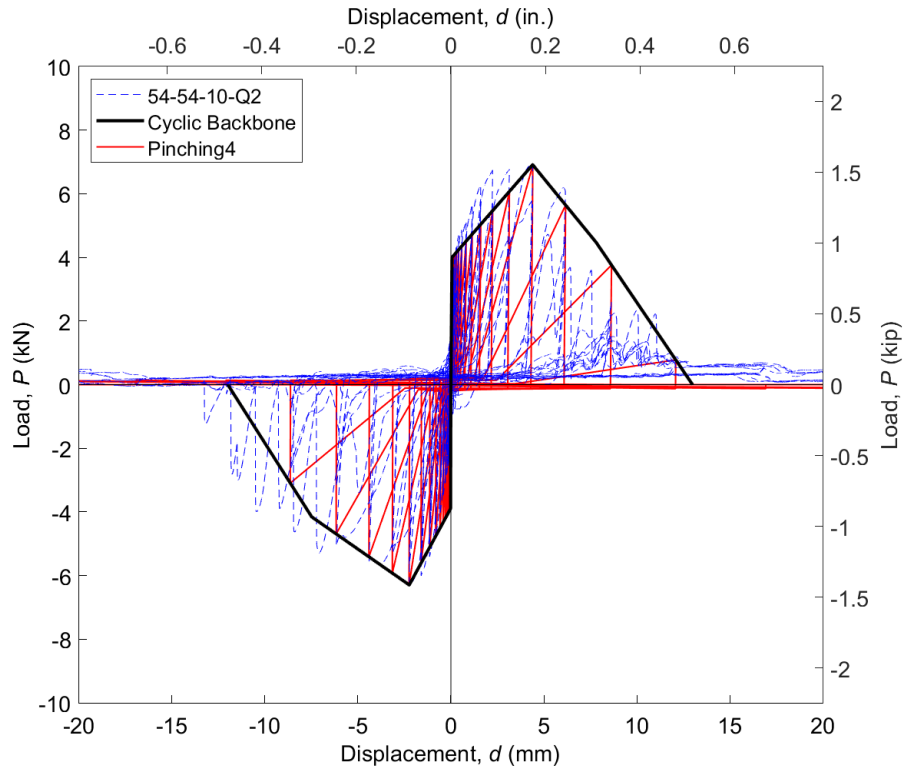


Fig. A-2: Cyclic load-displacement response for 54-54-10-Q2

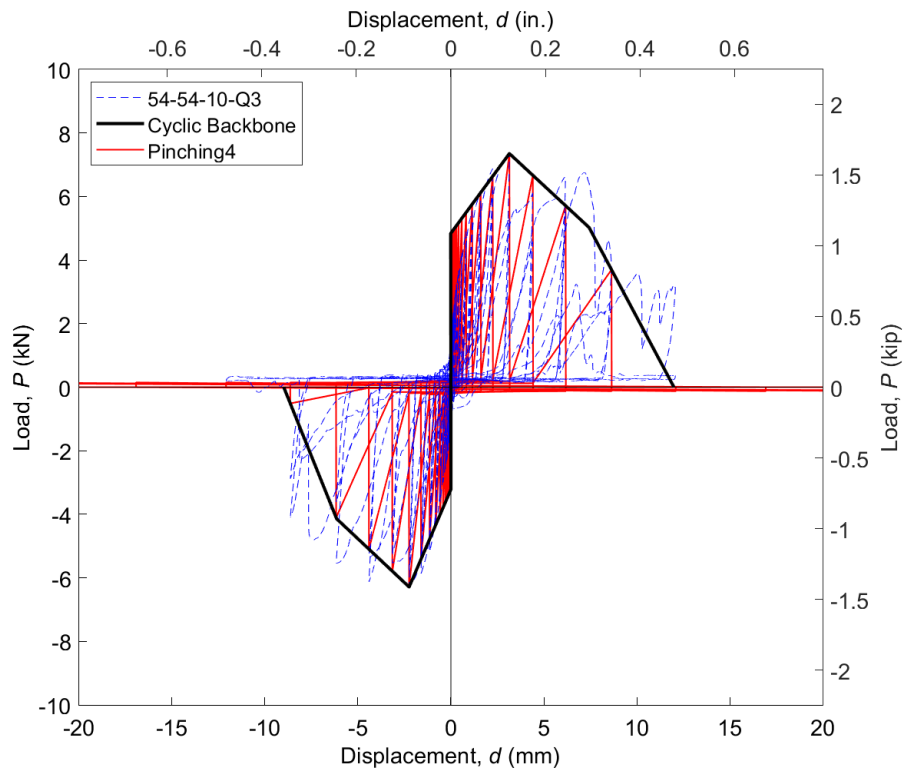


Fig. A-3: Cyclic load-displacement response for 54-54-10-Q3

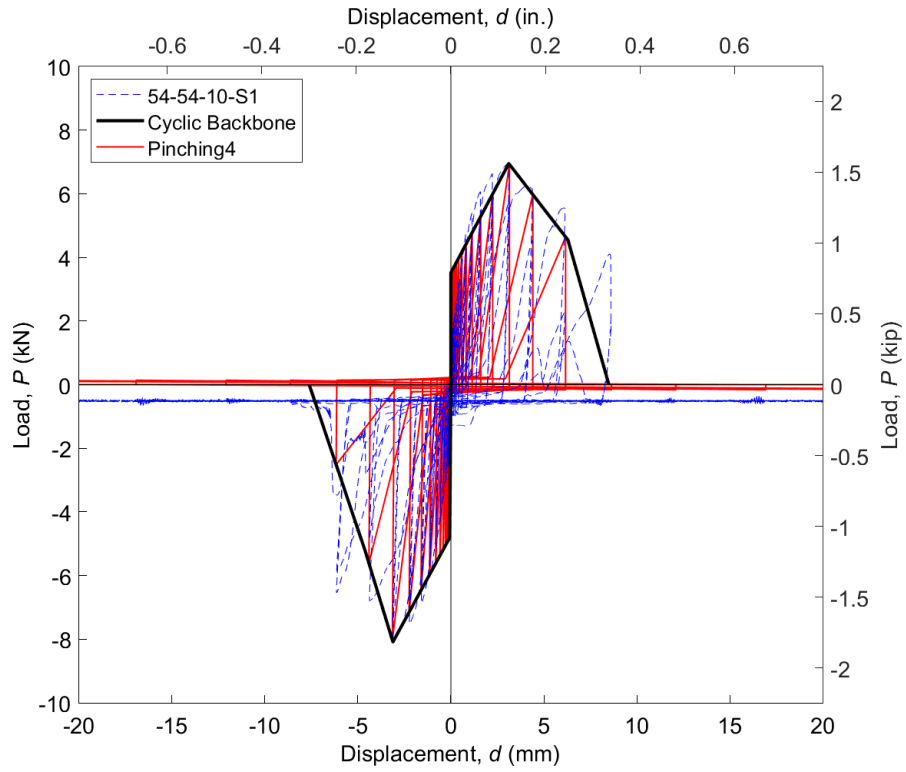


Fig. A-4: Cyclic load-displacement response for 54-54-10-S1

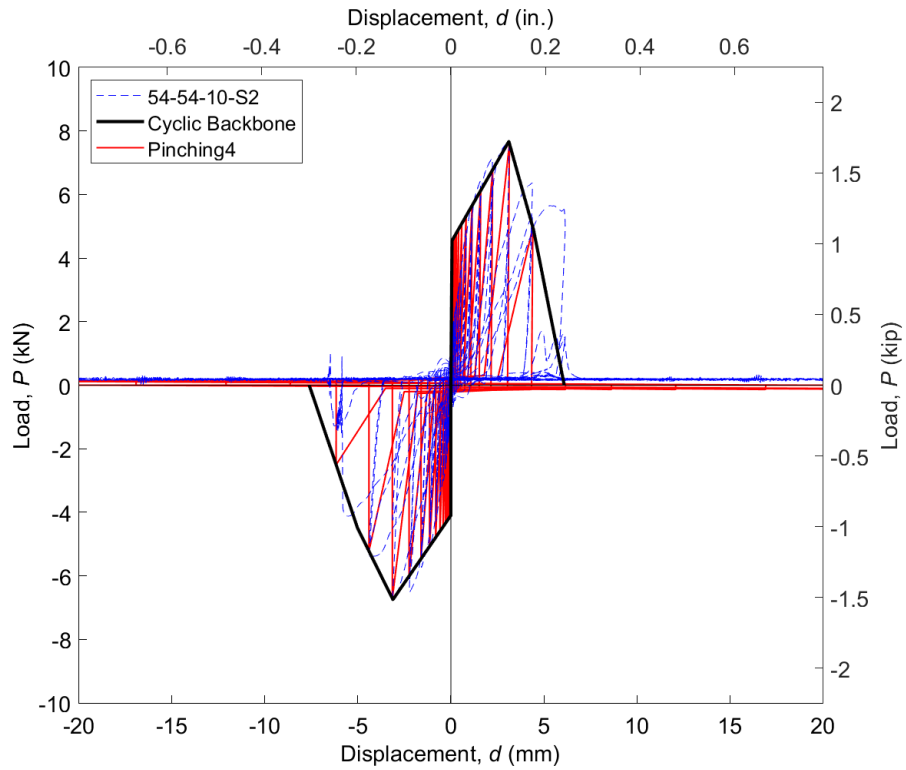


Fig. A-5: Cyclic load-displacement response for 54-54-10-S2

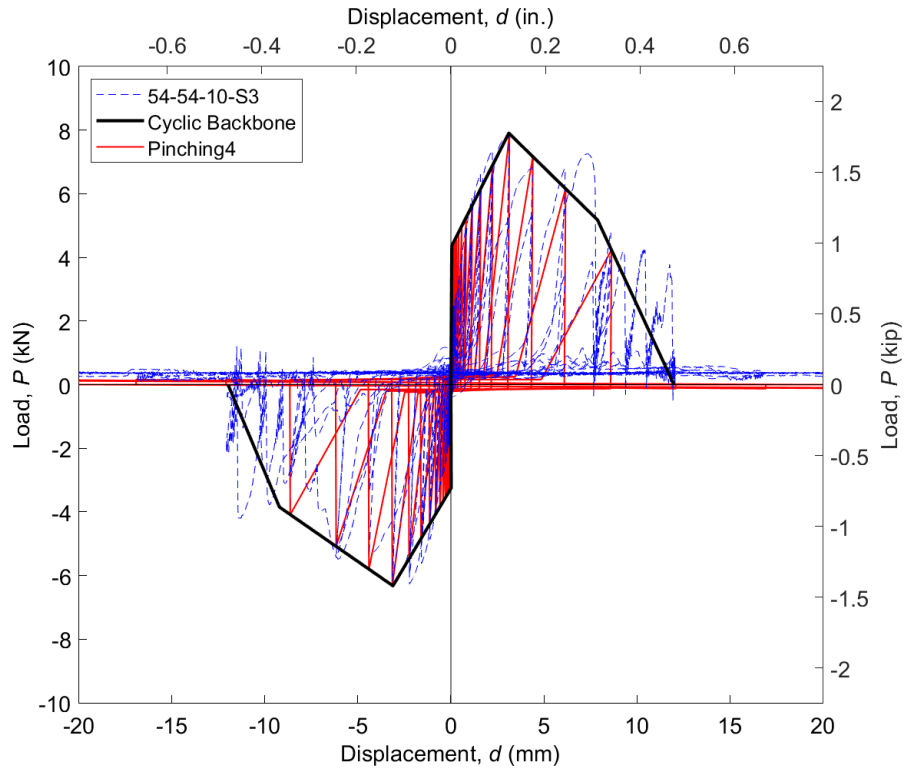


Fig. A-6: Cyclic load-displacement response for 54-54-10-S3

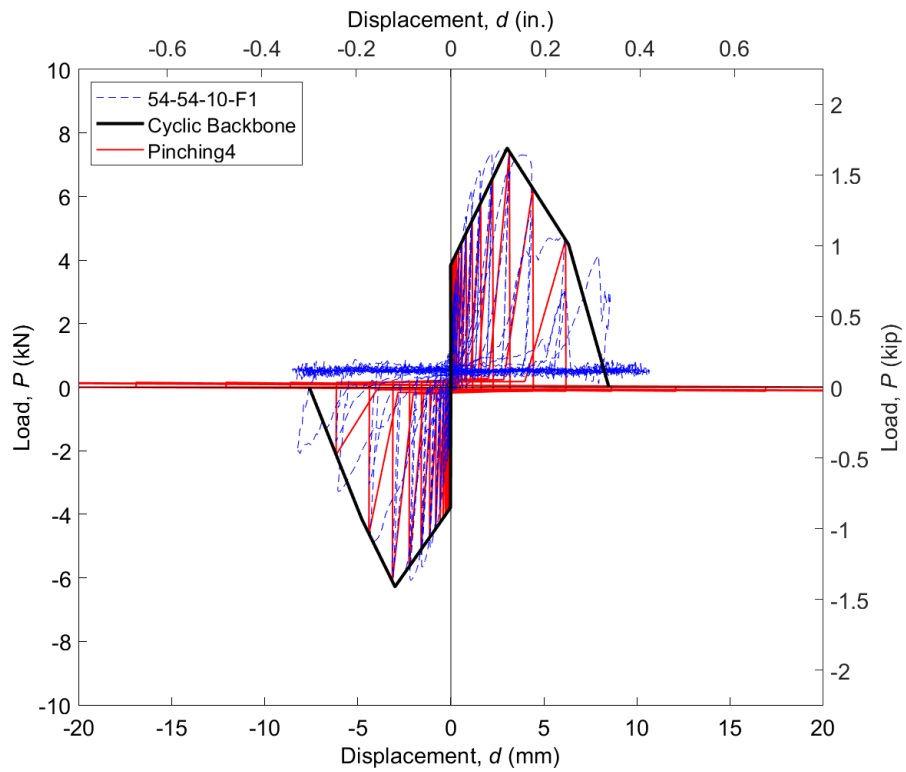


Fig. A-7: Cyclic load-displacement response for 54-54-10-F1

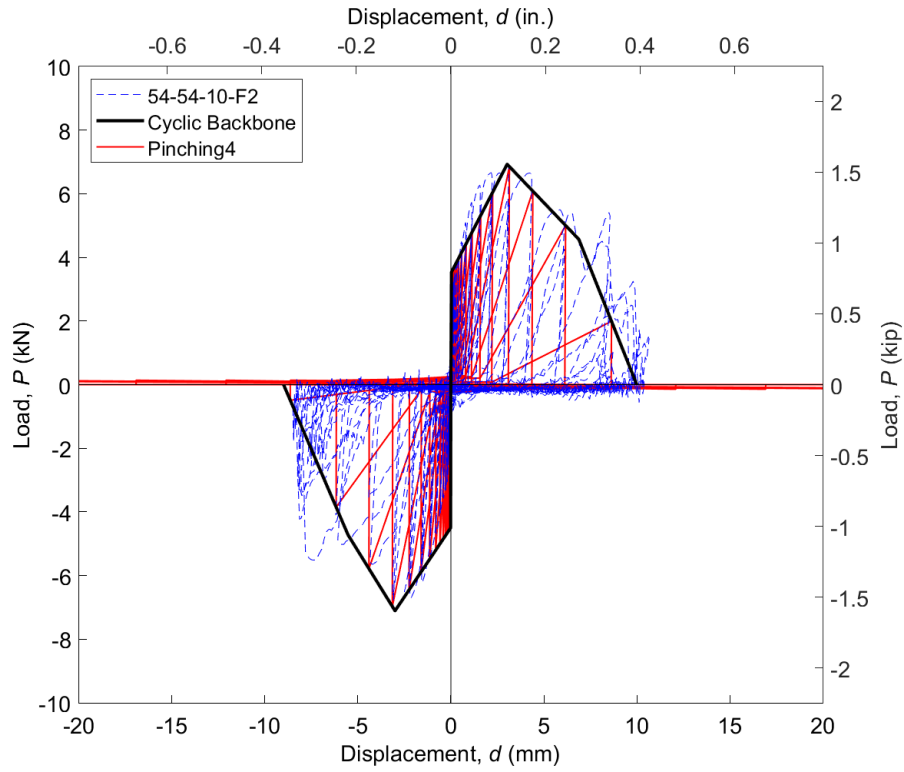


Fig. A-8: Cyclic load-displacement response for 54-54-10-F2

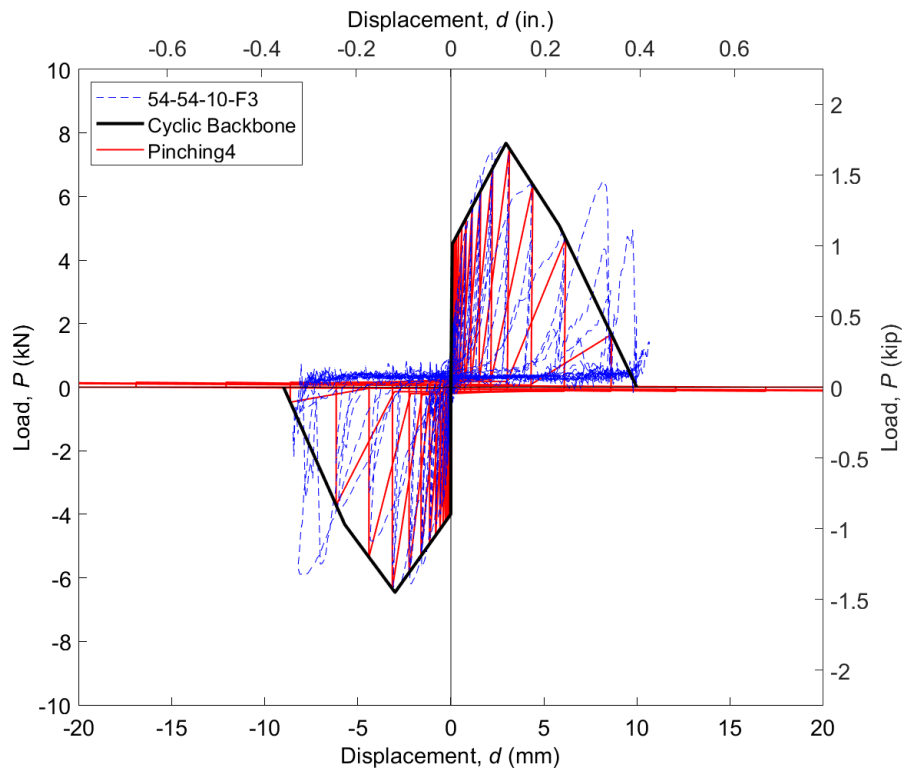


Fig. A-9: Cyclic load-displacement response for 54-54-10-F3

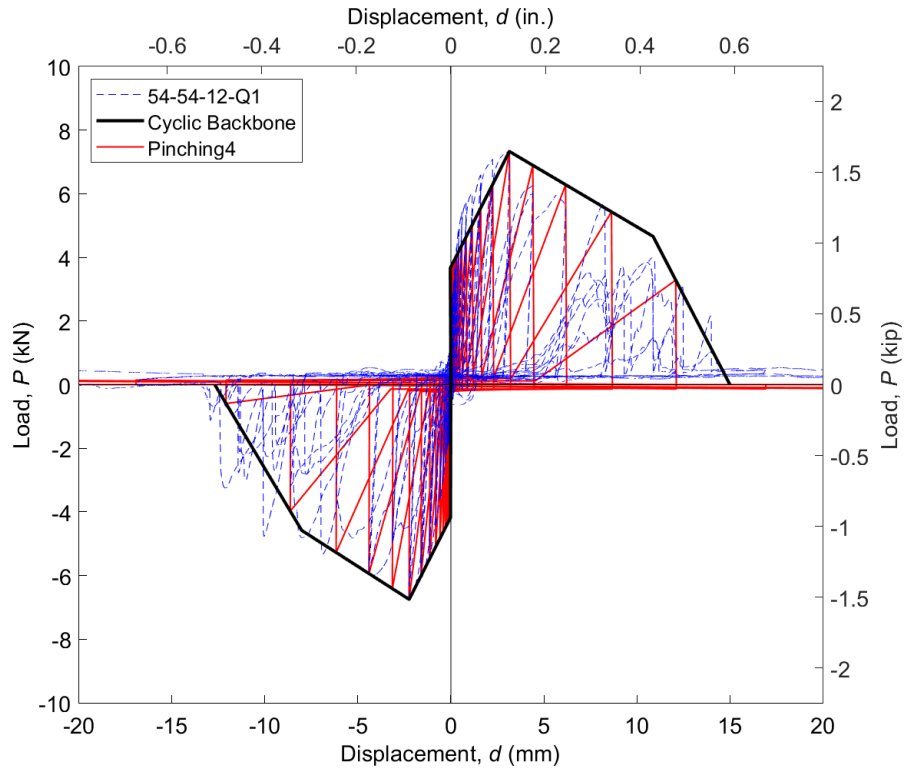


Fig. A-10: Cyclic load-displacement response for 54-54-12-Q1

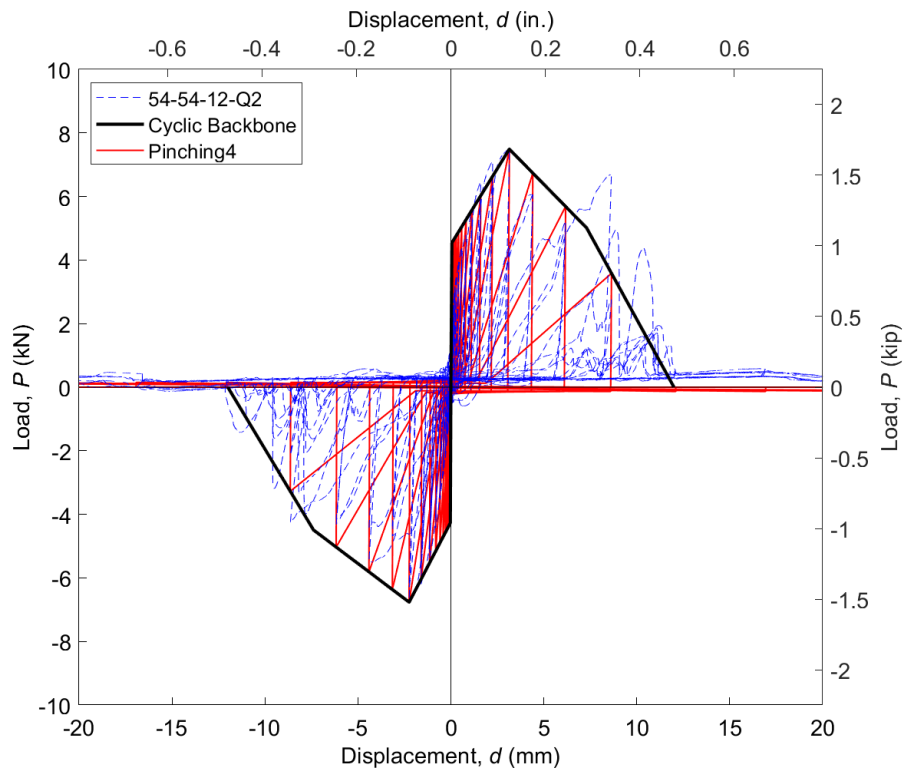


Fig. A-11: Cyclic load-displacement response for 54-54-12-Q2

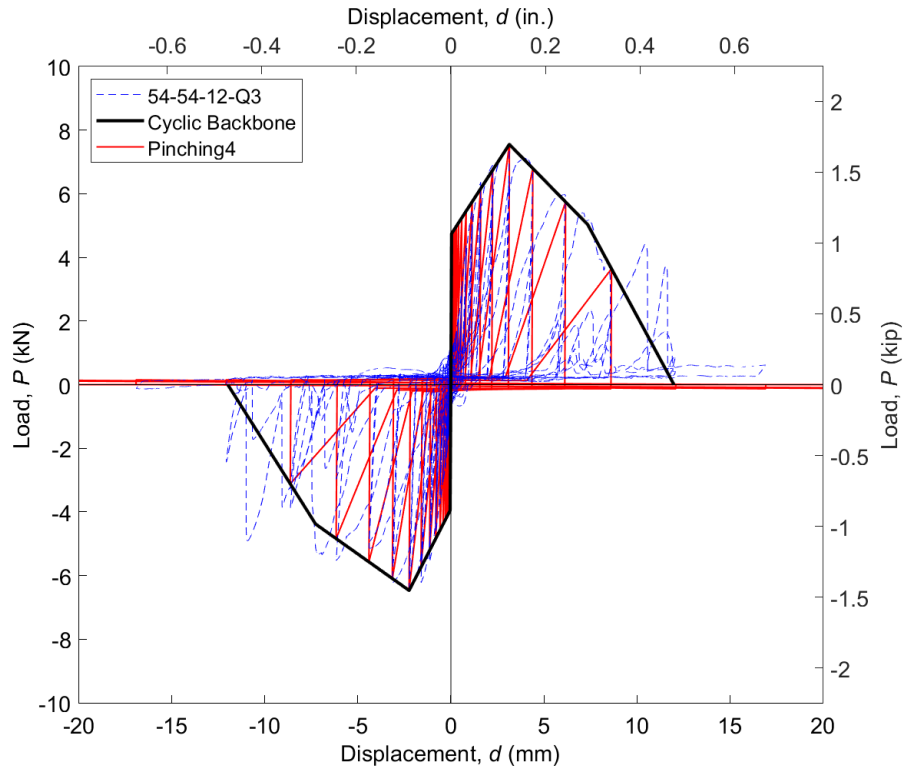


Fig. A-12: Cyclic load-displacement response for 54-54-12-Q3

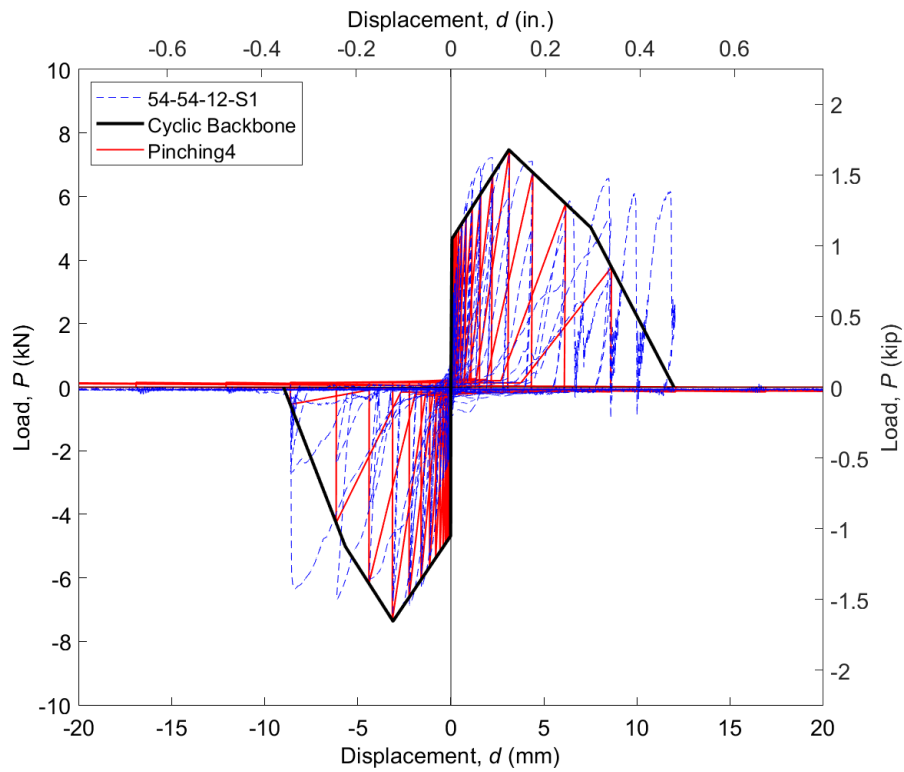


Fig. A-13: Cyclic load-displacement response for 54-54-12-S1

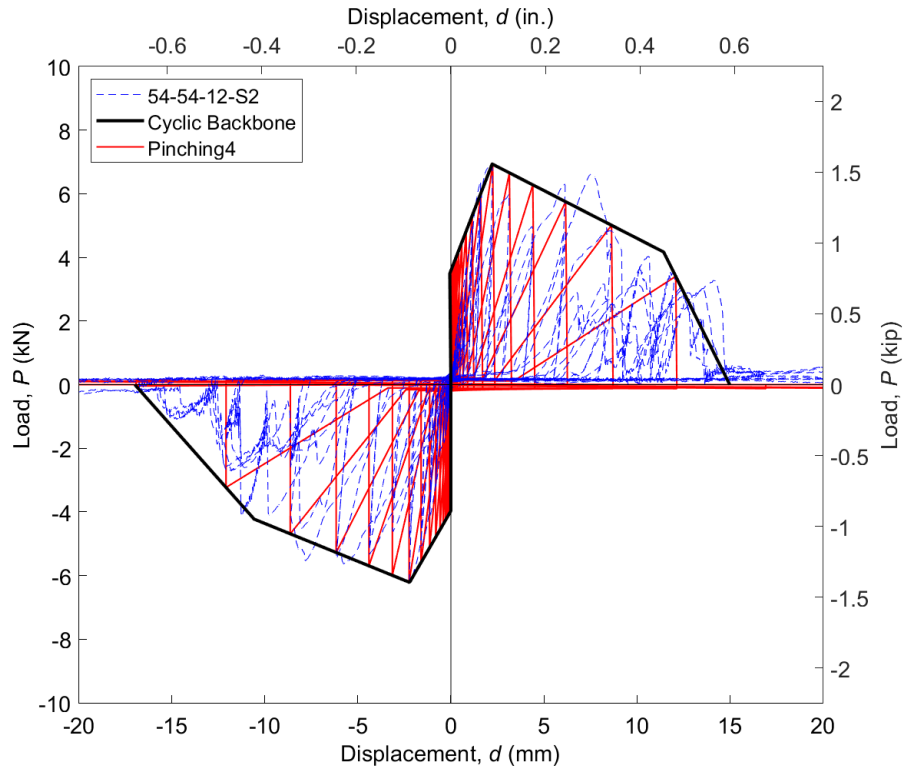


Fig. A-14: Cyclic load-displacement response for 54-54-12-S2

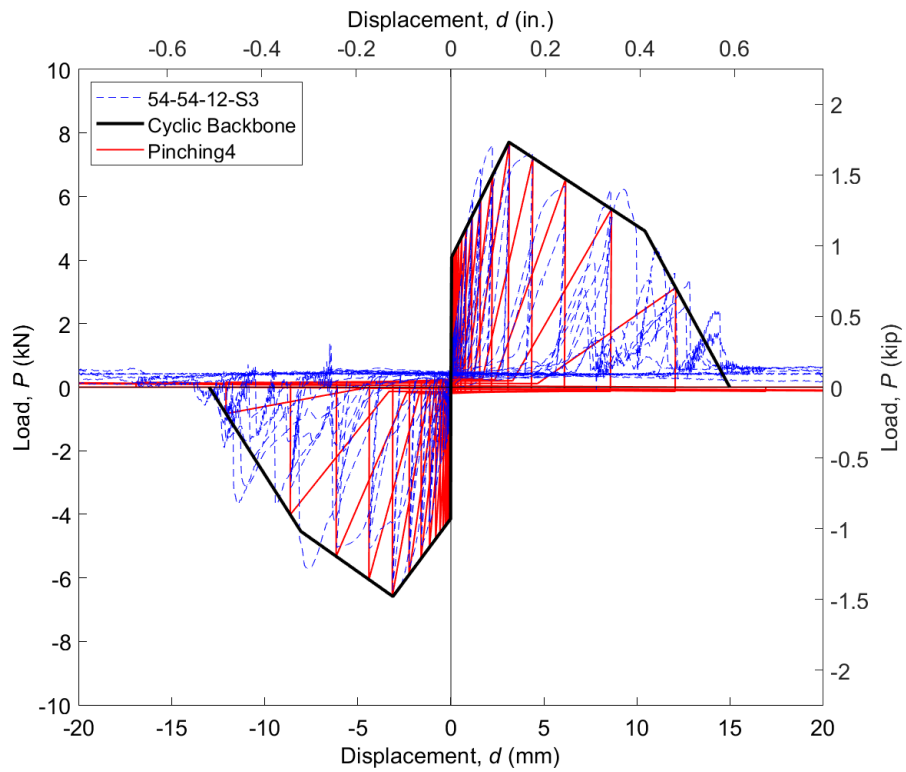


Fig. A-15: Cyclic load-displacement response for 54-54-12-S3

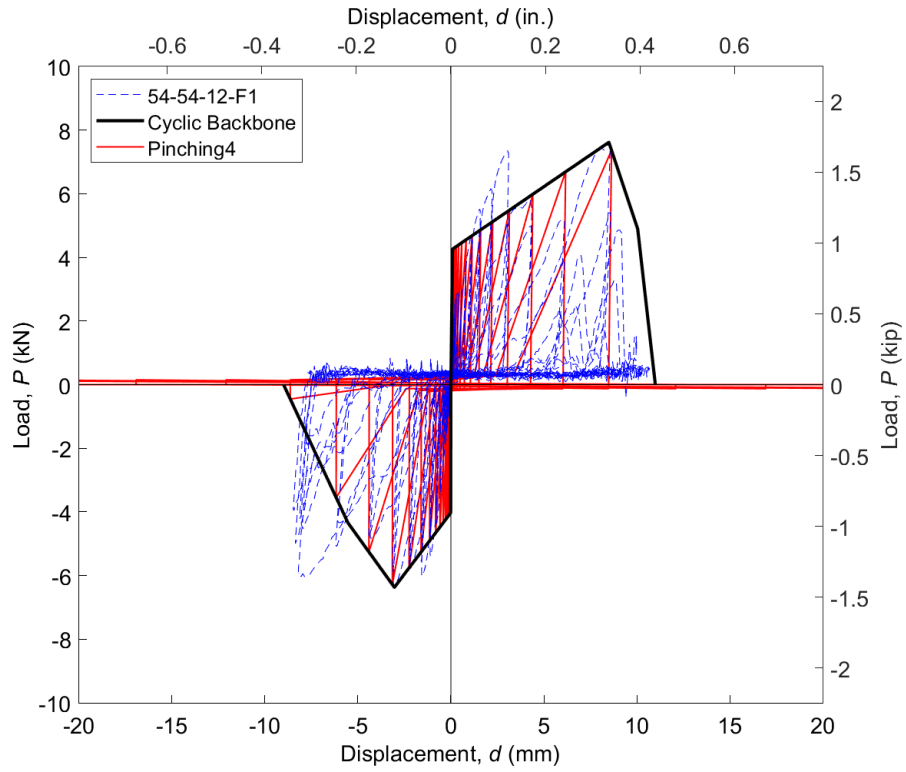


Fig. A-16: Cyclic load-displacement response for 54-54-12-F1

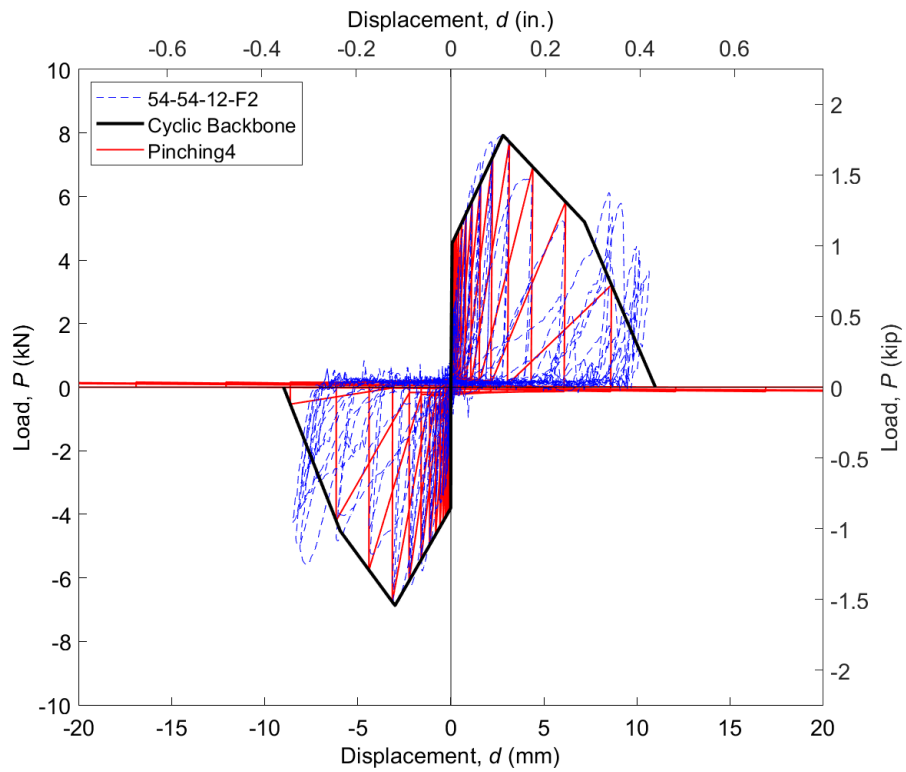


Fig. A-17: Cyclic load-displacement response for 54-54-12-F2

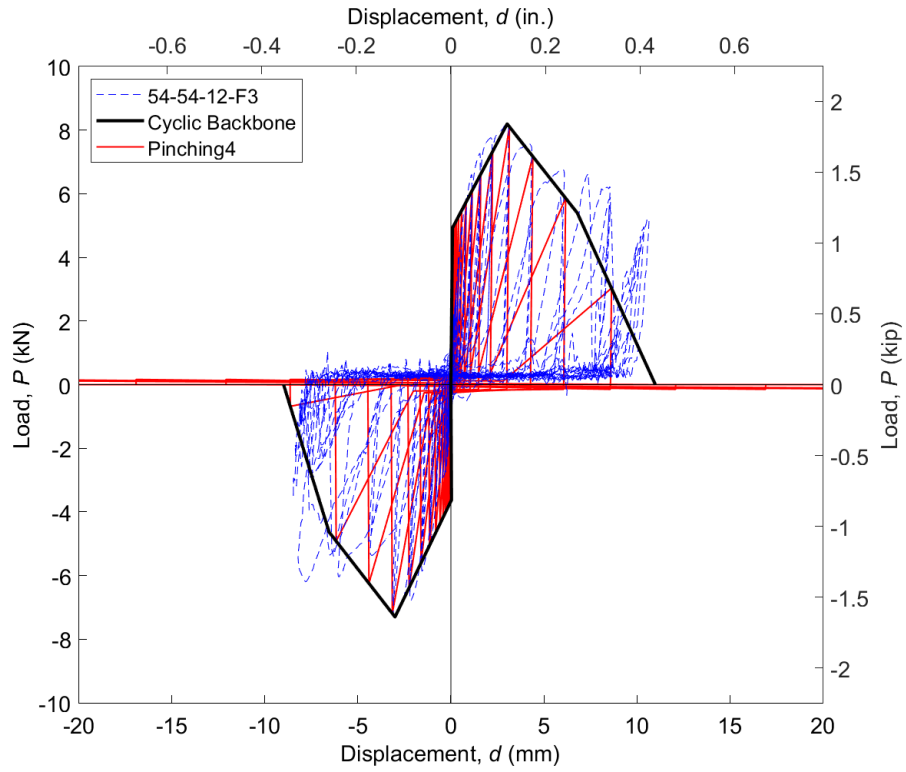


Fig. A-18: Cyclic load-displacement response for 54-54-12-F3

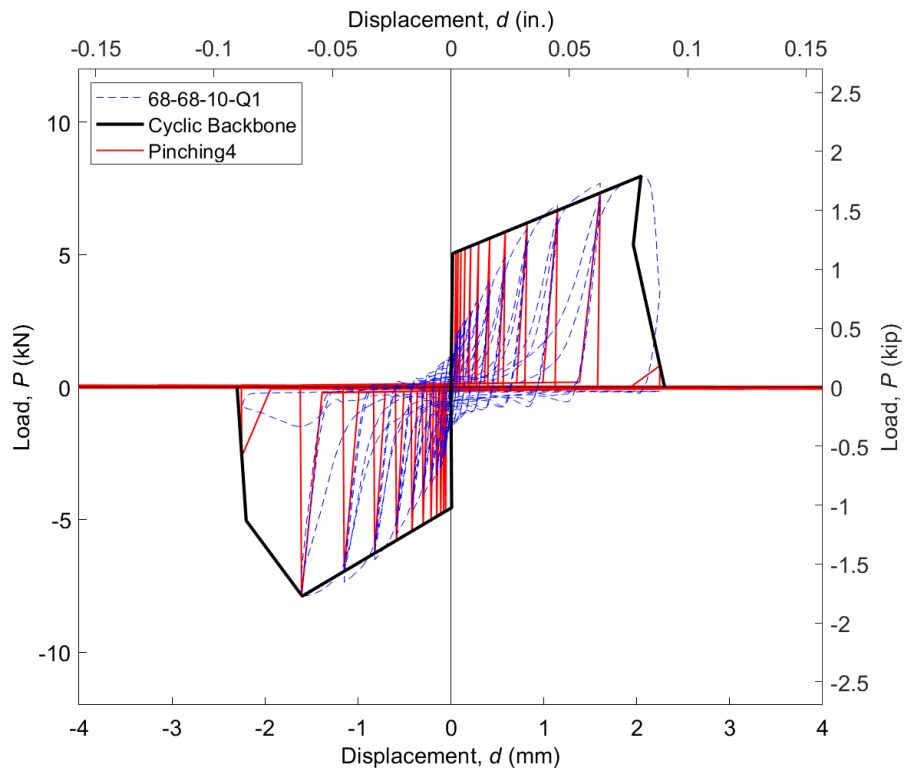


Fig. A-19: Cyclic load-displacement response for 68-68-10-Q1

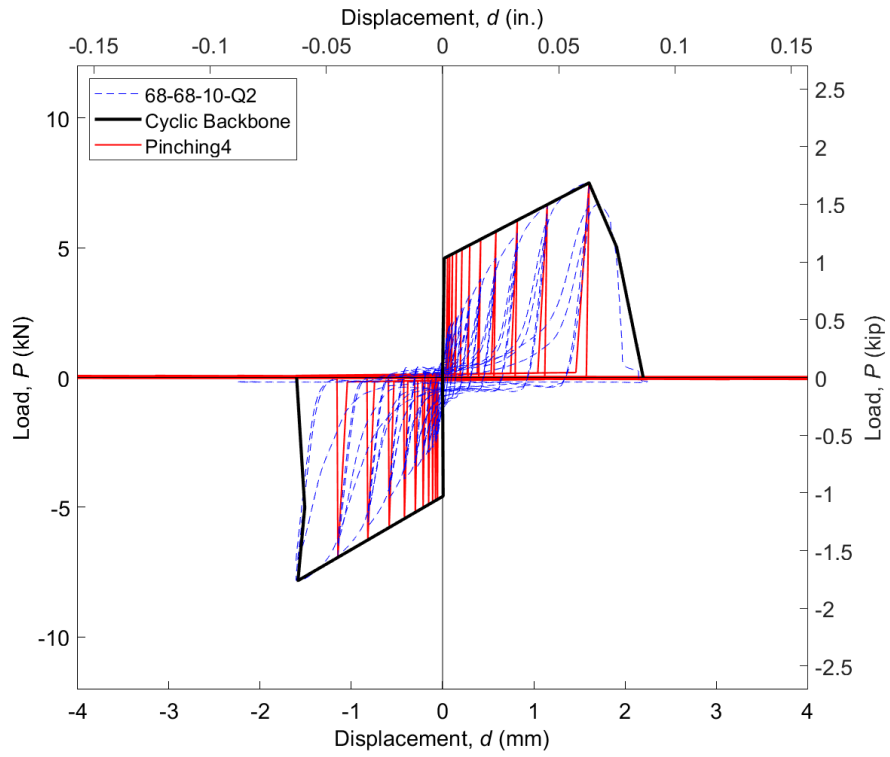


Fig. A-20: Cyclic load-displacement response for 68-68-10-Q2

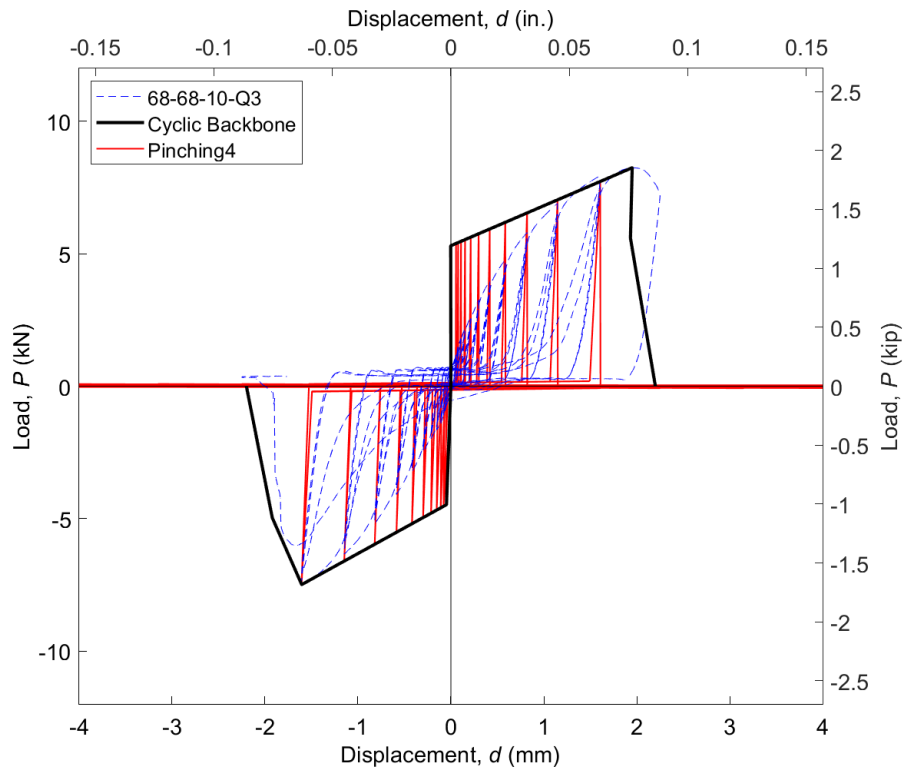


Fig. A-21: Cyclic load-displacement response for 68-68-10-Q3

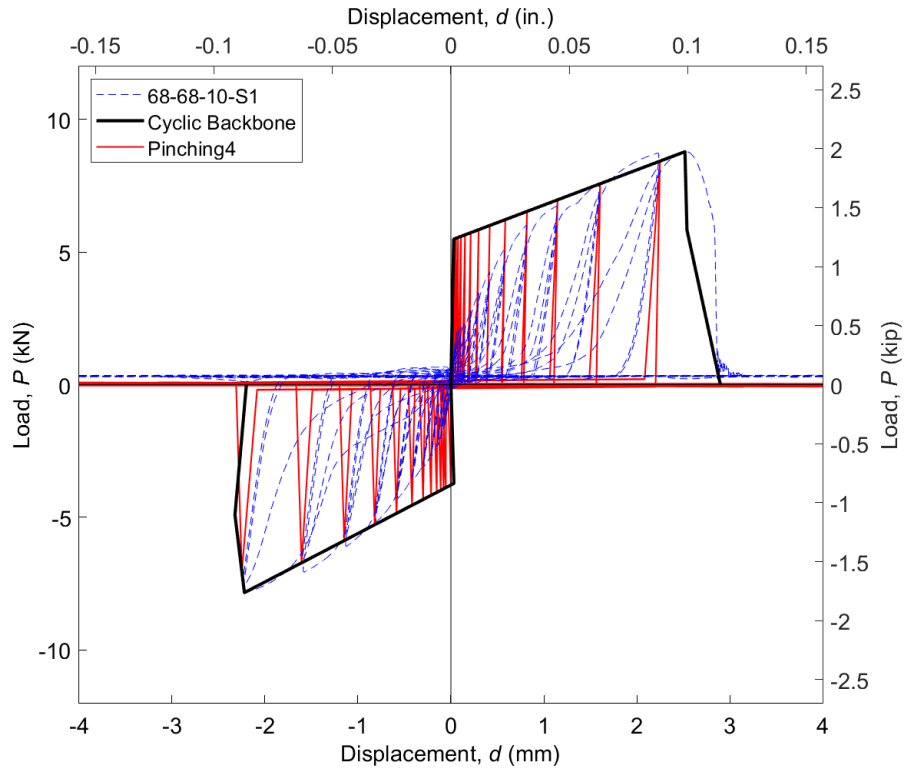


Fig. A. 22: Cyclic load-displacement response for 68-68-10-S1

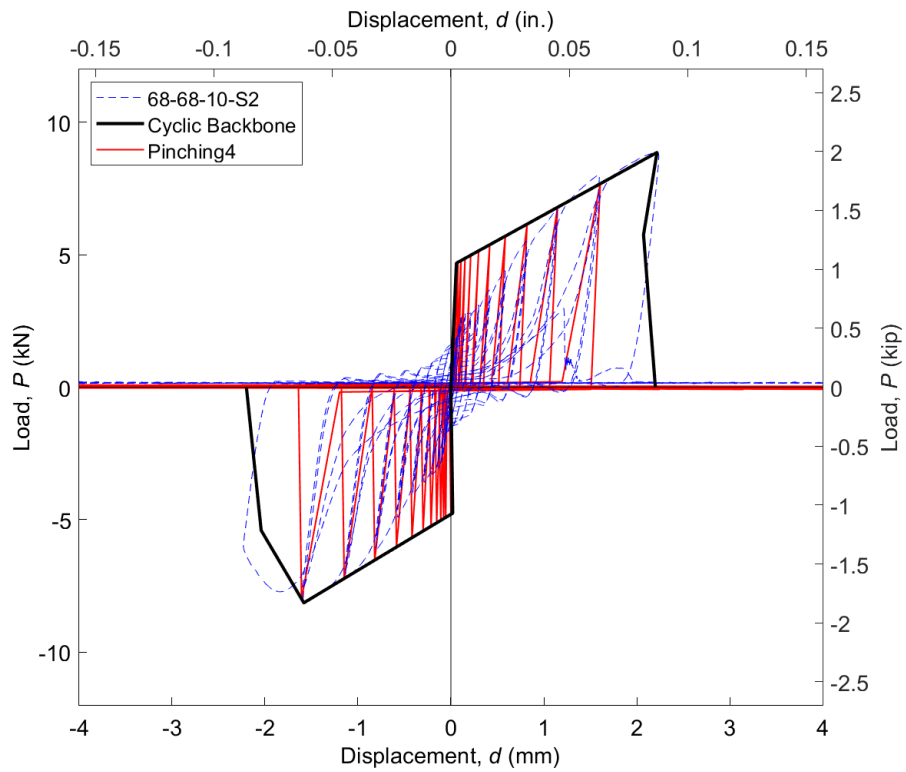


Fig. A-23: Cyclic load-displacement response for 68-68-10-S2

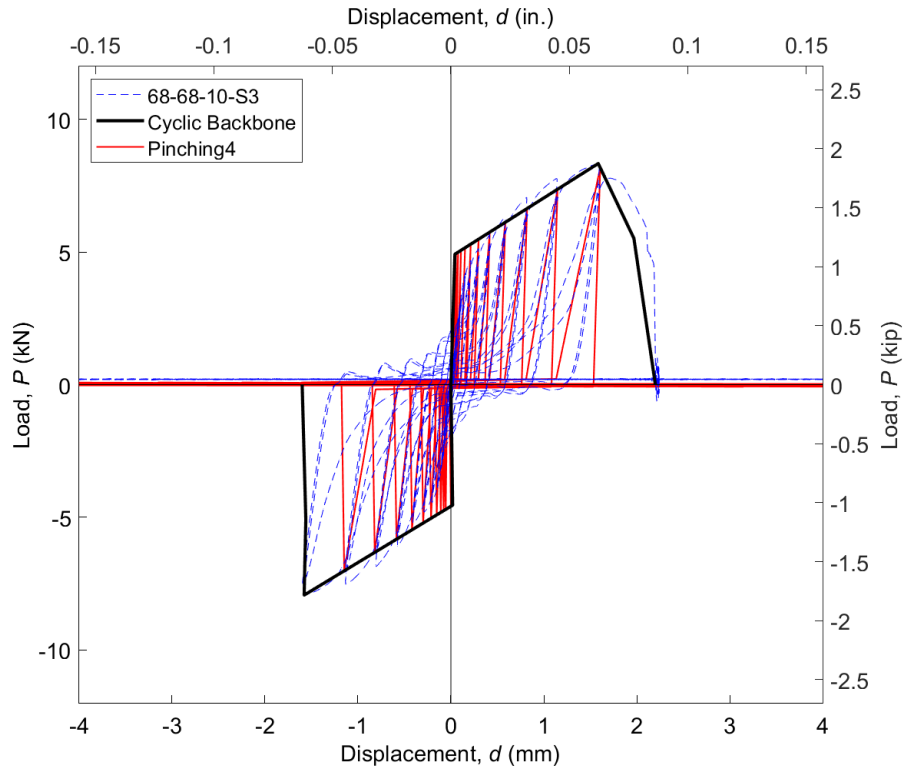


Fig. A-24: Cyclic load-displacement response for 68-68-10-S3

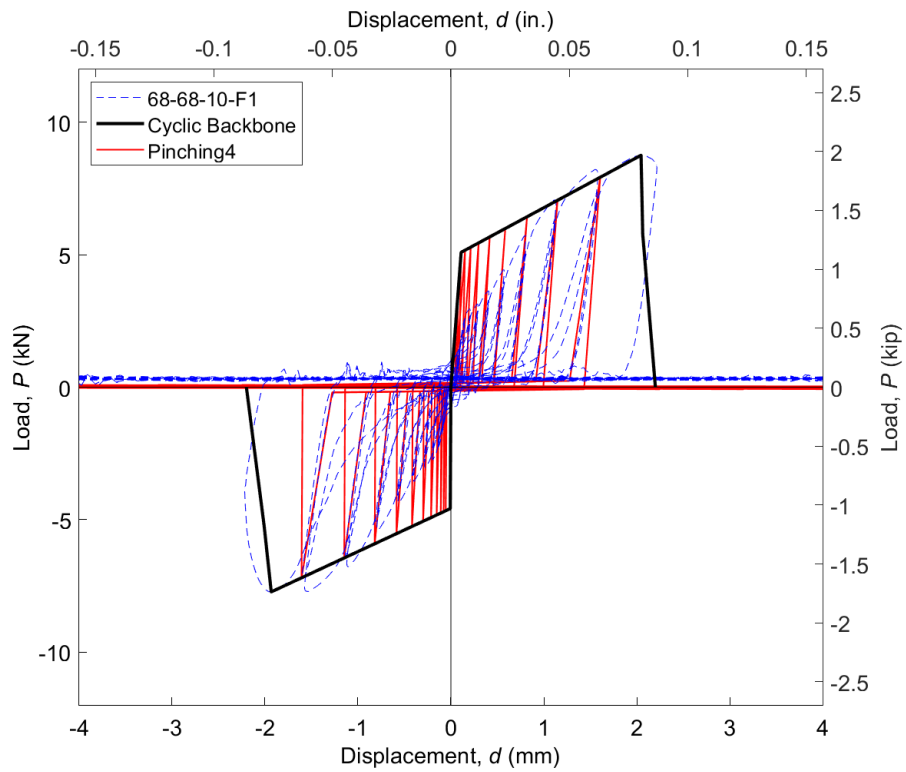


Fig. A-25: Cyclic load-displacement response for 68-68-10-F1

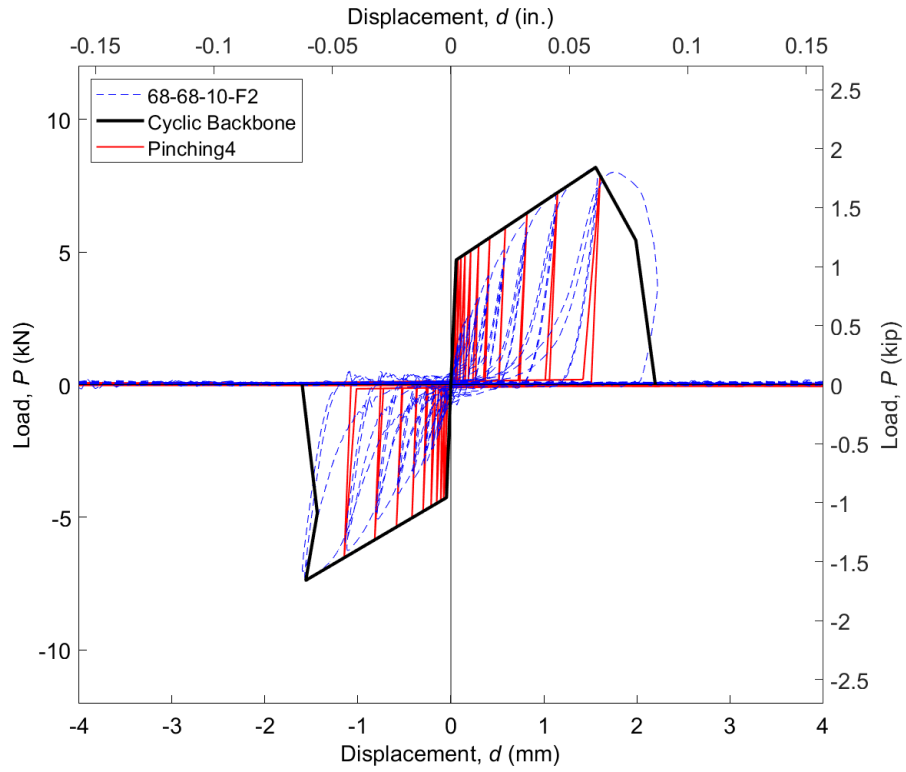


Fig. A-26: Cyclic load-displacement response for 68-68-10-F2

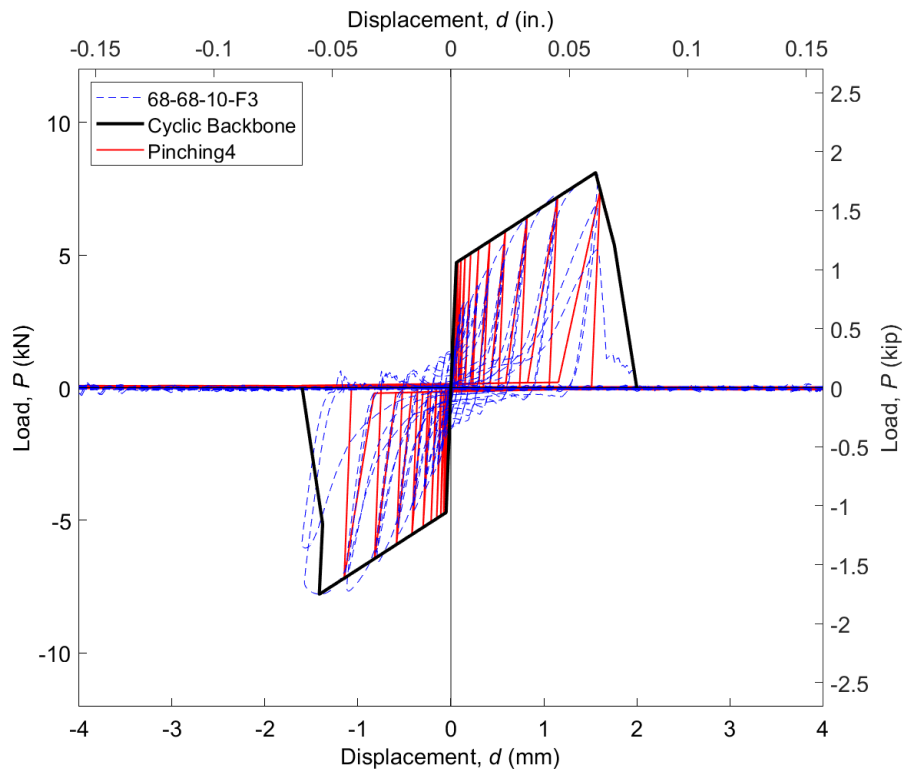


Fig. A-27: Cyclic load-displacement response for 68-68-10-F3

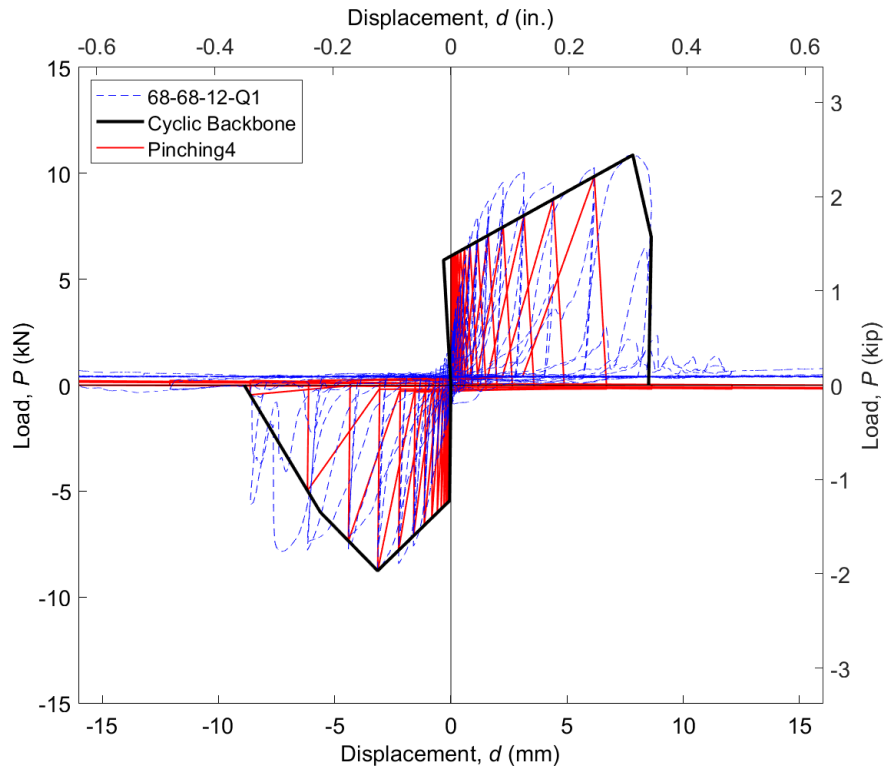


Fig. A-28: Cyclic load-displacement response for 68-68-12-Q1

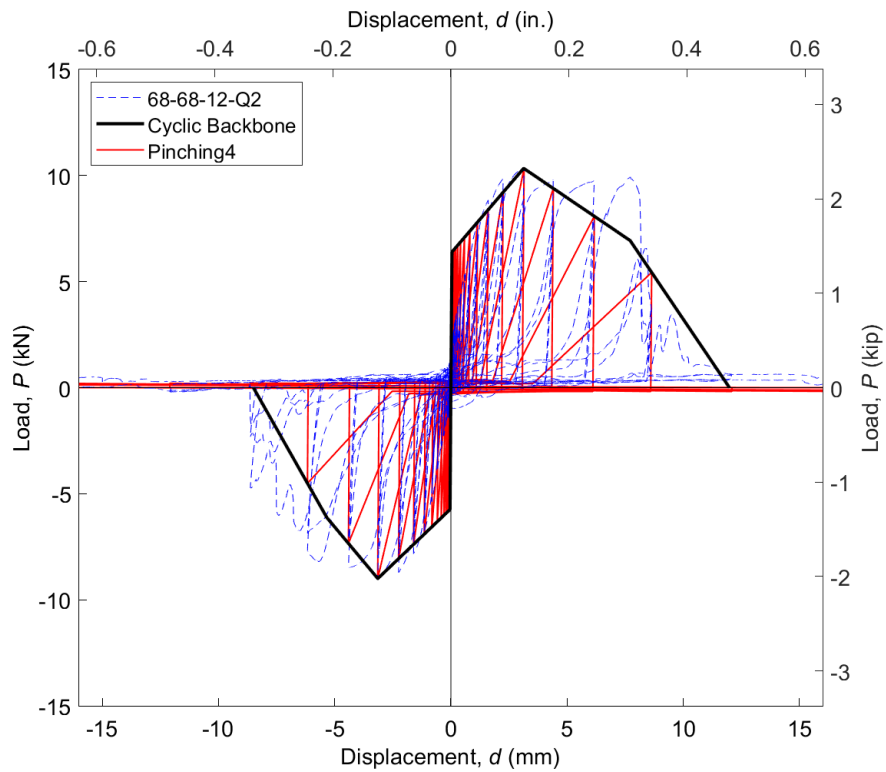


Fig. A-29: Cyclic load-displacement response for 68-68-12-Q2

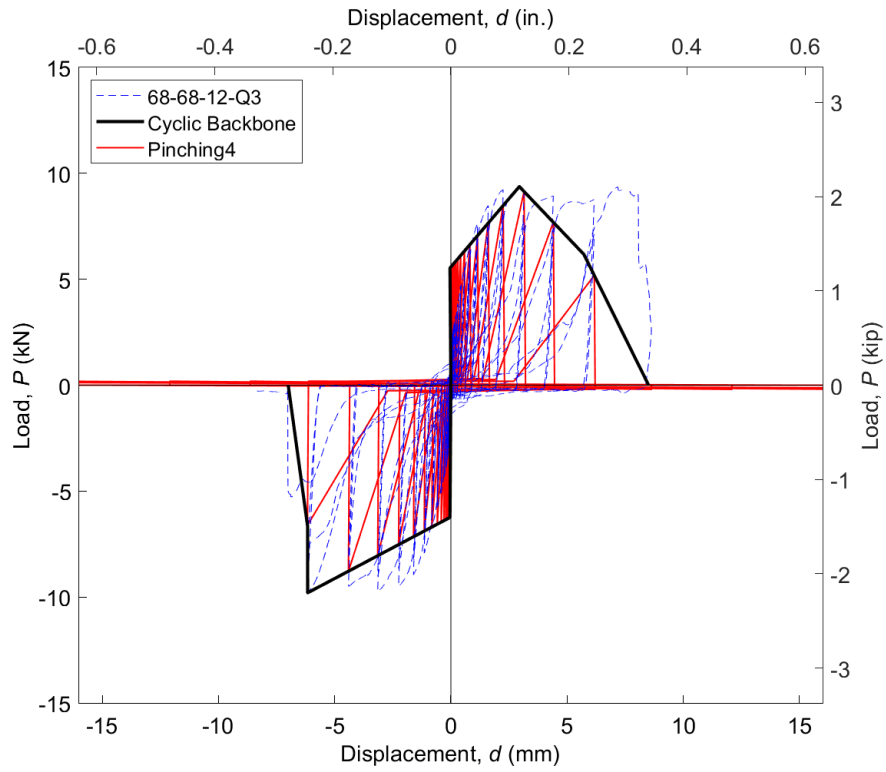


Fig. A-30: Cyclic load-displacement response for 68-68-12-Q3

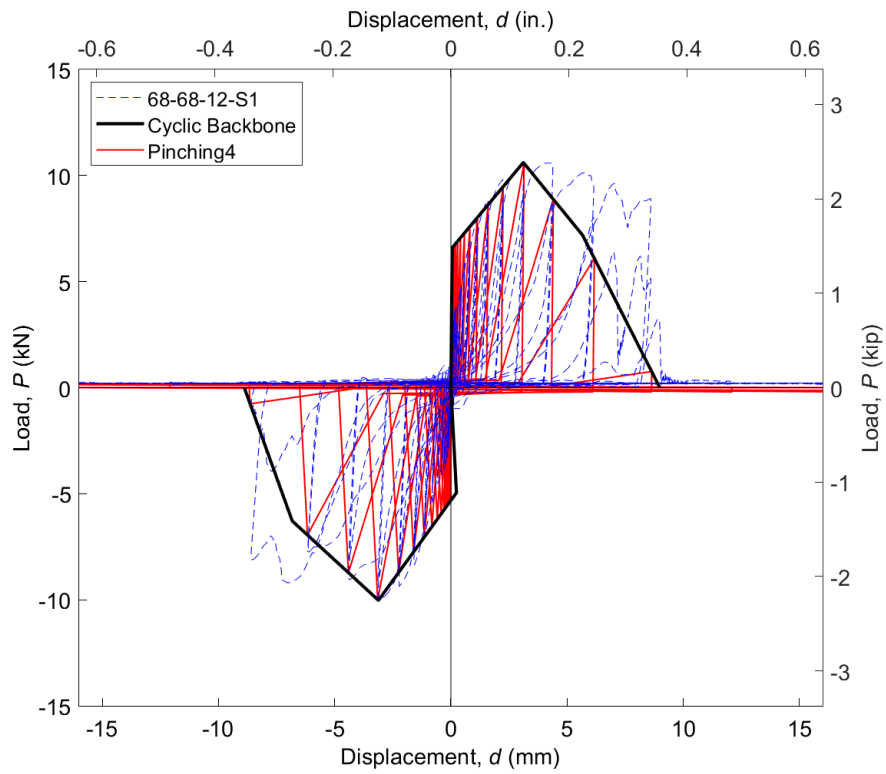


Fig. A-31: Cyclic load-displacement response for 68-68-12-S1

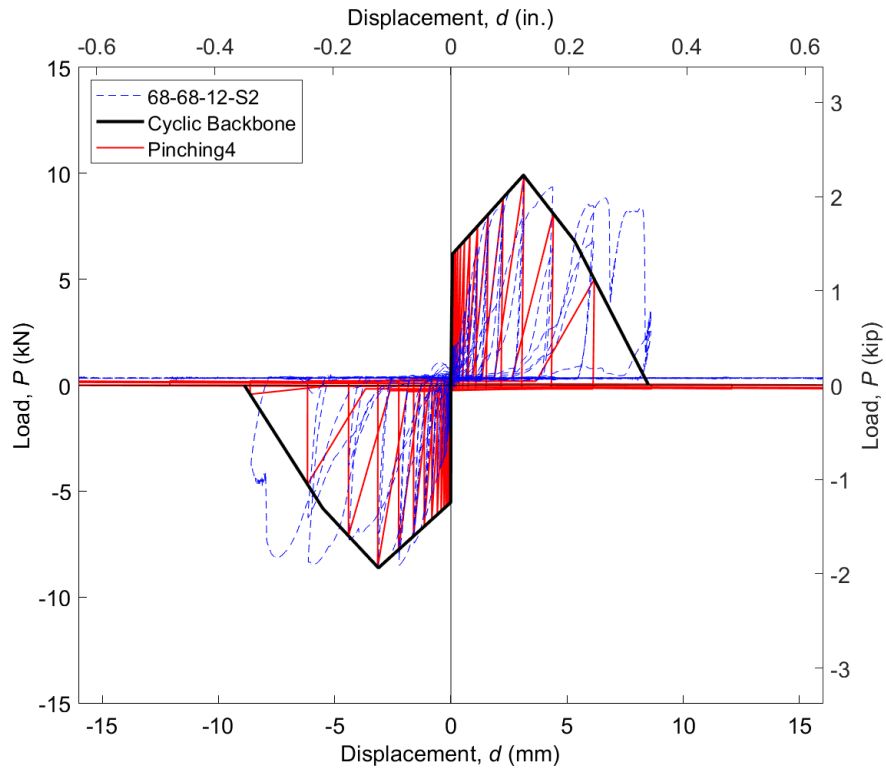


Fig. A-32: Cyclic load-displacement response for 68-68-12-S2

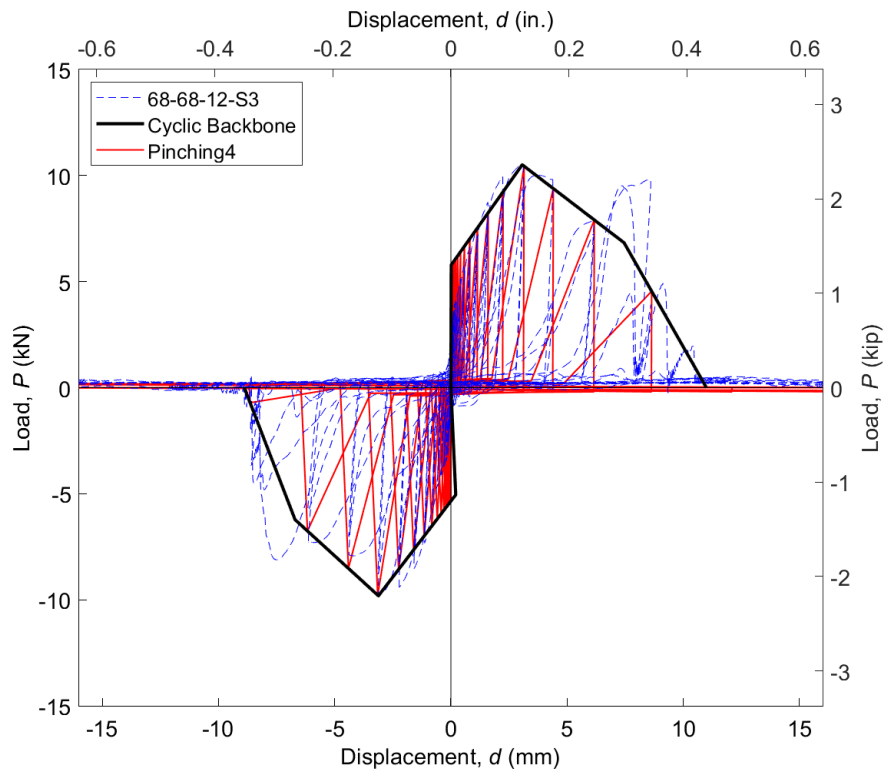


Fig. A-33: Cyclic load-displacement response for 68-68-12-S3

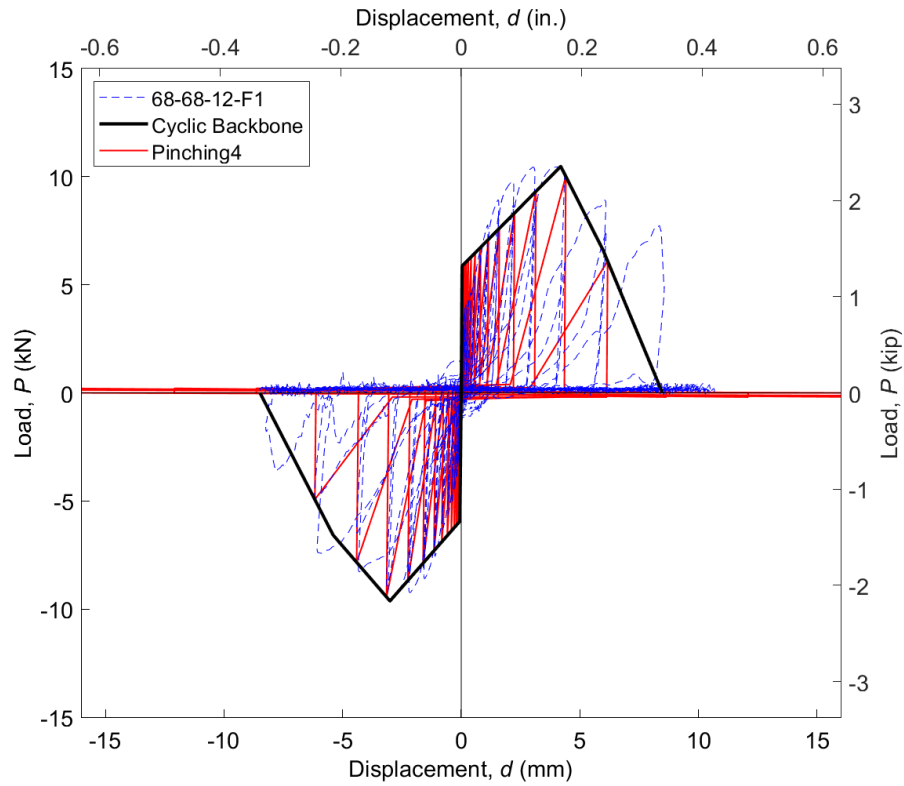


Fig. A-34: Cyclic load-displacement response for 68-68-12-F1

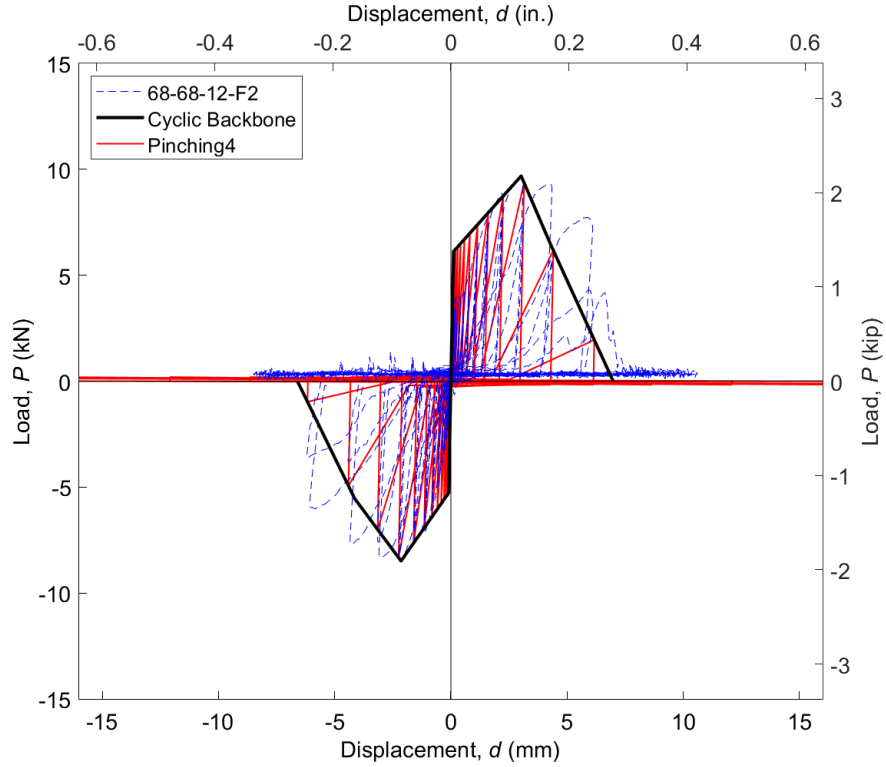


Fig. A-35: Cyclic load-displacement response for 68-68-12-F2

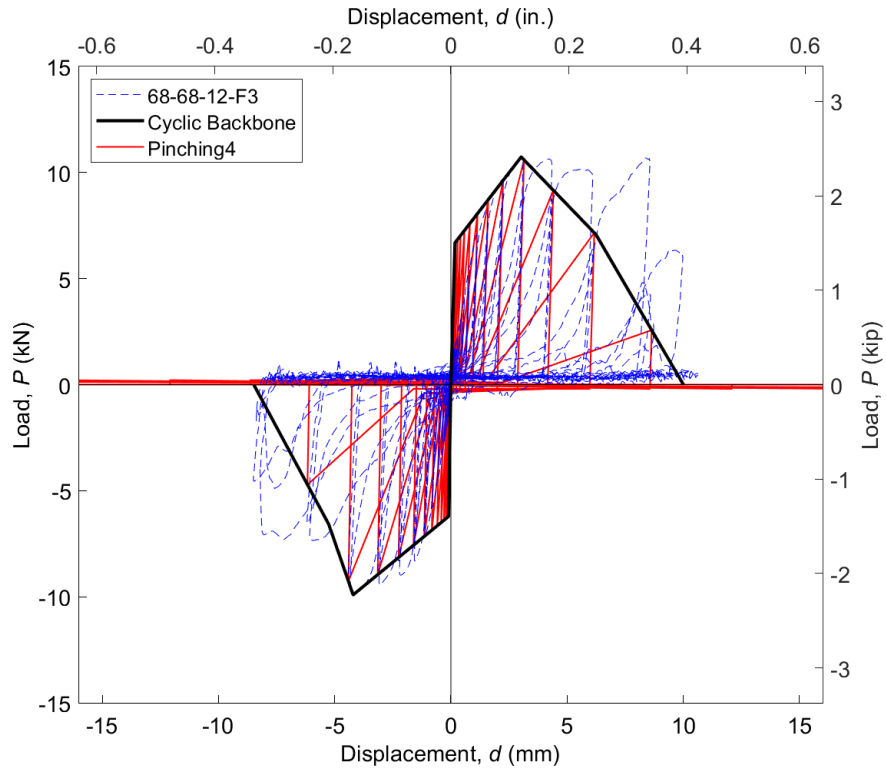


Fig. A-36: Cyclic load-displacement response for 68-68-12-F3

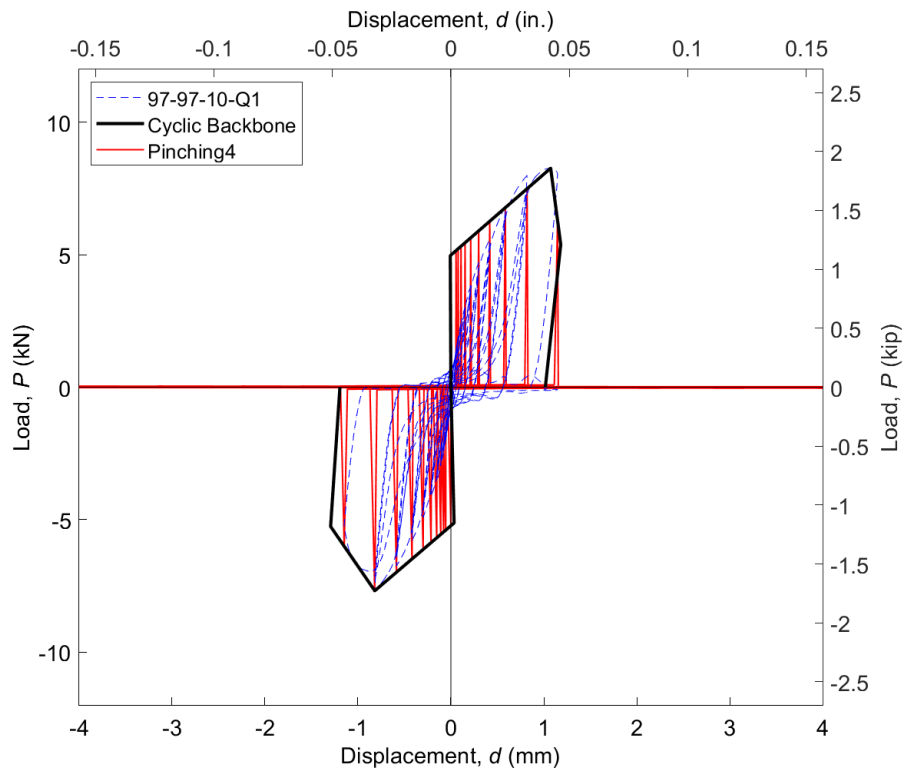


Fig. A-37: Cyclic load-displacement response for 97-97-10-Q1

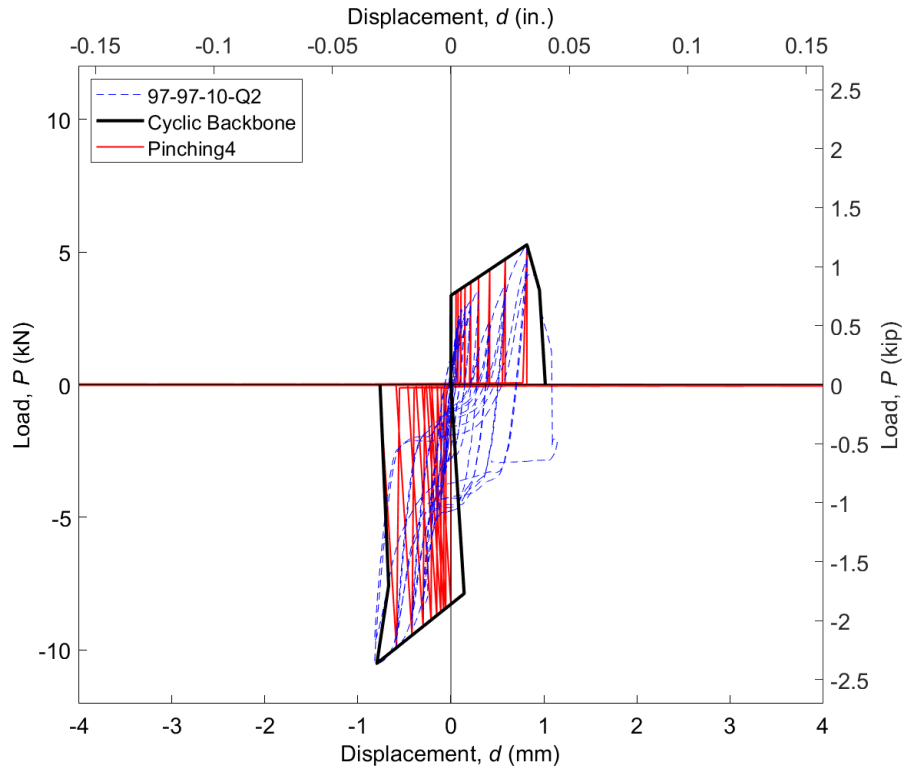


Fig. A-38: Cyclic load-displacement response for 97-97-10-Q2

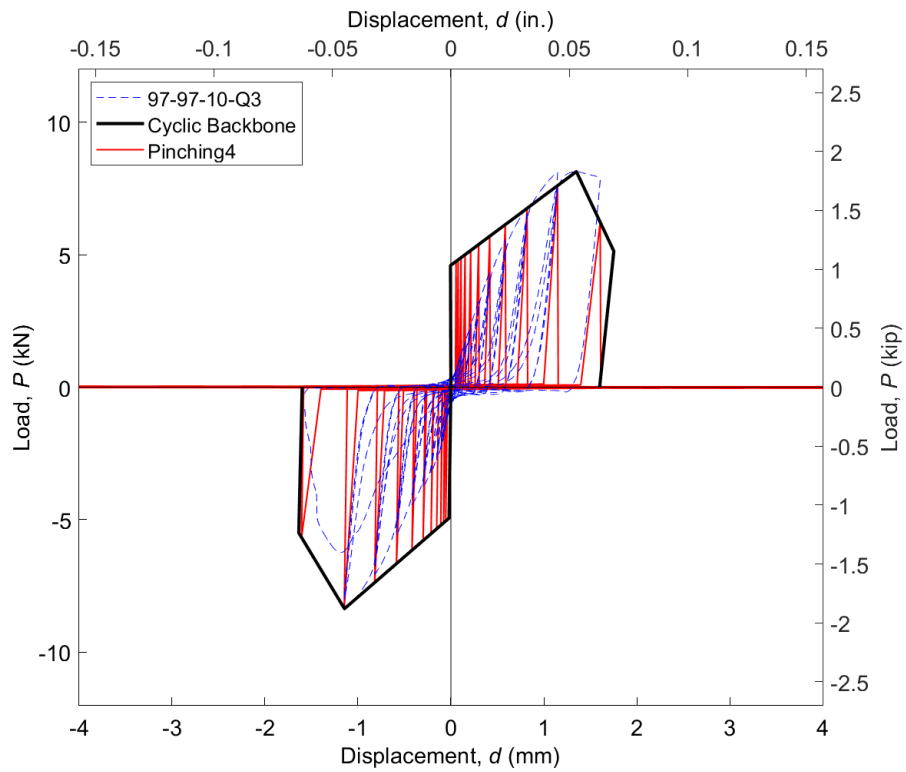


Fig. A-39: Cyclic load-displacement response for 97-97-10-Q3

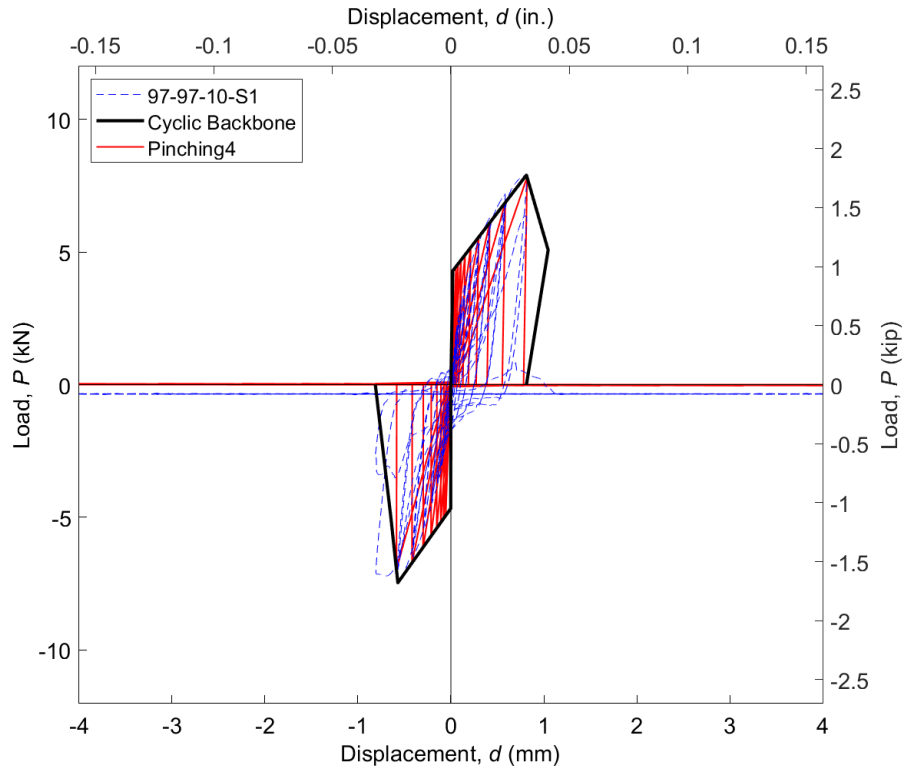


Fig. A-40: Cyclic load-displacement response for 97-97-10-S1

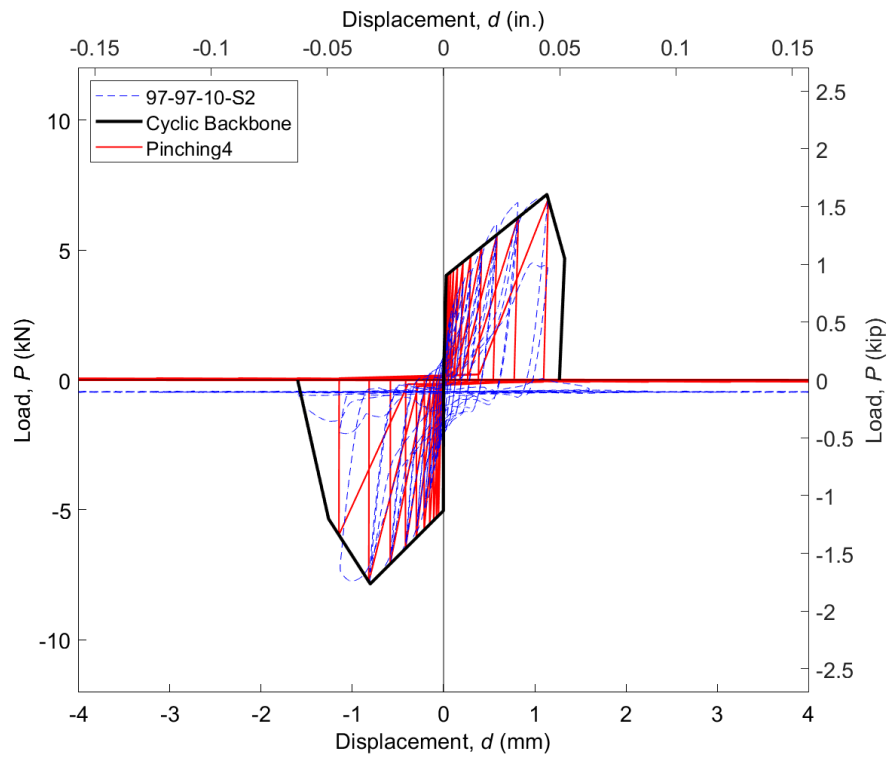


Fig. A-41: Cyclic load-displacement response for 97-97-10-S2

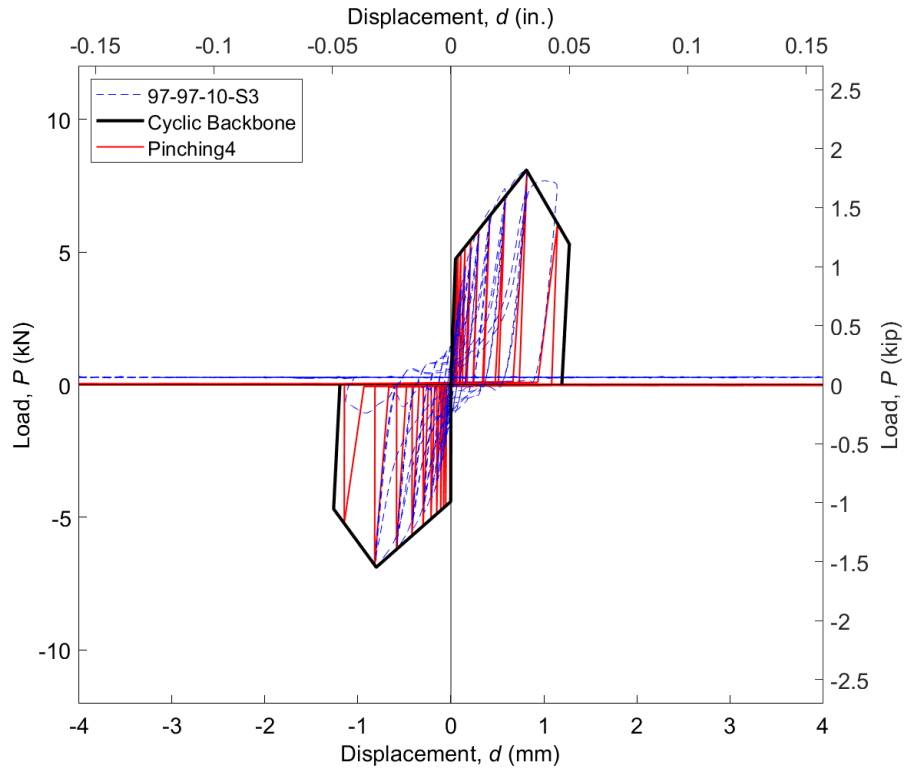


Fig. A-42: Cyclic load-displacement response for 97-97-10-S3

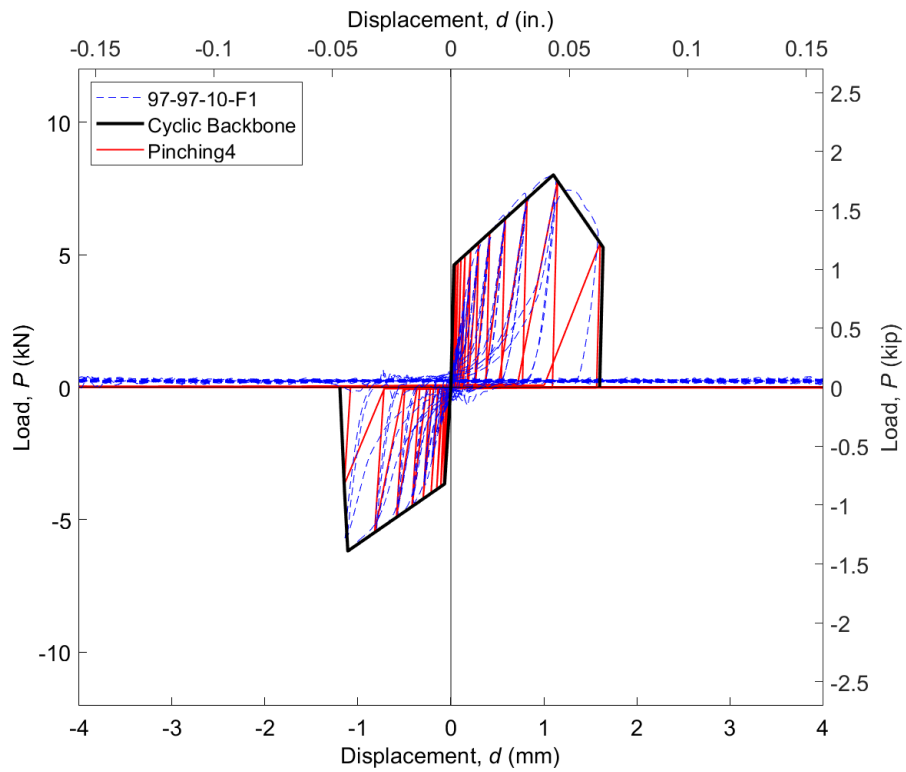


Fig. A-43: Cyclic load-displacement response for 97-97-10-F1

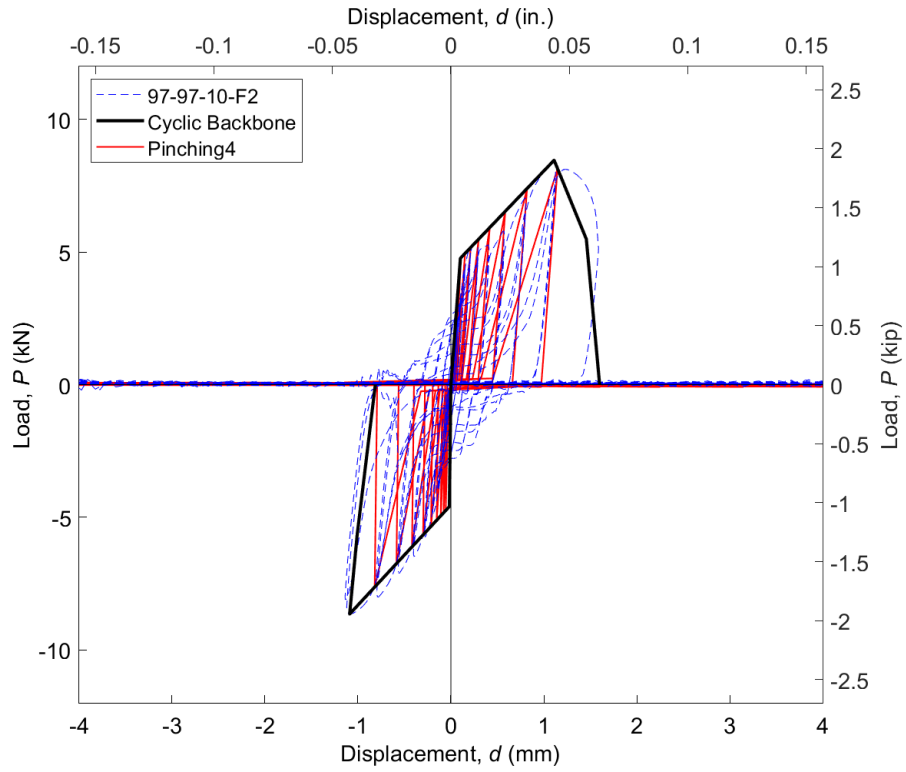


Fig. A-44: Cyclic load-displacement response for 97-97-10-F2

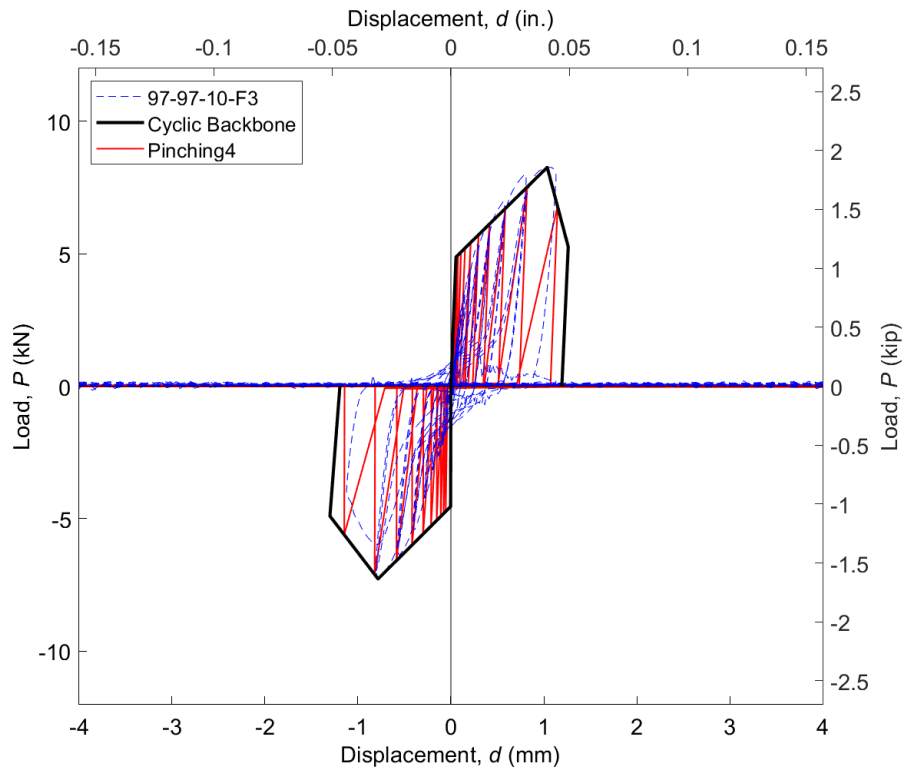


Fig. A-45: Cyclic load-displacement response for 97-97-10-F3

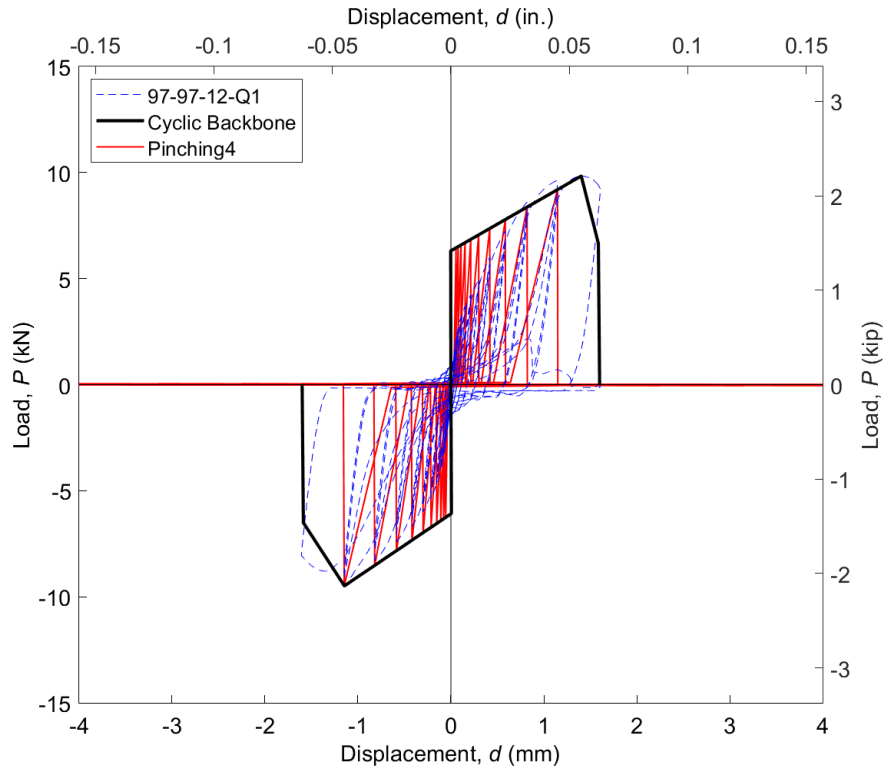


Fig. A-46: Cyclic load-displacement response for 97-97-12-Q1

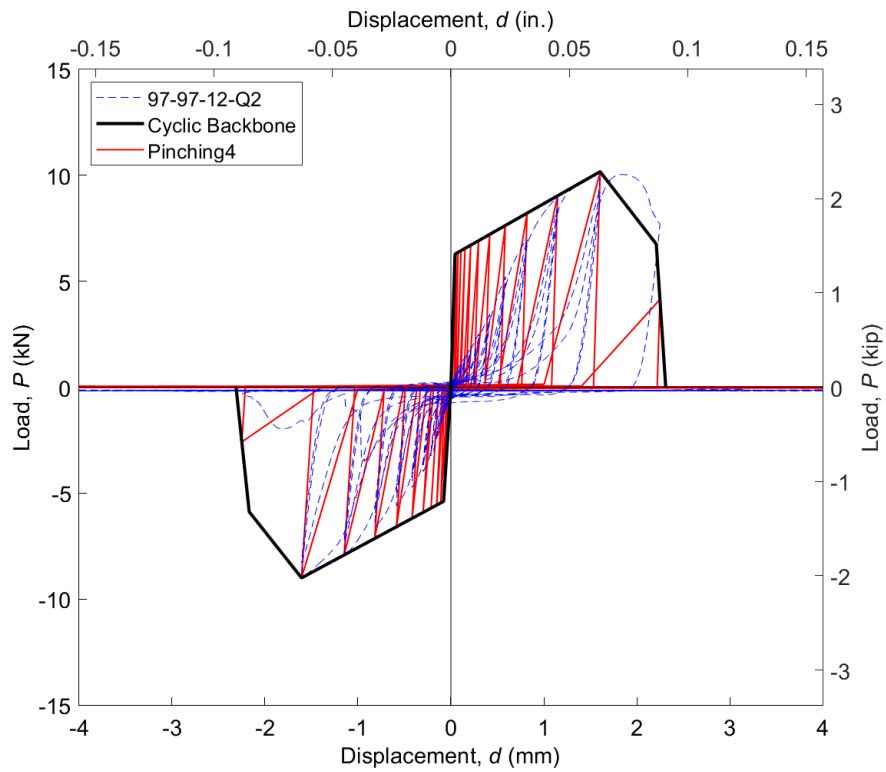


Fig. A-47: Cyclic load-displacement response for 97-97-12-Q2

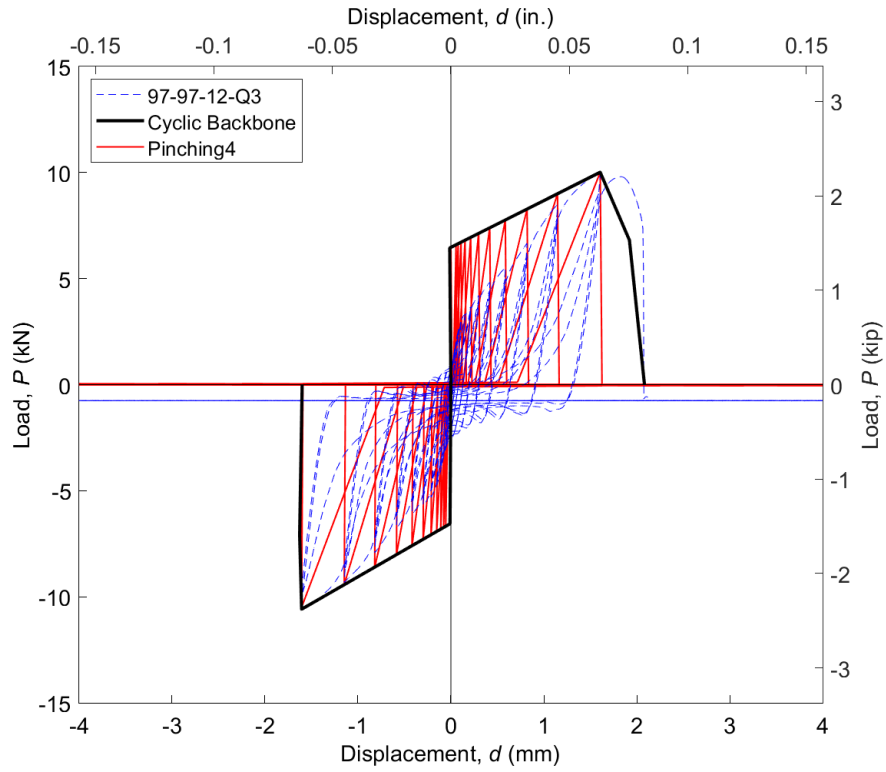


Fig. A-48: Cyclic load-displacement response for 97-97-12-Q3

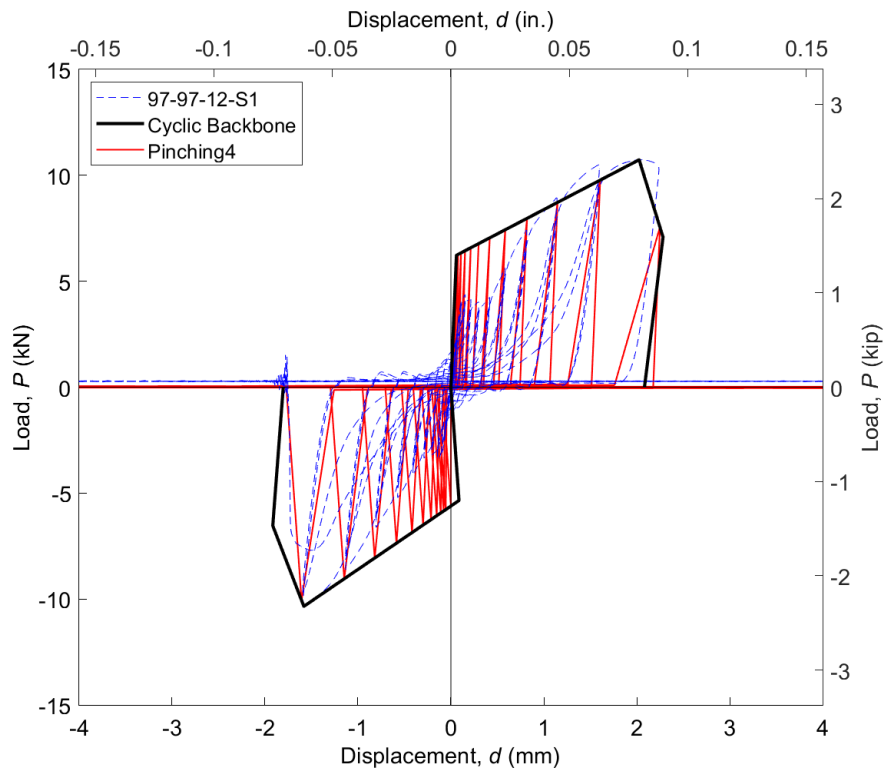


Fig. A-49: Cyclic load-displacement response for 97-97-12-S1

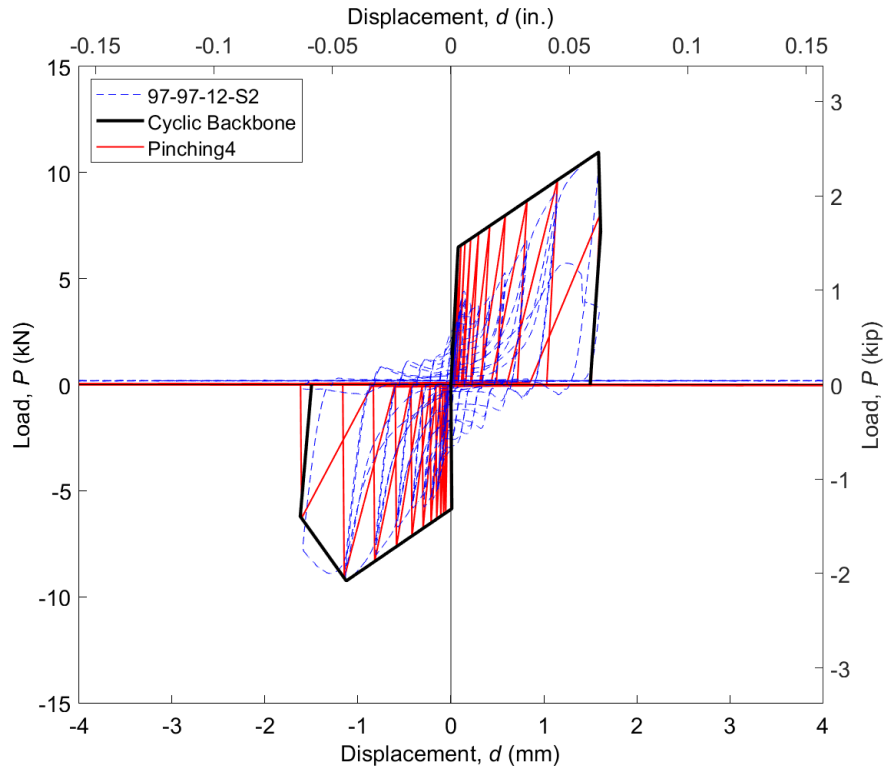


Fig. A-50: Cyclic load-displacement response for 97-97-12-S2

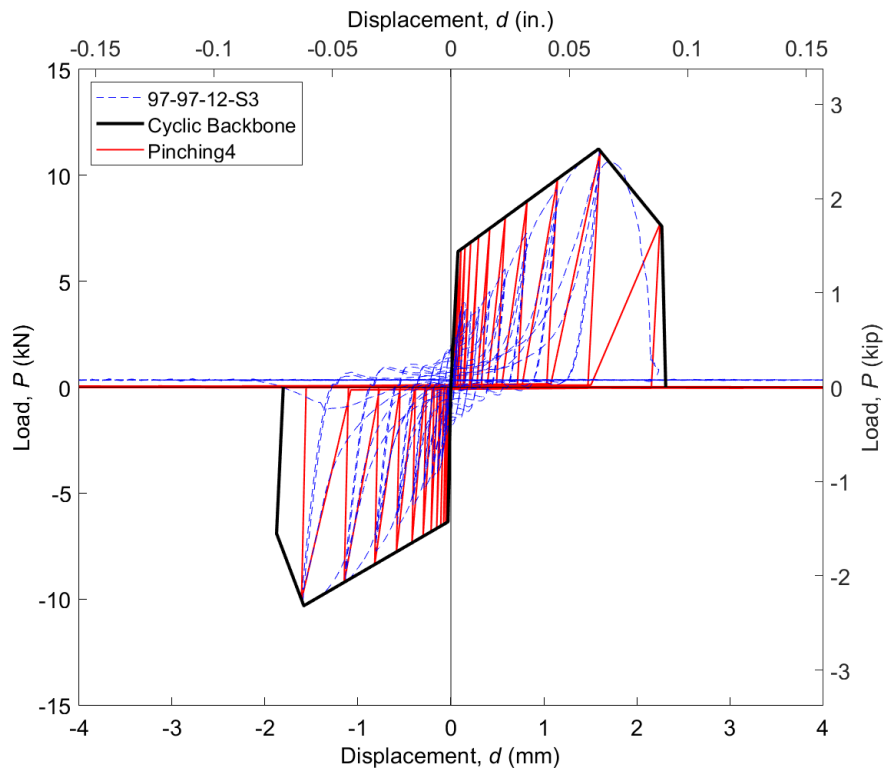


Fig. A-51: Cyclic load-displacement response for 97-97-12-S3

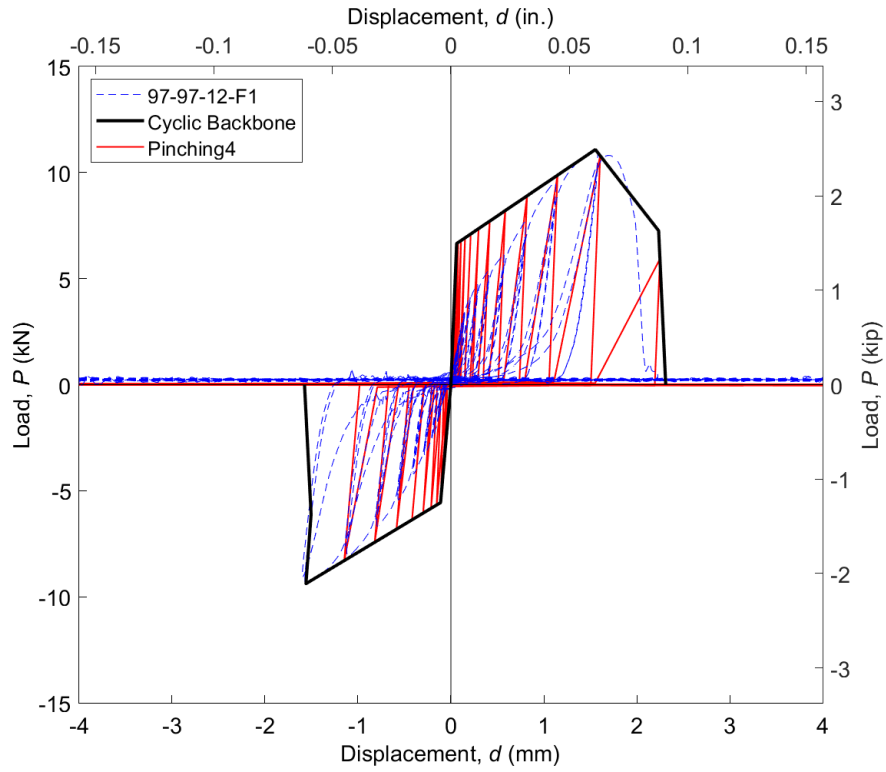


Fig. A-52: Cyclic load-displacement response for 97-97-12-F1

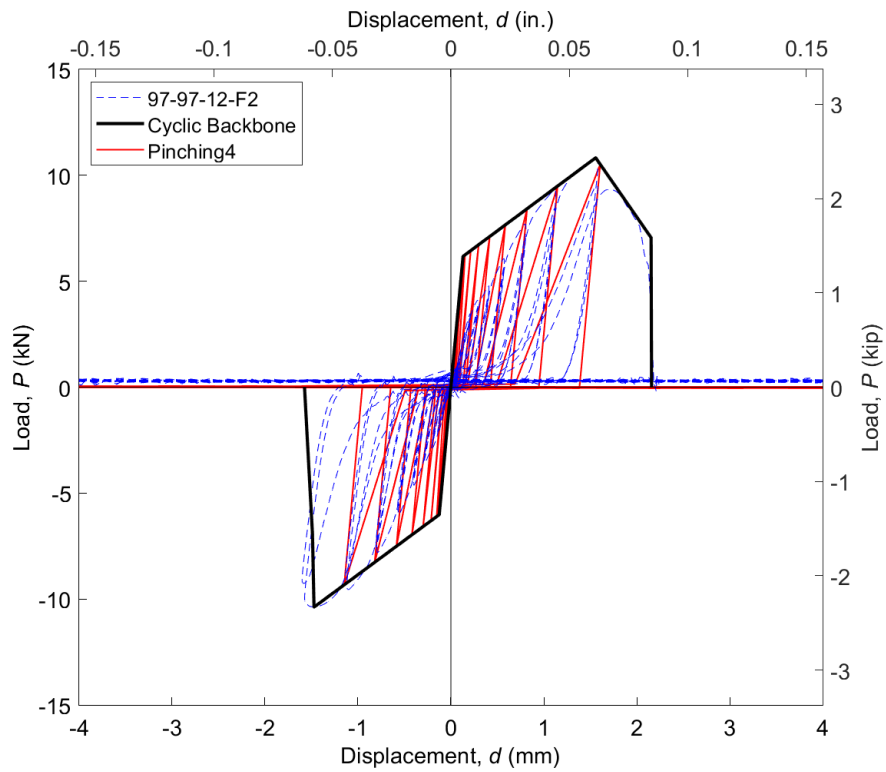


Fig. A-53: Cyclic load-displacement response for 97-97-12-F2

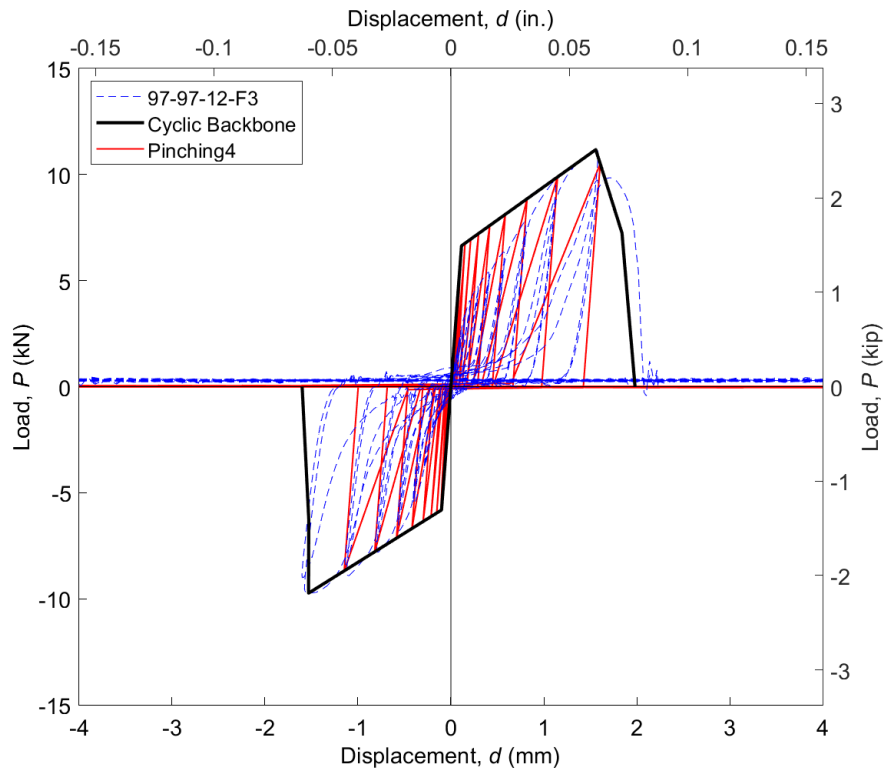


Fig. A-54: Cyclic load-displacement response for 97-97-12-F3

APPENDIX B: Cyclic Load-displacement Response (PAF)

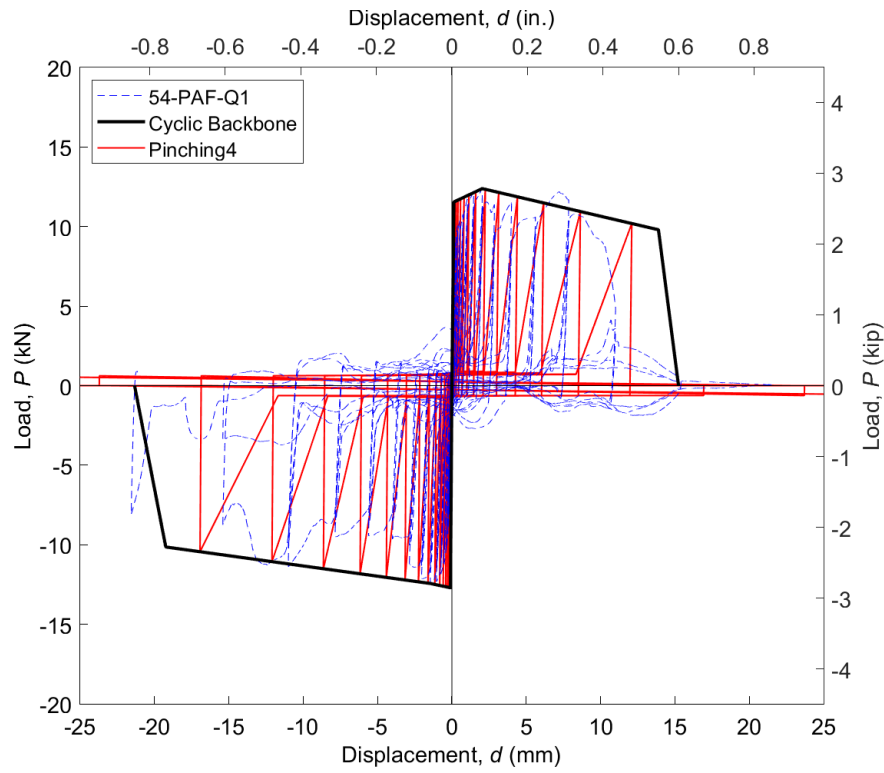


Fig. B-1: Cyclic load-displacement response for 54-PAF-Q1

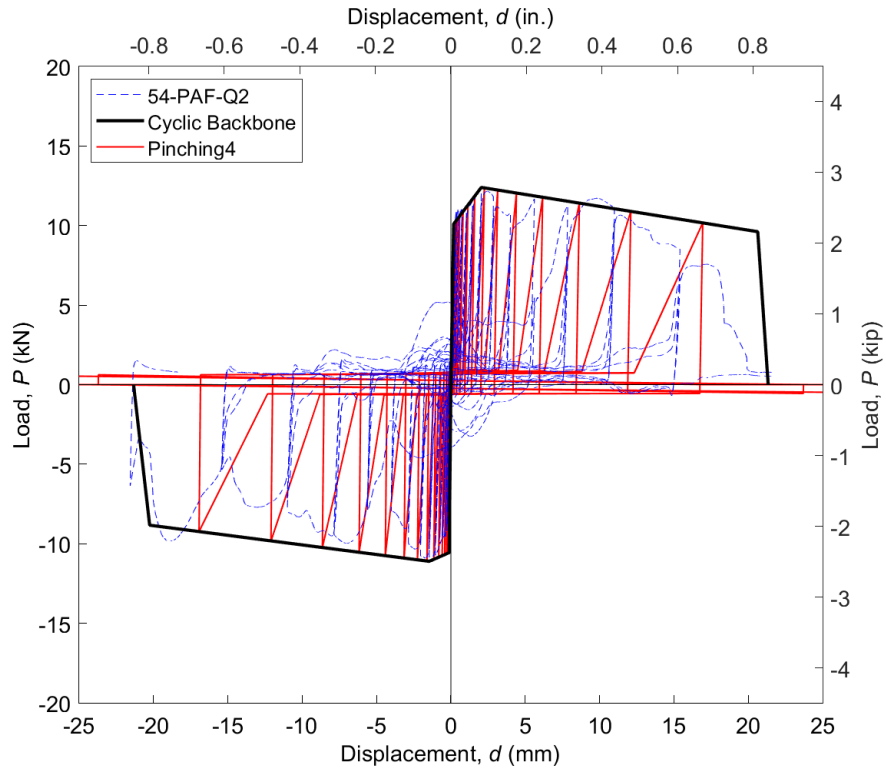


Fig. B-2: Cyclic load-displacement response for 54-PAF-Q2

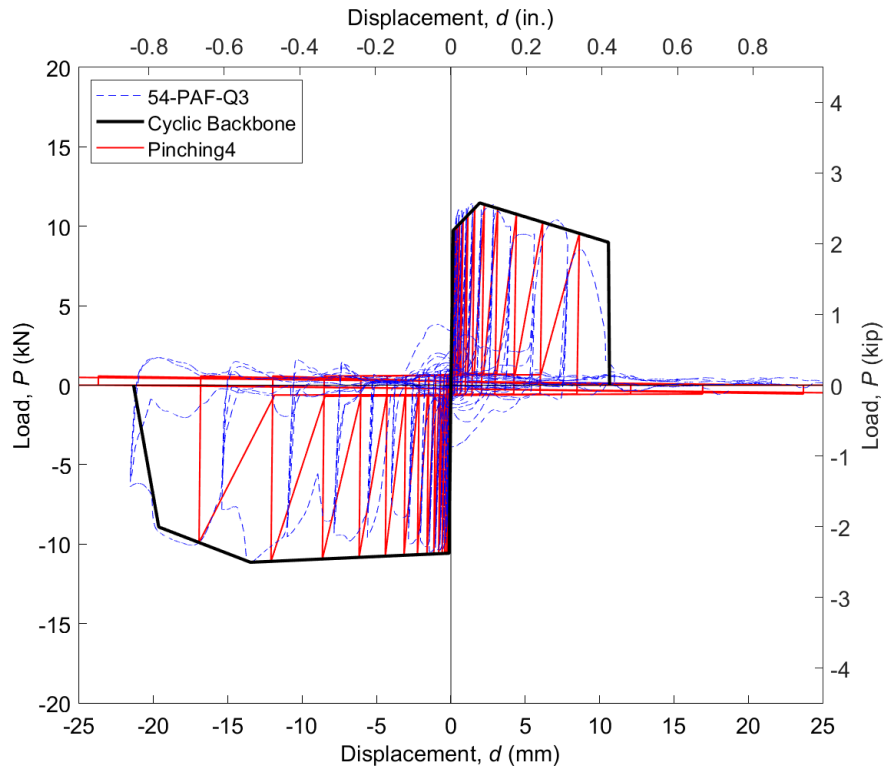


Fig. B-3: Cyclic load-displacement response for 54-PAF-Q3

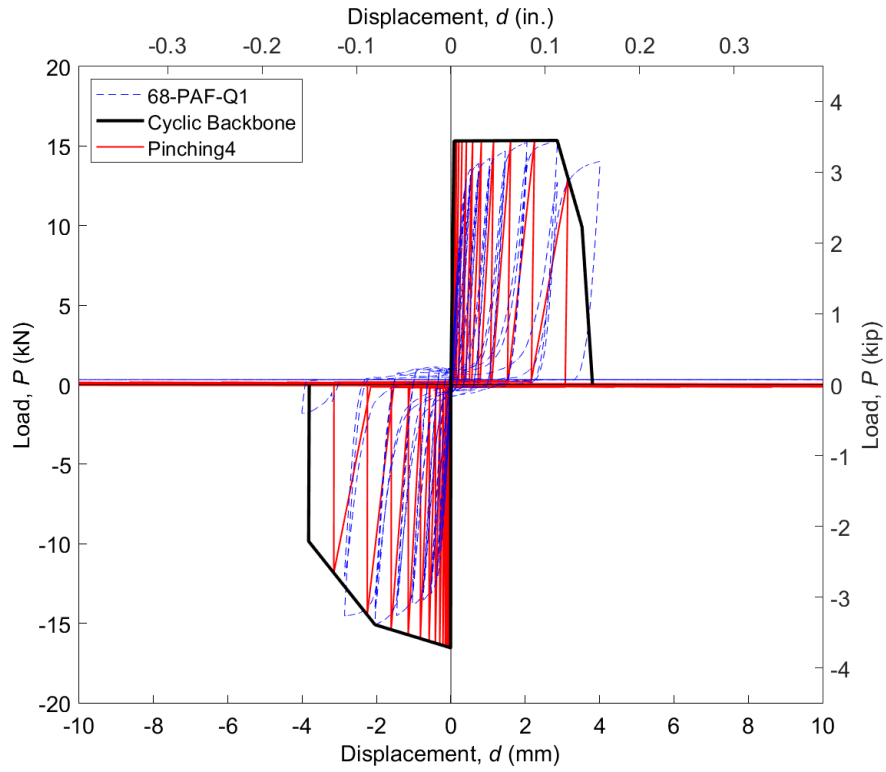


Fig. B-4: Cyclic load-displacement response for 68-PAF-Q1

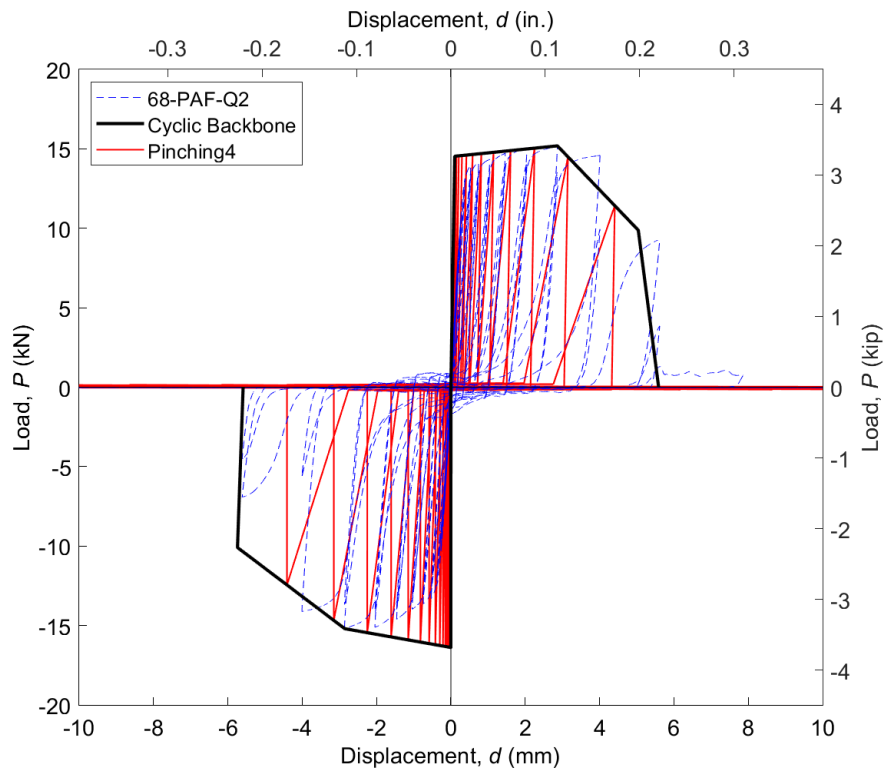


Fig. B-5: Cyclic load-displacement response for 68-PAF-Q2

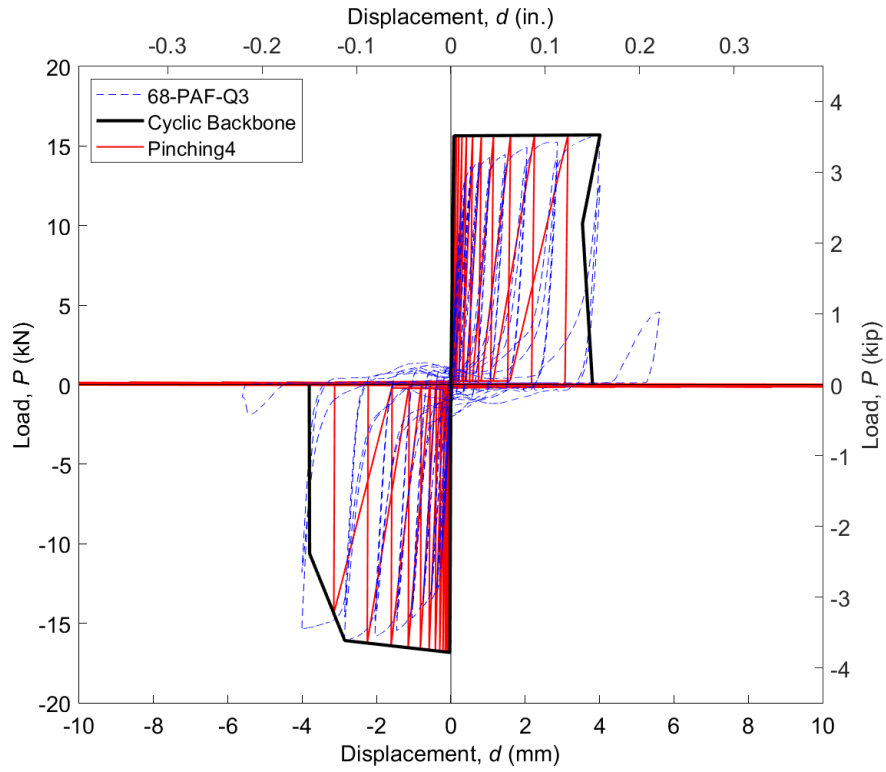


Fig. B-6: Cyclic load-displacement response for 68-PAF-Q3

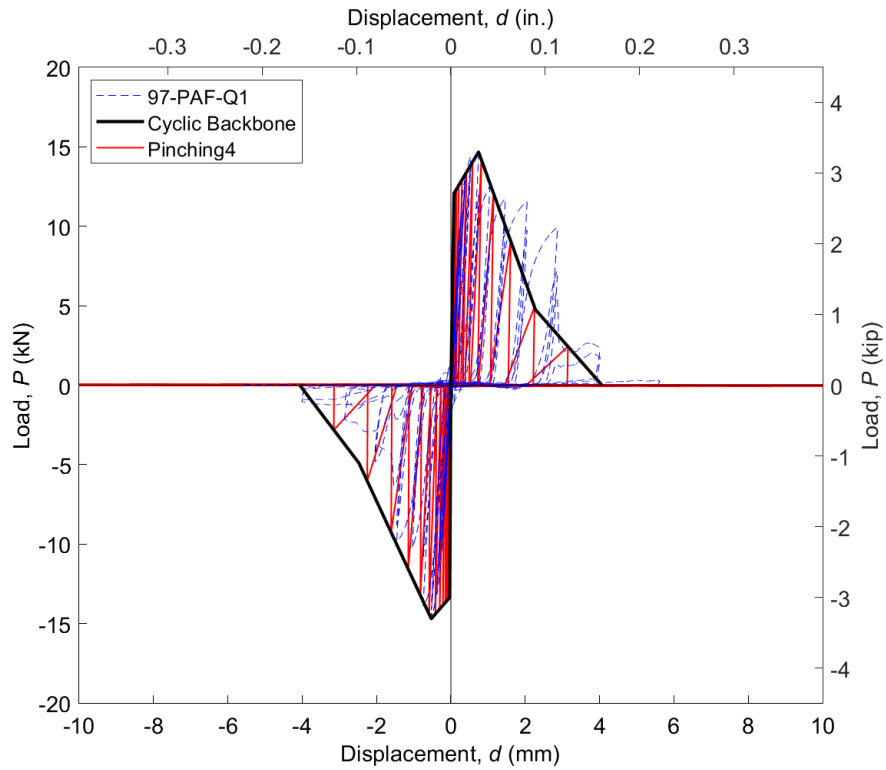


Fig. B-7: Cyclic load-displacement response for 97-PAF-Q1

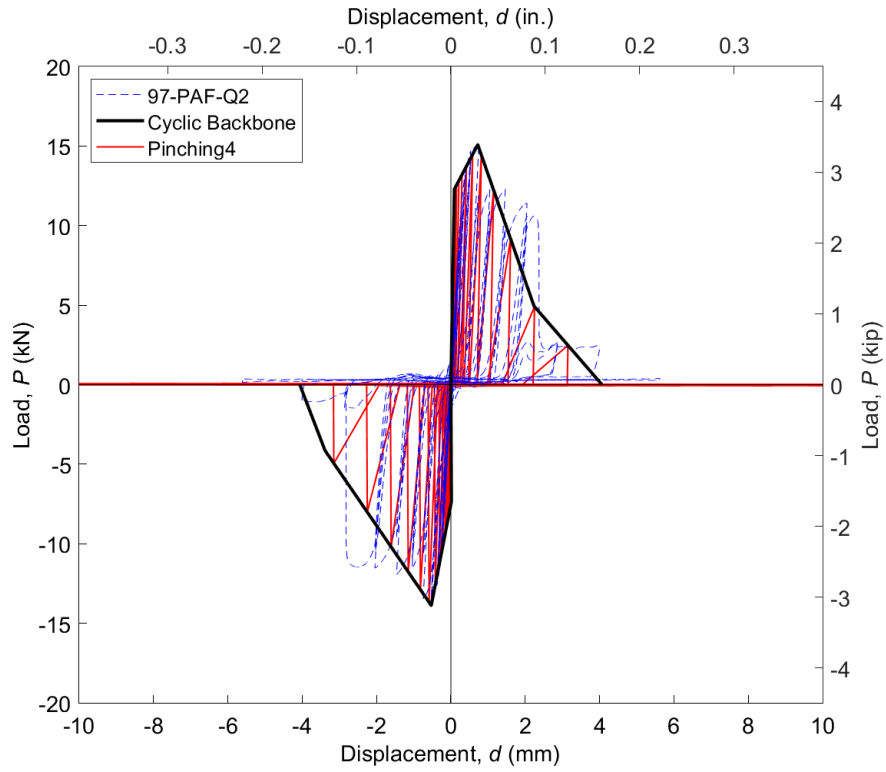


Fig. B-8: Cyclic load-displacement response for 97-PAF-Q2

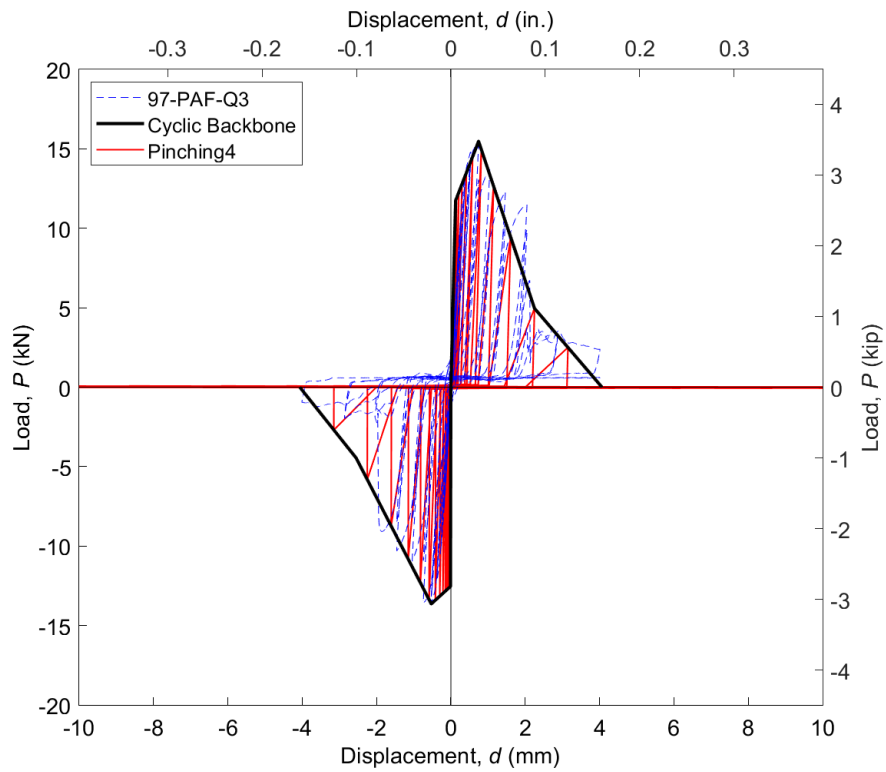


Fig. B-9: Cyclic load-displacement response for 97-PAF-Q3

APPENDIX C: Fastener Peak Load Summary

Test	Peak load	Peak load	Max. Peak	Failure	AISI/SDI	Ratio
	<i>P</i> +	<i>P</i> -	<i>P</i>	Mode	Max load	P/Max
	kN (kip)	kN (kip)	kN (kip)		kN (kip)	load
54-54-10-Q1	7.42 (1.67)	-6.03 (-1.35)	7.42 (1.67)	S.S	7.21 (1.62)	1.03
54-54-10-Q2	6.91 (1.55)	-6.29 (-1.41)	6.91 (1.55)	S.S	7.21 (1.62)	0.96
54-54-10-Q3	7.35 (1.65)	-6.29 (-1.41)	7.35 (1.65)	S.S	7.21 (1.62)	1.02
54-54-10-S1	6.95 (1.56)	-8.09 (-1.82)	8.09 (1.82)	S.S	7.21 (1.62)	1.12
54-54-10-S2	7.67 (1.72)	-6.75 (-1.52)	7.67 (1.72)	S.S	7.21 (1.62)	1.06
54-54-10-S3	7.90 (1.78)	-6.32 (-1.42)	7.90 (1.78)	S.B	7.21 (1.62)	1.10
54-54-10-F1	7.52 (1.69)	-6.28 (-1.41)	7.52 (1.69)	S.S	7.21 (1.62)	1.04
54-54-10-F2	6.93 (1.56)	-7.11 (-1.60)	7.11 (1.60)	S.S	7.21 (1.62)	0.99
54-54-10-F3	7.68 (1.72)	-6.46 (-1.45)	7.68 (1.72)	S.B	7.21 (1.62)	1.06
54-54-12-Q1	7.33 (1.65)	-6.75 (-1.52)	7.33 (1.65)	T/B	10.07 (2.26)	0.73
54-54-12-Q2	7.49 (1.68)	-6.76 (-1.52)	7.49 (1.68)	T/B	10.07 (2.26)	0.74
54-54-12-Q3	7.55 (1.70)	-6.47 (-1.45)	7.55 (1.70)	T/B	10.07 (2.26)	0.75
54-54-12-S1	7.47 (1.68)	-7.36 (-1.65)	7.47 (1.68)	S.S	10.07 (2.26)	0.74
54-54-12-S2	6.93 (1.56)	-6.21 (-1.40)	6.93 (1.56)	T/B	10.07 (2.26)	0.69
54-54-12-S3	7.71 (1.73)	-6.59 (-1.48)	7.71 (1.73)	T/B	10.07 (2.26)	0.77
54-54-12-F1	7.62 (1.71)	-6.37 (-1.43)	7.62 (1.71)	T/B	10.07 (2.26)	0.76
54-54-12-F2	7.93 (1.78)	-6.87 (-1.54)	7.93 (1.78)	T/B	10.07 (2.26)	0.79
54-54-12-F3	8.19 (1.84)	-7.30 (-1.64)	8.19 (1.84)	T/B	10.07 (2.26)	0.81
68-68-10-Q1	7.97 (1.79)	-7.89 (-1.77)	7.97 (1.79)	S.S	7.21 (1.62)	1.10
68-68-10-Q2	7.50 (1.69)	-7.83 (-1.76)	7.83 (1.76)	S.S	7.21 (1.62)	1.09
68-68-10-Q3	8.25 (1.85)	-7.49 (-1.68)	8.25 (1.85)	S.S	7.21 (1.62)	1.14
68-68-10-S1	8.78 (1.97)	-7.84 (-1.76)	8.78 (1.97)	S.S	7.21 (1.62)	1.22
68-68-10-S2	8.86 (1.99)	-8.14 (-1.83)	8.86 (1.99)	S.S	7.21 (1.62)	1.23

<i>68-68-10-S3</i>	8.34 (1.87)	-7.94 (-1.78)	8.34 (1.87)	S.S	7.21 (1.62)	1.16
<i>68-68-10-F1</i>	8.76 (1.97)	-7.73 (-1.74)	8.76 (1.97)	S.S	7.21 (1.62)	1.21
<i>68-68-10-F2</i>	8.20 (1.84)	-7.38 (-1.66)	8.20 (1.84)	S.S	7.21 (1.62)	1.14
<i>68-68-10-F3</i>	8.11 (1.82)	-7.79 (-1.75)	8.11 (1.82)	S.S	7.21 (1.62)	1.12
<i>68-68-12-Q1</i>	10.86 (2.44)	-8.76 (-1.97)	10.86 (2.44)	S.S	11.21 (2.52)	0.97
<i>68-68-12-Q2</i>	10.34 (2.32)	-9.00 (-2.02)	10.34 (2.32)	S.S	11.21 (2.52)	0.92
<i>68-68-12-Q3</i>	9.37 (2.11)	-9.80 (-2.20)	9.80 (2.20)	S.S	11.21 (2.52)	0.87
<i>68-68-12-S1</i>	10.61 (2.39)	-10.02 (-2.25)	10.61 (2.39)	S.S	11.21 (2.52)	0.95
<i>68-68-12-S2</i>	9.91 (2.23)	-8.62 (-1.94)	9.91 (2.23)	S.S	11.21 (2.52)	0.88
<i>68-68-12-S3</i>	10.51 (2.36)	-9.81 (-2.20)	10.51 (2.36)	S.S	11.21 (2.52)	0.94
<i>68-68-12-F1</i>	10.48 (2.35)	-9.62 (-2.16)	10.48 (2.35)	S.S	11.21 (2.52)	0.93
<i>68-68-12-F2</i>	9.68 (2.18)	-8.49 (-1.91)	9.68 (2.18)	S.S	11.21 (2.52)	0.86
<i>68-68-12-F3</i>	10.73 (2.41)	-9.91 (-2.23)	10.73 (2.41)	S.S	11.21 (2.52)	0.96
<i>97-97-10-Q1</i>	8.27 (1.86)	-7.69 (-1.73)	8.27 (1.86)	S.S	7.21 (1.62)	1.15
<i>97-97-10-Q2</i>	5.28 (1.19)	-10.51 (-2.36)	10.51 (2.36)	S.S	7.21 (1.62)	1.46
<i>97-97-10-Q3</i>	8.14 (1.83)	-8.36 (-1.88)	8.36 (1.88)	S.S	7.21 (1.62)	1.16
<i>97-97-10-S1</i>	7.90 (1.78)	-7.47 (-1.68)	7.90 (1.78)	S.S	7.21 (1.62)	1.10
<i>97-97-10-S2</i>	7.14 (1.60)	-7.85 (-1.76)	7.85 (1.76)	S.S	7.21 (1.62)	1.09
<i>97-97-10-S3</i>	8.10 (1.82)	-6.88 (-1.55)	8.10 (1.82)	S.S	7.21 (1.62)	1.12
<i>97-97-10-F1</i>	8.02 (1.80)	-6.19 (-1.39)	8.02 (1.80)	S.S	7.21 (1.62)	1.11
<i>97-97-10-F2</i>	8.46 (1.90)	-8.65 (-1.94)	8.65 (1.94)	S.S	7.21 (1.62)	1.20
<i>97-97-10-F3</i>	8.26 (1.86)	-7.28 (-1.64)	8.26 (1.86)	S.S	7.21 (1.62)	1.15
<i>97-97-12-Q1</i>	9.83 (2.21)	-9.48 (-2.13)	9.83 (2.21)	S.S	11.21 (2.52)	0.88
<i>97-97-12-Q2</i>	10.17 (2.29)	-9.00 (-2.02)	10.17 (2.29)	S.S	11.21 (2.52)	0.91
<i>97-97-12-Q3</i>	10.01 (2.25)	-10.58 (-2.38)	10.58 (2.38)	S.S	11.21 (2.52)	0.94
<i>97-97-12-S1</i>	10.73 (2.41)	-10.34 (-2.32)	10.73 (2.41)	S.S	11.21 (2.52)	0.96
<i>97-97-12-S2</i>	10.95 (2.46)	-9.25 (-2.08)	10.95 (2.46)	S.S	11.21 (2.52)	0.98
<i>97-97-12-S3</i>	11.24 (2.53)	-10.32 (-2.32)	11.24 (2.53)	S.S	11.21 (2.52)	1.00
<i>97-97-12-F1</i>	11.08 (2.49)	-9.38 (-2.11)	11.08 (2.49)	S.S	11.21 (2.52)	0.99

97-97-12-F2	10.83 (2.43)	-10.38 (-2.33)	10.83 (2.43)	S.S	11.21 (2.52)	0.97
97-97-12-F3	11.17 (2.51)	-9.73 (-2.19)	11.17 (2.51)	S.S	11.21 (2.52)	1.00
54-PAF-Q1	12.38 (2.78)	-12.43 (-2.79)	12.43 (2.79)	T/O	13.39 (3.01)	0.93
54-PAF-Q2	12.40 (2.79)	-11.10 (-2.50)	12.40 (2.79)	T/O	13.39 (3.01)	0.93
54-PAF-Q3	11.47 (2.58)	-11.14 (-2.50)	11.47 (2.58)	T/O	13.39 (3.01)	0.86
68-PAF-Q1	15.35 (3.45)	-15.09 (-3.39)	15.35 (3.45)	T/O	16.46 (3.70)	0.93
68-PAF-Q2	15.19 (3.41)	-15.20 (-3.42)	15.20 (3.42)	T/O	16.46 (3.70)	0.92
68-PAF-Q3	15.70 (3.53)	-16.08 (-3.61)	16.08 (3.61)	T/O	16.46 (3.70)	0.98
97-PAF-Q1	14.68 (3.30)	-14.70 (-3.30)	14.70 (3.30)	P/O	21.99 (4.94)	0.67
97-PAF-Q2	15.08 (3.39)	-13.88 (-3.12)	15.08 (3.39)	P/O	21.99 (4.94)	0.69
97-PAF-Q3	15.47 (3.48)	-13.64 (-3.06)	15.47 (3.48)	P/O	21.99 (4.94)	0.70

Key

S.S- Screw shear

T/B- Screw tilting and bearing

T/O- Fastener tear out

P/O- Fastener pull out

APPENDIX D: Positive Backbone Parameters

Test	<i>ePd1</i>	<i>ePd2</i>	<i>ePd3</i>	<i>ePd4</i>
	mm (in.)	mm (in.)	mm (in.)	mm (in.)
<i>54-54-10-Q1</i>	0.030 (0.0012)	3.1 (0.12)	9.5 (0.38)	15.0 (0.59)
<i>54-54-10-Q2</i>	0.059 (0.0023)	4.4 (0.17)	7.8 (0.31)	13.0 (0.51)
<i>54-54-10-Q3</i>	0.000 (0.0000)	3.1 (0.12)	7.4 (0.29)	12.0 (0.47)
<i>54-54-10-S1</i>	0.001 (0.0001)	3.1 (0.12)	6.3 (0.25)	8.5 (0.33)
<i>54-54-10-S2</i>	0.061 (0.0024)	3.1 (0.12)	4.4 (0.18)	6.1 (0.24)
<i>54-54-10-S3</i>	0.049 (0.0019)	3.1 (0.12)	7.9 (0.31)	12.0 (0.47)
<i>54-54-10-F1</i>	0.000 (0.0000)	3.0 (0.12)	6.3 (0.25)	8.5 (0.33)
<i>54-54-10-F2</i>	0.031 (0.0012)	3.0 (0.12)	6.9 (0.27)	10.0 (0.39)
<i>54-54-10-F3</i>	0.069 (0.0027)	3.0 (0.12)	5.8 (0.23)	10.0 (0.39)
<i>54-54-12-Q1</i>	0.000 (0.0000)	3.1 (0.12)	10.9 (0.43)	15.0 (0.59)
<i>54-54-12-Q2</i>	0.055 (0.0022)	3.1 (0.12)	7.3 (0.29)	12.0 (0.47)
<i>54-54-12-Q3</i>	0.036 (0.0014)	3.1 (0.12)	7.4 (0.29)	12.0 (0.47)
<i>54-54-12-S1</i>	0.055 (0.0022)	3.1 (0.12)	7.5 (0.30)	12.0 (0.47)
<i>54-54-12-S2</i>	0.000 (0.0000)	2.2 (0.09)	11.4 (0.45)	15.0 (0.59)
<i>54-54-12-S3</i>	0.041 (0.0016)	3.1 (0.12)	10.4 (0.41)	15.0 (0.59)
<i>54-54-12-F1</i>	0.090 (0.0035)	8.5 (0.33)	10.1 (0.40)	11.0 (0.43)
<i>54-54-12-F2</i>	0.064 (0.0025)	2.8 (0.11)	7.2 (0.28)	11.0 (0.43)
<i>54-54-12-F3</i>	0.087 (0.0034)	3.0 (0.12)	6.8 (0.27)	11.0 (0.43)
<i>68-68-10-Q1</i>	0.019 (0.0008)	2.0 (0.08)	2.0 (0.08)	2.3 (0.09)
<i>68-68-10-Q2</i>	0.018 (0.0007)	1.6 (0.06)	1.9 (0.08)	2.2 (0.09)
<i>68-68-10-Q3</i>	0.000 (0.0000)	2.0 (0.08)	1.9 (0.08)	2.2 (0.09)
<i>68-68-10-S1</i>	0.030 (0.0012)	2.5 (0.10)	2.5 (0.10)	2.9 (0.11)
<i>68-68-10-S2</i>	0.060 (0.0023)	2.2 (0.09)	2.1 (0.08)	2.2 (0.09)
<i>68-68-10-S3</i>	0.043 (0.0017)	1.6 (0.06)	2.0 (0.08)	2.2 (0.09)
<i>68-68-10-F1</i>	0.111 (0.0044)	2.0 (0.08)	2.1 (0.08)	2.2 (0.09)
<i>68-68-10-F2</i>	0.058 (0.0023)	1.6 (0.06)	2.0 (0.08)	2.2 (0.09)

<i>68-68-10-F3</i>	0.059 (0.0023)	1.6 (0.06)	1.8 (0.07)	2.0 (0.08)
<i>68-68-12-Q1</i>	0.000 (0.0000)	7.8 (0.31)	8.6 (0.34)	8.5 (0.34)
<i>68-68-12-Q2</i>	0.047 (0.0018)	3.1 (0.12)	7.7 (0.30)	12.0 (0.47)
<i>68-68-12-Q3</i>	0.000 (0.0000)	2.9 (0.12)	5.7 (0.23)	8.5 (0.34)
<i>68-68-12-S1</i>	0.058 (0.0023)	3.1 (0.12)	5.7 (0.22)	9.0 (0.35)
<i>68-68-12-S2</i>	0.063 (0.0025)	3.1 (0.12)	5.3 (0.21)	8.5 (0.34)
<i>68-68-12-S3</i>	0.015 (0.0006)	3.1 (0.12)	7.5 (0.29)	11.0 (0.43)
<i>68-68-12-F1</i>	0.037 (0.0014)	4.2 (0.17)	6.0 (0.24)	8.5 (0.33)
<i>68-68-12-F2</i>	0.116 (0.0045)	3.0 (0.12)	4.3 (0.17)	7.0 (0.28)
<i>68-68-12-F3</i>	0.176 (0.0069)	3.0 (0.12)	6.2 (0.25)	10.0 (0.39)
<i>97-97-10-Q1</i>	0.000 (0.0000)	1.1 (0.04)	1.2 (0.05)	1.0 (0.04)
<i>97-97-10-Q2</i>	0.002 (0.0001)	0.8 (0.03)	1.0 (0.04)	1.0 (0.04)
<i>97-97-10-Q3</i>	0.000 (0.0000)	1.3 (0.05)	1.8 (0.07)	1.6 (0.06)
<i>97-97-10-S1</i>	0.021 (0.0008)	0.8 (0.03)	1.0 (0.04)	0.8 (0.03)
<i>97-97-10-S2</i>	0.029 (0.0011)	1.1 (0.04)	1.3 (0.05)	1.3 (0.05)
<i>97-97-10-S3</i>	0.050 (0.0020)	0.8 (0.03)	1.3 (0.05)	1.2 (0.05)
<i>97-97-10-F1</i>	0.033 (0.0013)	1.1 (0.04)	1.6 (0.06)	1.6 (0.06)
<i>97-97-10-F2</i>	0.102 (0.0040)	1.1 (0.04)	1.5 (0.06)	1.6 (0.06)
<i>97-97-10-F3</i>	0.055 (0.0022)	1.0 (0.04)	1.3 (0.05)	1.2 (0.05)
<i>97-97-12-Q1</i>	0.000 (0.0000)	1.4 (0.06)	1.6 (0.06)	1.6 (0.06)
<i>97-97-12-Q2</i>	0.045 (0.0018)	1.6 (0.06)	2.2 (0.09)	2.3 (0.09)
<i>97-97-12-Q3</i>	0.000 (0.0000)	1.6 (0.06)	1.9 (0.08)	2.1 (0.08)
<i>97-97-12-S1</i>	0.060 (0.0024)	2.0 (0.08)	2.3 (0.09)	2.1 (0.08)
<i>97-97-12-S2</i>	0.078 (0.0031)	1.6 (0.06)	1.6 (0.06)	1.5 (0.06)
<i>97-97-12-S3</i>	0.076 (0.0030)	1.6 (0.06)	2.3 (0.09)	2.3 (0.09)
<i>97-97-12-F1</i>	0.062 (0.0024)	1.6 (0.06)	2.2 (0.09)	2.3 (0.09)
<i>97-97-12-F2</i>	0.131 (0.0051)	1.6 (0.06)	2.2 (0.08)	2.2 (0.09)
<i>97-97-12-F3</i>	0.115 (0.0045)	1.6 (0.06)	1.8 (0.07)	2.0 (0.08)
<hr/>				
<i>54-PAF-Q1</i>	0.136 (0.0054)	2.0 (0.08)	13.9 (0.55)	15.2 (0.60)
<i>54-PAF-Q2</i>	0.188 (0.0074)	2.0 (0.08)	20.6 (0.81)	21.3 (0.84)
<i>54-PAF-Q3</i>	0.157 (0.0062)	1.9 (0.08)	10.6 (0.42)	10.7 (0.42)

<i>68-PAF-Q1</i>	0.083 (0.0033)	2.9 (0.11)	3.5 (0.14)	3.8 (0.15)
<i>68-PAF-Q2</i>	0.102 (0.0040)	2.9 (0.11)	4.9 (0.19)	5.6 (0.22)
<i>68-PAF-Q3</i>	0.080 (0.0031)	4.0 (0.16)	3.5 (0.14)	3.8 (0.15)
<i>97-PAF-Q1</i>	0.085 (0.0034)	0.7 (0.03)	2.3 (0.09)	4.1 (0.16)
<i>97-PAF-Q2</i>	0.094 (0.0037)	0.7 (0.03)	2.2 (0.09)	4.1 (0.16)
<i>97-PAF-Q3</i>	0.128 (0.0050)	0.7 (0.03)	2.3 (0.09)	4.1 (0.16)

Test	<i>ePf1</i> kN (kip)	<i>ePf2</i> kN (kip)	<i>ePf3</i> kN (kip)	<i>ePf4</i> kN (kip)
<i>54-54-10-Q1</i>	0.030 (0.0012)	3.1 (0.12)	9.5 (0.38)	15.0 (0.59)
<i>54-54-10-Q2</i>	0.059 (0.0023)	4.4 (0.17)	7.8 (0.31)	13.0 (0.51)
<i>54-54-10-Q3</i>	0.000 (0.0000)	3.1 (0.12)	7.4 (0.29)	12.0 (0.47)
<i>54-54-10-S1</i>	0.001 (0.0001)	3.1 (0.12)	6.3 (0.25)	8.5 (0.33)
<i>54-54-10-S2</i>	0.061 (0.0024)	3.1 (0.12)	4.4 (0.18)	6.1 (0.24)
<i>54-54-10-S3</i>	0.049 (0.0019)	3.1 (0.12)	7.9 (0.31)	12.0 (0.47)
<i>54-54-10-F1</i>	0.000 (0.0000)	3.0 (0.12)	6.3 (0.25)	8.5 (0.33)
<i>54-54-10-F2</i>	0.031 (0.0012)	3.0 (0.12)	6.9 (0.27)	10.0 (0.39)
<i>54-54-10-F3</i>	0.069 (0.0027)	3.0 (0.12)	5.8 (0.23)	10.0 (0.39)
<i>54-54-12-Q1</i>	0.000 (0.0000)	3.1 (0.12)	10.9 (0.43)	15.0 (0.59)
<i>54-54-12-Q2</i>	0.055 (0.0022)	3.1 (0.12)	7.3 (0.29)	12.0 (0.47)
<i>54-54-12-Q3</i>	0.036 (0.0014)	3.1 (0.12)	7.4 (0.29)	12.0 (0.47)
<i>54-54-12-S1</i>	0.055 (0.0022)	3.1 (0.12)	7.5 (0.30)	12.0 (0.47)
<i>54-54-12-S2</i>	0.000 (0.0000)	2.2 (0.09)	11.4 (0.45)	15.0 (0.59)
<i>54-54-12-S3</i>	0.041 (0.0016)	3.1 (0.12)	10.4 (0.41)	15.0 (0.59)
<i>54-54-12-F1</i>	0.090 (0.0035)	8.5 (0.33)	10.1 (0.40)	11.0 (0.43)
<i>54-54-12-F2</i>	0.064 (0.0025)	2.8 (0.11)	7.2 (0.28)	11.0 (0.43)
<i>54-54-12-F3</i>	0.087 (0.0034)	3.0 (0.12)	6.8 (0.27)	11.0 (0.43)
<i>68-68-10-Q1</i>	0.019 (0.0008)	2.0 (0.08)	2.0 (0.08)	2.3 (0.09)
<i>68-68-10-Q2</i>	0.018 (0.0007)	1.6 (0.06)	1.9 (0.08)	2.2 (0.09)
<i>68-68-10-Q3</i>	0.000 (0.0000)	2.0 (0.08)	1.9 (0.08)	2.2 (0.09)
<i>68-68-10-S1</i>	0.030 (0.0012)	2.5 (0.10)	2.5 (0.10)	2.9 (0.11)
<i>68-68-10-S2</i>	0.060 (0.0023)	2.2 (0.09)	2.1 (0.08)	2.2 (0.09)
<i>68-68-10-S3</i>	0.043 (0.0017)	1.6 (0.06)	2.0 (0.08)	2.2 (0.09)
<i>68-68-10-F1</i>	0.111 (0.0044)	2.0 (0.08)	2.1 (0.08)	2.2 (0.09)
<i>68-68-10-F2</i>	0.058 (0.0023)	1.6 (0.06)	2.0 (0.08)	2.2 (0.09)
<i>68-68-10-F3</i>	0.059 (0.0023)	1.6 (0.06)	1.8 (0.07)	2.0 (0.08)
<i>68-68-12-Q1</i>	0.000 (0.0000)	7.8 (0.31)	8.6 (0.34)	8.5 (0.34)
<i>68-68-12-Q2</i>	0.047 (0.0018)	3.1 (0.12)	7.7 (0.30)	12.0 (0.47)

<i>68-68-12-Q3</i>	0.000 (0.0000)	2.9 (0.12)	5.7 (0.23)	8.5 (0.34)
<i>68-68-12-S1</i>	0.058 (0.0023)	3.1 (0.12)	5.7 (0.22)	9.0 (0.35)
<i>68-68-12-S2</i>	0.063 (0.0025)	3.1 (0.12)	5.3 (0.21)	8.5 (0.34)
<i>68-68-12-S3</i>	0.015 (0.0006)	3.1 (0.12)	7.5 (0.29)	11.0 (0.43)
<i>68-68-12-F1</i>	0.037 (0.0014)	4.2 (0.17)	6.0 (0.24)	8.5 (0.33)
<i>68-68-12-F2</i>	0.116 (0.0045)	3.0 (0.12)	4.3 (0.17)	7.0 (0.28)
<i>68-68-12-F3</i>	0.176 (0.0069)	3.0 (0.12)	6.2 (0.25)	10.0 (0.39)
<i>97-97-10-Q1</i>	0.000 (0.0000)	1.1 (0.04)	1.2 (0.05)	1.0 (0.04)
<i>97-97-10-Q2</i>	0.002 (0.0001)	0.8 (0.03)	1.0 (0.04)	1.0 (0.04)
<i>97-97-10-Q3</i>	0.000 (0.0000)	1.3 (0.05)	1.8 (0.07)	1.6 (0.06)
<i>97-97-10-S1</i>	0.021 (0.0008)	0.8 (0.03)	1.0 (0.04)	0.8 (0.03)
<i>97-97-10-S2</i>	0.029 (0.0011)	1.1 (0.04)	1.3 (0.05)	1.3 (0.05)
<i>97-97-10-S3</i>	0.050 (0.0020)	0.8 (0.03)	1.3 (0.05)	1.2 (0.05)
<i>97-97-10-F1</i>	0.033 (0.0013)	1.1 (0.04)	1.6 (0.06)	1.6 (0.06)
<i>97-97-10-F2</i>	0.102 (0.0040)	1.1 (0.04)	1.5 (0.06)	1.6 (0.06)
<i>97-97-10-F3</i>	0.055 (0.0022)	1.0 (0.04)	1.3 (0.05)	1.2 (0.05)
<i>97-97-12-Q1</i>	0.000 (0.0000)	1.4 (0.06)	1.6 (0.06)	1.6 (0.06)
<i>97-97-12-Q2</i>	0.045 (0.0018)	1.6 (0.06)	2.2 (0.09)	2.3 (0.09)
<i>97-97-12-Q3</i>	0.000 (0.0000)	1.6 (0.06)	1.9 (0.08)	2.1 (0.08)
<i>97-97-12-S1</i>	0.060 (0.0024)	2.0 (0.08)	2.3 (0.09)	2.1 (0.08)
<i>97-97-12-S2</i>	0.078 (0.0031)	1.6 (0.06)	1.6 (0.06)	1.5 (0.06)
<i>97-97-12-S3</i>	0.076 (0.0030)	1.6 (0.06)	2.3 (0.09)	2.3 (0.09)
<i>97-97-12-F1</i>	0.062 (0.0024)	1.6 (0.06)	2.2 (0.09)	2.3 (0.09)
<i>97-97-12-F2</i>	0.131 (0.0051)	1.6 (0.06)	2.2 (0.08)	2.2 (0.09)
<i>97-97-12-F3</i>	0.115 (0.0045)	1.6 (0.06)	1.8 (0.07)	2.0 (0.08)
<hr/>				
<i>54-PAF-Q1</i>	0.136 (0.0054)	2.0 (0.08)	13.9 (0.55)	15.2 (0.60)
<i>54-PAF-Q2</i>	0.188 (0.0074)	2.0 (0.08)	20.6 (0.81)	21.3 (0.84)
<i>54-PAF-Q3</i>	0.157 (0.0062)	1.9 (0.08)	10.6 (0.42)	10.7 (0.42)
<i>68-PAF-Q1</i>	0.083 (0.0033)	2.9 (0.11)	3.5 (0.14)	3.8 (0.15)
<i>68-PAF-Q2</i>	0.102 (0.0040)	2.9 (0.11)	4.9 (0.19)	5.6 (0.22)
<i>68-PAF-Q3</i>	0.080 (0.0031)	4.0 (0.16)	3.5 (0.14)	3.8 (0.15)

<i>97-PAF-Q1</i>	0.085 (0.0034)	0.7 (0.03)	2.3 (0.09)	4.1 (0.16)
<i>97-PAF-Q2</i>	0.094 (0.0037)	0.7 (0.03)	2.2 (0.09)	4.1 (0.16)
<i>97-PAF-Q3</i>	0.128 (0.0050)	0.7 (0.03)	2.3 (0.09)	4.1 (0.16)

APPENDIX E: Negative Backbone Parameters

Test	<i>eNd1</i> mm (in.)	<i>eNd2</i> mm (in.)	<i>eNd3</i> mm (in.)	<i>eNd4</i> mm (in.)
<i>54-54-10-Q1</i>	0.000 (0.0000)	-2.2 (-0.09)	-9.3 (-0.37)	-12.7 (-0.50)
<i>54-54-10-Q2</i>	-0.016 (-0.0006)	-2.2 (-0.09)	-7.5 (-0.29)	-12.0 (-0.47)
<i>54-54-10-Q3</i>	0.000 (0.0000)	-2.2 (-0.09)	-6.1 (-0.24)	-9.0 (-0.35)
<i>54-54-10-S1</i>	-0.060 (-0.0024)	-3.1 (-0.12)	-4.6 (-0.18)	-7.6 (-0.30)
<i>54-54-10-S2</i>	-0.002 (-0.0001)	-3.1 (-0.12)	-5.0 (-0.20)	-7.6 (-0.30)
<i>54-54-10-S3</i>	0.000 (0.0000)	-3.1 (-0.12)	-9.2 (-0.36)	-12.0 (-0.47)
<i>54-54-10-F1</i>	-0.021 (-0.0008)	-3.0 (-0.12)	-4.8 (-0.19)	-7.6 (-0.30)
<i>54-54-10-F2</i>	-0.014 (-0.0005)	-3.0 (-0.12)	-5.5 (-0.22)	-9.0 (-0.35)
<i>54-54-10-F3</i>	-0.005 (-0.0002)	-3.0 (-0.12)	-5.7 (-0.22)	-9.0 (-0.35)
<i>54-54-12-Q1</i>	-0.020 (-0.0008)	-2.2 (-0.09)	-8.0 (-0.32)	-12.7 (-0.50)
<i>54-54-12-Q2</i>	-0.029 (-0.0012)	-2.2 (-0.09)	-7.4 (-0.29)	-12.0 (-0.47)
<i>54-54-12-Q3</i>	-0.042 (-0.0016)	-2.2 (-0.09)	-7.3 (-0.29)	-12.0 (-0.47)
<i>54-54-12-S1</i>	-0.011 (-0.0005)	-3.1 (-0.12)	-5.7 (-0.22)	-9.0 (-0.35)
<i>54-54-12-S2</i>	-0.004 (-0.0001)	-2.2 (-0.09)	-10.6 (-0.42)	-17.0 (-0.67)
<i>54-54-12-S3</i>	-0.014 (-0.0006)	-3.1 (-0.12)	-8.1 (-0.32)	-13.0 (-0.51)
<i>54-54-12-F1</i>	-0.011 (-0.0004)	-3.0 (-0.12)	-5.5 (-0.22)	-9.0 (-0.35)
<i>54-54-12-F2</i>	-0.007 (-0.0003)	-3.0 (-0.12)	-6.0 (-0.23)	-9.0 (-0.35)
<i>54-54-12-F3</i>	0.000 (0.0000)	-3.0 (-0.12)	-6.6 (-0.26)	-9.0 (-0.35)
<i>68-68-10-Q1</i>	0.000 (0.0000)	-1.6 (-0.06)	-2.2 (-0.09)	-2.3 (-0.09)
<i>68-68-10-Q2</i>	0.000 (0.0000)	-1.6 (-0.06)	-1.5 (-0.06)	-1.6 (-0.06)
<i>68-68-10-Q3</i>	-0.047 (-0.0019)	-1.6 (-0.06)	-1.9 (-0.08)	-2.2 (-0.09)
<i>68-68-10-S1</i>	0.000 (0.0000)	-2.2 (-0.09)	-2.3 (-0.09)	-2.2 (-0.09)
<i>68-68-10-S2</i>	0.000 (0.0000)	-1.6 (-0.06)	-2.0 (-0.08)	-2.2 (-0.09)
<i>68-68-10-S3</i>	0.000 (0.0000)	-1.6 (-0.06)	-1.6 (-0.06)	-1.6 (-0.06)
<i>68-68-10-F1</i>	-0.007 (-0.0003)	-1.9 (-0.08)	-2.0 (-0.08)	-2.2 (-0.09)
<i>68-68-10-F2</i>	-0.047 (-0.0019)	-1.6 (-0.06)	-1.4 (-0.06)	-1.6 (-0.06)

<i>68-68-10-F3</i>	-0.051 (-0.0020)	-1.4 (-0.06)	-1.4 (-0.05)	-1.6 (-0.06)
<i>68-68-12-Q1</i>	-0.053 (-0.0021)	-3.2 (-0.12)	-5.6 (-0.22)	-8.9 (-0.35)
<i>68-68-12-Q2</i>	-0.036 (-0.0014)	-3.1 (-0.12)	-5.3 (-0.21)	-8.5 (-0.33)
<i>68-68-12-Q3</i>	-0.039 (-0.0015)	-6.2 (-0.24)	-6.2 (-0.24)	-7.0 (-0.28)
<i>68-68-12-S1</i>	0.000 (0.0000)	-3.1 (-0.12)	-6.8 (-0.27)	-8.9 (-0.35)
<i>68-68-12-S2</i>	-0.006 (-0.0002)	-3.1 (-0.12)	-5.5 (-0.22)	-8.9 (-0.35)
<i>68-68-12-S3</i>	0.000 (0.0000)	-3.1 (-0.12)	-6.7 (-0.26)	-8.9 (-0.35)
<i>68-68-12-F1</i>	-0.057 (-0.0023)	-3.0 (-0.12)	-5.4 (-0.21)	-8.5 (-0.33)
<i>68-68-12-F2</i>	-0.095 (-0.0037)	-2.1 (-0.08)	-4.1 (-0.16)	-6.6 (-0.26)
<i>68-68-12-F3</i>	-0.101 (-0.0040)	-4.2 (-0.17)	-5.3 (-0.21)	-8.5 (-0.33)
<i>97-97-10-Q1</i>	0.000 (0.0000)	-0.8 (-0.03)	-1.3 (-0.05)	-1.2 (-0.05)
<i>97-97-10-Q2</i>	0.000 (0.0000)	-0.8 (-0.03)	-0.7 (-0.03)	-0.8 (-0.03)
<i>97-97-10-Q3</i>	-0.019 (-0.0008)	-1.1 (-0.05)	-1.6 (-0.06)	-1.6 (-0.06)
<i>97-97-10-S1</i>	-0.002 (-0.0001)	-0.6 (-0.02)	-0.6 (-0.03)	-0.8 (-0.03)
<i>97-97-10-S2</i>	-0.002 (-0.0001)	-0.8 (-0.03)	-1.3 (-0.05)	-1.6 (-0.06)
<i>97-97-10-S3</i>	-0.002 (-0.0001)	-0.8 (-0.03)	-1.3 (-0.05)	-1.2 (-0.05)
<i>97-97-10-F1</i>	-0.068 (-0.0027)	-1.1 (-0.04)	-1.1 (-0.05)	-1.2 (-0.05)
<i>97-97-10-F2</i>	-0.016 (-0.0006)	-1.1 (-0.04)	-1.0 (-0.04)	-0.8 (-0.03)
<i>97-97-10-F3</i>	-0.003 (-0.0001)	-0.8 (-0.03)	-1.3 (-0.05)	-1.2 (-0.05)
<i>97-97-12-Q1</i>	0.000 (0.0000)	-1.1 (-0.05)	-1.6 (-0.06)	-1.6 (-0.06)
<i>97-97-12-Q2</i>	-0.078 (-0.0031)	-1.6 (-0.06)	-2.2 (-0.09)	-2.3 (-0.09)
<i>97-97-12-Q3</i>	-0.009 (-0.0004)	-1.6 (-0.06)	-1.6 (-0.06)	-1.6 (-0.06)
<i>97-97-12-S1</i>	0.000 (0.0000)	-1.6 (-0.06)	-1.9 (-0.08)	-1.8 (-0.07)
<i>97-97-12-S2</i>	0.000 (0.0000)	-1.1 (-0.04)	-1.6 (-0.06)	-1.5 (-0.06)
<i>97-97-12-S3</i>	-0.031 (-0.0012)	-1.6 (-0.06)	-1.9 (-0.07)	-1.8 (-0.07)
<i>97-97-12-F1</i>	-0.111 (-0.0044)	-1.6 (-0.06)	-1.5 (-0.06)	-1.6 (-0.06)
<i>97-97-12-F2</i>	-0.125 (-0.0049)	-1.5 (-0.06)	-1.5 (-0.06)	-1.6 (-0.06)
<i>97-97-12-F3</i>	-0.101 (-0.0040)	-1.5 (-0.06)	-1.5 (-0.06)	-1.6 (-0.06)
<i>54-PAF-Q1</i>	-0.094 (-0.0037)	-1.5 (-0.06)	-19.2 (-0.76)	-21.3 (-0.84)
<i>54-PAF-Q2</i>	-0.114 (-0.0045)	-1.5 (-0.06)	-20.3 (-0.80)	-21.3 (-0.84)
<i>54-PAF-Q3</i>	-0.113 (-0.0045)	-13.5 (-0.53)	-19.6 (-0.77)	-21.3 (-0.84)

<i>68-PAF-Q1</i>	-0.006 (-0.0002)	-2.0 (-0.08)	-3.8 (-0.15)	-3.8 (-0.15)
<i>68-PAF-Q2</i>	0.000 (0.0000)	-2.9 (-0.11)	-5.7 (-0.23)	-5.6 (-0.22)
<i>68-PAF-Q3</i>	-0.027 (-0.0010)	-2.9 (-0.11)	-3.8 (-0.15)	-3.8 (-0.15)
<i>97-PAF-Q1</i>	-0.030 (-0.0012)	-0.5 (-0.02)	-2.5 (-0.10)	-4.1 (-0.16)
<i>97-PAF-Q2</i>	0.000 (0.0000)	-0.5 (-0.02)	-3.4 (-0.13)	-4.1 (-0.16)
<i>97-PAF-Q3</i>	-0.010 (-0.0004)	-0.5 (-0.02)	-2.5 (-0.10)	-4.1 (-0.16)

Test	<i>eNf1</i> kN (kip)	<i>eNf2</i> kN (kip)	<i>eNf3</i> kN (kip)	<i>eNf4</i> kN (kip)
<i>54-54-10-Q1</i>	-3.22 (-0.72)	-6.0 (-1.35)	-3.7 (-0.83)	0.0 (0.00)
<i>54-54-10-Q2</i>	-3.90 (-0.88)	-6.3 (-1.41)	-4.2 (-0.93)	0.0 (0.00)
<i>54-54-10-Q3</i>	-3.21 (-0.72)	-6.3 (-1.41)	-4.1 (-0.93)	0.0 (0.00)
<i>54-54-10-S1</i>	-4.80 (-1.08)	-8.1 (-1.82)	-5.2 (-1.18)	0.0 (0.00)
<i>54-54-10-S2</i>	-4.10 (-0.92)	-6.7 (-1.52)	-4.5 (-1.01)	0.0 (0.00)
<i>54-54-10-S3</i>	-3.25 (-0.73)	-6.3 (-1.42)	-3.8 (-0.86)	0.0 (0.00)
<i>54-54-10-F1</i>	-3.79 (-0.85)	-6.3 (-1.41)	-4.2 (-0.94)	0.0 (0.00)
<i>54-54-10-F2</i>	-4.50 (-1.01)	-7.1 (-1.60)	-4.7 (-1.06)	0.0 (0.00)
<i>54-54-10-F3</i>	-4.00 (-0.90)	-6.5 (-1.45)	-4.3 (-0.97)	0.0 (0.00)
<i>54-54-12-Q1</i>	-4.18 (-0.94)	-6.7 (-1.52)	-4.6 (-1.03)	0.0 (0.00)
<i>54-54-12-Q2</i>	-4.27 (-0.96)	-6.8 (-1.52)	-4.5 (-1.01)	0.0 (0.00)
<i>54-54-12-Q3</i>	-3.95 (-0.89)	-6.5 (-1.45)	-4.4 (-0.98)	0.0 (0.00)
<i>54-54-12-S1</i>	-4.68 (-1.05)	-7.4 (-1.65)	-5.0 (-1.13)	0.0 (0.00)
<i>54-54-12-S2</i>	-3.97 (-0.89)	-6.2 (-1.40)	-4.2 (-0.95)	0.0 (0.00)
<i>54-54-12-S3</i>	-4.14 (-0.93)	-6.6 (-1.48)	-4.5 (-1.02)	0.0 (0.00)
<i>54-54-12-F1</i>	-4.03 (-0.91)	-6.4 (-1.43)	-4.3 (-0.98)	0.0 (0.00)
<i>54-54-12-F2</i>	-3.81 (-0.86)	-6.9 (-1.54)	-4.5 (-1.02)	0.0 (0.00)
<i>54-54-12-F3</i>	-3.62 (-0.81)	-7.3 (-1.64)	-4.6 (-1.04)	0.0 (0.00)
<i>68-68-10-Q1</i>	-4.55 (-1.02)	-7.9 (-1.77)	-5.0 (-1.13)	0.0 (0.00)
<i>68-68-10-Q2</i>	-4.57 (-1.03)	-7.8 (-1.76)	-5.0 (-1.13)	0.0 (0.00)
<i>68-68-10-Q3</i>	-4.47 (-1.01)	-7.5 (-1.68)	-5.0 (-1.12)	0.0 (0.00)
<i>68-68-10-S1</i>	-3.72 (-0.84)	-7.8 (-1.76)	-4.9 (-1.10)	0.0 (0.00)
<i>68-68-10-S2</i>	-4.76 (-1.07)	-8.1 (-1.83)	-5.4 (-1.22)	0.0 (0.00)
<i>68-68-10-S3</i>	-4.55 (-1.02)	-7.9 (-1.78)	-5.1 (-1.14)	0.0 (0.00)
<i>68-68-10-F1</i>	-4.59 (-1.03)	-7.7 (-1.74)	-5.2 (-1.18)	0.0 (0.00)
<i>68-68-10-F2</i>	-4.26 (-0.96)	-7.4 (-1.66)	-4.8 (-1.09)	0.0 (0.00)
<i>68-68-10-F3</i>	-4.71 (-1.06)	-7.8 (-1.75)	-5.1 (-1.15)	0.0 (0.00)
<i>68-68-12-Q1</i>	-5.45 (-1.22)	-8.8 (-1.97)	-6.0 (-1.35)	0.0 (0.00)
<i>68-68-12-Q2</i>	-5.74 (-1.29)	-9.0 (-2.02)	-6.1 (-1.38)	0.0 (0.00)

<i>68-68-12-Q3</i>	-6.24 (-1.40)	-9.8 (-2.20)	-6.7 (-1.50)	0.0 (0.00)
<i>68-68-12-S1</i>	-4.95 (-1.11)	-10.0 (-2.25)	-6.3 (-1.41)	0.0 (0.00)
<i>68-68-12-S2</i>	-5.53 (-1.24)	-8.6 (-1.94)	-5.8 (-1.31)	0.0 (0.00)
<i>68-68-12-S3</i>	-5.05 (-1.13)	-9.8 (-2.20)	-6.2 (-1.40)	0.0 (0.00)
<i>68-68-12-F1</i>	-5.94 (-1.33)	-9.6 (-2.16)	-6.6 (-1.48)	0.0 (0.00)
<i>68-68-12-F2</i>	-5.27 (-1.19)	-8.5 (-1.91)	-5.5 (-1.25)	0.0 (0.00)
<i>68-68-12-F3</i>	-6.21 (-1.40)	-9.9 (-2.23)	-6.6 (-1.48)	0.0 (0.00)
<i>97-97-10-Q1</i>	-5.13 (-1.15)	-7.7 (-1.73)	-5.3 (-1.18)	0.0 (0.00)
<i>97-97-10-Q2</i>	-7.88 (-1.77)	-10.5 (-2.36)	-7.6 (-1.70)	0.0 (0.00)
<i>97-97-10-Q3</i>	-4.94 (-1.11)	-8.4 (-1.88)	-5.5 (-1.24)	0.0 (0.00)
<i>97-97-10-S1</i>	-4.67 (-1.05)	-7.5 (-1.68)	-5.0 (-1.13)	0.0 (0.00)
<i>97-97-10-S2</i>	-5.04 (-1.13)	-7.9 (-1.76)	-5.3 (-1.20)	0.0 (0.00)
<i>97-97-10-S3</i>	-4.41 (-0.99)	-6.9 (-1.55)	-4.7 (-1.05)	0.0 (0.00)
<i>97-97-10-F1</i>	-3.65 (-0.82)	-6.2 (-1.39)	-3.9 (-0.88)	0.0 (0.00)
<i>97-97-10-F2</i>	-4.60 (-1.03)	-8.6 (-1.94)	-5.7 (-1.28)	0.0 (0.00)
<i>97-97-10-F3</i>	-4.55 (-1.02)	-7.3 (-1.64)	-4.9 (-1.10)	0.0 (0.00)
<i>97-97-12-Q1</i>	-6.07 (-1.36)	-9.5 (-2.13)	-6.5 (-1.46)	0.0 (0.00)
<i>97-97-12-Q2</i>	-5.39 (-1.21)	-9.0 (-2.02)	-5.9 (-1.32)	0.0 (0.00)
<i>97-97-12-Q3</i>	-6.56 (-1.47)	-10.6 (-2.38)	-7.1 (-1.59)	0.0 (0.00)
<i>97-97-12-S1</i>	-5.35 (-1.20)	-10.3 (-2.32)	-6.5 (-1.47)	0.0 (0.00)
<i>97-97-12-S2</i>	-5.85 (-1.31)	-9.2 (-2.08)	-6.2 (-1.40)	0.0 (0.00)
<i>97-97-12-S3</i>	-6.36 (-1.43)	-10.3 (-2.32)	-6.9 (-1.55)	0.0 (0.00)
<i>97-97-12-F1</i>	-5.56 (-1.25)	-9.4 (-2.11)	-6.1 (-1.37)	0.0 (0.00)
<i>97-97-12-F2</i>	-6.02 (-1.35)	-10.4 (-2.33)	-6.9 (-1.56)	0.0 (0.00)
<i>97-97-12-F3</i>	-5.81 (-1.31)	-9.7 (-2.19)	-6.3 (-1.41)	0.0 (0.00)
<hr/>				
<i>54-PAF-Q1</i>	-12.70 (-2.85)	-12.4 (-2.79)	-10.1 (-2.28)	0.0 (0.00)
<i>54-PAF-Q2</i>	-10.56 (-2.37)	-11.1 (-2.50)	-8.8 (-1.98)	0.0 (0.00)
<i>54-PAF-Q3</i>	-10.57 (-2.38)	-11.1 (-2.50)	-8.9 (-2.01)	0.0 (0.00)
<i>68-PAF-Q1</i>	-16.50 (-3.71)	-15.1 (-3.39)	-9.9 (-2.22)	0.0 (0.00)
<i>68-PAF-Q2</i>	-16.38 (-3.68)	-15.2 (-3.42)	-10.1 (-2.27)	0.0 (0.00)
<i>68-PAF-Q3</i>	-16.83 (-3.78)	-16.1 (-3.61)	-10.6 (-2.38)	0.0 (0.00)

<i>97-PAF-Q1</i>	-13.36 (-3.00)	-14.7 (-3.30)	-4.9 (-1.10)	0.0 (0.00)
<i>97-PAF-Q2</i>	-7.35 (-1.65)	-13.9 (-3.12)	-4.1 (-0.93)	0.0 (0.00)
<i>97-PAF-Q3</i>	-12.54 (-2.82)	-13.6 (-3.06)	-4.5 (-1.00)	0.0 (0.00)

APPENDIX F: Unloading-reloading Parameters

Test	<i>rDispP</i>	<i>rForceP</i>	<i>rDispN</i>	<i>rForceN</i>	<i>uForceP</i>	<i>uForceN</i>
<i>54-54-10-Q1</i>	0.614	0.035	0.614	0.035	0.020	0.020
<i>54-54-10-Q2</i>	0.285	0.037	0.285	0.035	0.020	0.020
<i>54-54-10-Q3</i>	0.510	0.033	0.510	0.039	0.020	0.020
<i>54-54-10-S1</i>	0.475	0.042	0.475	0.041	0.020	0.020
<i>54-54-10-S2</i>	0.570	0.043	0.570	0.039	0.020	0.020
<i>54-54-10-S3</i>	0.563	0.038	0.563	0.037	0.020	0.020
<i>54-54-10-F1</i>	0.645	0.041	0.645	0.040	0.020	0.020
<i>54-54-10-F2</i>	0.255	0.040	0.255	0.037	0.020	0.020
<i>54-54-10-F3</i>	0.492	0.039	0.492	0.038	0.020	0.020
<i>54-54-12-Q1</i>	0.375	0.036	0.375	0.034	0.020	0.020
<i>54-54-12-Q2</i>	0.220	0.036	0.220	0.035	0.020	0.020
<i>54-54-12-Q3</i>	0.472	0.035	0.472	0.035	0.020	0.020
<i>54-54-12-S1</i>	0.436	0.036	0.436	0.037	0.020	0.020
<i>54-54-12-S2</i>	0.280	0.034	0.280	0.032	0.020	0.020
<i>54-54-12-S3</i>	0.385	0.036	0.385	0.034	0.020	0.020
<i>54-54-12-F1</i>	0.390	0.040	0.390	0.037	0.020	0.020
<i>54-54-12-F2</i>	0.360	0.038	0.360	0.040	0.020	0.020
<i>54-54-12-F3</i>	0.327	0.038	0.327	0.040	0.020	0.020
<i>68-68-10-Q1</i>	0.862	0.026	0.862	0.024	0.010	0.010
<i>68-68-10-Q2</i>	0.910	0.026	0.910	0.029	0.010	0.010
<i>68-68-10-Q3</i>	0.930	0.024	0.930	0.026	0.010	0.010
<i>68-68-10-S1</i>	0.927	0.024	0.927	0.027	0.010	0.010
<i>68-68-10-S2</i>	0.745	0.030	0.745	0.025	0.010	0.010
<i>68-68-10-S3</i>	0.705	0.026	0.705	0.029	0.010	0.010
<i>68-68-10-F1</i>	0.795	0.030	0.795	0.027	0.010	0.010
<i>68-68-10-F2</i>	0.885	0.024	0.885	0.027	0.009	0.009
<i>68-68-10-F3</i>	0.720	0.027	0.720	0.029	0.010	0.010

68-68-12-Q1	0.500	0.041	0.500	0.038	0.020	0.020
68-68-12-Q2	0.410	0.036	0.410	0.038	0.020	0.020
68-68-12-Q3	0.440	0.038	0.440	0.039	0.020	0.020
68-68-12-S1	0.470	0.038	0.470	0.039	0.020	0.020
68-68-12-S2	0.595	0.039	0.595	0.037	0.020	0.020
68-68-12-S3	0.560	0.038	0.560	0.039	0.020	0.020
68-68-12-F1	0.470	0.041	0.470	0.039	0.020	0.020
68-68-12-F2	0.410	0.043	0.410	0.042	0.020	0.020
68-68-12-F3	0.260	0.041	0.260	0.041	0.020	0.020
97-97-10-Q1	0.970	0.014	0.970	0.012	0.005	0.005
97-97-10-Q2	0.945	0.015	0.945	0.014	0.005	0.005
97-97-10-Q3	0.870	0.013	0.870	0.013	0.005	0.005
97-97-10-S1	0.076	0.016	0.076	0.017	0.005	0.005
97-97-10-S2	0.340	0.029	0.340	0.027	0.010	0.010
97-97-10-S3	0.815	0.014	0.815	0.013	0.005	0.005
97-97-10-F1	0.625	0.013	0.625	0.015	0.005	0.005
97-97-10-F2	0.395	0.032	0.395	0.035	0.010	0.010
97-97-10-F3	0.620	0.015	0.620	0.013	0.005	0.005
97-97-12-Q1	0.559	0.013	0.559	0.013	0.005	0.005
97-97-12-Q2	0.625	0.012	0.625	0.013	0.005	0.005
97-97-12-Q3	0.446	0.012	0.446	0.013	0.005	0.005
97-97-12-S1	0.783	0.013	0.783	0.013	0.005	0.005
97-97-12-S2	0.530	0.014	0.530	0.012	0.005	0.005
97-97-12-S3	0.670	0.013	0.670	0.013	0.005	0.005
97-97-12-F1	0.690	0.012	0.690	0.016	0.005	0.005
97-97-12-F2	0.430	0.015	0.430	0.017	0.005	0.005
97-97-12-F3	0.404	0.014	0.404	0.016	0.005	0.005
54-PAF-Q1	0.690	0.069	0.690	0.060	0.050	0.050
54-PAF-Q2	0.728	0.072	0.728	0.063	0.050	0.050
54-PAF-Q3	0.700	0.079	0.700	0.063	0.050	0.050
68-PAF-Q1	0.685	0.017	0.685	0.015	0.010	0.010

<i>68-PAF-Q2</i>	0.625	0.016	0.625	0.014	0.010	0.010
<i>68-PAF-Q3</i>	0.506	0.016	0.506	0.015	0.010	0.010
<i>97-PAF-Q1</i>	0.648	0.011	0.648	0.010	0.005	0.005
<i>97-PAF-Q2</i>	0.615	0.011	0.615	0.011	0.005	0.005
<i>97-PAF-Q3</i>	0.640	0.012	0.640	0.010	0.005	0.005

APPENDIX G: Sample Matlab code for generating *pinching4* parameters

```
close all

s_x=25.4; s_y=4.45; %x and y scaling factors

% figure

%54-54-10-Cyclic

for i = 1:9

    filename = ['specimen',num2str(i+6),'.dat'];

    data_sp.(['sp',num2str(i)]) = importdata(filename);

    data_sp.(['sp',num2str(i)]) = data_sp.(['sp',num2str(i)])...

        ( ~any( isnan(data_sp.(['sp',num2str(i)]) )...

            | isinf( data_sp.(['sp',num2str(i)]) ), 2 ),: );

    [CD1(i,1),I1(i,1)] = min(data_sp.(['sp',num2str(i)]) (:,2));

    dcc1 = data_sp.(['sp',num2str(i)])(I1(i,1),1);

    [CD2(i,1),I2(i,1)] = max(data_sp.(['sp',num2str(i)]) (:,2));

    dcc2 = data_sp.(['sp',num2str(i)])(I2(i,1),1);

    ke_ini(i,1) = data_sp.(['sp',num2str(i)])( ...

        find(data_sp.(['sp',num2str(i)]) (:,1) >= 0.0022,1),2)

    ...

    / 0.0022;

AA = [CD2,CD1,ke_ini];
```

```

%Initial Backbone parameters

do1=Bckb5410.do1(i);Po1=Bckb5410.Po1(i);

dc1=dcc1 ; Pc1=CD1(i);

dr1=Bckb5410.dr1(i);Pr1=0.6*Pc1;

Py1=0.4*Pc1; dy1=Py1/min(ke_ini(:,1));

do2=Bckb5410.do2(i);Po2=Bckb5410.Po2(i);

dc2=dcc2;Pc2=CD2(i);

dr2=Bckb5410.dr2(i);Pr2=0.6*Pc2;

Py2=0.4*Pc2;dy2=Py2/min(ke_ini(:,1));

ke1=Py1/dy1; ke2=Py1/dy1;

ks1=(Pc1-Py1)/(dc1-dy1); ks2=(Pc2-Py2)/(dc2-dy2);

kc1=(Pr1-Pc1)/(dc1-dr1); kc2=(Pr2-Pc2)/(dc2-dr2);

kr1=(Pr1-Po1)/(do1-dr1); kr2=(Pr2-Po2)/(do2-dr2);

%OPTIMIZING BACKBONE

x1=data_sp.(['sp',num2str(i)])(:,1); %Experimental results
y1=data_sp.(['sp',num2str(i)])(:,2); %Experimental results

k=boundary(x1,y1,1.0);

```

```

% Boundary values

x1bound = x1(k);

y1bound = y1(k);

posloc =find(x1bound>=0 & y1bound>=0);

negloc =find(x1bound<0 & y1bound<0);

%Positive boundary

boundpos=[x1bound(posloc),y1bound(posloc)];

boundneg=[x1bound(negloc),y1bound(negloc)];

%set limits

[max_disp,I3]=max(boundpos(:,1));

[min_disp,I4]=min(boundneg(:,1));

boundpos_x = boundpos(I3:end,1);

boundpos_y = boundpos(I3:end,2);

boundneg_x = boundneg(I4:end,1);

boundneg_y = boundneg(I4:end,2);

%Optimizing backbone

xdata1 = boundneg_x;

ydata1 = boundneg_y;

xdata2 = boundpos_x;

ydata2 = boundpos_y;

```

```

fun = @(x) sseval(x, Pc1, dc1, do1, xdata1, ydata1);
fun1 = @(z) sseval1(z, Pc2, dc2, do2, xdata2, ydata2);

x0 = [Py1, dy1, Pr1, dr1];
z0 = [Py2, dy2, Pr2, dr2];

bestxn(i, :) = fminsearch(fun, x0)
bestxp(i, :) = fminsearch(fun1, z0)

%Optimized backbone parameters

Py3 = bestxn(i, 1); dy3 = bestxn(i, 2);
Pr3 = bestxn(i, 3); dr3 = bestxn(i, 4);
Py4 = bestxp(i, 1); dy4 = bestxp(i, 2);
Pr4 = bestxp(i, 3); dr4 = bestxp(i, 4);

x2=[do1;dr3;dc1;dy3;0;dy4;dc2;dr4;do2];
y2=[Po1;Pr3;Pc1;Py3;0;Py4;Pc2;Pr4;Po2];

    for j=1:height(dminmax)

%Backbone

        dminmax2 = table2array(dminmax);

%Pinching4 initial parameters

            dmax=dminmax2(:,1);
            dmin=dminmax2(:,2);
            ky4=Py4/dy4; kc4=(Pc2-Py4)/(dc2-dy4);
            kr4=(Pr4-Pc2)/(dr4-dc2); ko4=-Pr4/(do2-dr4);

                if 0<=dmax(j) && dmax(j)<dy4

                    y(j)=(dmax(j))*ky4;

```

```

elseif dy4<=dmax(j) && dmax(j)<dc2
    y(j)=Py4+kc4*(dmax(j)-dy4);
elseif dc2<=dmax(j) && dmax(j)<dr4
    y(j)=Pc2+kr4*(dmax(j)-dc2);
elseif dr4<=dmax(j) && dmax(j)<do2
    y(j)=Pr4+ko4*(dmax(j)-dr4);
elseif dmax(j)>=do2
    y(j)=0;
    end

    ky3=Py3/dy3; kc3=(Pc1-Py3)/(dc1-dy3);
kr3=(Pr3-Pc1)/(dr3-dc1); ko3=-Pr3/(do1-dr3);
    if dmin(j)<=0 && dmin(j)>dy3
        yy(j)=(dmin(j))*ky3;
    elseif dmin(j)<=dy3 && dmin(j)>dc1
        yy(j)=Py3-kc3*(dy3-dmin(j));
    elseif dmin(j)<=dc1 && dmin(j)>dr3
        yy(j)=Pc1-kr3*(dc1-dmin(j));
    elseif dmin(j)<=dr3 && dmin(j)>do1
        yy(j)=Pr3-ko3*(dr3-dmin(j));
    elseif dmin(j)<=do1
        yy(j)=0;
    end

```

```
rDispP=[0.614,0.285,0.510,0.475,0.570,0.563,0.645,0.255,0.492]';
```

```
rDispN=[0.614,0.285,0.510,0.475,0.570,0.563,0.645,0.255,0.492]';
```

```

uForceP=[0.02,0.02,0.02,0.02,0.02,0.02,0.02,0.02,0.02]';
uForceN=[0.02,0.02,0.02,0.02,0.02,0.02,0.02,0.02,0.02]';
AvgForceN(i,:) = mean(yy);
AvgForceP(i,:) = mean(y);
rForceP(i,:) = (Pc2/AvgForceP(i,1))*uForceP(i);
rForceN(i,:) = (Pc1/AvgForceN(i,1))*uForceN(i);

    d2 =(y(j)-uForceN(i)*(Pc1))/ky4;      %unloading offset
    d1 =(yy(j)-uForceP(i)*(Pc2))/ky3;      %unloading offset

x3=[rDispP(i)*dmax(j),dmax(j),(dmax(j)-
d2),rDispN(i)*dmin(j),...
    dmin(j),(dmin(j)-d1),rDispP(i)*dmax(j)];
y3=[rForceP(i,1)*y(j),y(j),uForceN(i)*(Pc1),rForceN(i,1)*yy(j),y
y(j),...
    uForceP(i)*(Pc2),rForceP(i)*y(j)];
% % Areas comparison
    HysA(j,i)=polyarea(x3,y3);
    PinchingArea(1,i) = sum(HysA(:,i));
TestArea(1,i)=trapz(x1,y1);%Area of Test data
Optimum(i,:)= [(PinchingArea(i)/TestArea(i))]
    figure(i)
    hold on
P3= plot(x3*s_x,y3*s_y,'Color','r','LineWidth',1); %Pinching4
%
```

```

end

P1= plot(x1*s_x,y1*s_y,'--b','LineWidth',0.5);
P2= plot(x2*s_x,y2*s_y,'Color','k','LineWidth',2);

Lgd_name(i)=string(Filenames.Name(i+6));

Pinching(i,:)=

[Lgd_name(i);rDispP(i);rForceP(i,1);rDispN(i);rForceN(i,1);...
    uForceP(i);uForceN(i)];

Backbone(i,:) = [do1,dr3,Pr3,dc1,Pc1,dy3,Py3,...
    0,dy4,Py4,dc2,Pc2,dr4,Pr4,do2]';

%change legend for each different group
legend([P1,P2,P3],Lgd_name(i),'Cyclic
Backbone','Pinching4','location','northwest')
xlim([-20 20]); ylim([-10 10])
ax1 = gca; % current axes
set(gca,'box','off')
ax1.FontSize = 14;
ax1.XColor = 'k';
ax1.YColor = 'k'; ax1_pos = ax1.Position; % position of first
axes

```

```

xlabel('Displacement, \itd\rm (mm)', 'FontName',
'Arial', 'FontSize', 14);
ylabel('Load, \itP\rm (kN)', 'FontName', 'Arial', 'FontSize', 14)
%Secondary Axis
ax2 = axes('Position', ax1_pos, ...
'XAxisLocation', 'top', ...
'YAxisLocation', 'right', ...
'Color', 'none');
ax2.FontSize = 14;
s_x1=x1/s_x; s_y1=y1/s_y; %Divide by scaling factors
line(s_x1, s_y1, 'Parent', ax2, 'Color', 'none')
xlim([-0.787 0.787]); ylim([-2.2472 2.2472])
xlabel('Displacement, \itd\rm (in.)', 'FontName', 'Arial', ...
'FontSize', 14, 'Color', 'k')
ylabel('Load, \itP\rm (kip)', 'FontSize', 14)

axh = gca; % use current axes
line(get(axh, 'XLim'), [0 0], 'Color', 'k', 'LineStyle', '-');
line([0 0], get(axh, 'YLim'), 'Color', 'k', 'LineStyle', '-');
fig = gcf;
fig.Position = [0 0 800 800]; % window size
foldernameset = '54-10-cyc' % change folder name
filenamefig = ['54-54-10-', num2str(i), '.fig'] % change file name
filenameimg = ['54-54-10-', num2str(i), '.png'] % change file name

```

```
saveas(gcf,fullfile(foldernamefig,filenameefig))
saveas(gcf,fullfile(foldernameimg,filenameimg))
    hold off
end
```

```

function sse = sseval(x,Pc1,dc1,dol,xdata1,ydata1)

Py1 = x(1);
dy1 = x(2);
Pr1 = x(3);
dr1 = x(4);

for ii=1:length(xdata1)

    if 0>=xdata1(ii,1) && xdata1(ii,1)>dy1

        ff =xdata1(ii,1)*(Py1/dy1);

    elseif dy1>=xdata1(ii,1) && xdata1(ii,1)>dc1

        ff=Py1+(xdata1(ii,1)-dy1)*((Pc1-Py1)/(dc1-dy1));

    elseif dc1>=xdata1(ii,1) && xdata1(ii,1)>dr1;

        ff=Pc1+(xdata1(ii,1)-dc1)*((Pr1-Pc1)/(dr1-dc1));

    elseif dr1>=xdata1(ii,1) && xdata1(ii,1)>dol

        ff =Pr1-(xdata1(ii,1)-dc1)*(Pr1/(dol-dr1));

    elseif xdata1(ii,1)<=dol

        ff =0;

    end

end

sse = sum((ydata1-ff).^2);

```

```

function sse1 = sseval1(z,Pc2,dc2,do2,xdata2,ydata2)

Py2 = z(1);
dy2 = z(2);
Pr2 = z(3);
dr2 = z(4);

for jj=1:length(xdata2)
    if 0<=xdata2(jj,1) && xdata2(jj,1)<dy2
        ff1 =xdata2(jj,1)*(Py2/dy2);
    elseif dy2<=xdata2(jj,1) && xdata2(jj,1)<dc2
        ff1=Py2+(xdata2(jj,1)-dy2)*((Pc2-Py2)/(dc2-dy2));
    elseif dc2<=xdata2(jj,1) && xdata2(jj,1)<dr2
        ff1=Pc2+(xdata2(jj,1)-dc2)*((Pr2-Pc2)/(dr2-dc2));
    elseif dr2<=xdata2(jj,1) && xdata2(jj,1)<do2
        ff1 =Pr2-(xdata2(jj,1)-dc2)*(Pr2/(do2-dr2));
    elseif xdata2(jj,1)>=do2
        ff1 =0;
    end
end

sse1 = sum((ydata2-ff1).^2);

```

APPENDIX H: Photos of Test Frame Construction and Floor Assembly



Fig. H-1: Typical frame corner brace



Fig. H-2: Typical bearing support



Fig. H- 3: Assembled frame



Fig. H-4: 980 kN (220 kip) Actuator attachment



Fig. H-5: Final floor assembly for diaphragm testing

APPENDIX I: Individual gage readings for diaphragm tests

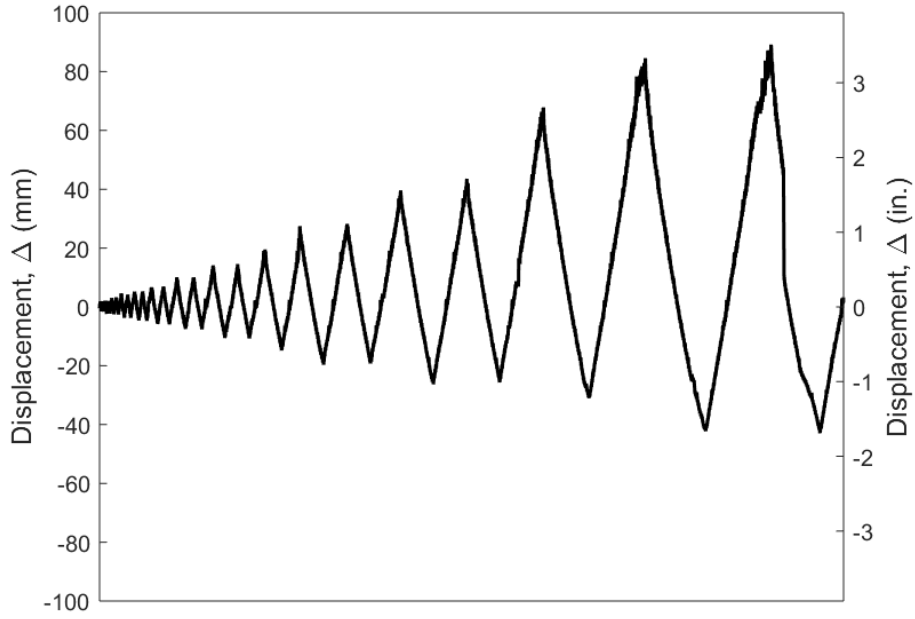


Fig. I-1: Floor 1 - Gage 1

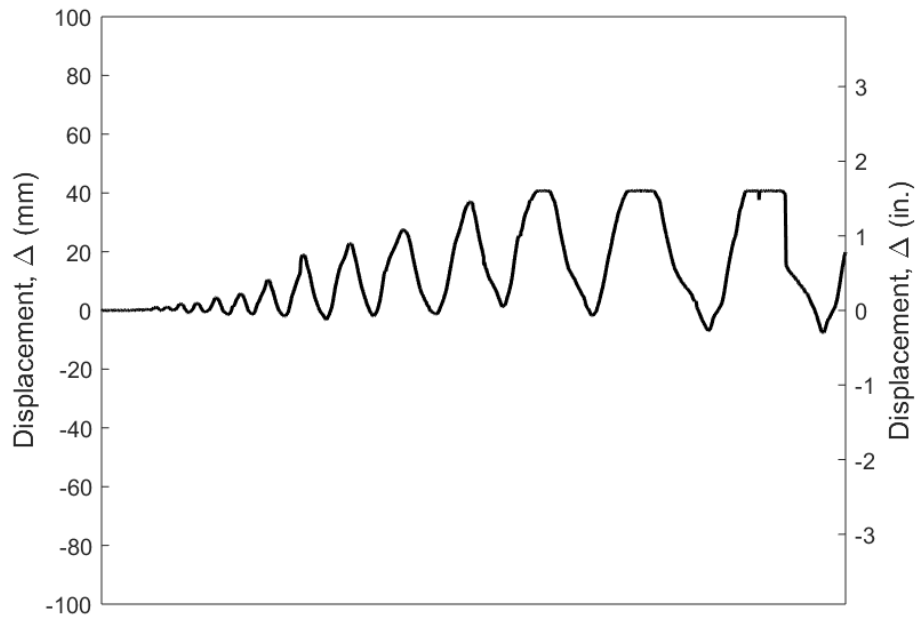


Fig. I-2: Floor 1 - Gage 2

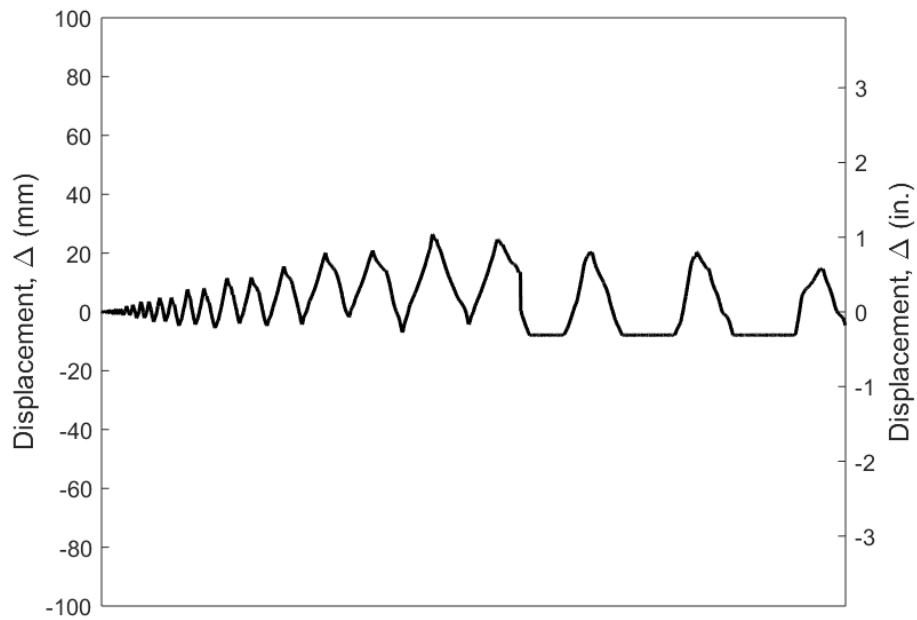


Fig. I-3: Floor 1 - Gage 3

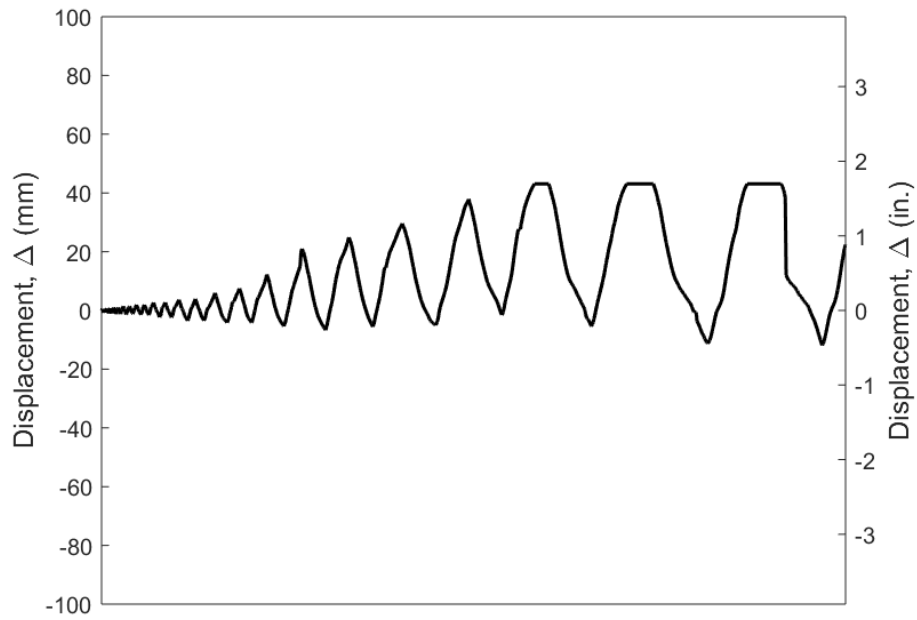


Fig. I-4: Floor 1 - Gage 4

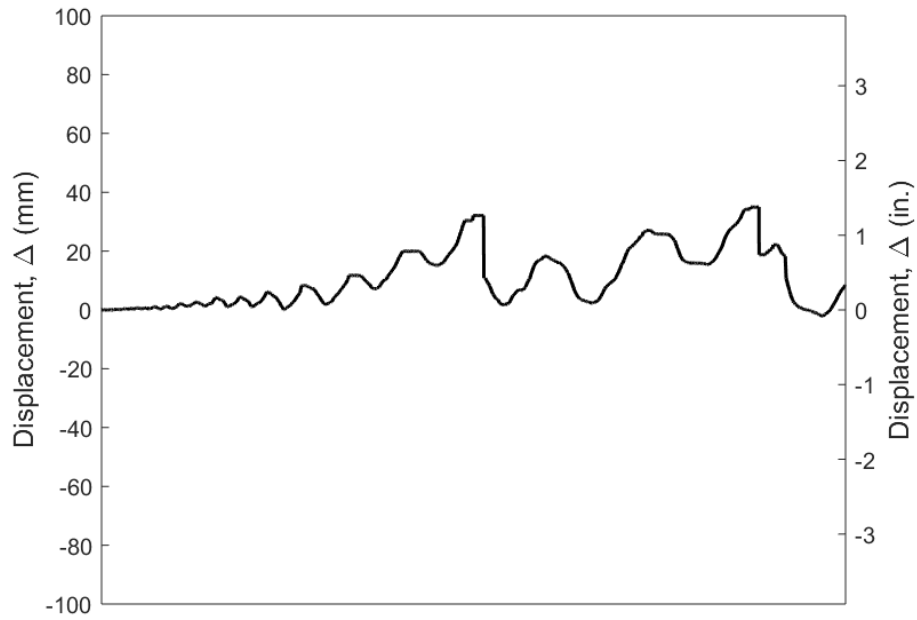


Fig. I-5: Floor 1 - Gage 5

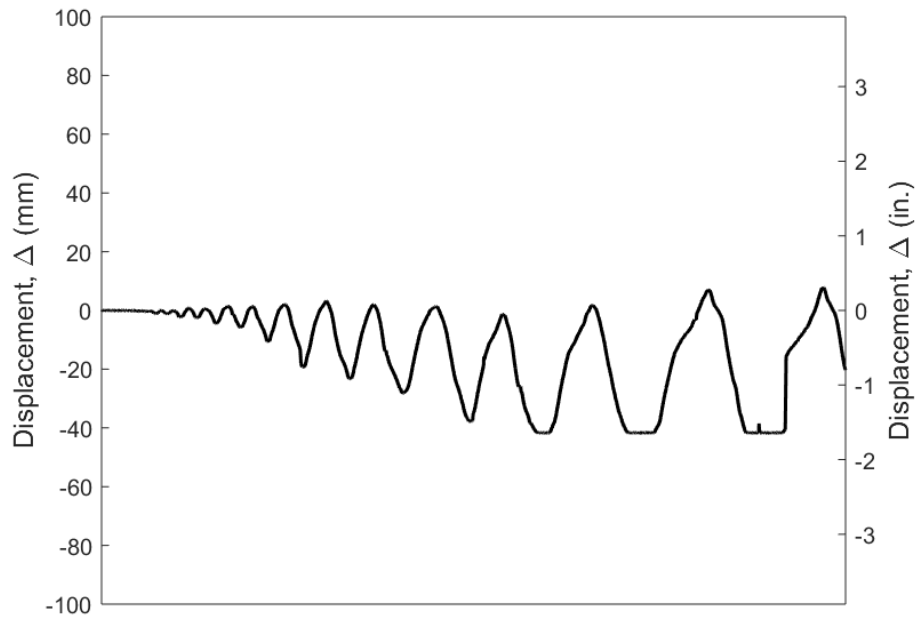


Fig. I-6: Floor 1 - Gage 6

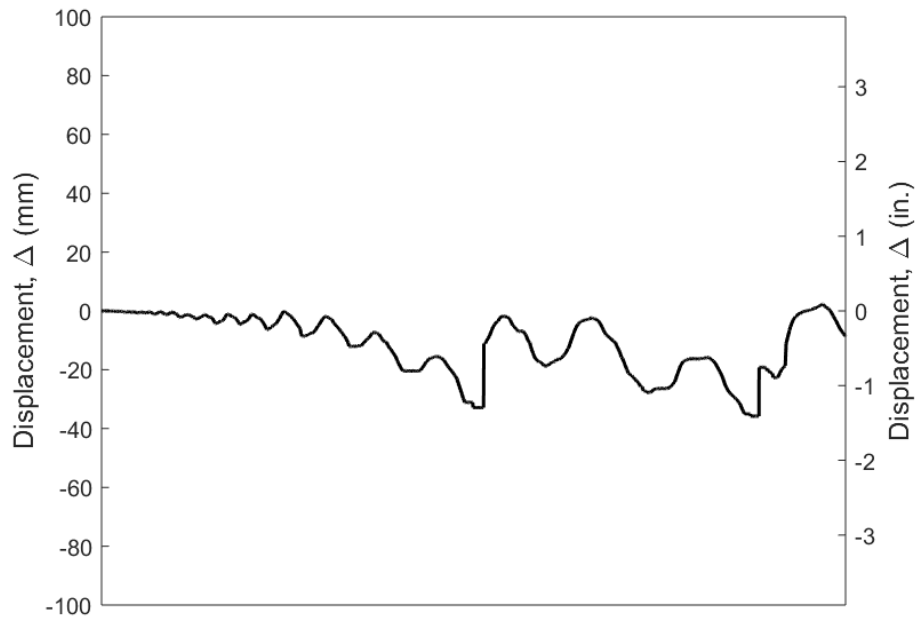


Fig. I-7: Floor 1 - Gage 7

APPENDIX J: Test Frame Shop Drawings

Table J-1. Test frame bill of materials

Name	Item	Length	Qty
Free side support	W16x67	1'	3
Columns	W14x90	3'	4
Girders	W14x90	17-10 9/16"	2
		26'	2
Kickers	W6x25	SEE DRAWINGS	5
Anchor channels	C12x30	6'	6
		8'	2
		9'-2"	4
		9'-6"	4
HSS supports	HSS 6x6x1/4	1'	2
Angle	L6x6x3/8	10"	24
	L4x4x5/8	8"	12
	L10x6x1/2	2'	42
Anchor plates	PL 110x14x1	-	2
	PL 114x14x1	-	2
	PL96x16.5x1	-	1
	PL72x9.5x1	-	3
Endplate	PL20x18x1	-	1
HSS endplates	PL 8x8x1/2	-	4
Plate Girder	PL18x48x1	-	2
	PL16x48x1	-	1
Web Stiffeners	PL13x7x1/2	SEE DRAWINGS	16
	PL16x8.5x1/2	SEE DRAWINGS	4

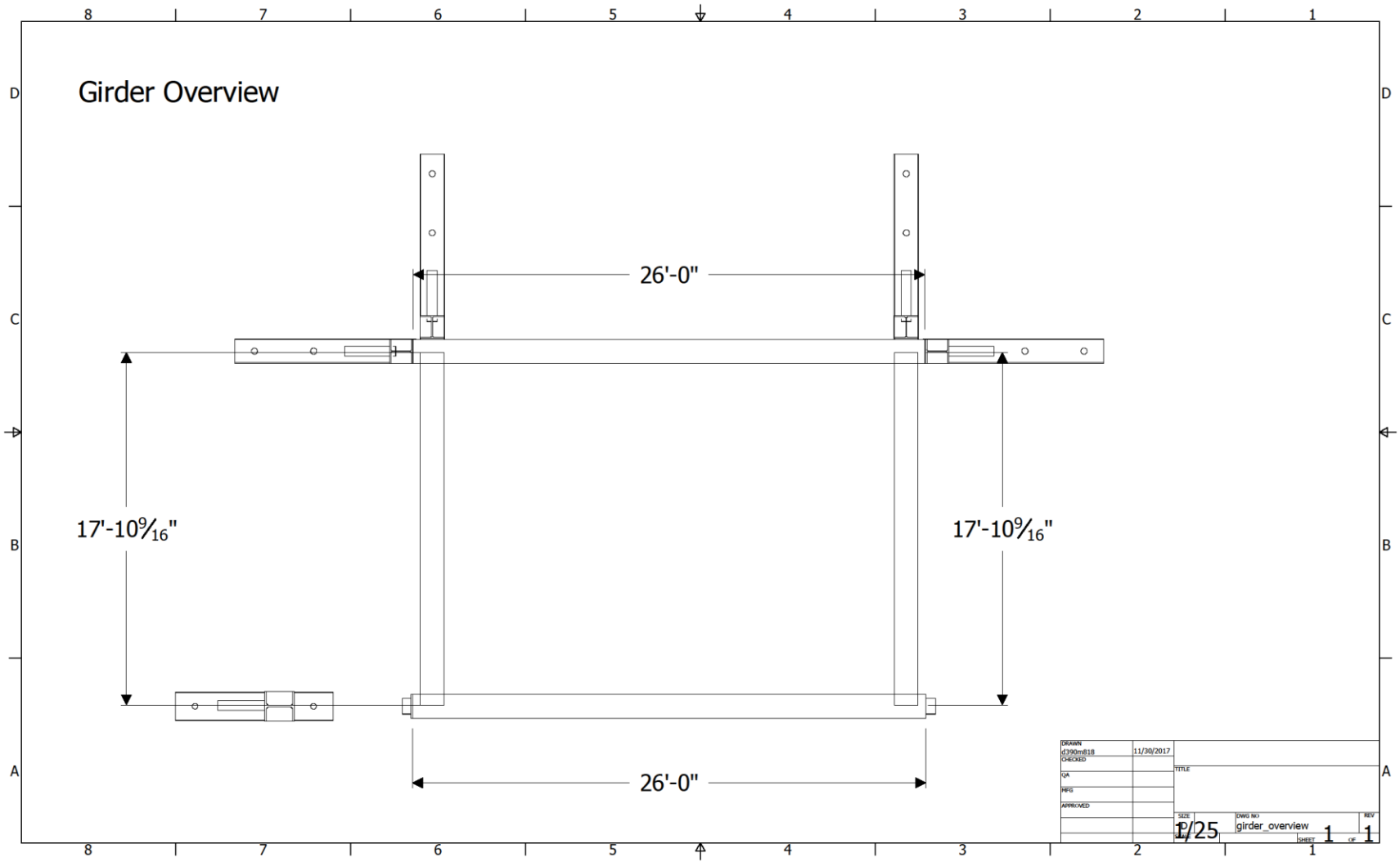


Fig. J-1. Test frame girder overview

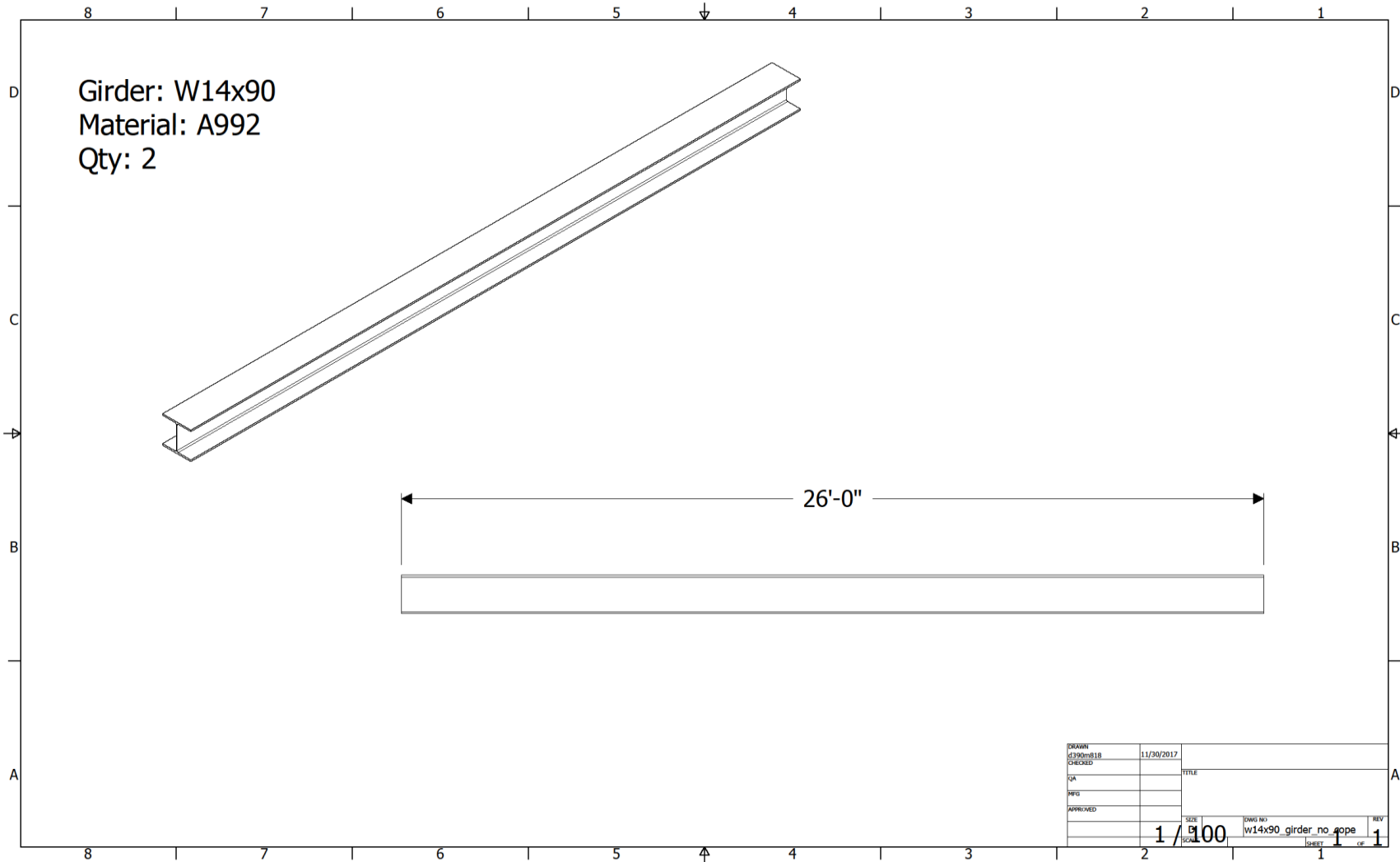


Fig. J-2. Test frame girder, longitudinal span

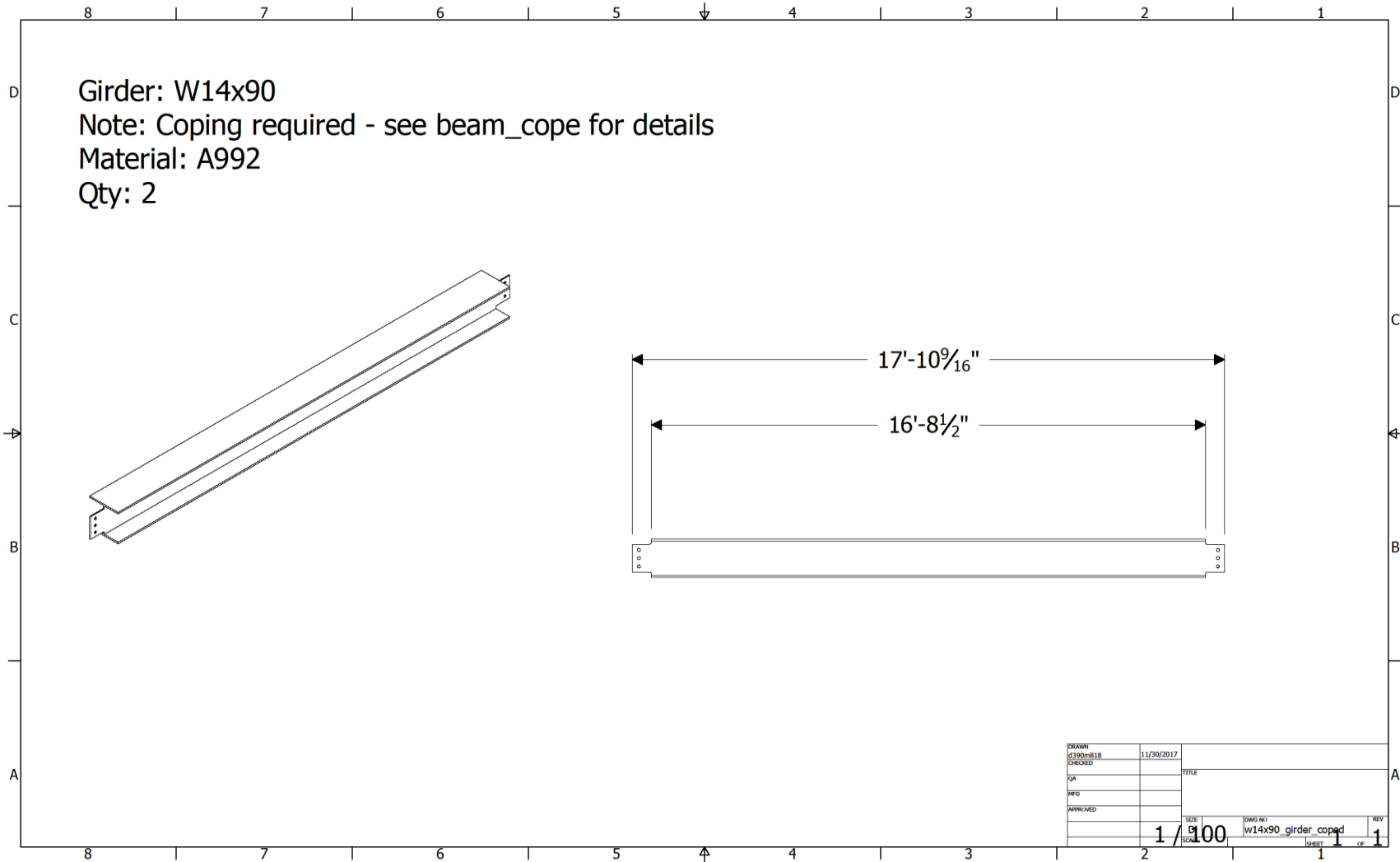


Fig. J-3. Coped girder

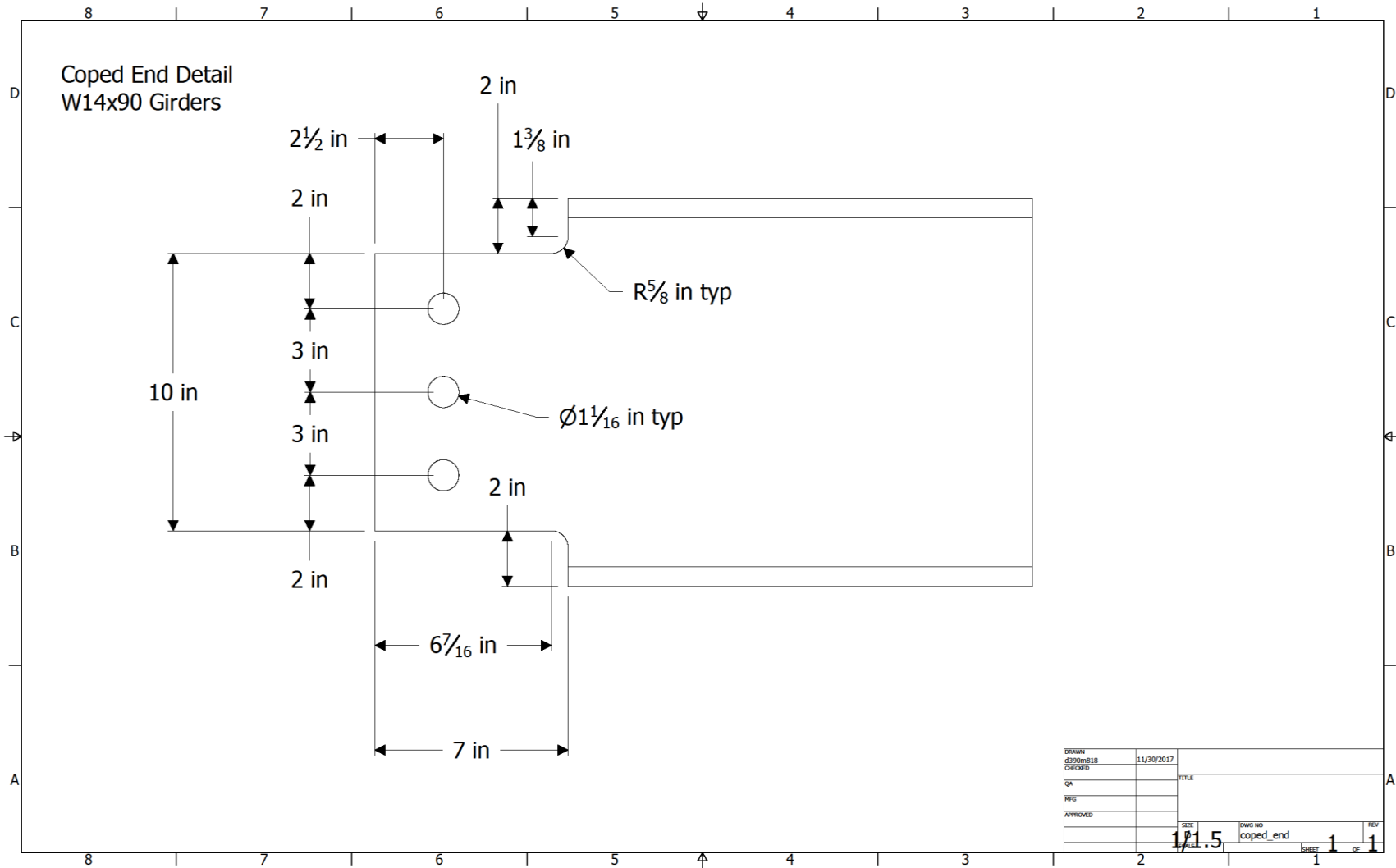


Fig. J-4. Coped end details

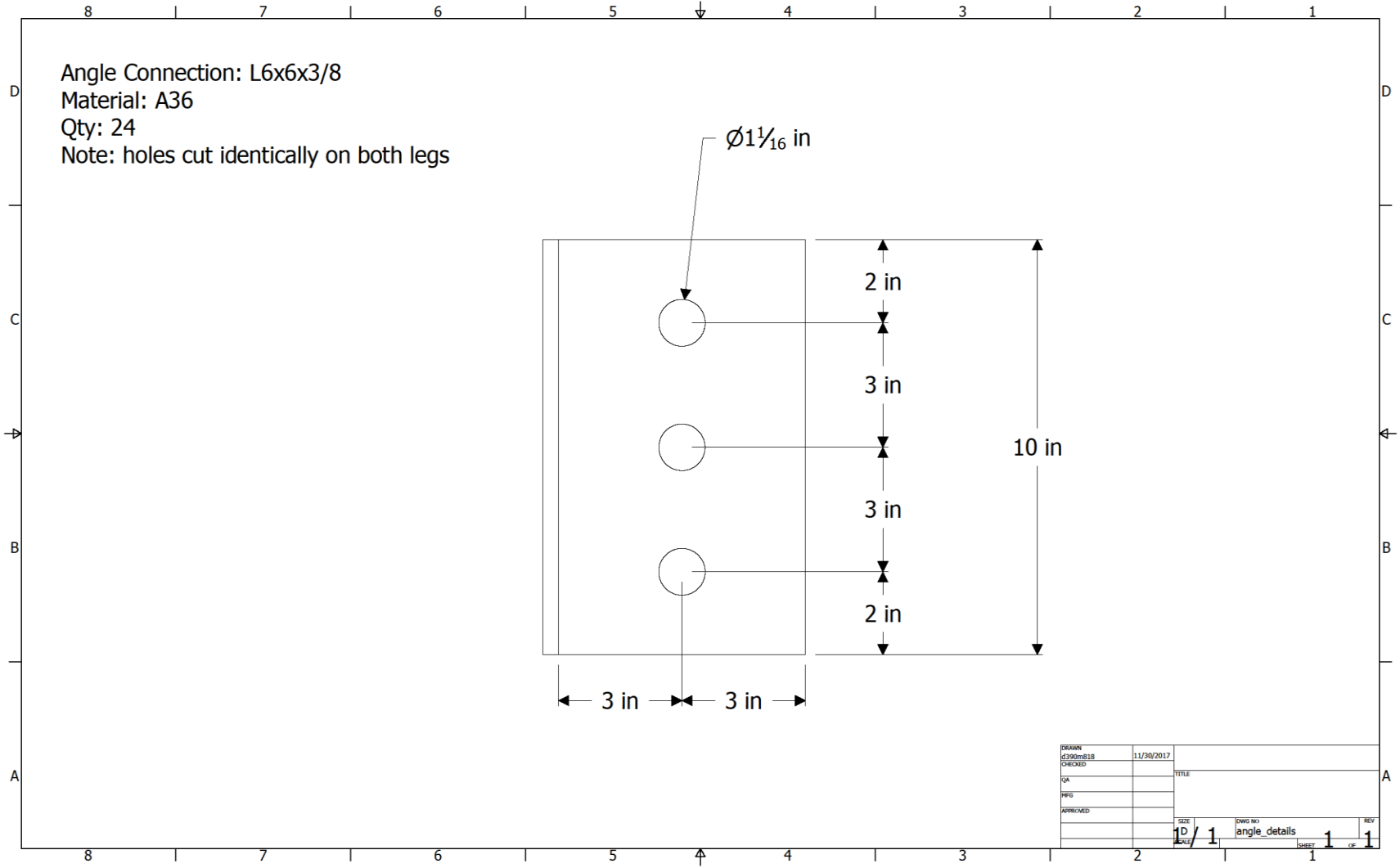


Fig. J-5. Angle connection details

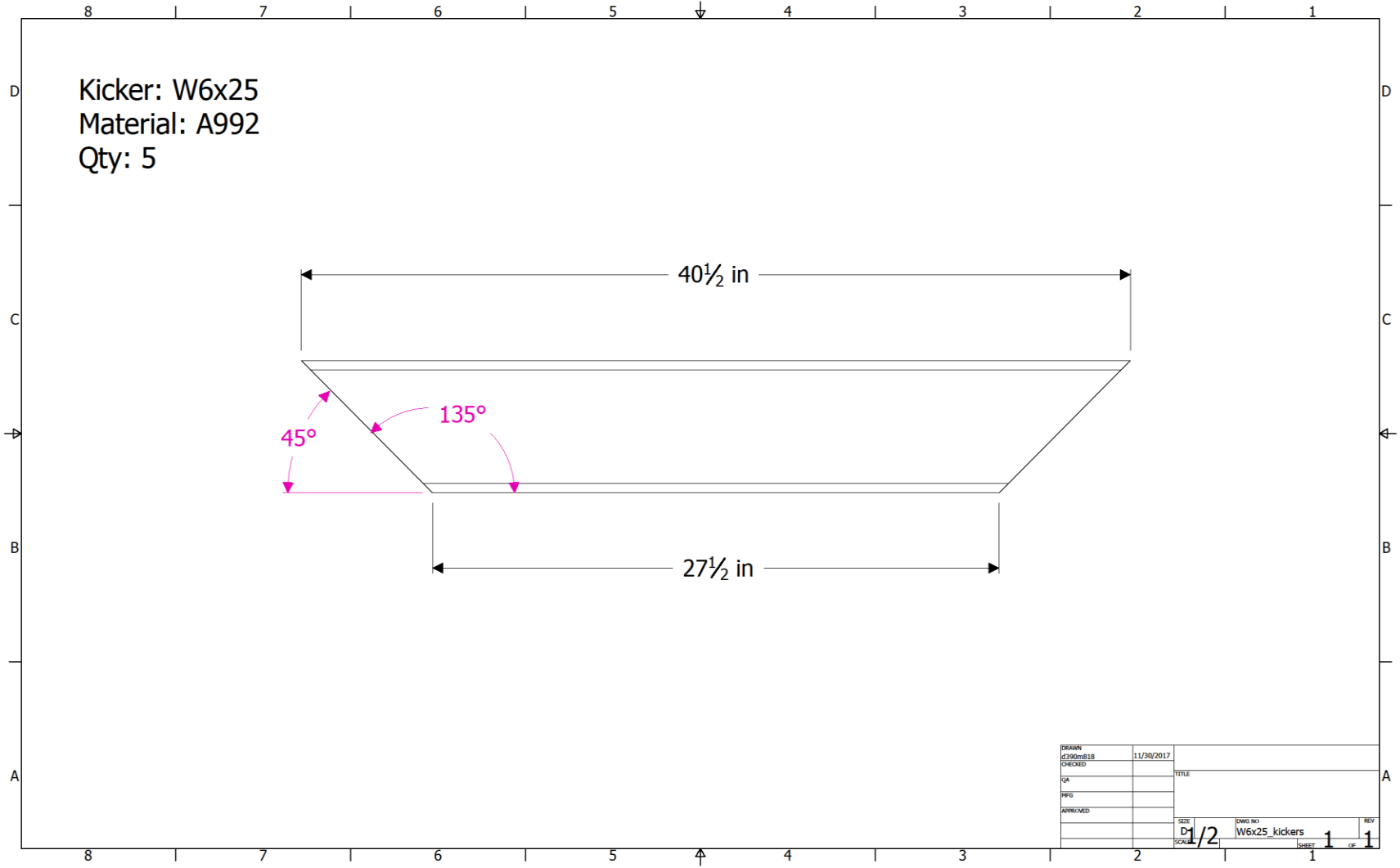


Fig. J-6. Brace kicker detail

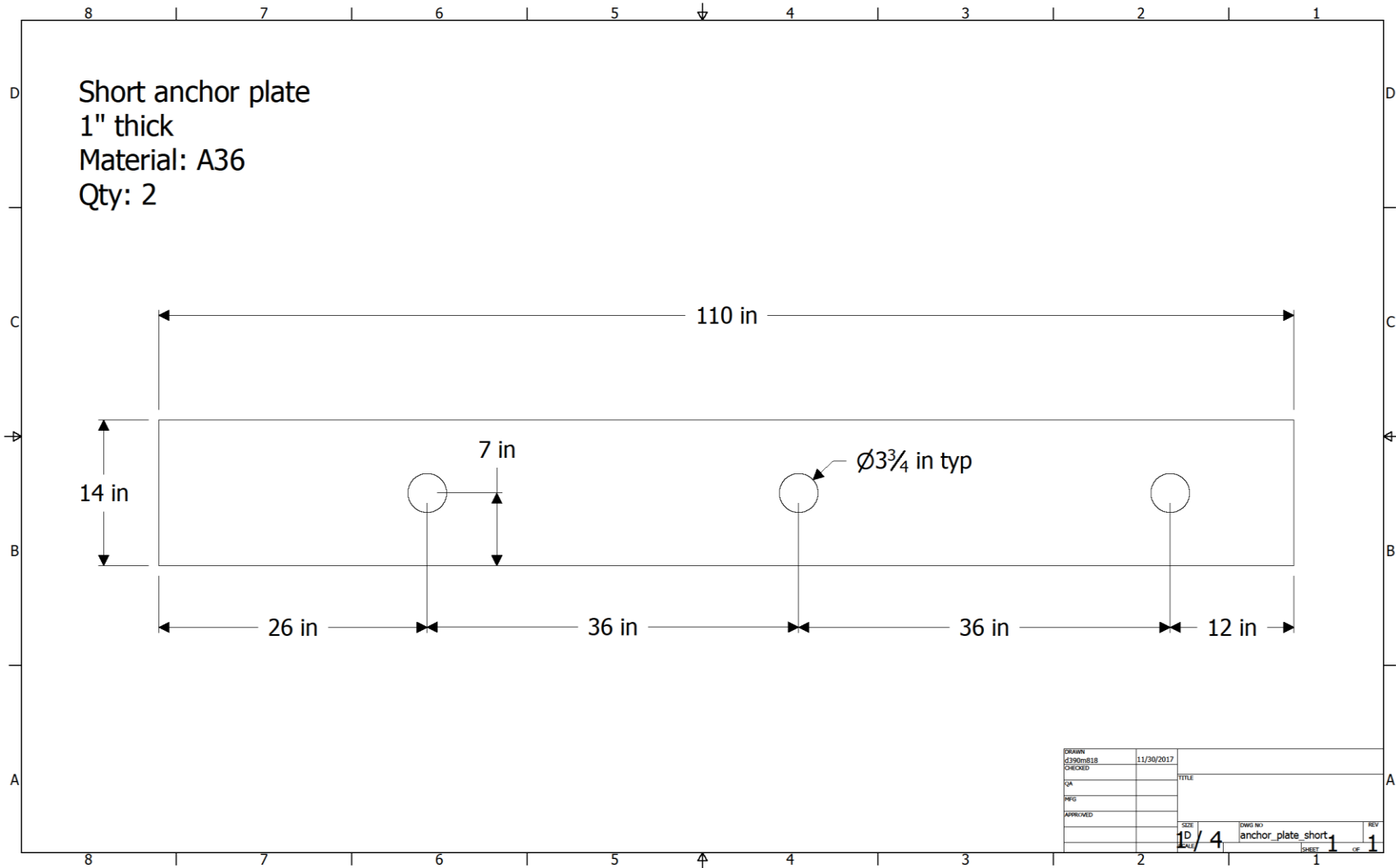


Fig. J-7. Brace type one anchor plate detail

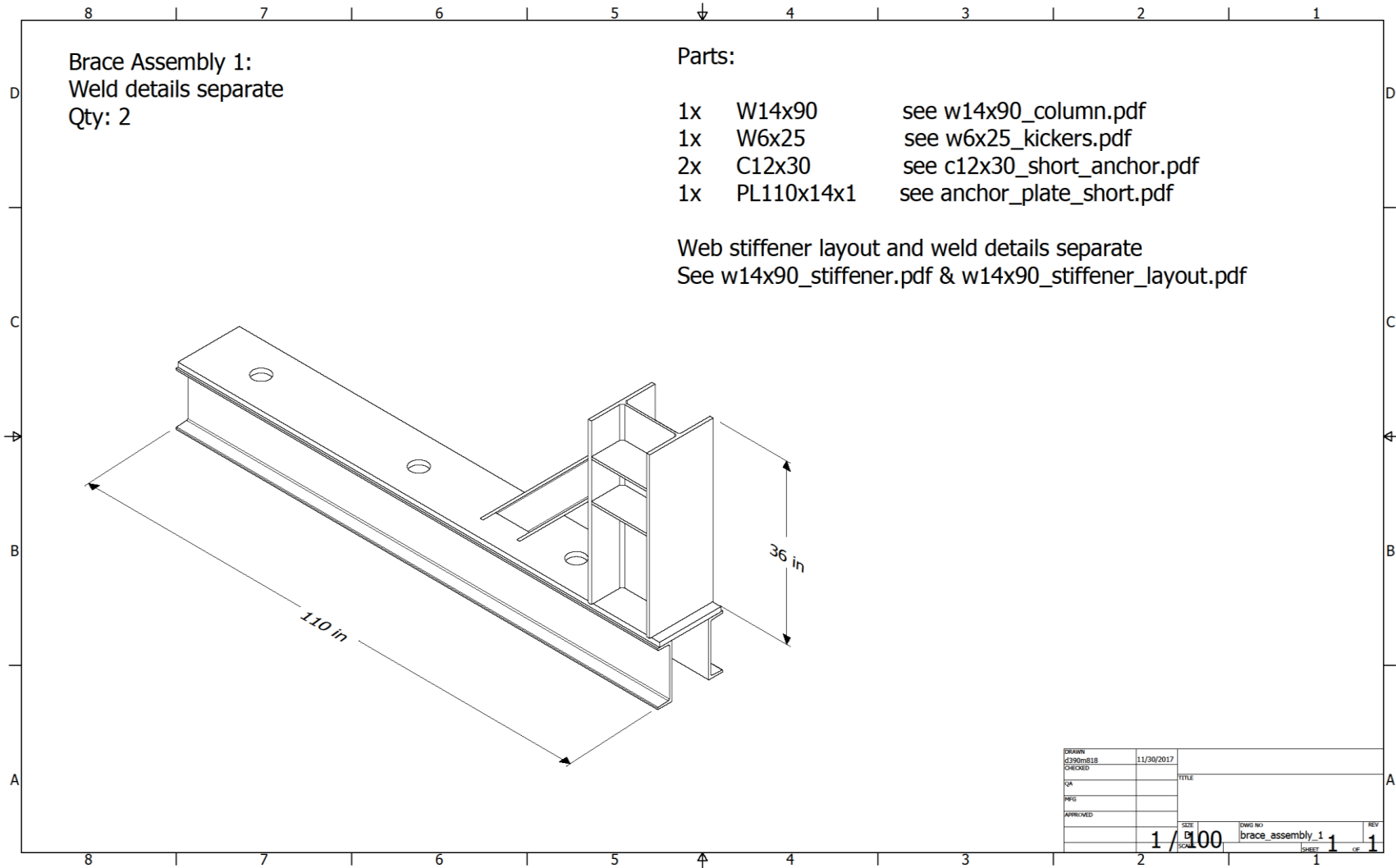


Fig. J-8. Brace type one assembly

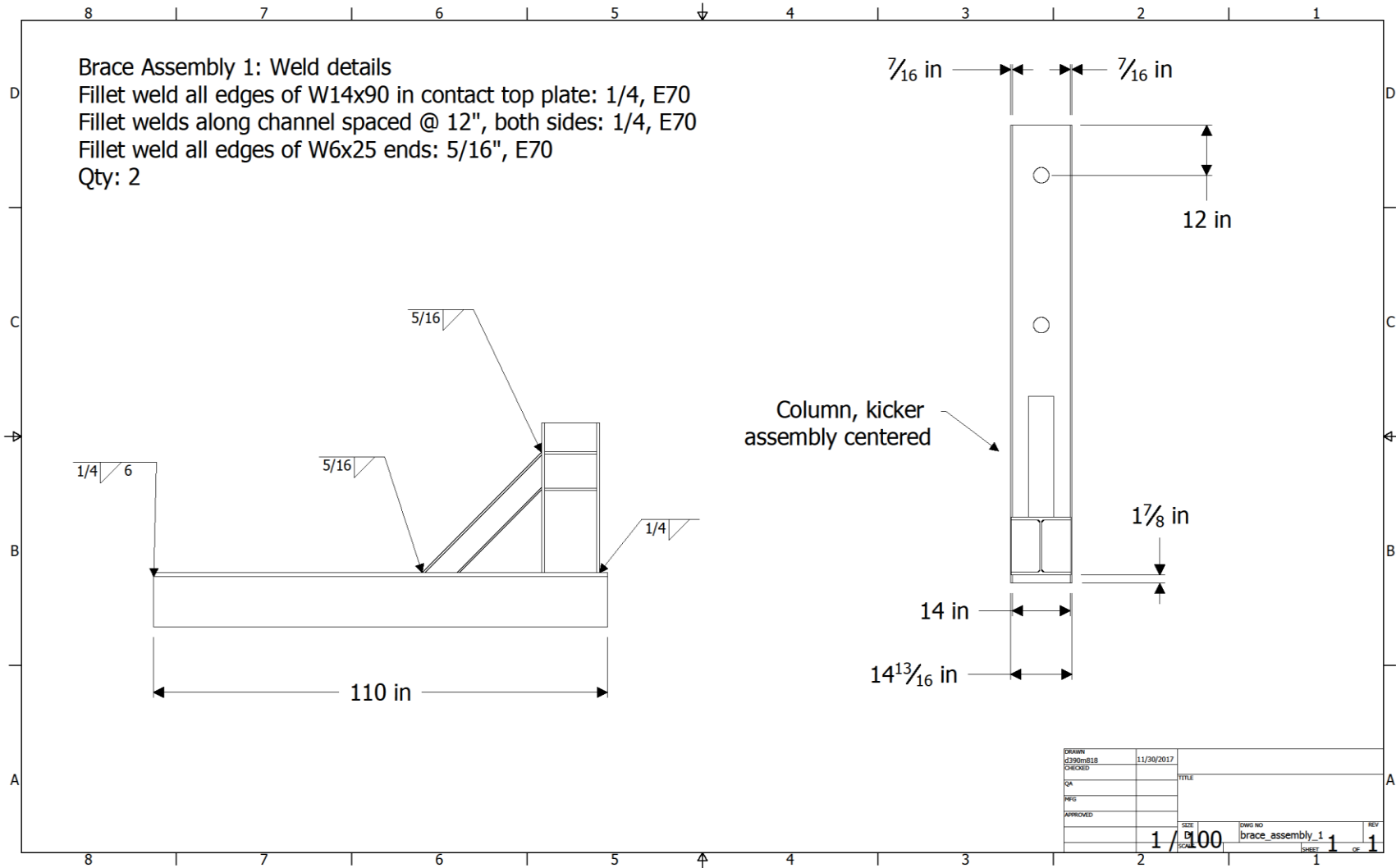


Fig. J-9. Brace type one assembly details

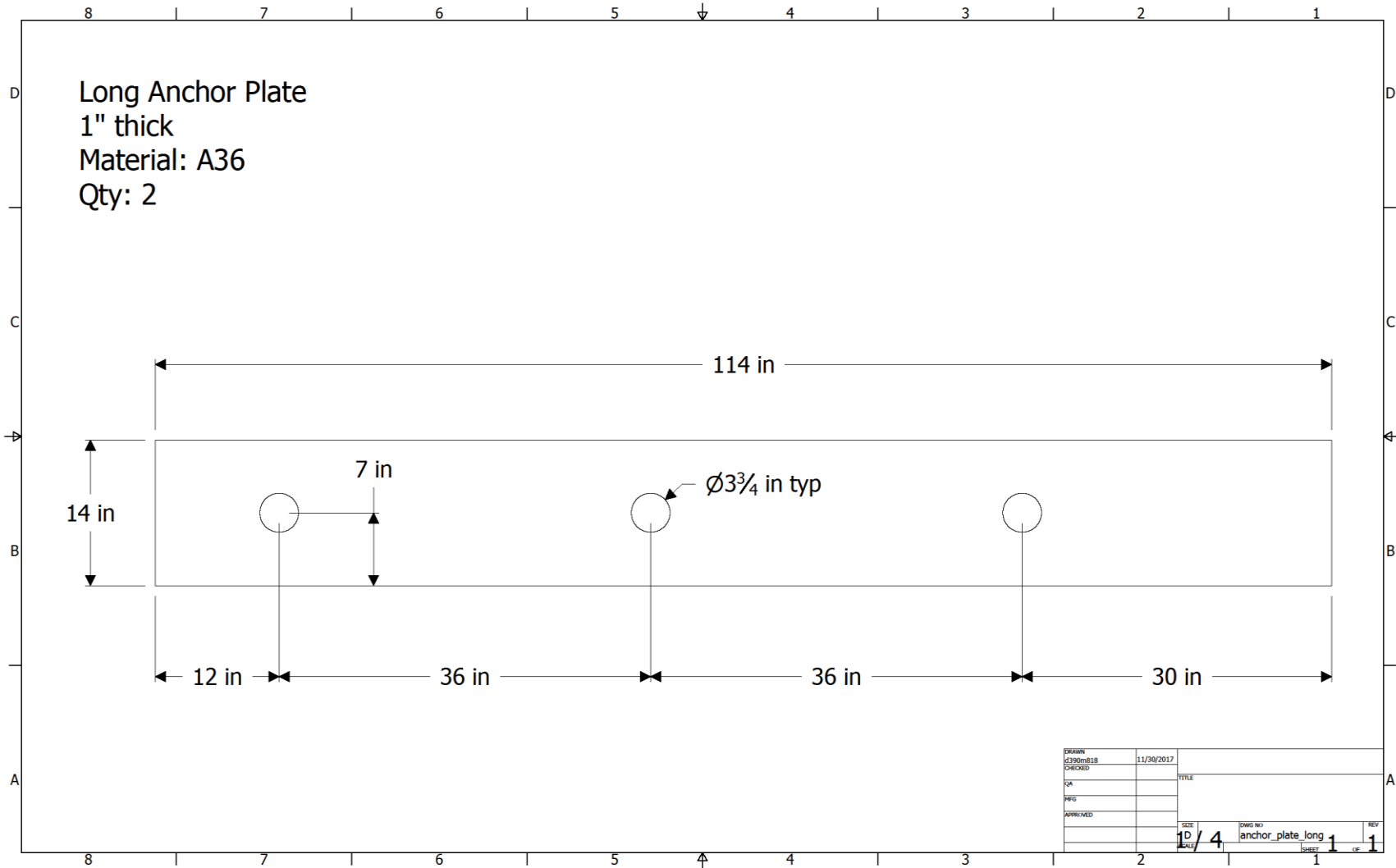


Fig. J-10. Brace type two anchor plate detail

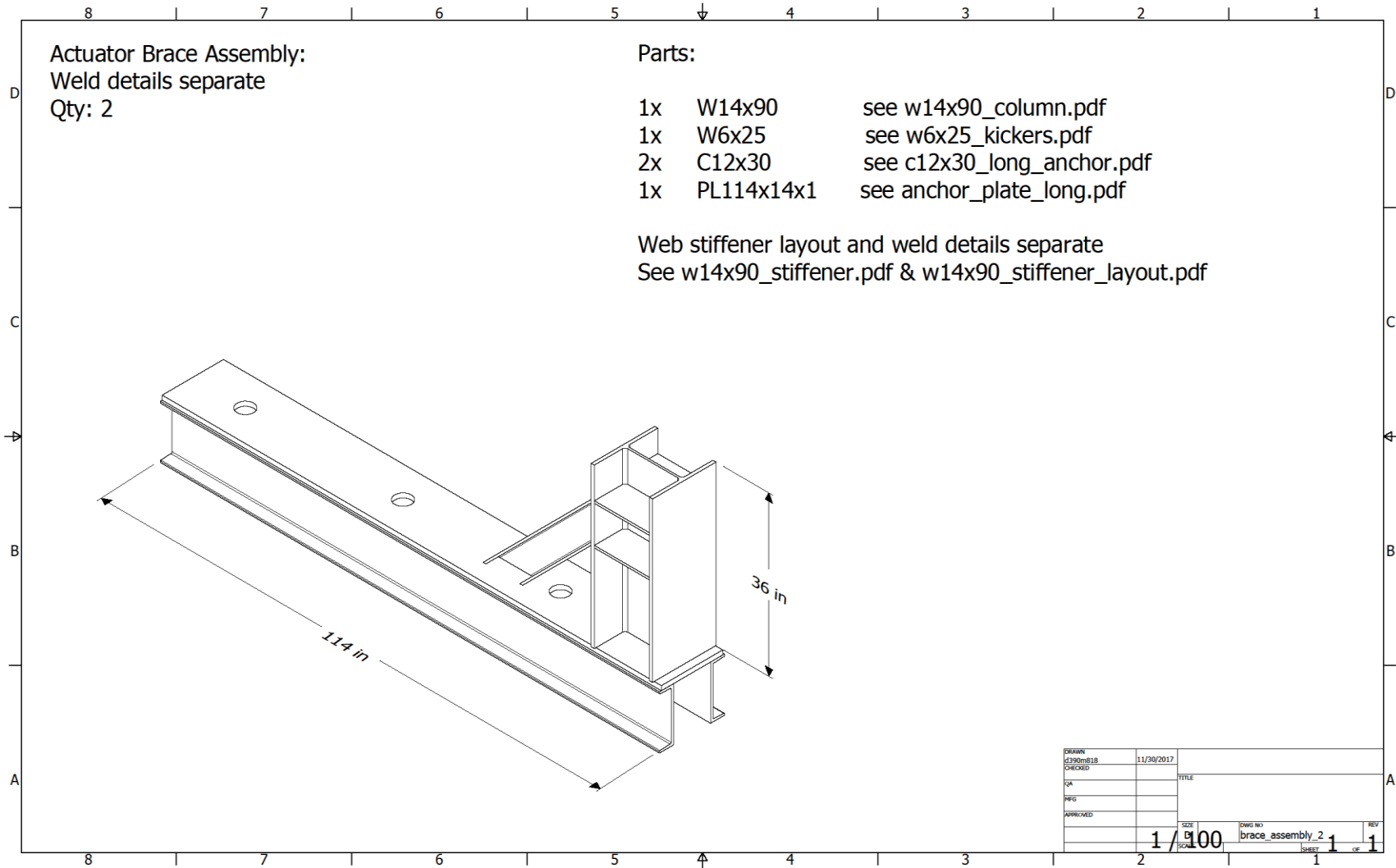


Fig. J-11. Brace type two assembly

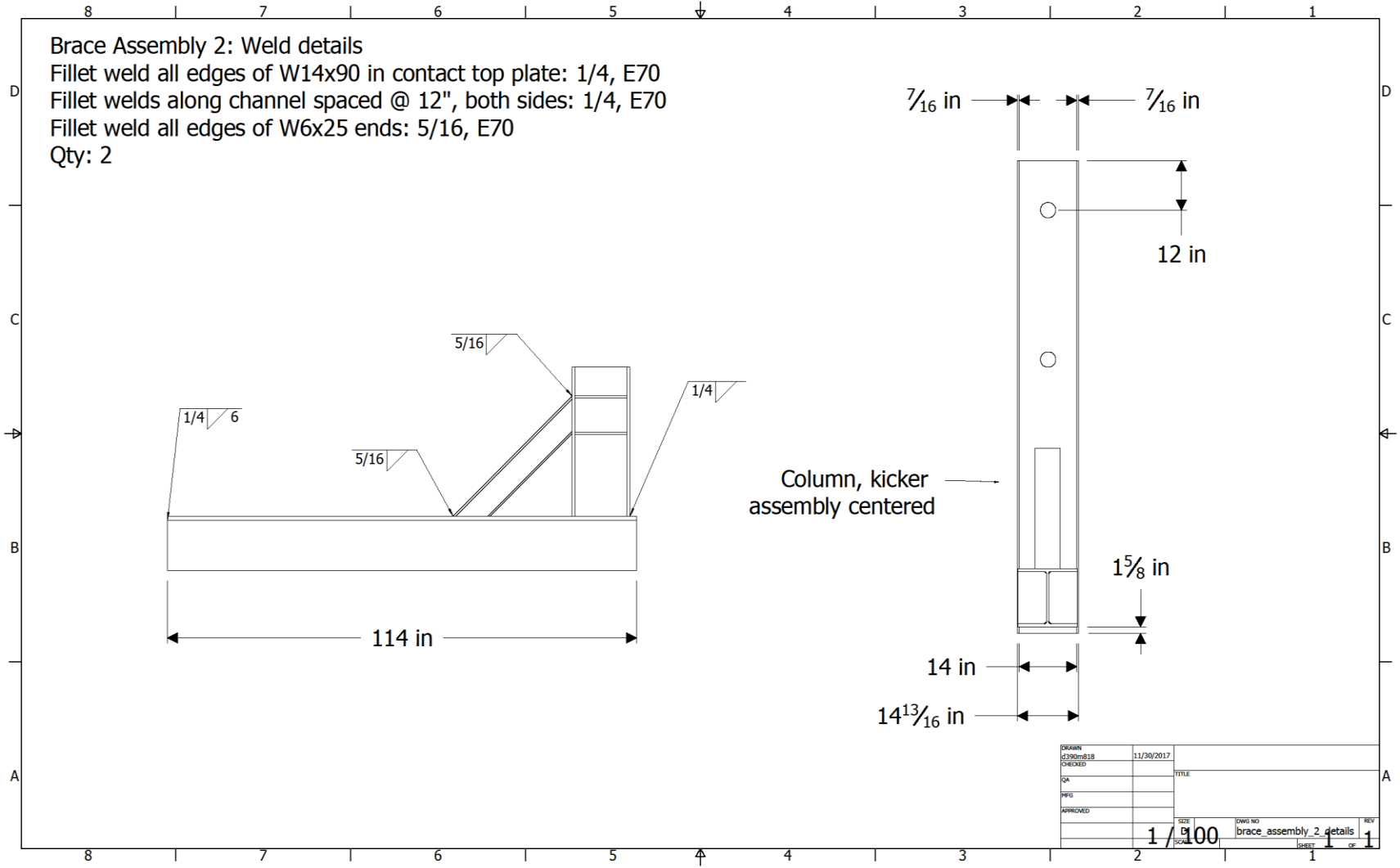


Fig. J-12. Brace type two assembly details

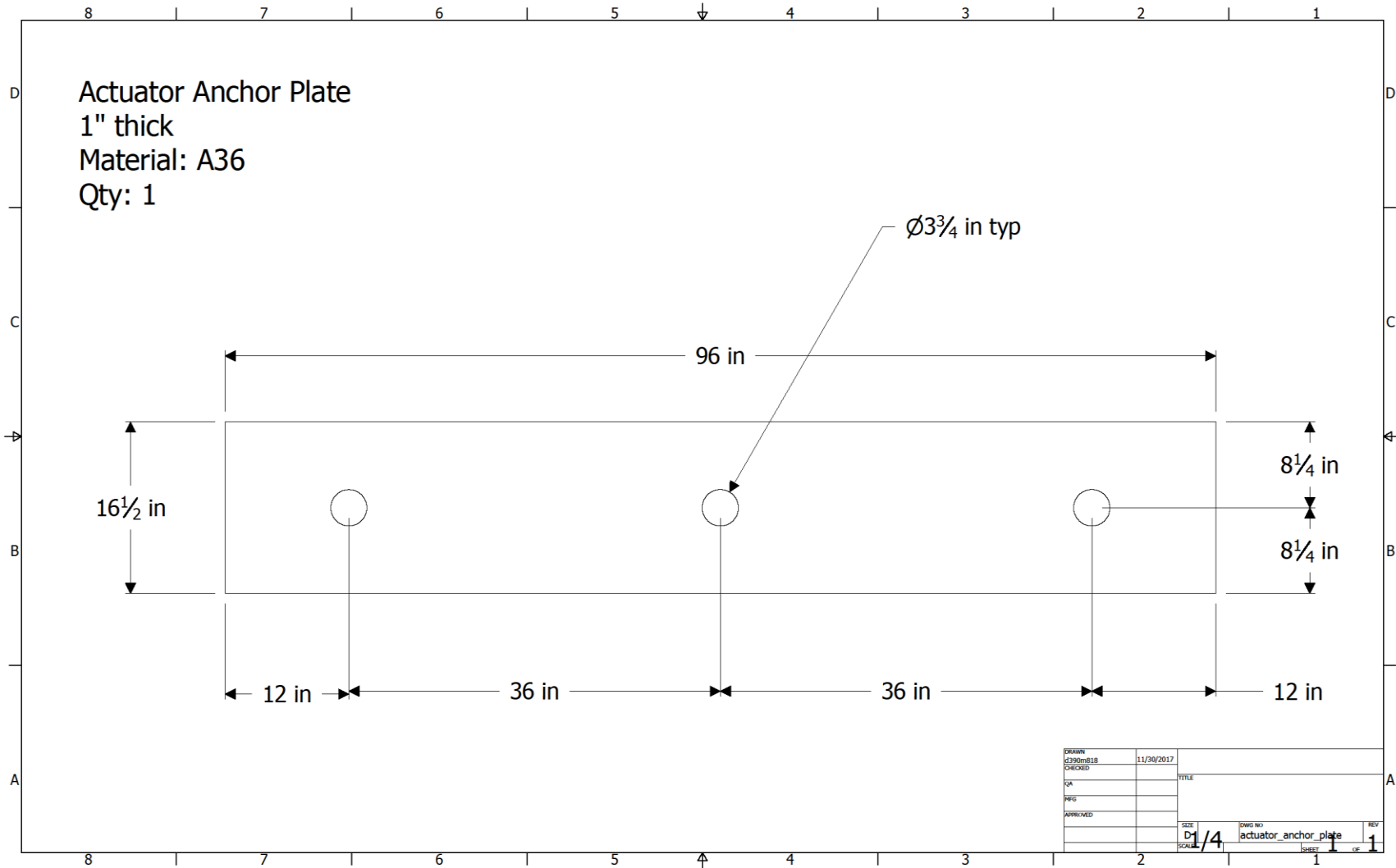


Fig. J-13. Actuator brace anchor plate detail

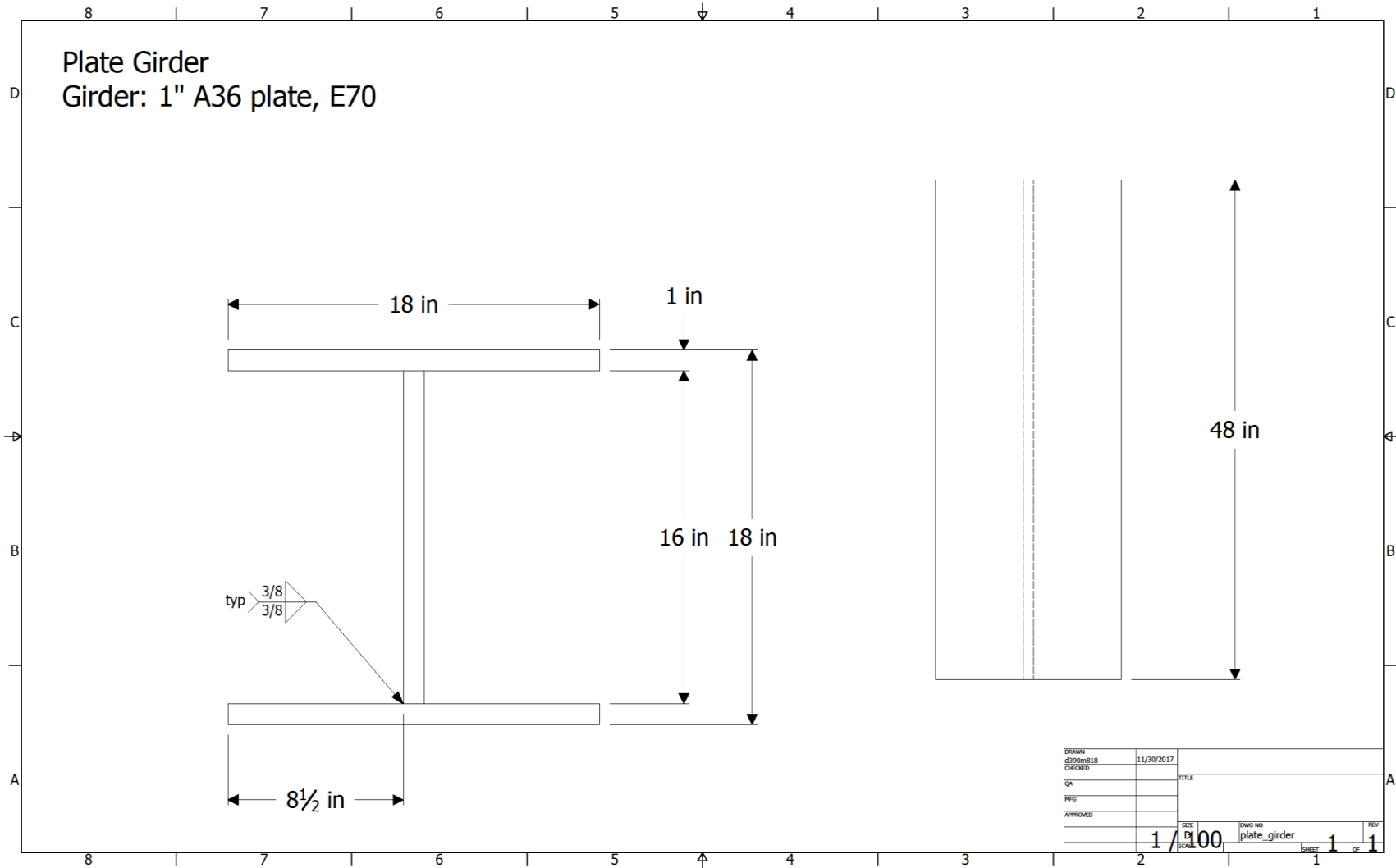


Fig. J-14. Actuator brace plate girder details

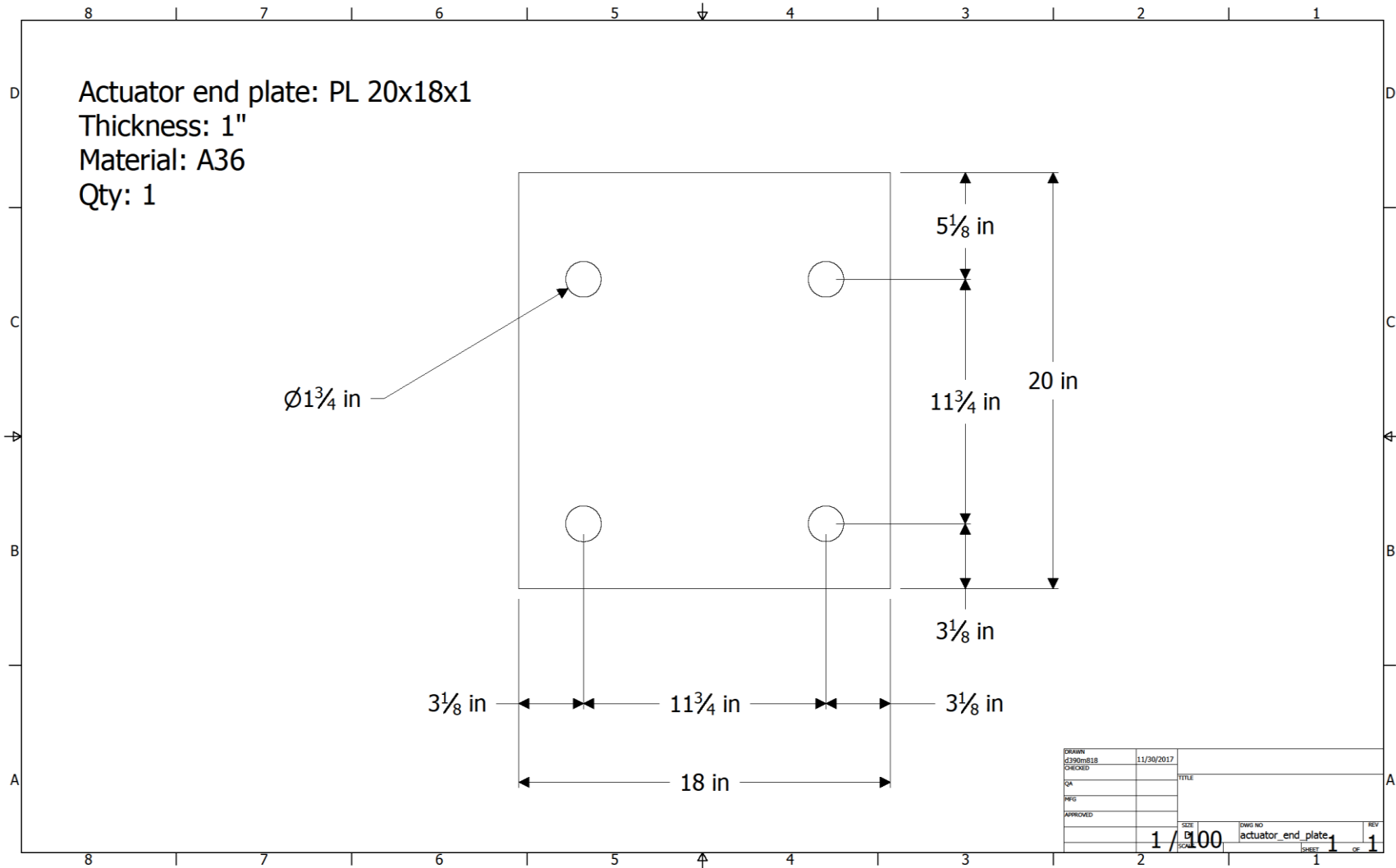
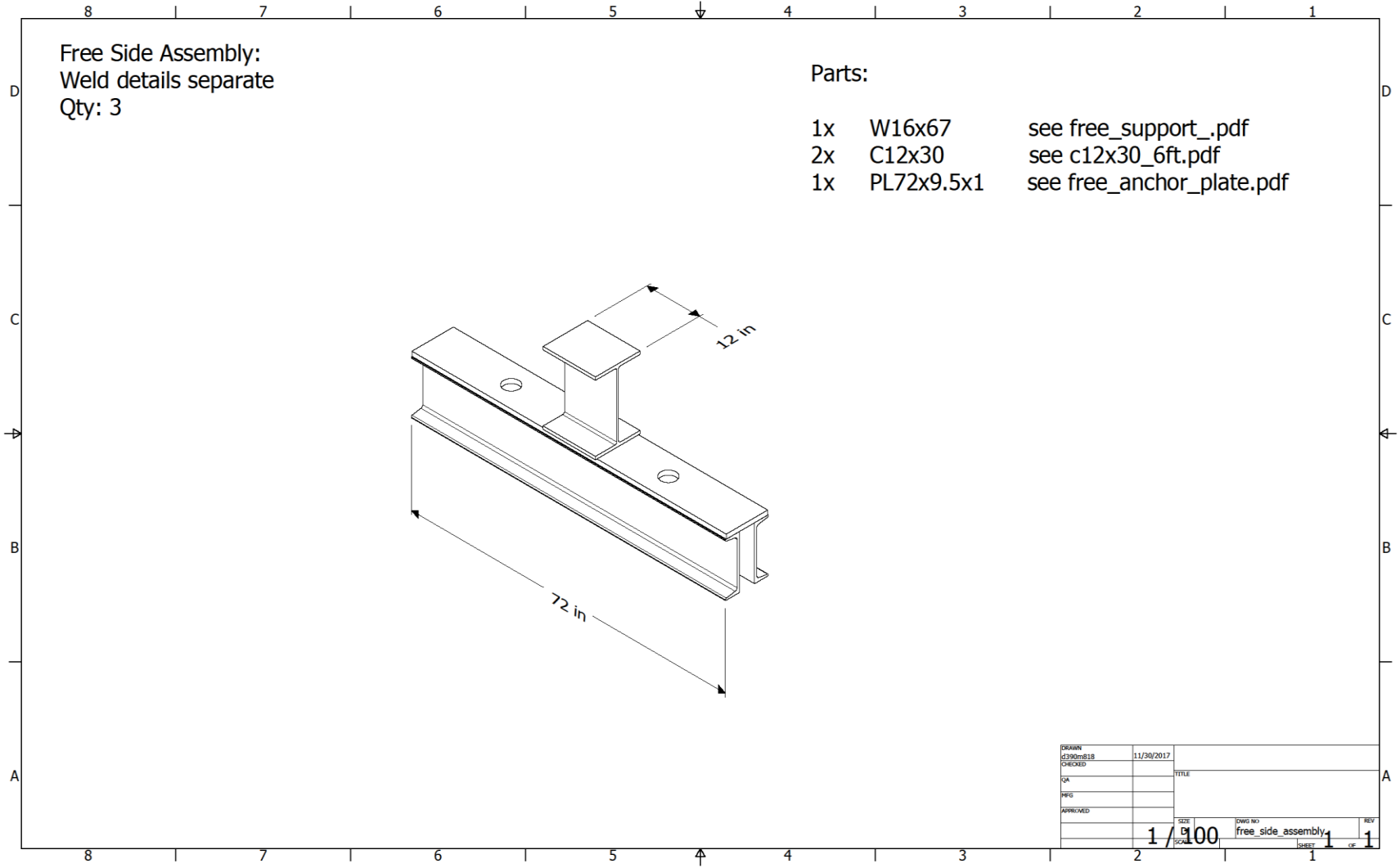


Fig. J-15. Actuator end plate detail



Free Side Assembly:
Weld details separate
Qty: 3

- Parts:
- 1x W16x67 see free_support_.pdf
 - 2x C12x30 see c12x30_6ft.pdf
 - 1x PL72x9.5x1 see free_anchor_plate.pdf

DESIGN	11/30/2017		
CHECKED		TITLE	
QA			
MFG			
APPROVED			
	SIZE	DWG NO	REV
	1/100	free_side_assembly	1
	SCALE	SHEET	1 of 1

Fig. J-16. Bearing support

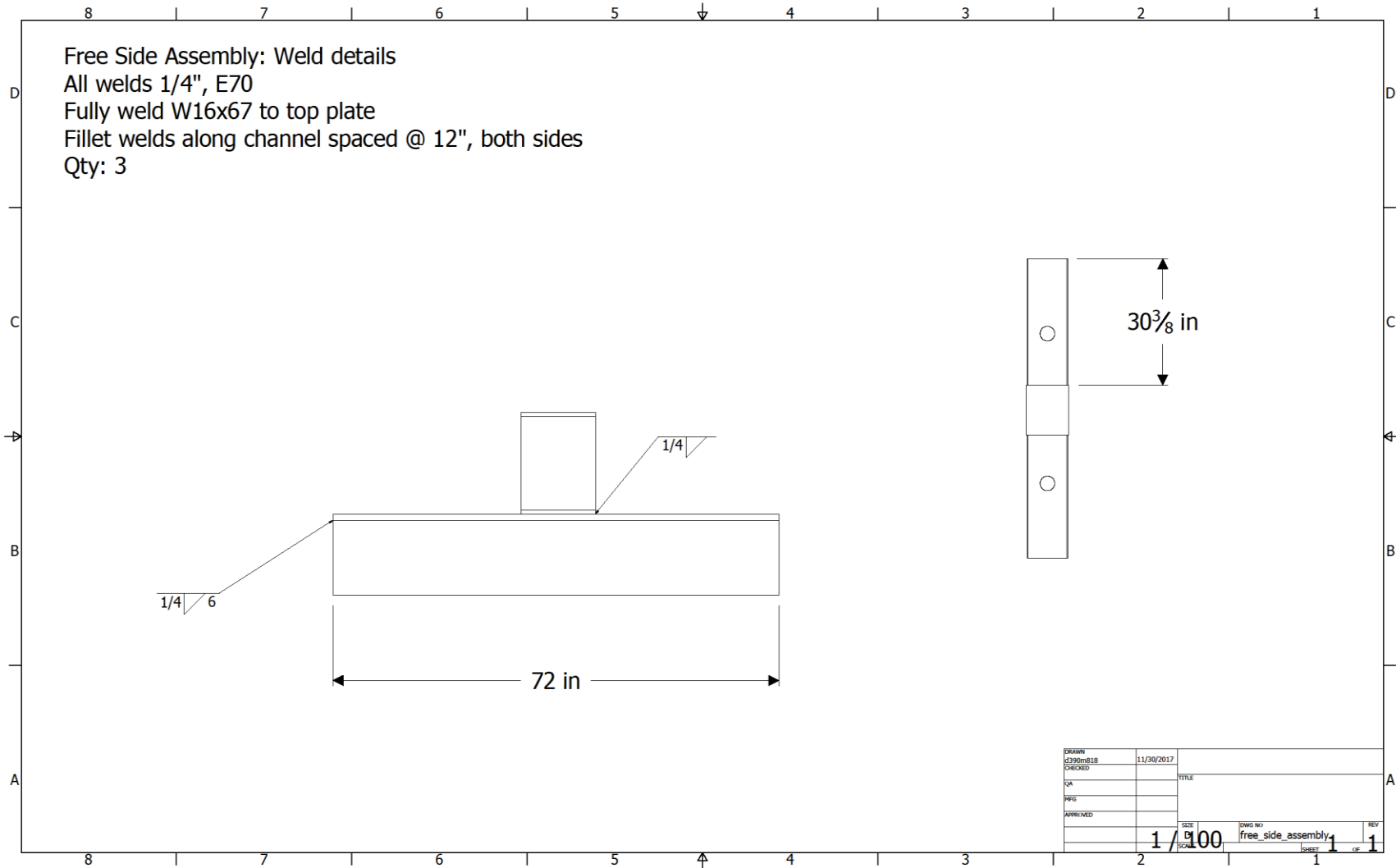


Fig. J-17. Bearing support assembly details

Chapter 9: APPENDIX K: Test Frame Construction Photos



Fig. K-1. Typical brace assembly



Fig. K-2. Bearing support assembly



Fig. K-3. Actuator brace assembly



Fig. K-4. Constructed test frame

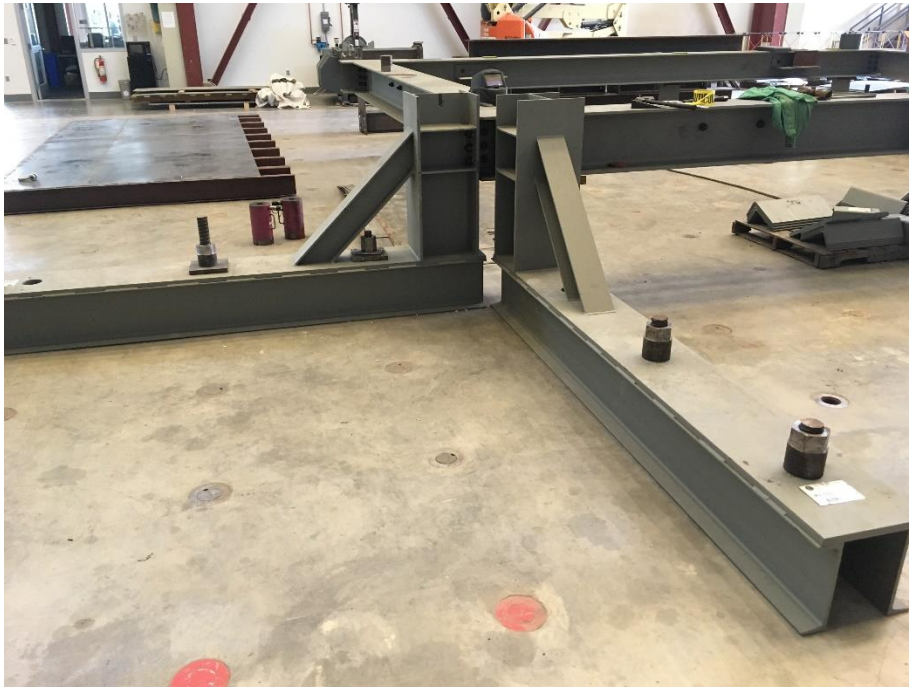


Fig. K-5. Brace support detail

APPENDIX L: Floor Fabrication Drawings

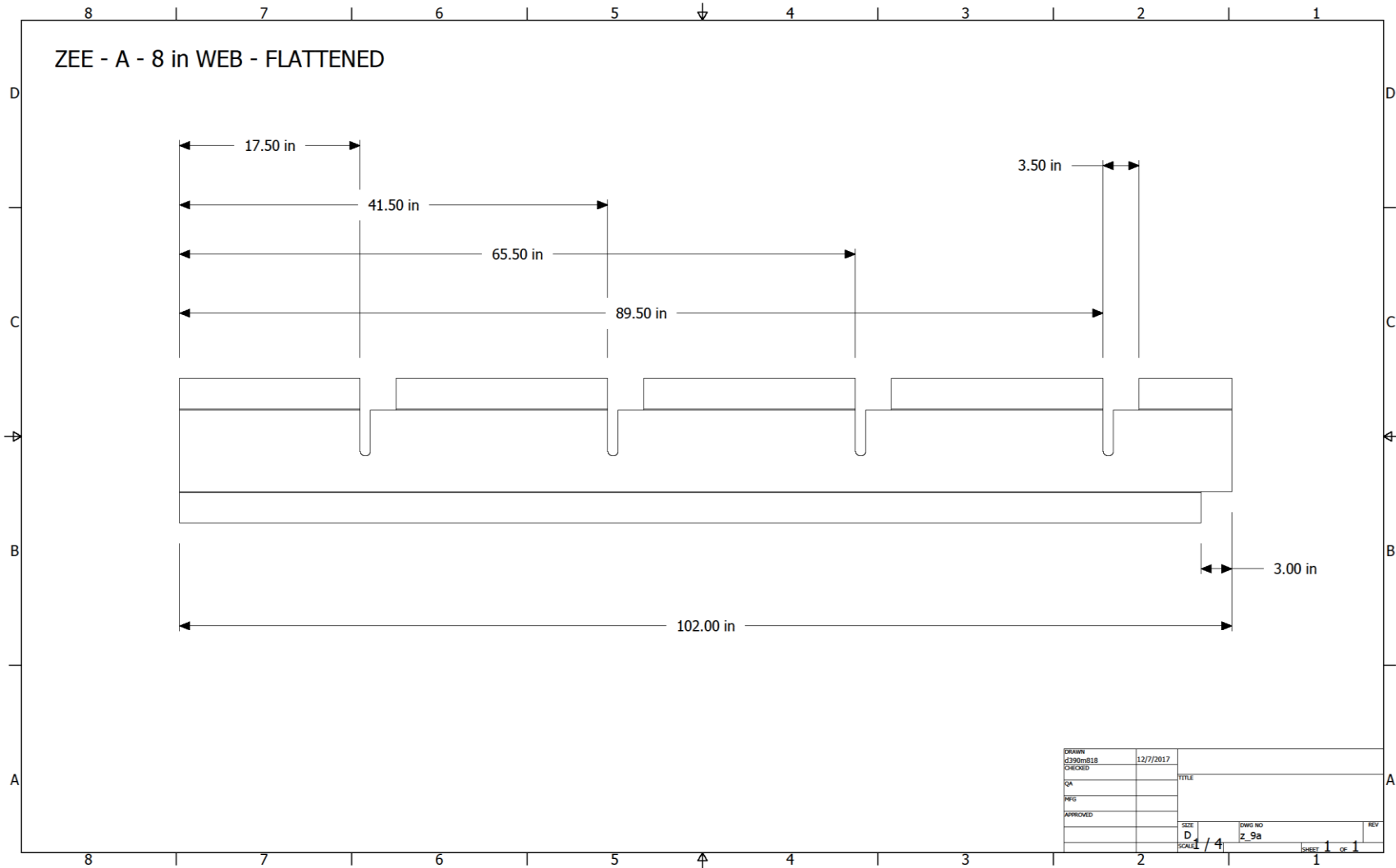


Fig. L-1. Typical purlin torching pattern for edge panel type A

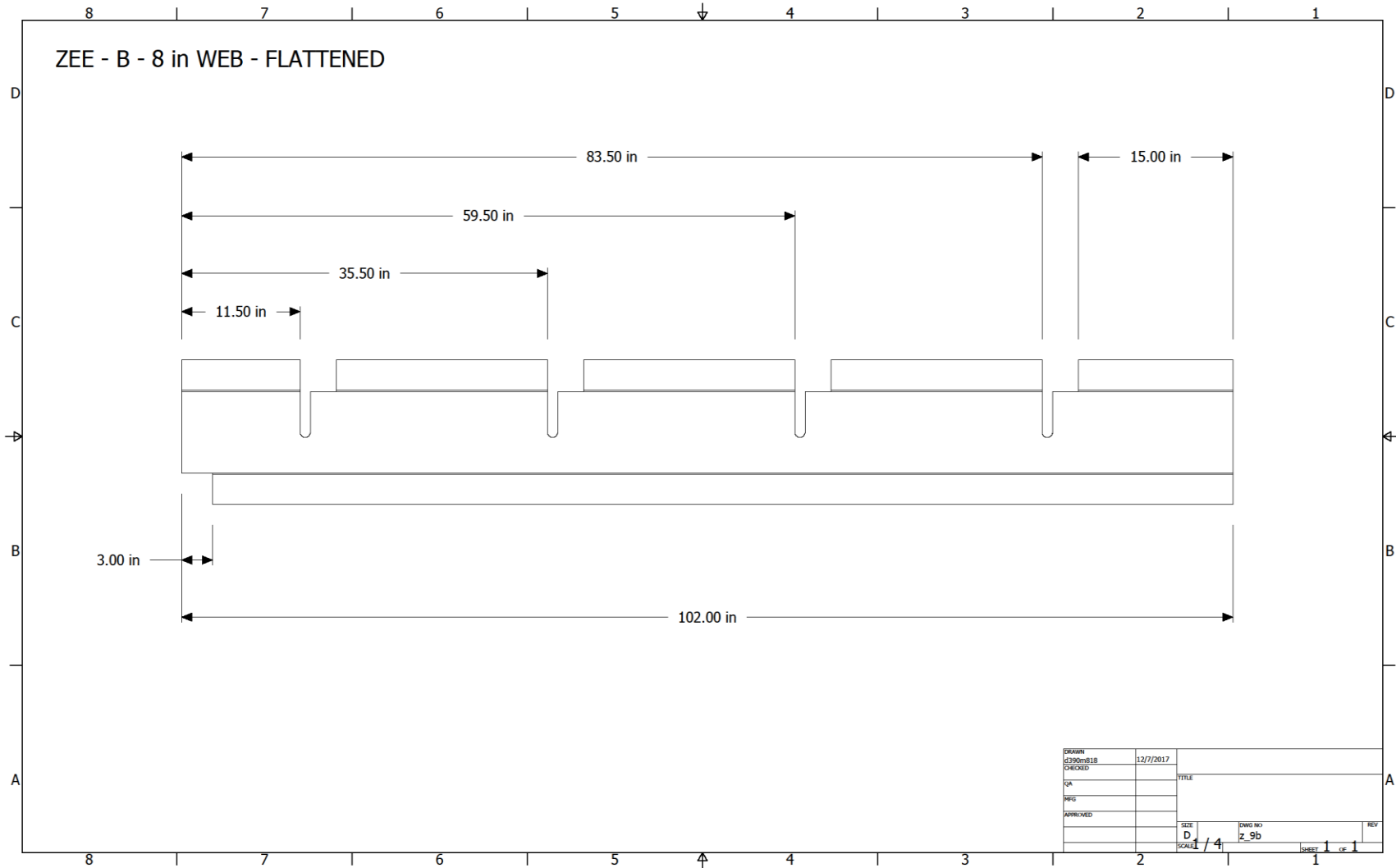


Fig. L-1. Typical purlin torching pattern for edge panel type B

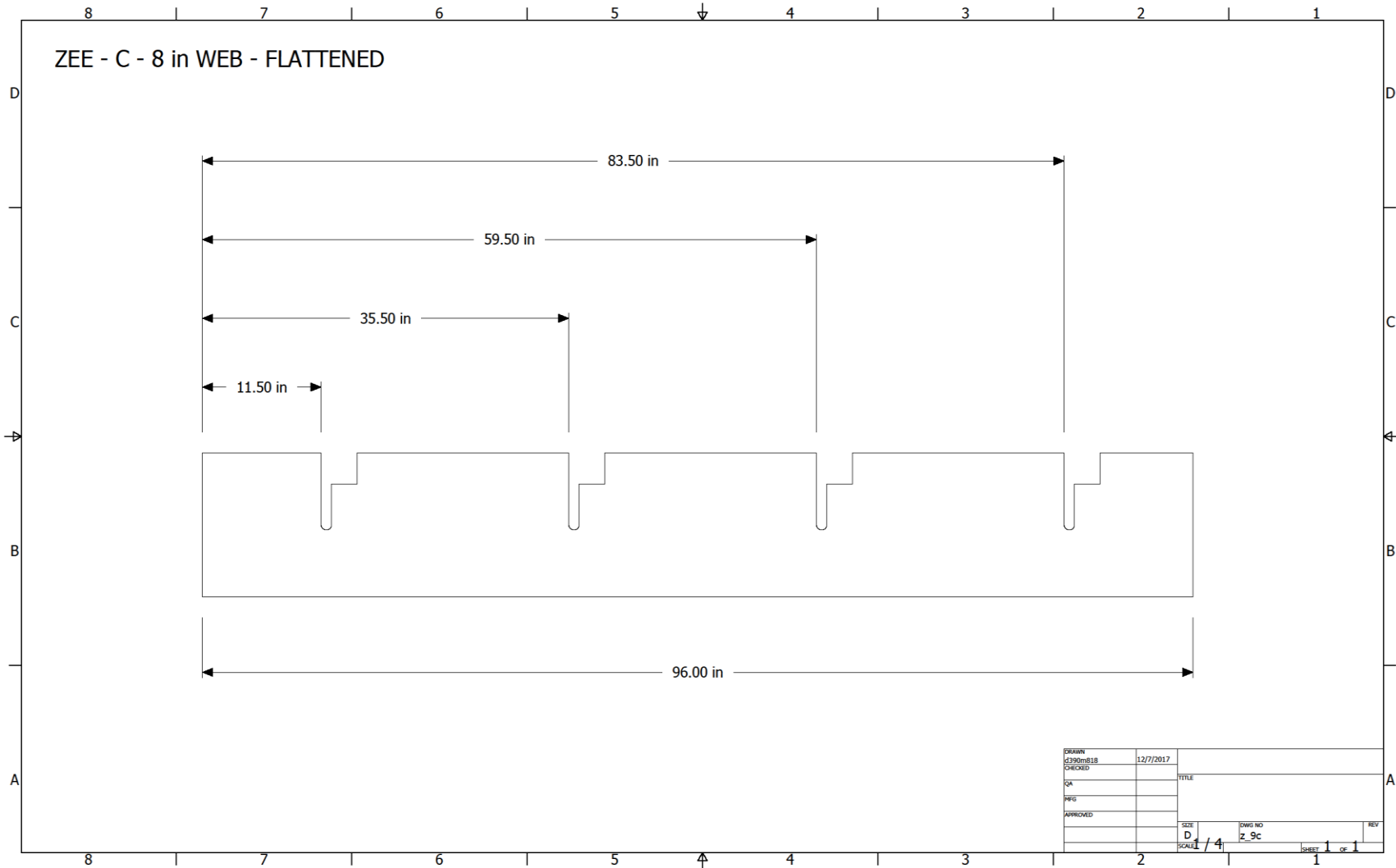


Fig. L-2. Typical purlin torching pattern for edge panel type C

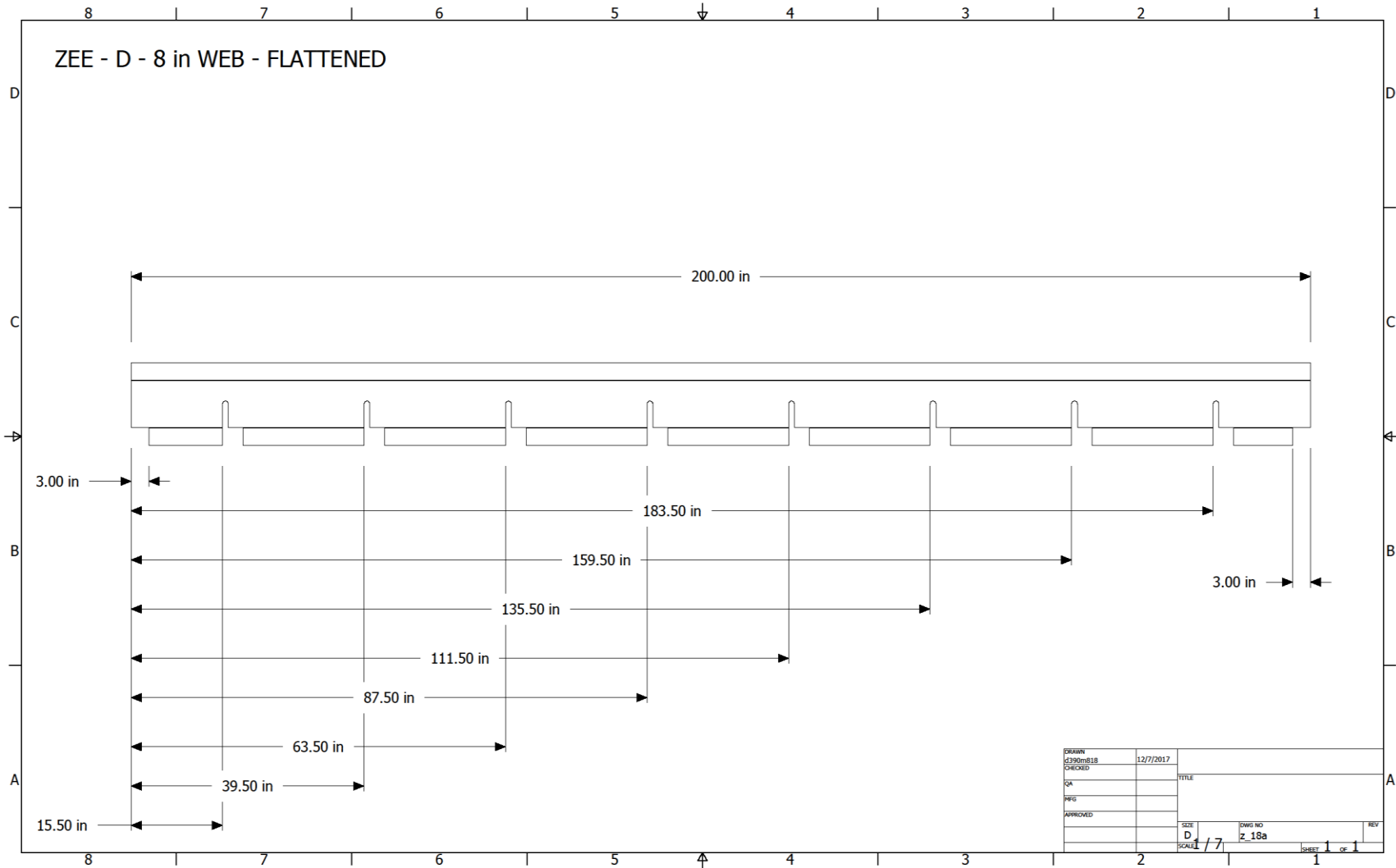


Fig. L-3. Typical torching pattern for transverse purlins in all panels

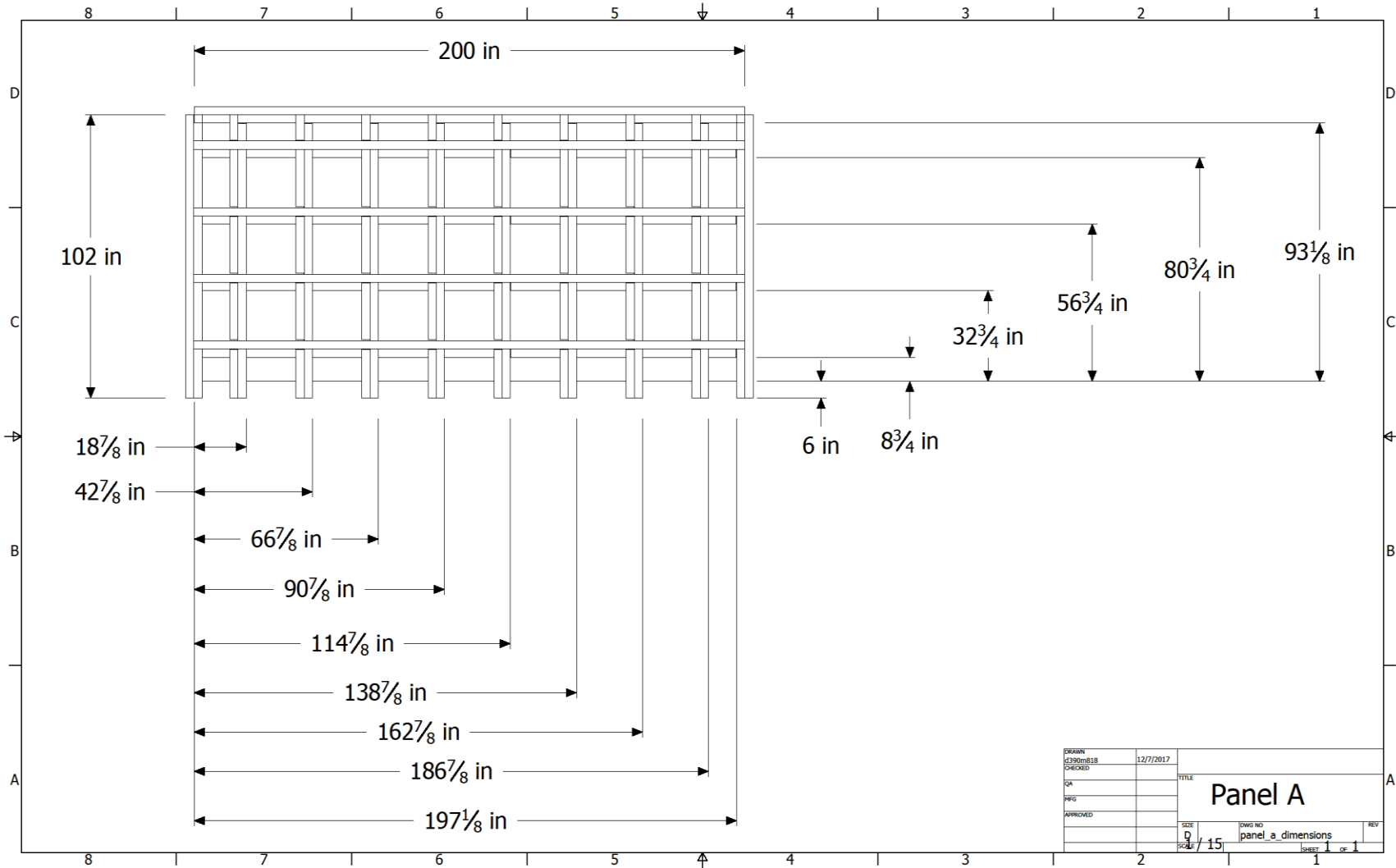


Fig. L-4. Purlin layout Panel A

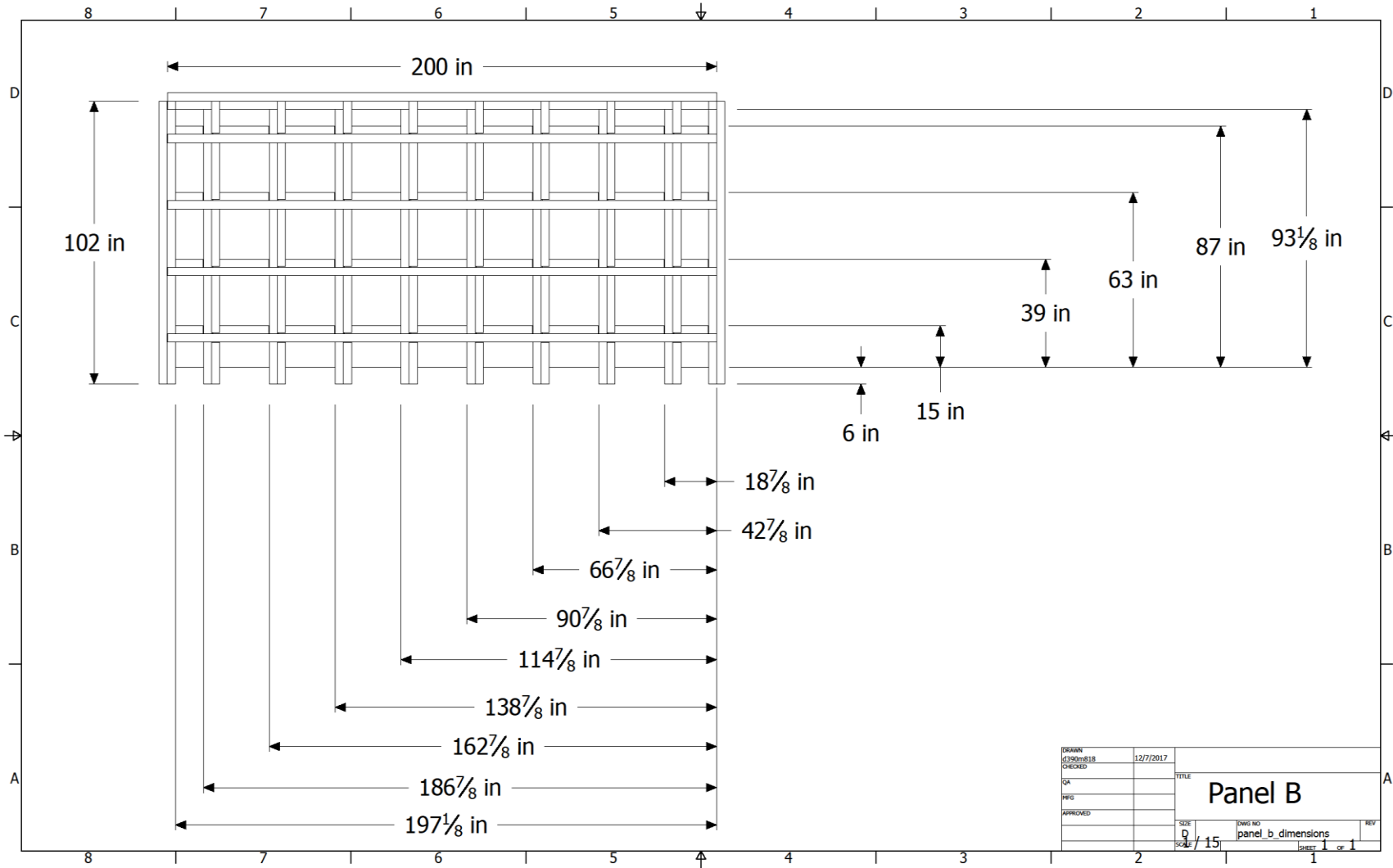


Fig. L-5. Purlin layout Panel B

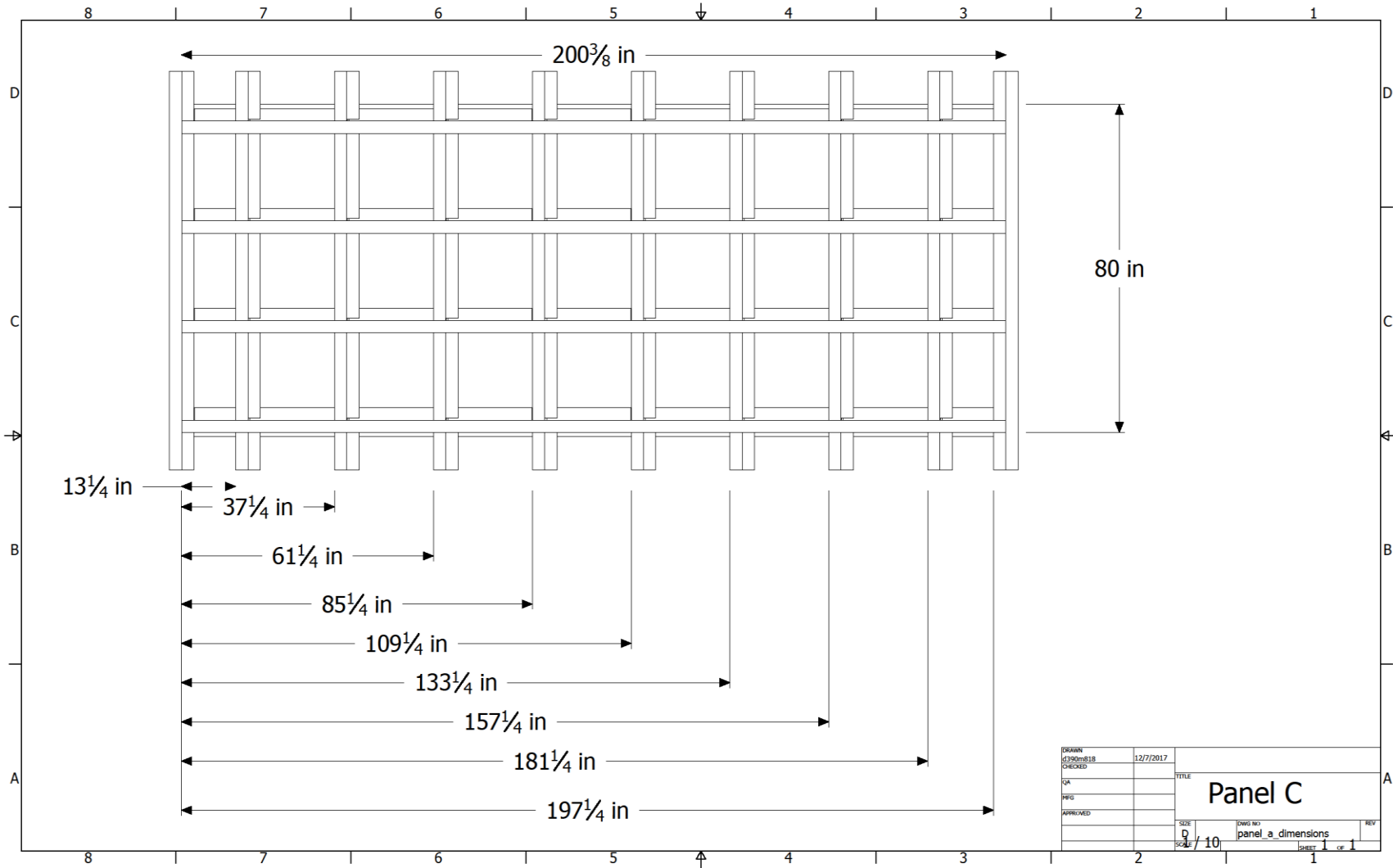


Fig. L-6. Purlin layout Panel C

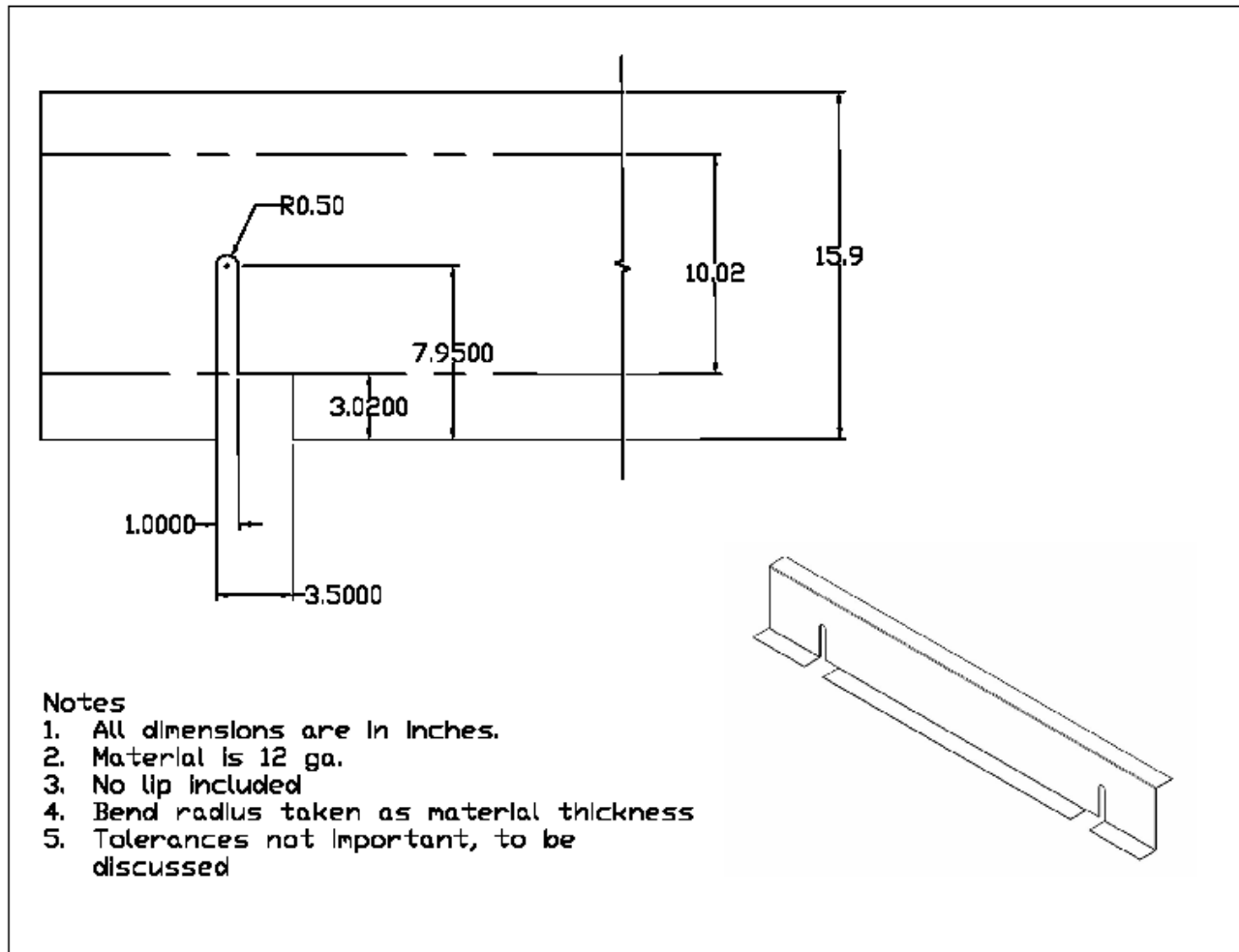


Fig. L-7. Junction cutout profile for 10 in. purlin. Depth of profile cutout in web is equal to half the purlin depth plus the bend radius

Chapter 10: APPENDIX M: Floor Fabrication Photos



Fig. M-1. Junction cutout marking



Fig. M -2. Torch cutting junction cutout



Fig. M -3. Junction cutout



Fig. M -4. Purlin intersection



Fig. M -5. Plate cutting



Fig. M -6. Typical process of welding top and bottom plates with stiffeners to reduce warping

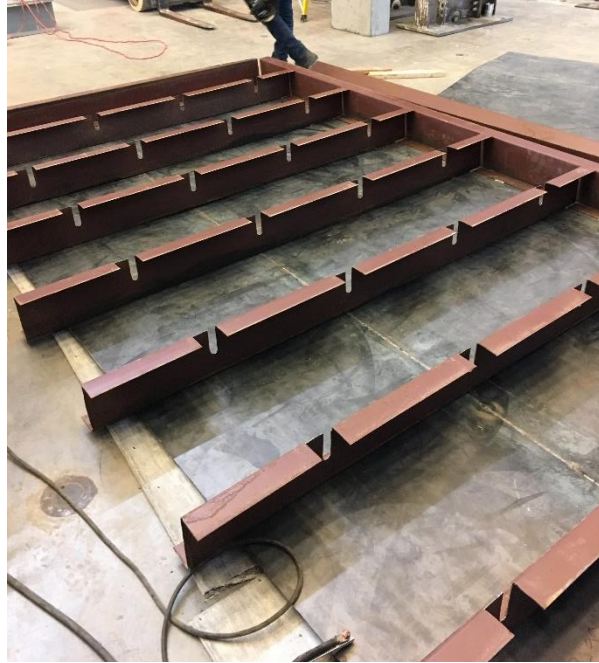


Fig. M -7. Transverse purlins laid out inside perimeter purlins

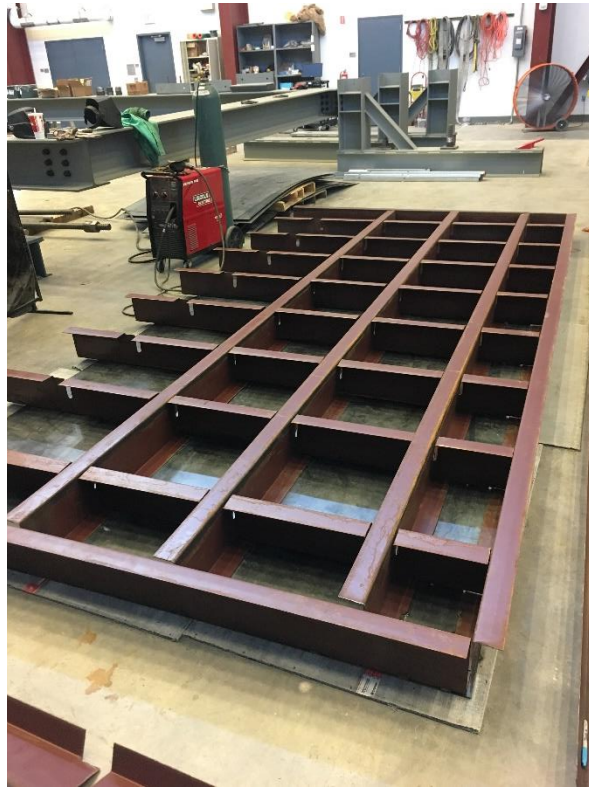


Fig. M -8. Longitudinal purlins laid out to form interior grid



Fig. M -9. Top plate set in place to form single panel



Fig. M -10. Center panel with top and bottom plate notches for joining with edge panels

APPENDIX N: Instrumentation and Testing for Serviceability

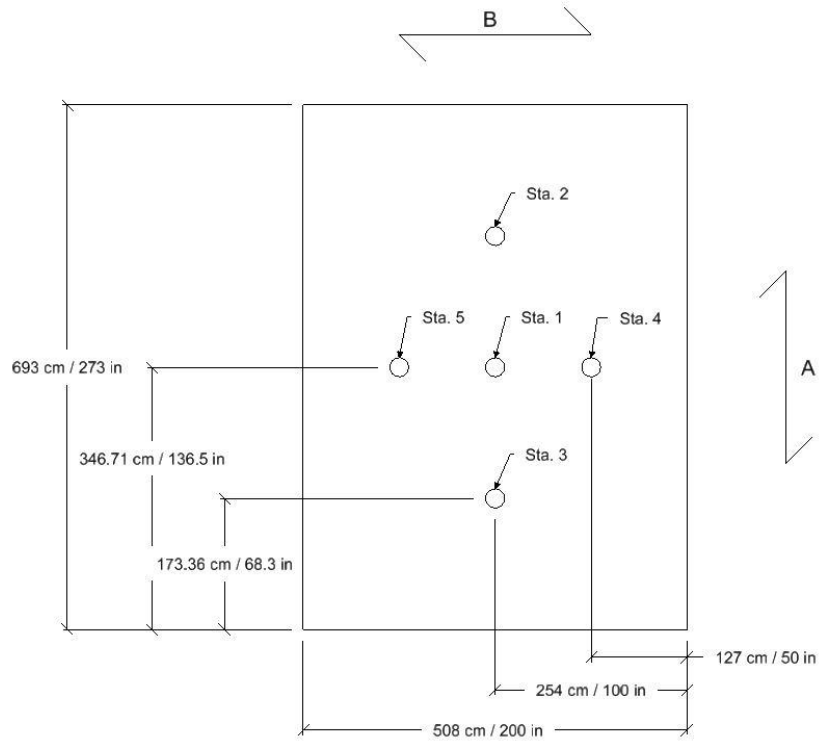


Fig. N-1. Instrumentation plan for accelerometers in the longitudinal (A) direction and transverse (B) direction

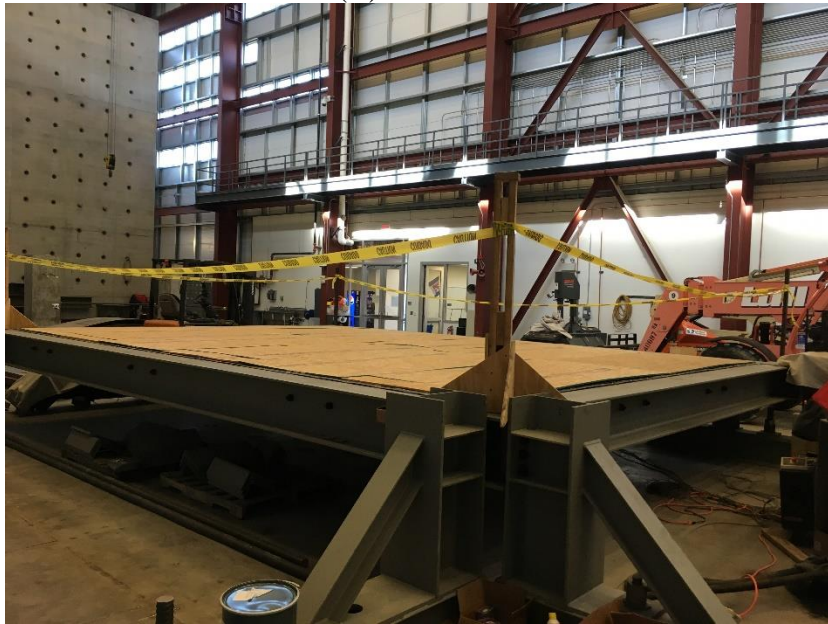


Fig. N-2. Floor with decking prepared for heel drop and walking testing



Fig. N-5. Monitoring station in foreground with walking testing in background

APPENDIX O: Heel Drop Response Spectra Plots, Floor D203

(D8)

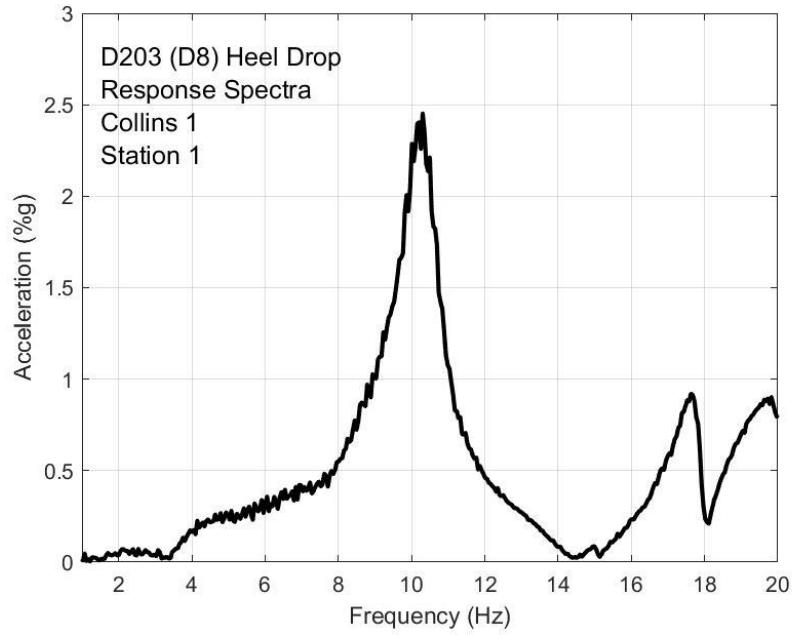


Fig. O-1. Heel drop response, Collins test 1 station 1

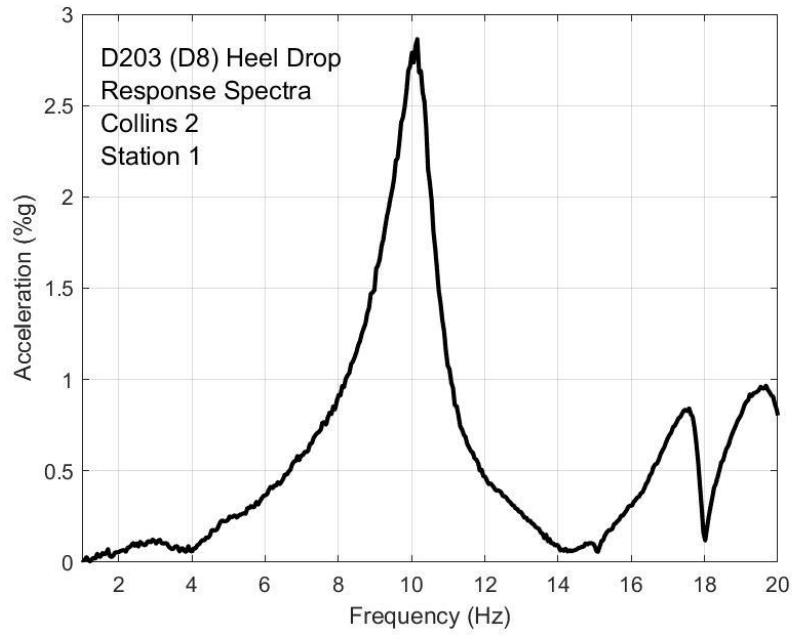


Fig. O-2. Heel drop response, Collins test 2 station 1

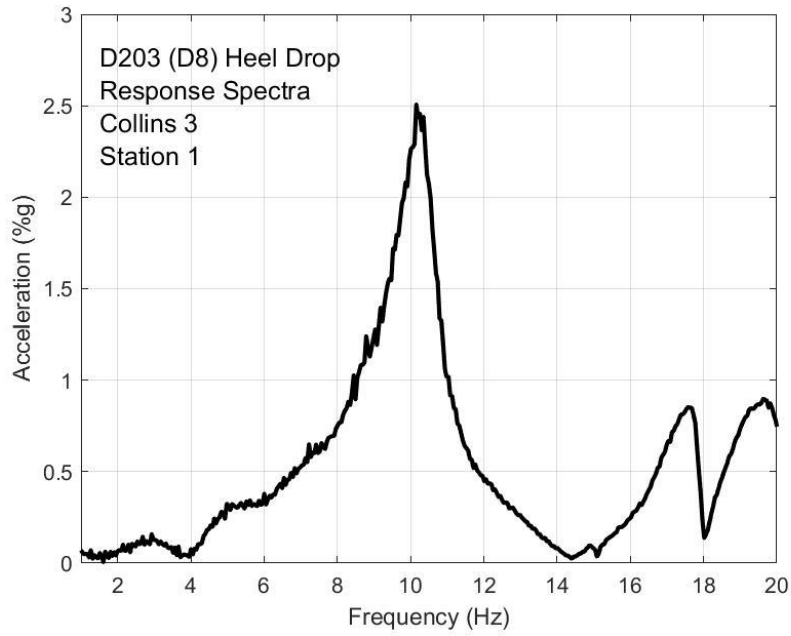


Fig. O-3. Heel drop response, Collins test 3 station 1

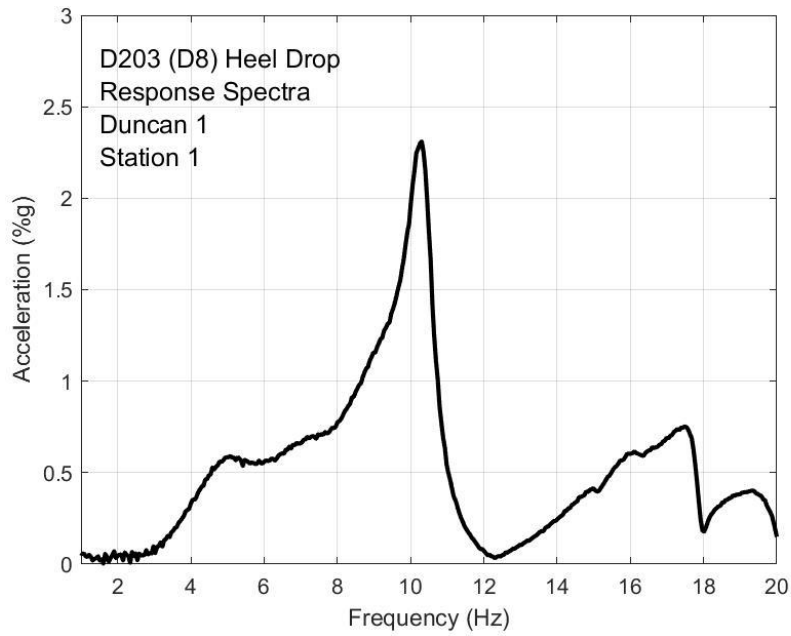


Fig. O-4. Heel drop response, Duncan test 1 station 1

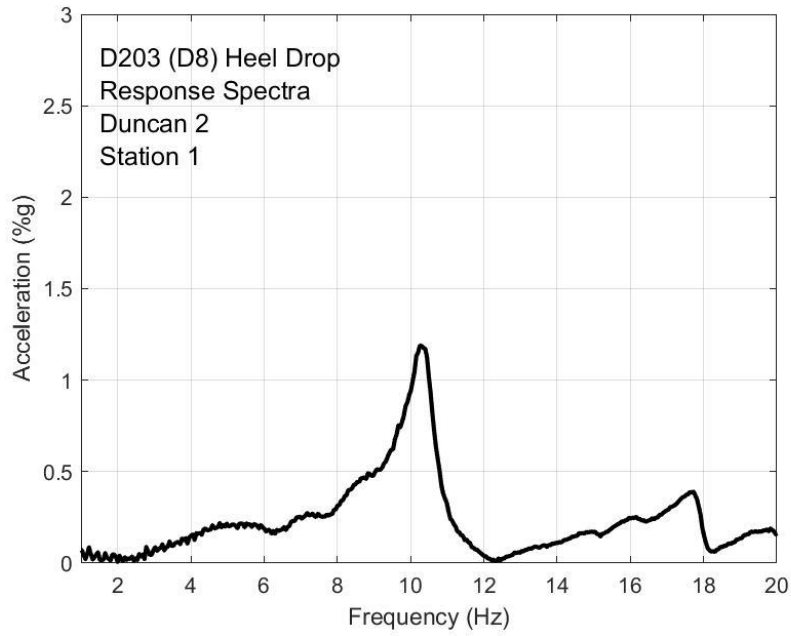


Fig. O-5. Heel drop response, Duncan test 2 station 1

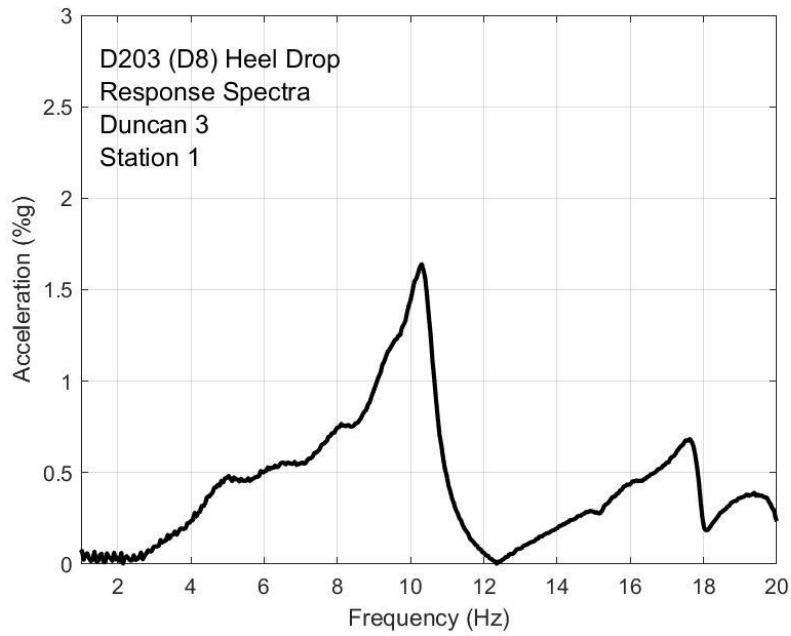


Fig. O-6. Heel drop response, Duncan test 3 station 1

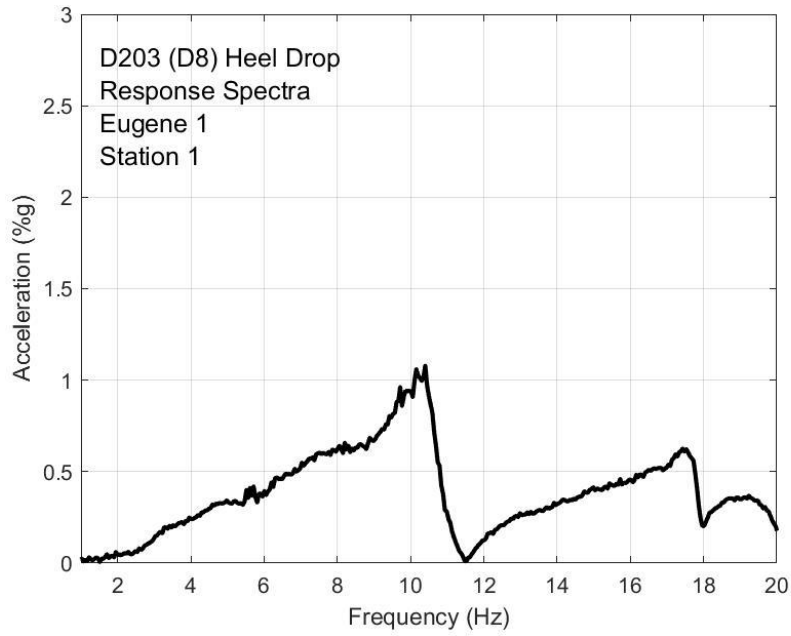


Fig. O-7. Heel drop response, Eugene test 1 station 1

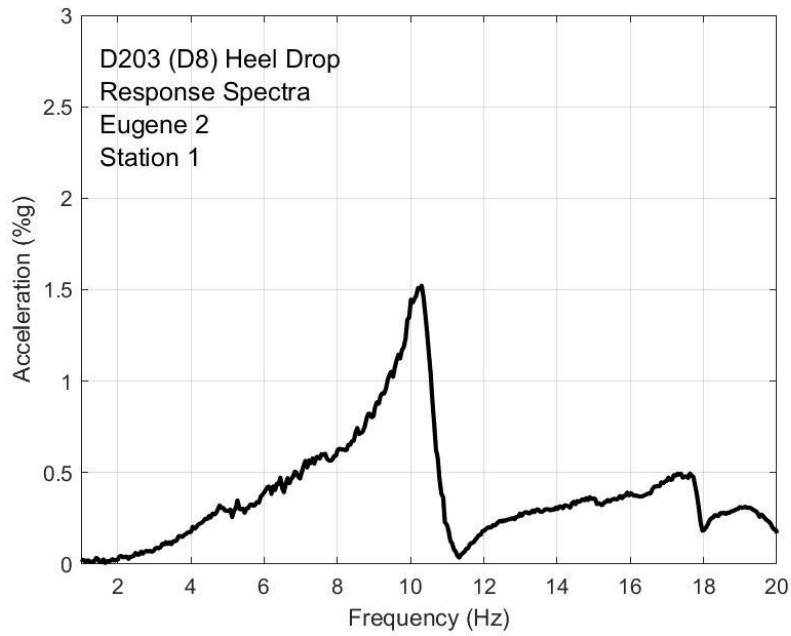


Fig. O-8. Heel drop response, Eugene test 2 station 1

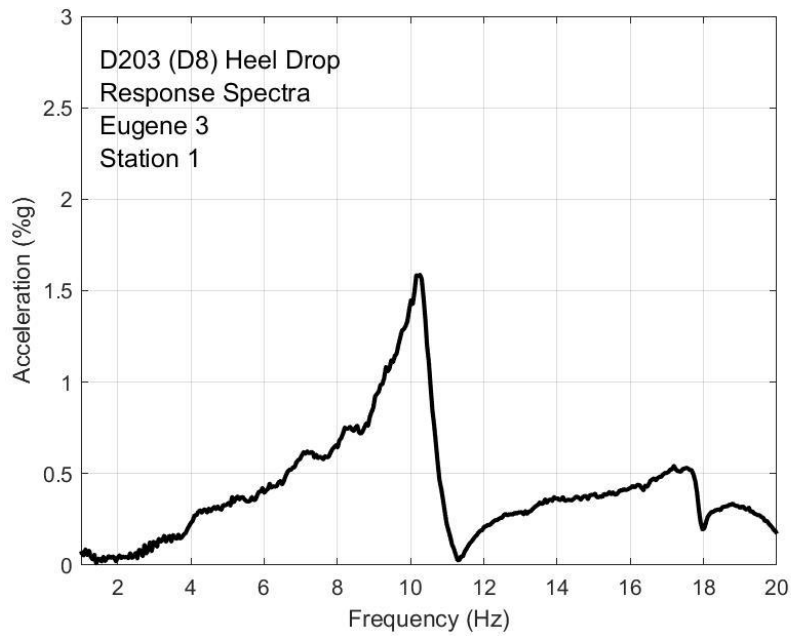


Fig. O-9. Heel drop response, Eugene test 3 station 1

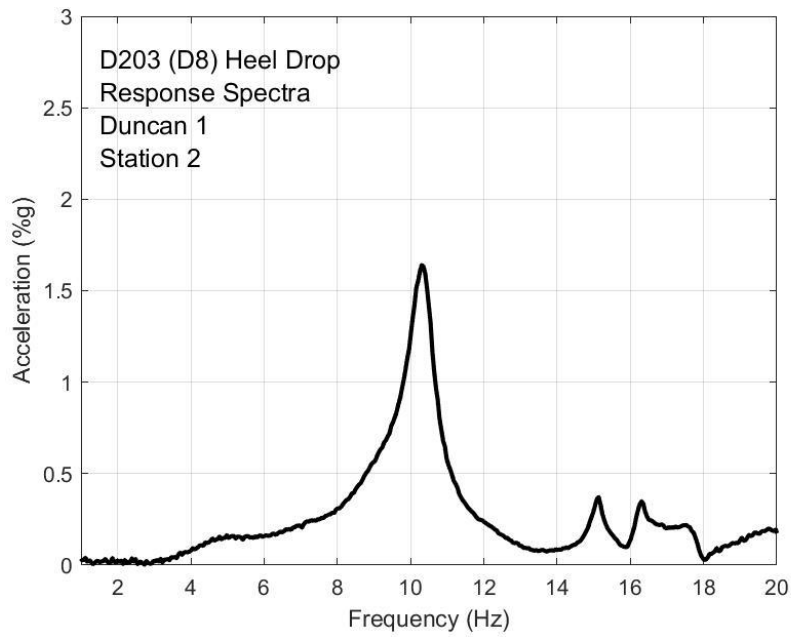


Fig. O-10. Heel drop response, Duncan test 1 station 2

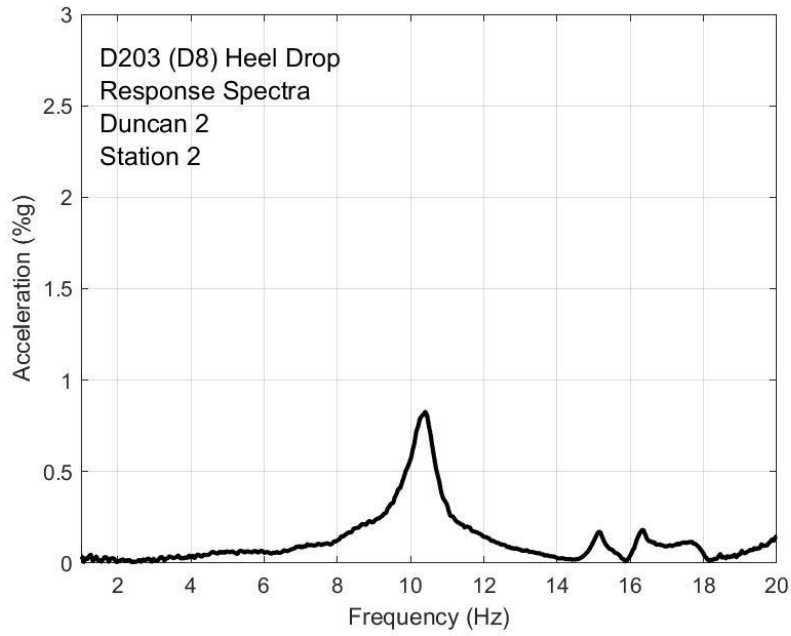


Fig. O-11. Heel drop response, Duncan test 1 station 2

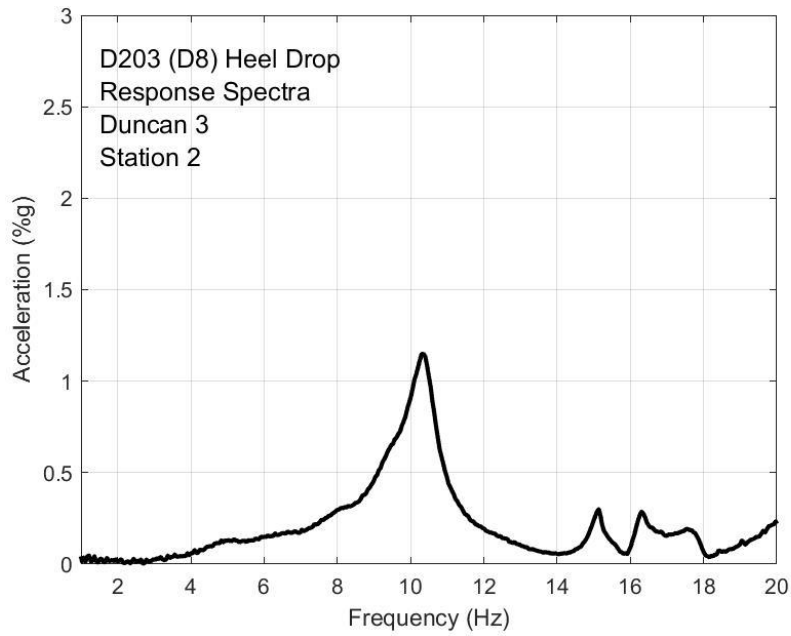


Fig. O-12. Heel drop response, Duncan test 3 station 2

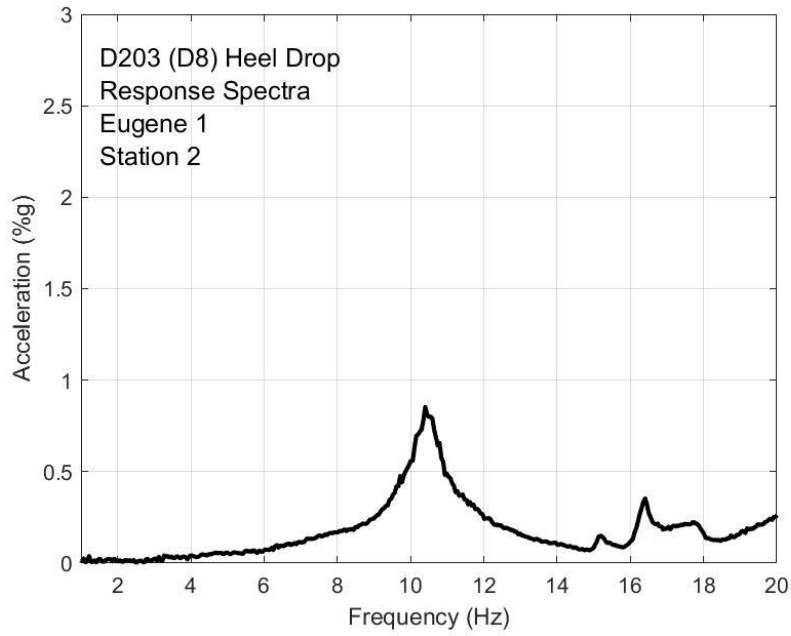


Fig. O-13. Heel drop response, Eugene test 1 station 2

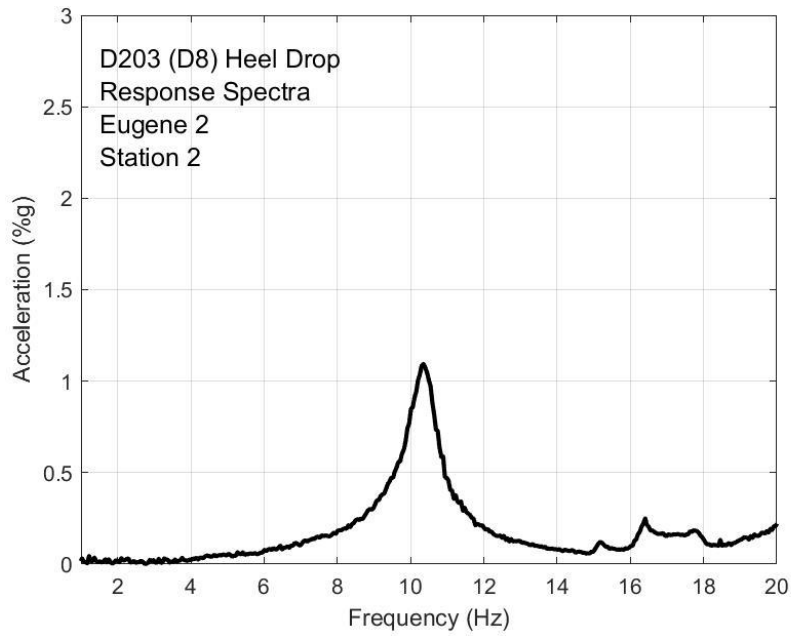


Fig. O-14. Heel drop response, Eugene test 2 station 2

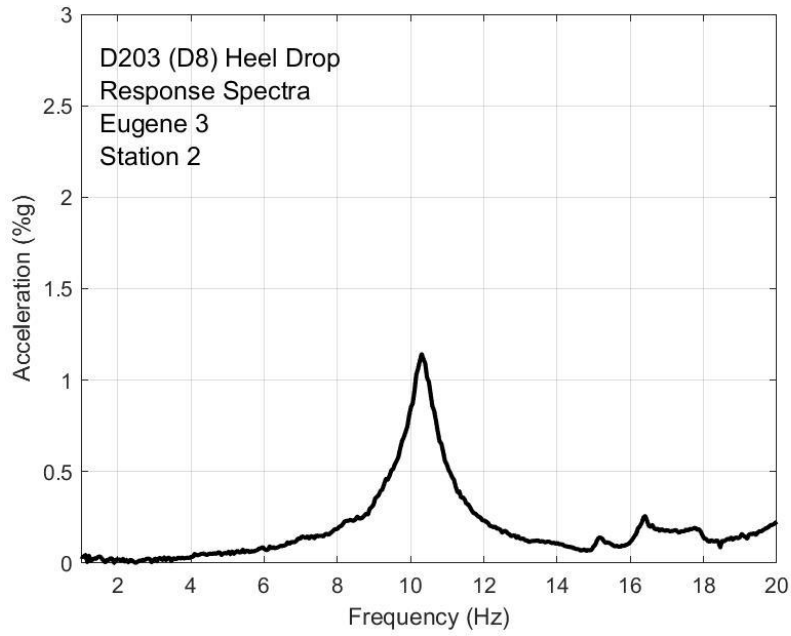


Fig. O-15. Heel drop response, Eugene test 3 station 2

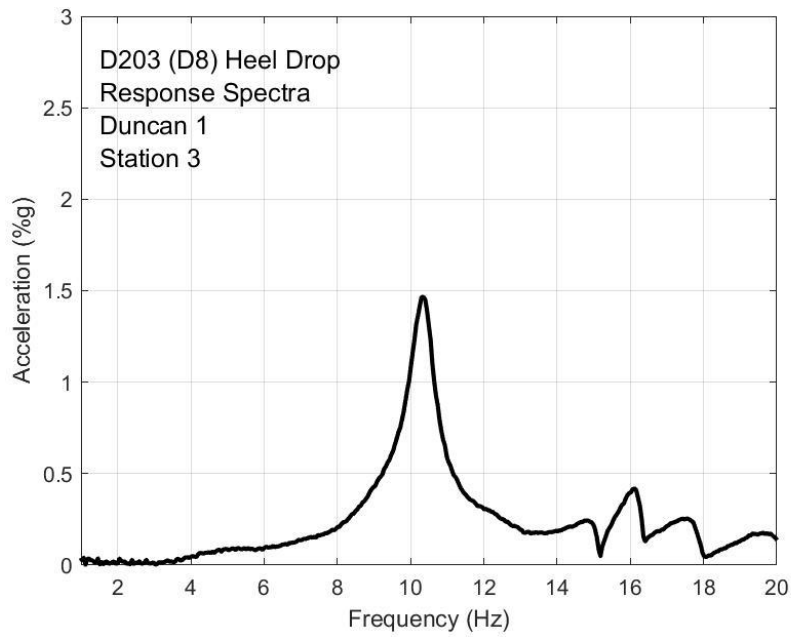


Fig. O-16. Heel drop response, Duncan test 1 station 3

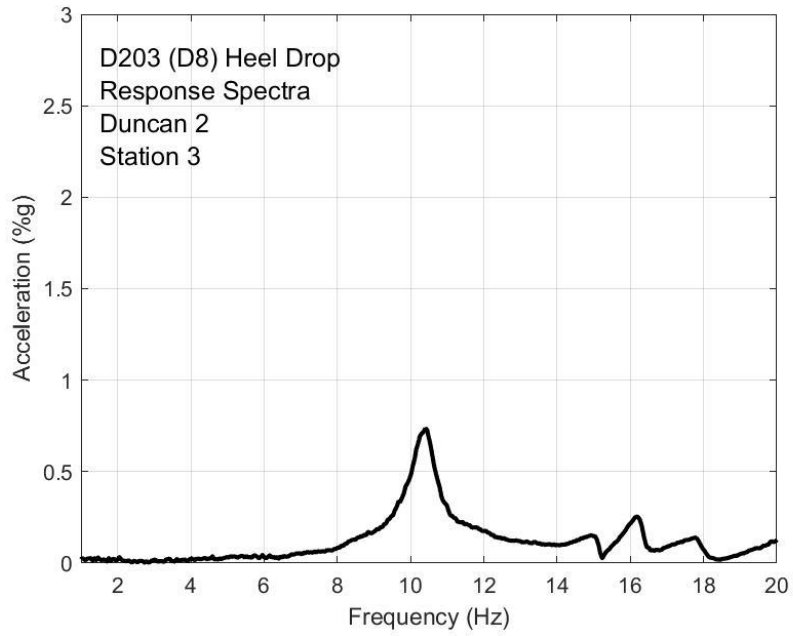


Fig. O-17. Heel drop response, Duncan test 2 station 3

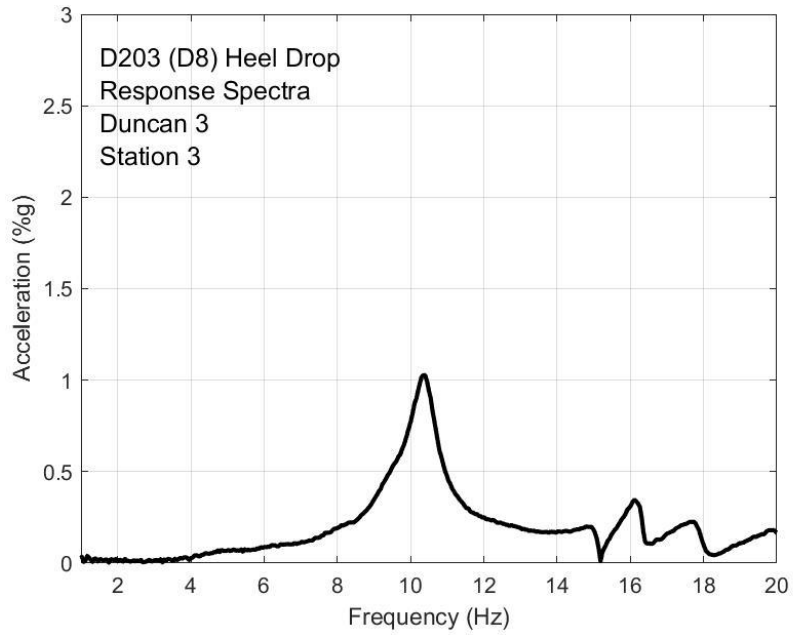


Fig. O-18. Heel drop response, Duncan test 3 station 3

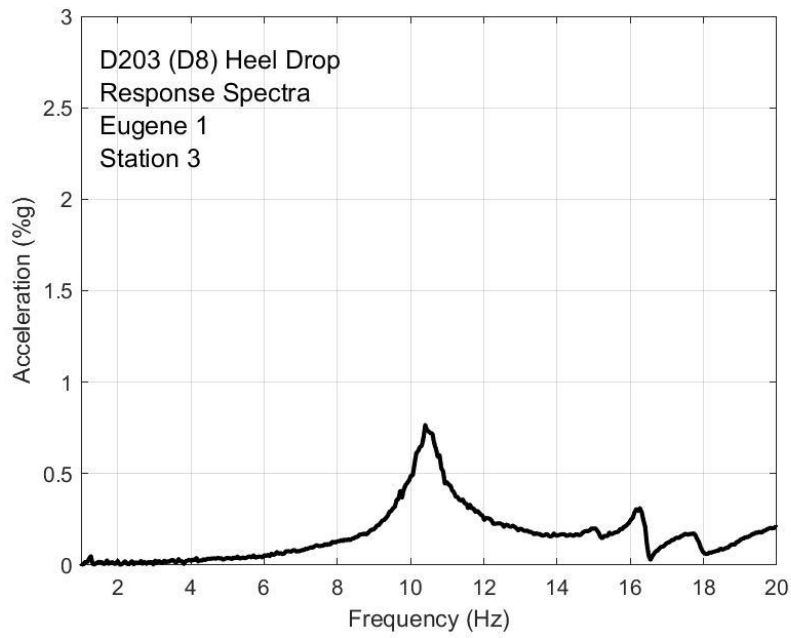


Fig. O-19. Heel drop response, Eugene test 1 station 3

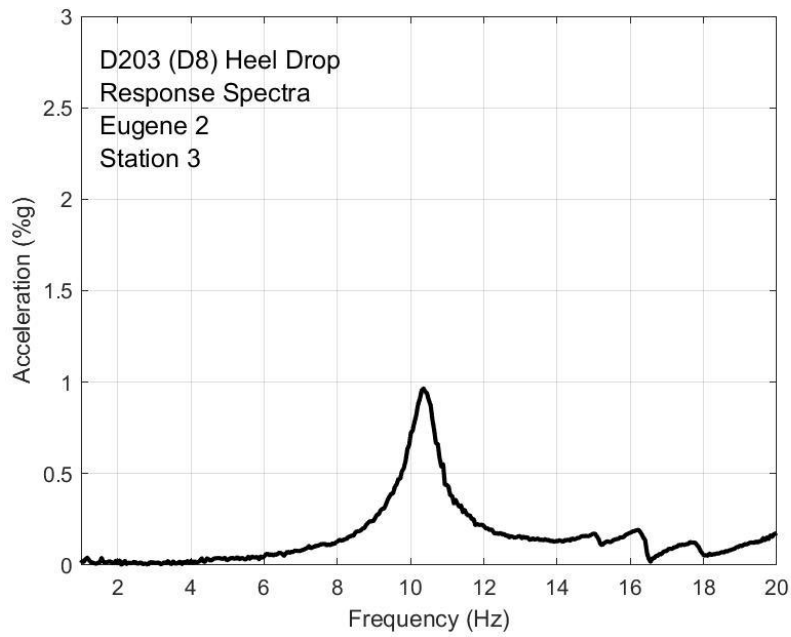


Fig. O-20. Heel drop response, Eugene test 2 station 3

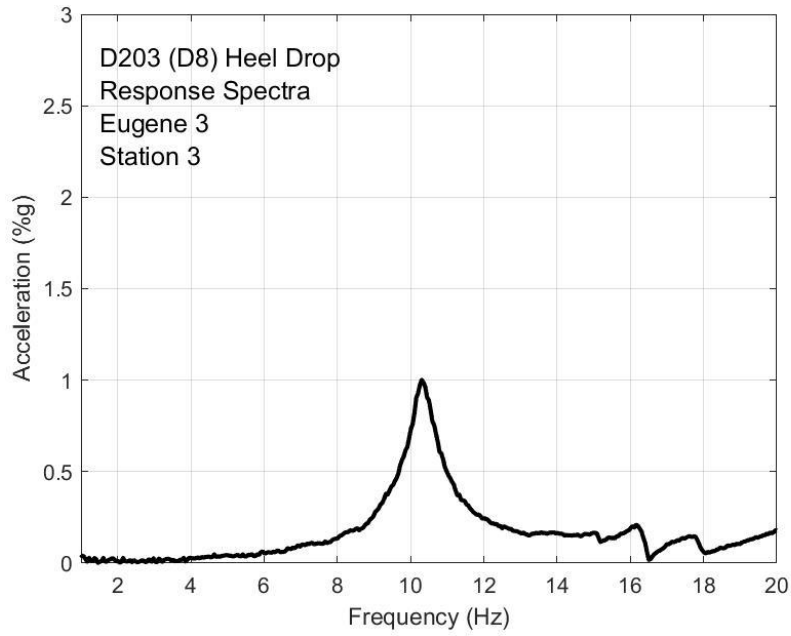


Fig. O-21. Heel drop response, Eugene test 3 station 3

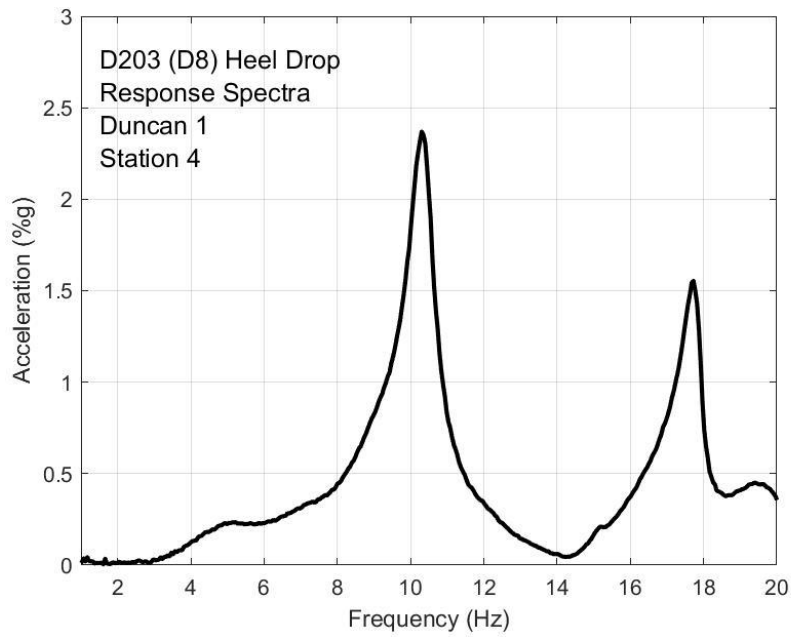


Fig. O-22. Heel drop response, Duncan test 1 station 4

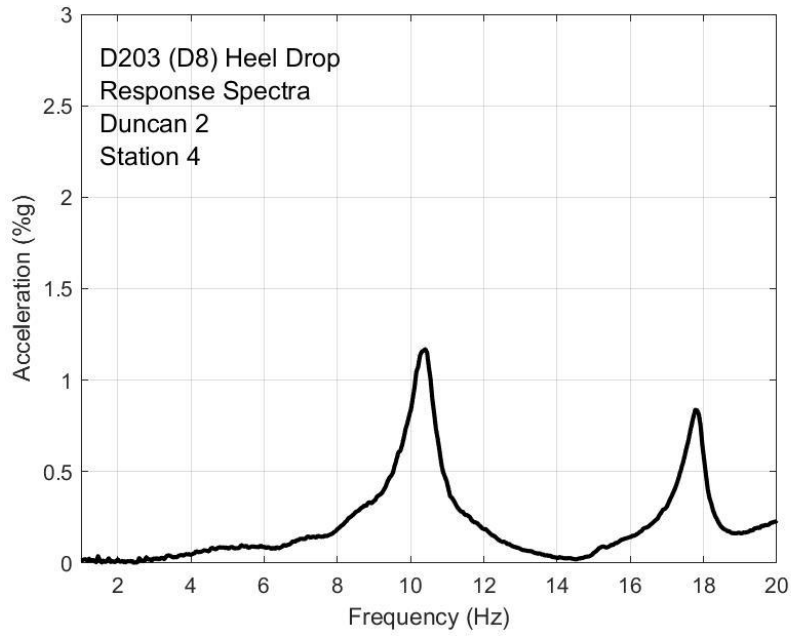


Fig. O-23. Heel drop response, Duncan test 2 station 4

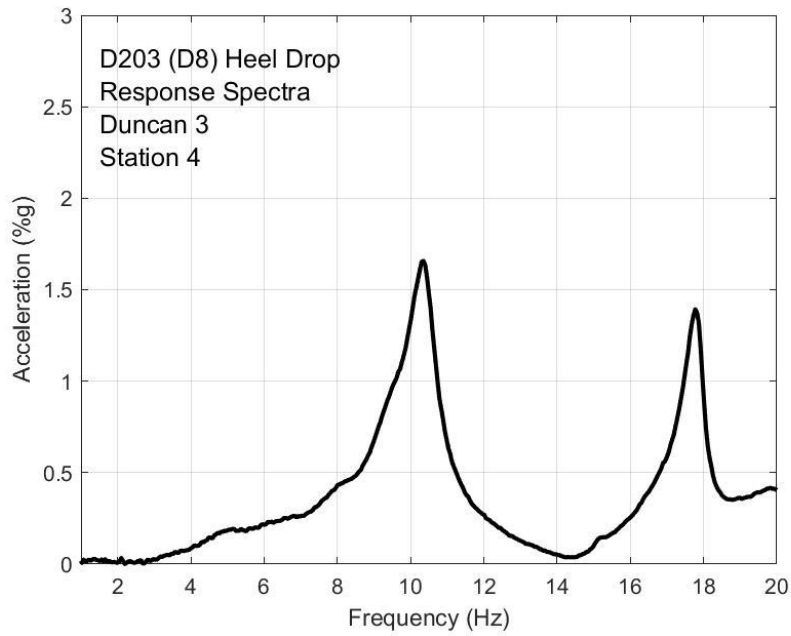


Fig. O-24. Heel drop response, Duncan test 3 station 4

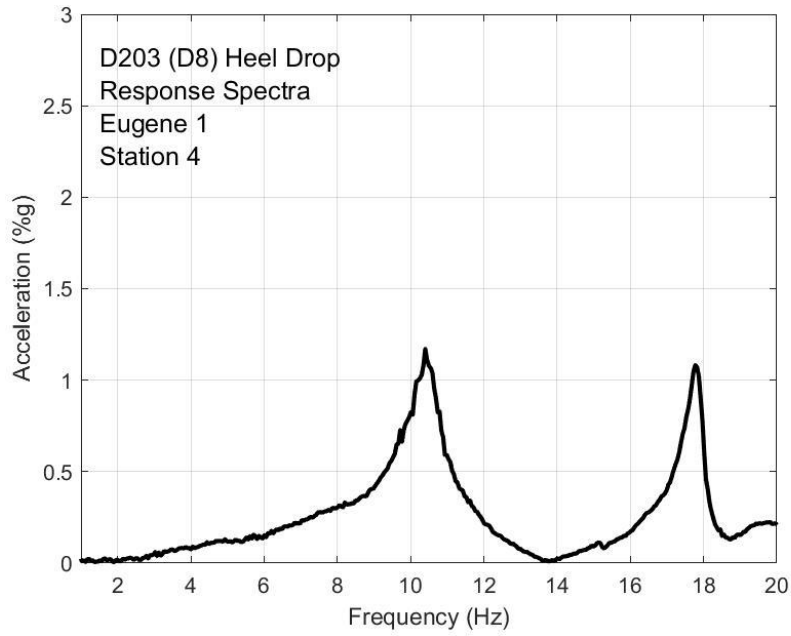


Fig. O-25. Heel drop response, Eugene test 1 station 4

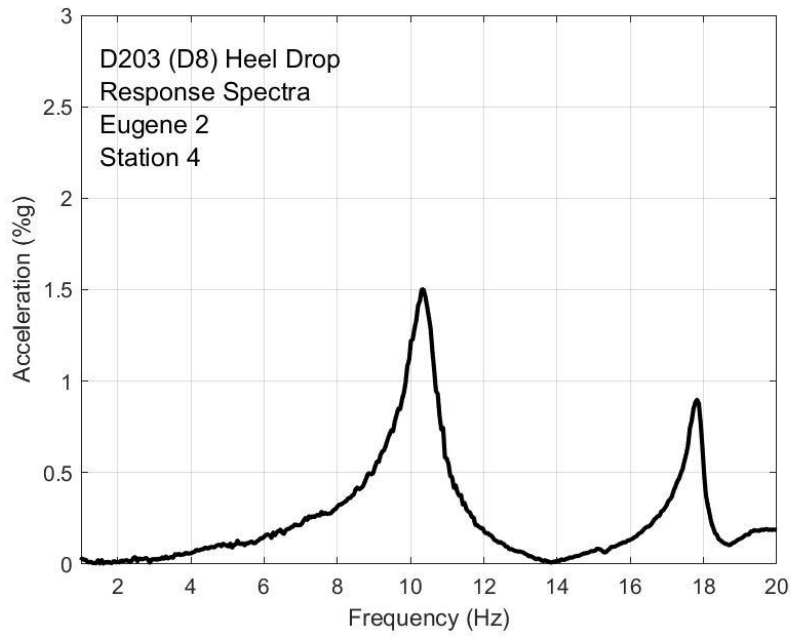


Fig. O-26. Heel drop response, Eugene test 2 station 4

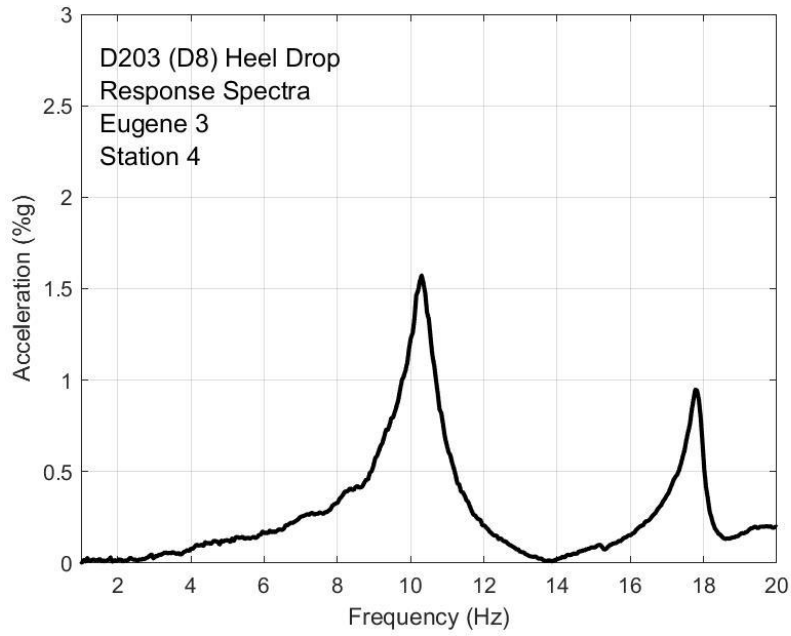


Fig. O-27. Heel drop response, Eugene test 3 station 4

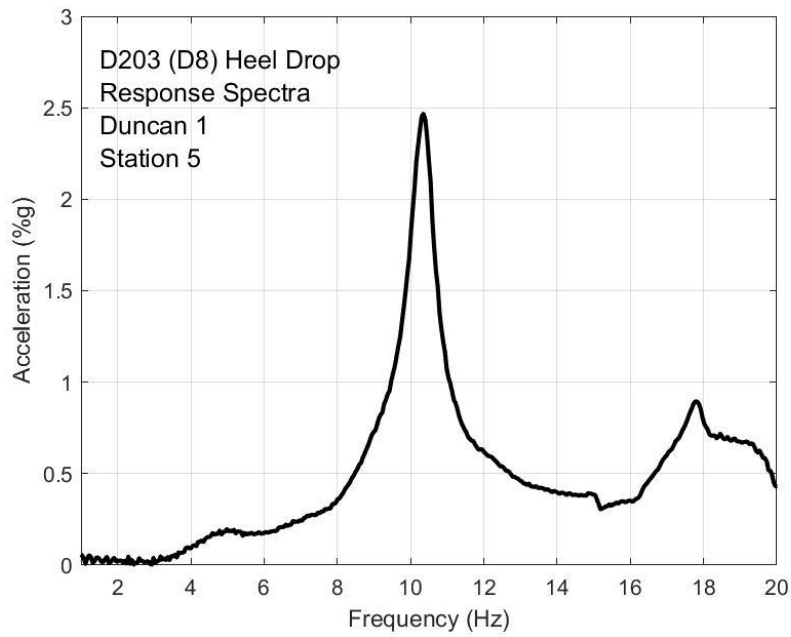


Fig. O-28. Heel drop response, Duncan test 1 station 5

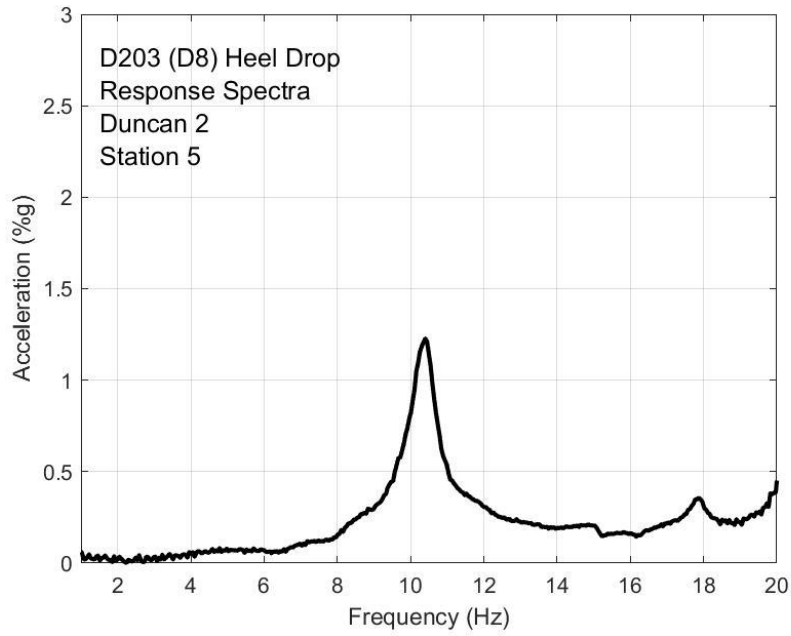


Fig. O-29. Heel drop response, Duncan test 2 station 5

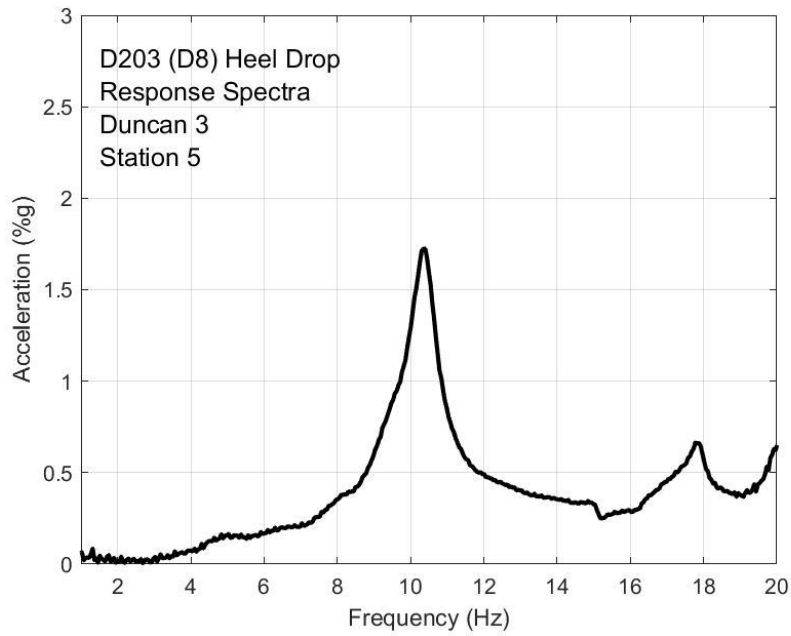


Fig. O-30. Heel drop response, Duncan test 3 station 5

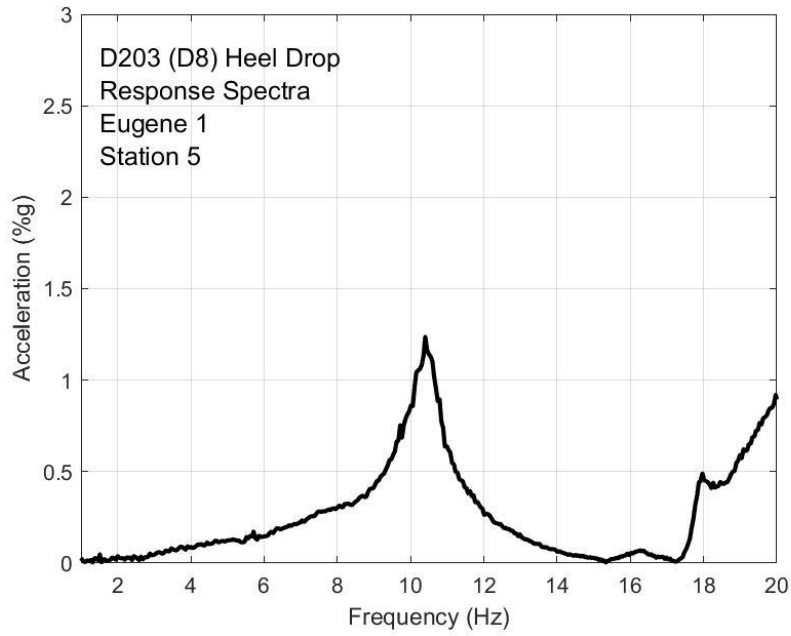


Fig. O-31. Heel drop response, Eugene test 1 station 5

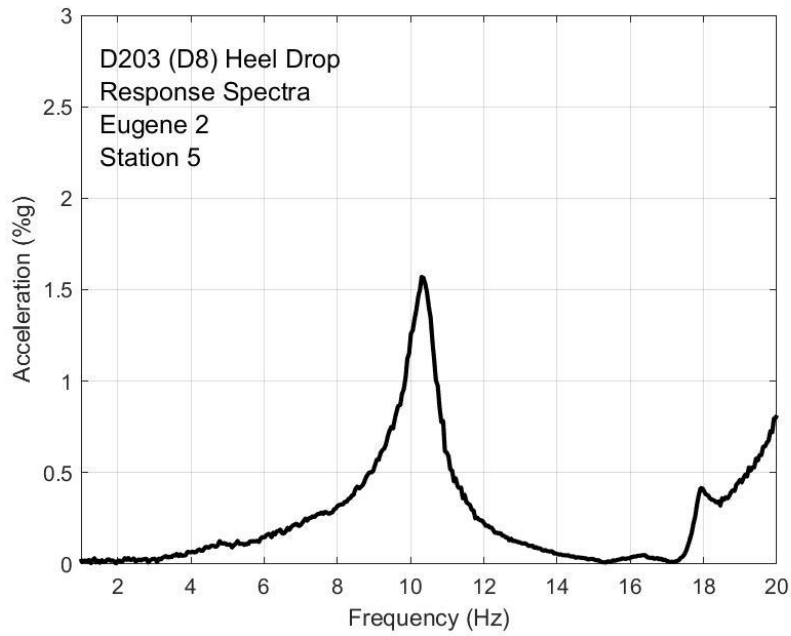


Fig. O-32. Heel drop response, Eugene test 2 station 5

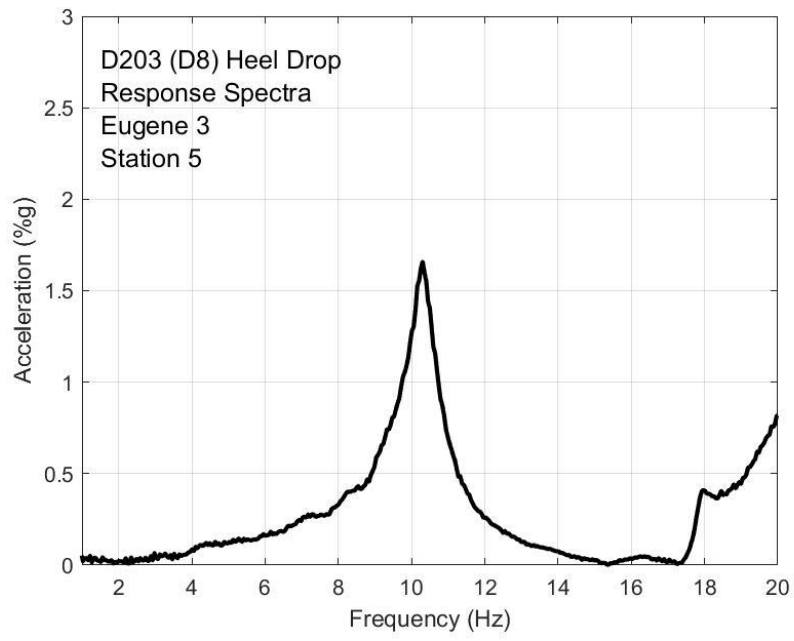


Fig. O-33. Heel drop response, Eugene test 3 station 5

APPENDIX P: Walking Testing, Floor D203 (D8)

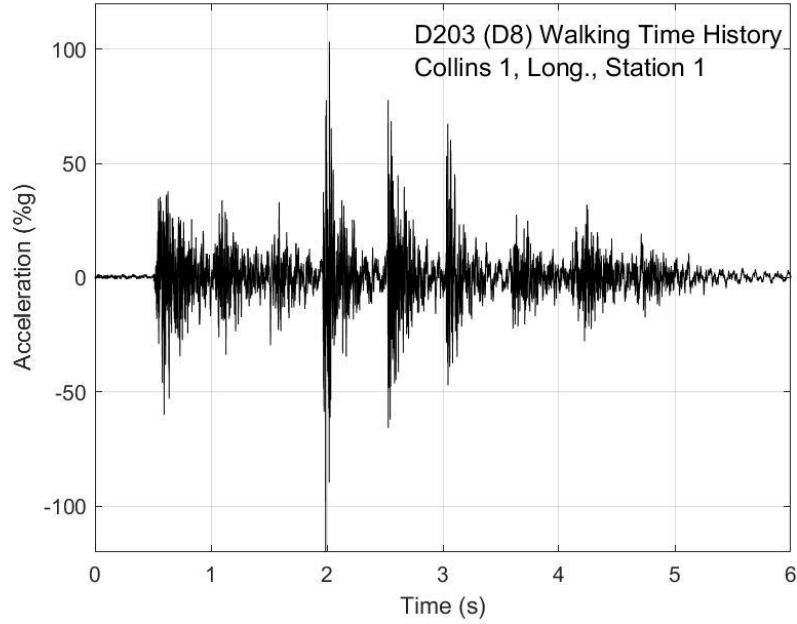


Fig. P-1. Walking time history, Collins test 1, longitudinal direction, station 1

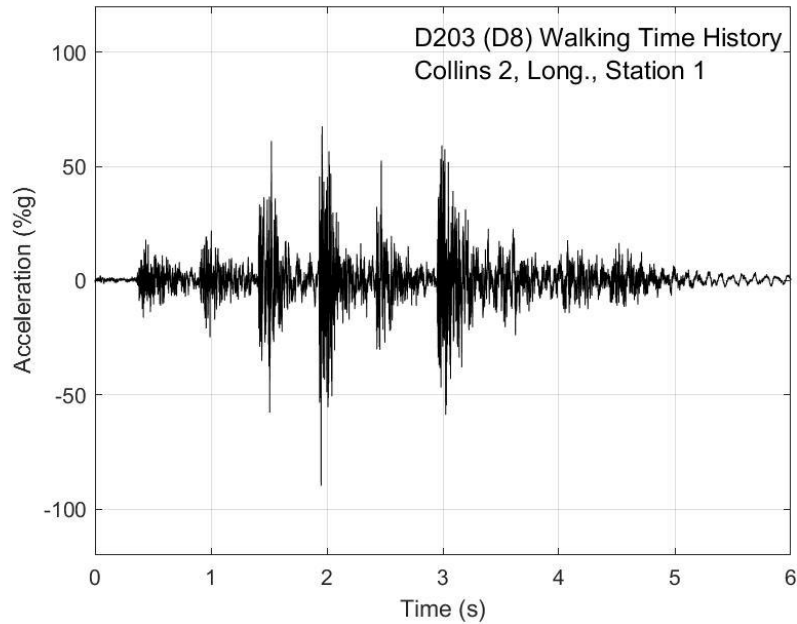


Fig. P-2. Walking time history, Collins test 2, longitudinal direction, station 1

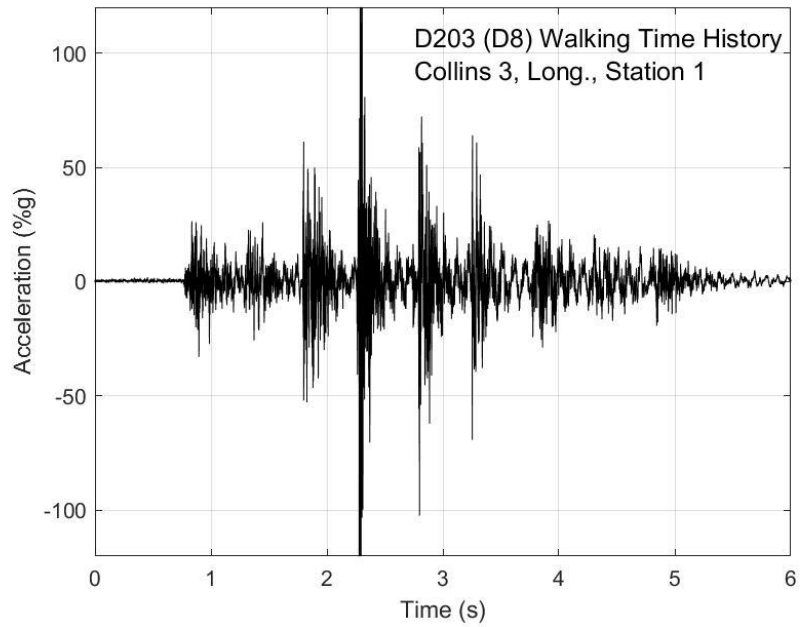


Fig. P-3. Walking time history, Collins test 3, longitudinal direction, station 1

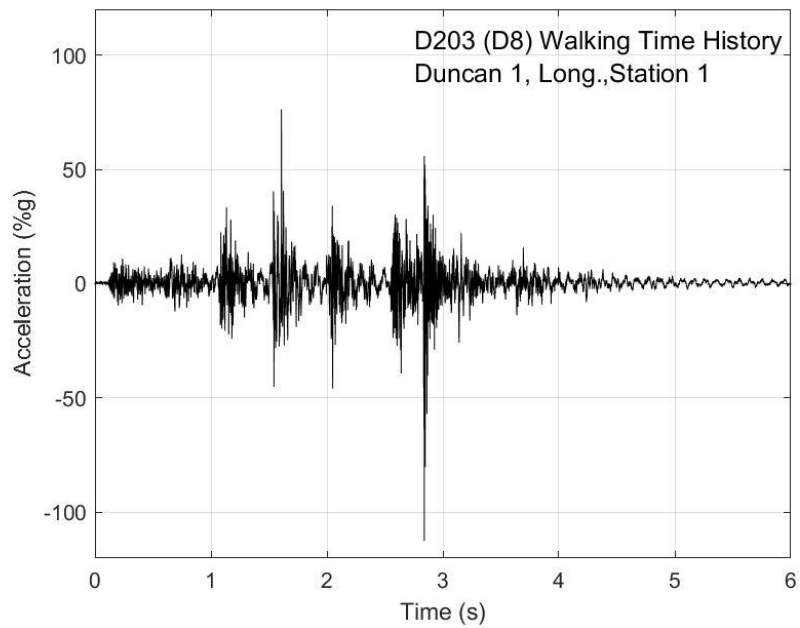


Fig. P-4. Walking time history, Duncan test 1, longitudinal direction, station 1

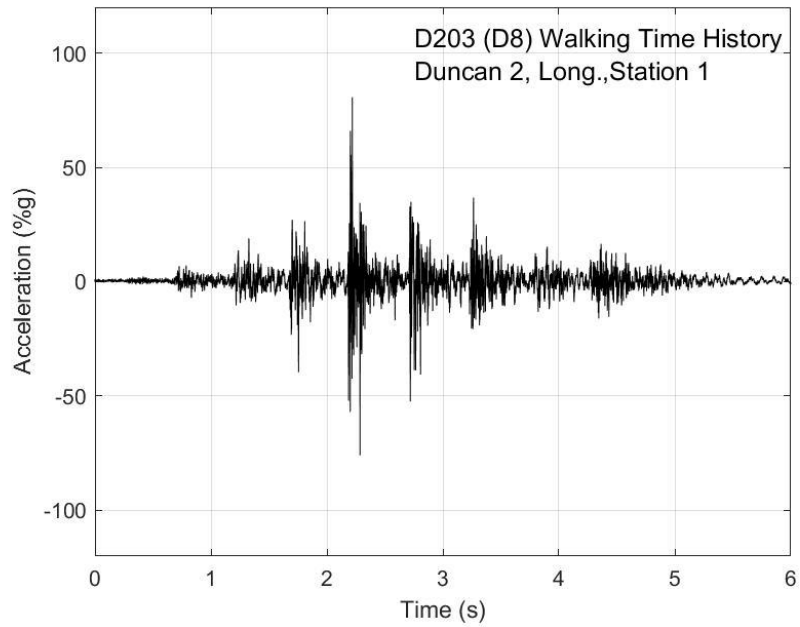


Fig. P-5. Walking time history, Duncan test 2, longitudinal direction, station 1

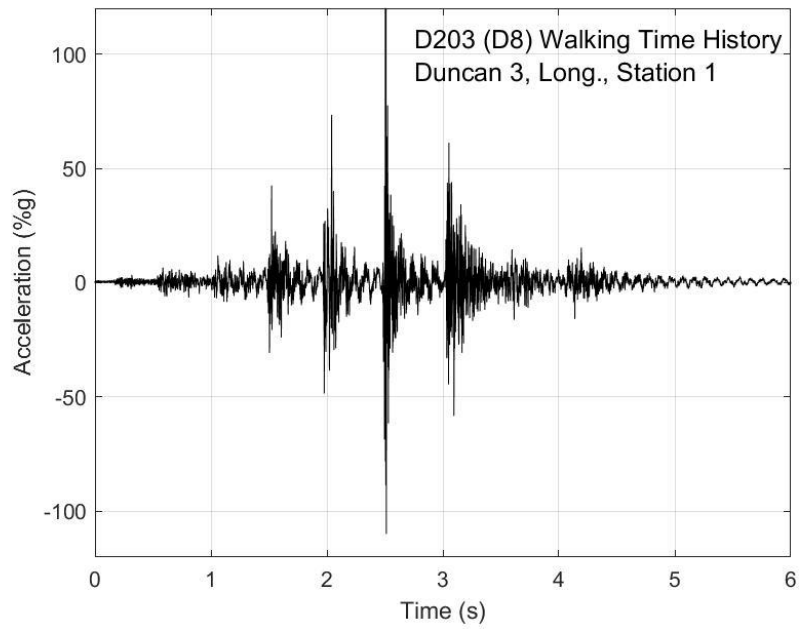


Fig. P-6. Walking time history, Duncan test 3, longitudinal direction, station 1

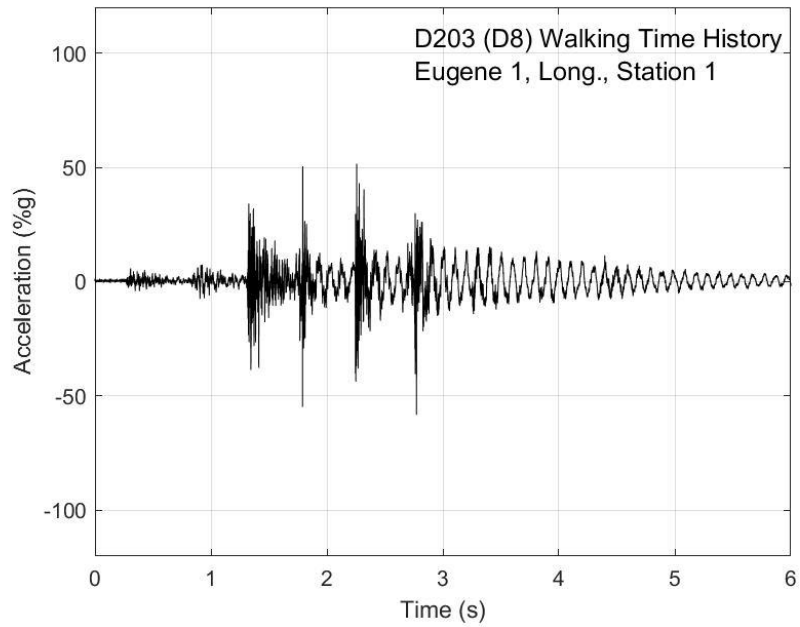


Fig. P-7. Walking time history, Eugene test 1, longitudinal direction, station 1

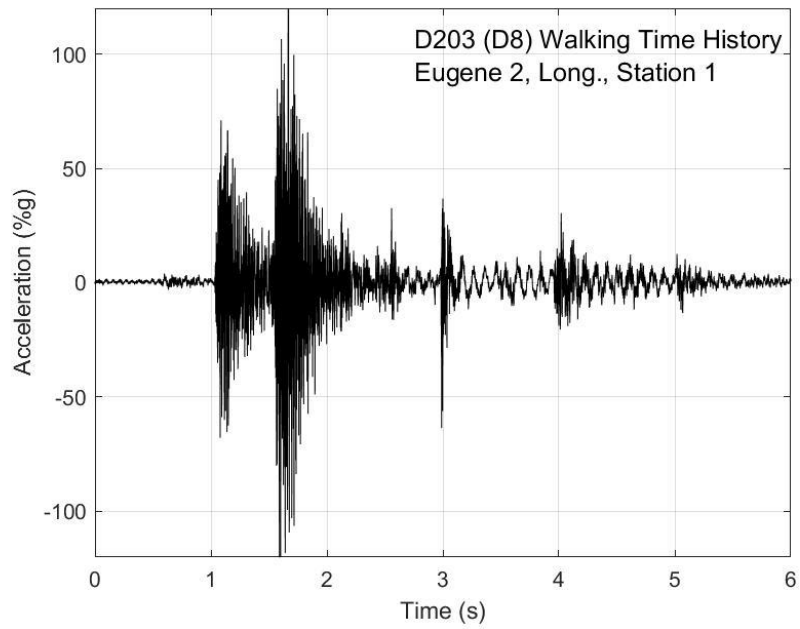


Fig. P-8. Walking time history, Eugene test 2, longitudinal direction, station 1

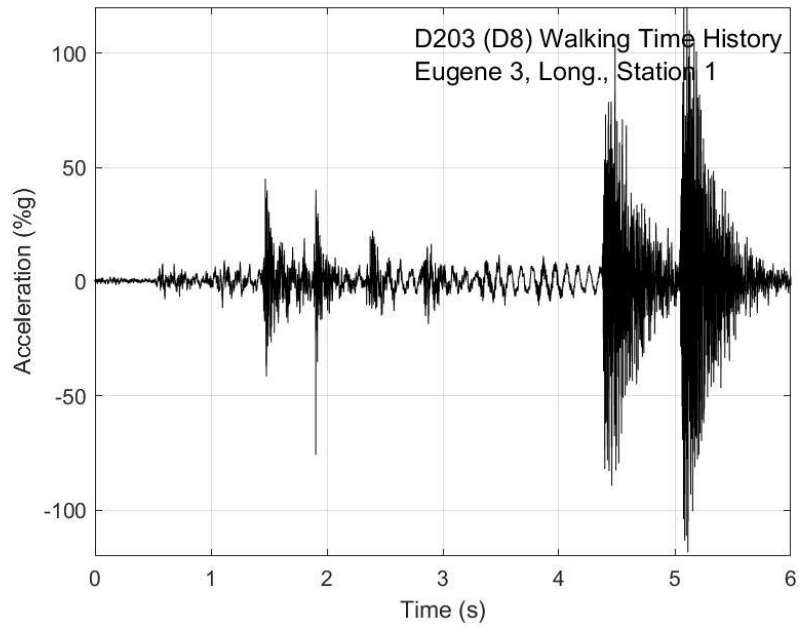


Fig. P-9. Walking time history, Eugene test 3, longitudinal direction, station 1

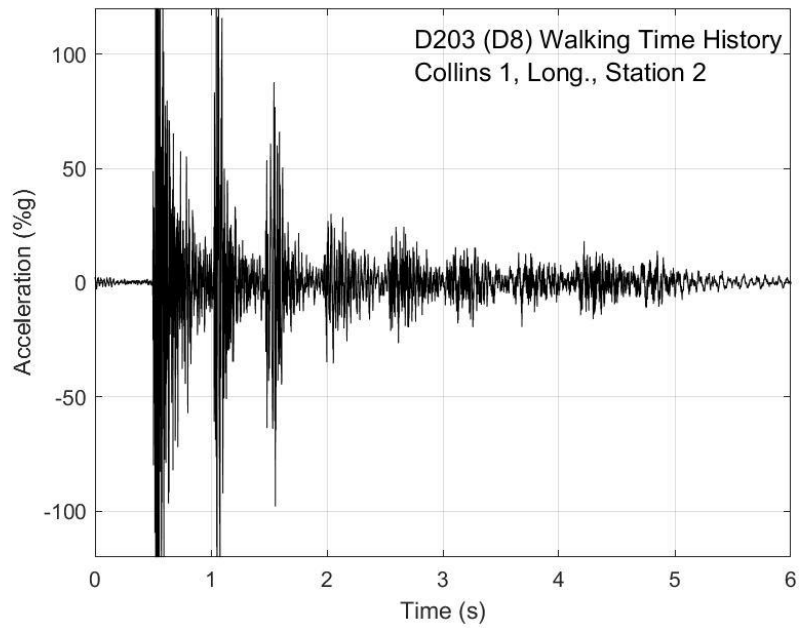


Fig. P-10. Walking time history, Collins test 1, longitudinal direction, station 2

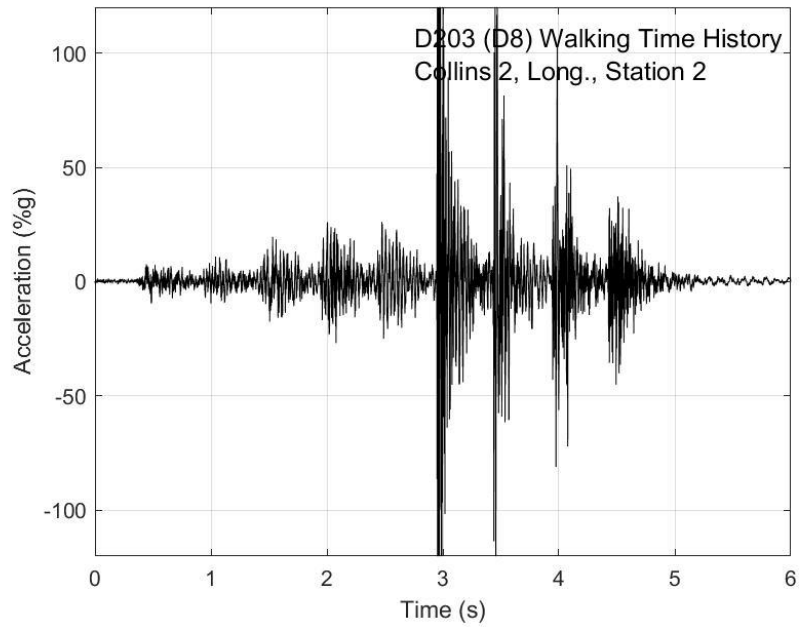


Fig. P-11. Walking time history, Collins test 2, longitudinal direction, station 2

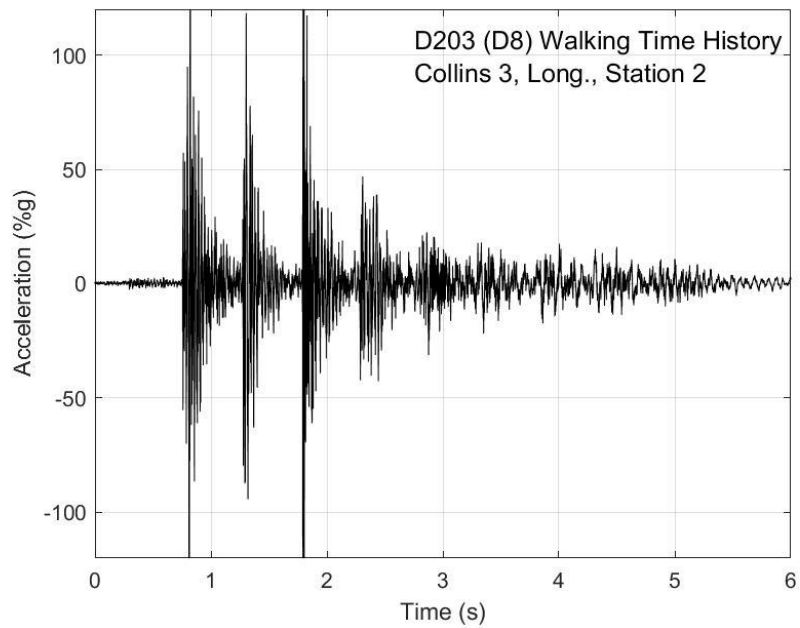


Fig. P-12. Walking time history, Collins test 3, longitudinal direction, station 2

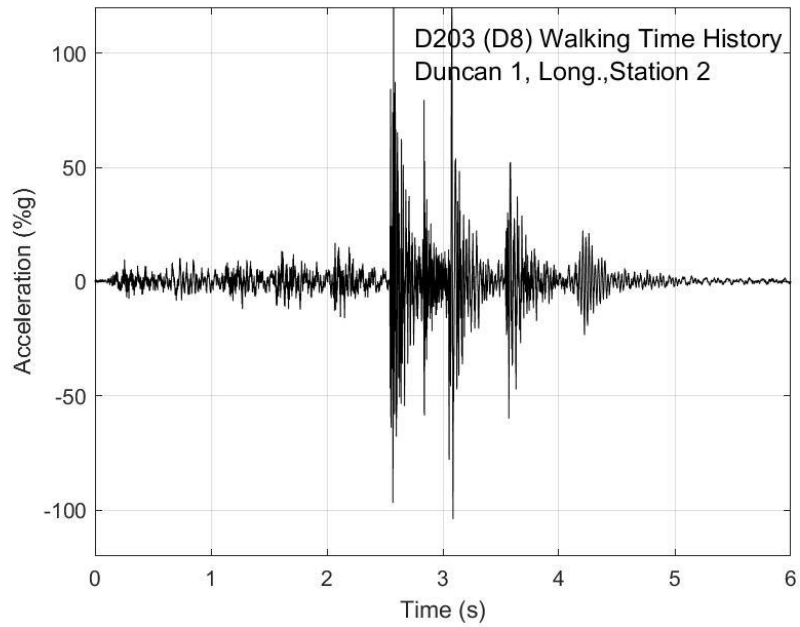


Fig. P-13. Walking time history, Duncan test 1, longitudinal direction, station 2

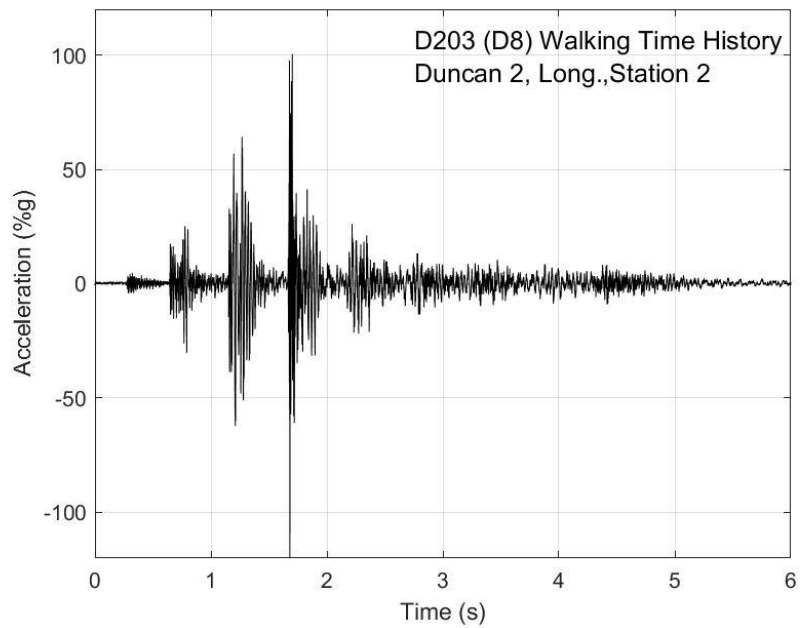


Fig. P-14. Walking time history, Duncan test 2, longitudinal direction, station 2

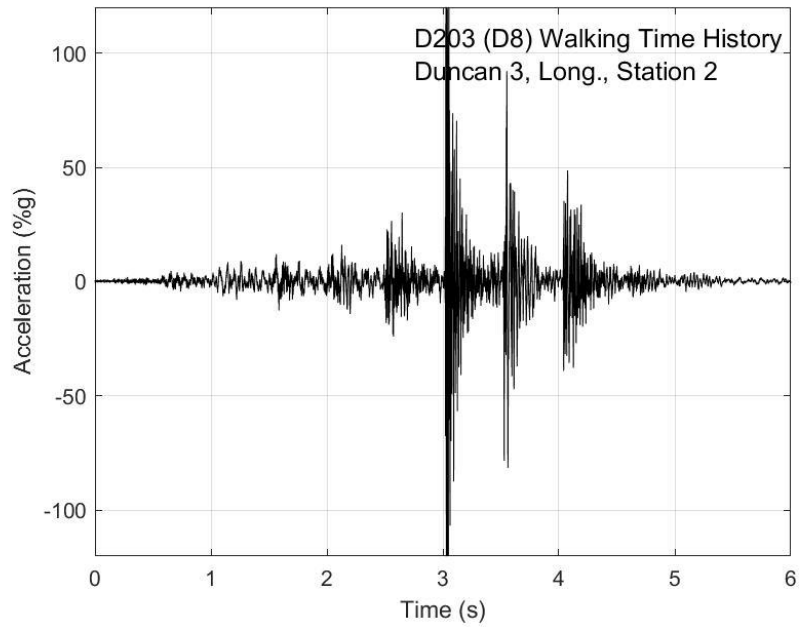


Fig. P-15. Walking time history, Duncan test 3, longitudinal direction, station 2

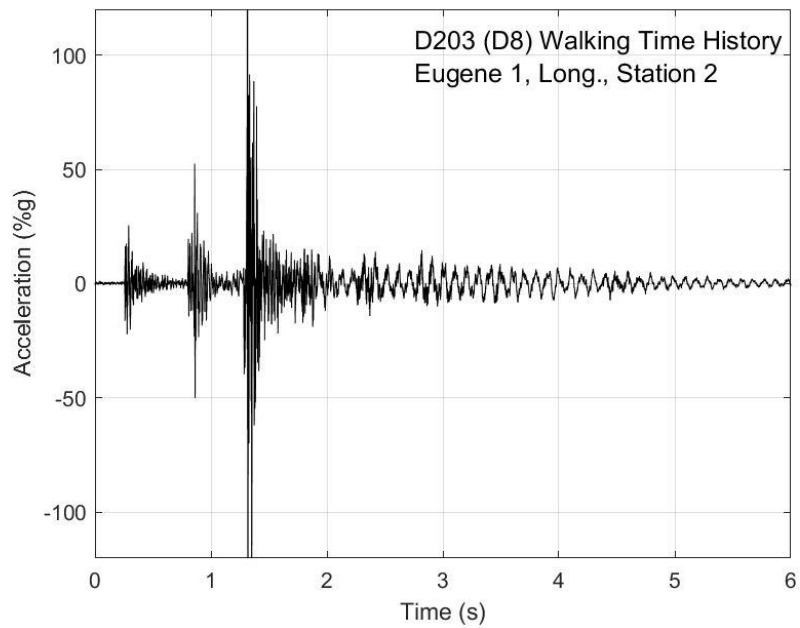


Fig. P-16. Walking time history, Eugene test 1, longitudinal direction, station 2

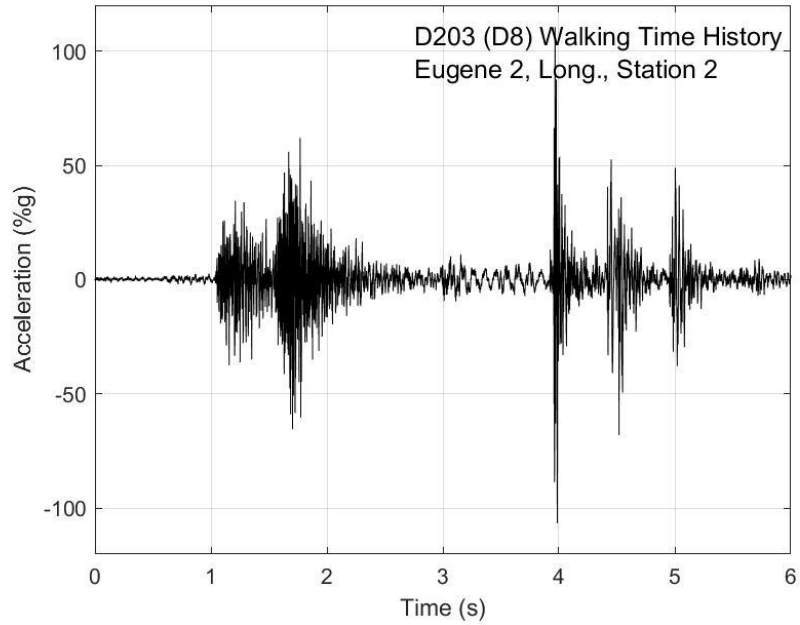


Fig. P-17. Walking time history, Eugene test 2, longitudinal direction, station 2

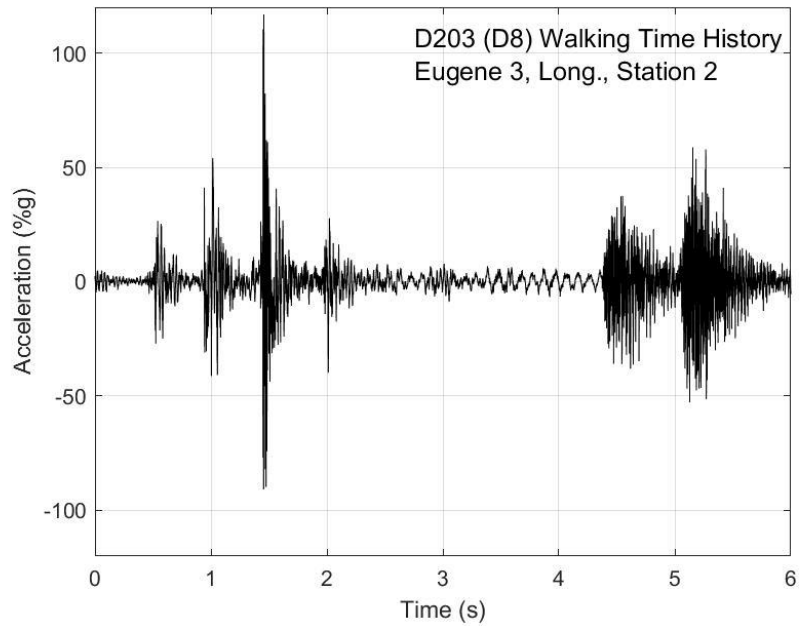


Fig. P-18. Walking time history, Eugene test 3, longitudinal direction, station 2

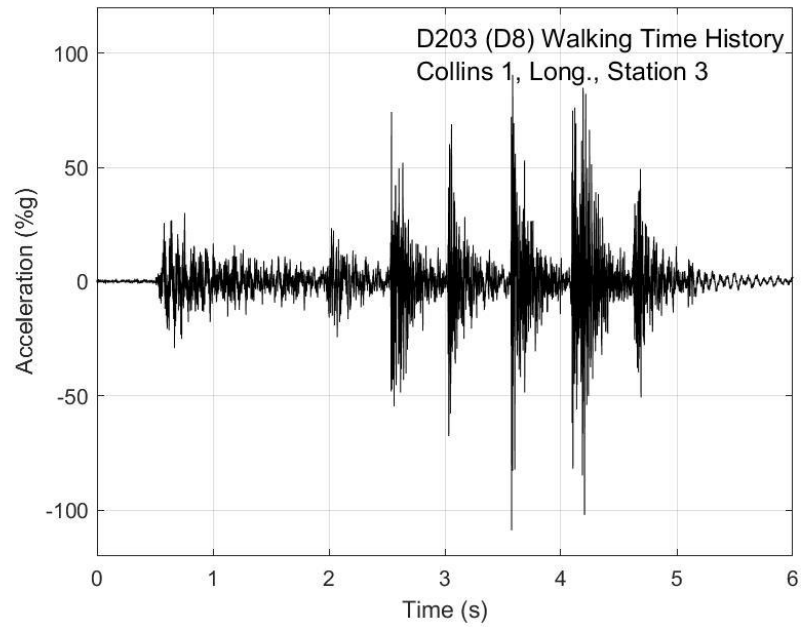


Fig. P-19. Walking time history, Collins test 1, longitudinal direction, station 3

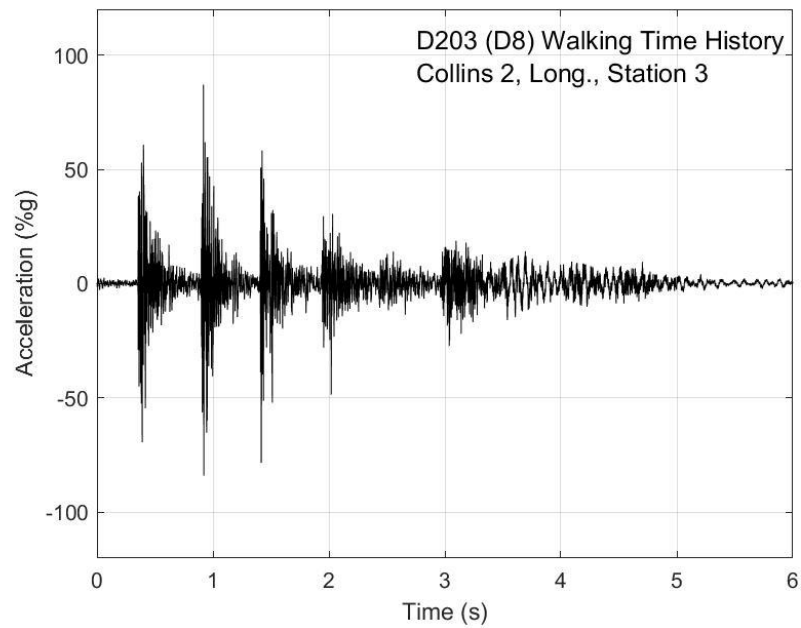


Fig. P-20. Walking time history, Collins test 2, longitudinal direction, station 3

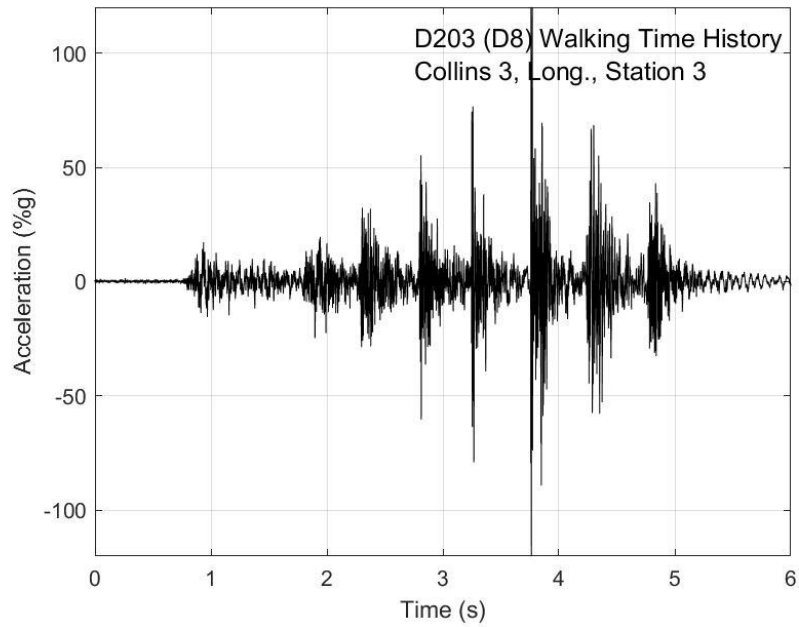


Fig. P-21. Walking time history, Collins test 3, longitudinal direction, station 3

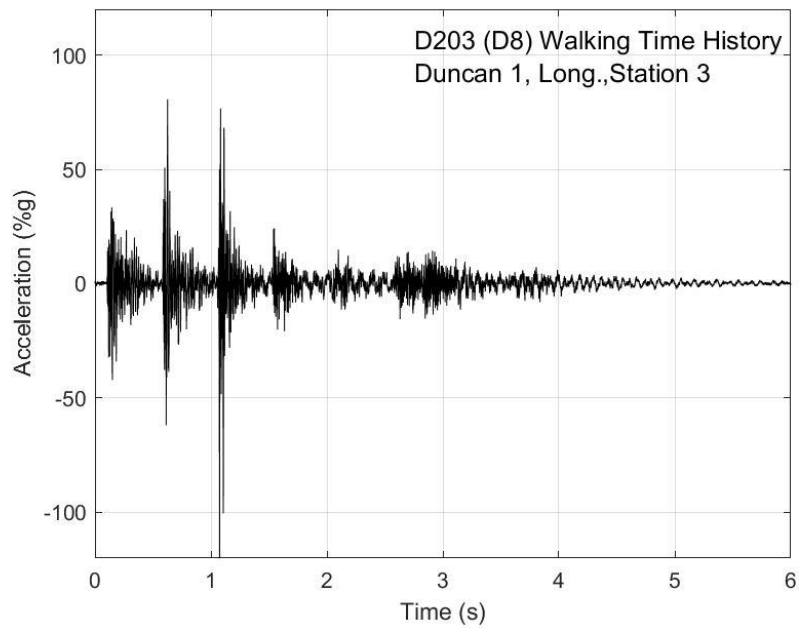


Fig. P-22. Walking time history, Duncan test 1, longitudinal direction, station 3

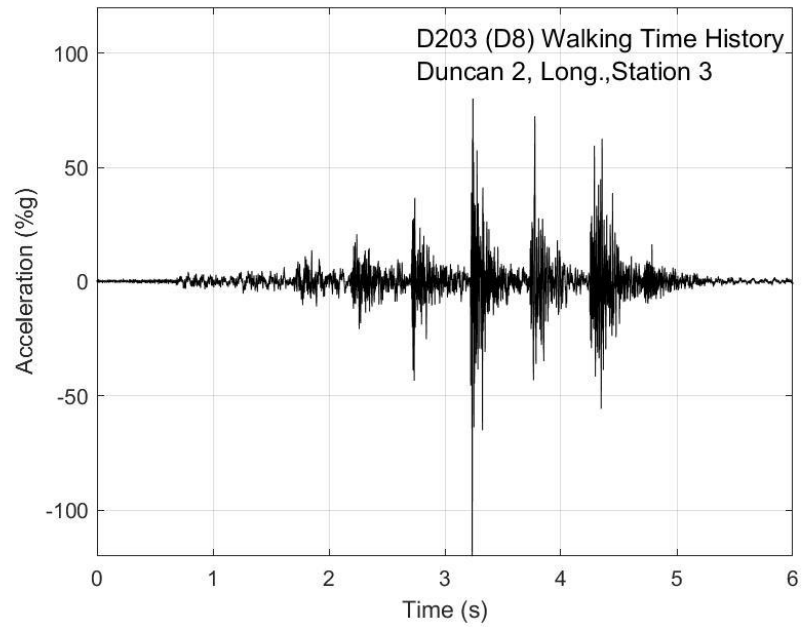


Fig. P-23. Walking time history, Duncan test 2, longitudinal direction, station 3

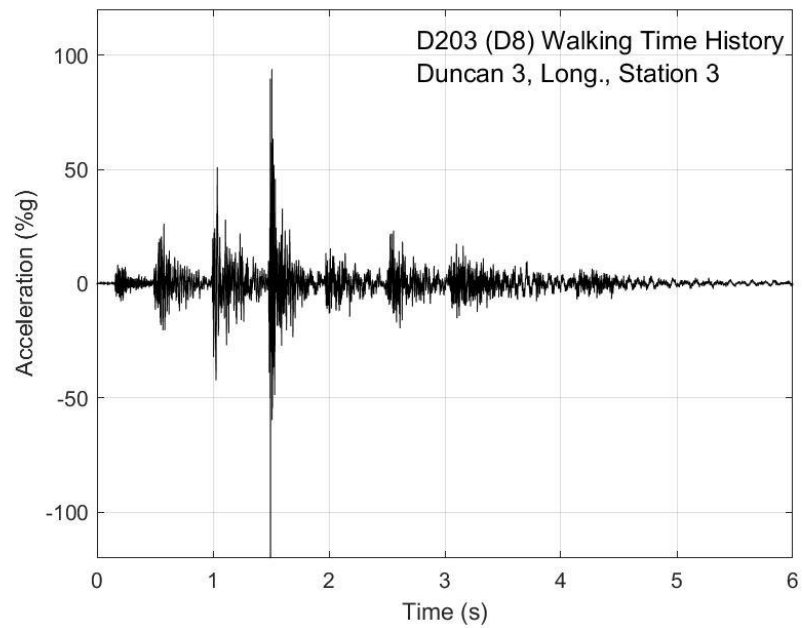


Fig. P-24. Walking time history, Duncan test 3, longitudinal direction, station 3

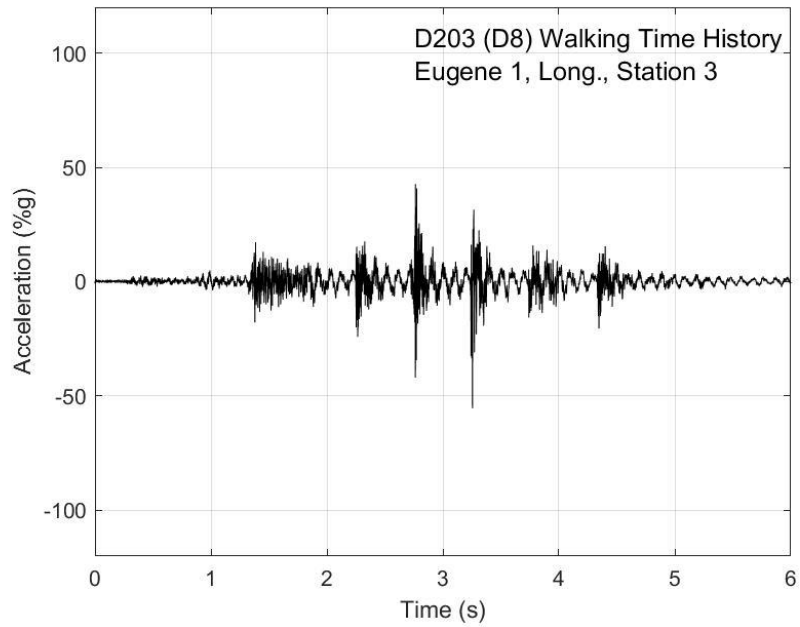


Fig. P-25. Walking time history, Eugene test 1, longitudinal direction, station 3

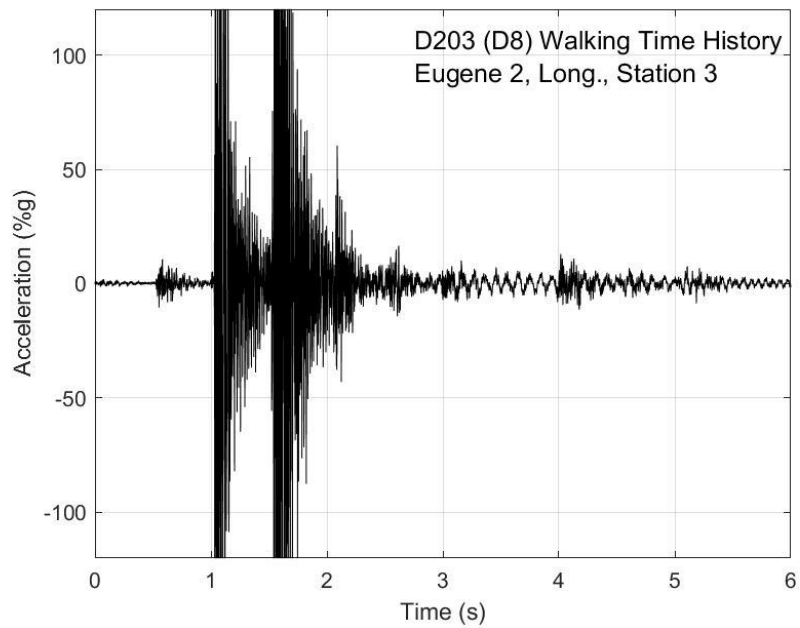


Fig. P-26. Walking time history, Eugene test 2, longitudinal direction, station 3

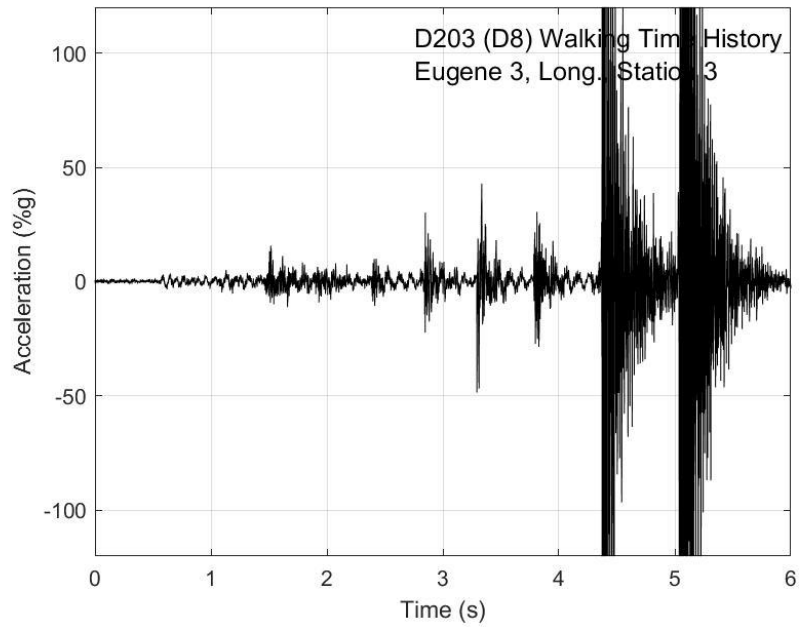


Fig. P-27. Walking time history, Eugene test 3, longitudinal direction, station 3

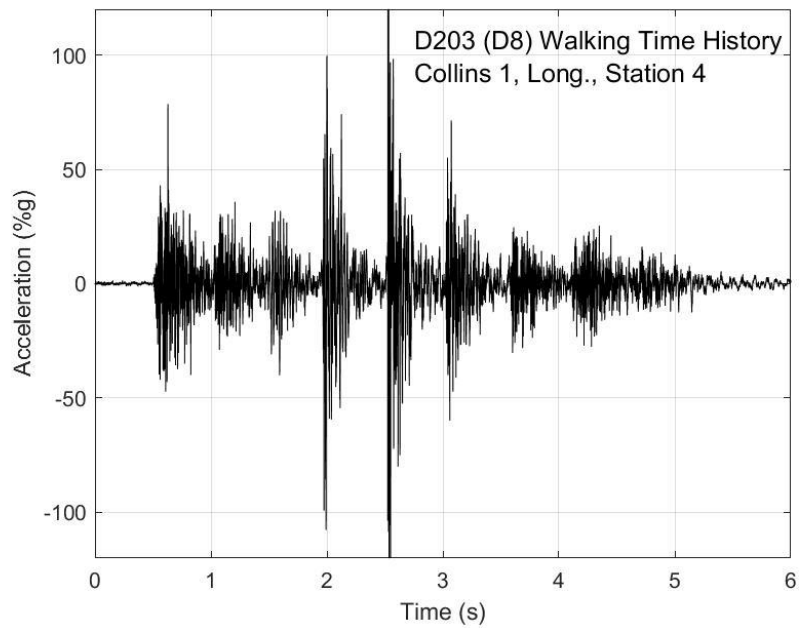


Fig. P-28. Walking time history, Collins test 1, longitudinal direction, station 4

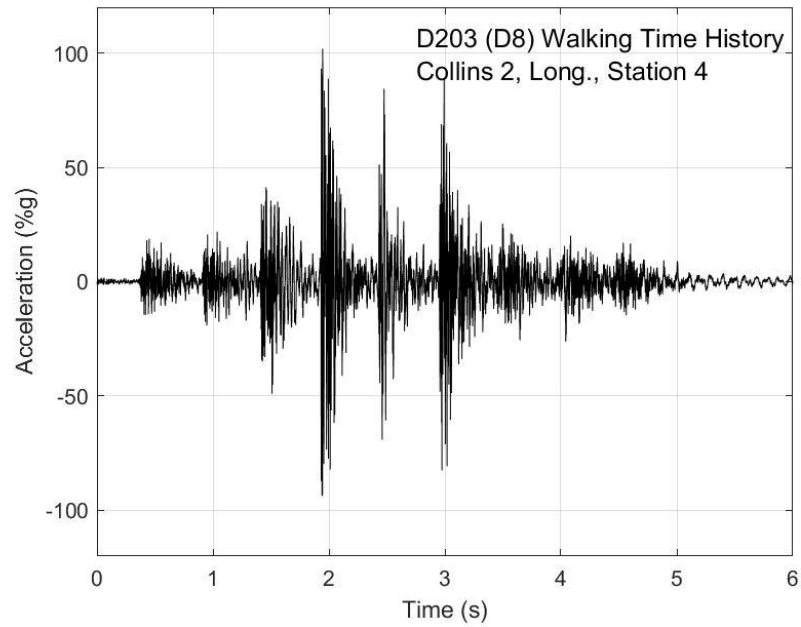


Fig. P-29. Walking time history, Collins test 2, longitudinal direction, station 4

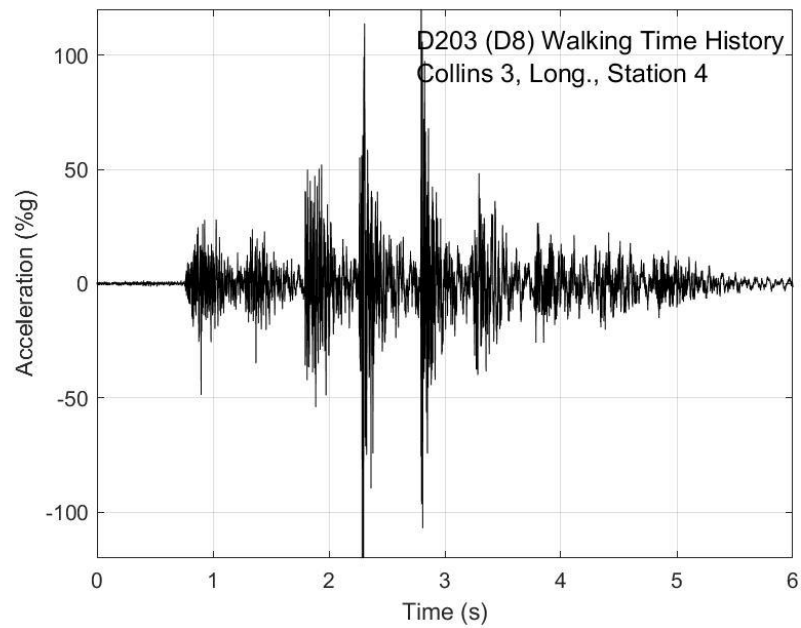


Fig. P-30. Walking time history, Collins test 3, longitudinal direction, station 4

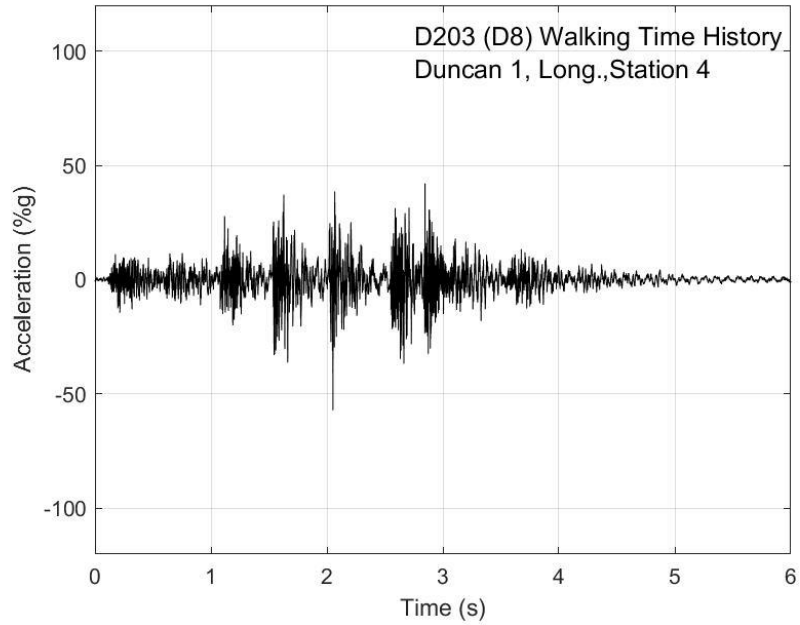


Fig. P-31. Walking time history, Duncan test 1, longitudinal direction, station 4

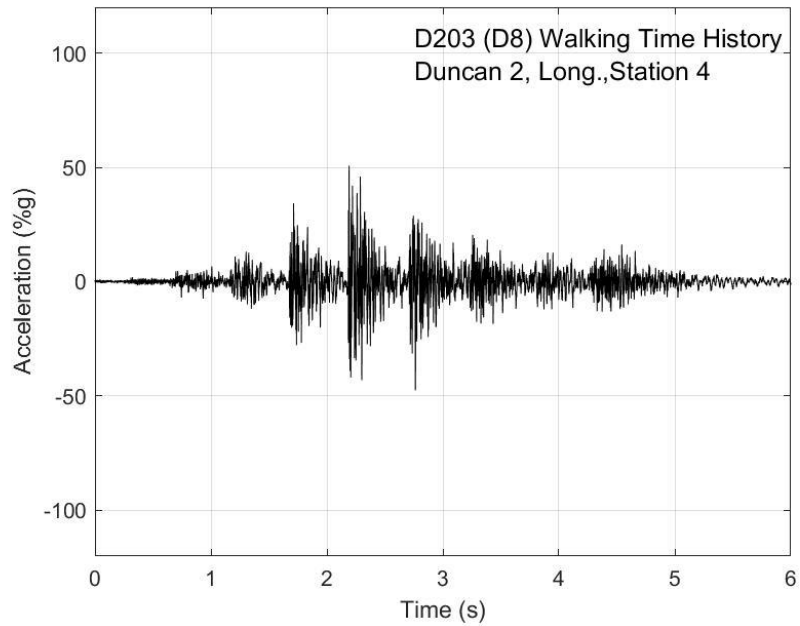


Fig. P-32. Walking time history, Duncan test 2, longitudinal direction, station 4

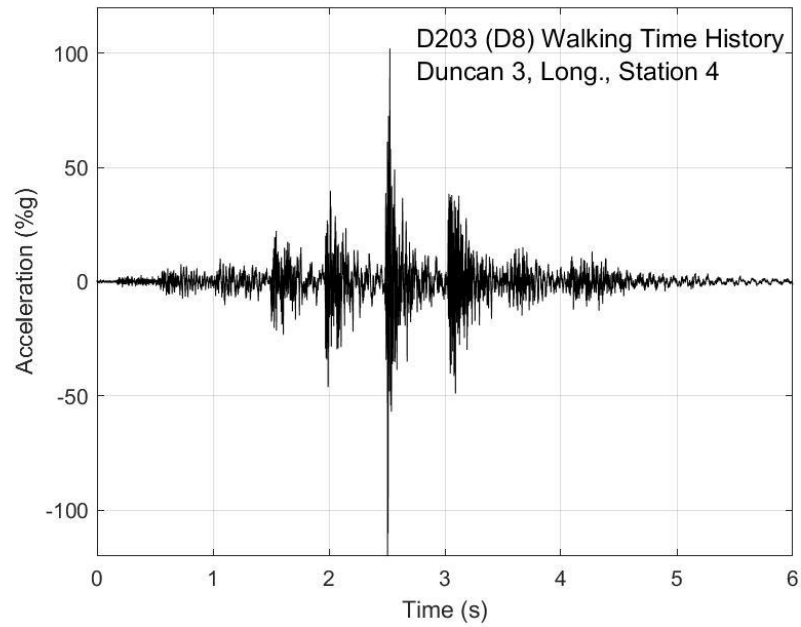


Fig. P-33. Walking time history, Duncan test 3, longitudinal direction, station 4

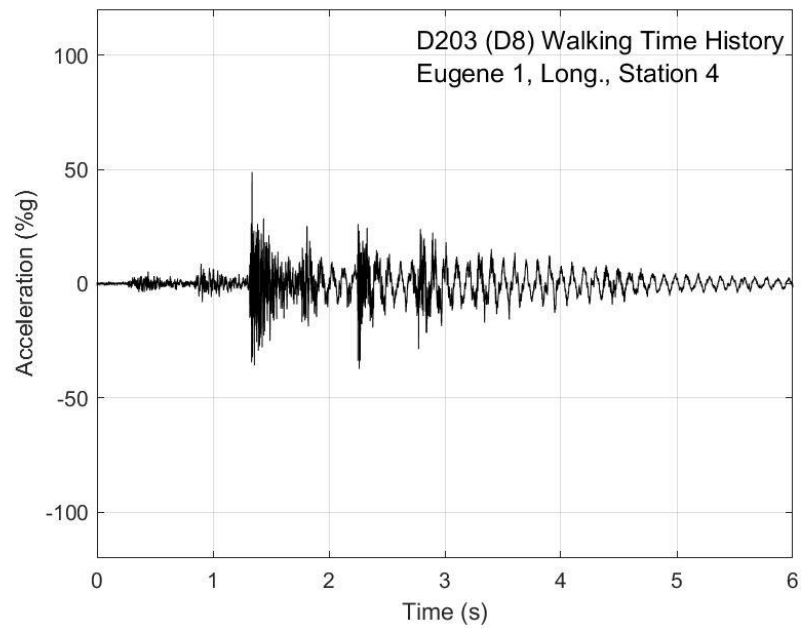


Fig. P-34. Walking time history, Eugene test 1, longitudinal direction, station 4

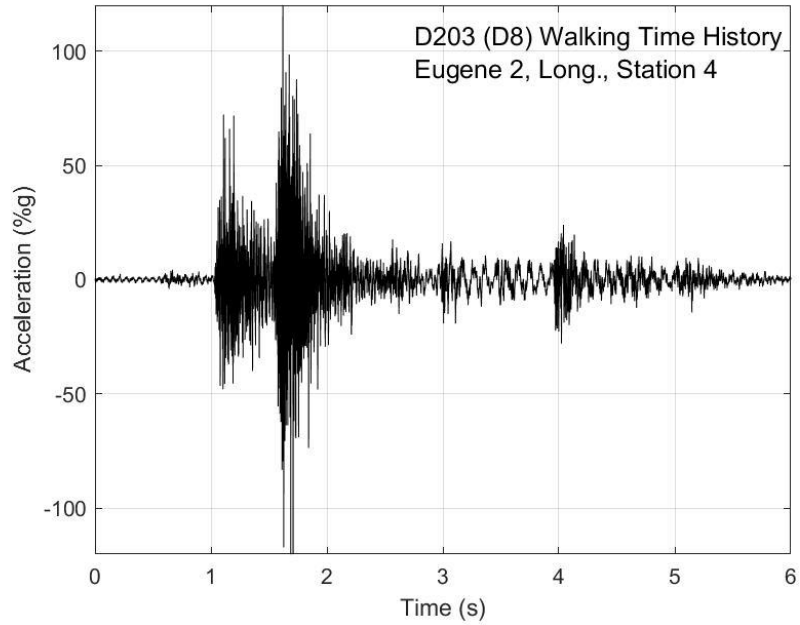


Fig. P-35. Walking time history, Eugene test 2, longitudinal direction, station 4

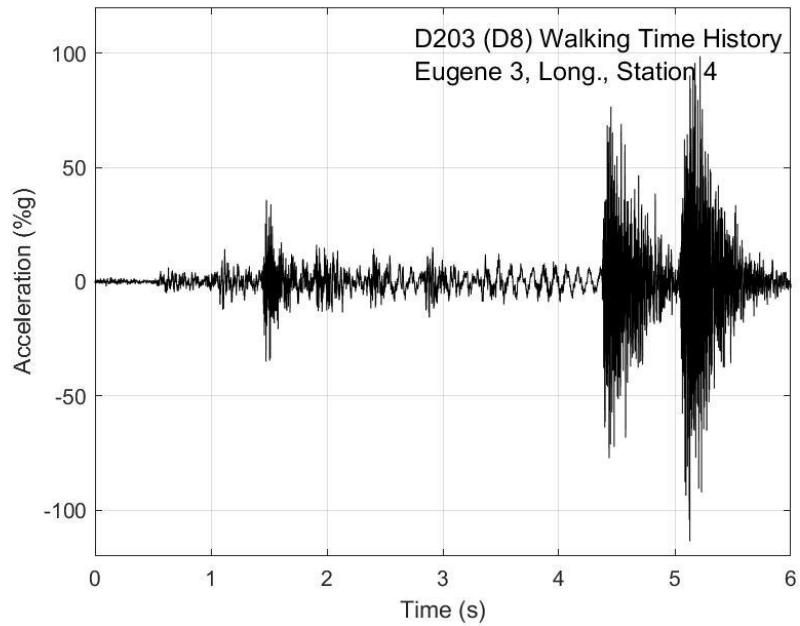


Fig. P-36. Walking time history, Eugene test 3, longitudinal direction, station 4

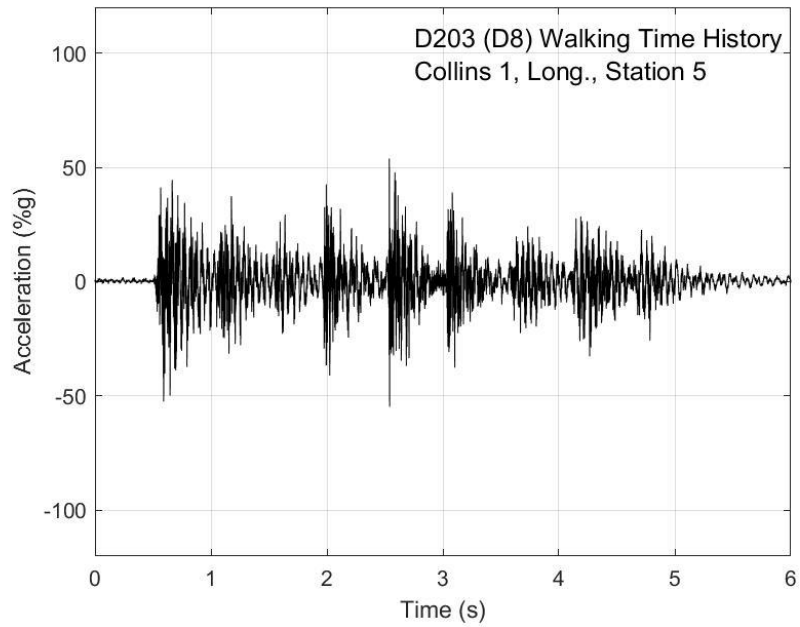


Fig. P-37. Walking time history, Collins test 1, longitudinal direction, station 5

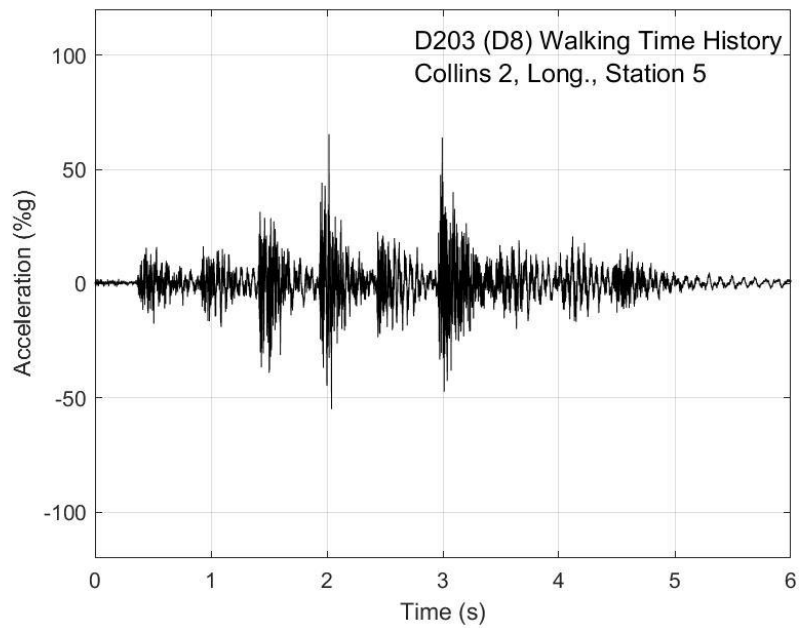


Fig. P-38. Walking time history, Collins test 2, longitudinal direction, station 5

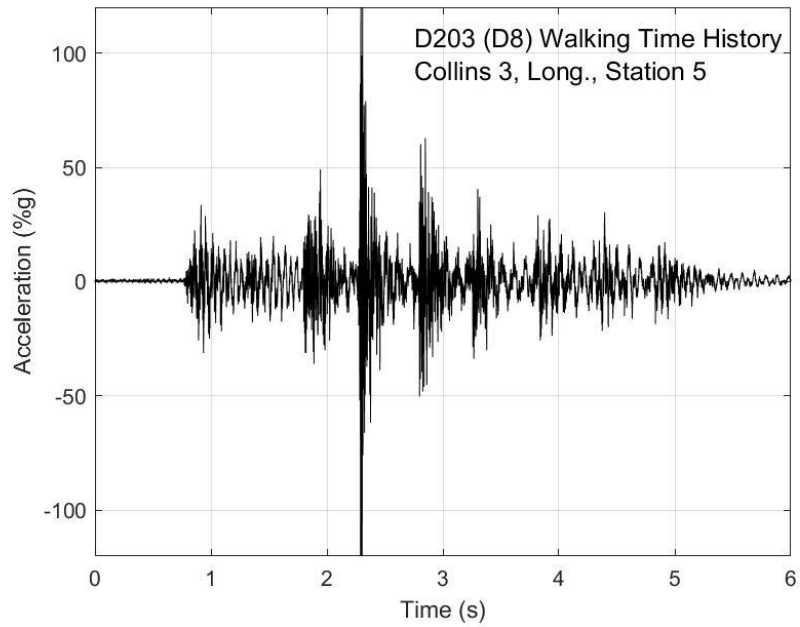


Fig. P-39. Walking time history, Collins test 3, longitudinal direction, station 5

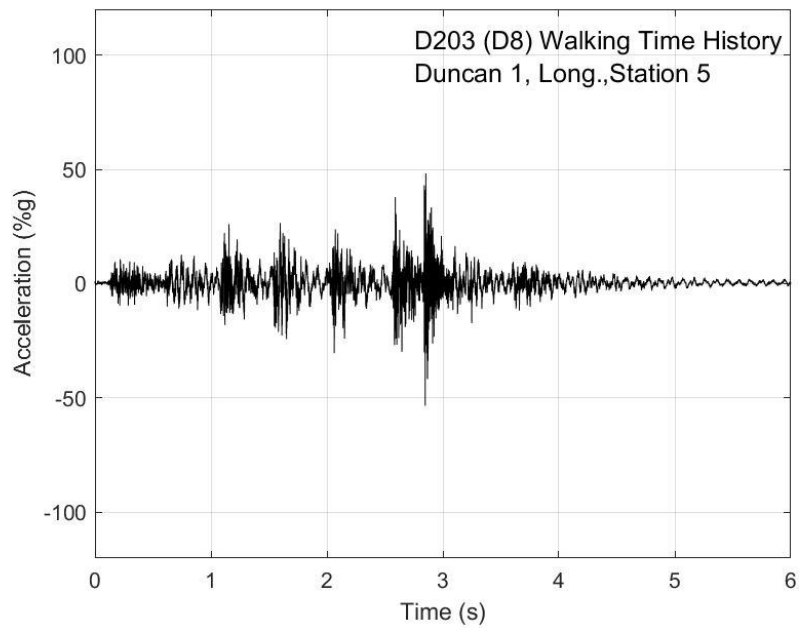


Fig. P-40. Walking time history, Duncan test 1, longitudinal direction, station 5

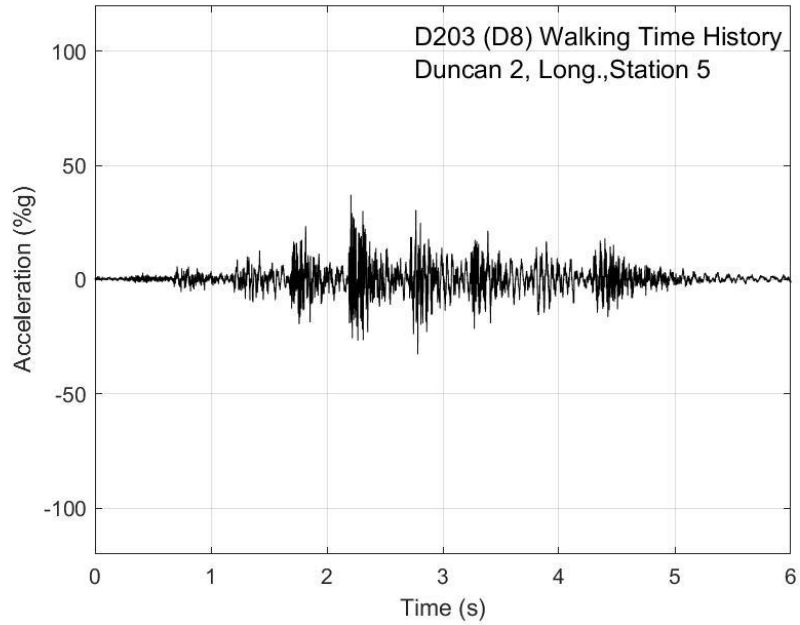


Fig. P-41. Walking time history, Duncan test 2, longitudinal direction, station 5

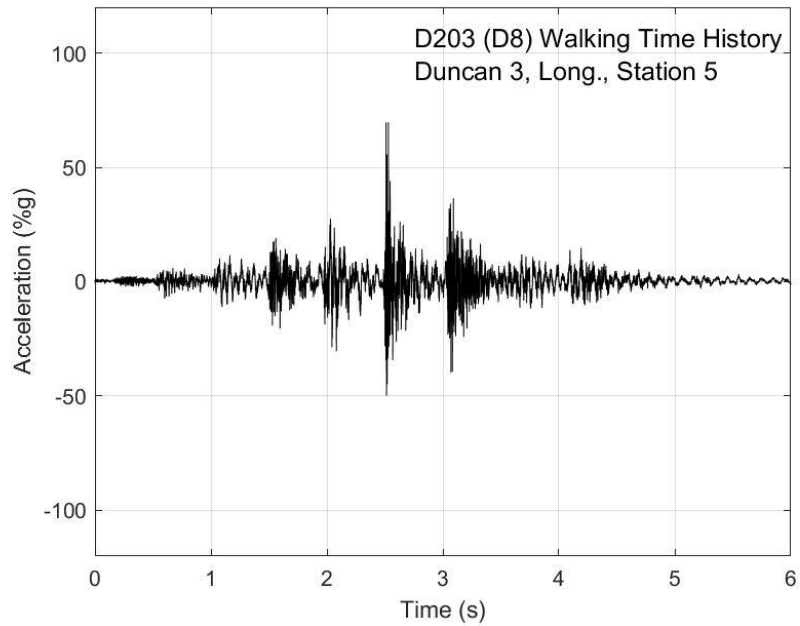


Fig. P-42. Walking time history, Duncan test 3, longitudinal direction, station 5

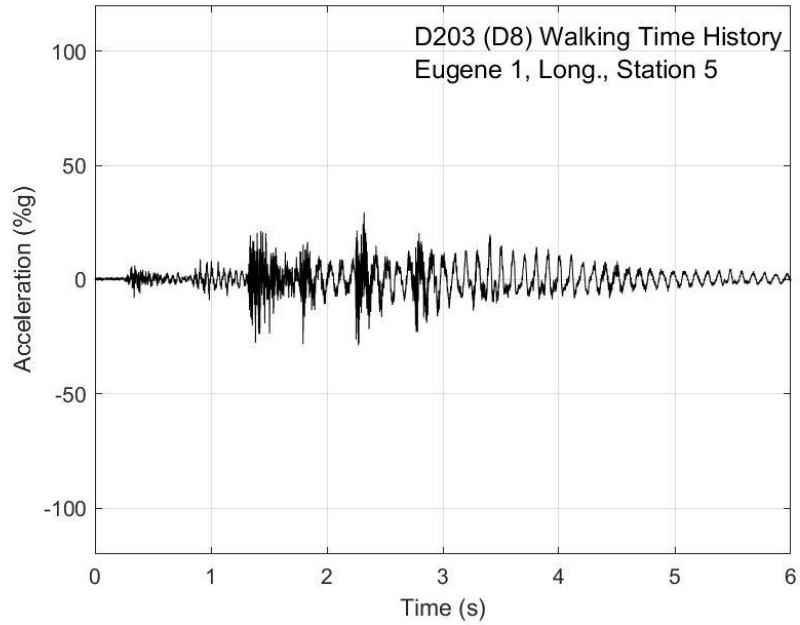


Fig. P-43. Walking time history, Eugene test 1, longitudinal direction, station 5

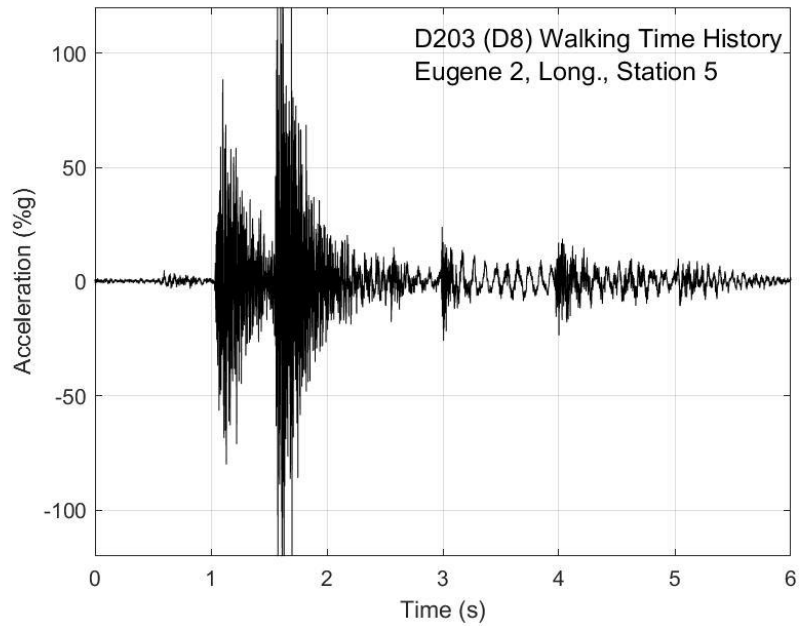


Fig. P-44. Walking time history, Eugene test 2, longitudinal direction, station 5

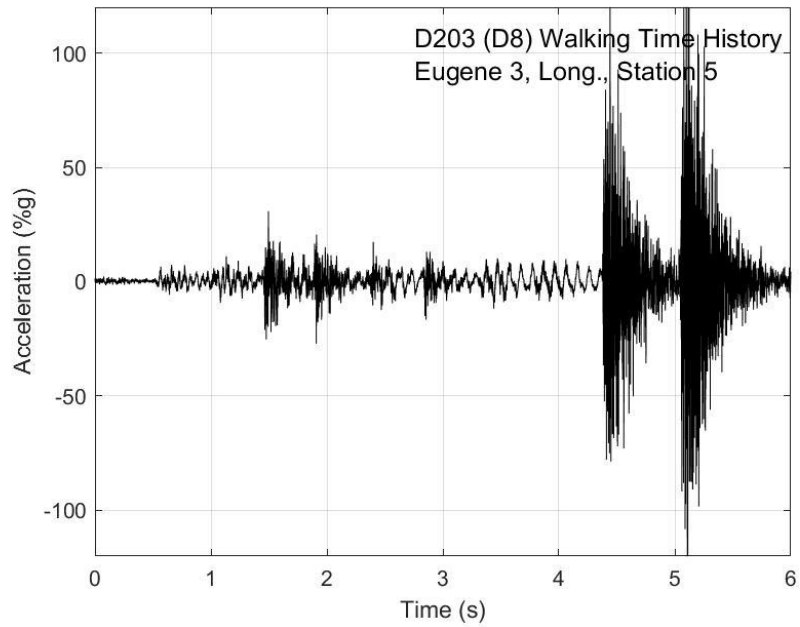


Fig. P-45. Walking time history, Eugene test 3, longitudinal direction, station 5

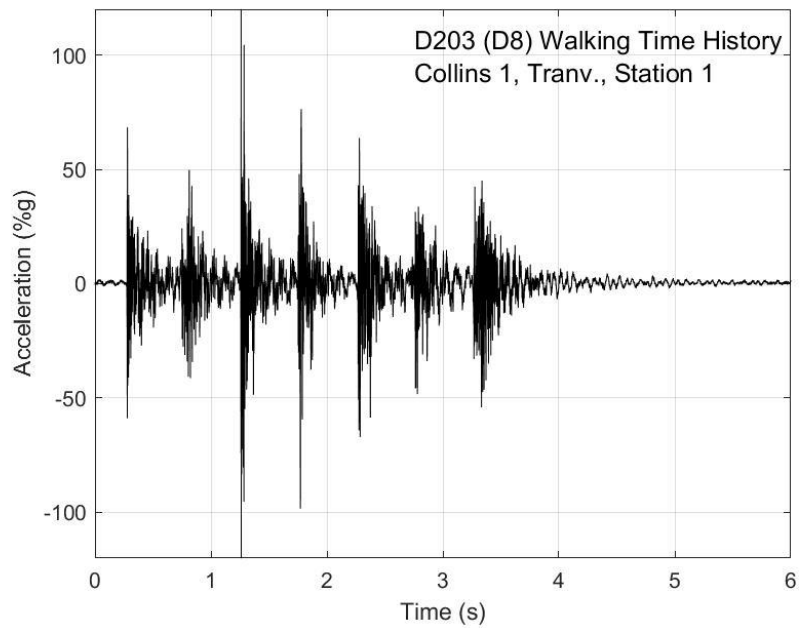


Fig. P-46. Walking time history, Collins test 1, transverse direction, station 1

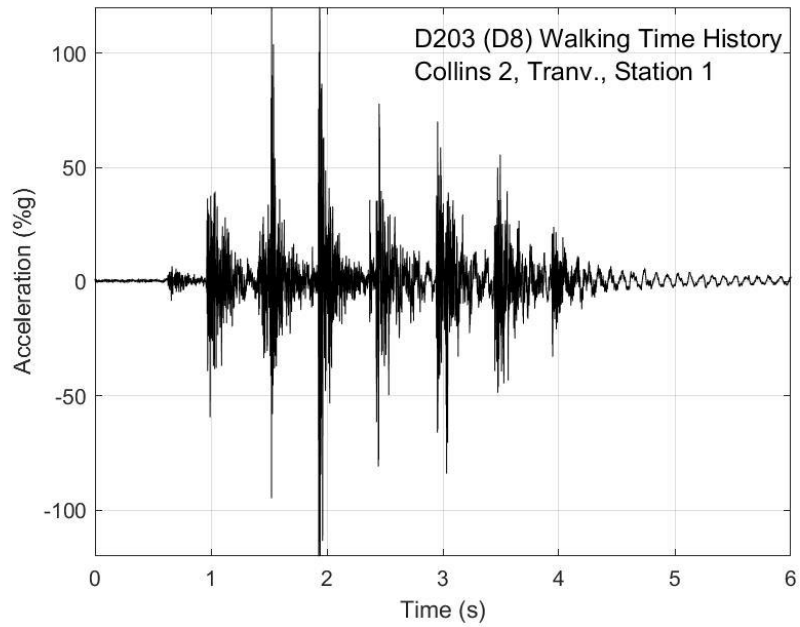


Fig. P-47. Walking time history, Collins test 2, transverse direction, station 1

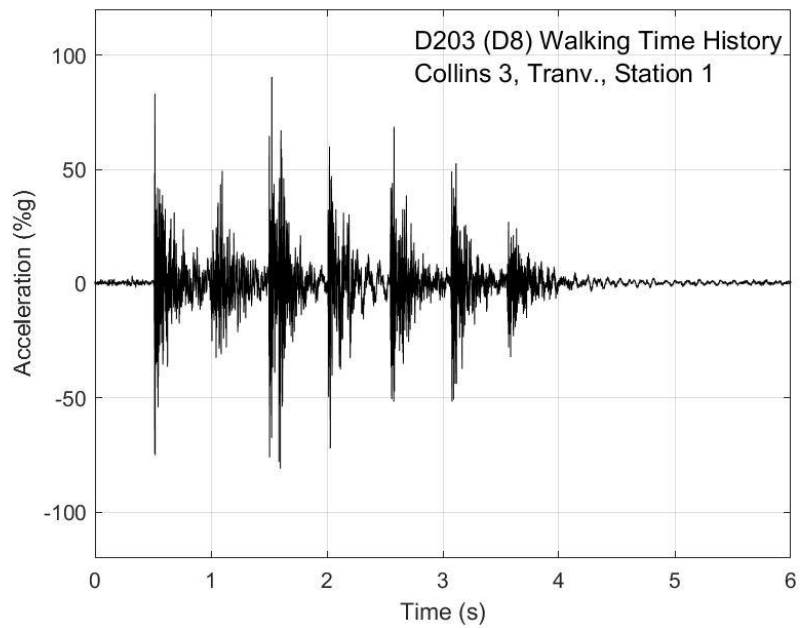


Fig. P-48. Walking time history, Collins test 3, transverse direction, station 1

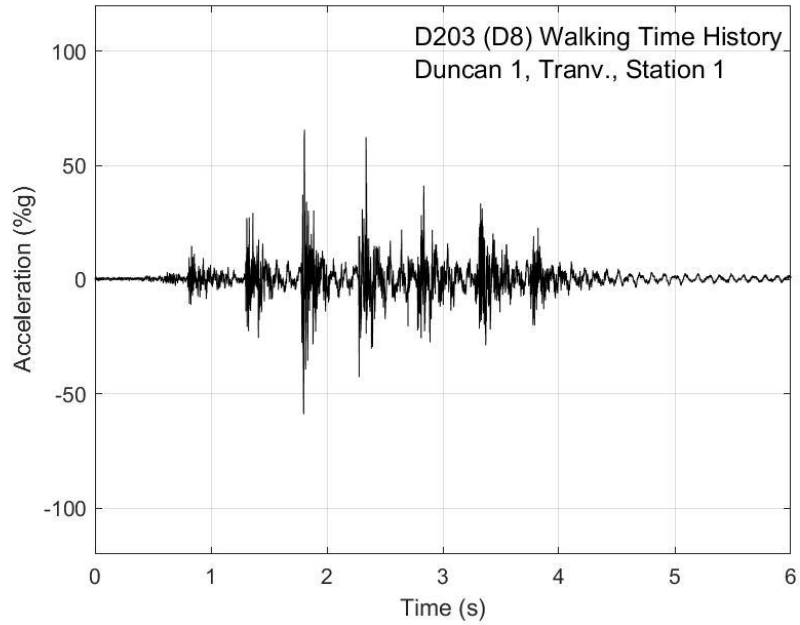


Fig. P-49. Walking time history, Duncan test 1, transverse direction, station 1

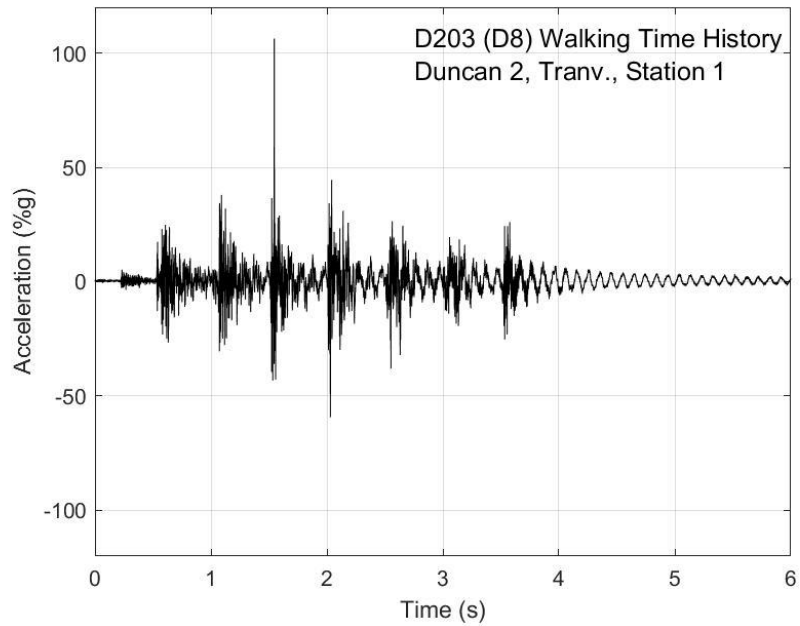


Fig. P-50. Walking time history, Duncan test 2, transverse direction, station 1

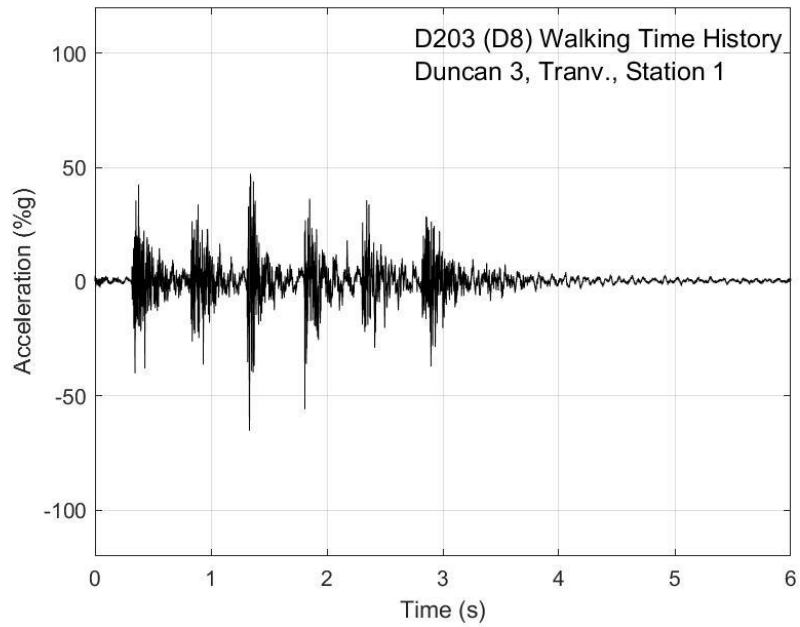


Fig. P-51. Walking time history, Duncan test 3, transverse direction, station 1

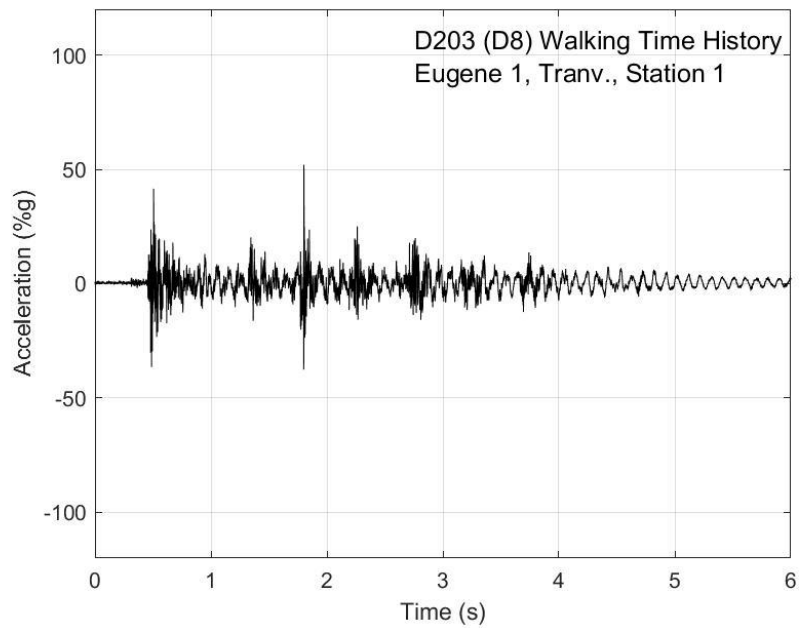


Fig. P-52. Walking time history, Eugene test 1, transverse direction, station 1

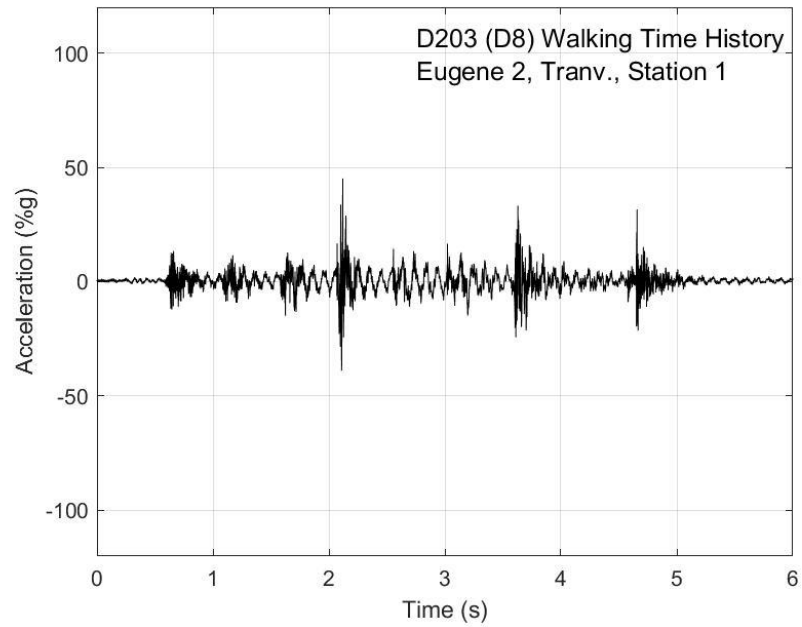


Fig. P-53. Walking time history, Eugene test 2, transverse direction, station 1

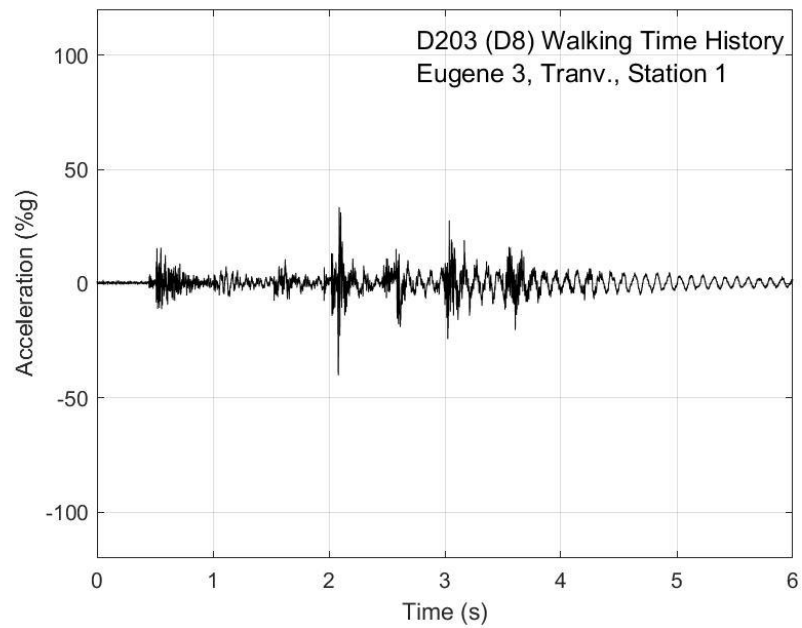


Fig. P-54. Walking time history, Eugene test 3, transverse direction, station 1

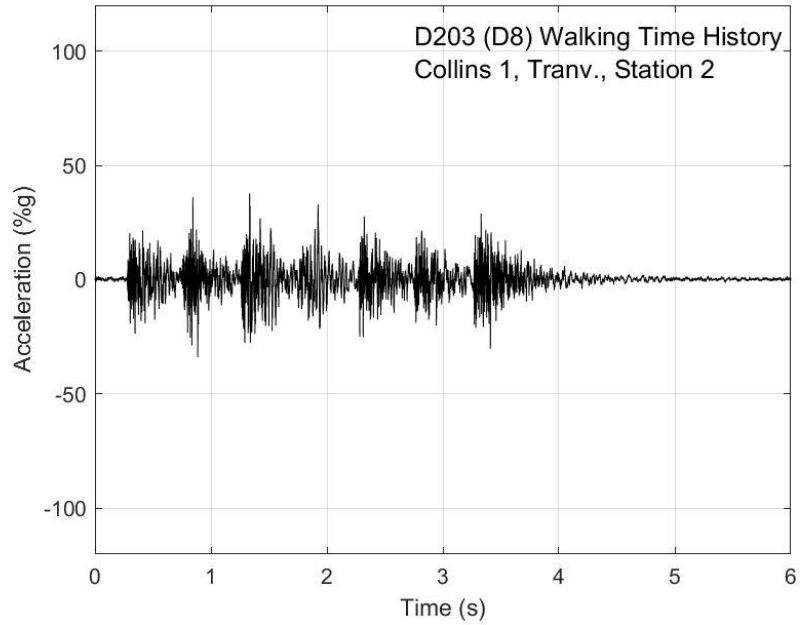


Fig. P-55. Walking time history, Collins test 1, transverse direction, station 2

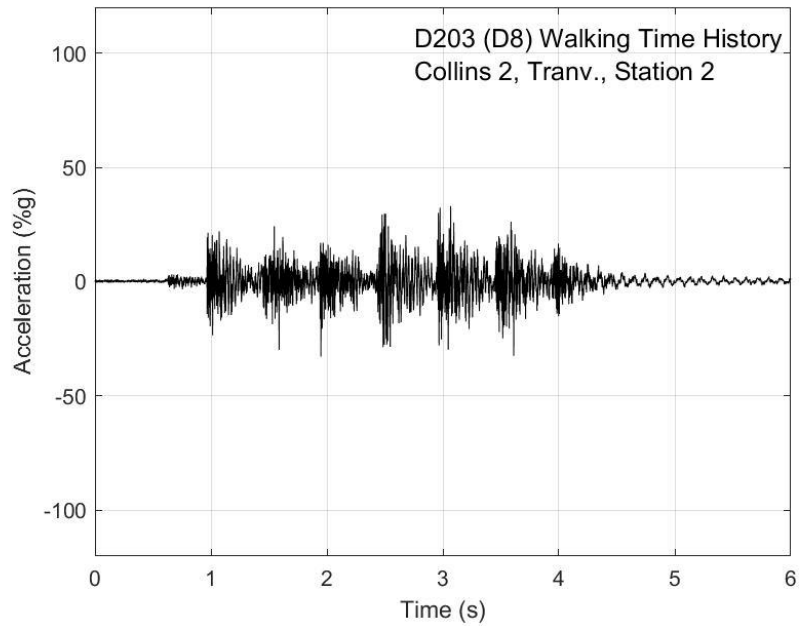


Fig. P-56. Walking time history, Collins test 2, transverse direction, station 2

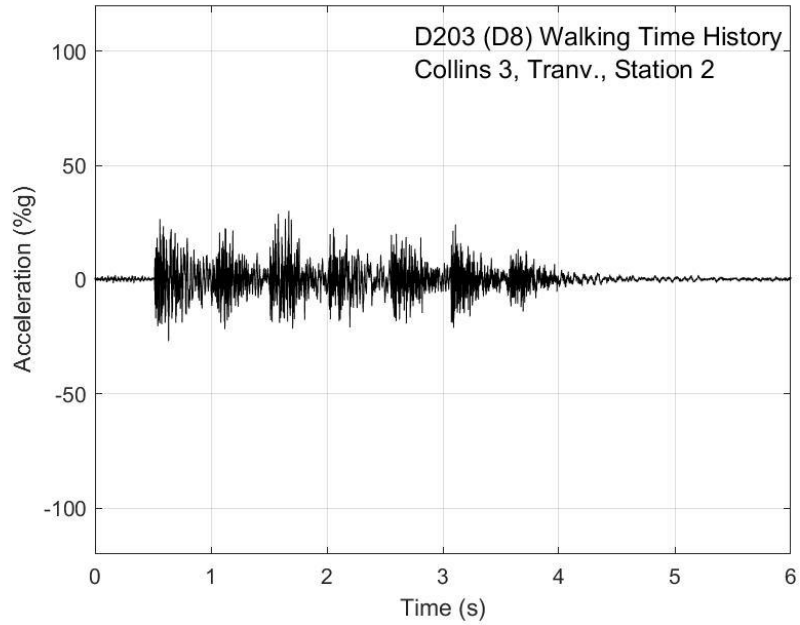


Fig. P-57. Walking time history, Collins test 3, transverse direction, station 2

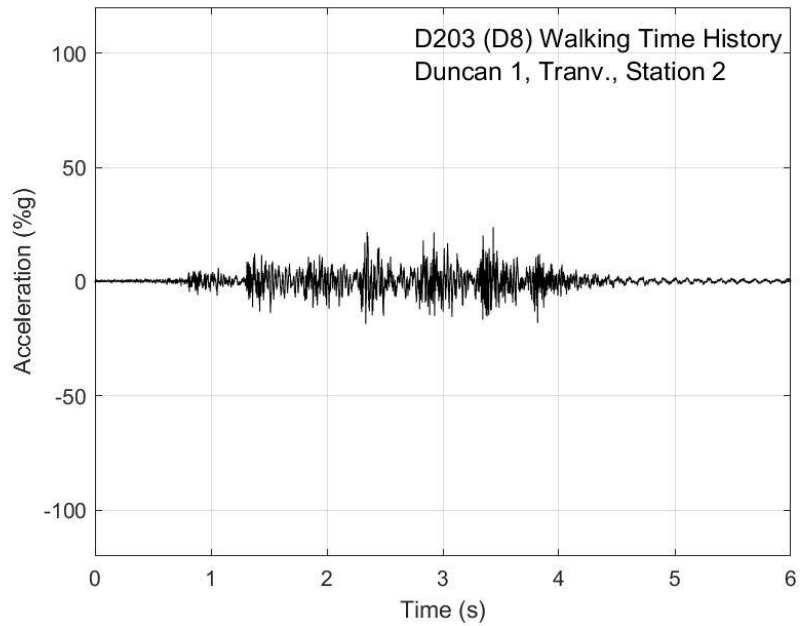


Fig. P-58. Walking time history, Duncan test 1, transverse direction, station 2

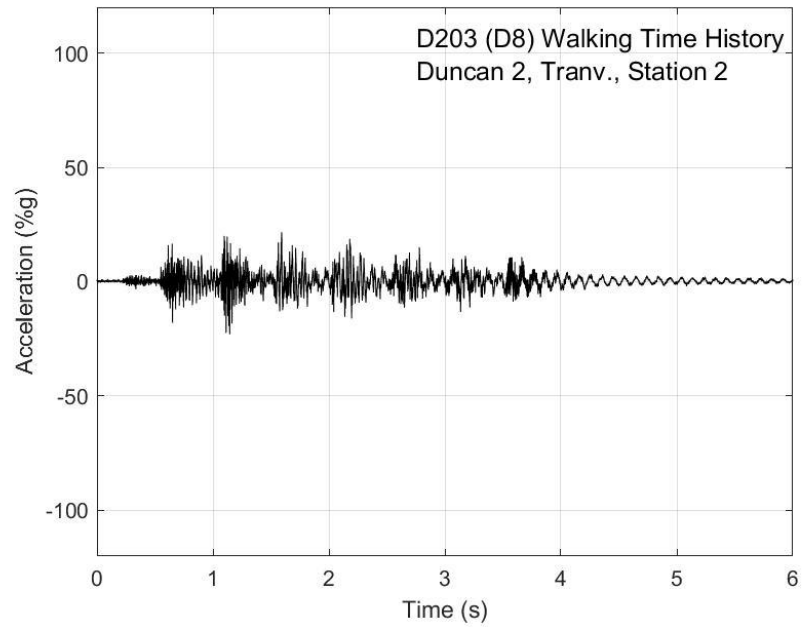


Fig. P-59. Walking time history, Duncan test 2, transverse direction, station 2

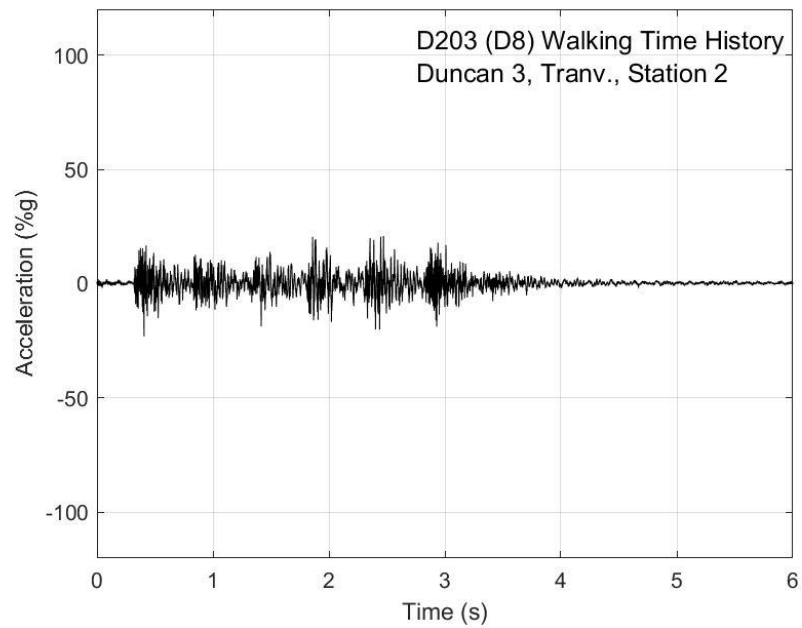


Fig. P-60. Walking time history, Duncan test 3, transverse direction, station 2

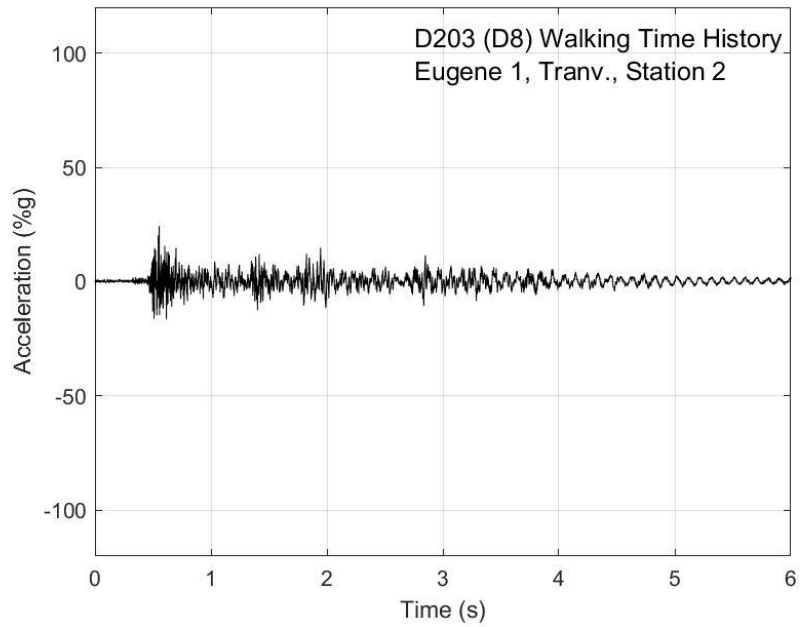


Fig. P-61. Walking time history, Eugene test 1, transverse direction, station 2

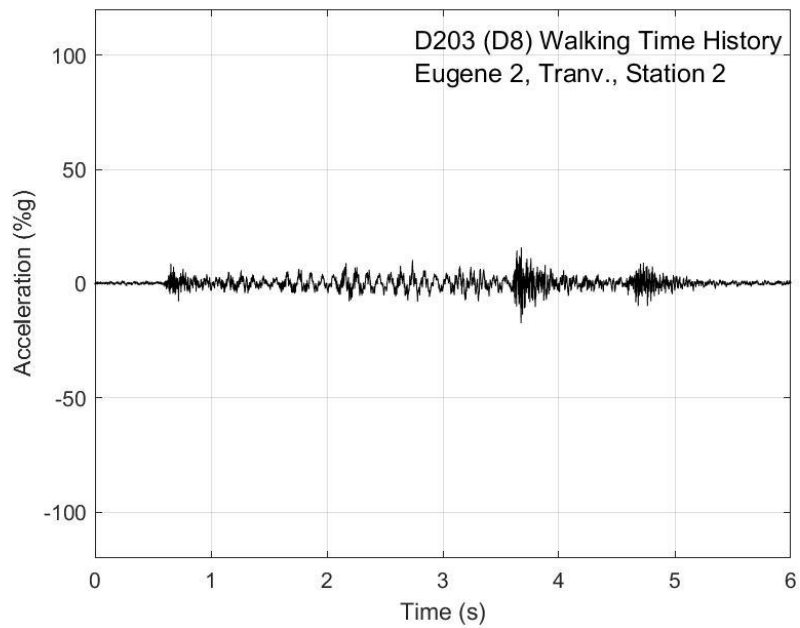


Fig. P-62. Walking time history, Eugene test 2, transverse direction, station 2

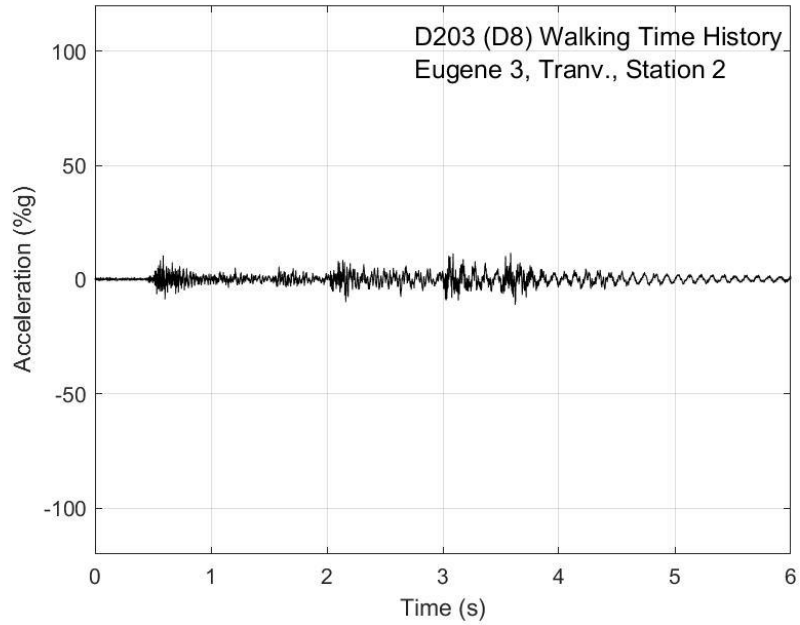


Fig. P-63. Walking time history, Eugene test 3, transverse direction, station 2

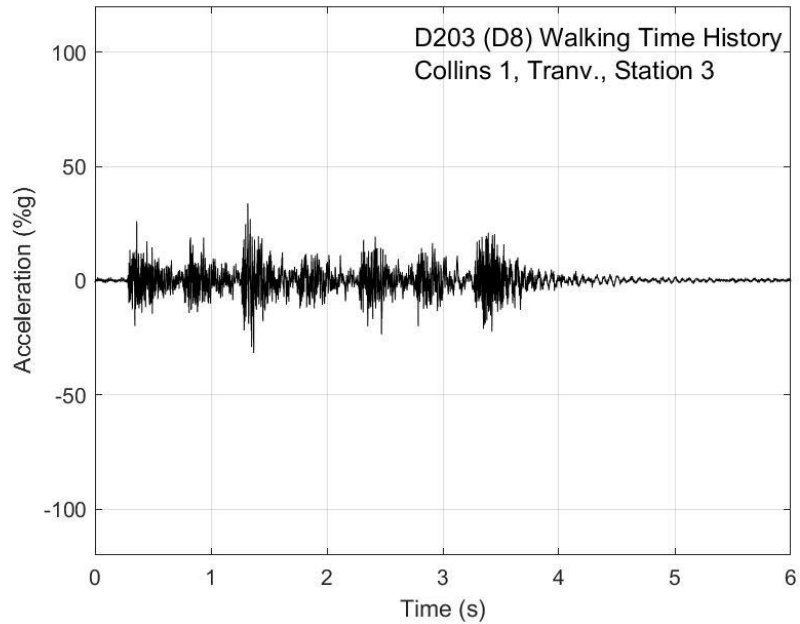


Fig. P-64. Walking time history, Collins test 1, transverse direction, station 3

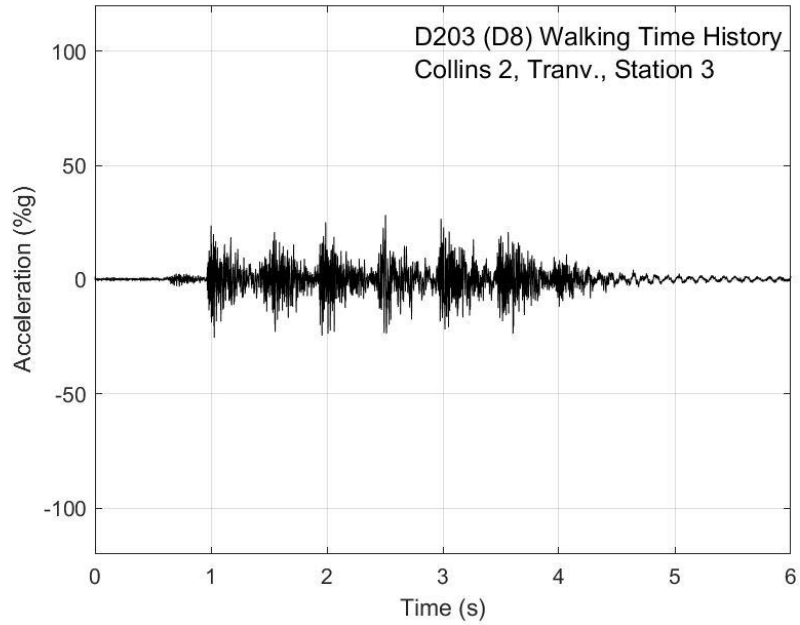


Fig. P-65. Walking time history, Collins test 2, transverse direction, station 3

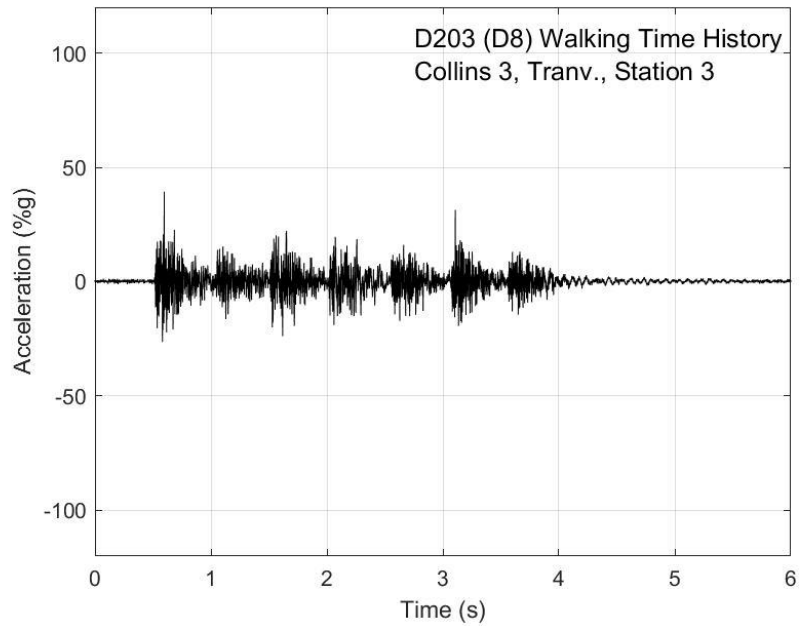


Fig. P-66. Walking time history, Collins test 3, transverse direction, station 3

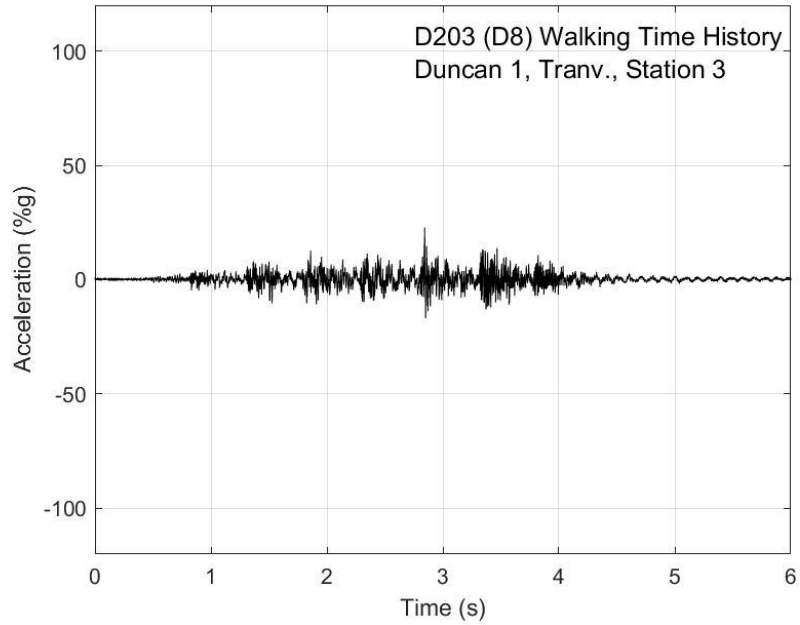


Fig. P-67. Walking time history, Duncan test 1, transverse direction, station 3

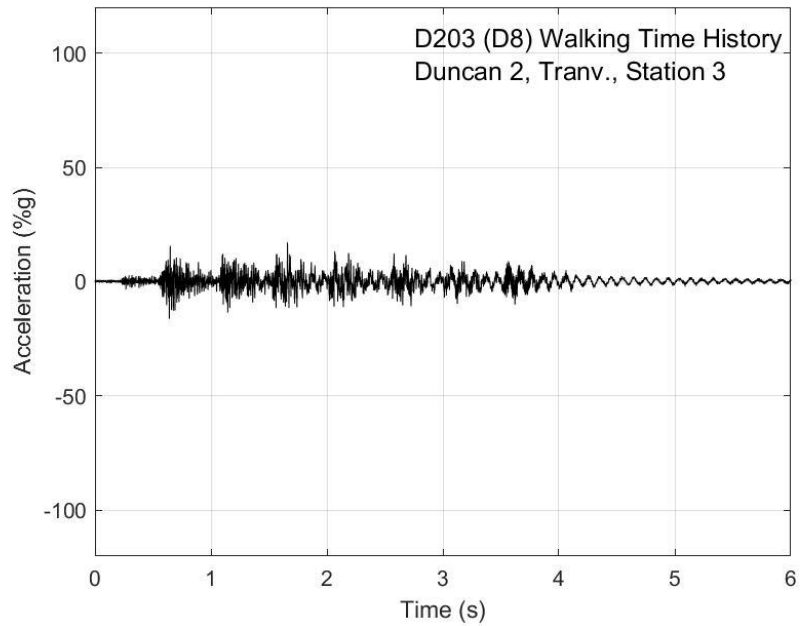


Fig. P-68. Walking time history, Duncan test 2, transverse direction, station 3

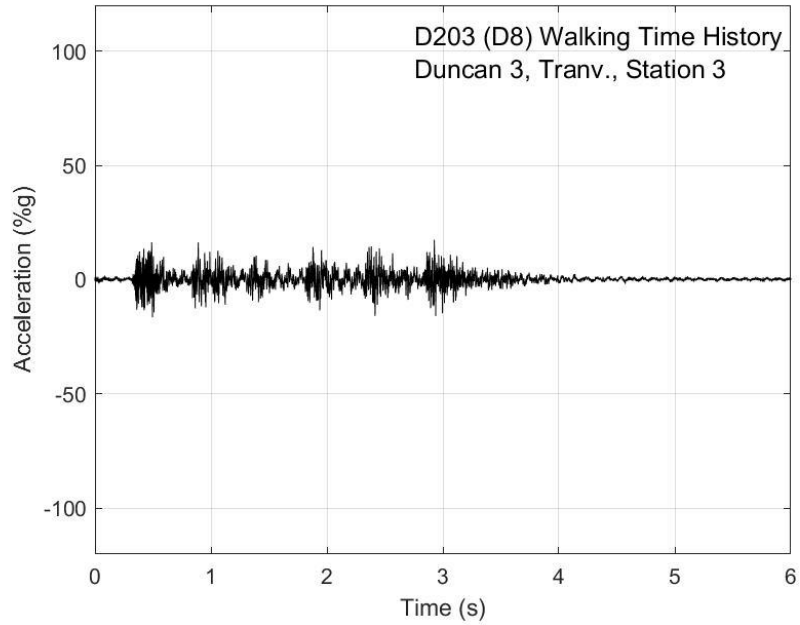


Fig. P-69. Walking time history, Duncan test 3, transverse direction, station 3

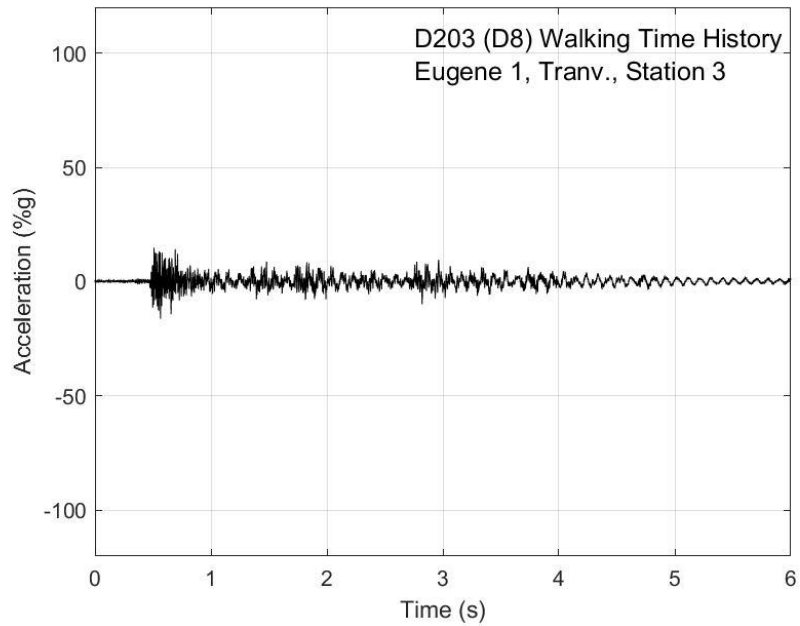


Fig. P-70. Walking time history, Eugene test 1, transverse direction, station 3

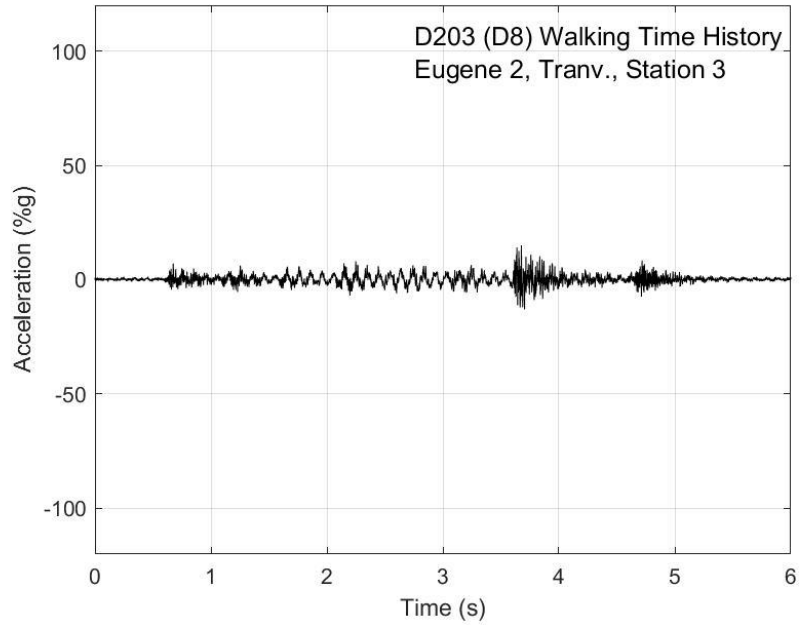


Fig. P-71. Walking time history, Eugene test 2, transverse direction, station 3

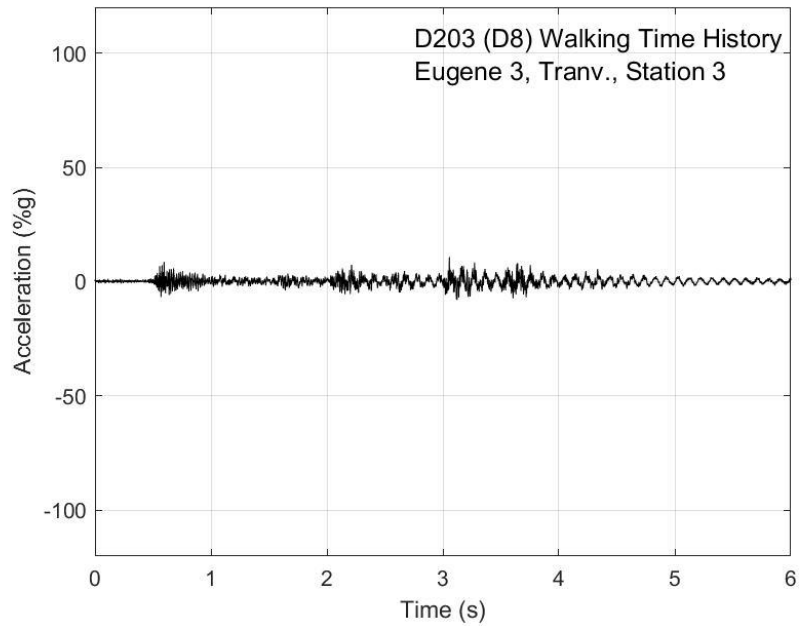


Fig. P-72. Walking time history, Eugene test 3, transverse direction, station 3

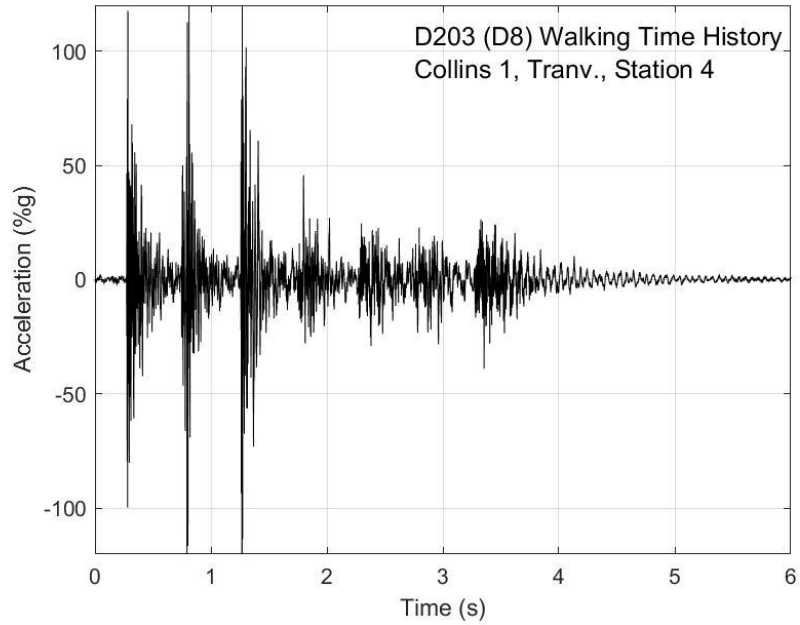


Fig. P-73. Walking time history, Collins test 1, transverse direction, station 4

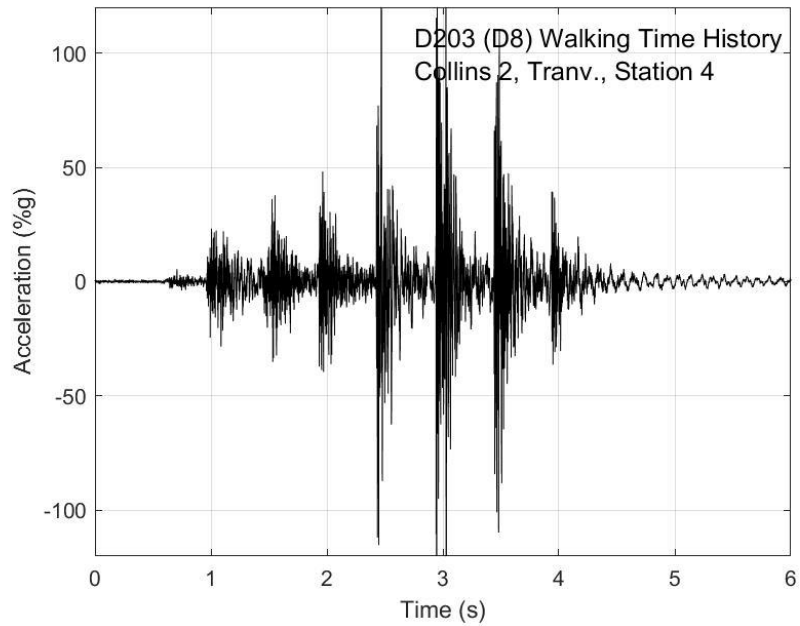


Fig. P-74. Walking time history, Collins test 2, transverse direction, station 4

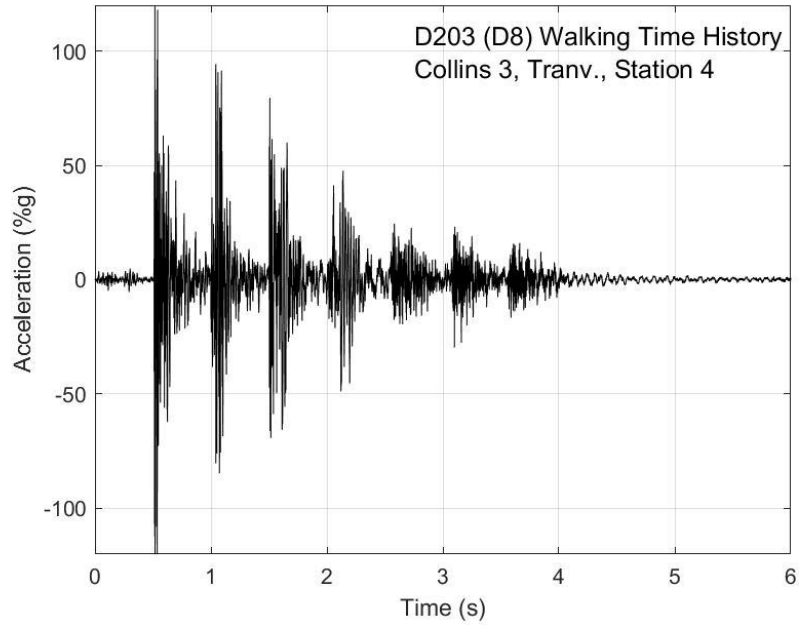


Fig. P-75. Walking time history, Collins test 3, transverse direction, station 4

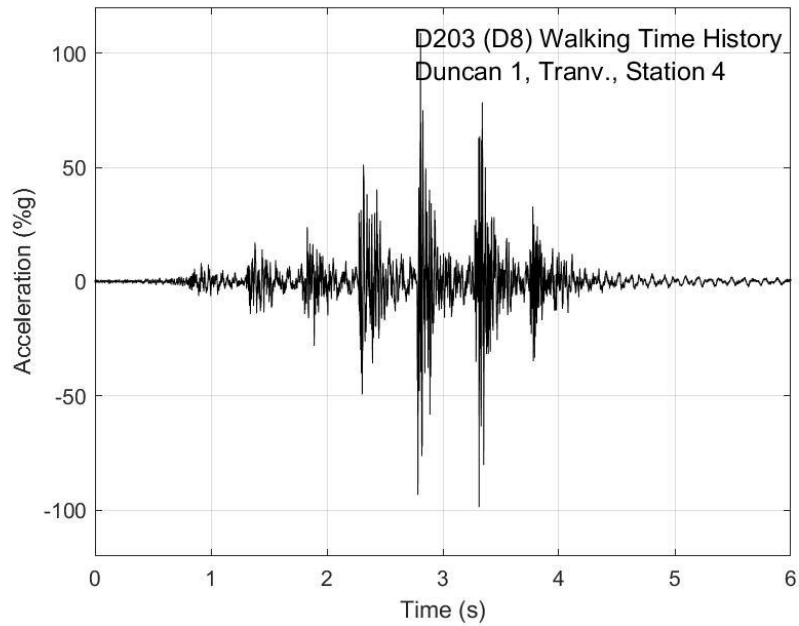


Fig. P-76. Walking time history, Duncan test 1, transverse direction, station 4

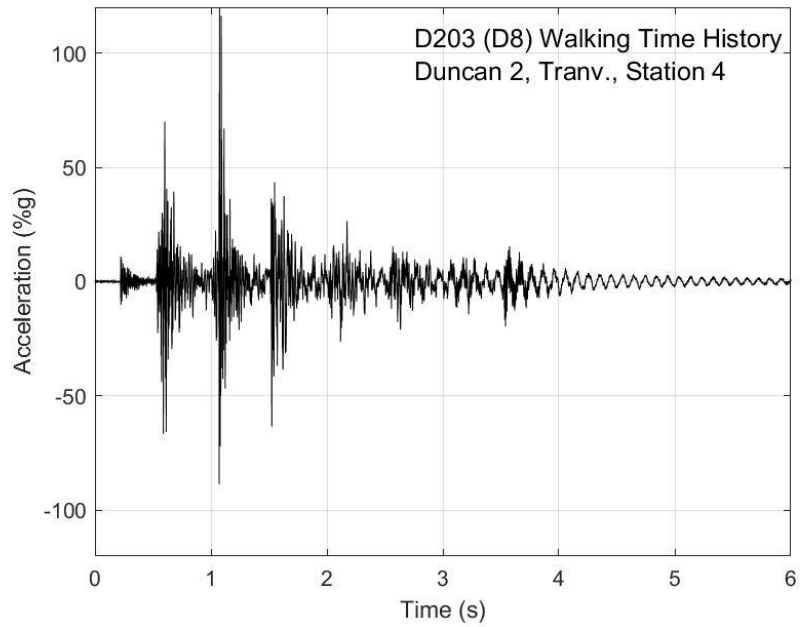


Fig. P-77. Walking time history, Duncan test 2, transverse direction, station 4

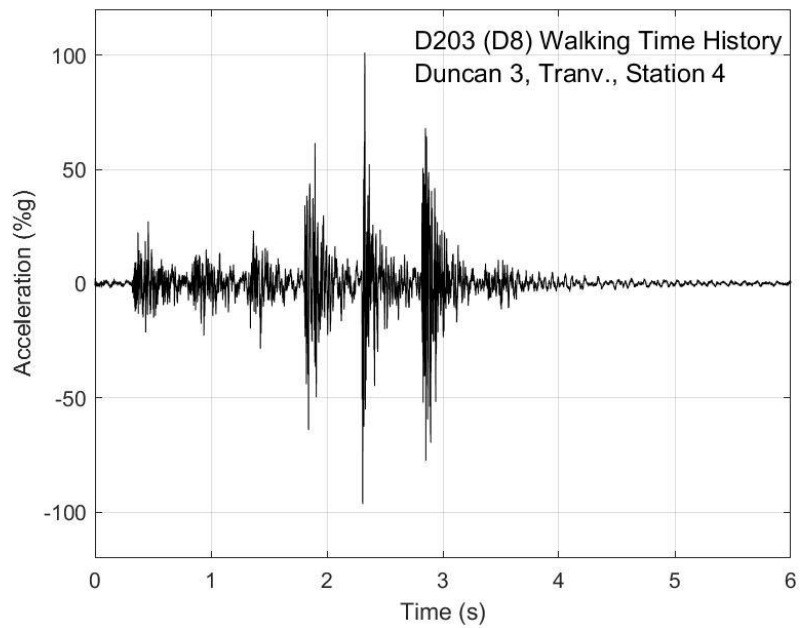


Fig. P-78. Walking time history, Duncan test 3, transverse direction, station 4

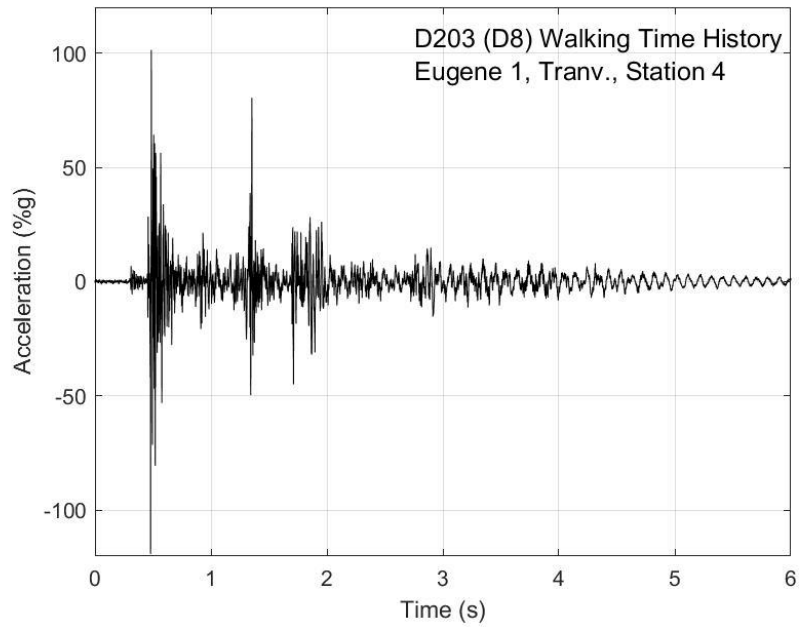


Fig. P-79. Walking time history, Eugene test 1, transverse direction, station 4

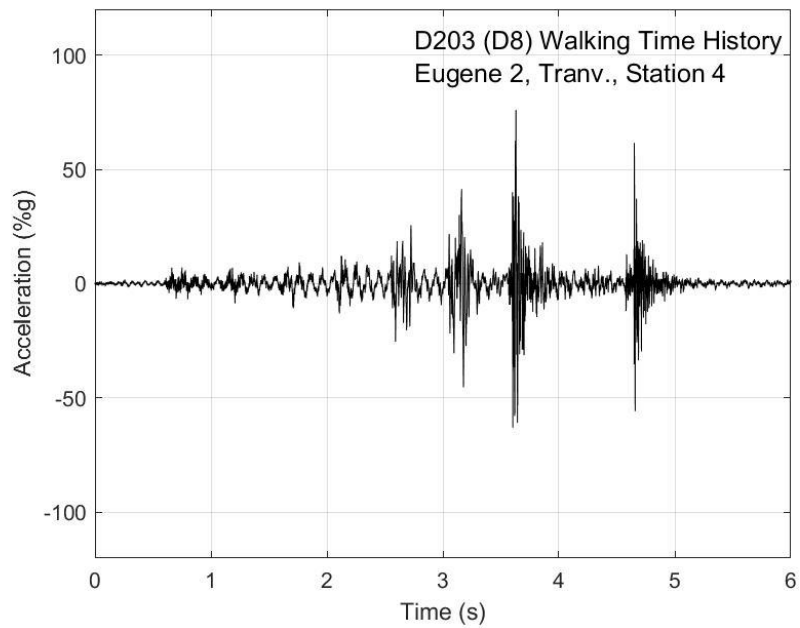


Fig. P-80. Walking time history, Eugene test 2, transverse direction, station 4

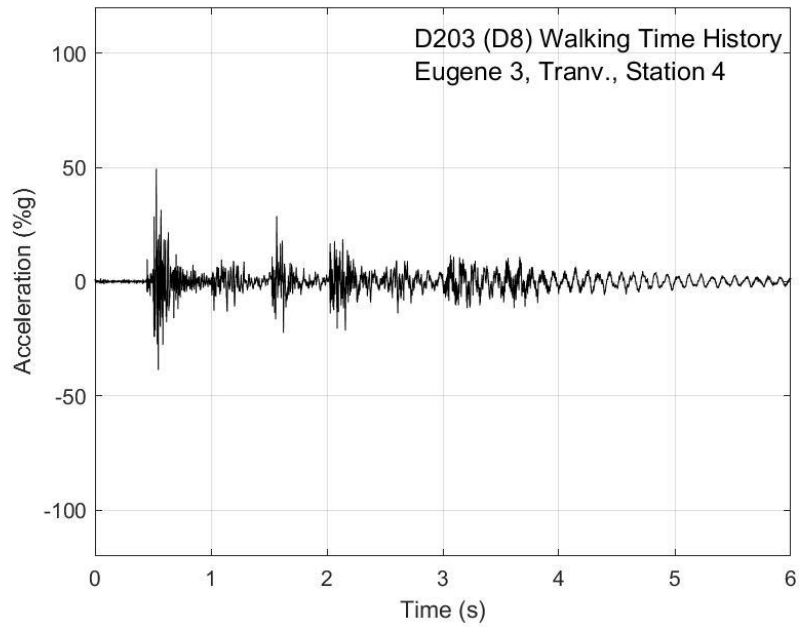


Fig. P-81. Walking time history, Eugene test 2, transverse direction, station 4

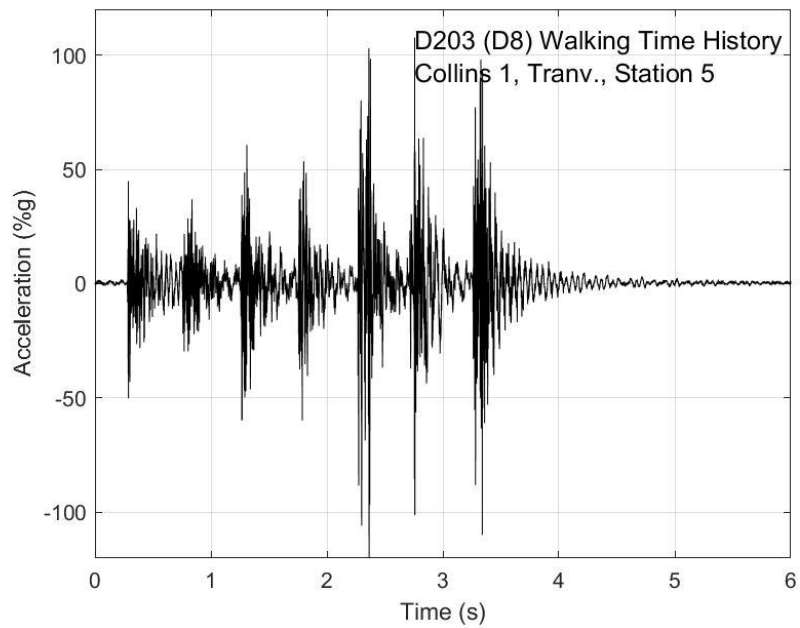


Fig. P-82. Walking time history, Collins test 1, transverse direction, station 5

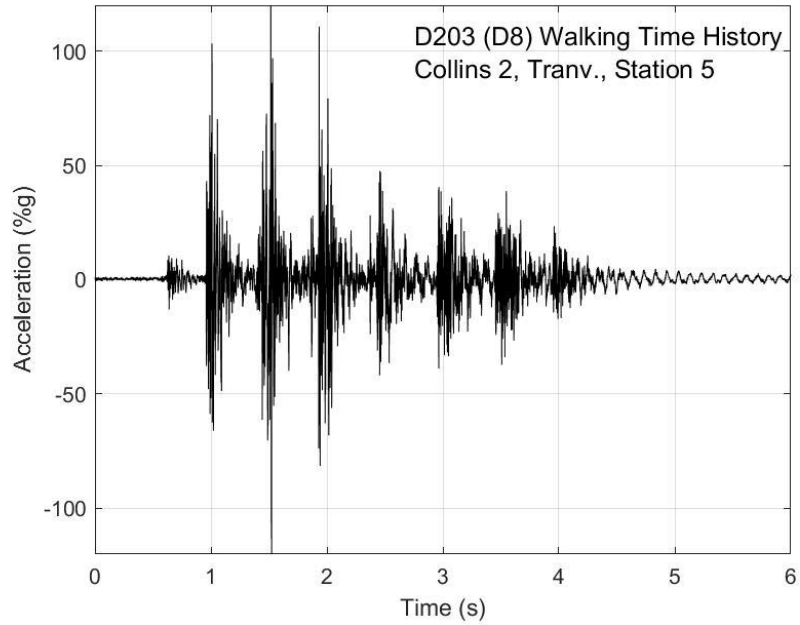


Fig. P-83. Walking time history, Collins test 2, transverse direction, station 5

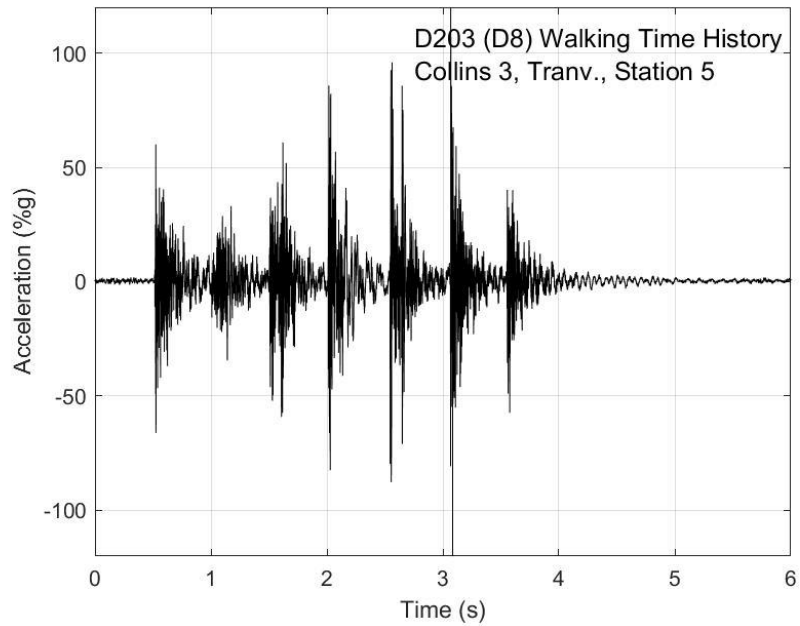


Fig. P-84. Walking time history, Collins test 3, transverse direction, station 5

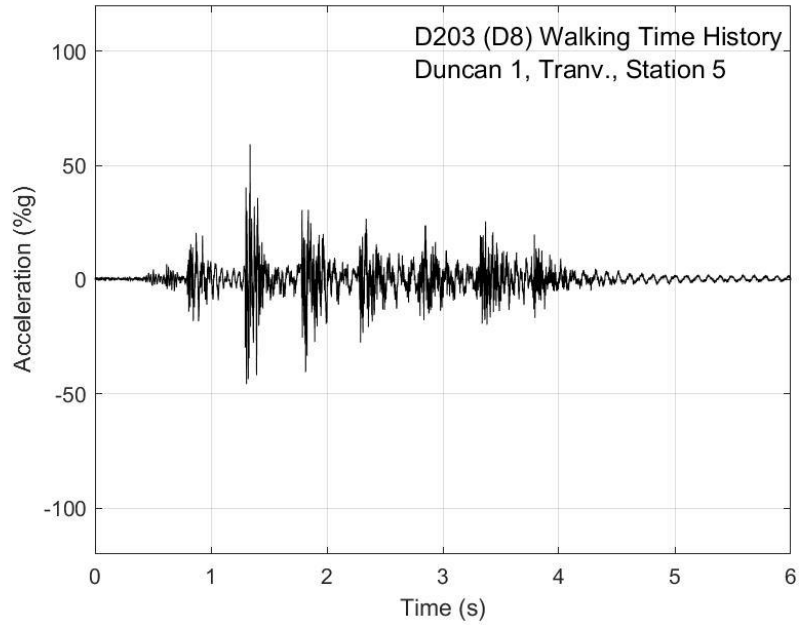


Fig. P-85. Walking time history, Duncan test 1, transverse direction, station 5

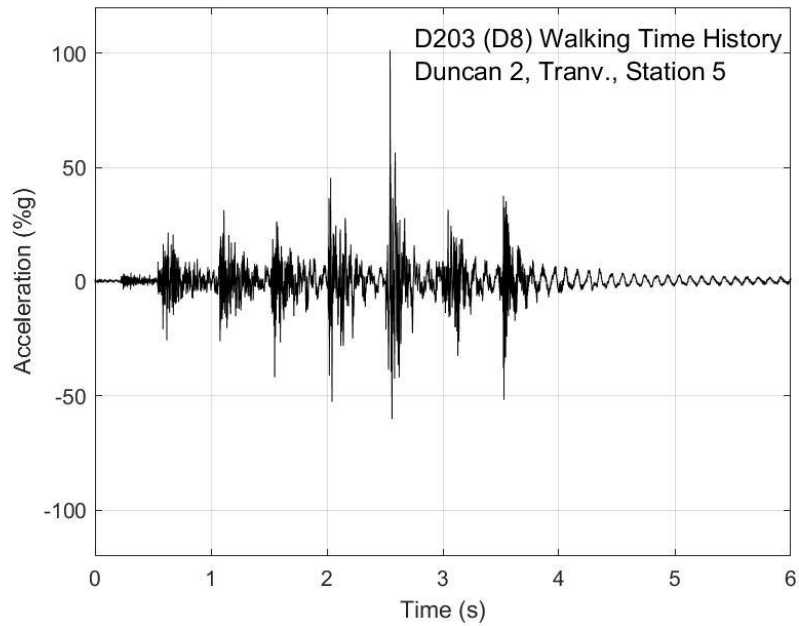


Fig. P-86. Walking time history, Duncan test 2, transverse direction, station 5

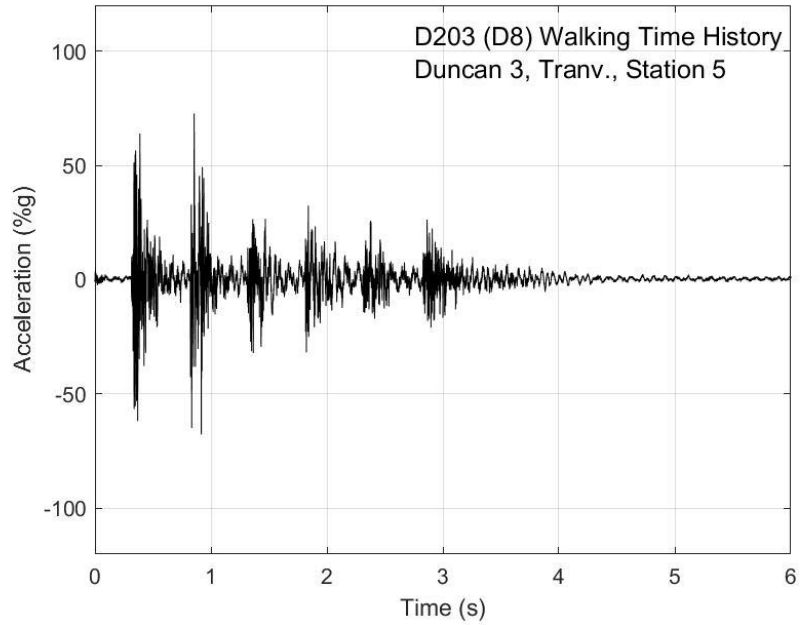


Fig. P-87. Walking time history, Duncan test 3, transverse direction, station 5

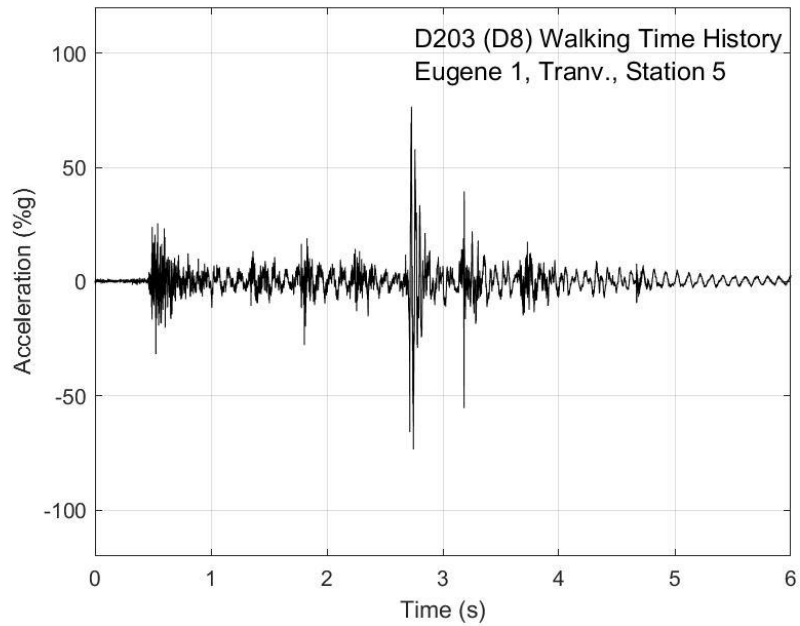


Fig. P-88. Walking time history, Eugene test 1, transverse direction, station 5

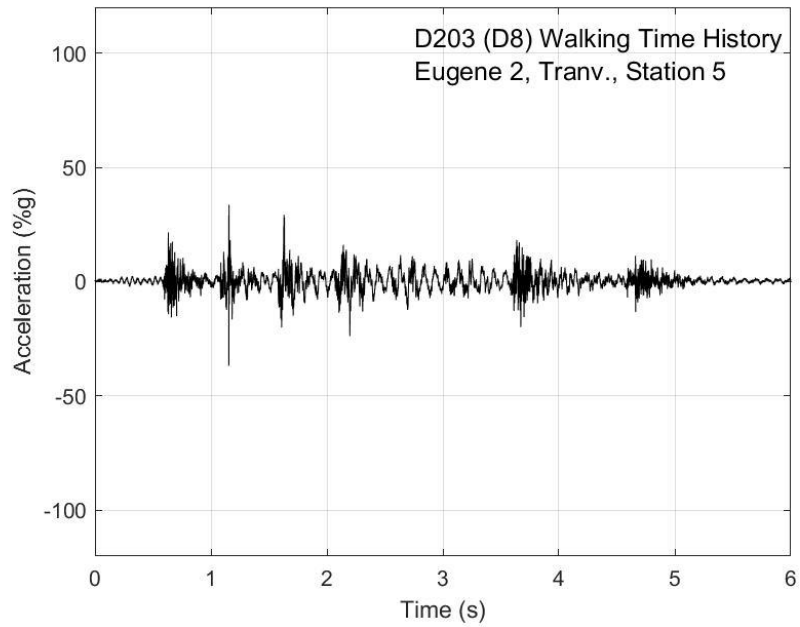


Fig. P-89. Walking time history, Eugene test 2, transverse direction, station 5

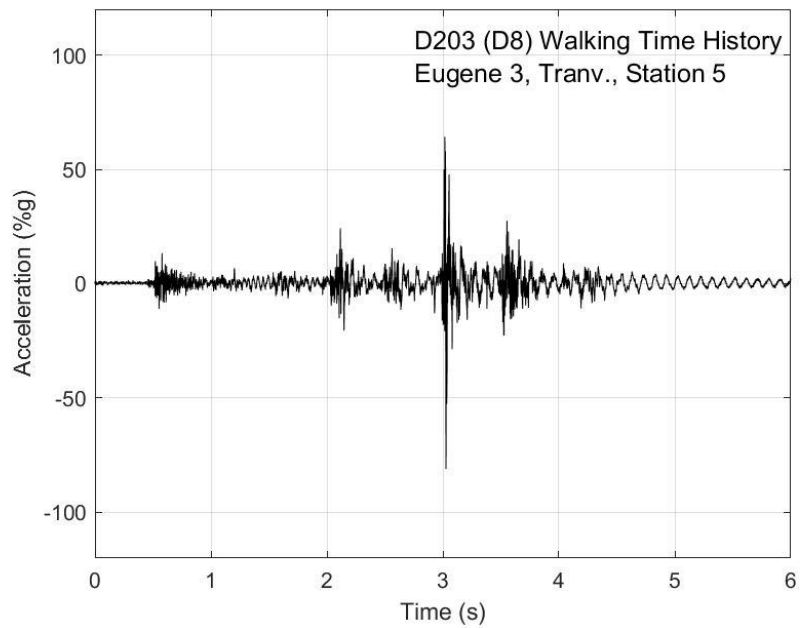


Fig. P-90. Walking time history, Eugene test 3, transverse direction, station 5

APPENDIX Q: Heel Drop Response Spectra Plots, Floor D254

(D10)

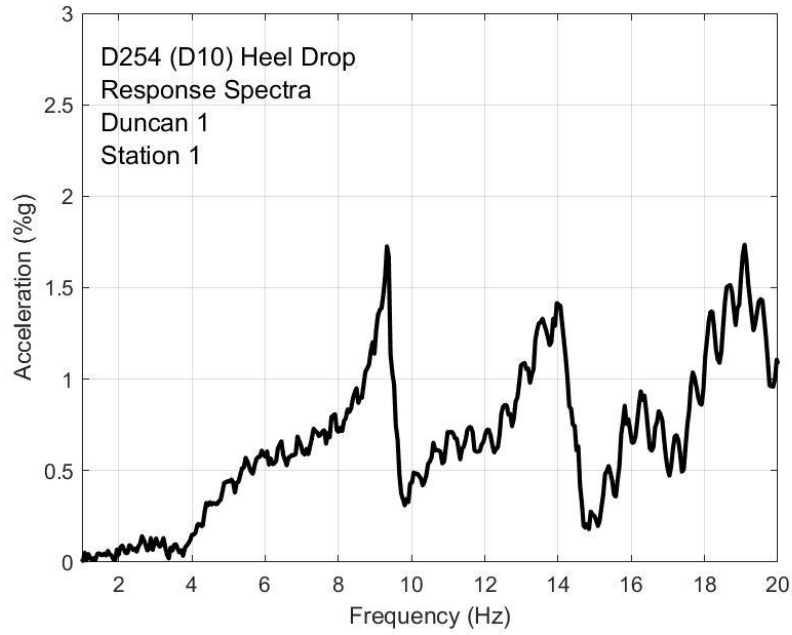


Fig. Q-1. Heel drop response, Duncan test 1 station 1

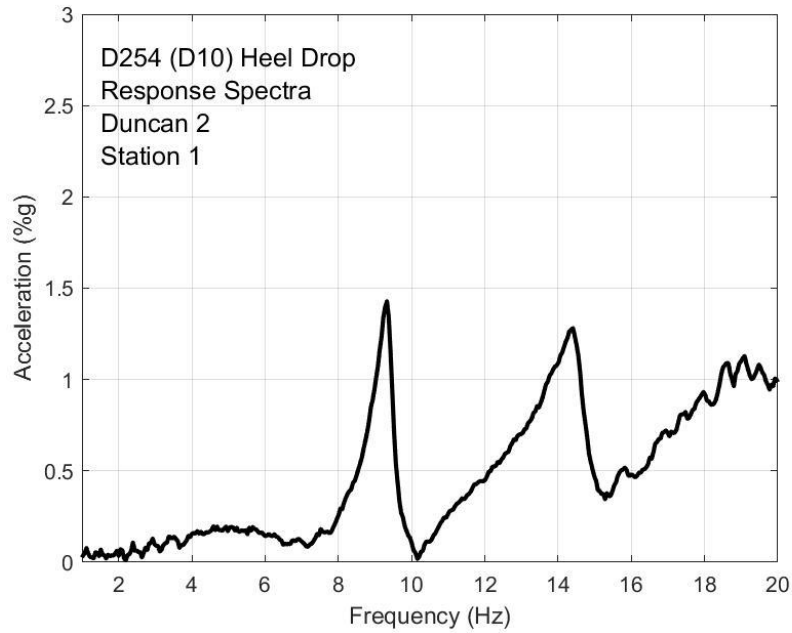


Fig. Q-2. Heel drop response, Duncan test 2 station 1

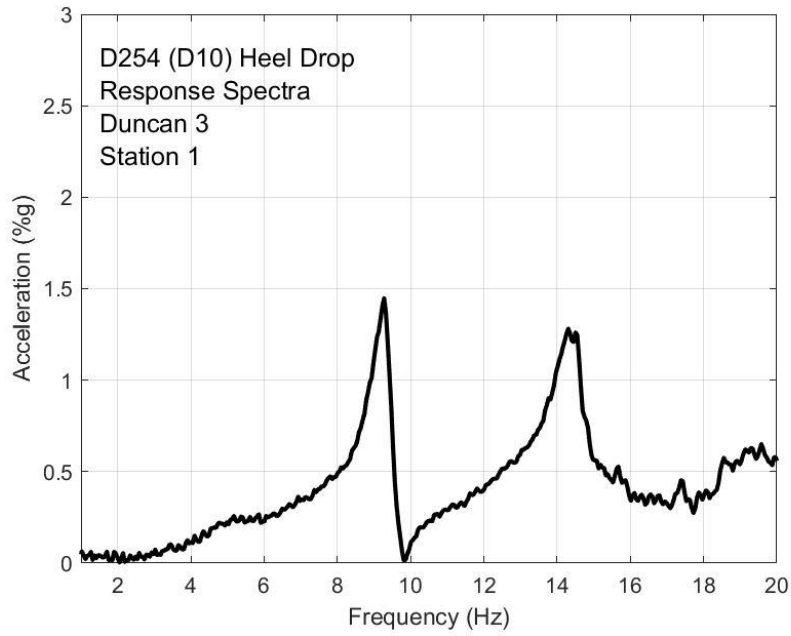


Fig. Q-3. Heel drop response, Duncan test 3 station 1

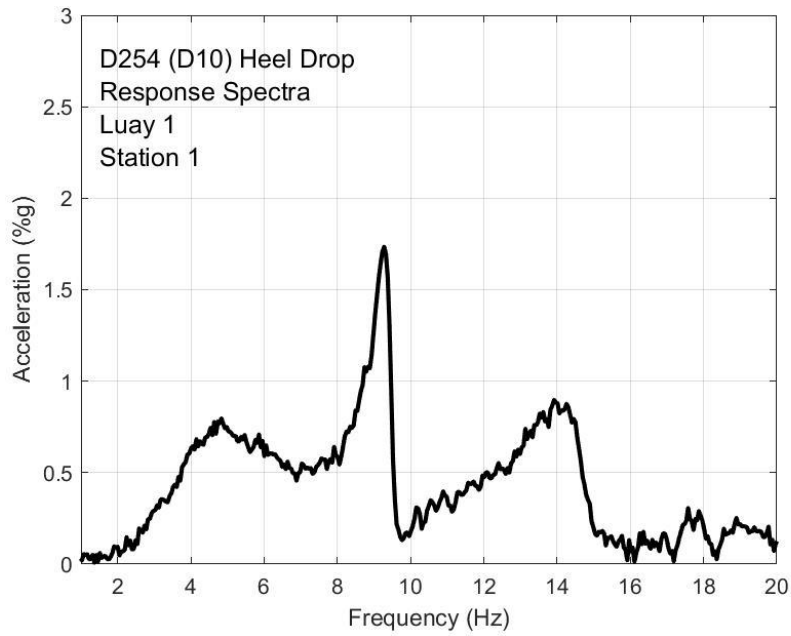


Fig. Q-4. Heel drop response, Luay test 1 station 1

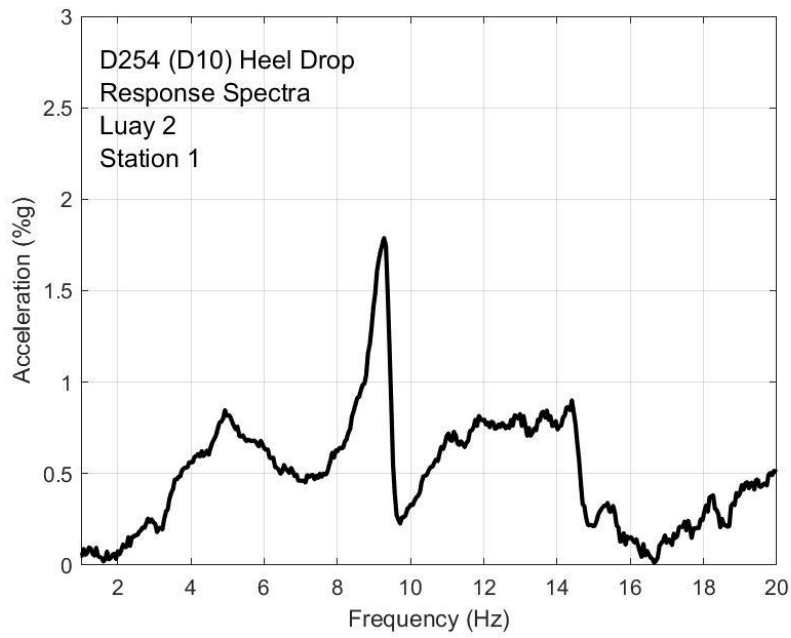


Fig. Q-5. Heel drop response, Luay test 2 station 1

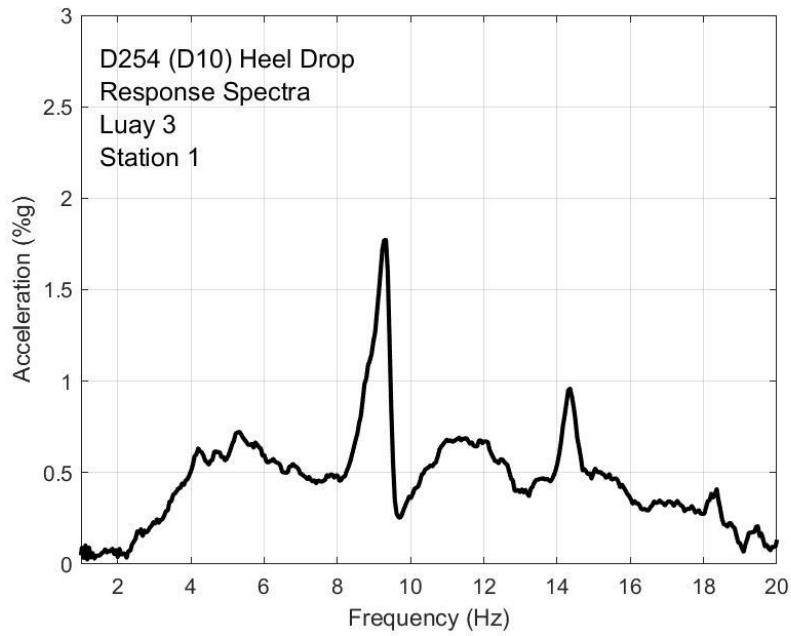


Fig. Q-6. Heel drop response, Luay test 3 station 1

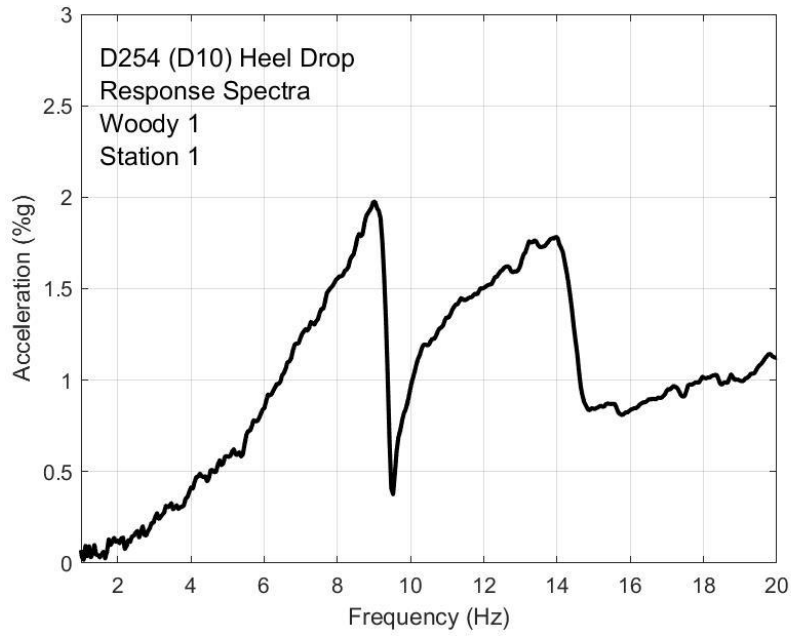


Fig. Q-7. Heel drop response, Woody test 1 station 1

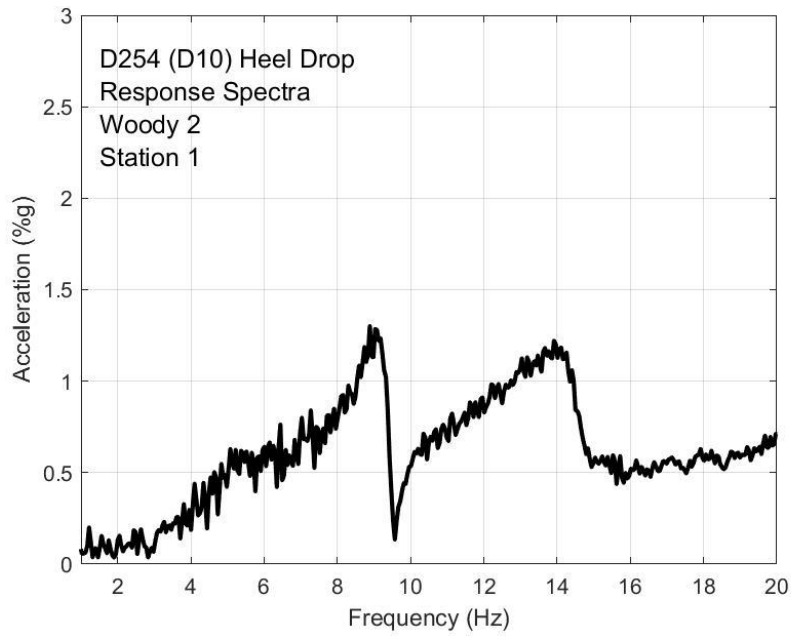


Fig. Q-8. Heel drop response, Woody test 2 station 1

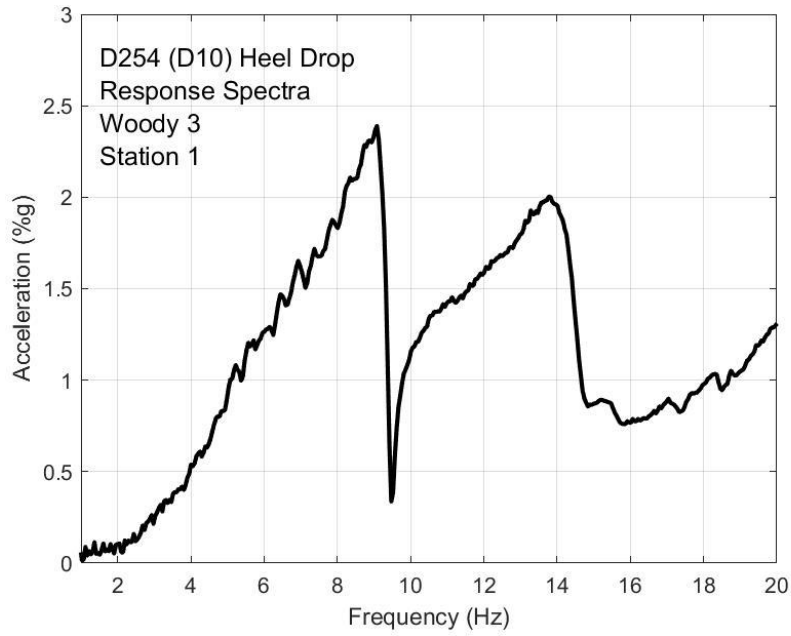


Fig. Q-9. Heel drop response, Woody test 3 station 1

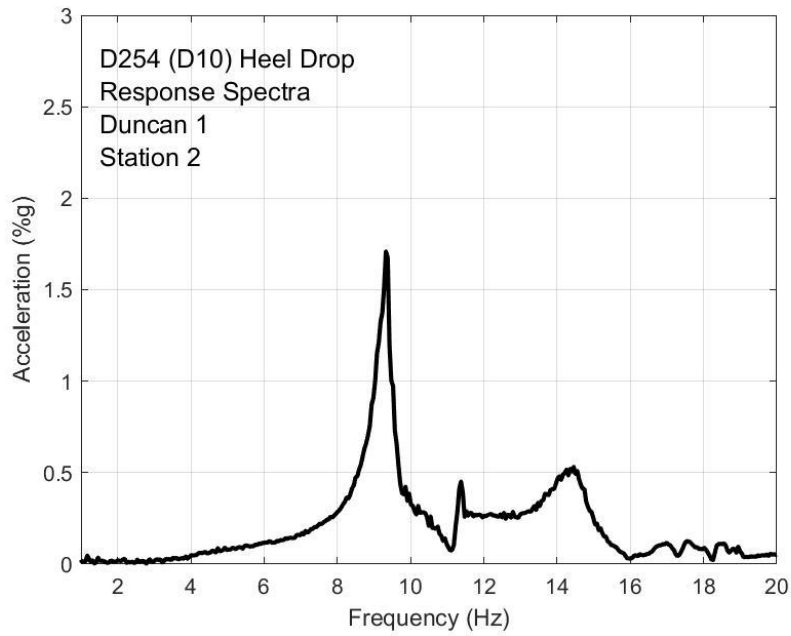


Fig. Q-10. Heel drop response, Duncan test 1 station 2

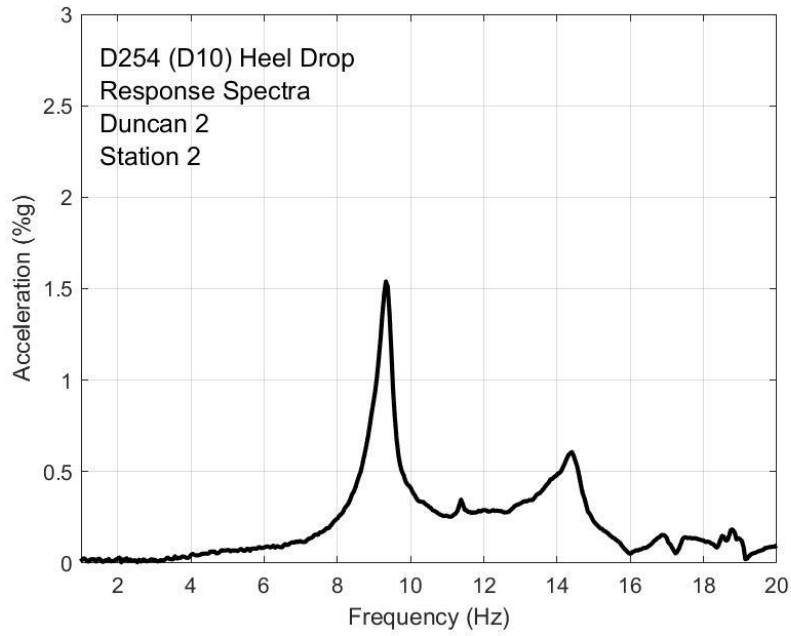


Fig. Q-11. Heel drop response, Duncan test 2 station 2

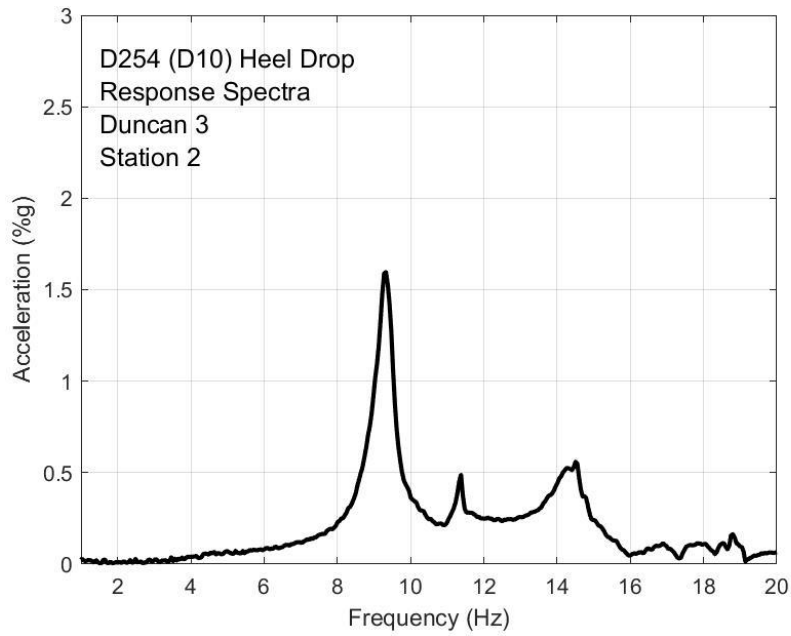


Fig. Q-12. Heel drop response, Duncan test 3 station 2

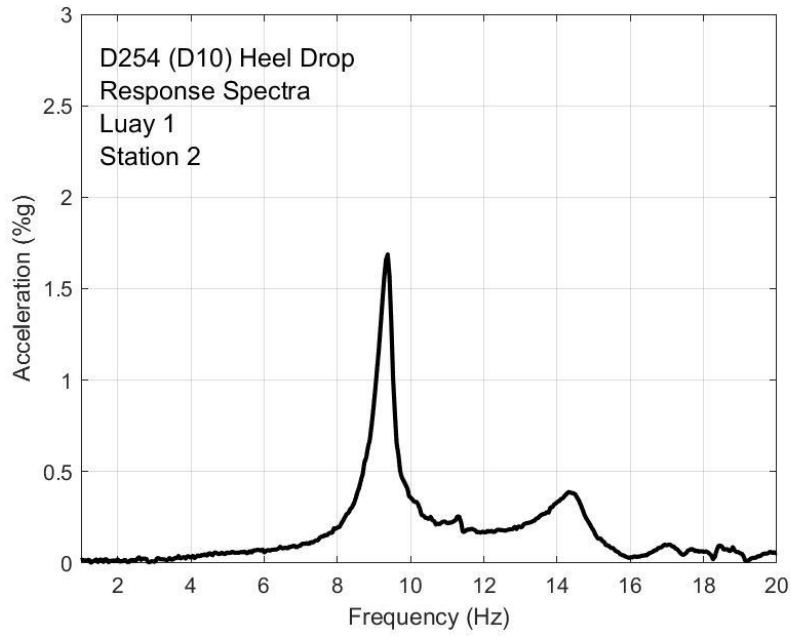


Fig. Q-13. Heel drop response, Luay test 1 station 2

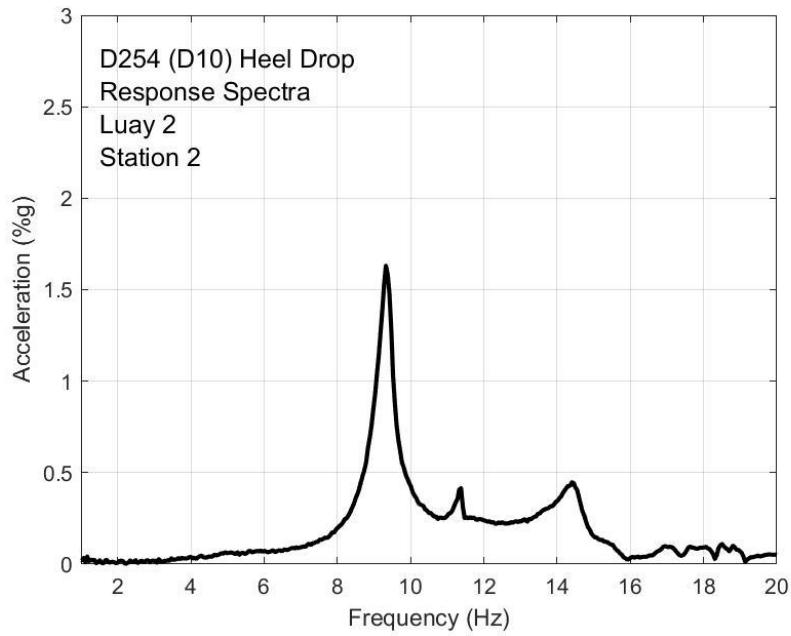


Fig. Q-14. Heel drop response, Luay test 2 station 2

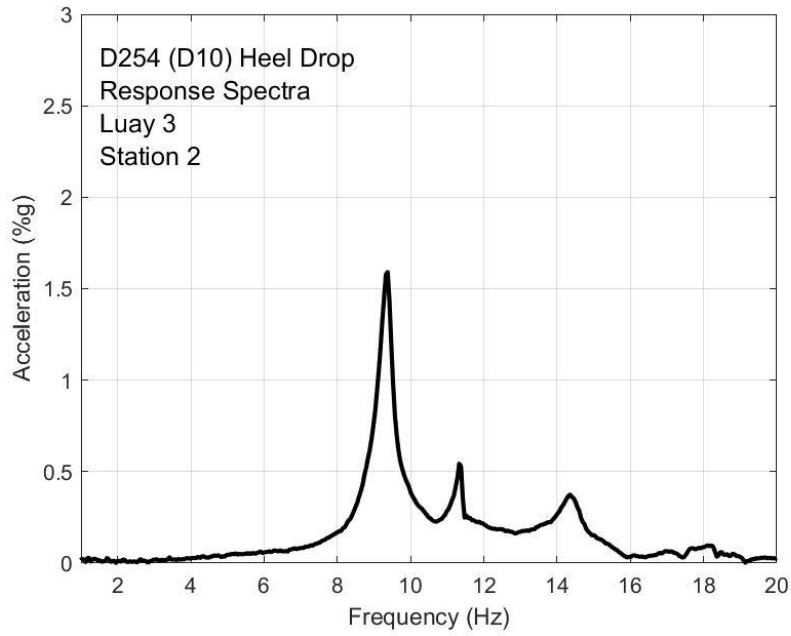


Fig. Q-15. Heel drop response, Luay test 3 station 2

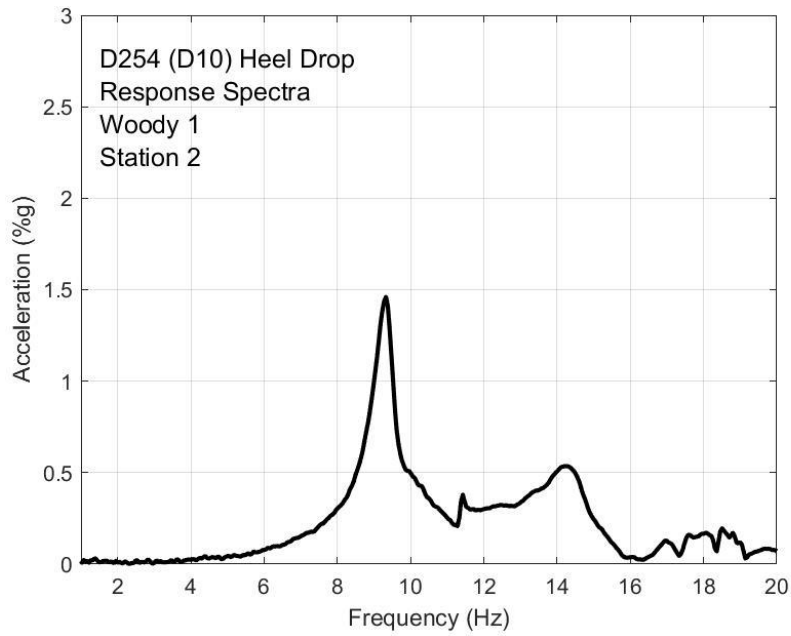


Fig. Q-16. Heel drop response, Woody test 1 station 2

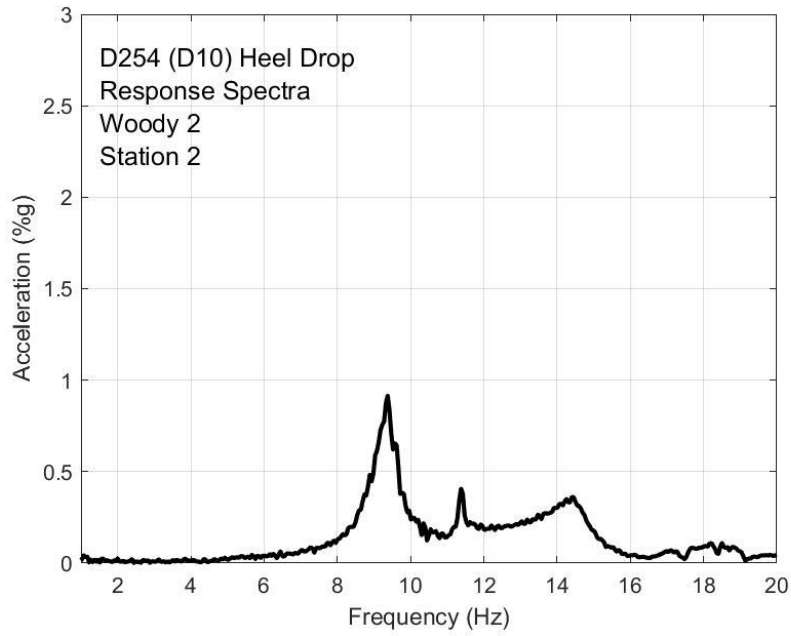


Fig. Q-17. Heel drop response, Woody test 2 station 2

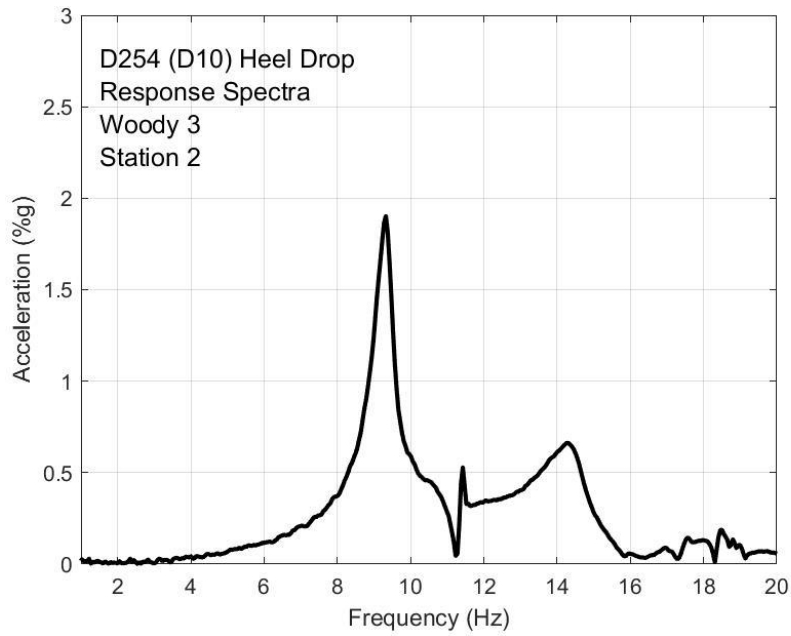


Fig. Q-18. Heel drop response, Woody test 3 station 2

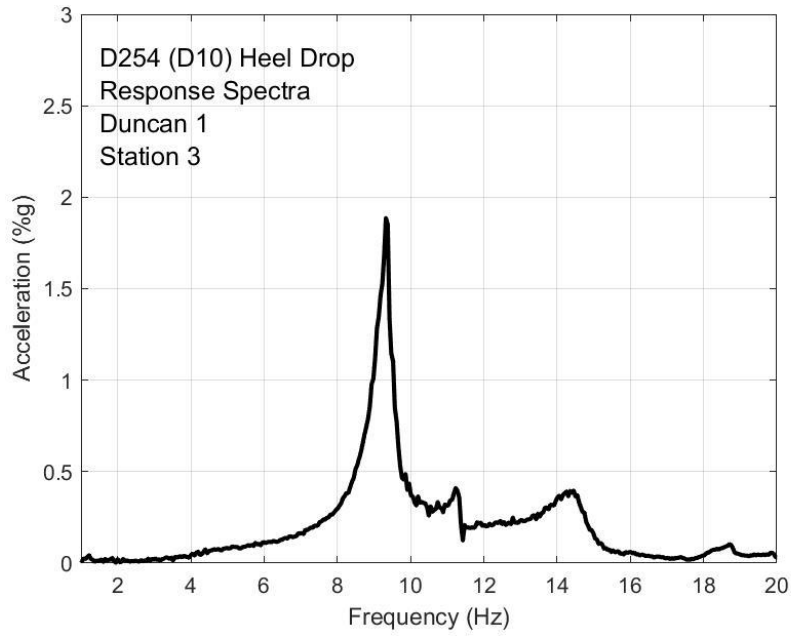


Fig. Q-19. Heel drop response, Duncan test 1 station 3

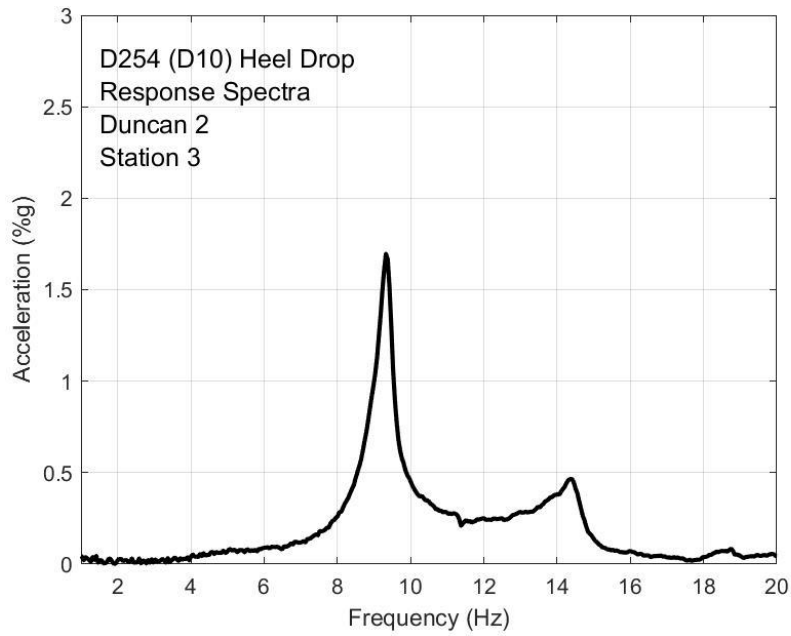


Fig. Q-20. Heel drop response, Duncan test 2 station 3

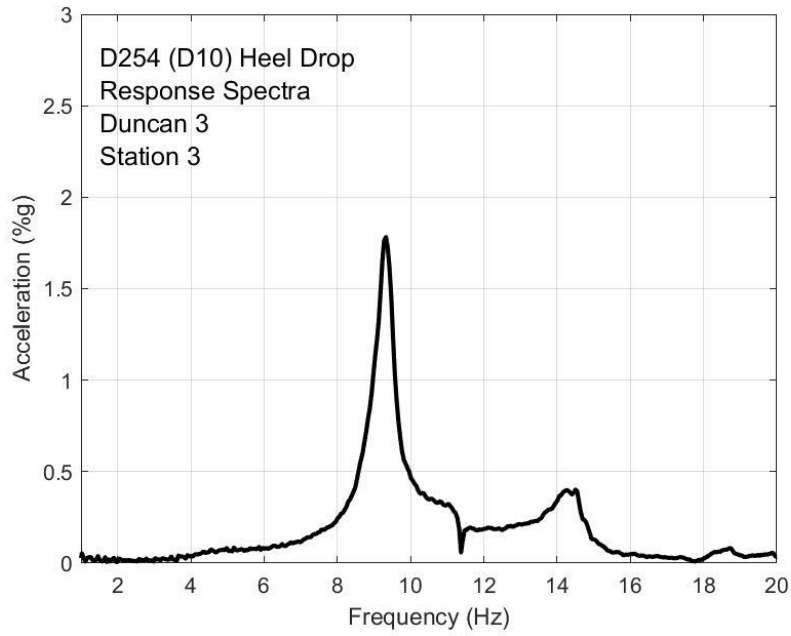


Fig. Q-21. Heel drop response, Duncan test 3 station 3

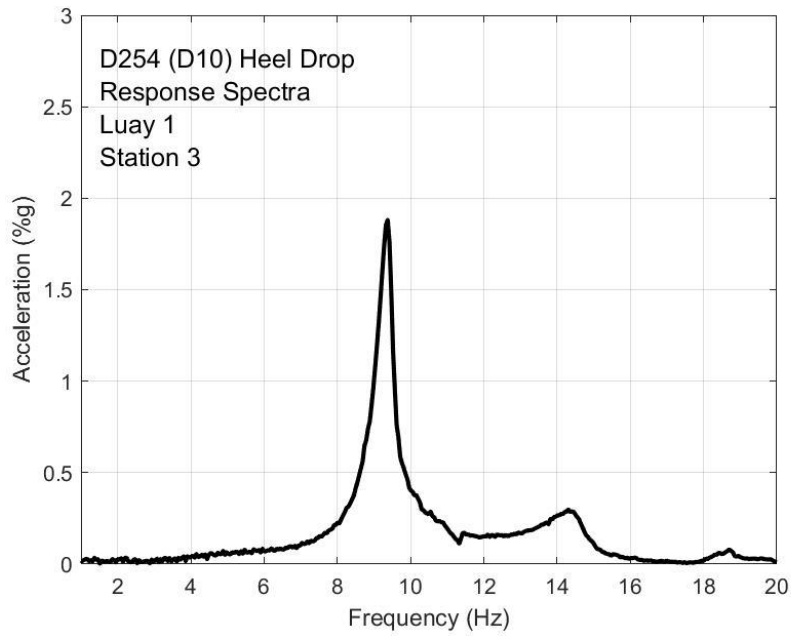


Fig. Q-22. Heel drop response, Luay test 1 station 3

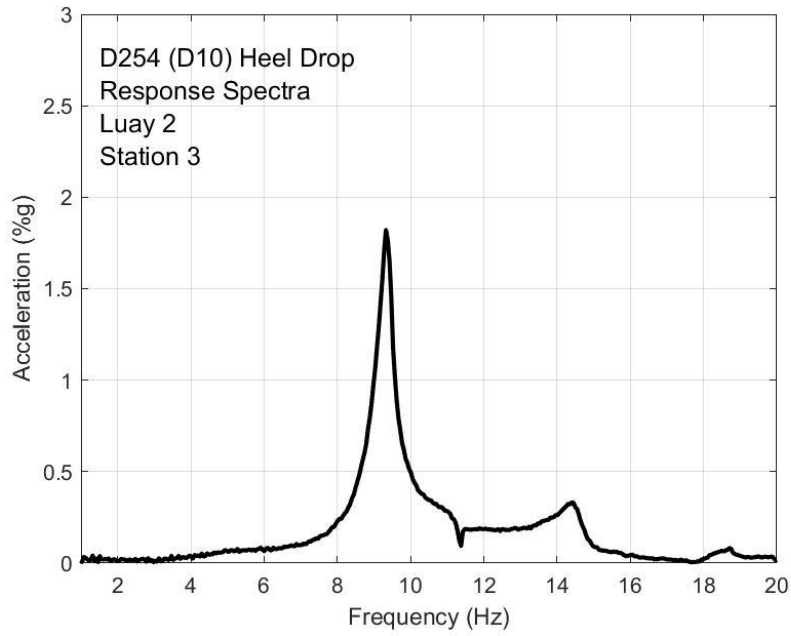


Fig. Q-23. Heel drop response, Luay test 2 station 3

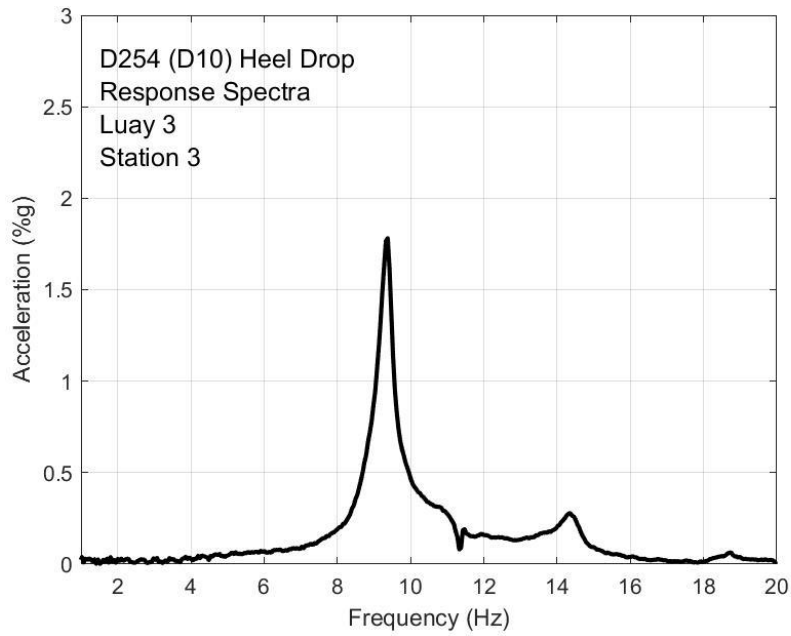


Fig. Q-24. Heel drop response, Luay test 3 station 3

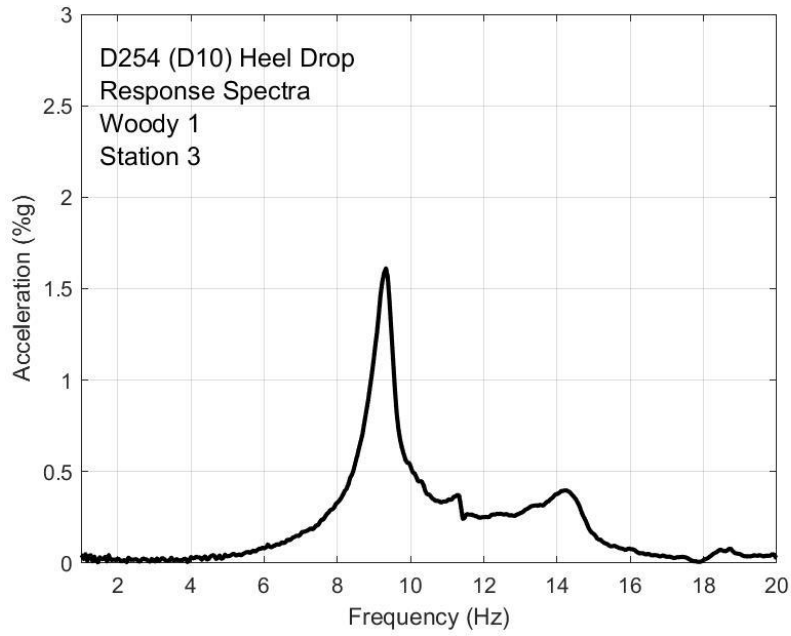


Fig. Q-25. Heel drop response, Woody test 1 station 3

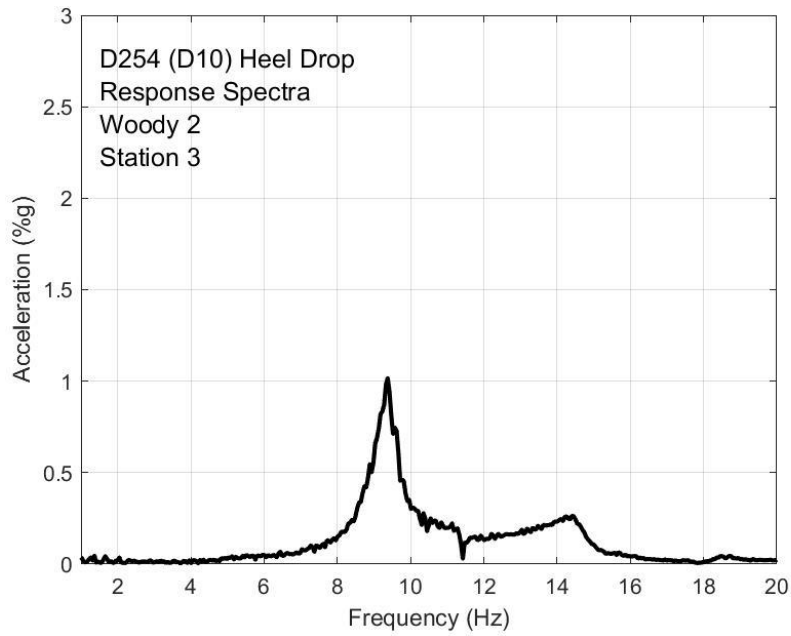


Fig. Q-26. Heel drop response, Woody test 2 station 3

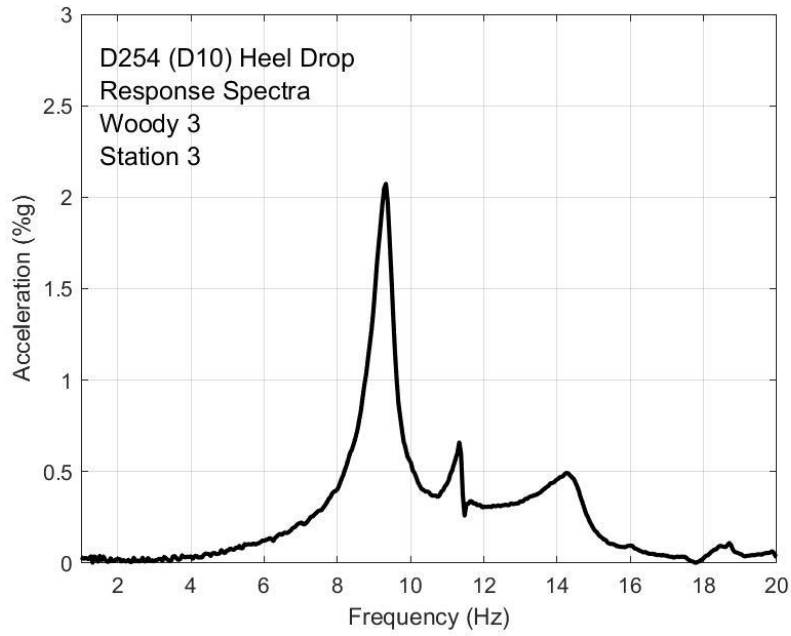


Fig. Q-27. Heel drop response, Woody test 3 station 3

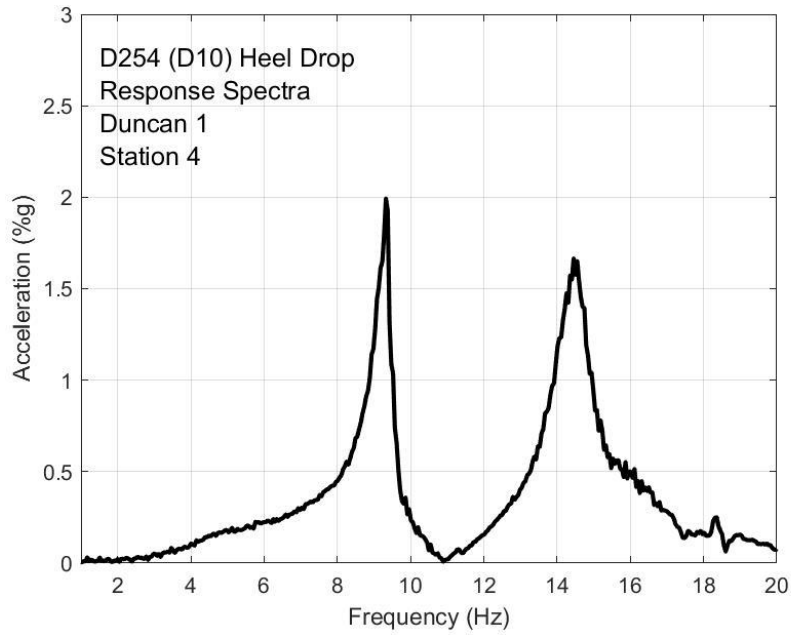


Fig. Q-28. Heel drop response, Duncan test 1 station 4

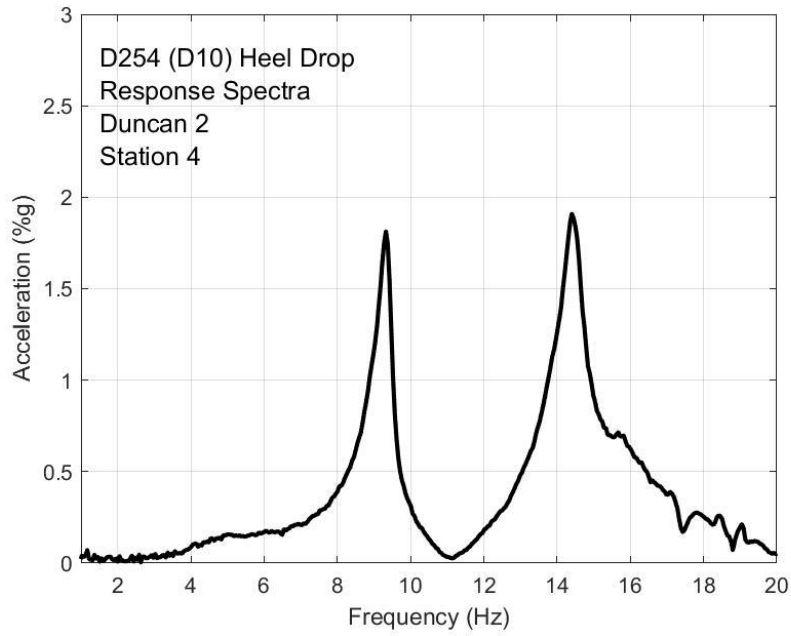


Fig. Q-29. Heel drop response, Duncan test 2 station 4

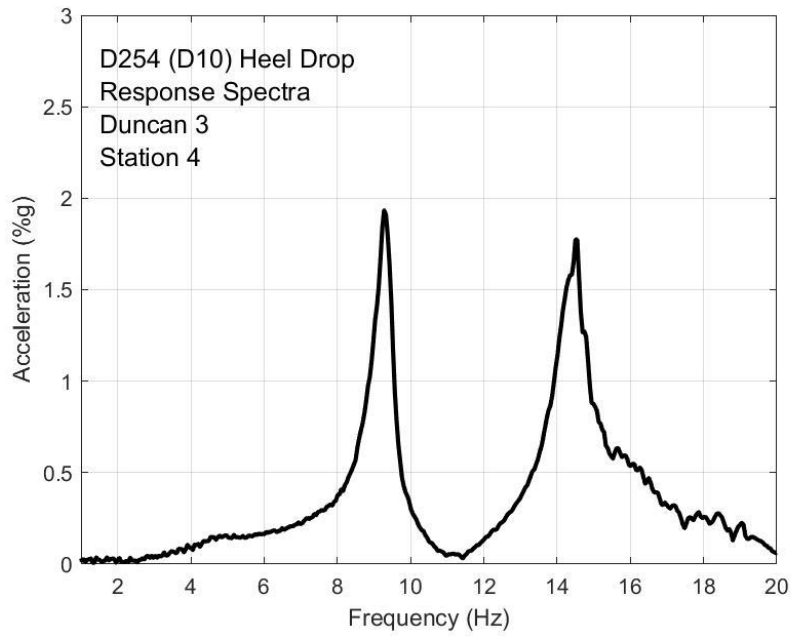


Fig. Q-30. Heel drop response, Duncan test 3 station 4

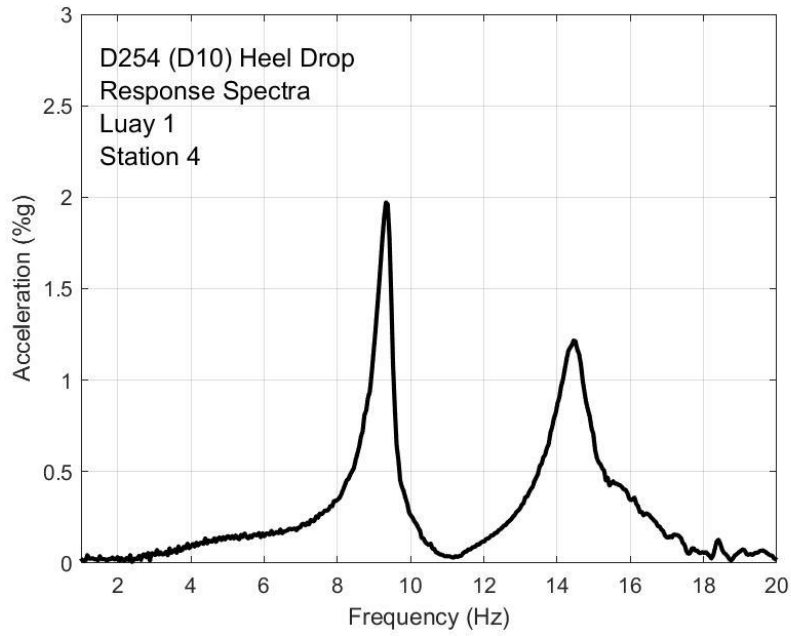


Fig. Q-31. Heel drop response, Luay test 1 station 4

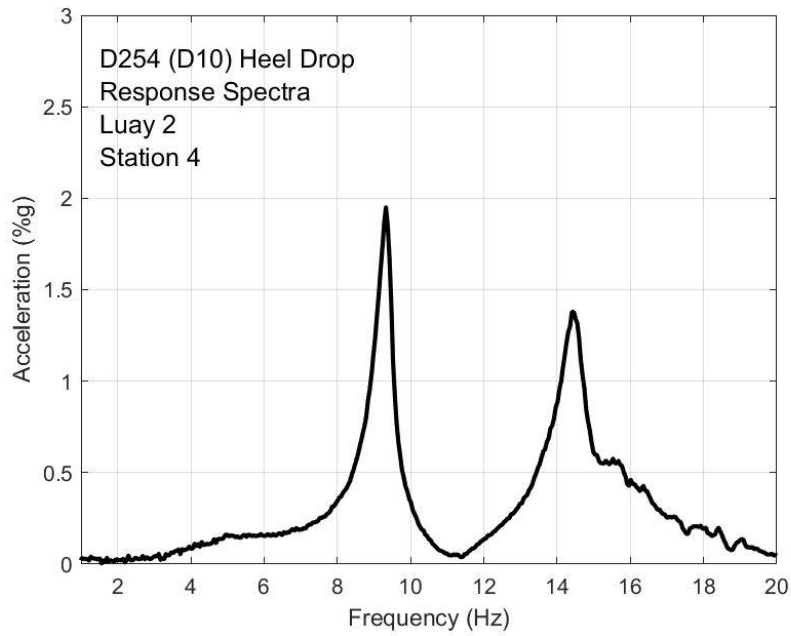


Fig. Q-32. Heel drop response, Luay test 2 station 4

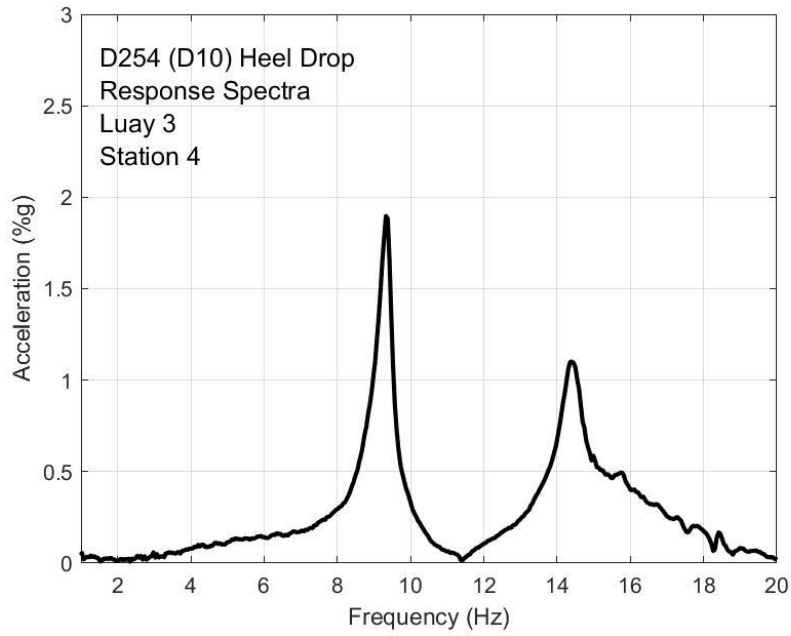


Fig. Q-33. Heel drop response, Luay test 3 station 4

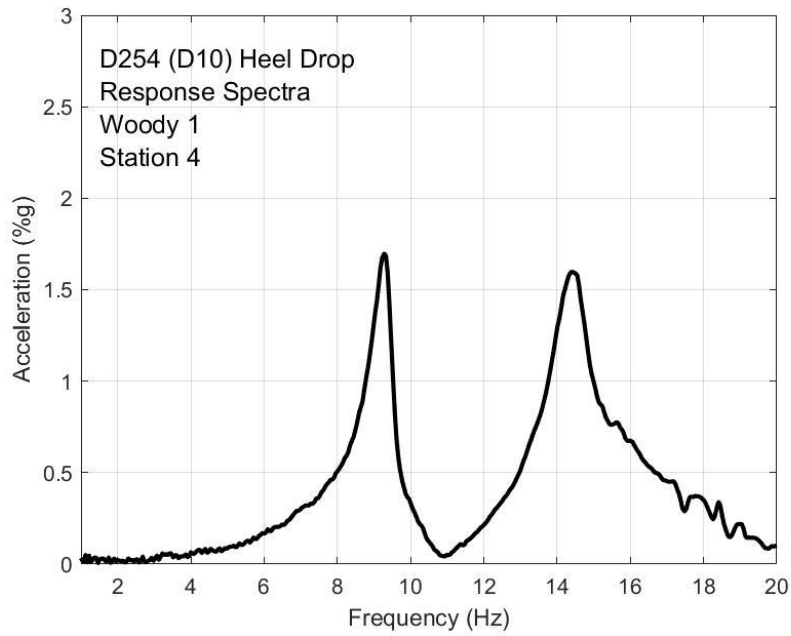


Fig. Q-34. Heel drop response, Woody test 1 station 4

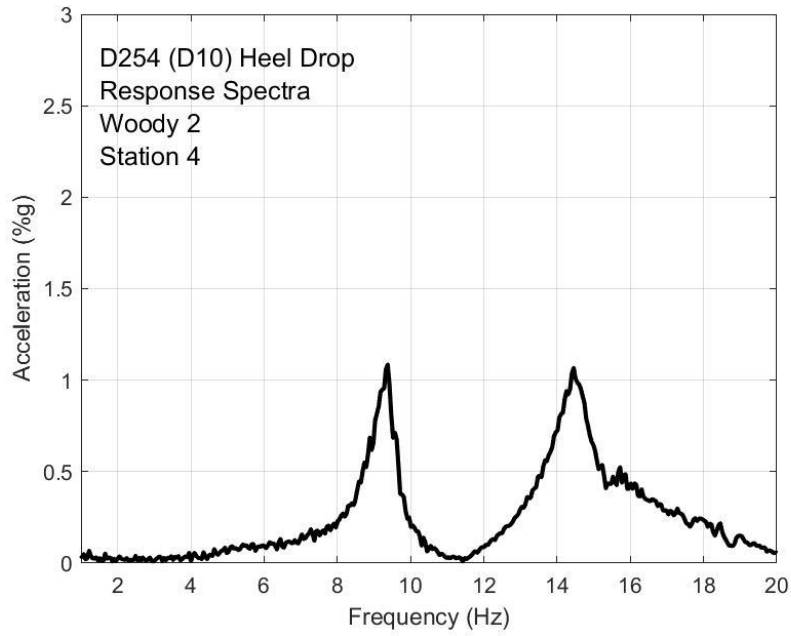


Fig. Q-35. Heel drop response, Woody test 2 station 4

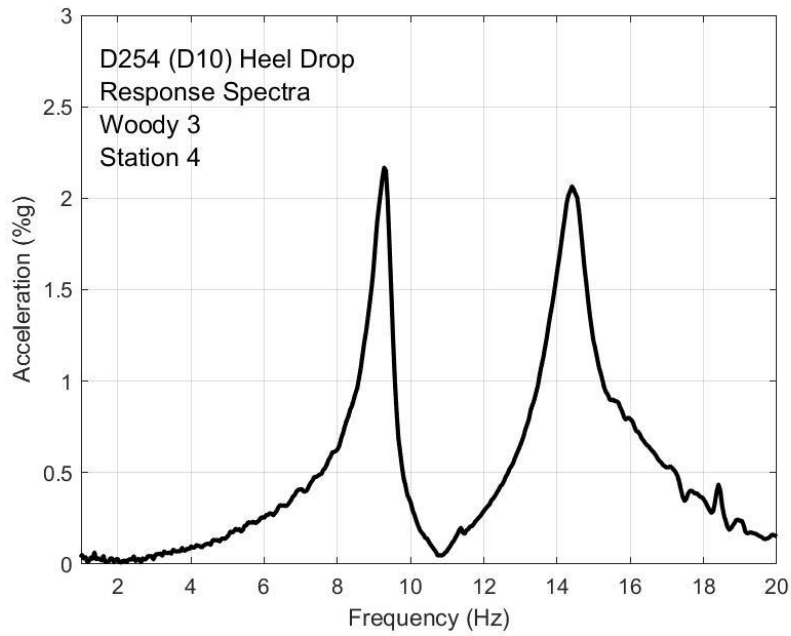


Fig. Q-36. Heel drop response, Woody test 3 station 4

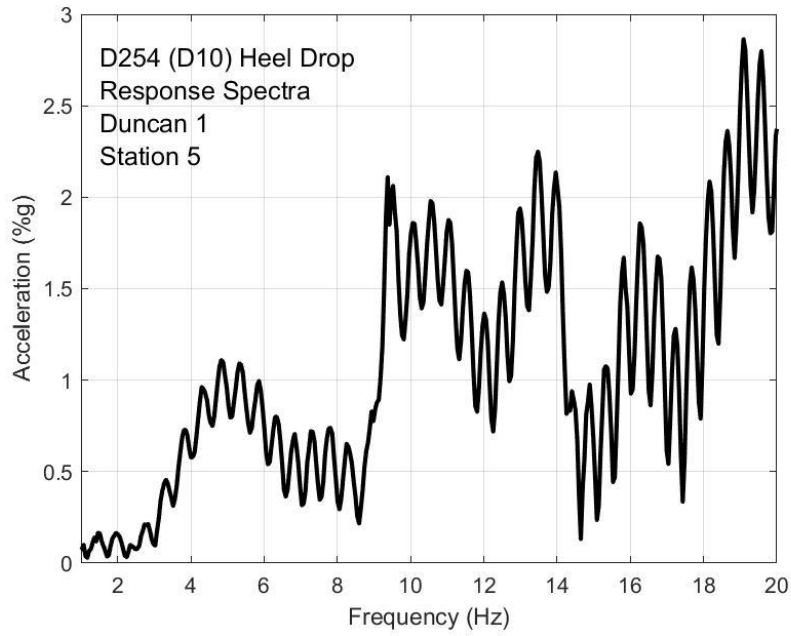


Fig. Q-37. Heel drop response, Duncan test 1 station 5

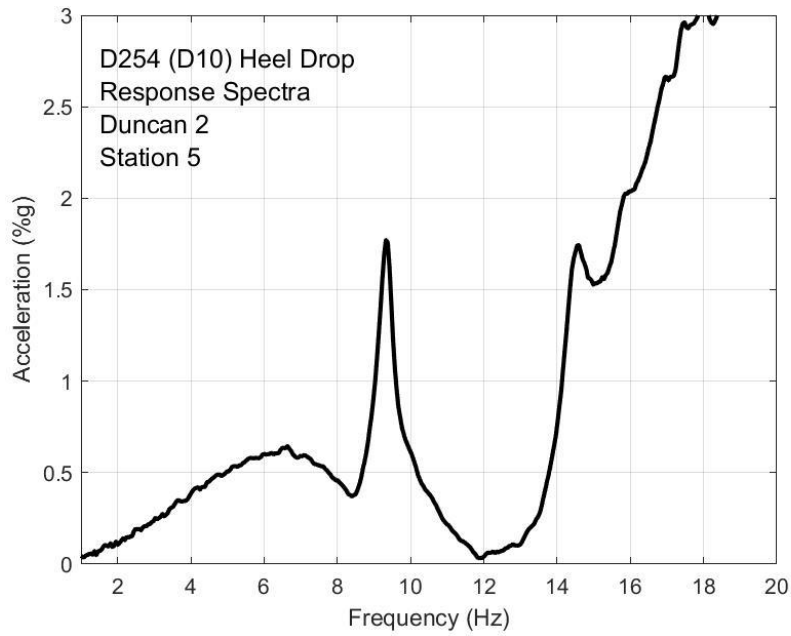


Fig. Q-38. Heel drop response, Duncan test 2 station 5

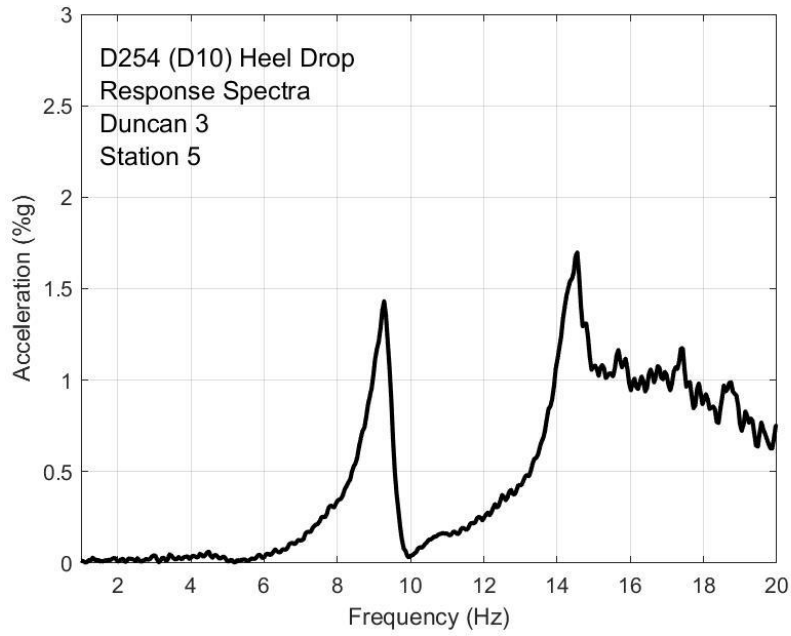


Fig. Q-39. Heel drop response, Duncan test 3 station 5

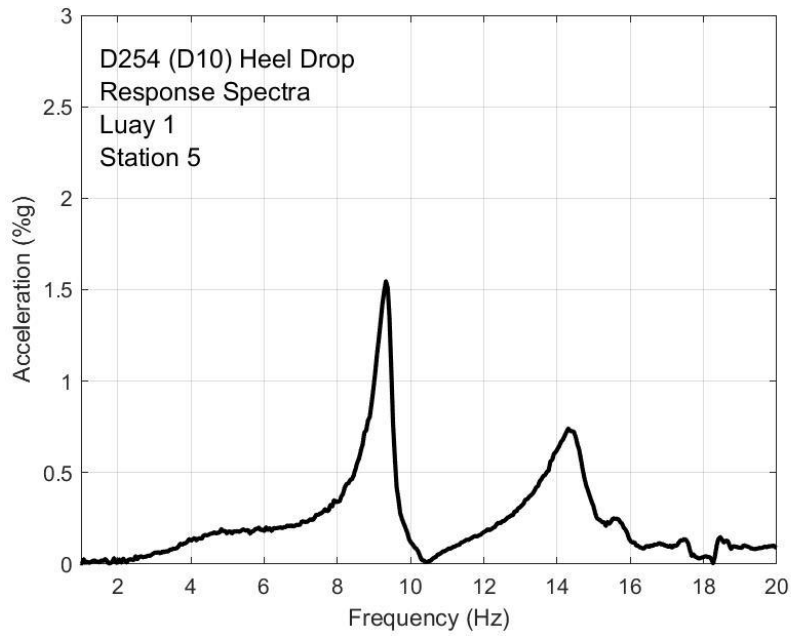


Fig. Q-40. Heel drop response, Luay test 1 station 5

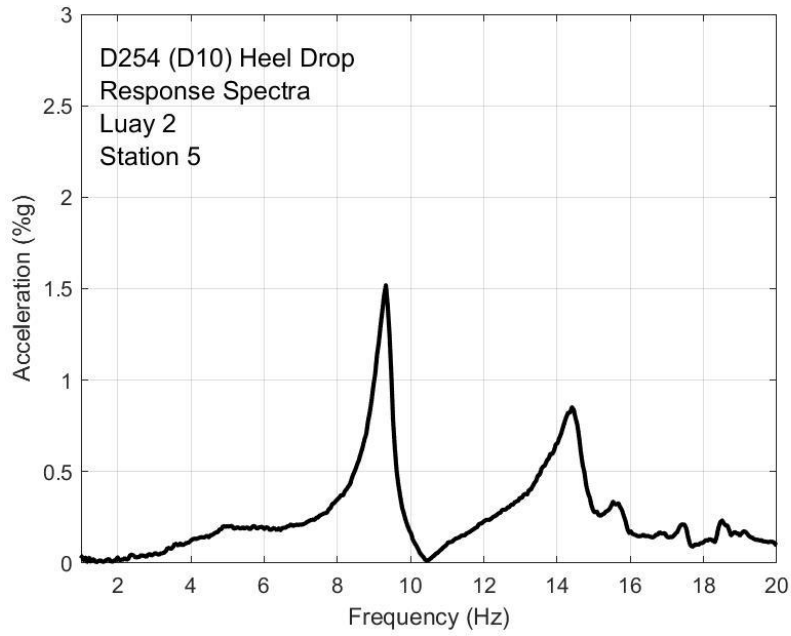


Fig. Q-41. Heel drop response, Luay test 2 station 5

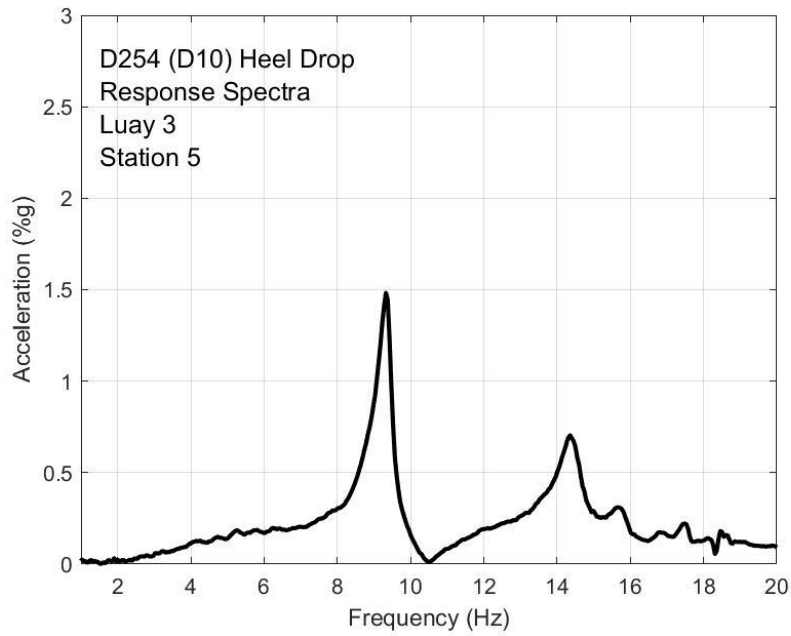


Fig. Q-42. Heel drop response, Luay test 3 station 5

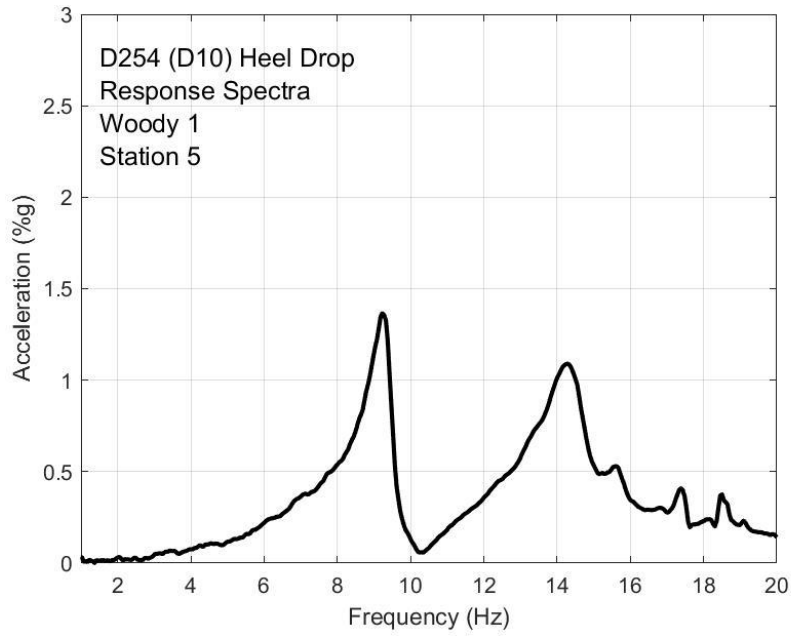


Fig. Q-43. Heel drop response, Woody test 1 station 5

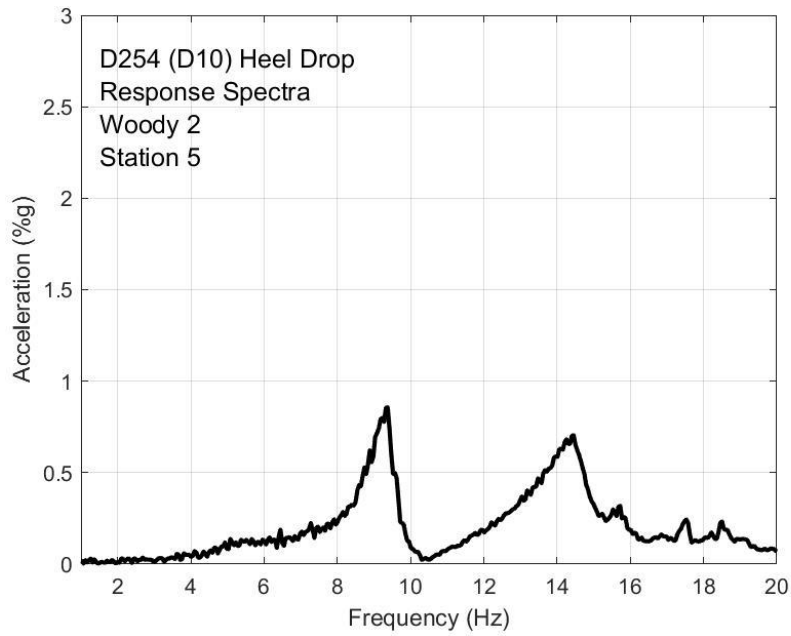


Fig. Q-44. Heel drop response, Woody test 2 station 5

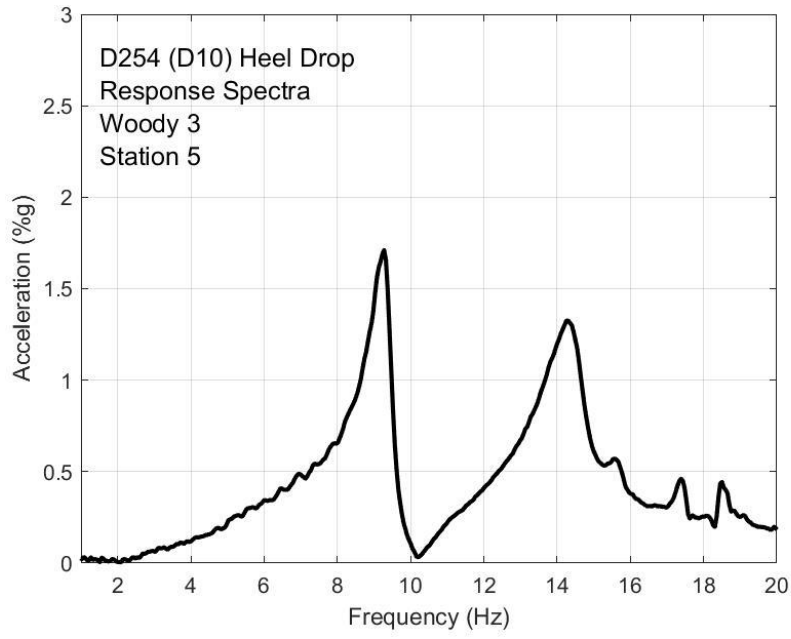


Fig. Q-45. Heel drop response, Woody test 3 station 5

APPENDIX R: Walking Testing, Floor D254 (D10)

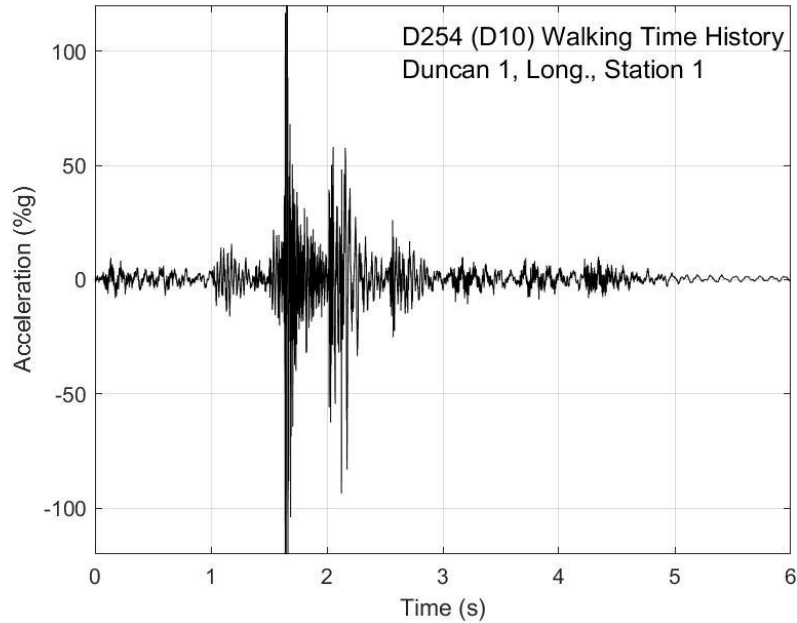


Fig. R-1. Walking time history, Duncan test 1, longitudinal direction, station 1

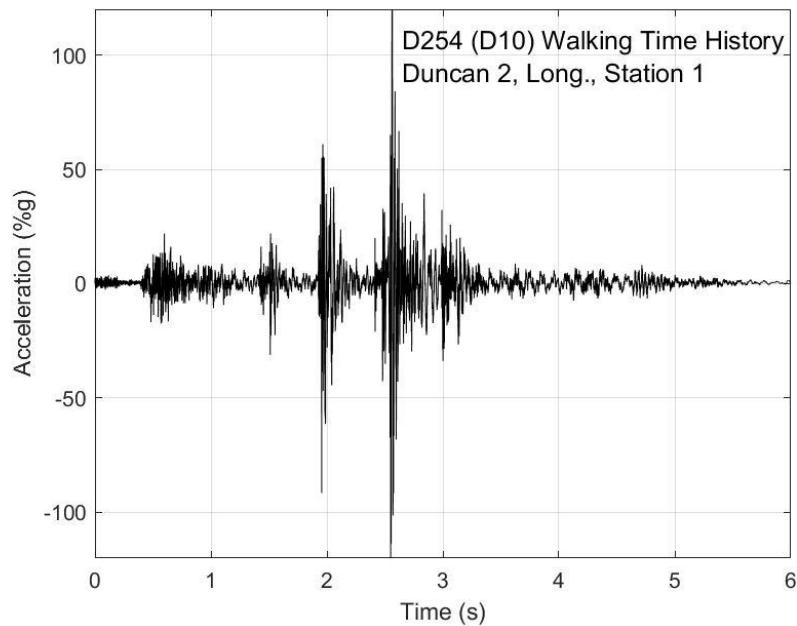


Fig. R-2. Walking time history, Duncan test 2, longitudinal direction, station 1

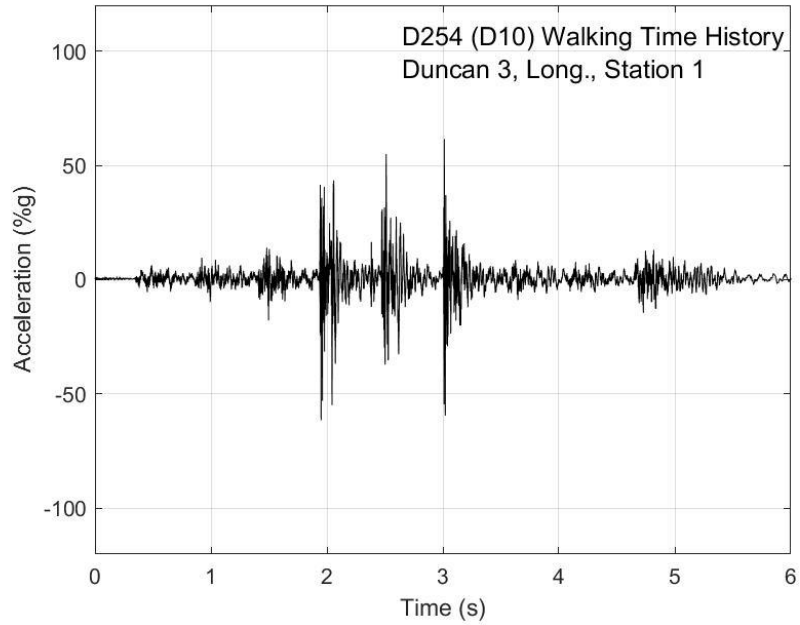


Fig. R-3. Walking time history, Duncan test 3, longitudinal direction, station 1

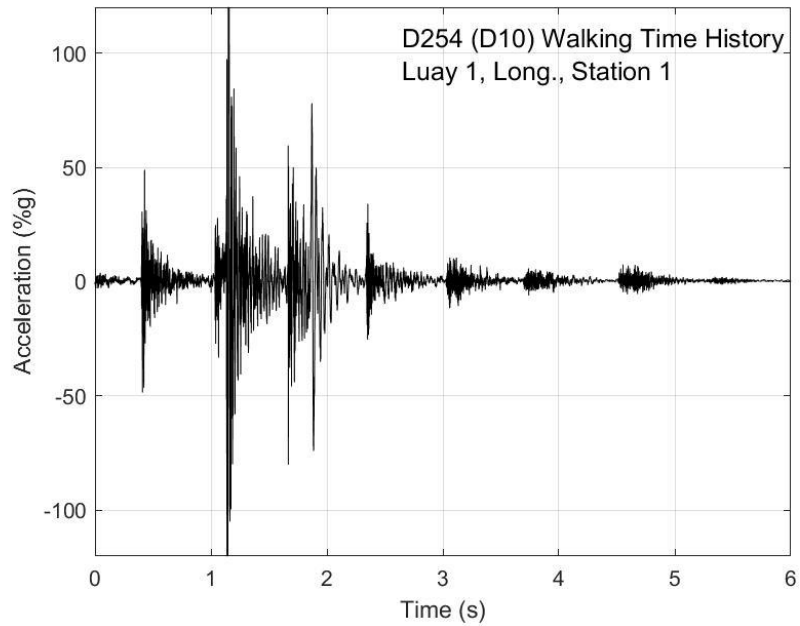


Fig. R-4. Walking time history, Luay test 1, longitudinal direction, station 1

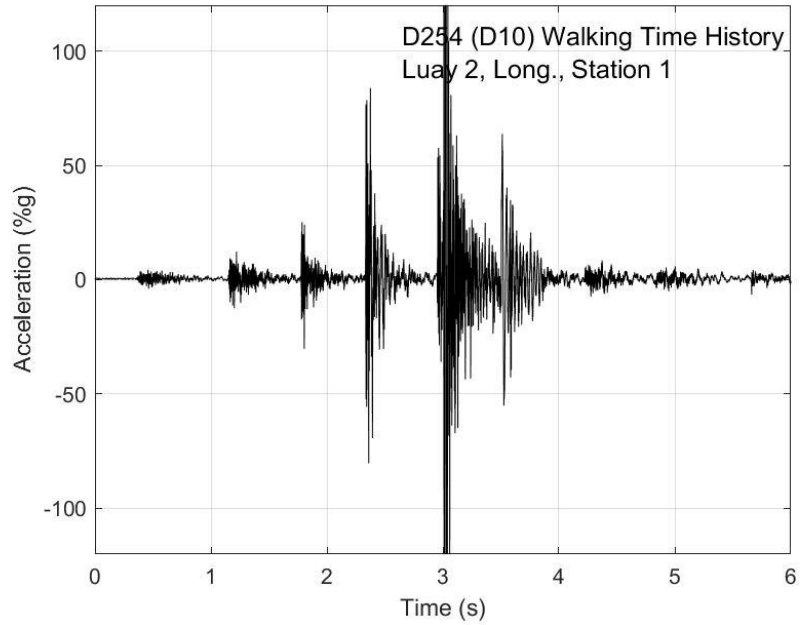


Fig. R-5. Walking time history, Luay test 2, longitudinal direction, station 1

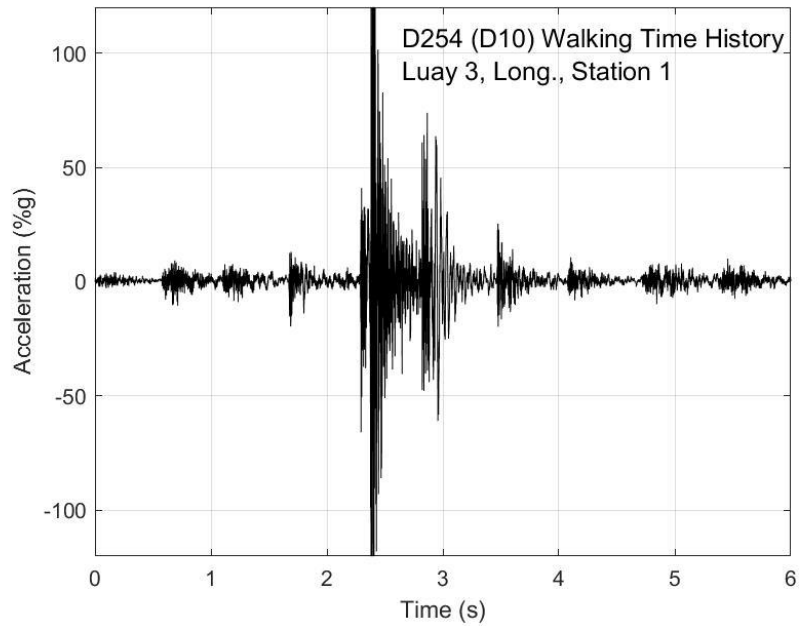


Fig. R-6. Walking time history, Luay test 3, longitudinal direction, station 1

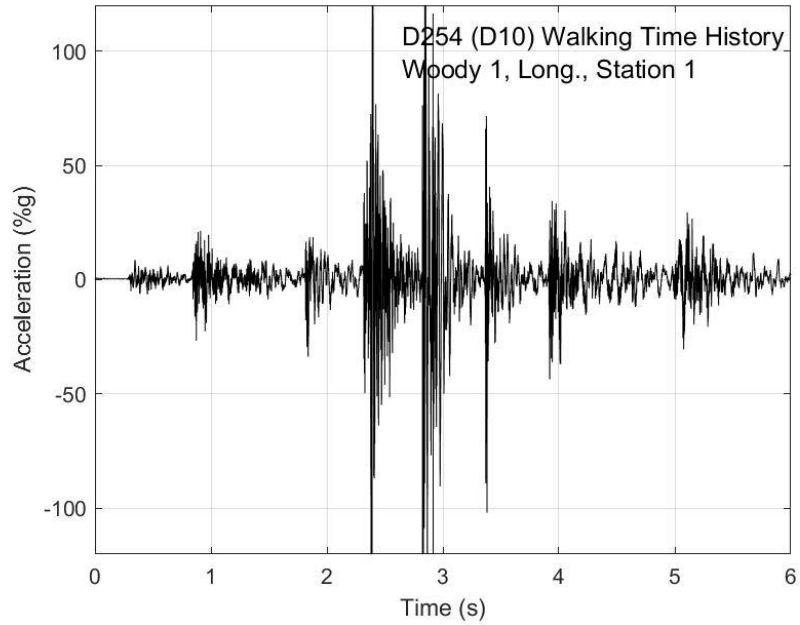


Fig. R-7. Walking time history, Woody test 1, longitudinal direction, station 1

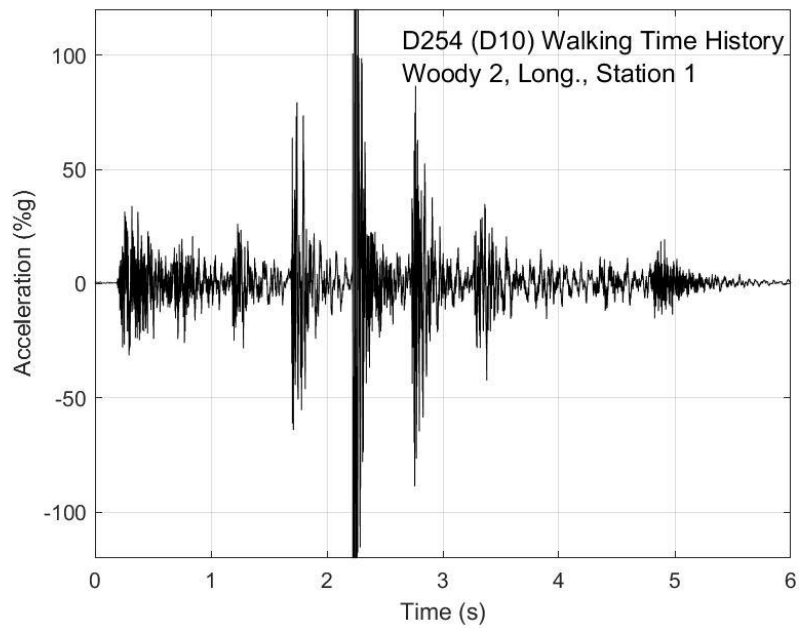


Fig. R-8. Walking time history, Woody test 2, longitudinal direction, station 1

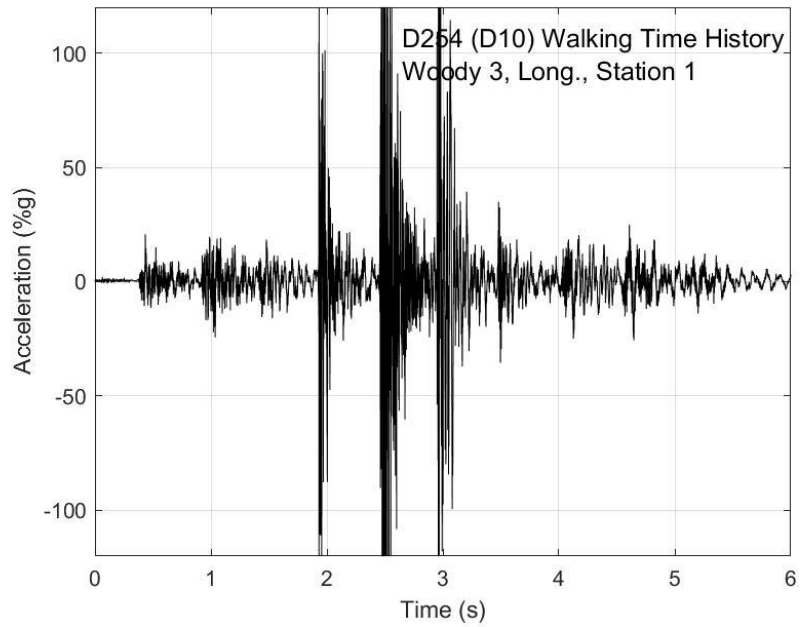


Fig. R-9. Walking time history, Woody test 3, longitudinal direction, station 1

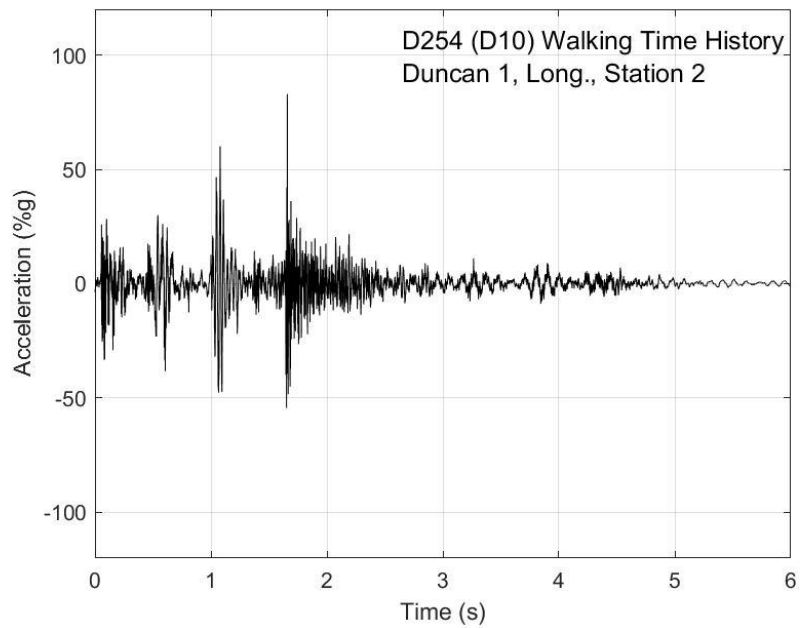


Fig. R-10. Walking time history, Duncan test 1, longitudinal direction, station 2

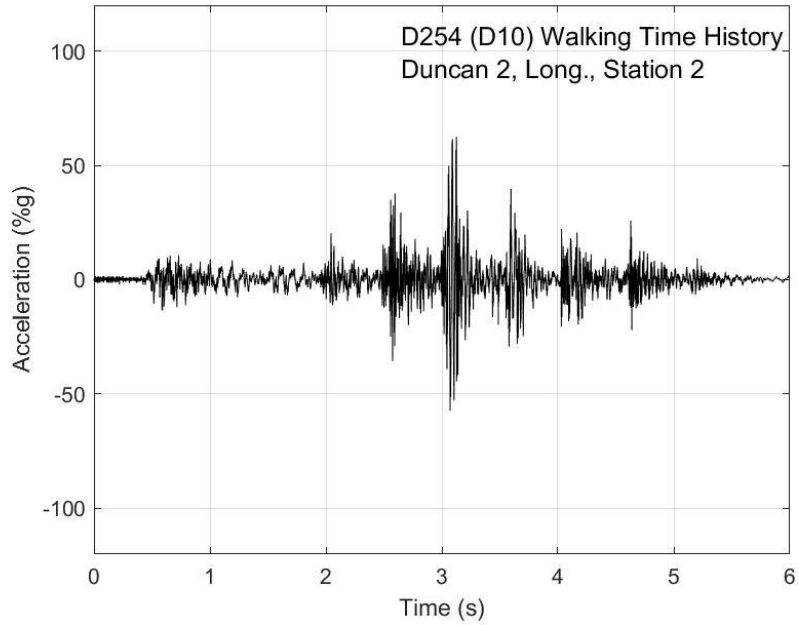


Fig. R-11. Walking time history, Duncan test 2, longitudinal direction, station 2

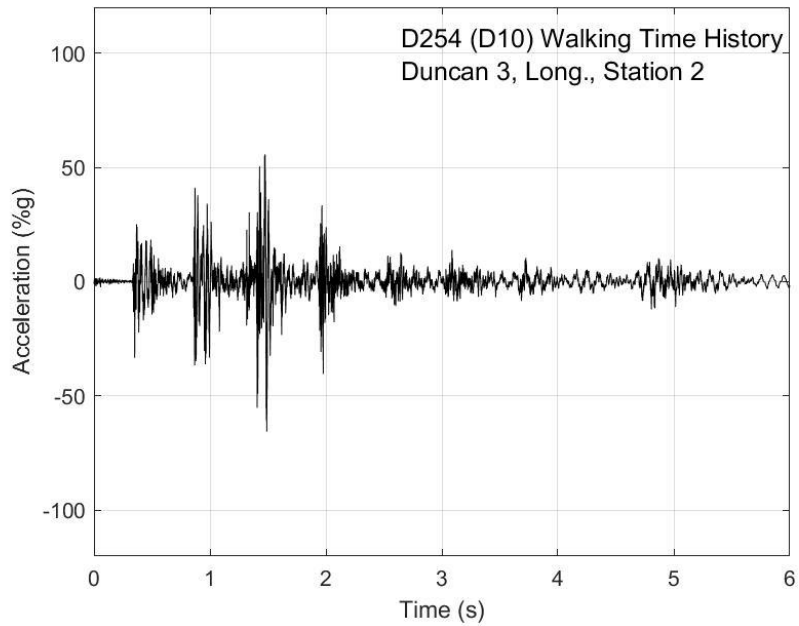


Fig. R-12. Walking time history, Duncan test 3, longitudinal direction, station 2

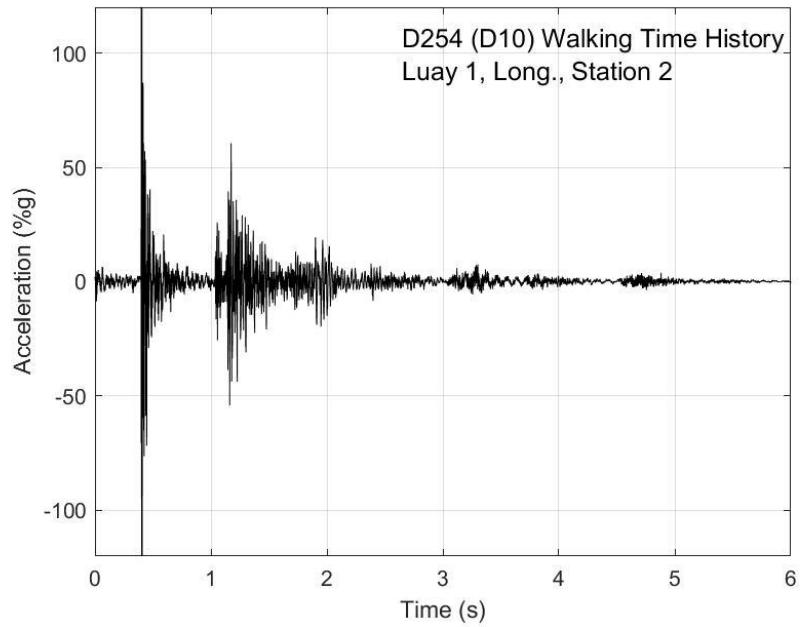


Fig. R-13. Walking time history, Luay test 1, longitudinal direction, station 2

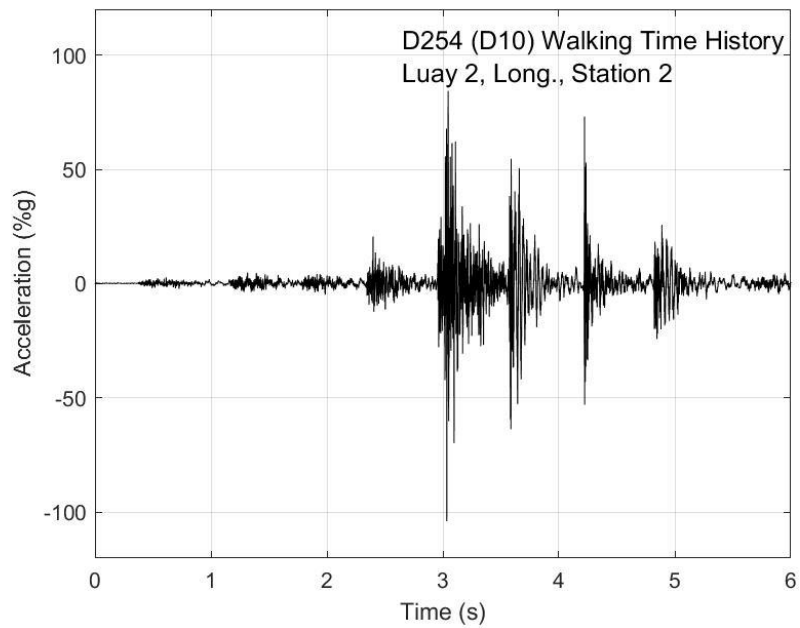


Fig. R-14. Walking time history, Luay test 2, longitudinal direction, station 2

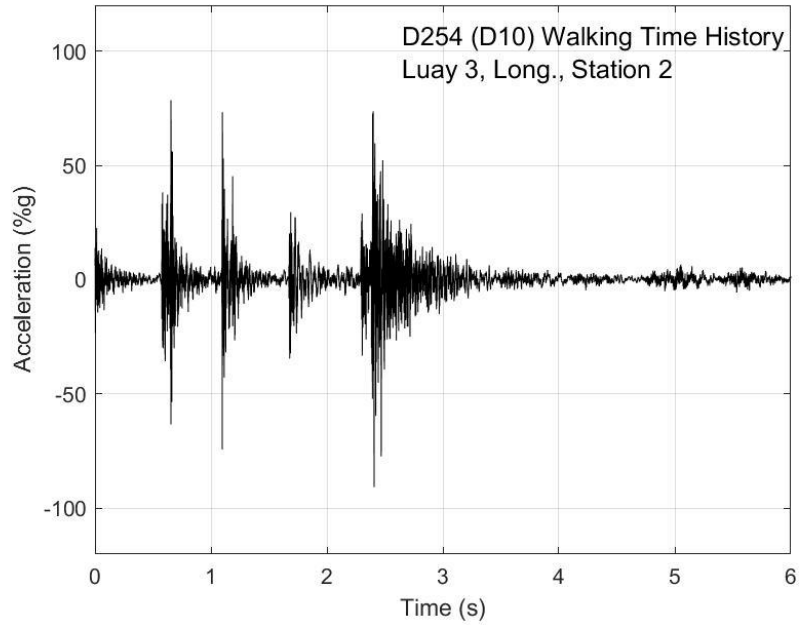


Fig. R-15. Walking time history, Luay test 3, longitudinal direction, station 2

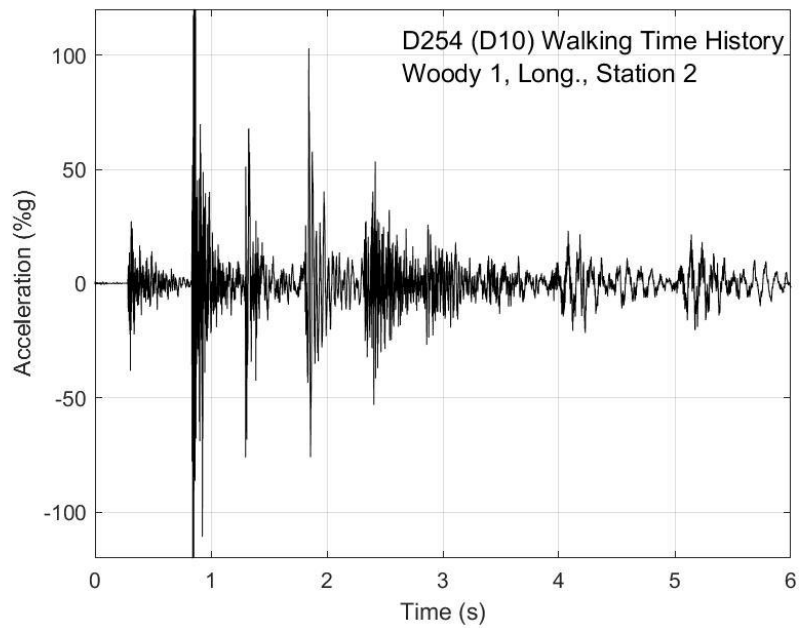


Fig. R-16. Walking time history, Woody test 1, longitudinal direction, station 2

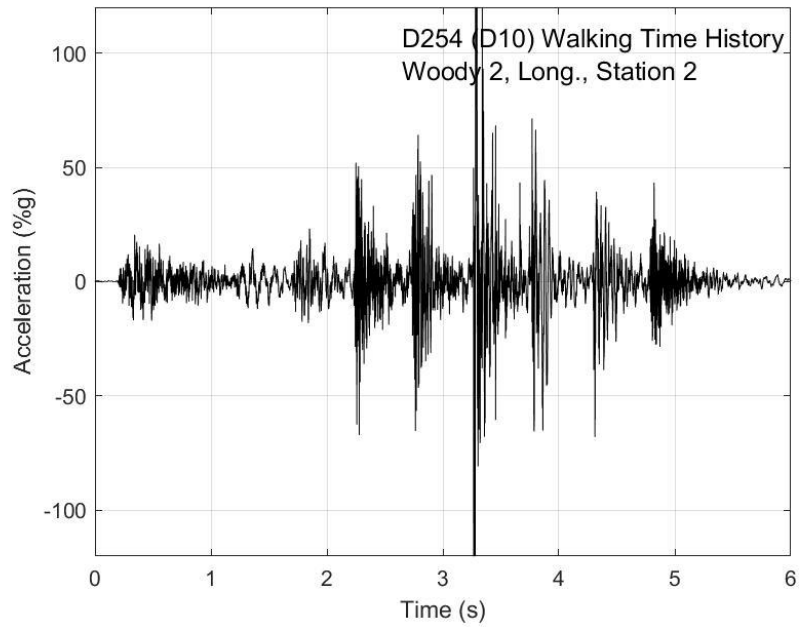


Fig. R-17. Walking time history, Woody test 2, longitudinal direction, station 2

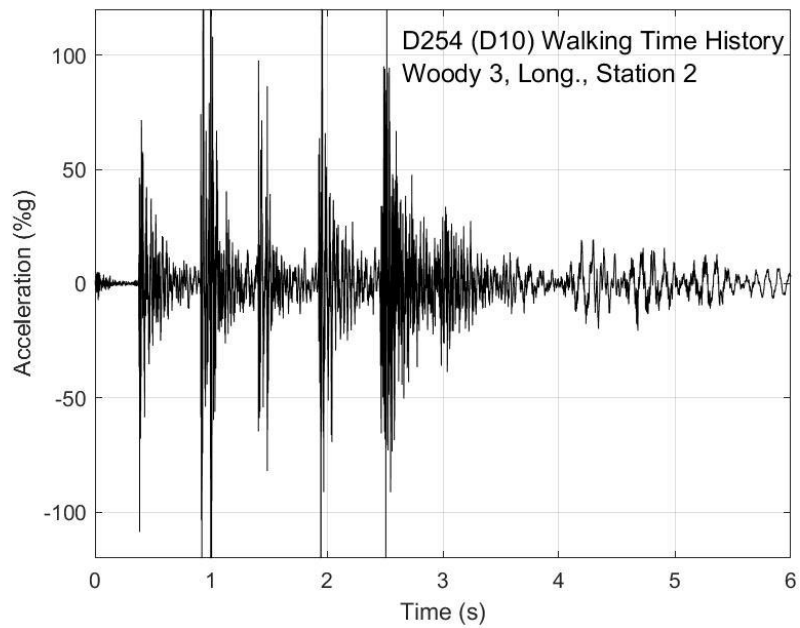


Fig. R-18. Walking time history, Woody test 3, longitudinal direction, station 2

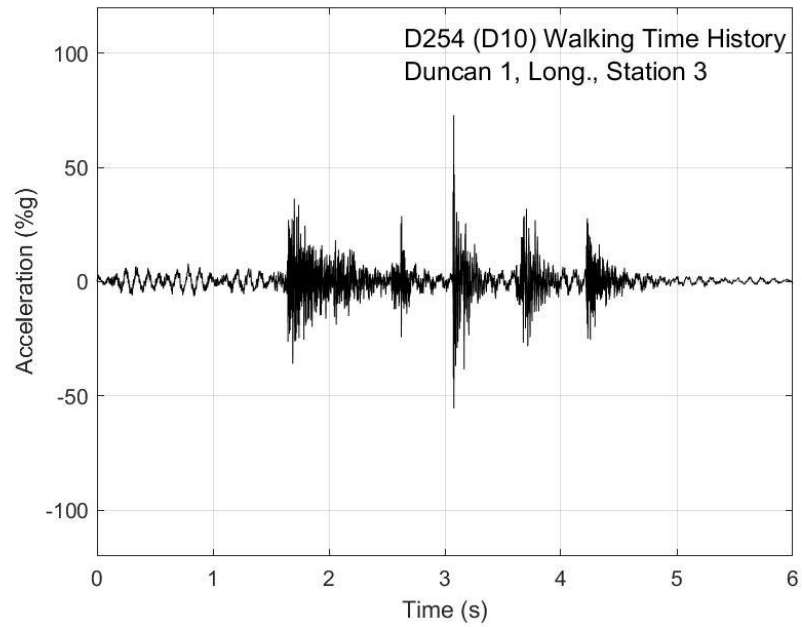


Fig. R-19. Walking time history, Duncan test 1, longitudinal direction, station 3

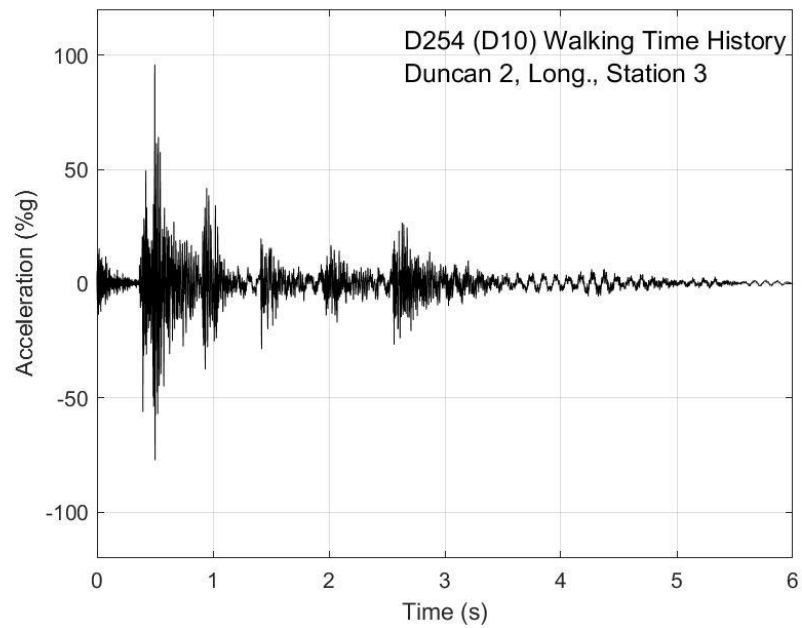


Fig. R-20. Walking time history, Duncan test 2, longitudinal direction, station 3

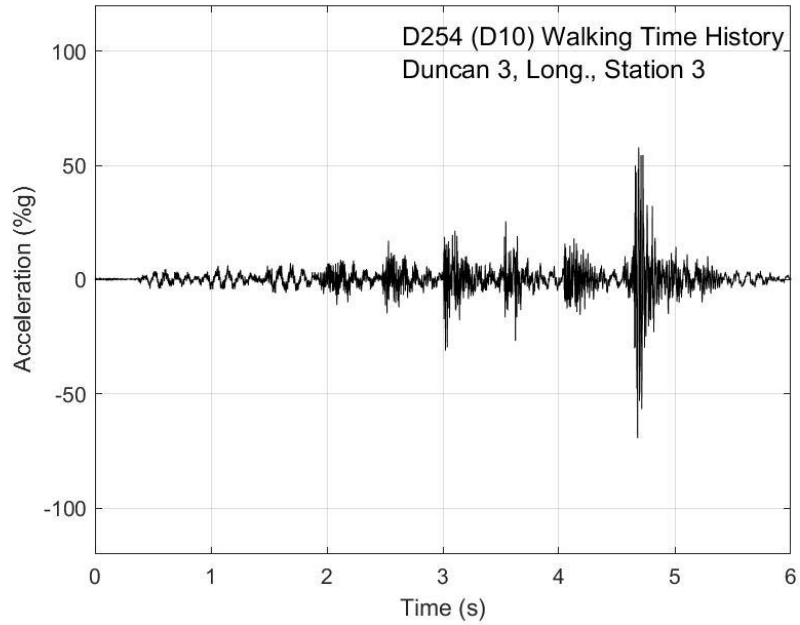


Fig. R-21. Walking time history, Duncan test 3, longitudinal direction, station 3

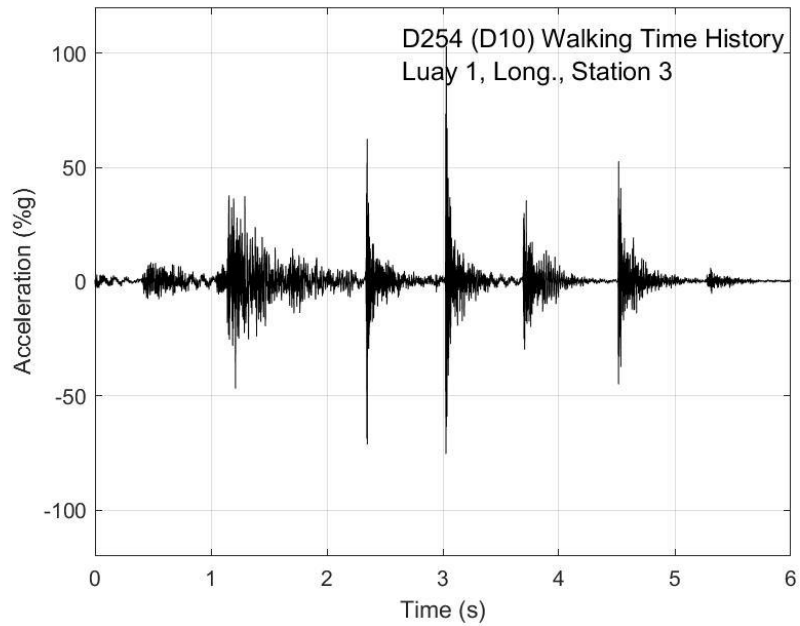


Fig. R-22. Walking time history, Luay test 1, longitudinal direction, station 3

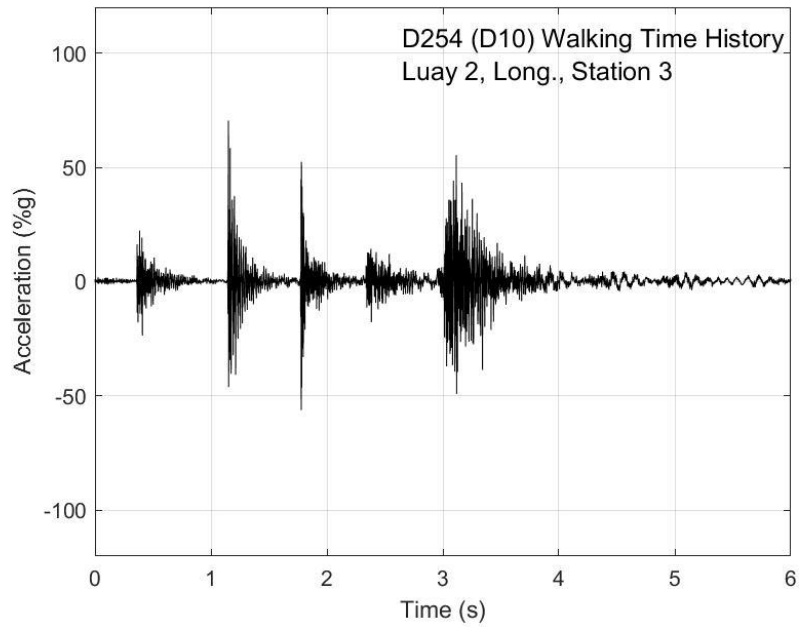


Fig. R-23. Walking time history, Luay test 2, longitudinal direction, station 3

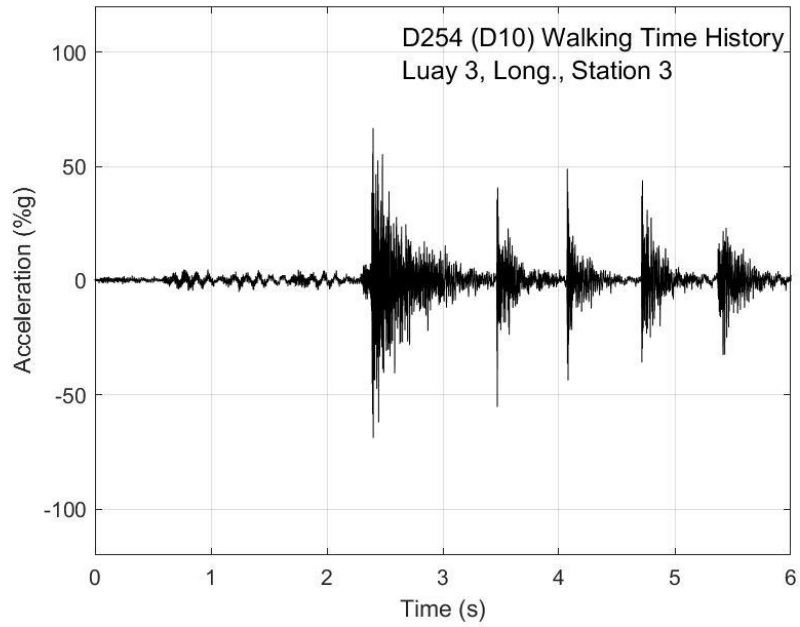


Fig. R-24. Walking time history, Luay test 3, longitudinal direction, station 3

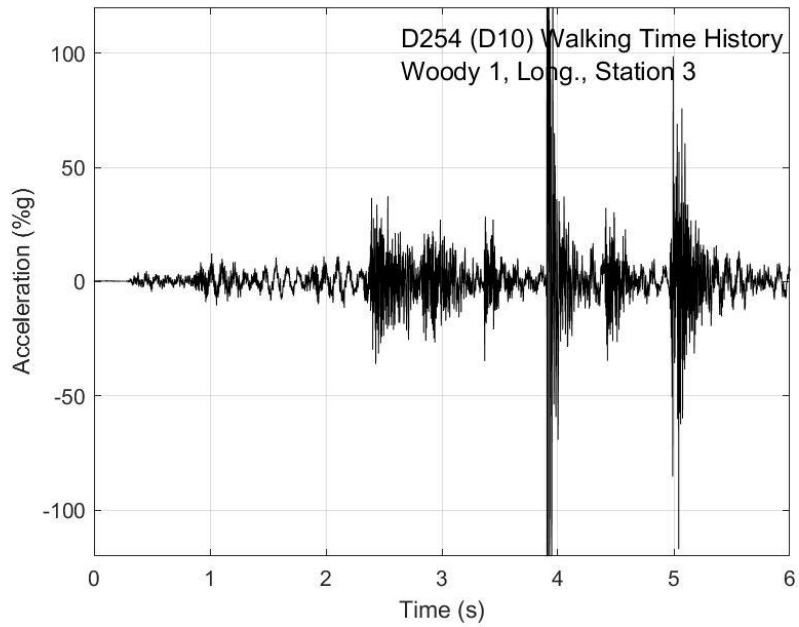


Fig. R-25. Walking time history, Woody test 1, longitudinal direction, station 3

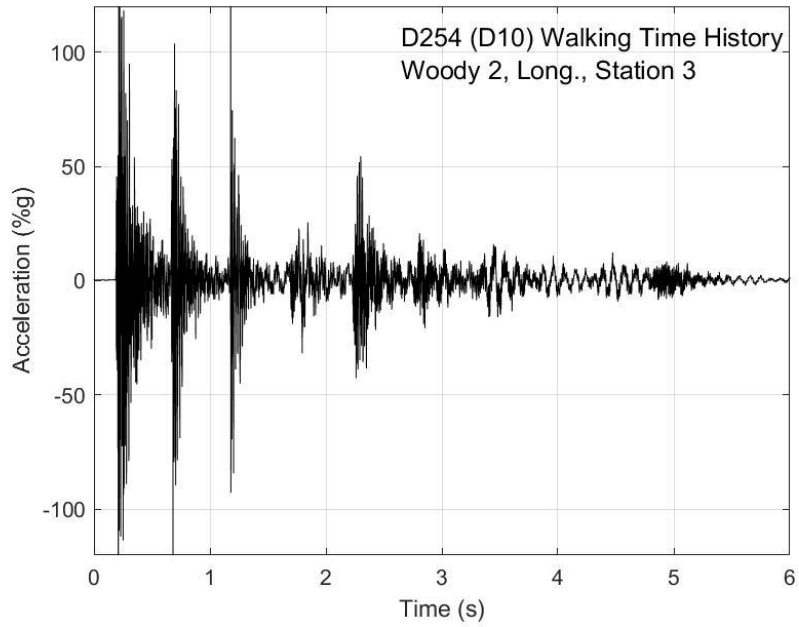


Fig. R-26. Walking time history, Woody test 2, longitudinal direction, station 3

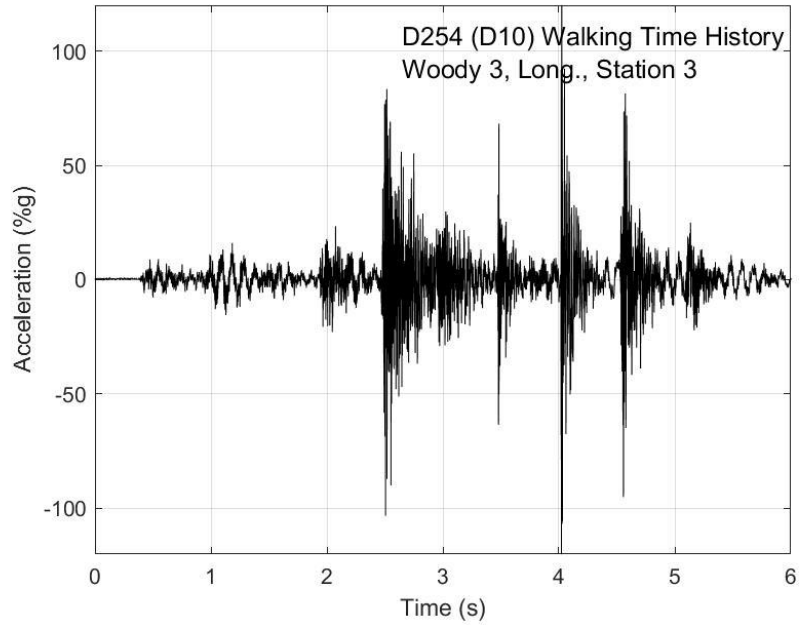


Fig. R-27. Walking time history, Woody test 3, longitudinal direction, station 3

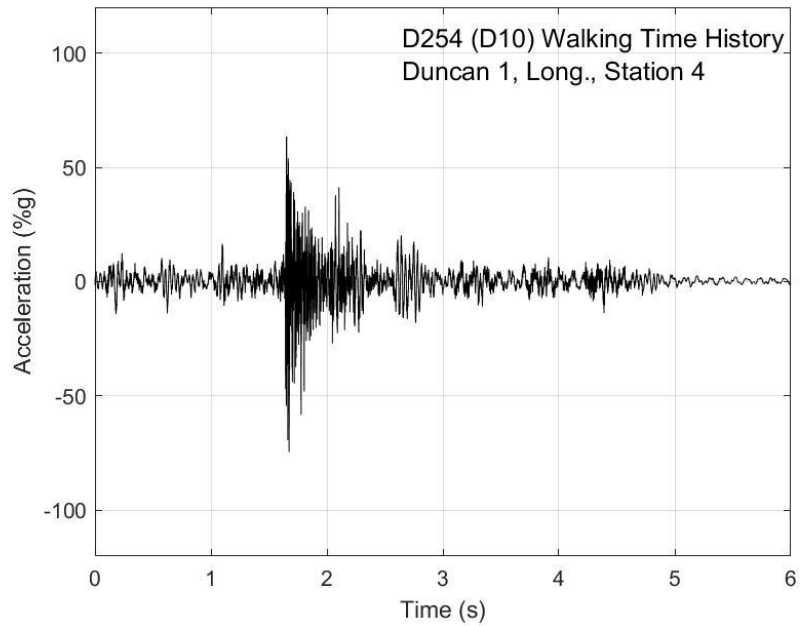


Fig. R-28. Walking time history, Duncan test 1, longitudinal direction, station 4

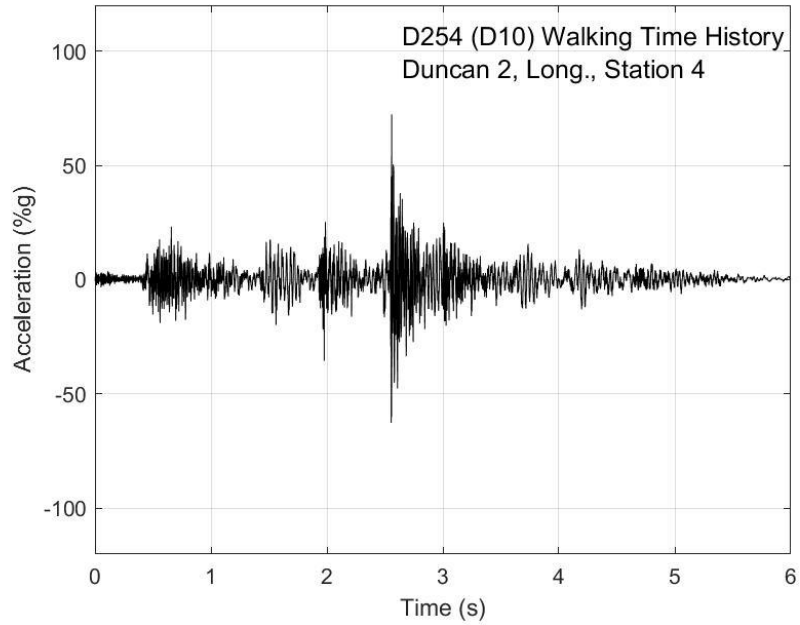


Fig. R-29. Walking time history, Duncan test 2, longitudinal direction, station 4

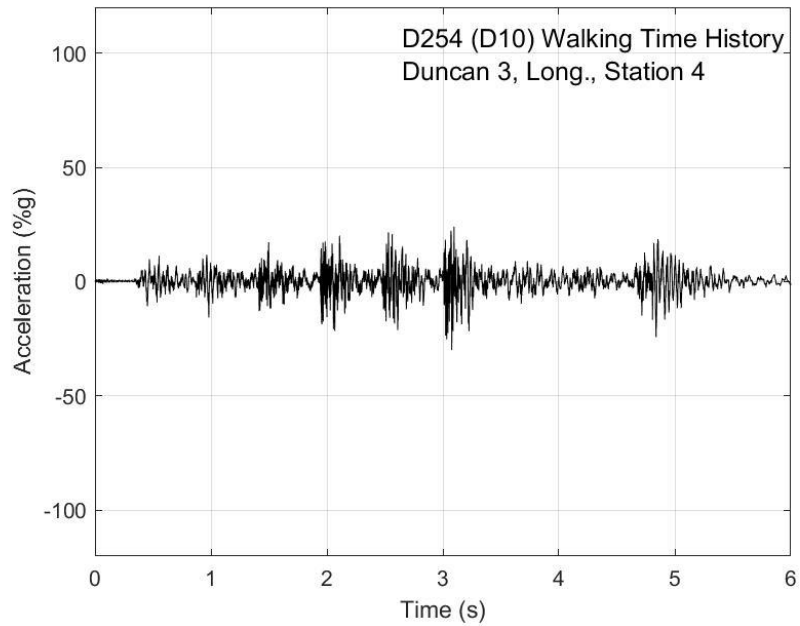


Fig. R-30. Walking time history, Duncan test 3, longitudinal direction, station 4

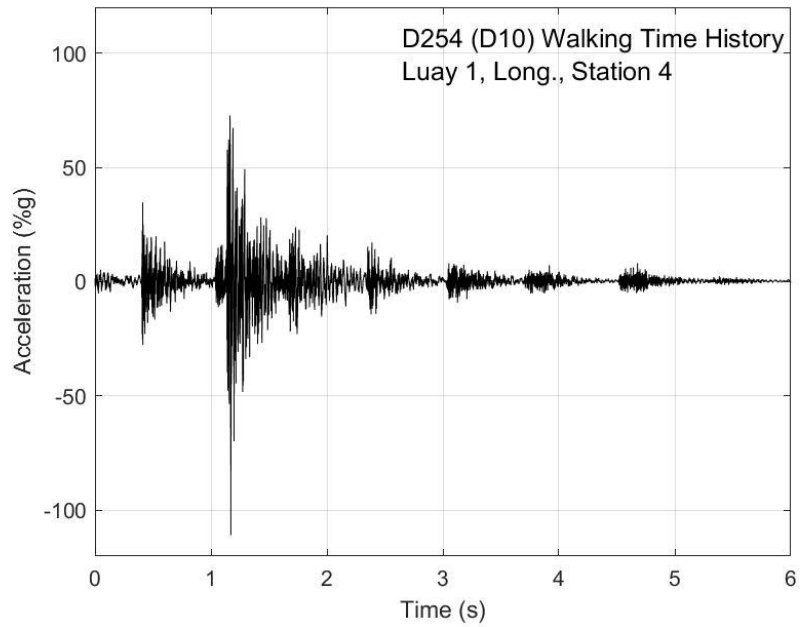


Fig. R-31. Walking time history, Luay test 1, longitudinal direction, station 4

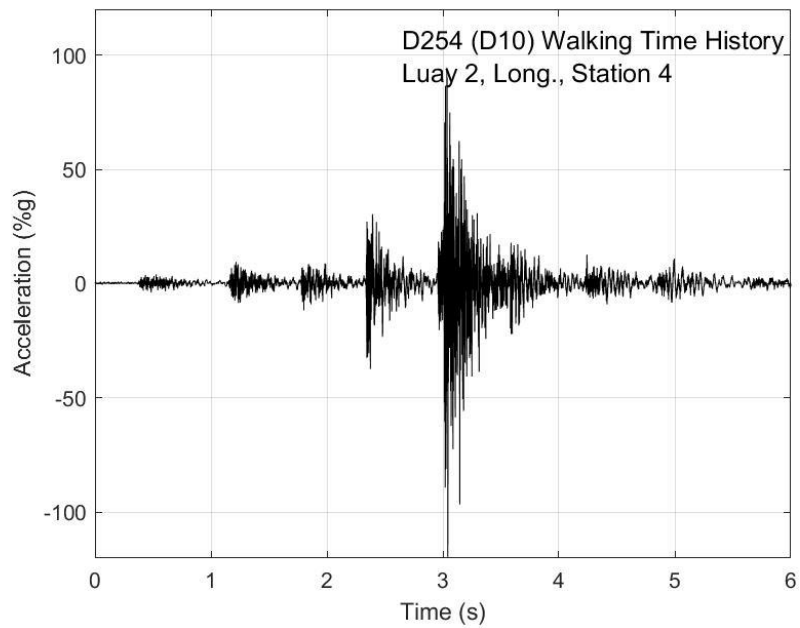


Fig. R-32. Walking time history, Luay test 2, longitudinal direction, station 4

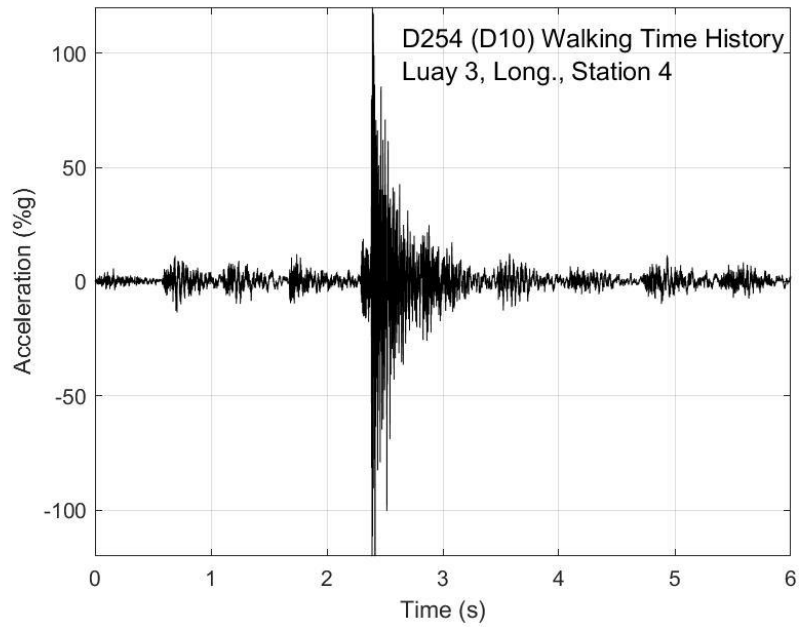


Fig. R-33. Walking time history, Luay test 3, longitudinal direction, station 4

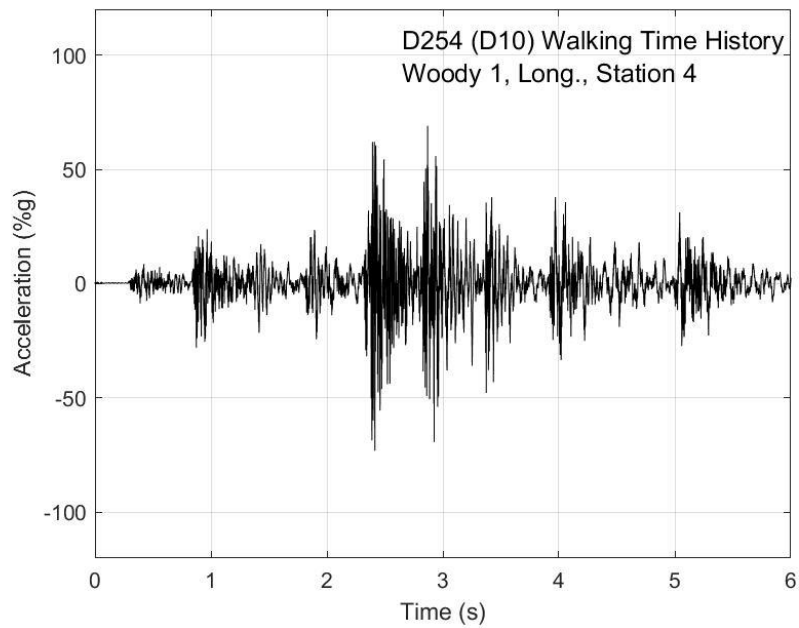


Fig. R-34. Walking time history, Woody test 1, longitudinal direction, station 4

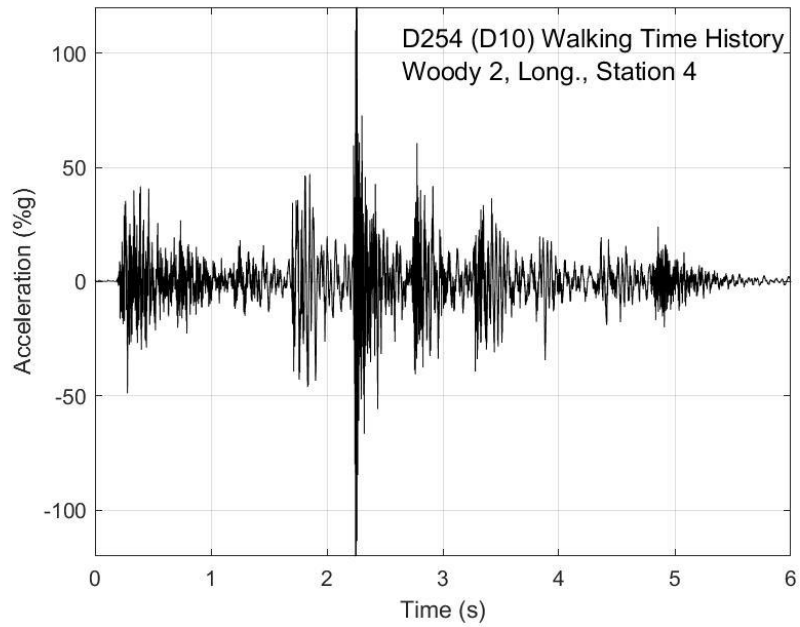


Fig. R-35. Walking time history, Woody test 2, longitudinal direction, station 4

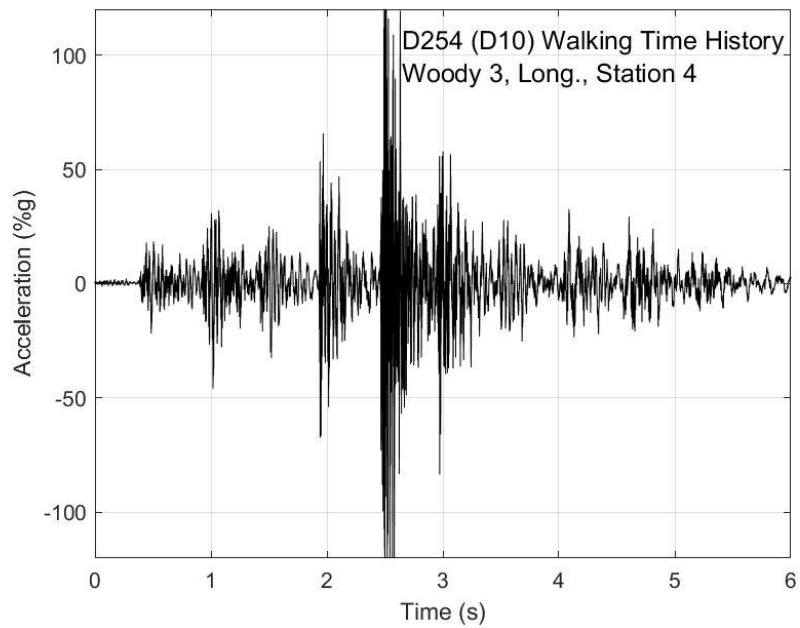


Fig. R-36. Walking time history, Woody test 3, longitudinal direction, station 4

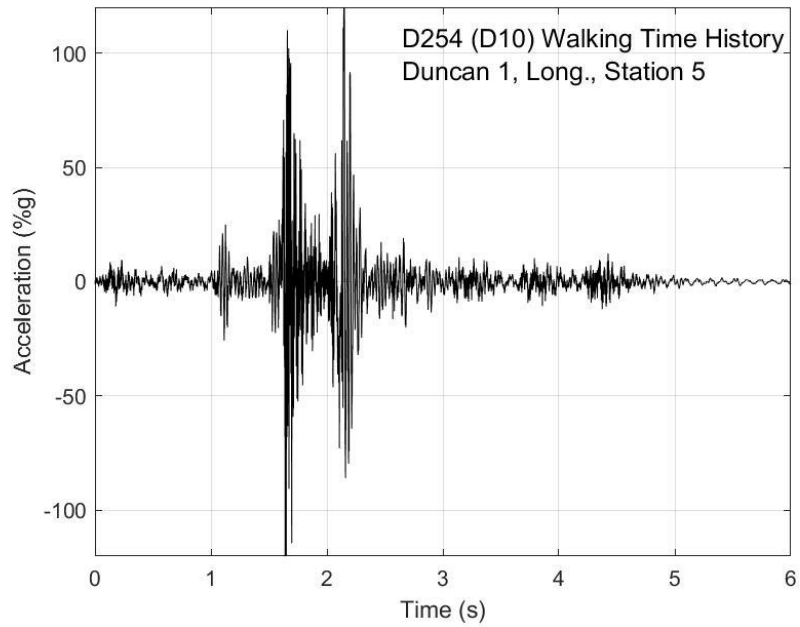


Fig. R-37. Walking time history, Duncan test 1, longitudinal direction, station 5

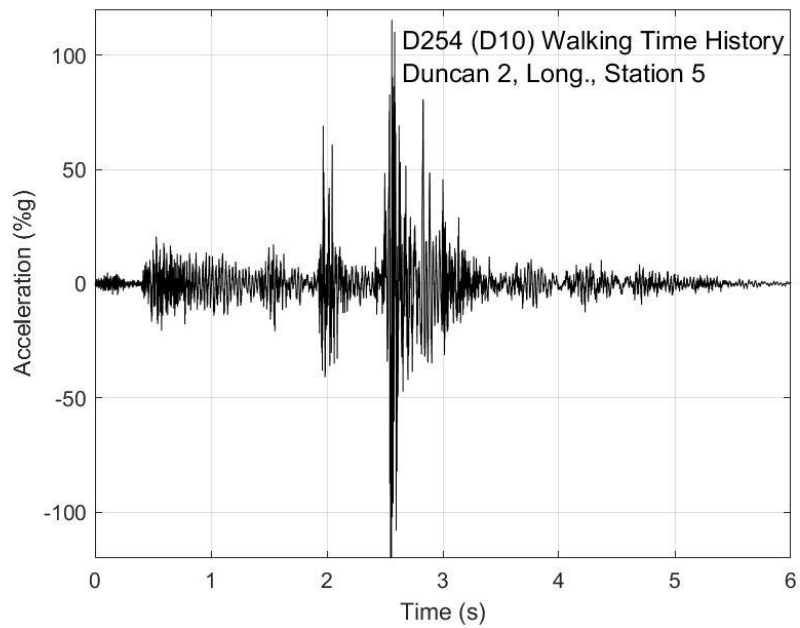


Fig. R-38. Walking time history, Duncan test 2, longitudinal direction, station 5

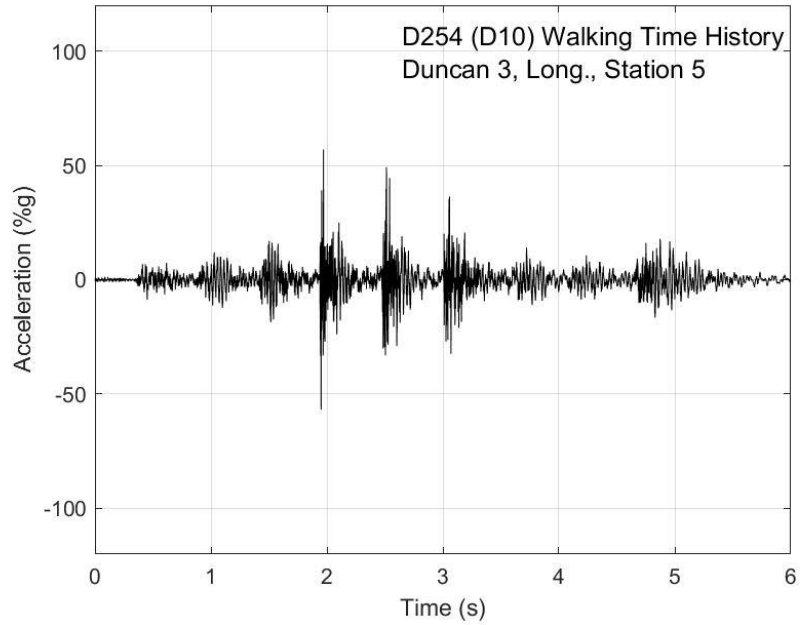


Fig. R-39. Walking time history, Duncan test 3, longitudinal direction, station 5

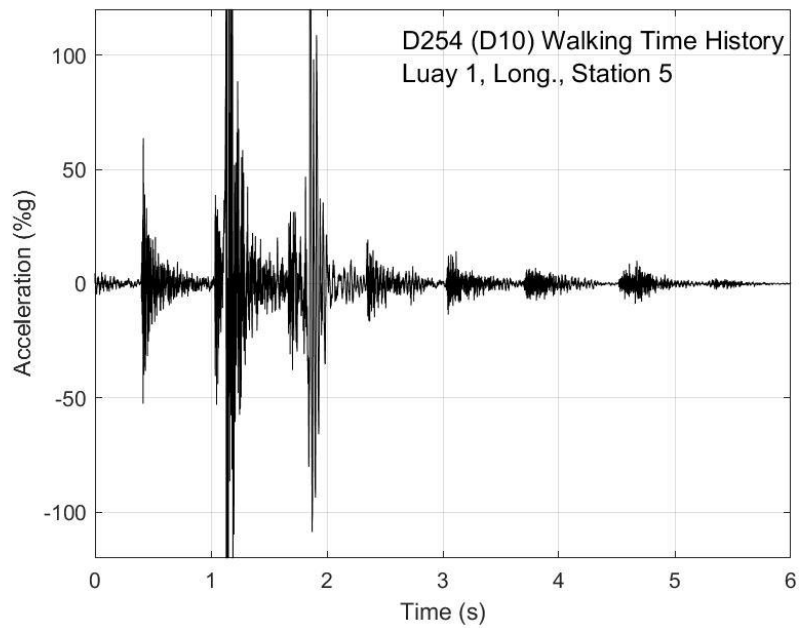


Fig. R-40. Walking time history, Luay test 1, longitudinal direction, station 5

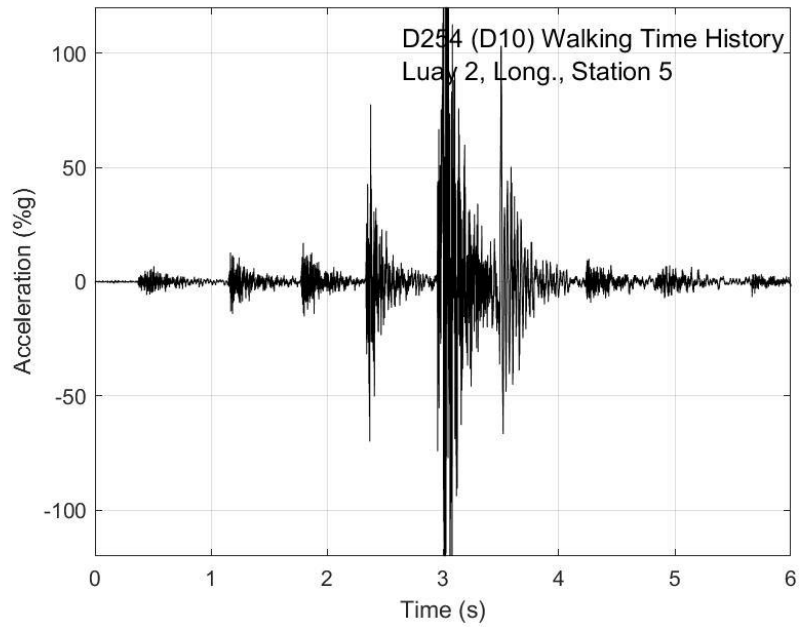


Fig. R-41. Walking time history, Luay test 2, longitudinal direction, station 5

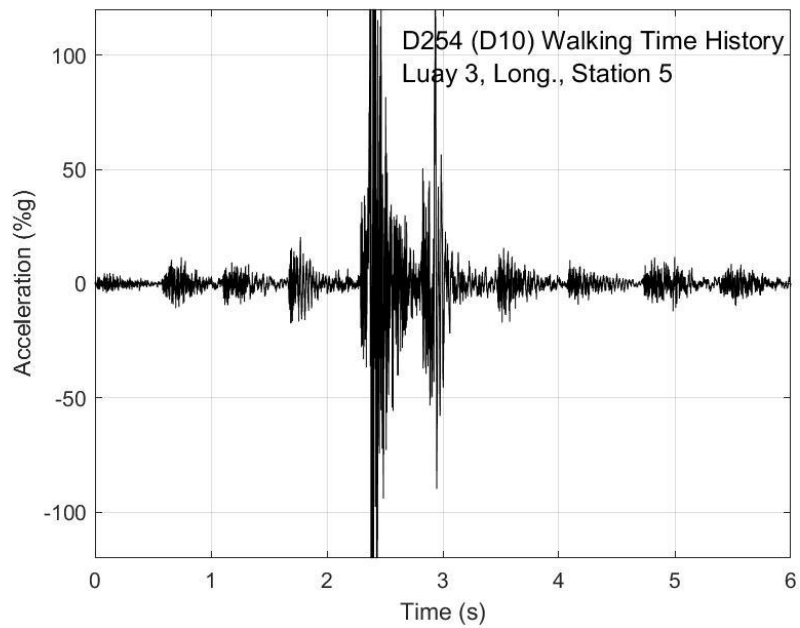


Fig. R-42. Walking time history, Luay test 3, longitudinal direction, station 5

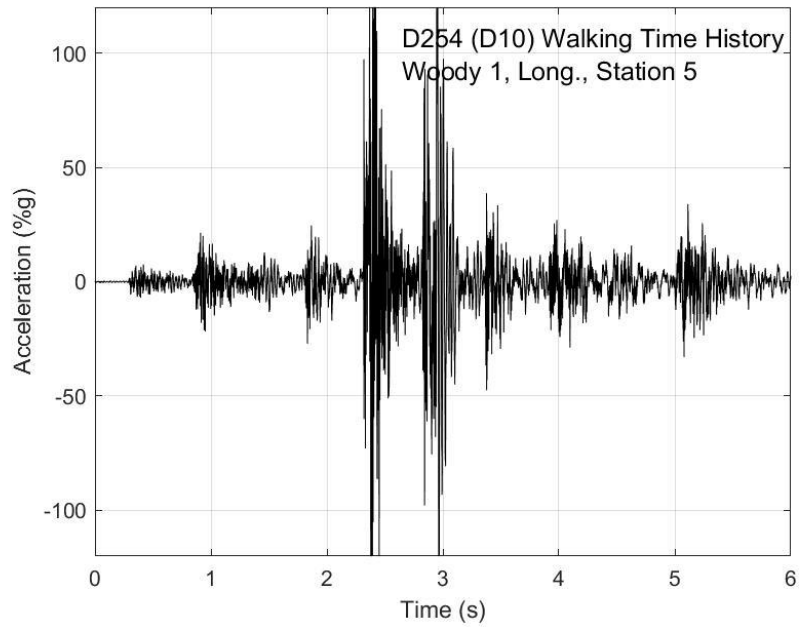


Fig. R-43. Walking time history, Woody test 1, longitudinal direction, station 5

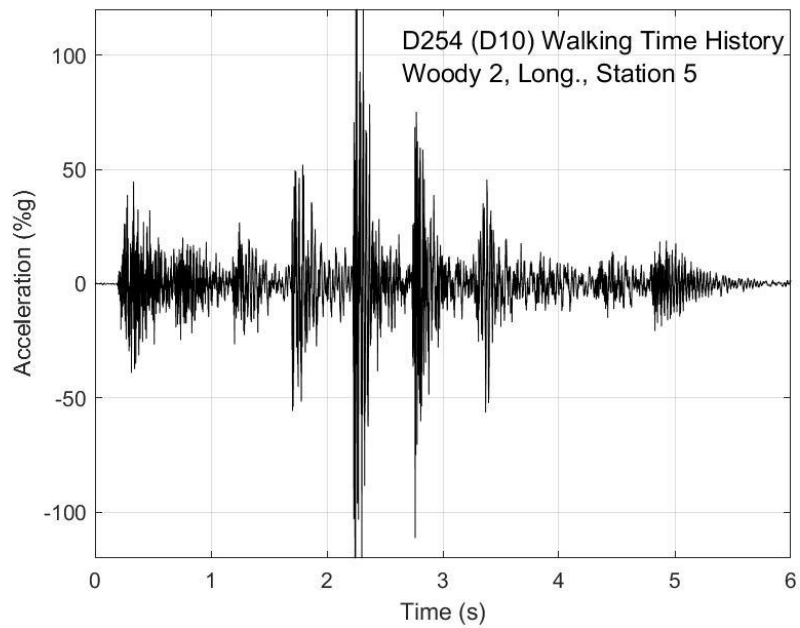


Fig. R-44. Walking time history, Woody test 2, longitudinal direction, station 5

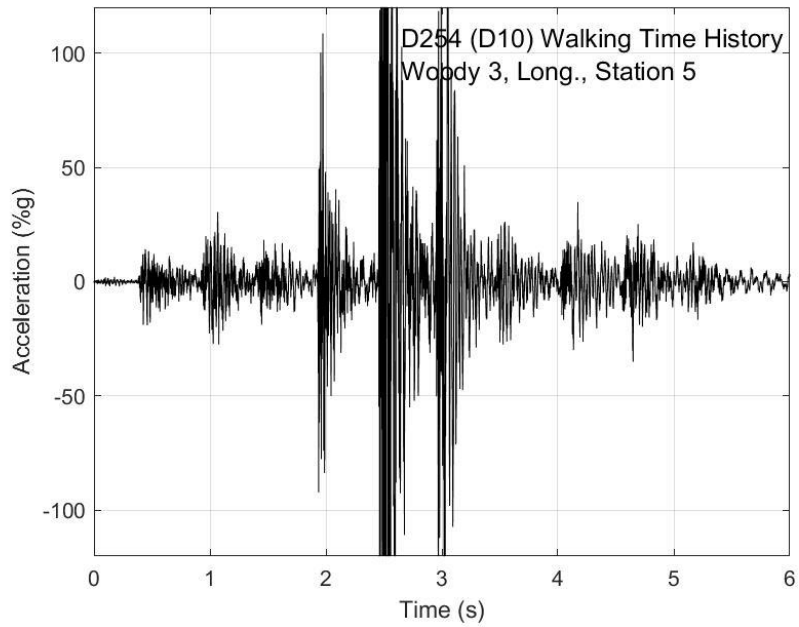


Fig. R-45. Walking time history, Woody test 3, longitudinal direction, station 5

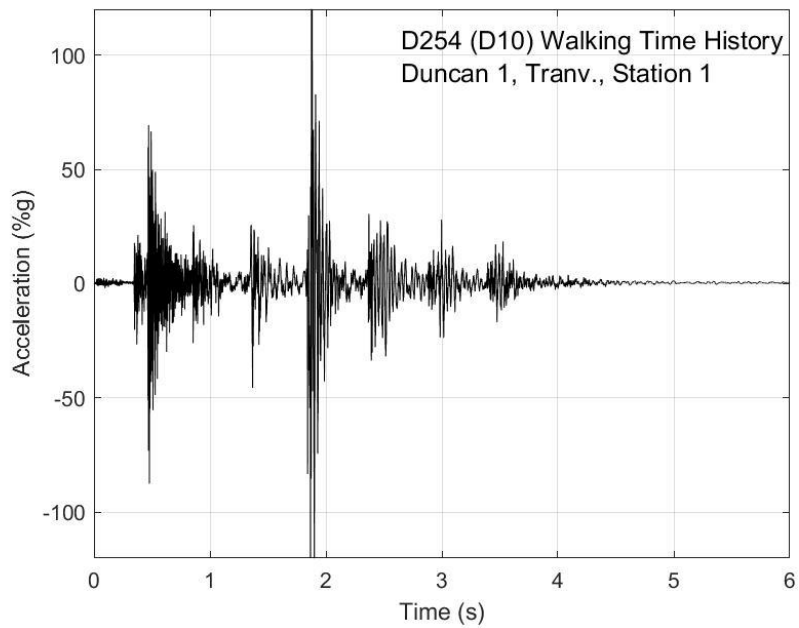


Fig. R-46. Walking time history, Duncan test 1, transverse direction, station 1

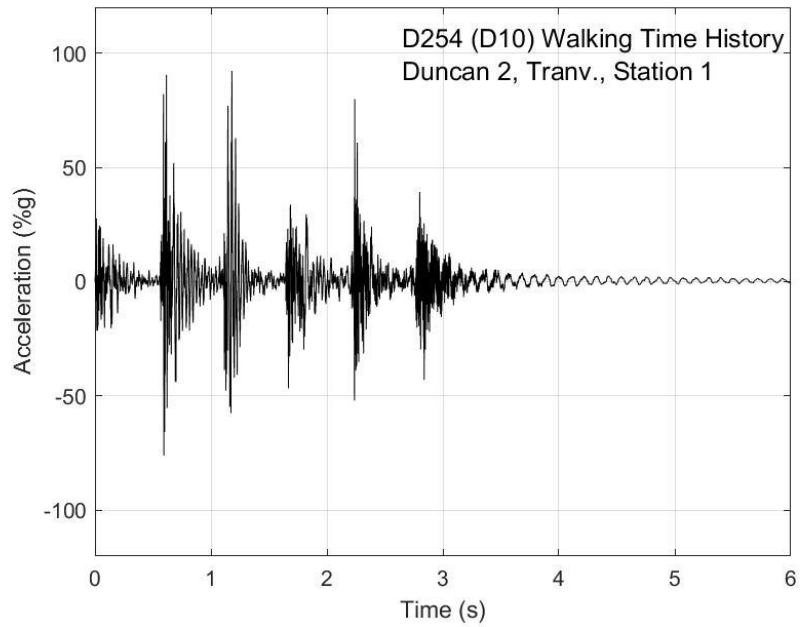


Fig. R-47. Walking time history, Duncan test 2, transverse direction, station 1

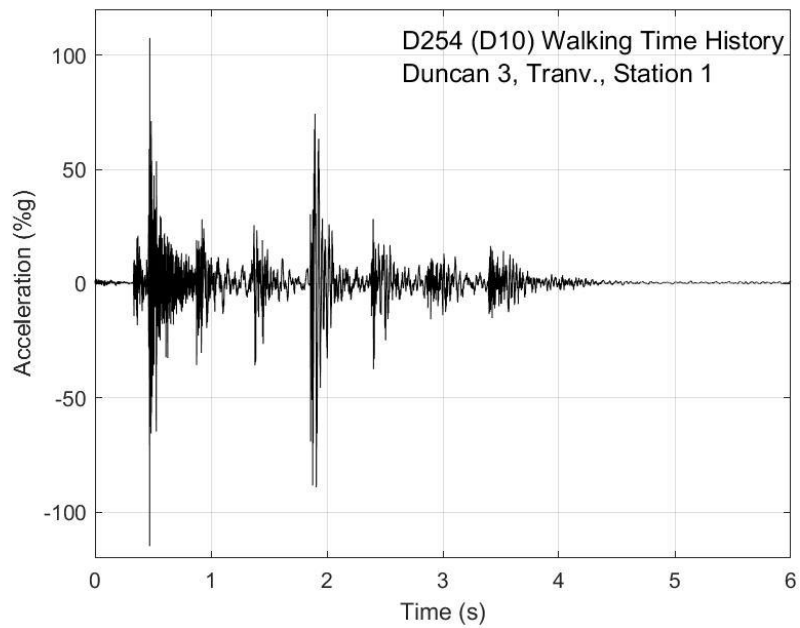


Fig. R-48. Walking time history, Duncan test 3, transverse direction, station 1

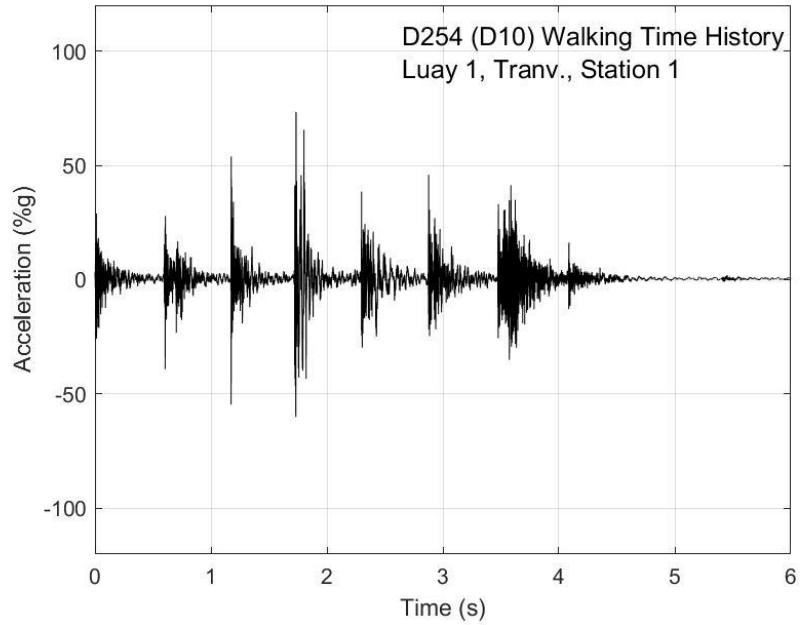


Fig. R-49. Walking time history, Luay test 1, transverse direction, station 1

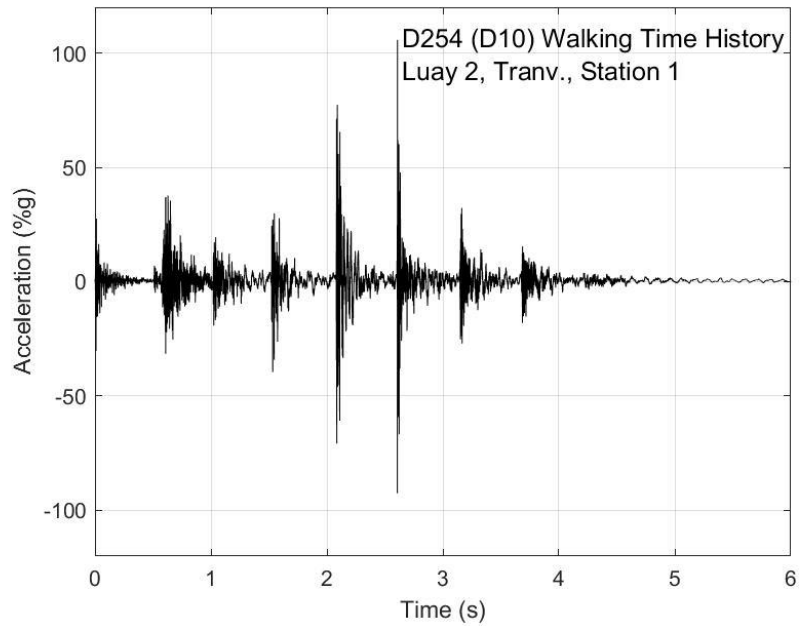


Fig. R-50. Walking time history, Luay test 2, transverse direction, station 1

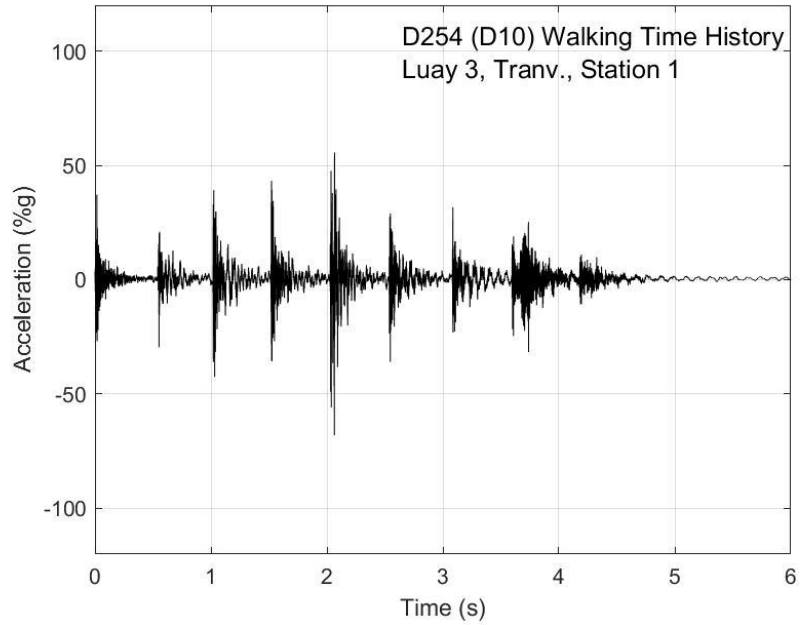


Fig. R-51. Walking time history, Luay test 3, transverse direction, station 1

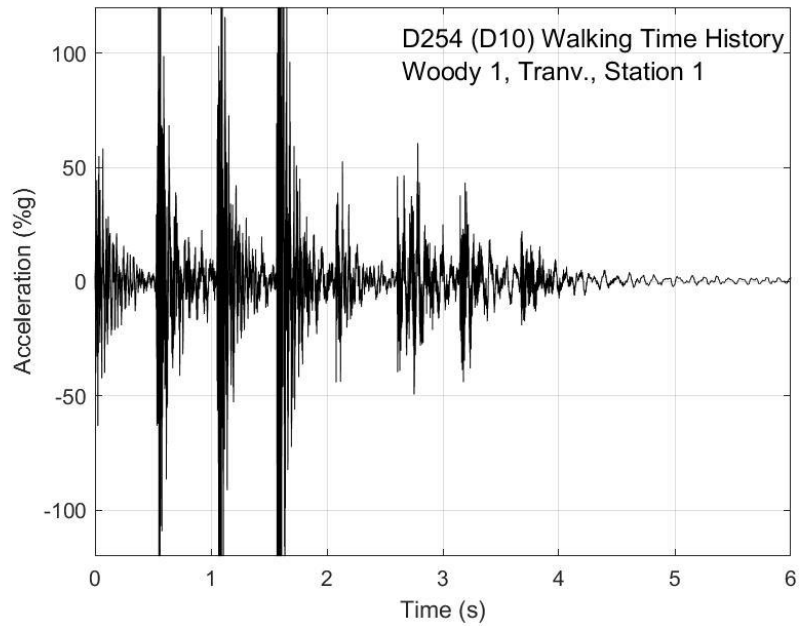


Fig. R-52. Walking time history, Woody test 1, transverse direction, station 1

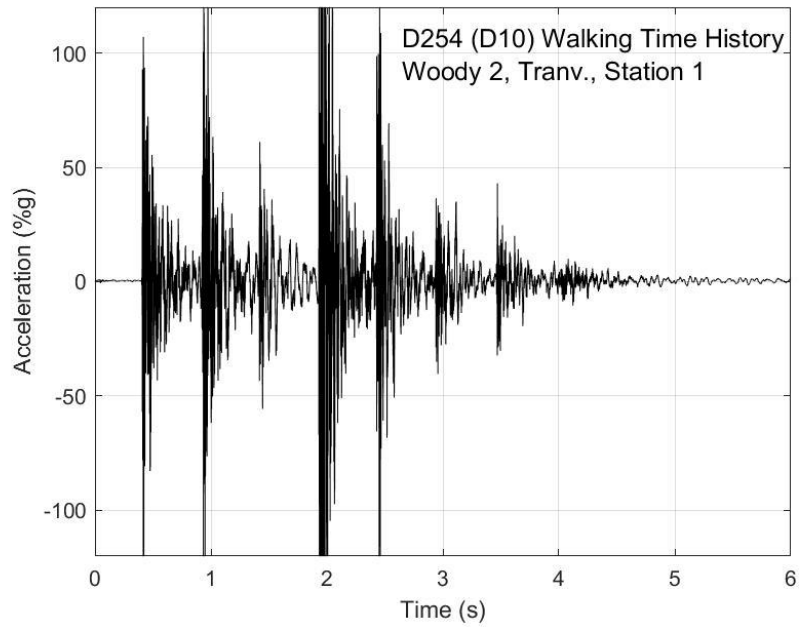


Fig. R-53. Walking time history, Woody test 2, transverse direction, station 1

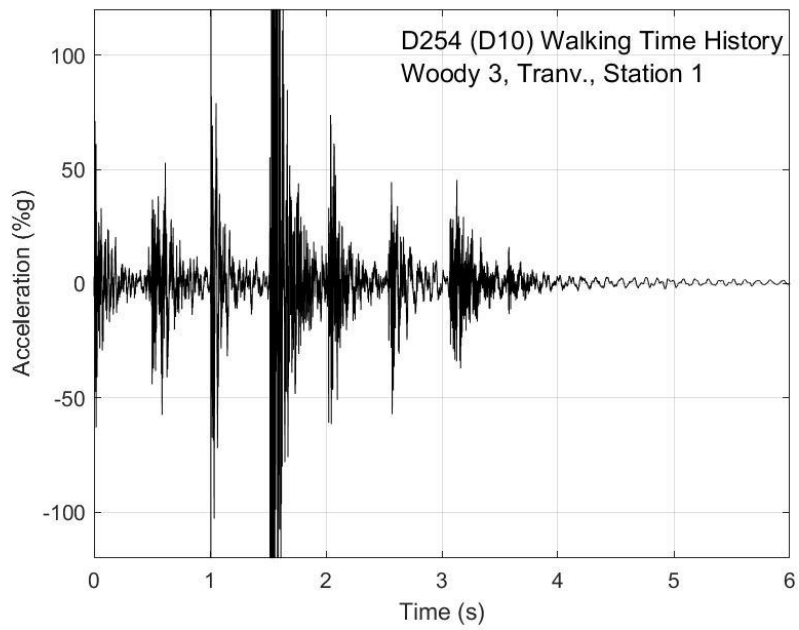


Fig. R-54. Walking time history, Woody test 3, transverse direction, station 1

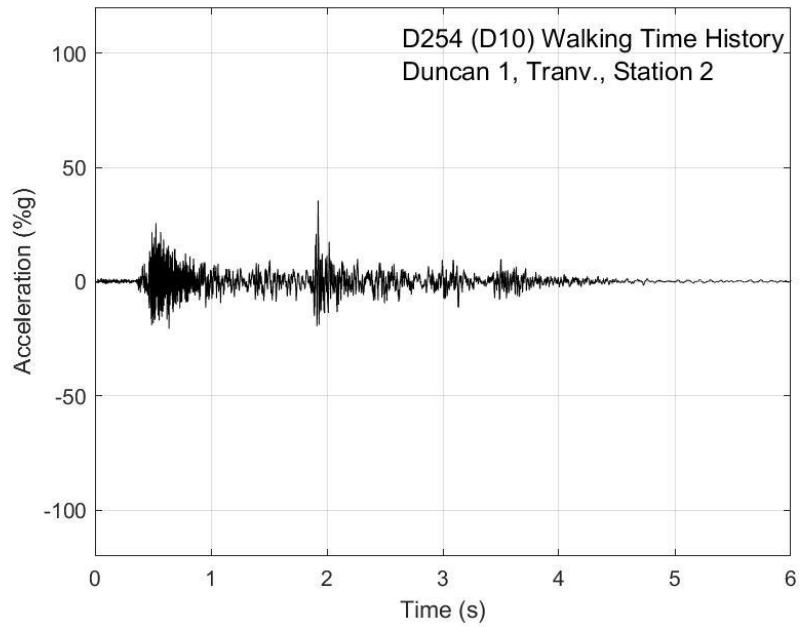


Fig. R-55. Walking time history, Duncan test 1, transverse direction, station 2

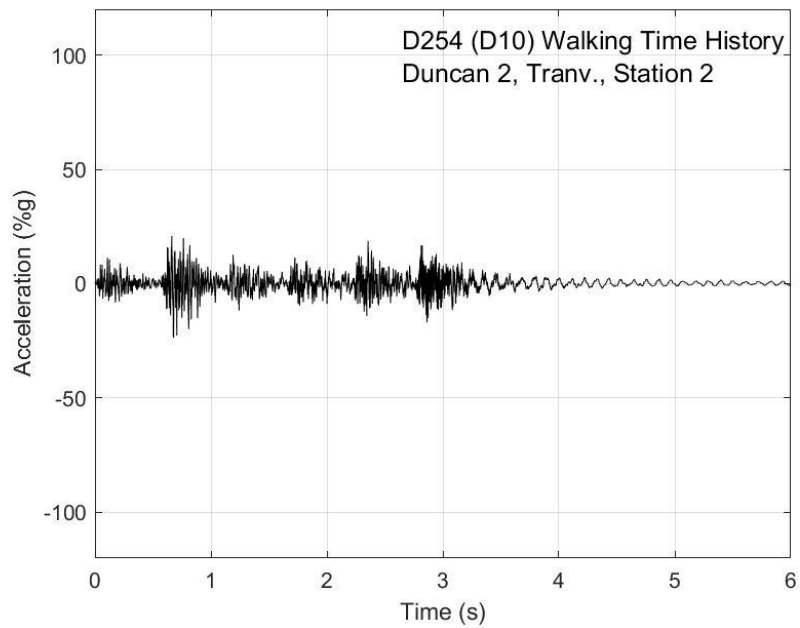


Fig. R-56. Walking time history, Duncan test 2, transverse direction, station 2

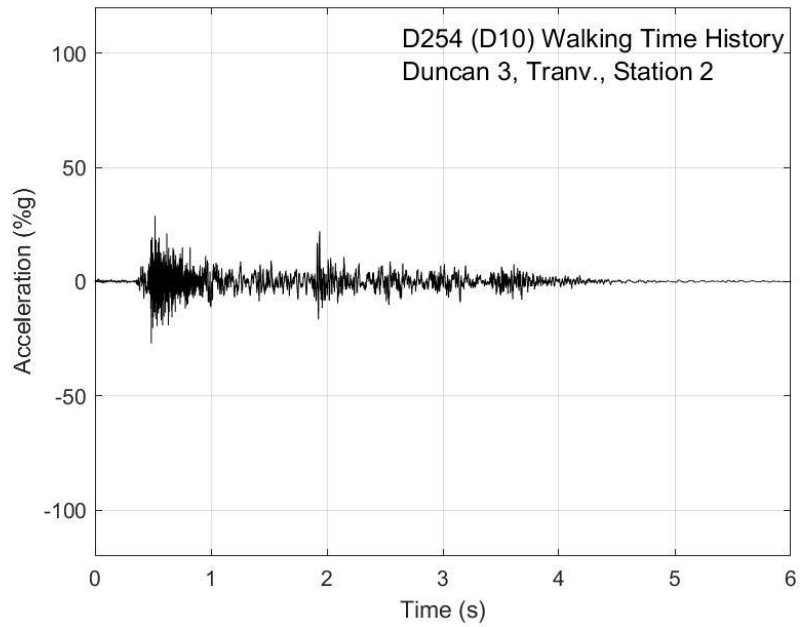


Fig. R-57. Walking time history, Duncan test 3, transverse direction, station 2

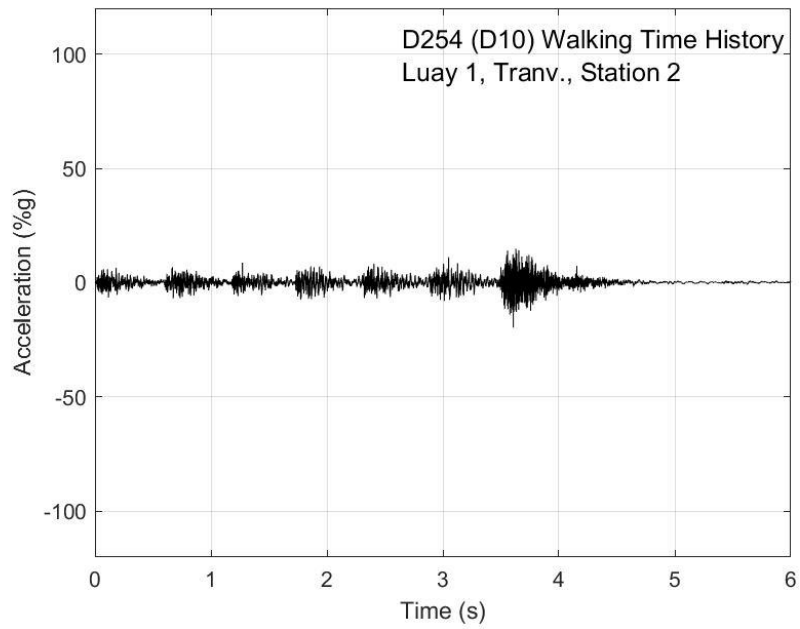


Fig. R-58. Walking time history, Luay test 1, transverse direction, station 2

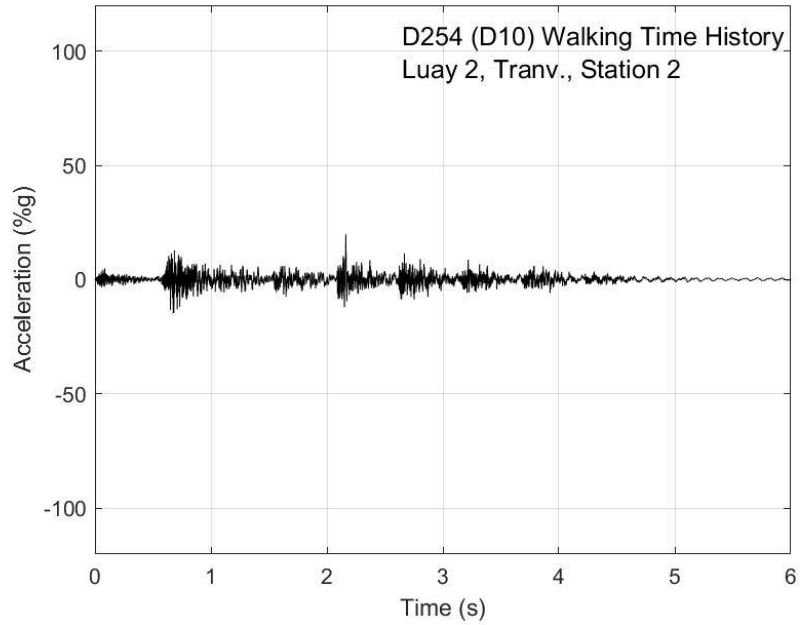


Fig. R-59. Walking time history, Luay test 2, transverse direction, station 2

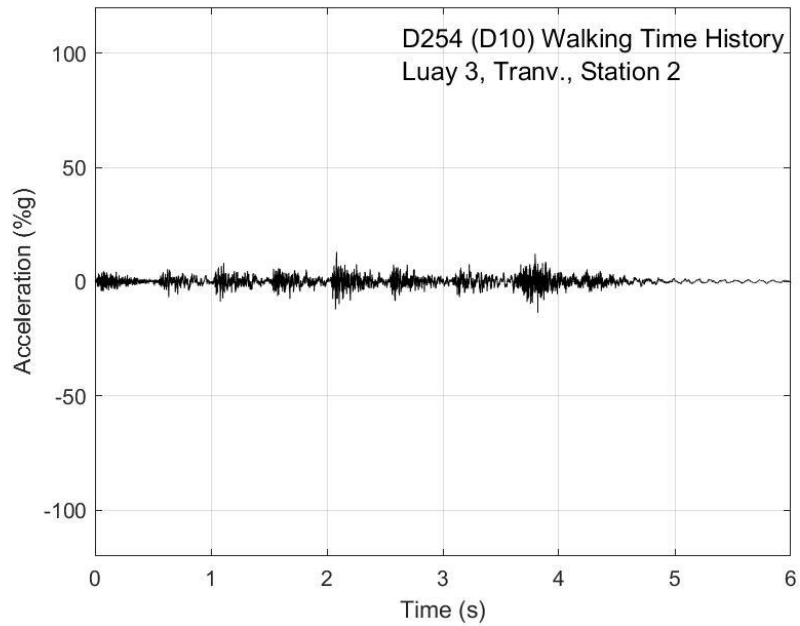


Fig. R-60. Walking time history, Luay test 3, transverse direction, station 2

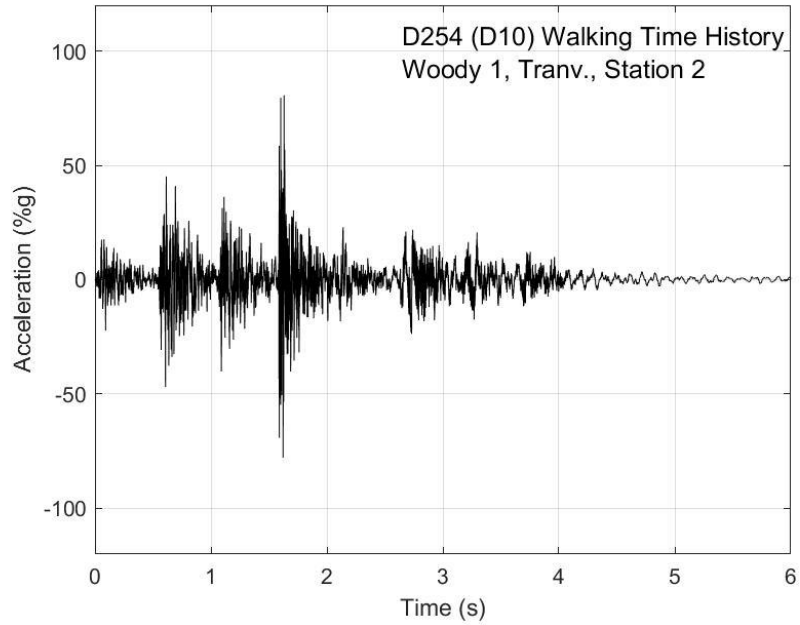


Fig. R-61. Walking time history, Woody test 1, transverse direction, station 2

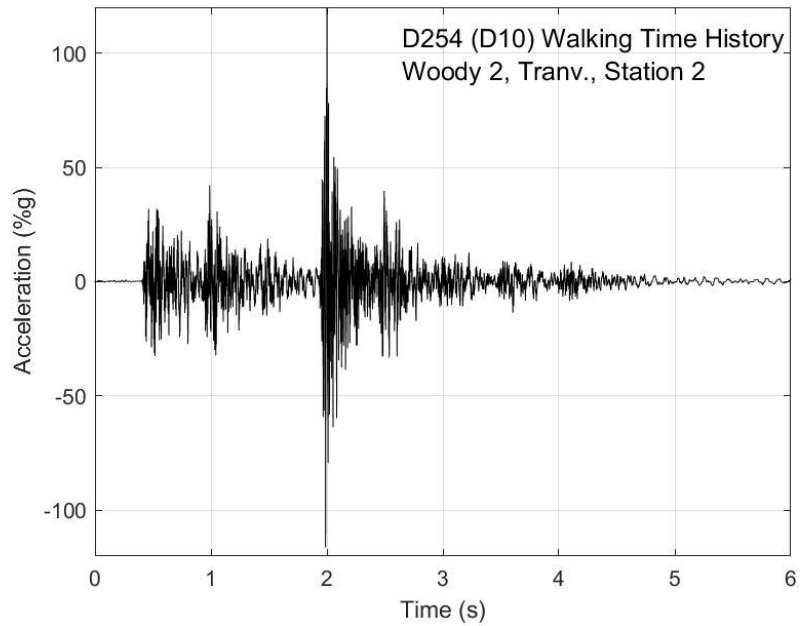


Fig. R-62. Walking time history, Woody test 2, transverse direction, station 2

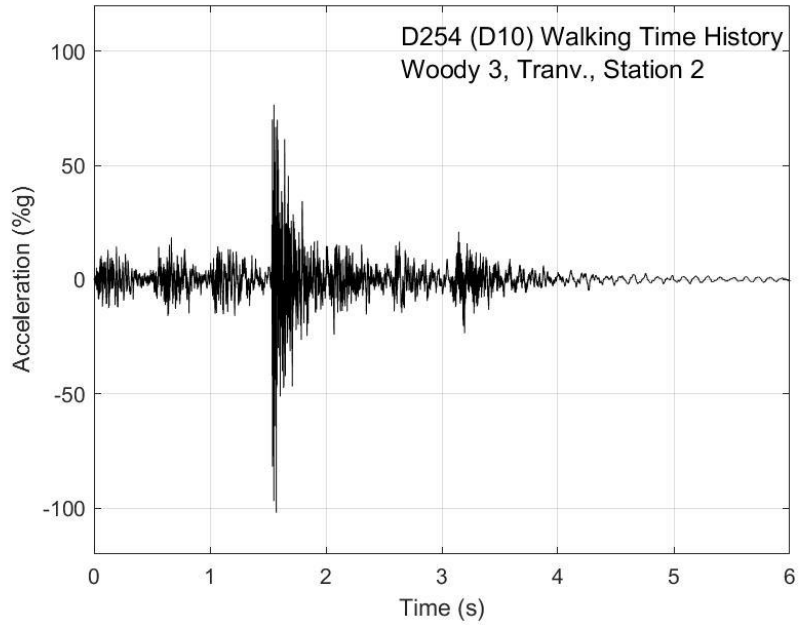


Fig. R-63. Walking time history, Woody test 3, transverse direction, station 2

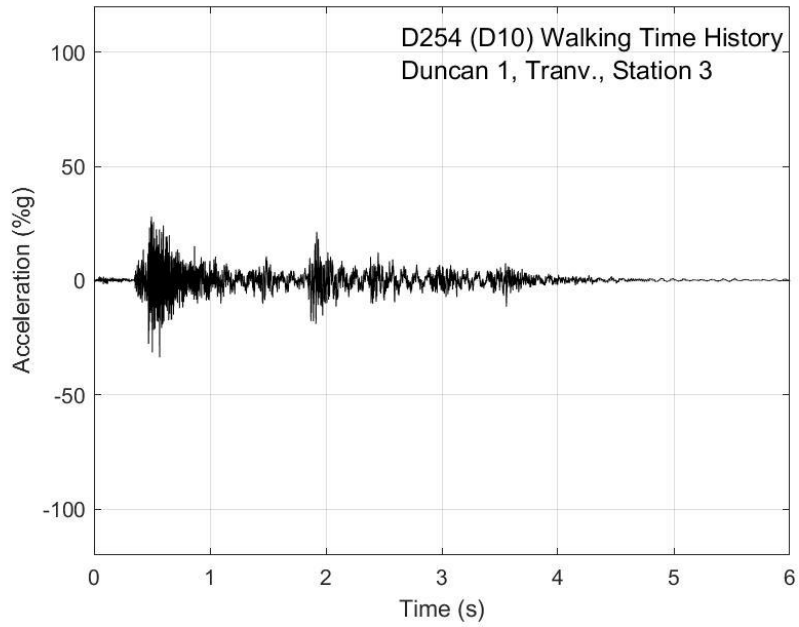


Fig. R-64. Walking time history, Duncan test 1, transverse direction, station 3

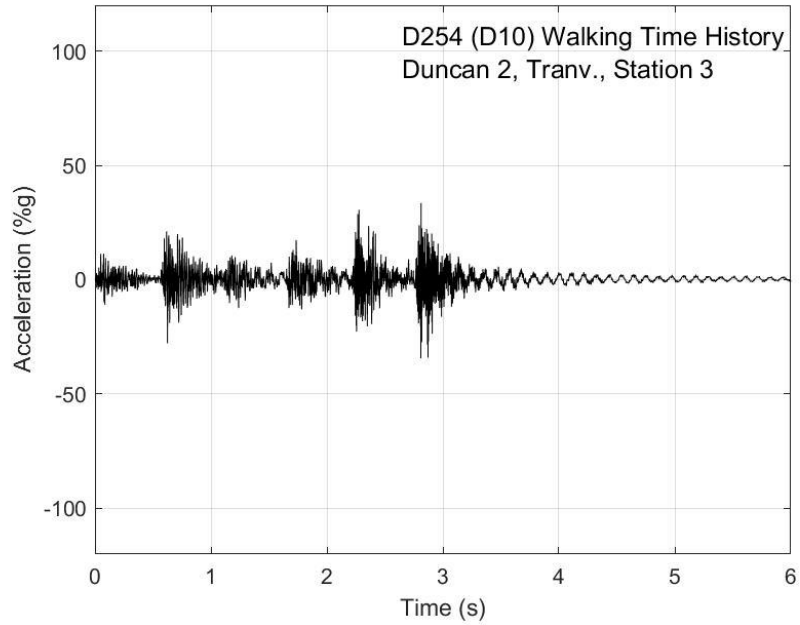


Fig. R-65. Walking time history, Duncan test 2, transverse direction, station 3

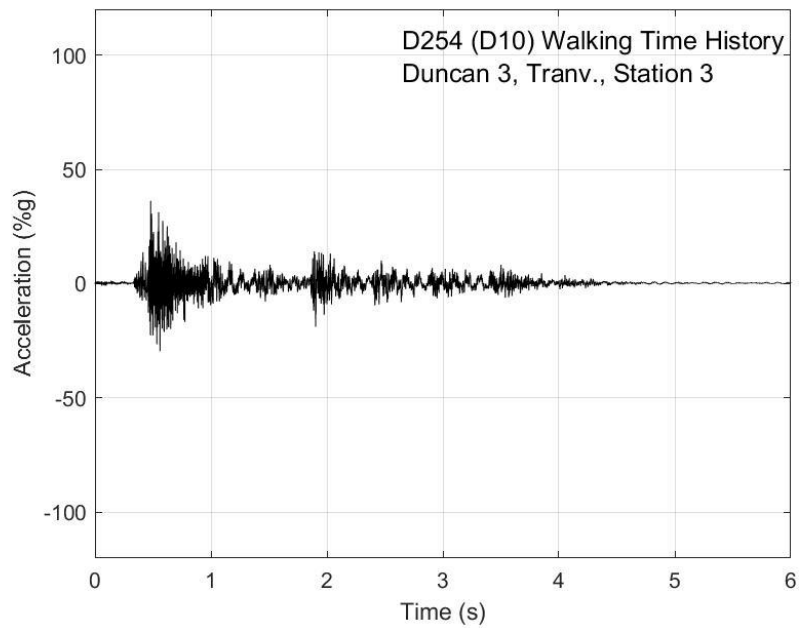


Fig. R-66. Walking time history, Duncan test 3, transverse direction, station 3

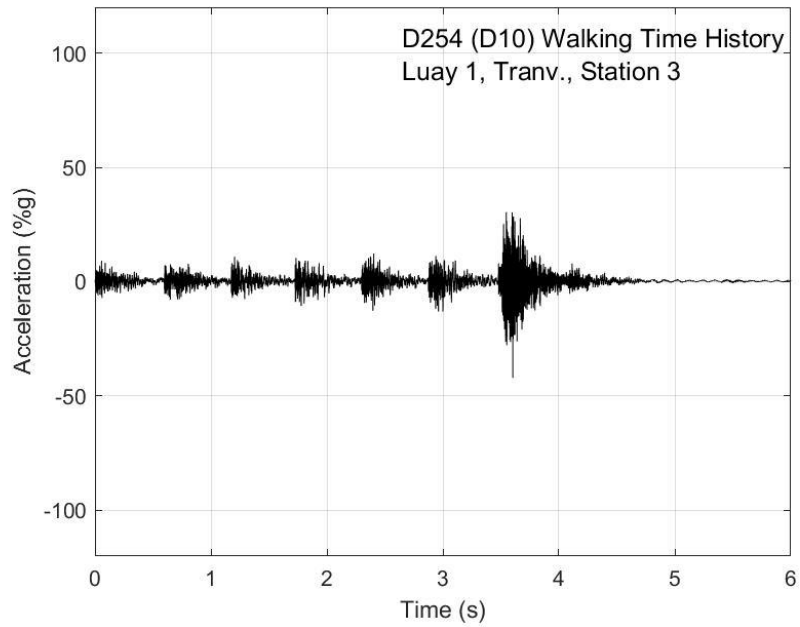


Fig. R-67. Walking time history, Luay test 1, transverse direction, station 3

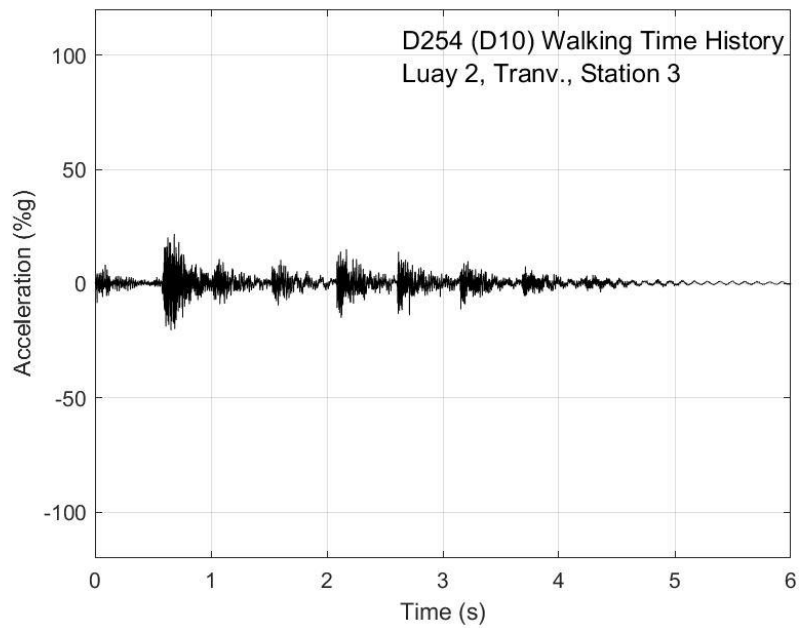


Fig. R-68. Walking time history, Luay test 2, transverse direction, station 3

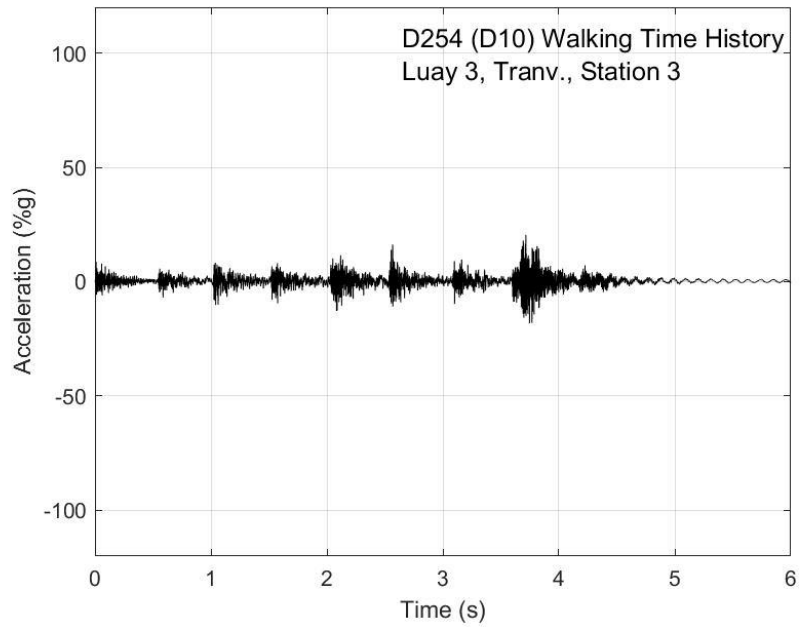


Fig. R-69. Walking time history, Luay test 3, transverse direction, station 3

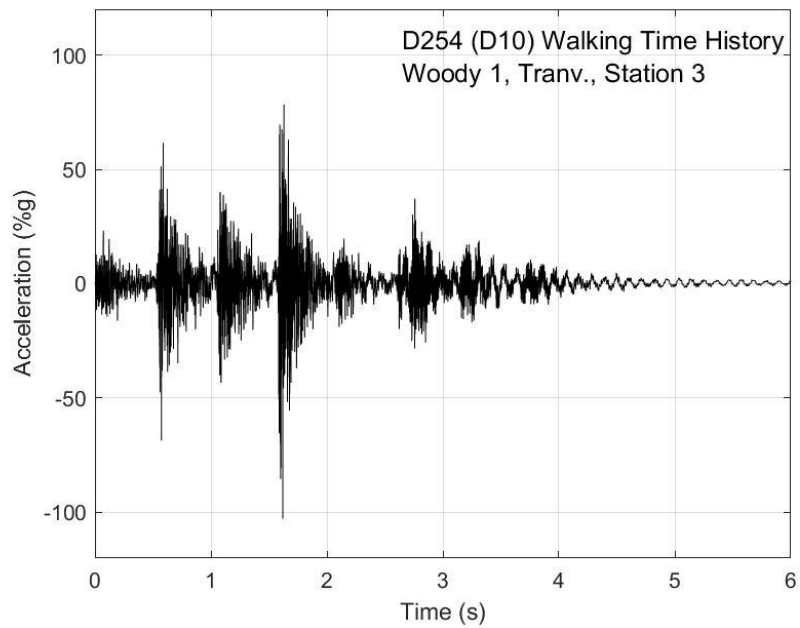


Fig. R-70. Walking time history, Woody test 1, transverse direction, station 3

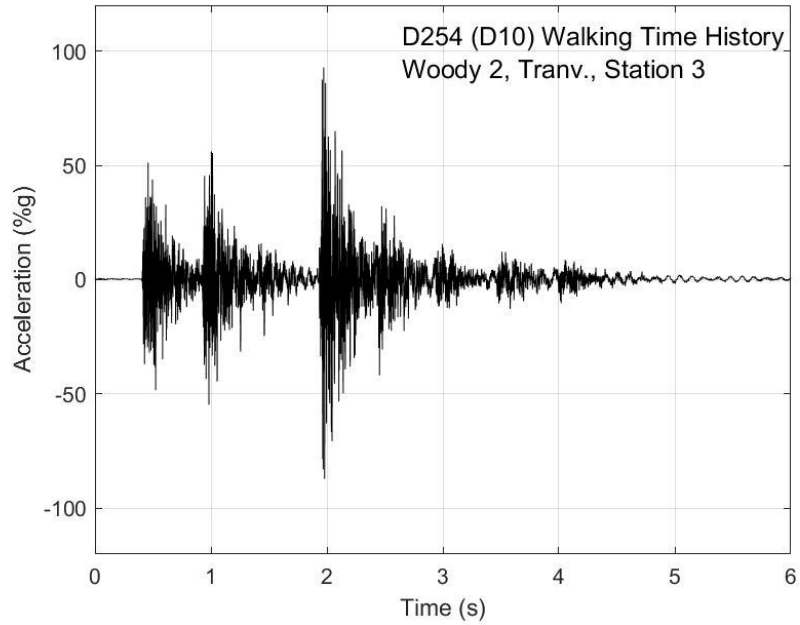


Fig. R-71. Walking time history, Woody test 2, transverse direction, station 3

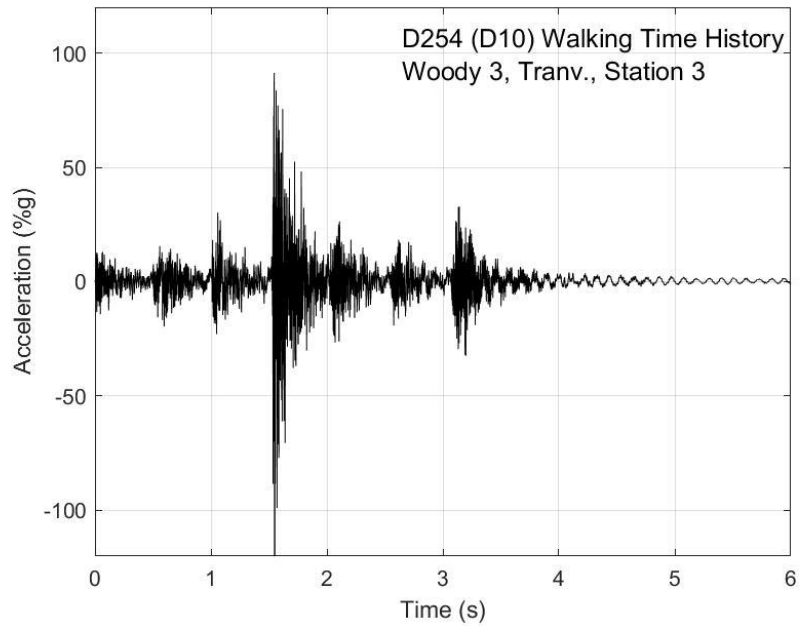


Fig. R-72. Walking time history, Woody test 3, transverse direction, station 3

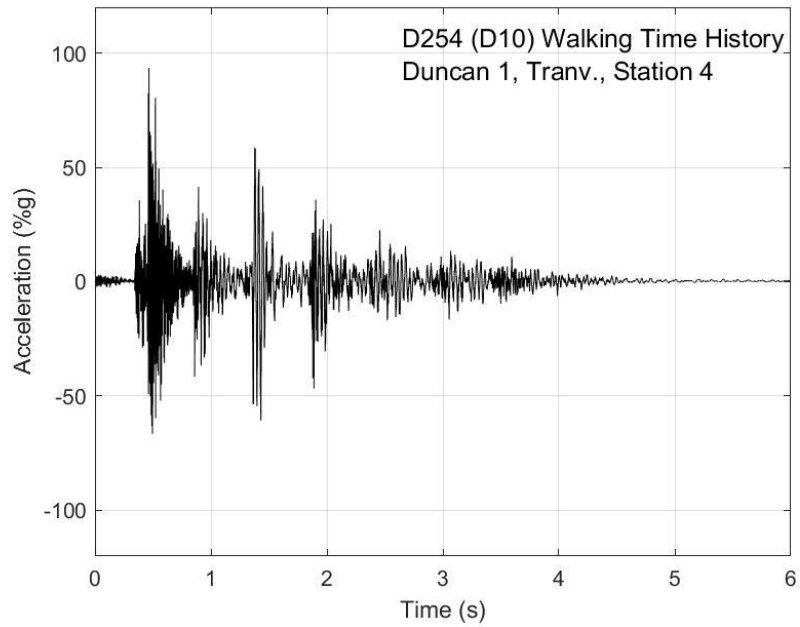


Fig. R-73. Walking time history, Duncan test 1, transverse direction, station 4

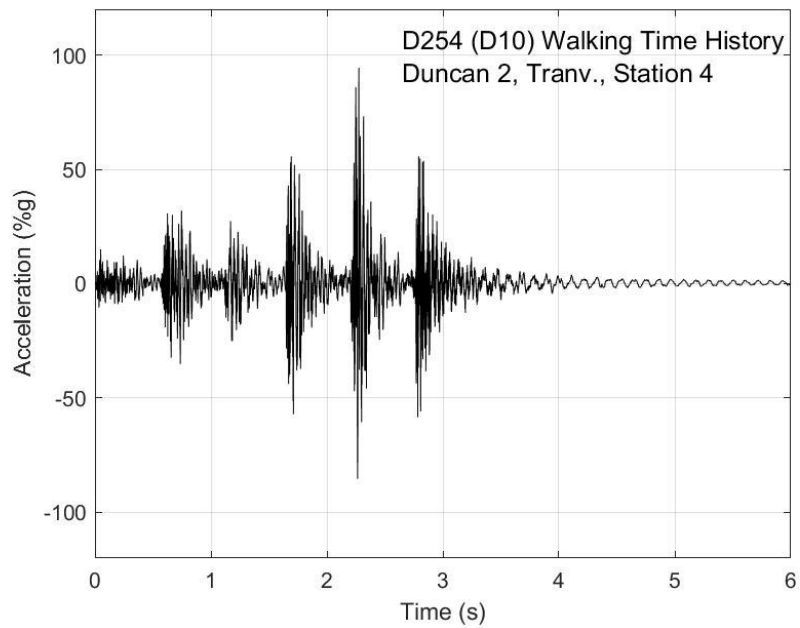


Fig. R-74. Walking time history, Duncan test 2, transverse direction, station 4

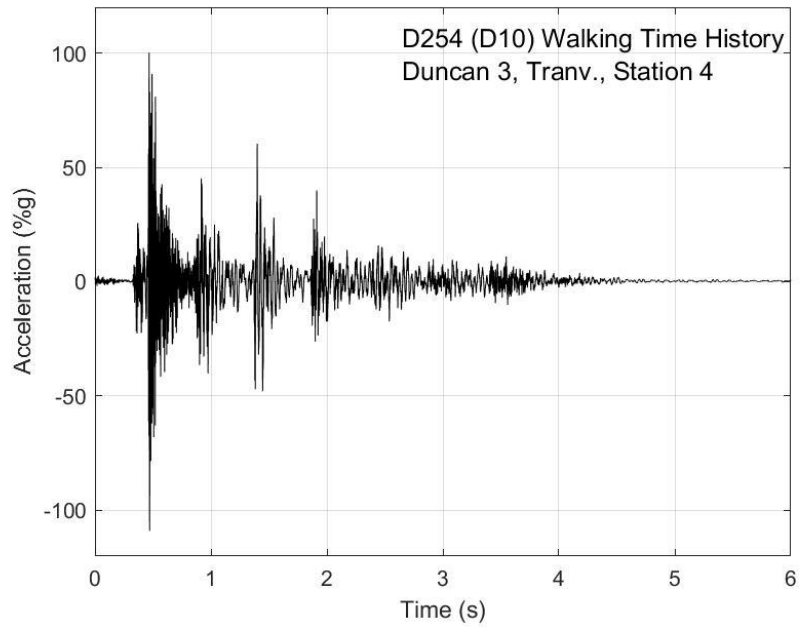


Fig. R-75. Walking time history, Duncan test 3, transverse direction, station 4

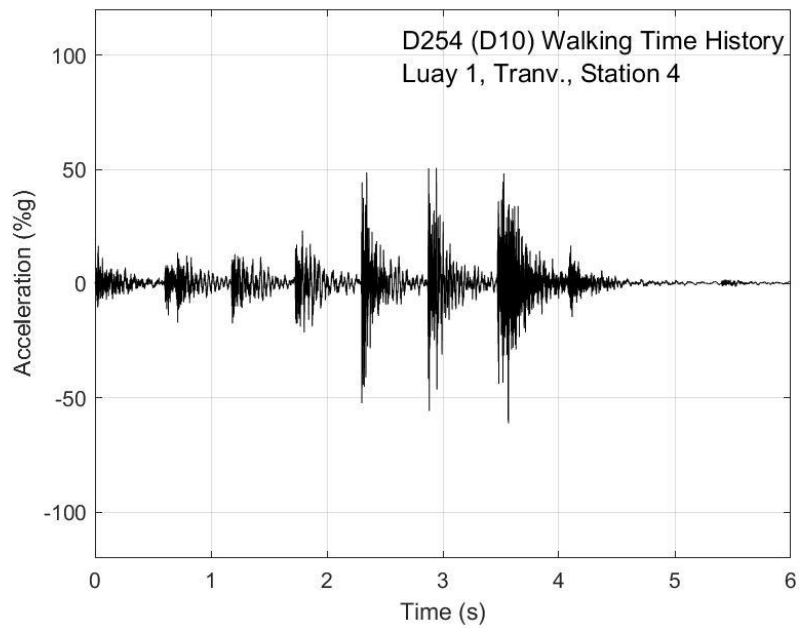


Fig. R-76. Walking time history, Luay test 1, transverse direction, station 4

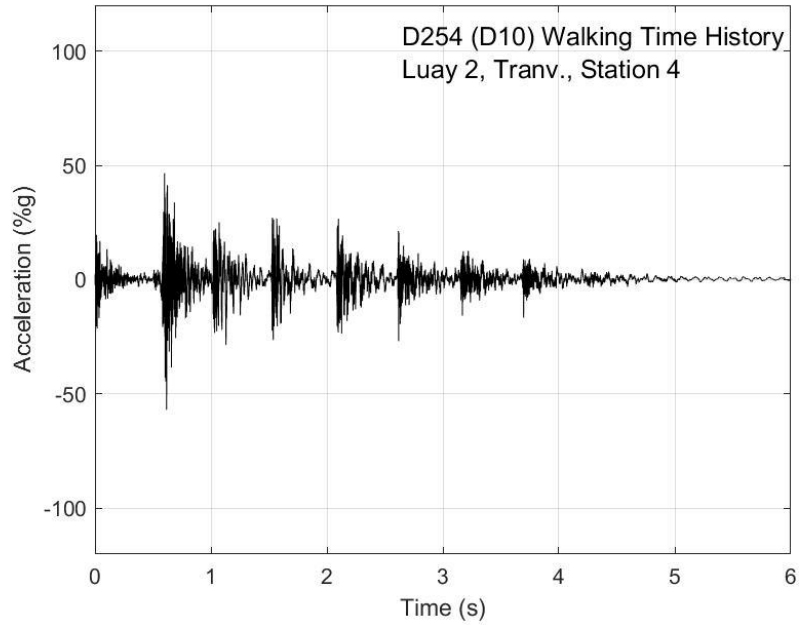


Fig. R-77. Walking time history, Luay test 2, transverse direction, station 4

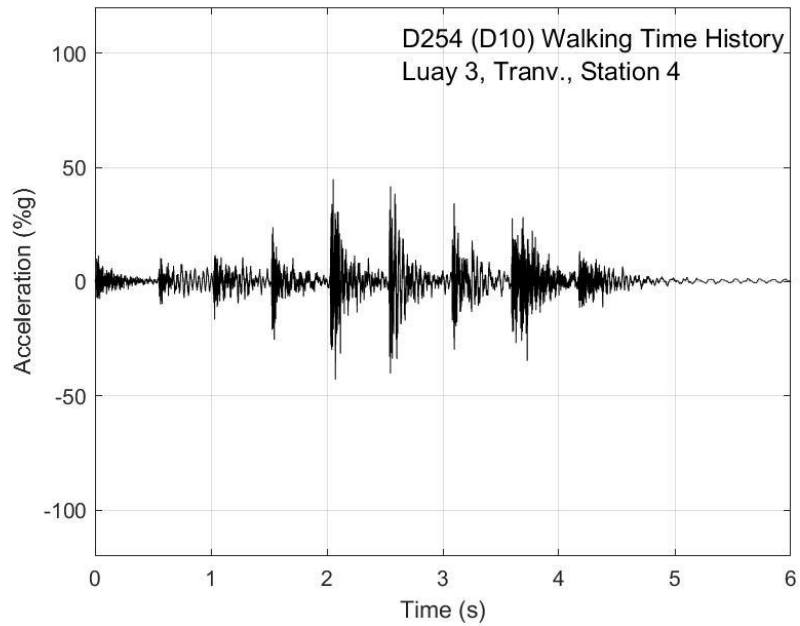


Fig. R-78. Walking time history, Luay test 3, transverse direction, station 4

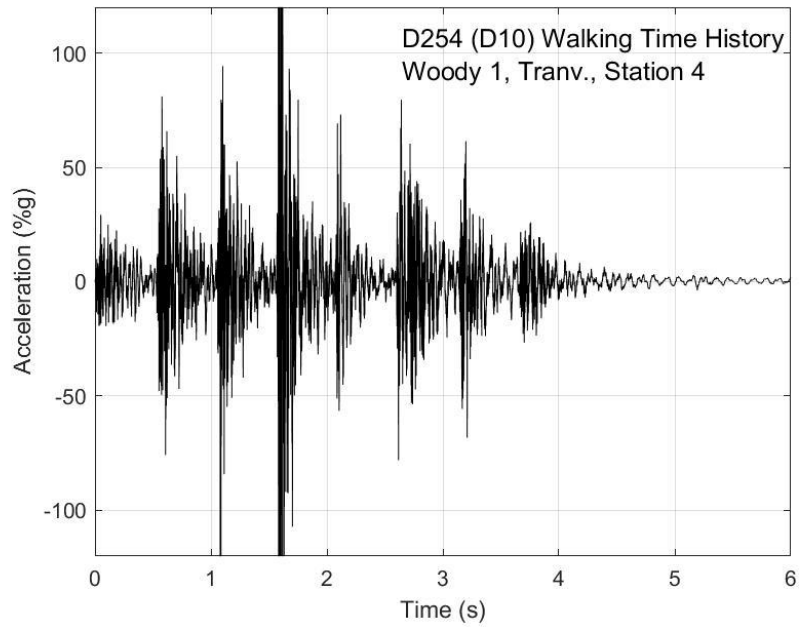


Fig. R-79. Walking time history, Woody test 1, transverse direction, station 4

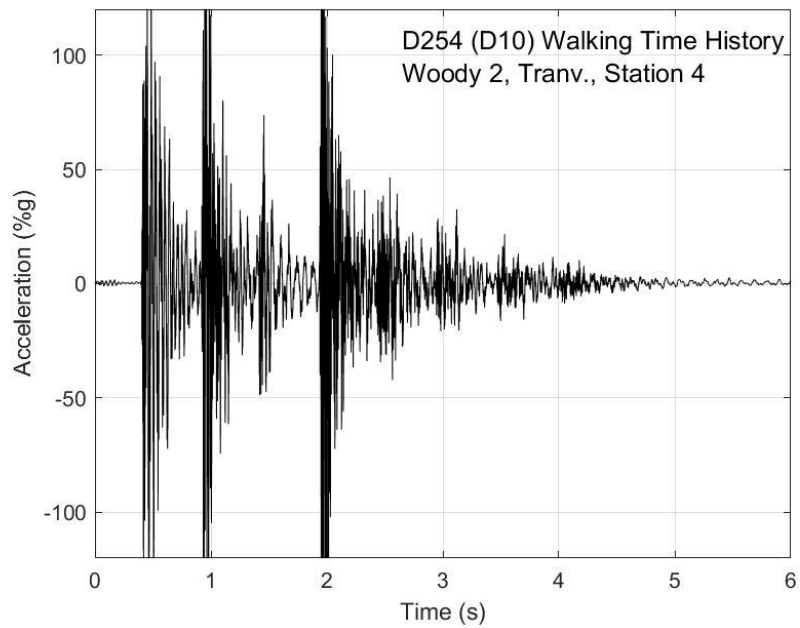


Fig. R-80. Walking time history, Woody test 2, transverse direction, station 4

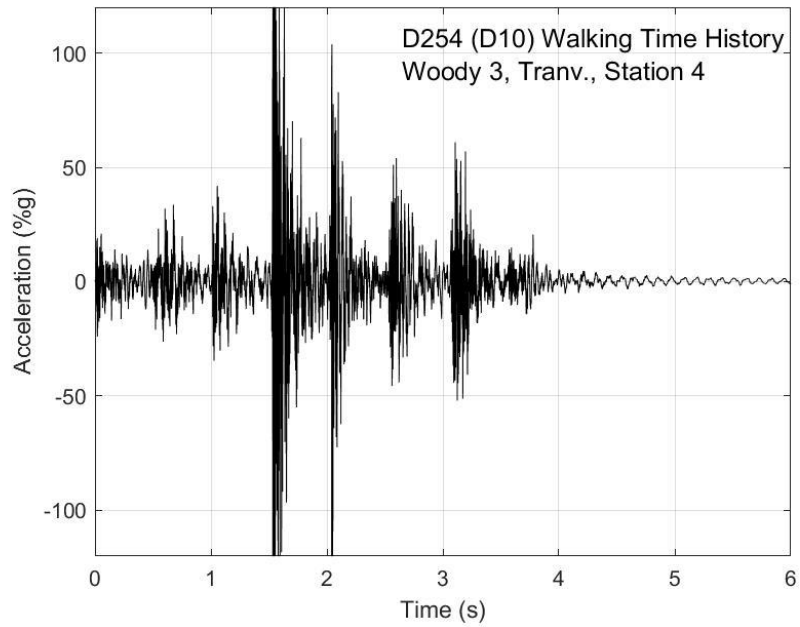


Fig. R-81. Walking time history, Woody test 3, transverse direction, station 4

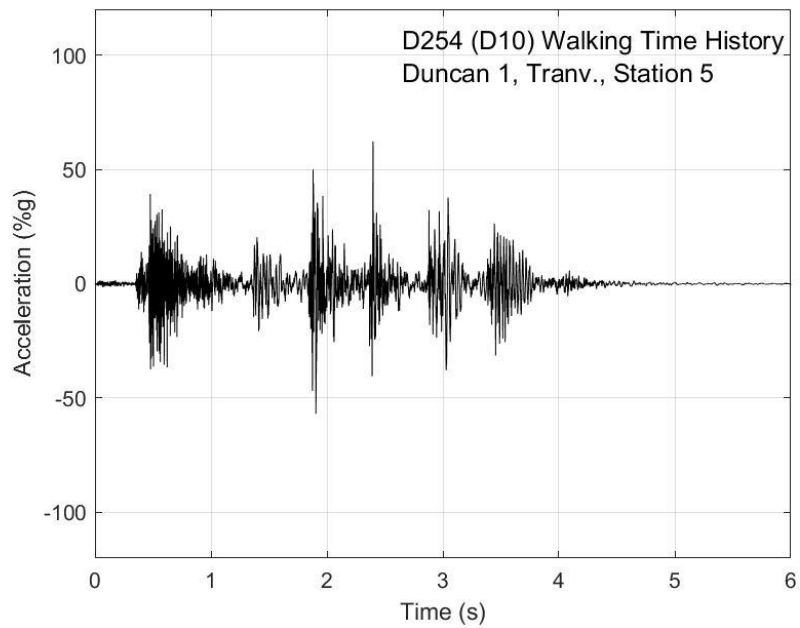


Fig. R-82. Walking time history, Duncan test 1, transverse direction, station 5

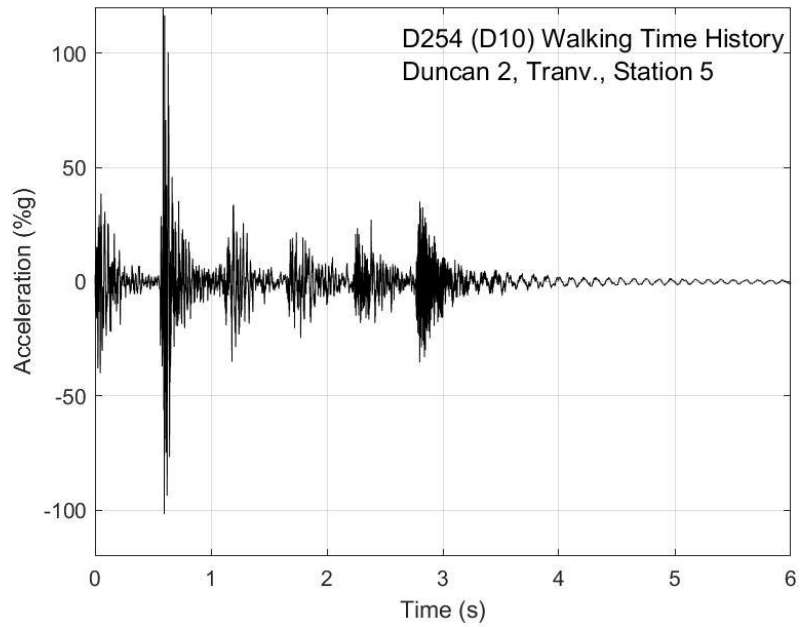


Fig. R-83. Walking time history, Duncan test 2, transverse direction, station 5

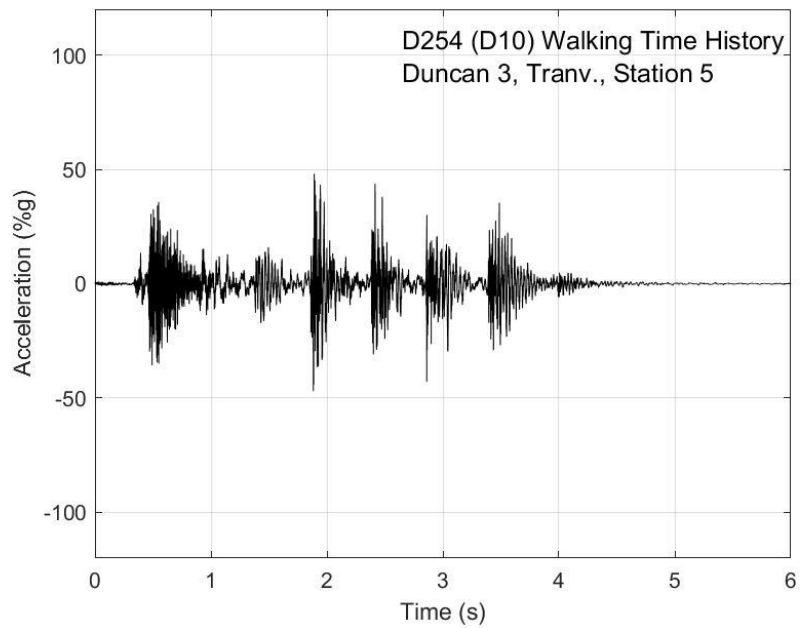


Fig. R-84. Walking time history, Duncan test 3, transverse direction, station 5

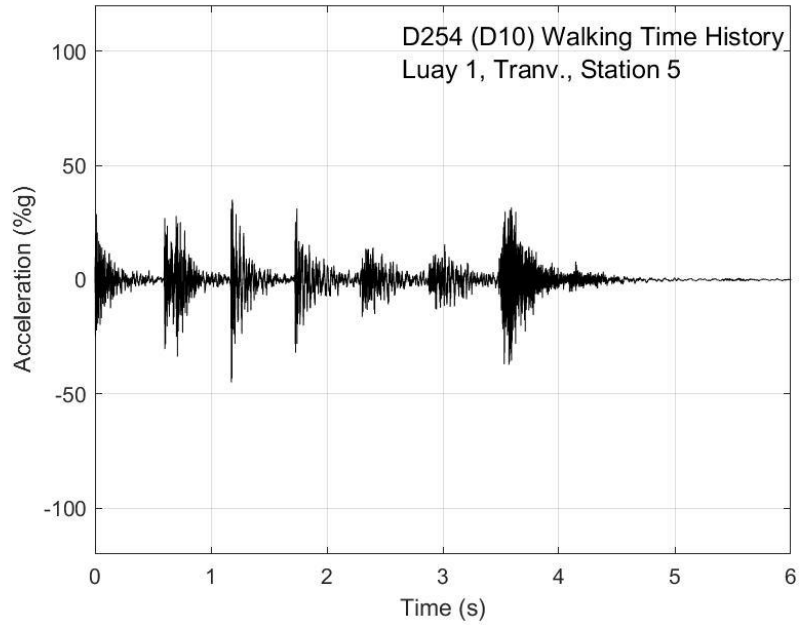


Fig. R-85. Walking time history, Luay test 1, transverse direction, station 5

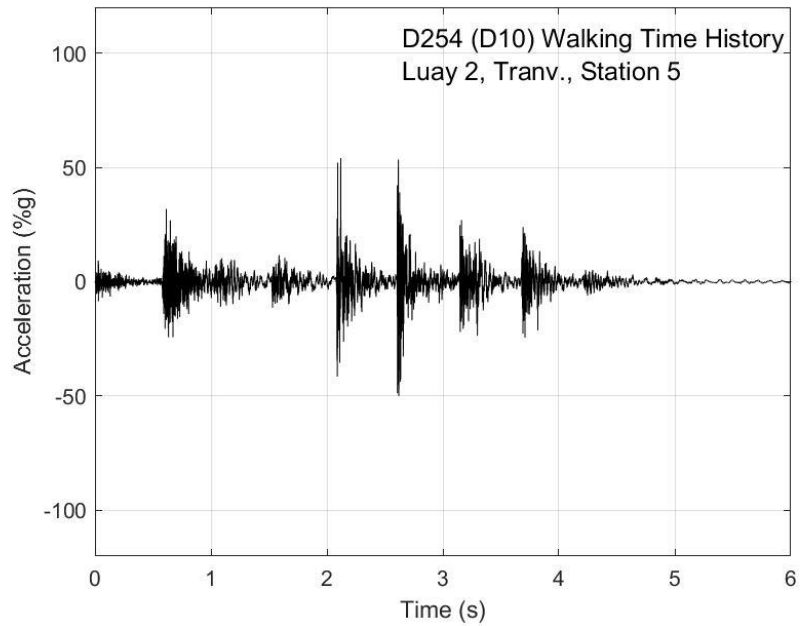


Fig. R-86. Walking time history, Luay test 2, transverse direction, station 5

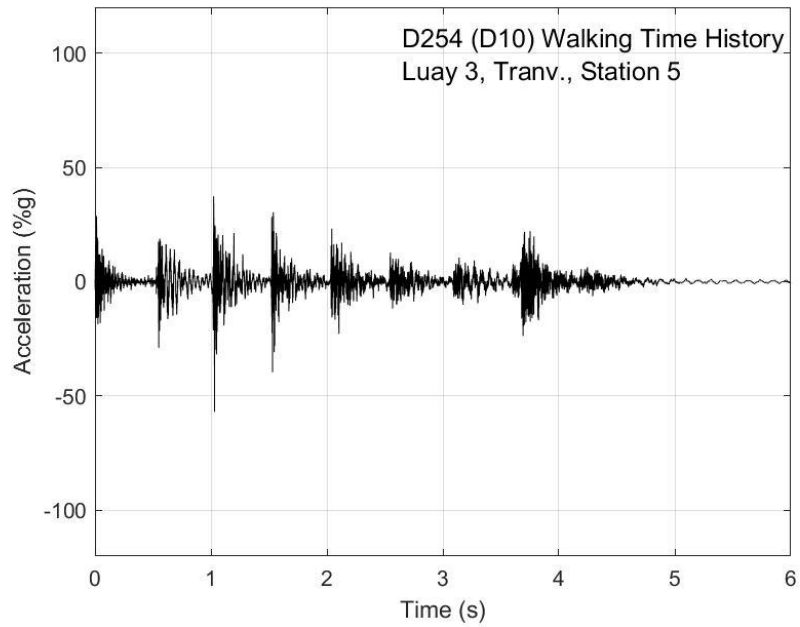


Fig. R-87. Walking time history, Luay test 3, transverse direction, station 5

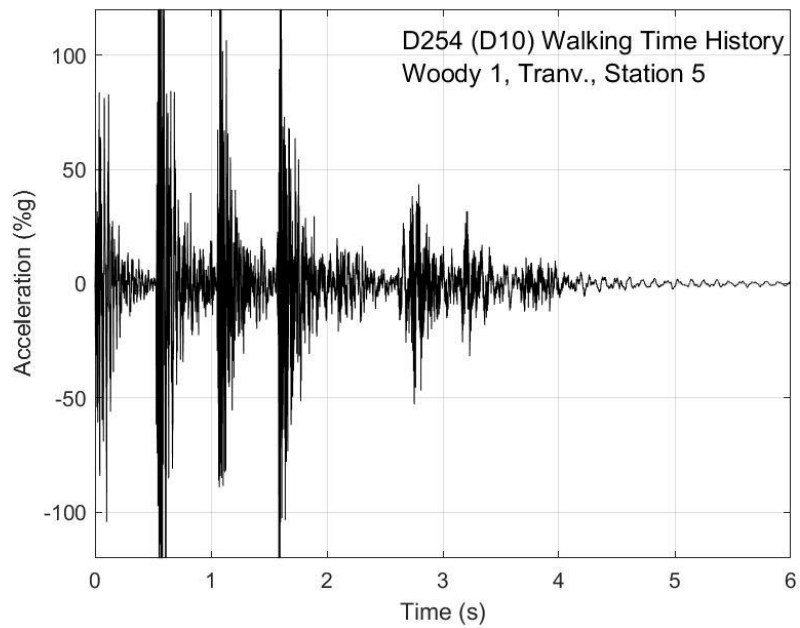


Fig. R-88. Walking time history, Woody test 1, transverse direction, station 5

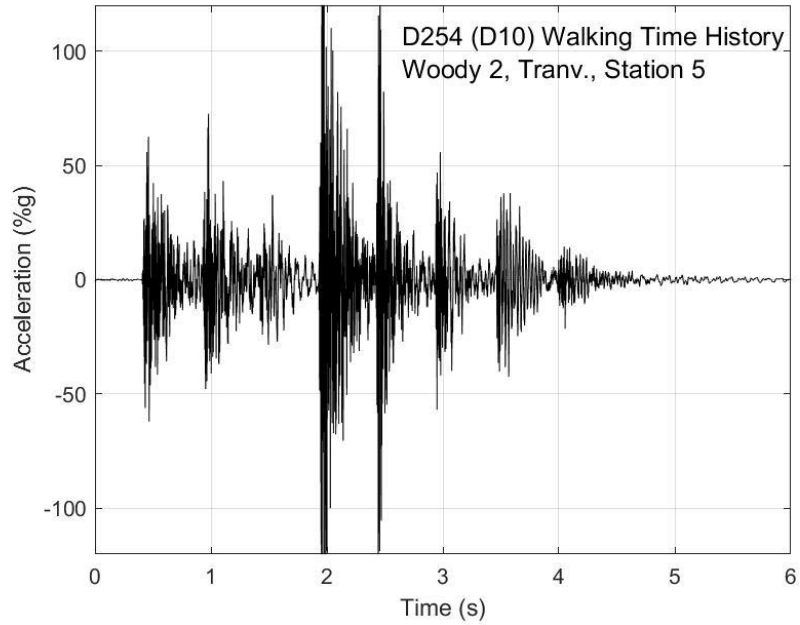


Fig. R-89. Walking time history, Woody test 2, transverse direction, station 5

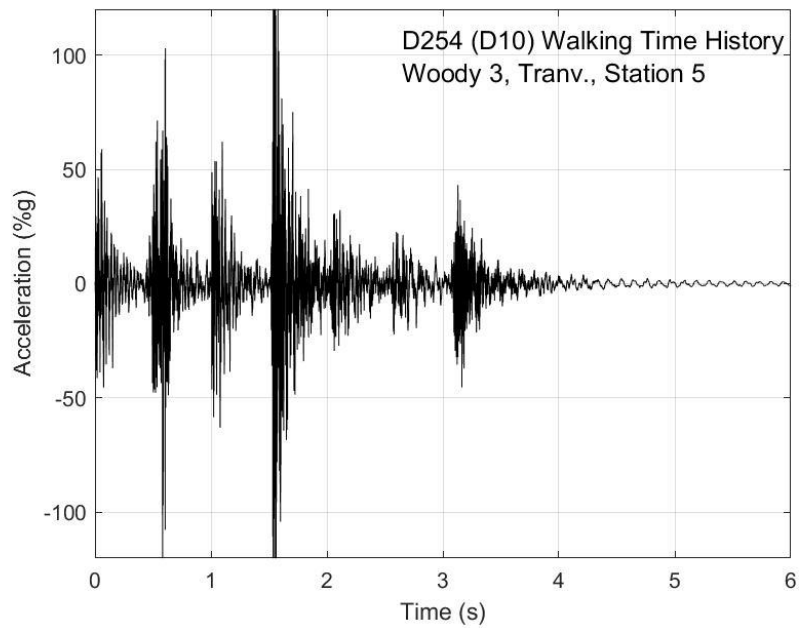


Fig. R-90. Walking time history, Woody test 3, transverse direction, station 5

APPENDIX S: Sample FORTRAN Code

```
      SUBROUTINE DLOAD(F,KSTEP,KINC,TIME,NOEL,NPT,LAYER,KSPT,  
1 COORDS,JLTYP,SNAME)  
C  
C   INCLUDE 'ABA_PARAM.INC'  
C  
      DIMENSION TIME(2), COORDS (3)  
      CHARACTER*80 SNAME  
  
      if((coords(1).gt.188.5).and.(coords(1).lt.191.5))then  
        loadpath = 1  
      endif  
  
      if(loadpath.eq.1)then  
        heel_1 = 0.0  
        toe_1 = 12.0  
  
        heel_2 = 30.0  
        toe_2 = 42.0  
  
        heel_3 = 60.0  
        toe_3 = 72.0  
  
        heel_4 = 90.0  
        toe_4 = 102.0  
  
        heel_5 = 120.0  
        toe_5 = 132.0  
  
        heel_6 = 150.0  
        toe_6 = 162.0  
  
        heel_7 = 180.0  
        toe_7 = 192.0  
  
        heel_8 = 210.0  
        toe_8 = 222.0  
      endif  
  
      step_velocity = 24.0      ! Step duration is 0.5s hence step_velocity = 2.0 ft/s  
      foot_pressure = 4.67     ! psi. Loading area = 3" x 12" = 168 lb  
      f = 0.  
  
      if((time(1).gt.0).and.(time(1).lt.0.5))then  
        heel = heel_1 + step_velocity*time(1)  
        toe = toe_1 + step_velocity*time(1)  
      endif  
  
      if((coords(2).ge.heel).and.(coords(2).le.toe))then  
        f=foot_pressure  
      endif  
  
      if((time(1).gt.1).and.(time(1).lt.1.5))then  
        heel = heel_2 + step_velocity*time(1)  
        toe = toe_2 + step_velocity*time(1)  
      endif
```

```

if((coords(2).ge.heel).and.(coords(2).le.toe))then
  f=foot_pressure
endif

if((time(1).gt.2).and.(time(1).lt.2.5))then
  heel = heel_3 + step_velocity*time(1)
  toe = toe_3 + step_velocity*time(1)
endif

if((coords(2).ge.heel).and.(coords(2).le.toe))then
  f=foot_pressure
endif

if((time(1).gt.3).and.(time(1).lt.3.5))then
  heel = heel_4 + step_velocity*time(1)
  toe = toe_4 + step_velocity*time(1)
endif

if((coords(2).ge.heel).and.(coords(2).le.toe))then
  f=foot_pressure
endif

if((time(1).gt.4).and.(time(1).lt.4.5))then
  heel = heel_5 + step_velocity*time(1)
  toe = toe_5 + step_velocity*time(1)
endif

if((coords(2).ge.heel).and.(coords(2).le.toe))then
  f=foot_pressure
endif

if((time(1).gt.5).and.(time(1).lt.5.5))then
  heel = heel_6 + step_velocity*time(1)
  toe = toe_6 + step_velocity*time(1)
endif

if((coords(2).ge.heel).and.(coords(2).le.toe))then
  f=foot_pressure
endif

if((time(1).gt.6).and.(time(1).lt.6.5))then
  heel = heel_7 + step_velocity*time(1)
  toe = toe_7 + step_velocity*time(1)
endif

if((coords(2).ge.heel).and.(coords(2).le.toe))then
  f=foot_pressure
endif

if((time(1).gt.7).and.(time(1).lt.7.5))then
  heel = heel_8 + step_velocity*time(1)
  toe = toe_8 + step_velocity*time(1)
endif

if((coords(2).ge.heel).and.(coords(2).le.toe))then
  f=foot_pressure
endif

return
end

```